Roughing up wings

Boundary layer separation over static and dynamic roughness elements

Pietro Servini

PhD in Mathematics

supervised by Prof. Frank Smith

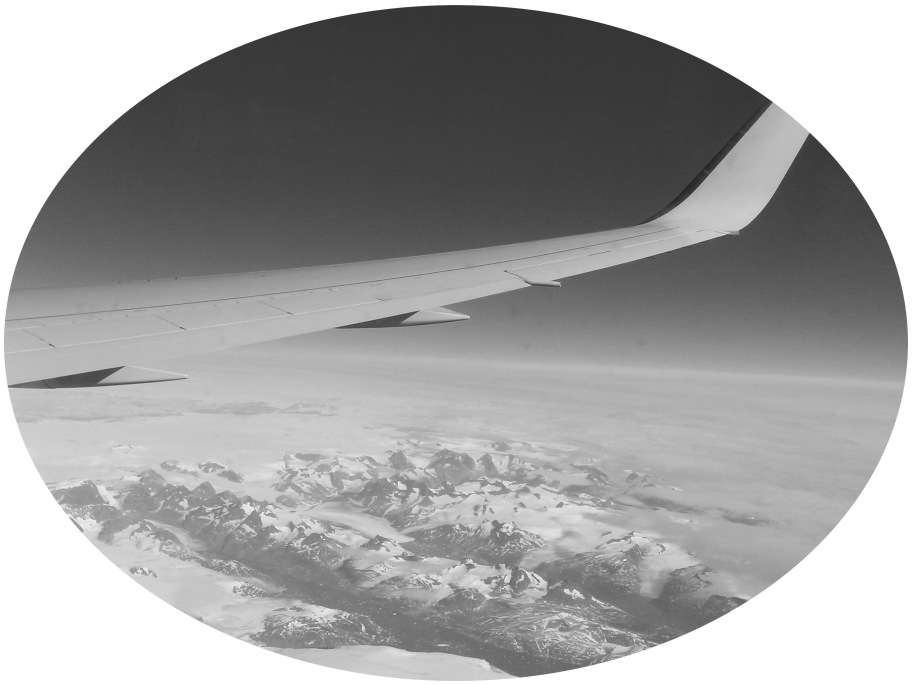

University College London

February 2018

I, Pietro Servini, confirm that the work presented in this thesis is my own. Where information has been derived from other sources, I confirm that this has been indicated in the thesis.

Acknowledgements

We asked God's permission and walked on His carpet. Up and up to a high mountain pass, then down and down through the valley of Eden, around distant cliffs, brown and pink and gold, farther than the eye could see, to Gwahgot, where a masterly irrigation system keeps the fields robed in shades of green and yellow. We waded along dry riverbeds: the wind and the memory of the rainy season formed ripples in the sand.

Thank you to mamma and papá, who, from when I was young, gave me the freedom and encouragement to go out and explore. It has been, however, their continued and unceasing presence, support and love that has allowed me to keep walking. Thank you to Marianna, not for the many friends I have met along the way that may or may not have been her friends first, but for being herself the very best friend a brother could have. Cara famiglia, grazie: grazie per ciò che siete; grazie per ciò che siamo.

To all those who have passed through the KLB, or who continue to inhabit it: thank you. It has been an honour to get to know you and a joy to spend time with you: the sometimes lonely existence of PhD life has been greatly alleviated by your presence, especially during lunches—even though there were those who partially disagreed with my views—and at the deep watering holes that are pubs. A special thank you to Niko Laaksonen, for all those steps we took together.

It has been a privilege, over the last three years, to have worked as part of the wonderful, evolving team that turned *Chalkdust* from a foolish dream into the success it has become, as well as to have partaken in various public engagement events at the side of so many enthusiastic people. These have formed some of the greatest highlights of my PhD.

Of course, none of that which is contained herein would have been possible without my supervisor Frank Smith, whose patient help, advice and encouragement have not only been of immense support, but have also been an invaluable example to me for the future: thank you, Frank, for your great humanity. Thank you also to Alric Rothmayer of Iowa State University for his hospitality and our various discussions—and for pointing me in the direction of Iowa's superb beer. This work was part-funded by the United States Air Force Office of Scientific Research and their financial assistance, extending also to various trips to the US, is gratefully acknowledged.

Finally, to all those in the UK and around the world who I have met, who have taught me something about life and who I have had the privilege to go on to call "friend" over the course of my long journey: you have enriched it and given it colour. Thank you.

We spent the night in Paradise, and were woken by the crow of a cockerel and the songs of birds. Chicken, sheep, goats and cows slept outside our door. A donkey kept watch over the entrance. Retracing our steps the next day with the rising sun, an old man overtook us with his long stick and continued to talk to us as he receded into the distance, where the world of mortals awaited.

. . . for those who could, but can't.

Abstract

The separation of a boundary layer from an aeroplane wing can have severe effects on aeroplane safety and efficiency, as its occurrence directly results in decreases in lift and increases in drag. Similar considerations apply to other technologies that rely on airfoils, such as drones, helicopters, propellers and wind turbines. Hence recent experimental and numerical work on dynamic roughness elements—small bumps that are made to oscillate up and down at a given frequency—is exciting, as it suggests that these elements are able to delay separation or increase the angle of attack at which it occurs, provided that the Reynolds number is such that the flow remains laminar [33, 40, 41, 66].

Our aims are to gain further insight into whether this is indeed the case; to determine the possible impact of the roughness parameters on the separation of a boundary layer from a surface; and to attempt to understand the physical mechanisms that may be involved, with our focus very much on the pressure gradient. To this end, we will make use of a mathematical approach and exploit asymptotic methods throughout.

Three scenarios will be considered, and we will study both dynamic and static roughnesses. The first consists of small roughness elements, which are able to modify the mean flow pressure gradient, on a flat plate. The second will revolve around flow over a hump within a condensed boundary layer, first described by Smith & Daniels [85], but with the addition of roughness elements on its lee side, in the region in which local separation occurs and the advent of full breakaway separation is seen. The final scenario is set near the leading edge of an airfoil, inclined to the oncoming flow at or near the critical angle of attack, where marginally separated flow exists and a small separation bubble is possible [70, 90].

Note

In a filing system that must have made sense at the time, but now looks unfathomable, there is paper after paper after paper. Somewhere in the world, a forest wept. (Or perhaps, to paraphrase the words of that great thinker, Anon, every time I open a journal and read it, "a tree smiles knowing there's life after death".) On my laptop are many more and within the vast expanses of the internet is a repository that makes the great libraries of antiquity (Alexandria, Gundishapur, Pergamum, ...) seem mere household collections.

All, undoubtedly, are informative. There are many, however, that are as dry as the Sahara that surrounds Timbuktu, home to hundreds of thousands of manuscripts of medieval Arabic, Islamic and North African learning. I enjoy writing and I like words—playing with them, moving them around, fitting them together in lots of different ways. We'll encounter a fair bit of asymptotics on our journey, and the flow of sentences might stutter at times, like a mountain torrent that falls into rocky pools, before overflowing and continuing on to the plains. Apart from that, the written style of this thesis might be different to most others, and some people might not find it quite appropriate, but you've got to read it, and I've got to write it, so we might as well try to have fun.

"If you have a strong first world and a strong set of relationships, then in some part of you, you are always free: you can walk the world because you know where you belong, you have some place to come back to."

Seamus Heaney

"When there's a smile in your heart
There's no better time to start [. . .]
You can fly!"

Peter Pan (Disney)

Contents

List of Figures

1

The mountains of the future and the mountains of the past

"Men wanted for hazardous journey. Low wages, bitter cold, long hours of complete darkness. Safe return doubtful. Honour and recognition in event of success."

Sir Ernest Shackleton, advert (probably apocryphal) for the Imperial Trans-Antarctic Expedition, 1914

I have always liked walking in the mountains, feeling the crunch of stones and loose rock under sturdy boots, or the soft springiness of earth, the fresh air on bare skin, the smell of pines and grass and everything else that is green and brown and therefore good in the world. There's a sense, too, of the unknown, the belief that you're off to see something new and you'll never know exactly what it is that you'll find over the top of the next peak.

But at the start it's always the same. You're fresh and full of energy and enthusiasm, your heavy pack is on your shoulders but you're still standing tall and straight, and you are quite certain that you have everything that you could possibly need. You look ahead and the path is clear and well delineated, marked perhaps by fields or a stream or an alpine fence; and the peak of the first mountain that looms in your way is distinctly visible and sharply in focus and it doesn't, after all, seem overly tall. So off you set, briskly, not a care in the world, happily oblivious, without pausing to question what lies in wait or whether it's the right direction to walk in at all; wondering only what Shackleton was on about and determinedly confident that all one has to do is to follow the path...

1.1 The mountains of the past

In the words of Huebsch (2006)—the author who, as far as I'm aware, first studied them—dynamic roughness elements are

> *"small time-dependent perturbations to the airfoil or wing surface [...] humps placed in the leading-edge region of the wing that would have the ability to expand and contract at a specific frequency and reach a maximum height"* [40].

Their effect is either to move the point where the flow separates from the surface farther downstream, remove it altogether or increase the angle of attack at which it occurs. Separation of a fluid, whether liquid or gas, from a surface can be due to the presence of adverse (positive) pressure gradients, which result in fluid particles having to move from regions of low pressure to regions of high pressure. The expenditure of kinetic energy to overcome this pressure increase retards them and, if the gradient is large enough, brings near-wall particles to a standstill. At this point, both the fluid velocity at the surface (due to the no-slip condition) *and* the first derivative of the streamwise velocity taken in the direction normal to the surface (and evaluated at the surface) are zero. The fluid then detaches itself from the wall and forms a shear layer, below which a region of slower, recirculating fluid develops.

This adverse pressure gradient inevitably occurs on airfoils and, indeed, is a consequence of the fact that the very purpose of an aeroplane is that of flying in the air. Figure 1.1 gives the pressure distribution (in terms of the pressure coefficient, C_p) over a NACA 0012[1] airfoil flying at an angle of attack of 5°, generated on XFOIL[2] using an inviscid flow solver.

If we note the reversed orientation of the y-axis, the incoming flow hits the stagnation point at the base of the airfoil (where pressure is highest) and then, as it moves around the leading edge from the base to the top of the airfoil, it rapidly expands and accelerates, with the pressure dropping precipitously to a negative peak. It is this negative suction pressure that keeps the aeroplane in the air and, at the same time, the downstream pressure recovery that gives rise to the adverse pressure gradient, which, if sufficiently strong, will drive separation.

Separation has, however, a detrimental effect on the flow properties in most aerodynamic scenarios. The first impact is on drag. An aircraft wing contributes approximately 25% of the total drag experienced by an aeroplane cruising at subsonic speeds [27] and thus cutting drag there could have a great impact on reducing fuel usage and flight costs, as well as allowing for larger range, payloads and speeds: all are important, to a greater or lesser extent, in civilian and military applications. Details on monthly fuel usage and cost are provided by the US government [97] for both commercial airline

[1] A symmetrical 4-digit NACA airfoil, of chord length c and maximum thickness t (expressed as a fraction of the chord) is given by

$$y = 5t\left[0.2969\left(\frac{x}{c}\right)^{\frac{1}{2}} - 0.1260\left(\frac{x}{c}\right) - 0.3516\left(\frac{x}{c}\right)^{2} + 0.2843\left(\frac{x}{c}\right)^{3} - 0.1015\left(\frac{x}{c}\right)^{4}\right] \text{[47]}.$$

[2] XFOIL is a code developed by Mark Drela at MIT in 1986, in collaboration later with Harold Youngren. The latest version is available at `http://web.mit.edu/drela/Public/web/xfoil/` (last accessed 12 May 2017).

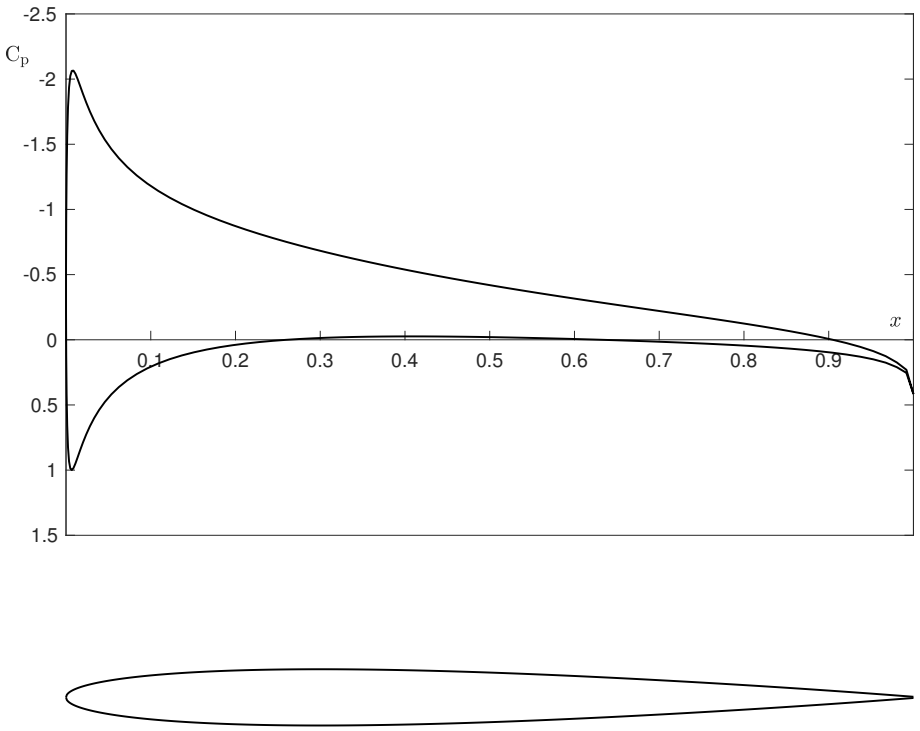

FIGURE 1.1: Pressure distribution (top) over a NACA 0012 airfoil (bottom) at an angle of attack of 5°, generated using inviscid theory on XFOIL (see footnote).

companies and the air force—figure 1.2 presents the yearly data for US-based commercial companies only and contains within its bars a plethora of interesting stories. The first is that we spend vast quantities of money on fuel, consistently reaching around US$50bn per year in 2011 to 2014. This figure is now decreasing, wholly due to the recent, well-publicised crash in the price of fuel. In fact, the year-on-year variation in cost per gallon of fuel takes a rollercoaster ride from 1977 (when published records begin) to 2016. Embedded within that journey are the sad tales of instability in the Middle East; as well, hopefully, of a more heart-warming trend of a decreased reliance on fossil fuels in response to the ever-nearing hoofbeats of the first of the modern Horsemen of the Apocalypse, climate change. Indeed, it is perhaps promising that the amount of fuel we use has not increased above 1999 levels, with total use remaining largely constant in the last few decades. It would be interesting to compare fuel usage over time with the number of individual flights made per year: perhaps, within that comparison, one can find the proof that hard work on flow control and drag reduction has been bearing its fruits.

The term drag is, in reality, an umbrella term for various types of resistive forces that occur as fluid flows past an object as complicated as an aeroplane. The first major component of drag is skin friction drag—the streamwise component of the integral of all tangential stresses acting over a surface. Its analogue would be the friction that occurs as a solid object is dragged over some other object: in fluid dynamics, it is

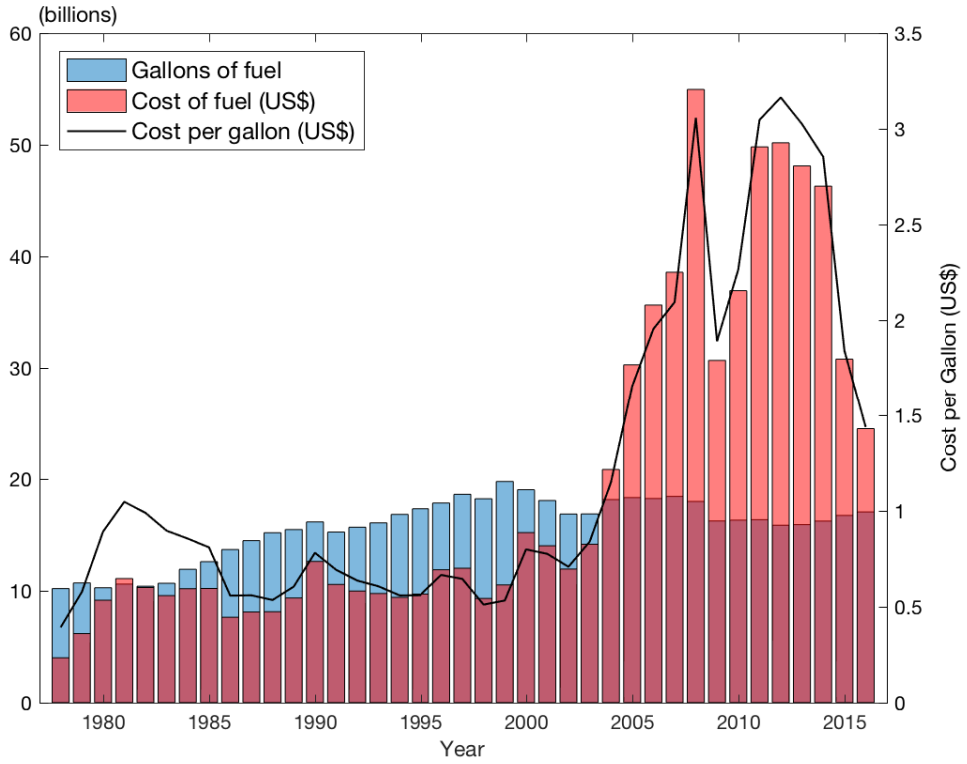

FIGURE 1.2: Amount of fuel (in billions of gallons) used, and associated cost (in billions of dollars), per year by US carriers. Data taken from [97].

the layers of fluid that are sliding over the surface and each other that give rise to a viscosity-related resistance. At this point, it is convenient to introduce the distinction between a laminar and turbulent boundary layer—the boundary layer being a thin layer of fluid near a surface where viscosity effects are important, to be discussed in more detail in chapter 2. The former can be thought of as layers of fluid sliding past each other in a somewhat orderly manner; the latter, on the other hand, is characterised by considerable mixing across the boundary layer, with large amounts of mass, momentum and energy being transferred from upper regions to near-wall regions, and vice versa. The difference, perhaps, between a stately ball and the average modern nightclub on a weekend. Due to this less 'chaotic' behaviour, a laminar flow has skin friction drag that can be lower by as much as 90% when compared to a turbulent boundary layer [45].

To reduce drag, then, a preference for laminar flow seems clear. But this is only part of the story: laminar boundary layers suffer the complication that they are far more likely to separate than their turbulent counterparts. This is largely due to the lack of mixing and the associated inability to bring energy-rich particles from upper regions to add momentum to the near-wall layers, which are moving under the influence of a retarding adverse pressure gradient. Once separation occurs, the eddies that exist in the wake result in a collapse in pressure at the rear of an airfoil and give rise to a dominant pressure drag, which is the streamwise component of the integral of all normal forces acting over a surface—small, provided that the flow remains attached; but considerable

if separation occurs. It is this desire to avoid large pressure drag that has driven research into tripping laminar boundary layers to become turbulent through the use of either active [94] or passive [61] roughness elements: the use of static roughness elements and their beneficial aerodynamic properties should be familiar to golfers, with the bumps that cover a golf ball making the air go turbulent and the ball travel farther. Sadly, the person wielding the club is still the major contributing factor to accuracy.

The second detrimental impact of separation is that on lift. Lift increases almost linearly with increasing angle of attack until a critical angle is reached and the lift coefficient collapses. This critical angle of attack is linked to the adverse pressure gradient (which has also increased with angle of attack) being strong enough to provoke separation near the airfoil leading edge; and the resultant formation of a wake covering the majority of the surface causes this dramatic decrease in lift in a phenomenon known as aerodynamic stall. This has been responsible for numerous air disasters in the past, including the disappearance of the Air France Flight 447 over the Atlantic Ocean in 2009 and the Indonesia AirAsia Flight 8501 crash in 2014.

As mentioned, laminar flows are more prone to separate than turbulent ones and cannot withstand strong adverse pressure gradients: the critical angle of attack for laminar boundary layers is therefore rather low. The existence of a laminar boundary layer is largely dependent on the Reynolds number, which is a ratio of inertial to viscous forces and will be introduced in chapter 2: for Reynolds numbers less than 10^6, the flow will be predominantly laminar and the imperative is then to prevent transition to turbulence (and its attendant larger skin friction drag) and avoid separation. Within this range of Reynolds numbers exist large soaring birds, the blades of wind turbines, helicopter propellers and drones [27, 50], which are becoming more and more prevalent in the civilian and military spheres. At lower Reynolds numbers, less than around 10^4, fly many insects, including the bumblebee. Interestingly, this last creature actually requires separation in order to generate enough lift to fly: on its downstroke, the flow separates near the leading edge, reattaching farther downstream to form a leading edge vortex that enhances lift [7]. A similar effect is also used on delta wings (such as those on a Concorde, when it was among us) to improve the lift on take-off and landing at subsonic speeds.

Laminar flows are also characterised by the formation of a laminar separation bubble near the leading edge of a lifting surface. At low angles of attack, the flow can separate and the separated shear layer can become turbulent due to, among other things, the amplification of Kelvin-Helmholtz instabilities [36] and the shedding of vortices [49]. The Reynolds stresses within this turbulent layer, provided that the angle of attack is low enough, then cause reattachment and the formation of this short leading edge bubble. If, however, the angle of attack (and thus adverse pressure gradient) increases further, or the Reynolds number decreases so that turbulent flow cannot form, the detached shear layer may fail to reattach immediately downstream and the bubble is said to "burst". Reattachment may occur farther downstream, forming a long bubble, or may

not take place at all, with separated flow existing over the entire downstream surface of the wing: in either case, lift decreases and drag increases [65]. One can attempt to avoid the laminar separation bubble altogether by activating or enhancing Tollmien-Schlichting waves upstream of the separation point through various techniques ably reviewed by Gad-el-Hak (2000) [27] that inject momentum into the flow and potentially advance the transition to turbulence.

Other mathematical explanations for the reattachment of the detached shear layer have also been proposed. Smith & Elliott (1985) point to a nonlinear mechanism arising from unsteady marginal separation theory (described in chapter 6), with reversed flow upstream of a 'shock' becoming forward flow just downstream of it [86]. This theory can also be used to describe the phenomenon of dynamic stall [82], which occurs due to a rapidly increasing angle of attack that can rise to values higher than its critical value without resulting in the aerodynamic stall described above. A leading edge vortex initially forms and then detaches, travelling downstream along the wing and briefly increasing lift, which then abruptly decreases as the vortex drops off the airfoil trailing edge. This process can be repeated multiple times with the creation of secondary and tertiary vortices, subjecting the wing structure to large and abrupt changes in forces, with catastrophic effects [52].

1.1.1 Avoiding separation

The aim, then, is to avoid separation and considerable investment in time and money has been spent trying to achieve this goal. The search is for an effective boundary layer control mechanism, described by Flatt (1961) as

> *"any mechanism or process through which the boundary layer of a fluid flow is caused to behave differently than it normally would were the flow developing naturally along a smooth straight surface"* [25],

which is an admirably all-inclusive definition. Most of all, it includes the actual streamlining of an object—hence we have been carrying out research into flow control techniques since we began to pick up stones and throw them, eventually realising that spears were a much more aerodynamically favourable shape. More recently (considerably so), Eastman Jacobs developed the laminar flow airfoil, which pushes the point of maximum thickness further back compared to standard airfoils and has a favourable pressure gradient for over 60% of its upper surface [3].

The strategy of extending the streamwise extent of the favourable pressure gradient, or reducing the magnitude of the adverse pressure gradient, makes sense from the arguments presented above. However, its favourable effect can also be seen by a study of the Navier–Stokes streamwise momentum equation, written at the wall:

$$\rho_{\mathrm{w}} \left.\frac{\partial u}{\partial t}\right|_{\mathrm{w}} + \rho_{\mathrm{w}} u_{\mathrm{w}} \left.\frac{\partial u}{\partial x}\right|_{\mathrm{w}} + \rho_{\mathrm{w}} v_{\mathrm{w}} \left.\frac{\partial u}{\partial y}\right|_{\mathrm{w}} + \left.\frac{\partial p}{\partial x}\right|_{\mathrm{w}} - \left.\frac{\partial \mu}{\partial y}\right|_{\mathrm{w}} \left.\frac{\partial u}{\partial y}\right|_{\mathrm{w}} = \mu \left.\frac{\partial^2 u}{\partial y^2}\right|_{\mathrm{w}} . \qquad (1.1)$$

A more detailed presentation of the governing Navier–Stokes equations awaits in chapter 2, but for our current purposes we note that u, v are the velocity components tangential and normal to the surface respectively, p is the pressure, ρ the fluid density, μ the viscosity and the subscript 'w' refers to evaluation at the wall. At the separation point, the curvature of u (u_{yy}) is positive and so the aim would be to keep the left-hand side of equation (1.1) negative. As we have already concluded, we see that we want to keep the pressure gradient at the wall negative (favourable) for as long as possible.

Another well-established technique to delay boundary layer separation (although the ancients were probably not aware of it) is that of suction, which would introduce a negative v_{w} in equation (1.1). Physically, suction can remove decelerated near-wall particles and entrain faster ones that still have the energy to overcome an adverse pressure gradient [59]. It can also be used as a method to delay transition, provided that the suction strength through the slot is not too strong [56]. Viscosity in gases increases with temperature, thus if we decrease the wall temperature (perhaps by running cryogenic fuel just below the surface), we can have a positive μ_y at the wall in equation (1.1), as required. The opposite is the case in liquids: viscosity decreases with increasing temperature. Although possible in theory [14], in practice this technique, as well as being difficult to implement, is not overly effective [73].

Alternative strategies involve the injection of momentum near the wall to help overcome the adverse pressure gradient. This includes the use of spanwise slots running along the length of a wing, higher pressure air from below flowing through the slot and acting as a jet to reinvigorate tired near-wall flow. Such an approach is especially important during take-off and landing, when the lower speeds mean that the aeroplane must fly at higher angles of attack to obtain the required lift: from this comes the deployment of leading edge slats and trailing edge flaps. Evolution has had similar ideas and got there first: to avoid stall when landing at high angles of attack, a set of feathers at the front of a bird's wings, known as the alula, pop out and act like a leading edge slat [2].

Fish also display an astonishing array of flow control techniques, whether that be through the use of protuberances like tubercles along the front of fins and flappers (as in the hammerhead shark or humpback whale), or riblets (as in the dermal denticles—tiny scales—on sharks) that break up spanwise vortices and decrease turbulence levels [13], or compliant skins that either trigger turbulence or can maintain attached laminar flow, or just by the way they move their bodies as they dart, glide and flash through the rivers and oceans. An excellent review of techniques in aquatic animals is provided by Fish & Lauder (2006) [24].

Of course, in the spirit of the quote that started this subsection, there are many other reasons for which one might want to modify the flow within a boundary layer. These include the augmentation of the mixing of fluid mass, momentum or energy and the suppression of noise. But engineering sets some constraints to our imagination: any flow technique we might come up with must operate reliably within as wide a range of realistic flow parameters as possible; be practical to implement, both in terms of

expense and complexity of equipment; and cannot introduce more drag, weight or energy requirements than it saves by favourably affecting the boundary layer flow.

1.2 The mountains of the future

These engineering considerations have made many promising flow control techniques unfeasible for aeronautical applications, including, due to the rather unwieldy plumbing that would have to be installed on an aircraft wing, the well-established strategy of suction. Dynamic roughness elements could be quite straightforward to incorporate on a surface and thus have the potential to circumvent many of the difficulties mentioned above. The roughness elements themselves could be considered as being either three-dimensional bumps or two-dimensional strips inserted spanwise along a wing (and, in fact, the 2D work described in this thesis will make use of this fact). The 3D version was constructed by Grager et al. (2012) [33] through the use of a thin sheet of latex rubber placed over the leading edge of an airfoil, within which was created a hollow, airtight chamber, with holes drilled through the surface. Cycles of pressurisation and depressurisation of this pressure plenum then caused the rubber to vibrate up and down, creating the oscillating roughness elements. The rapidly developing technology of micro electromechanical systems (MEMS) throws open the doors to more high-tech implementation methods; and dialectric electro-active polymers (which compress as a result of the application of electrostatic pressure) have been proposed as a means of creating dimples for skin friction drag reduction in the turbulent regime [18, 19, 31] and, indeed, to control the formation of the laminar separation bubble through the forcing of Kelvin–Helmholtz instabilities to cause early transition [20].

The dynamic roughness elements that have been studied and will be considered here can be classified as falling under the umbrella of oscillatory flow control techniques, beneath which oscillating flaps, strings or wires, acoustic vibrations and alternating blowing and suction also find shelter [34]. These oscillatory motions marked a departure from the predominantly steady techniques that had dominated work throughout most of the 20th century and were an acknowledgement that separation has a significant time-dependent component to it, most especially when turbulence, and the discovery of its attendant coherent structures, is considered as part of the separation and reattachment process.

The existing work on dynamic roughness elements, however, focuses on laminar flow and suggests that the boundary layer remains laminar over and downstream of the roughness. The first study on these elements was by Huebsch (2006), who showed, through the use of numerical computations, that dynamic roughness were able to suppress separation at constant angle of attack and delay the formation of the dynamic stall vortex during the rapid pitch-up of an airfoil [40]. For the former case (see figure 1.3), the chord Reynolds number was set at 70 000 and the airfoil was the NACA 0012 shown in figure 1.1, flying at an angle of attack of 21°. The clean airfoil (figure 1.3a) clearly shows the formation of recirculating bubbles near the leading edge, with

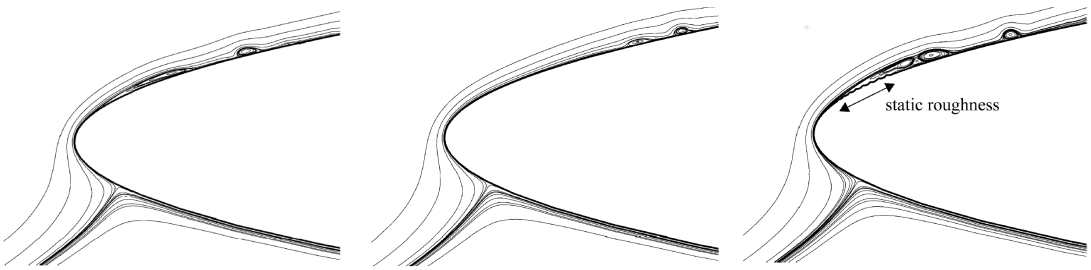

(A) Clean airfoil (B) Airfoil with dynamic roughness (C) Airfoil with static roughness

FIGURE 1.3: Comparison of the effects of a clean airfoil with an airfoil on which are mounted dynamic or static roughness elements, taken from figures 10–12 of [40]. The airfoil is a NACA 0012, the chord Reynolds number is 70 000 and the angle of attack is 21°. The maximum extension of the dynamic roughness elements corresponds to the height of the static elements and is approximately 70% of the boundary layer thickness. For the dynamic roughness elements, the oscillation frequency was 60 Hz.

shed vortices propagating downstream; while leading edge separation is absent when the dynamic roughness elements, which have an amplitude when fully extended that is reported as being approximately 70% of the local boundary layer height, are activated at a frequency of 60 Hz (figure 1.3b). Static roughness elements, on the other hand, have a detrimental effect in both scenarios: for constant angle of attack, they result in more unsteadiness in the flow (figure 1.3c) and there is a suggestion that they speed up the dynamic stall process.

Further confirmation of the potential successes of dynamic roughness, from both a numerical and experimental approach, arrived in 2012 in the papers of Huebsch et al. and Grager et al. The former found close agreement between computational simulations and experimental results for an array of 14 roughness elements starting just upstream of the expected separation point on a NACA 0012 airfoil. The Reynolds number this time was set at 100 000 and the airfoil angle of attack was either 9.5° or 12°, which, in the clean case, would form a short and long laminar separation bubble respectively. In both cases, the bubble was suppressed by roughness elements whose maximum extension was 22% of the local boundary layer height: in the first case the oscillation frequency was 60 Hz and in the second it had to be increased to 90 Hz [41].

The NACA 0012 airfoil was the setting also of the experiments of Grager et al. (2012), which used particle image velocimetry (PIV) measurements to visualise the impact of the roughness elements on the flow. The maximum height of the elements was again around 25% of the boundary layer height, with the paper giving further details regarding the configuration of the roughness array: the chord and span of the airfoil had lengths 150 mm and 300 mm respectively, the roughness region started at 1.07% and extended to 10.76% of chord, the roughness elements had diameters of 3 mm and their maximum height was of approximately 230 µm. The amplitude of oscillation using the pressure plenum contraption described previously was actually only 25% of the maximum height and thus the elements were never able to drop flush with the airfoil surface. Four

different chord Reynolds numbers were tested—25 000, 49 000, 73 000 and 97 000—and in all cases the angle of attack increases by two to three degrees before the occurrence of separation (figure 1.4).

Throughout all of the experimental and computational work here described, however, the existence of a favourable effect was heavily dependent on the physical parameters of the roughness elements or array. Most studies agree regarding the required location: in the vicinity of the separation point [40] and, if an array, starting just upstream of the separation point and ending at a position downstream where the resultant deceleration of the flow will not have an adverse impact [66]. Issues regarding height and frequency are more delicate. Undoubtedly, the roughness should lie completely within the boundary layer [40]; and heights of around 50–80% of the height of the boundary layer seem to be preferable (see, for example, figure 1.5) [33, 41]. However, lower heights, of around 4% of the boundary layer height, were also effective provided that the oscillation frequency was increased [41].

Initially, indications were, in fact, that there is an inverse relation between the roughness height and frequency of oscillation. The frequency range studied in the various papers covers the range 30–120 Hz, and the spectre of engineering considerations comes back to haunt what is achievable in real-life applications. Flow control for given flight parameters, according to Grager et al. (2012), is lost once the frequency decreases below a certain value, as shown in figure 1.6 [33]; and the analytical work of Rothmayer & Huebsch (2011) indicates that for height scales of order Re^{-1}, non-dimensionalised relative to the chord length and free-stream velocity, time also scales as Re^{-1}, which implies that the oscillation frequency should be of order the Reynolds number (taken to be much larger than unity) [66].

An analysis of the behaviour of a single roughness, rather than an array, perhaps paints a more complex and subtle picture. This was carried out by Rothmayer & Huebsch (2012) (both analytically and numerically) and focused on the shedding of vorticity from the roughness due to its upwards and downwards motion. Their numerical solutions indicated that on the upstroke, regions of negative and positive vorticity formed to the left and right of the roughness crest, and this was reversed on the downstroke. These regions are then ejected from the surface into the main boundary layer flow: given a low oscillation frequency, if the roughness height is small enough, this shed vorticity dissipates and the flow is unsteady, but attached. As the height increases, however, the ejected vortices become much more focused and concentrated, are not dissipated entirely and are convected downstream, as demonstrated in figure 1.7. Hence for a slow oscillation frequency, the maintenance of an attached flow requires a low roughness amplitude [67].

The vortex shedding process also becomes more visible as the frequency increases and unsteady flow separation begins to occur, with the possibility of dynamic stall (see figures 1.7e and 1.7f, for example). However, as we increase the frequency still further, becoming of order $\mathrm{Re}^{1/2}$ (figure 1.8), the shed vortices are no longer seen and the

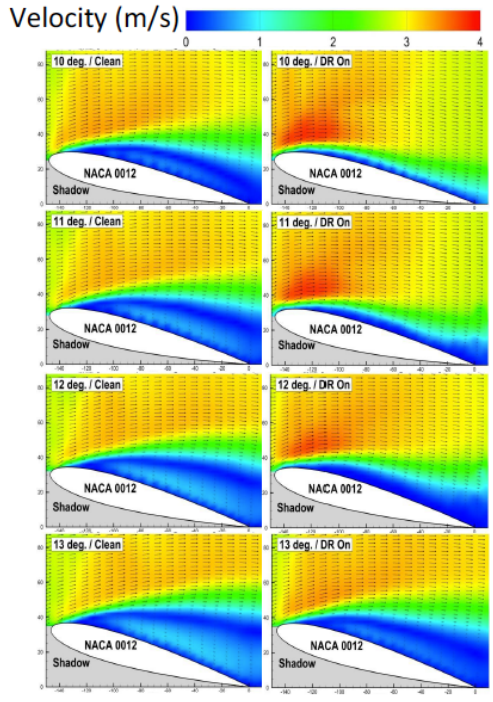

(A) Re = 25 000

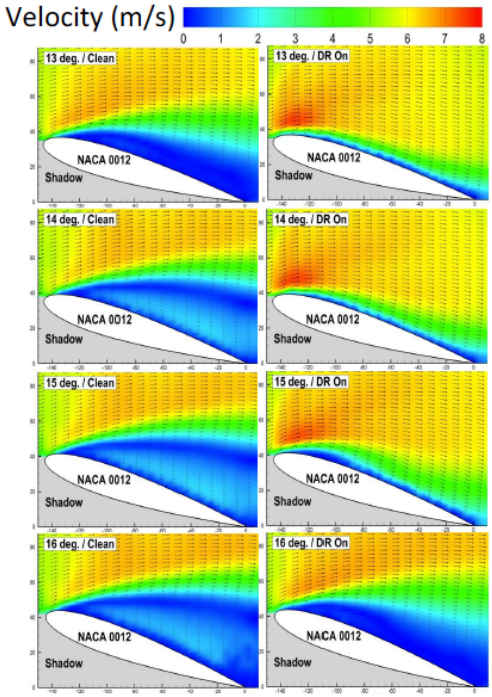

(B) Re = 49 000

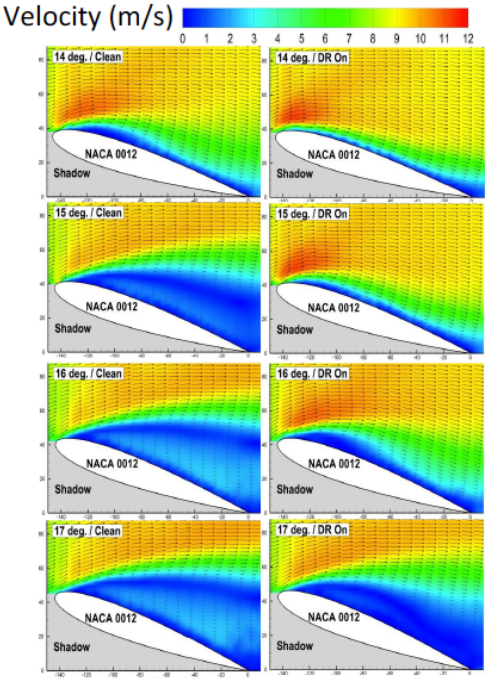

(C) Re = 73 000

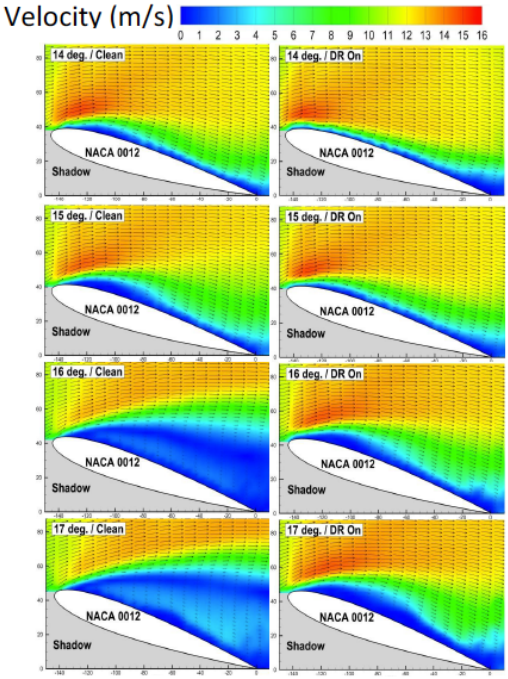

(D) Re = 97 000

FIGURE 1.4: Average velocity contours for the flow at varying chord Reynolds number, for various angles of attack, for both a clean NACA 0012 airfoil and one on which an array of dynamic roughness elements are actuated at a frequency of 90 Hz, as described in the text. Arrows show the direction of the flow. Taken from figures 7–10 of [33].

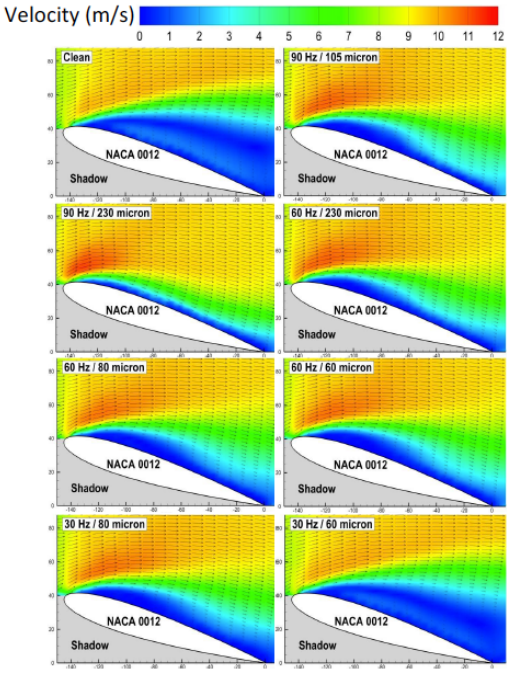

FIGURE 1.5: PIV measurements showing the effect of roughness height and frequency on separation control for an angle of attack of 15° and chord Reynolds number of 73 000, with the various heights and actuation frequencies given in the boxes in the top left-hand corner. The direction of the flow is given by the arrows. Both increasing height and frequency has a positive effect on separation delay. Taken from figure 17 of [33].

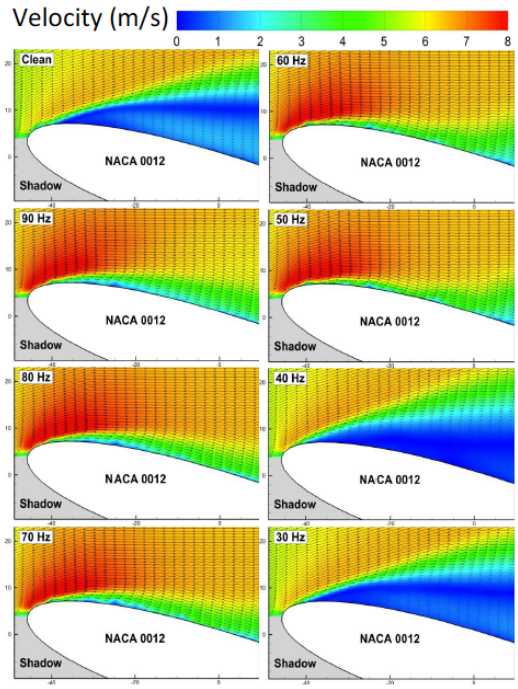

FIGURE 1.6: PIV measurements indicating the effect of frequency on flow separation over dynamic roughness elements of maximum height 230 µm, for an angle of attack of 14° and chord Reynolds number of 49 000. Arrows show the direction of the flow. Below a certain frequency—40 Hz for this configuration of flight parameters—separation is not suppressed. Taken from figure 12 of [33].

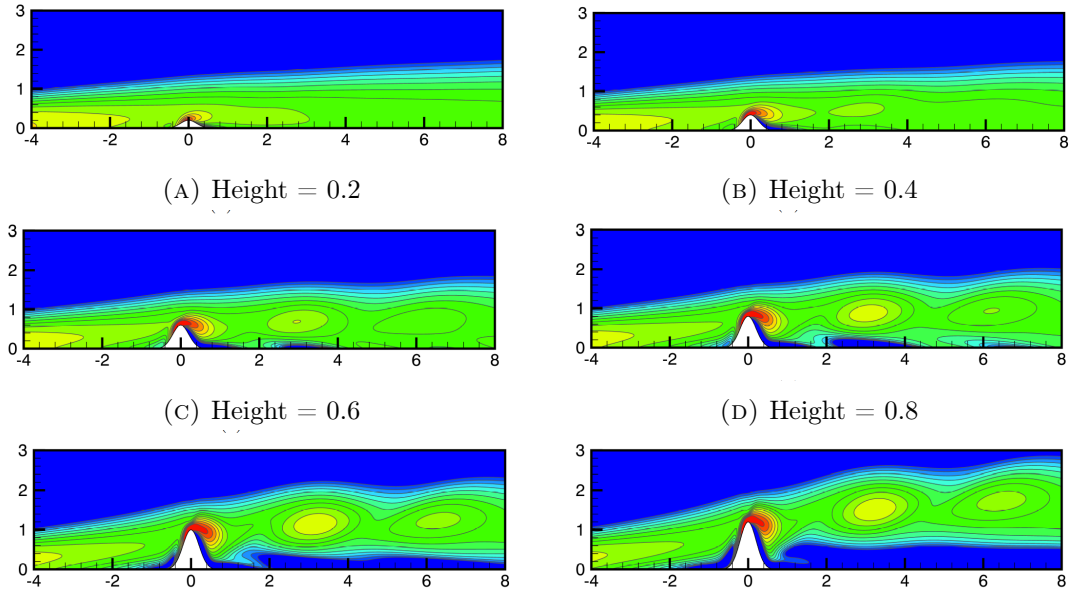

(A) Height = 0.2 (B) Height = 0.4

(C) Height = 0.6 (D) Height = 0.8

(E) Height = 1.0 (F) Height = 1.2

FIGURE 1.7: Numerical solutions for the vorticity over a single dynamic roughness element for a Reynolds number, based on the boundary layer thickness, of 100 (corresponding to a macroscopic Reynolds number of roughly 10 000). The solutions for various heights, non-dimensionalised to the local boundary layer thickness, are shown, indicating the development from attached flow to the shedding of vortices downstream as roughness height increases. The oscillation frequency is 1 and the flow shown is that which occurs approximately ten cycles into the solution, when the hump is near the maximum amplitude. Taken from figure 13 of [67], which uses the common colour map.

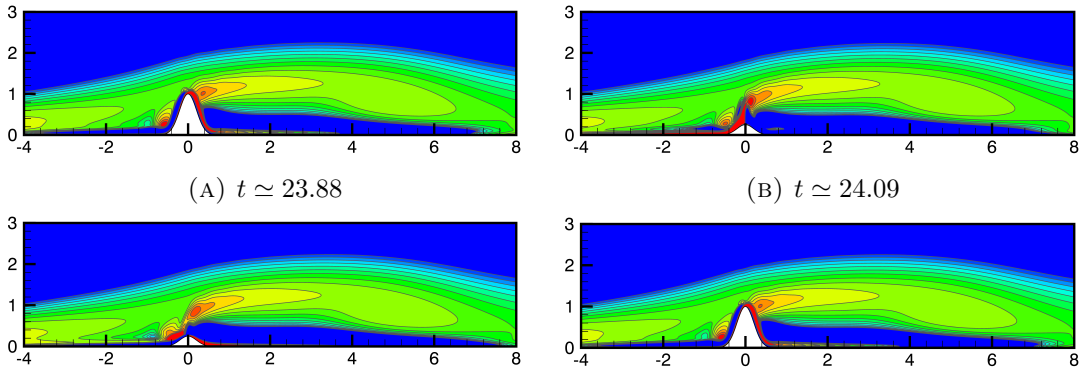

(A) $t \simeq 23.88$ (B) $t \simeq 24.09$

(C) $t \simeq 24.29$ (D) $t \simeq 24.50$

FIGURE 1.8: Numerical solutions for the vorticity over a single roughness element oscillating at a frequency of 10 and maximum roughness height of 1. The times represent the 40th cycle of oscillation; all other details are as in figure 1.7. Taken from figure 16 of [67], which uses the common colour map.

flow downstream of the roughness element becomes steady. Hence the conclusions are twofold: if the frequency is less than order $\mathrm{Re}^{1/2}$, then the roughness amplitude must be below a certain critical value to maintain attached flow, with that value decreasing with decreasing frequency; for frequencies of the order of $\mathrm{Re}^{1/2}$, however, the range of amplitudes for which a stabilising effect is seen increases and the maximum height can be of the order of the boundary layer height. This stabilising effect is due mainly to the injection of vorticity from a viscous sublayer around the oscillating roughness to the main boundary layer flow and only occurs once the amplitude is high enough: the implication, therefore, is that if separation control requires this injection of vorticity into the mean flow, then there exists a minimum effective height [67]. It should be noted, though, that unlike the other studies, this paper only examined the response of an oncoming, attached, Blasius boundary layer to a dynamic roughness element, rather than the impact of an array of them on flow that, in the absence of the roughness elements, would have undergone separation.

Other theories, linked and distinct to that of vorticity injection, have also been proposed to explain the effect of the dynamic roughness on flow separation. The asymptotic approach of Rothmayer & Huebsch (2011), matching between the multiple scales present in a long array of roughness elements all with a height and time scaling of order Re^{-1}, derived the dynamic roughness boundary layer equations, which were the result of an interaction between an inviscid core flow and a viscous sublayer (the Stokes layer). In these equations was the presence of a term that resembled the Reynolds stresses present in the equations that drive turbulent flows, except that here it was due to the velocity perturbations of the dynamic roughness rather than an averaging of the Navier–Stokes equations. In turn, this Reynolds stress gave rise to a mean pressure gradient that favourably modified the mean flow within the core of the boundary layer, allowing for attached flow at angles of attack that would normally result in separation [66].

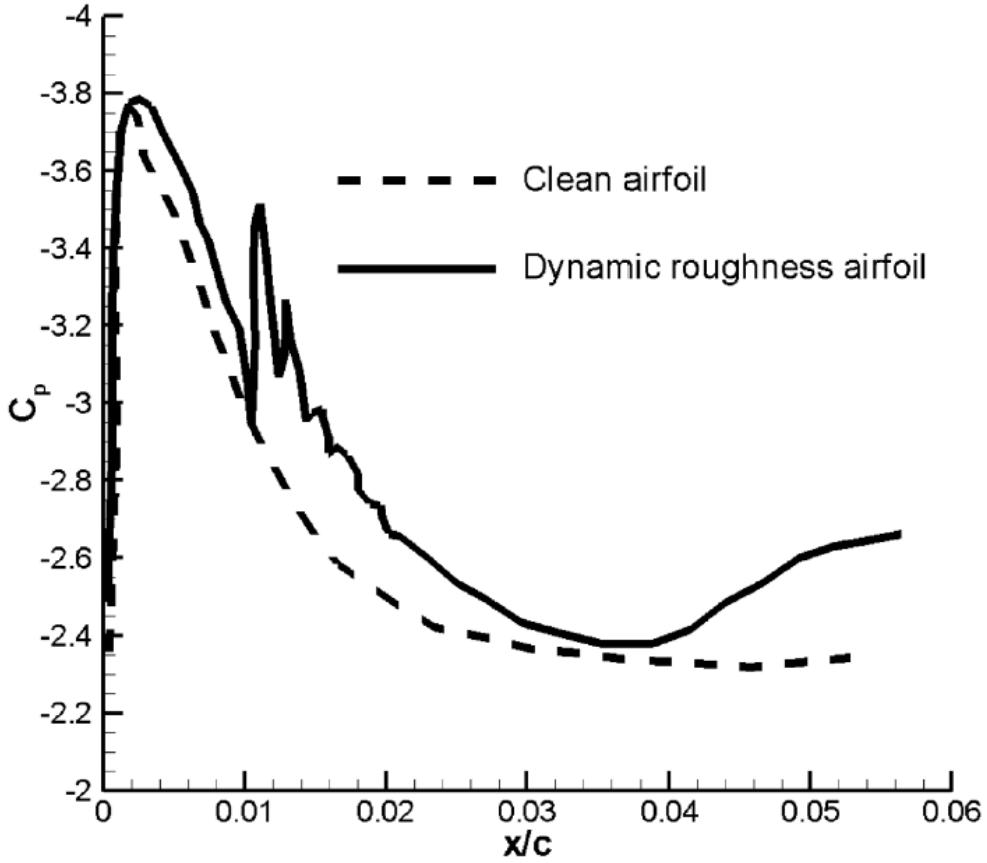

FIGURE 1.9: Leading edge (note the scale on the x-axis, c is the chord length) pressure coefficient (C_p) for flow over a clean NACA 0012 airfoil and one with an array of 14 dynamic roughness elements (the pressure coefficient has been time-averaged), of amplitude 50–80% of the boundary layer height, taken from figure 4 of [41]. The angle of attack was of 12° and the Reynolds number was equal to 100 000. The oscillation frequency was not given.

The introduction of regions of favourable pressure gradients as the flow processes over an array of dynamic roughness elements was also identified by Huebsch et al. (2012), as shown in figure 1.9 [41]. These favourable pressure gradients where the flow would normally expect to be fighting an adverse gradient can accelerate near-wall fluid particles and thereby delay separation [66], especially if the roughness is a significant proportion of the boundary layer height [67]. Commentary on the possible role of transition and the link between roughness elements and turbulence will be delayed until chapter 7.

1.3 On maps was written *'terra incognita'*

The role of the pressure gradient in provoking separation and its possible modification by dynamic roughness elements has played a significant part in our preparations thus far. Our journey will continue to focus on the pressure as the boundary layer flows over a single roughness element or an array of them in various scenarios. The first of these, the first snowy peak that lies ahead, consists of an array of dynamic roughness elements lying within a condensed layer embedded within the boundary layer (scenario

1). The array gives rise to multiple length scales—that of a single roughness and the array, which can have a much larger streamwise extent—and an interaction between a viscous near-wall layer and the inviscid core flow, in a similar way to that described by Rothmayer & Huebsch (2011) [66]. The oncoming flow will be that of a Blasius boundary layer developing on a flat plate: to begin with, it is only the effect of the pressure on the mean flow that will be of interest to us, rather than the presence of separation.

Separating flows will be our focus in scenarios 2 and 3. Both will deal mainly with single roughness elements, although some results for a limited array (with length scale that is the same as that of a sole roughness) will also be presented. The second scenario is set in the landscape of Smith & Daniels (1981) [85], where a hump within the boundary layer provokes separation. Within the relevant region of interest, which will drive the appropriate length, height and frequency scalings, will be placed our roughness element and the goal will be to determine its impact on the position of separation, as well as the role of the pressure in any shift in the separation point. The third scenario will move to a setting that is perhaps of more applicable interest: flow over an airfoil flying at or near the critical angle of attack. We will thus place the roughness elements in the context of the theory of marginal separation [69, 70, 90] and extend it to incorporate these unsteady roughnesses. This will then allow us to determine their impact on the critical angle of attack—with a view to seeing whether they can increase it before the airfoil stalls, as suggested by Grager et al. (2012) [33]; and their effect on separation—to find out whether fully attached flow can be maintained without the formation of a laminar separation bubble, as suggested by Huebsch et al. (2012) [41].

We are motivated also by a desire to investigate the various scalings that are important and the influence of the roughness parameters, especially the relationship between height and oscillation frequency. Although the work that set this study in motion dealt only with dynamic roughness, we will not ignore static elements, which will turn out to give rise to interesting results.

We aim, therefore, for the following markers: in chapter 2, the governing equations that will be used for the various scenarios will be introduced, with some indication of their historical setting; chapter 3 will describe scenario 1; we will encounter separation once more in chapter 4, and the Goldstein singularity will also make an appearance; this will be in preparation for the work of chapters 5 and 6 regarding scenarios 2 and 3 respectively; the end of the journey will come in chapter 7, where we will touch also on turbulence and realise that, in reality, the end of this journey is only the start of another.

Throughout, we will deal only with two-dimensional roughness elements: thus one might consider them instead to be strips placed spanwise along a surface. Three-dimensional effects are undoubtedly important, but we believe or hope that a 2D analysis is valid for an initial look at the impact of roughness elements on flow separation, as well as yielding some new findings and providing a basis for comparison with other work. Our

approach will be unashamedly analytical, and rely heavily on the theory of matched asymptotic expansions, with the Reynolds number taken to be much larger than 1. On the other hand, one should remember that we wish to remain within the laminar regime and thus physically we are grounded in the range of Reynolds numbers from 10^4 to 10^6.

Our belief is that an asymptotic approach is a valuable tool in shedding light on the physical mechanisms at play and providing a basis for deriving the relevant scaling laws. It was, in fact, a use of asymptotics that liberated us from a reliance on experimentation and which, from the Wright brothers' single person flyer, changed the course of the twentieth century and brought the power of flight to the whole of humanity.

1.4 Icarus flew

We've always wanted to fly. The ancient Greeks told of Daedalus, the master craftsman, who had built for King Minos of Crete the labyrinth that housed the Minotaur—the product of Pasiphaë's lust for a fierce and handsome bull—and yet he, too, found himself "imprisoned by the waves". Unhappy, but armed with his own ingenuity, he built for himself and his son wings of wax and feathers; and, warning Icarus "to take the middle way, in case the moisture weighs down your wings [. . . or] the sun scorches them", flew away [57]. The great Berber polymath, Abbas Ibn Firnas (810–887) who, living in the culturally vibrant Emirate of Córdoba, was most likely motivated by scientific curiosity rather than a desire to escape, launched himself from the top of a mountain. A few centuries later, the scholar Ahmed Mohammed al-Maqqari (1577–1632), drawing on the testimony of (possibly imaginary) witnesses, recounted that

> *"he [Ibn Firnas] flew a considerable distance, as if he had been a bird, but, in alighting again on the place whence he had started, his back was very much hurt, for not knowing that birds when they alight come down upon their tails, he forgot to provide himself with one"* [101].

Eilmer of Malmesbury, an eleventh century Benedictine monk from Wiltshire Abbey, presumably had not been informed of this oversight, for he too, despite flying for over 200 metres at some point between 1000 and 1010, also failed to equip himself with a tale. Consequently, in the words of William (also of Malmesbury), he "broke his legs, and was lame ever after" [101].

The flight of birds motivated other, arguably more successful, researchers. Leonardo da Vinci's *Codex on the Flight of Birds* described, often erroneously, the general flow characteristics around a flying bird; and his *Codex E* is a marked departure from the Aristotelian theory that stated that the propulsion of an object through the skies was due to air separating in front of the projectile and then filling in the space behind. Within da Vinci's work is the phrase that

> *"the air surrounding birds is above thinner than the usual thinness of the other air [that of the atmosphere], as below it is thicker than the same, and it is thinner behind than above in proportion to the velocity of the bird and its motion forwards, [. . .]; and in the same way the thickness of the air is thicker in front of the bird than below"*:

a description that is qualitatively correct once one replaces 'thinner/thicker' with 'lower/higher pressure' [3].

The empirical approach of da Vinci (1452–1519) dominated most of the early research in aerodynamics. The development of streamlined spears by our early ancestors, hunting in the African plains, was driven by trial and error and, millennia later, Sir George Cayley (1773–1857) designed, built and tested flyers over Brompton Dale with very flimsy theoretical foundations, despite his seminal (but largely forgotten) three-part treatise on flight (1809–10). Later, Samuel Pierpont Langley (1834–1906) in the USA and Otto Lilienthal (1848–96) in Germany took up Cayley's mantle and carried out experiments on lifting surfaces and various other aspects of glider design. The latter went a few kilometres further and ordered the construction of a 15 m high conical-shaped hill at Lichterfelde, from the top of which he could launch himself on his gliders regardless of wind direction, before dying on 9 August 1896 in the Rhinow Hills when his glider stalled. This experimental work ultimately culminated in the first powered heavier-than-air flight on the morning of 17 December 1903. The Wright Flyer had been built by Wilbur and Orville Wright off the back of an exhaustive programme of wind tunnel tests.

It was little surprise that experimentation had been at the forefront of humankind's journey to the skies. Theoretical aerodynamics at first could not describe what was being observed in reality and then, when it could, consisted of equations that were far too complicated to be of any practical use. The development of a more mathematical description of fluid flow began largely through the work of the triumvirate of Daniel Bernouilli (1700–82), Jean le Rond d'Alembert (1717–83) and Leonhard Euler (1707–83). The former, in his book *Hydrodynamica* (1738), derived a relationship between fluid velocity and pressure (thus giving his name to the Bernouilli equation); while d'Alembert's use of partial differential equations paved the way for Euler's continuity and momentum equations, which appeared in *General principles of the state of equilibrium of fluids* (1753).

Claude-Louis Navier (1785–1836), Augustin-Louis Cauchy (1789–1857), Siméon Poisson (1781–1840), Adhémar Jean Claude Barré de Saint-Venant (1797–1886) and George Stokes (1810–1903), despite disagreeing with each other, then all managed to derive what became known as the Navier–Stokes equations, which overcame the hurdle of d'Alembert's paradox [17]. These, however, were (and are) impossible to solve analytically except in only a small number of cases and were therefore left to one side to accumulate dust until Prandtl arrived with his genius, invented boundary layer theory and let the genie out of the bottle.

Prandtl's equations, to be discussed in chapter 2, moved aerodynamics away from its foundations of sand to more solid ground. His laboratory in Göttingen was a spectacular embodiment of the new marriage between mathematics and experimentation and was the breeding ground for many of the theories that would transform the Wright Flyer into the aeroplanes we know today. From Göttingen sprang forth, too, some of the protagonists of twentieth century fluid mechanics: Theodore von Kármán (1881–1963), Heinrich Blasius (1883–1970), Albert Betz (1885–1968), Max Munk (1890–1986) and Adolf Busemann (1901–1986).

This last figure was hugely influential in resolving the problem posed by the "compressibility burble" [88] as flight began to approach supersonic speeds. The separation of air over objects moving in the transonic range, first observed in post-First World War aeroplane propellers, was explained by Eastman Jacobs (1902–87) and John Stack (1906–72) who, in 1934, published schlieren photographs showing the formation of shock waves. At the Fifth Volta Conference in Rome, entitled *High velocities in aviation*, Busemann proposed the use of swept wings to counteract this and Mussolini announced the Italian invasion of Ethiopia. The former was ridiculed and ignored by the international community (the latter was condemned and sanctioned), but the concept—based on the fact that it is the component of the flow normal to a wing's leading edge that dominates the airspeed—was re-proposed in wartime USA by Robert Jones (1910–1999) and vindicated by the secret experiments being carried out by the Germans. These were related back to US aircraft manufacturers by George Schairer, who was part of von Kármán's team that went to Germany as resistance crumbled to see what research was being carried out there, and resulted in the revised design of the B-47 bomber, which inspired the iconic Boeing 747, bringing air travel to the masses [5].

All of which has ignored the contributions of countless others who have guided us from 36.5 m flown over sandy, bumpy ground at Kill Devil Hills near Kitty Hawk, North Carolina, in 1903 to breaking the sound barrier in 1947 and then heading into space. Icarus ignored his father's warning to "take the middle way, [. . . to] travel between the extremes" [57], but somewhere beyond the Milky Way, Voyager 1 is still flying.

2

From Euler to Navier–Stokes to Prandtl and beyond

"We dwelt on the fringes of an unspanned continent, where the chill breath of a vast, polar wilderness, quickening to the rushing might of eternal blizzards, surged to the northern seas. We had discovered an accursed country. We had found the home of the blizzard."

Sir Douglas Mawson, *The Home of the Blizzard*

Ludwig Prandtl, too, found himself on the fringes of an unexplored land, surveying the wilderness. At the end of 1903, the Wright Brothers had flown, but their success was based wholly on empirical testing and observations, rather than a sound mathematical and theoretical foundation. The Navier–Stokes equations, discovered (or defined, depending on your philosophical bent) in the first half of the 1800s, had at least cleared up D'Alembert's paradox—flow around a sphere and drag that didn't quite add up—but, for practical aeronautical applications in an era without computers, the equations were a little like Capability Brown and James Wyatt's Broadway Tower, constructed in the Cotswolds in 1794: mathematical follies, imposing (especially in the fog) and attractive, but of little actual use. (Although Broadway Tower eventually found purpose in monitoring nuclear fallout over Britain during the Cold War.)

In this chapter, we travel from Euler's equation to those of Navier and Stokes, passing by d'Alembert's paradox on the way, taking us to the impasse that confronted Prandtl at the turn of the twentieth century. Through his boundary layer theory and associated boundary layer equations, Prandtl gave us the equipment to penetrate into the wilderness and make sense of the blizzards. The boundary layer equations and, from them, the condensed layer equations and triple deck structures, form the basis of our study of the impact of roughness elements on flow separation.

Incidentally, Sir Douglas Mawson's Australasian Antarctic expedition (1911–13) was accompanied by a Vickers aeroplane: intended to be the first aeroplane to be flown in the Antarctic, it might have proved invaluable in the exploration of the continent, had it not been damaged in Australia before departure. It travelled on the Aurora nonetheless

and made it to Cape Denison, on the edge of unmapped territory immediately south of Australia, where it was to be converted for life as a tractor. In this, too, it sadly failed (it was too cold for the engine) and Mawson's own exploration met with hardship and disaster: with Lieutenant Belgrave Ninnis and Xavier Mertz, he found himself 507 km *away from base camp, deep in King George V land, when Ninnis and a sled fell into a crevasse, taking most of the supplies with them. Racing death back to base camp, Mawson and Mertz fed themselves on their sled dogs and poisoned themselves on the vitamin A in the huskies' livers. Mertz died; Mawson, despite himself falling twice into a crevasse, somehow survived [64].*

2.1 From Euler's equation to the Navier–Stokes

It was Daniel Bernouilli, in his book *Hydrodynamica*, published in 1738, who began to make progress in understanding the relationship between velocity and pressure that, in the century that followed, eventually became embedded in the Navier–Stokes equations; the book also giving rise to the name by which the study of fluid dynamics was to become known during the early days of its theoretical development. Within the pages of Bernouilli's work is the conclusion that if velocity increases, then the pressure must decrease, and vice versa: a finding that today is encapsulated in the Bernouilli equation, although the equation itself in its modern form—that

$$\frac{1}{2}\rho\left|\mathbf{u}\right|^2 + p = \text{constant} \tag{2.1}$$

along a streamline (to be defined shortly), with ρ the fluid density, $\mathbf{u}$ the velocity vector and p the pressure—does not actually appear in *Hydrodynamica*.

The derivation of Bernouilli's equation (2.1) follows directly from the integration of the steady version of Euler's equation, whose formulation became possible after d'Alembert first showed how partial differential equations could be used to model problems in physics and fluid dynamics. The paper *Essai d'une nouvelle théorie de la résistance des fluides*[1] was submitted to a prize competition run by the Berlin Academy in 1749 and, in a considerably opaque form, contains the precursor of the modern continuity equation (the paper, along with all the other entries, was rejected, but it was eventually published in 1752) [16]. It was Leonhard Euler's 1757 paper, *Principes généraux du mouvement des fluides*[2], that contains a more recognisable form of the continuity equation, which is actually the law of conservation of mass of a fluid in the absence of any sources or sinks. In current notation, the equation is given by

$$\frac{\partial\rho}{\partial t} + \nabla\cdot(\rho\mathbf{u}) = 0 \tag{2.2a}$$

[1] *Essay on a new theory of the resistance of fluids*
[2] *General principles on the movement of fluids*

or, equivalently,

$$\frac{1}{\rho}\frac{\mathrm{D}\rho}{\mathrm{D}t} + \nabla \cdot \mathbf{u} = 0. \tag{2.2b}$$

In the above, $\mathrm{D}/\mathrm{D}t$ is known as the substantive derivative: if we assume one fluid element at time t_1 and position $\mathbf{x_1} = (x_1, y_1, z_1)$, which, at time t_2, is at position $\mathbf{x_2} = (x_2, y_2, z_2)$, with $t_2 - t_1$ small; and if $f = f(\mathbf{x}, t)$ is some property of the flow, then a Taylor series expansion gives that

$$\begin{aligned} f(\mathbf{x_2}, t_2) \simeq f(\mathbf{x_1}, t_1) &+ \frac{\partial f}{\partial x}(\mathbf{x_1}, t_1)(x_2 - x_1) + \frac{\partial f}{\partial y}(\mathbf{x_1}, t_1)(y_2 - y_1) \\ &+ \frac{\partial f}{\partial z}(\mathbf{x_1}, t_1)(z_2 - z_1) + \frac{\partial f}{\partial t}(\mathbf{x_1}, t_1)(t_2 - t_1) + \cdots ; \end{aligned}$$

which, dividing by $t_2 - t_1$, gives

$$\begin{aligned} \frac{f(\mathbf{x_2}, t_2) - f(\mathbf{x_1}, t_1)}{t_2 - t_1} \simeq &\frac{\partial f}{\partial x}(\mathbf{x_1}, t_1)\frac{x_2 - x_1}{t_2 - t_1} + \frac{\partial f}{\partial y}(\mathbf{x_1}, t_1)\frac{y_2 - y_1}{t_2 - t_1} \\ &+ \frac{\partial f}{\partial z}(\mathbf{x_1}, t_1)\frac{z_2 - z_1}{t_2 - t_1} + \frac{\partial f}{\partial t}(\mathbf{x_1}, t_1) ; \end{aligned}$$

and, taking the limit $t_2 - t_1 \to 0$, gives

$$\frac{\mathrm{D}f}{\mathrm{D}t} = \mathbf{u} \cdot (\nabla f) + \frac{\partial f}{\partial t}.$$

The substantive derivative is, therefore, the sum of two terms: the convective and local derivatives.

For incompressible flows, where the density ρ is constant, equation (2.2b) reduces to

$$\nabla \cdot \mathbf{u} = 0 \tag{2.3}$$

and this is the continuity equation that will concern us. In two dimensions, it implies the existence of a stream function ψ, defined as

$$\psi - \psi_0 = \int_C (u\,\mathrm{d}y - v\,\mathrm{d}x)$$

—ψ_0 being the constant of integration associated with the line integral taken along some curve C from a reference point to the point (x, y)—and giving rise to the relationship

$$u = \frac{\partial \psi}{\partial y} \quad \text{and} \quad v = -\frac{\partial \psi}{\partial x}, \tag{2.4}$$

where (x, y) are the coordinates in a Cartesian system and (u, v) are the velocity components in the x and y directions respectively. Setting the stream function to be a constant gives a streamline and plotting these streamlines gives a picture of the flow, with the tangent to each streamline giving the velocity of the flow at that point at a particular instant in time.

Also appearing in *Principes généraux du mouvement des fluides* was the equation

$$\rho \frac{\mathrm{D}\mathbf{u}}{\mathrm{D}t} = -\nabla p, \tag{2.5}$$

which finally combined velocity and pressure in a single equation: Euler's equation. This, ultimately, is a result of Newton's second law of motion, that force equals mass times acceleration: the forces consist of both surface and body forces (the latter being those, such as gravity, that act over a distance and which, for our purposes, are ignored); and the acceleration is represented by the substantive derivative of the velocity, defined above.

Euler's equation, however, predicts zero drag on an object moving with a constant velocity in a flow—a finding that contradicted all experimental results. If we consider, for example, a circular cylinder placed transverse to the flow, then the radial and azimuthal velocity components are

$$u_r = -U\left(1 - \frac{R^2}{r^2}\right)\cos\theta \quad \text{and} \quad u_\theta = U\left(1 + \frac{R^2}{r^2}\right)\sin\theta$$

respectively, giving a velocity magnitude of

$$|\mathbf{u}|^2 = U^2\left[\left(1 - \frac{R^2}{r^2}\right)^2 \cos^2\theta + \left(1 + \frac{R^2}{r^2}\right)^2 \sin^2\theta\right],$$

where r is the radial distance from the centre of the cylinder's circular cross-section (of radius R), θ is the angle made with the horizontal and U is the magnitude of the upstream velocity of the flow, which is moving parallel to the horizontal axis. On the surface of the cylinder ($r = R$), therefore, the velocity magnitude is

$$|\mathbf{u}|^2 = 4U^2 \sin^2\theta;$$

while far upstream ($r \to -\infty$, $\theta \to 0$), it is

$$|\mathbf{u}|^2 = U^2.$$

Setting the upstream pressure equal to zero (without loss of generality), Bernouilli's equation (2.1) allows us to find the pressure on the surface of the cylinder as

$$p = \frac{1}{2}\rho U^2\left(1 - 4\sin^2\theta\right)$$

(see figure 2.1). Since the pressure is symmetric over the front and rear halves of the cylinder, there is no net force acting on it and the drag is zero [6].

This contradiction became known as d'Alembert's paradox, after Jean le Rond d'Alembert, who admitted that he could not see

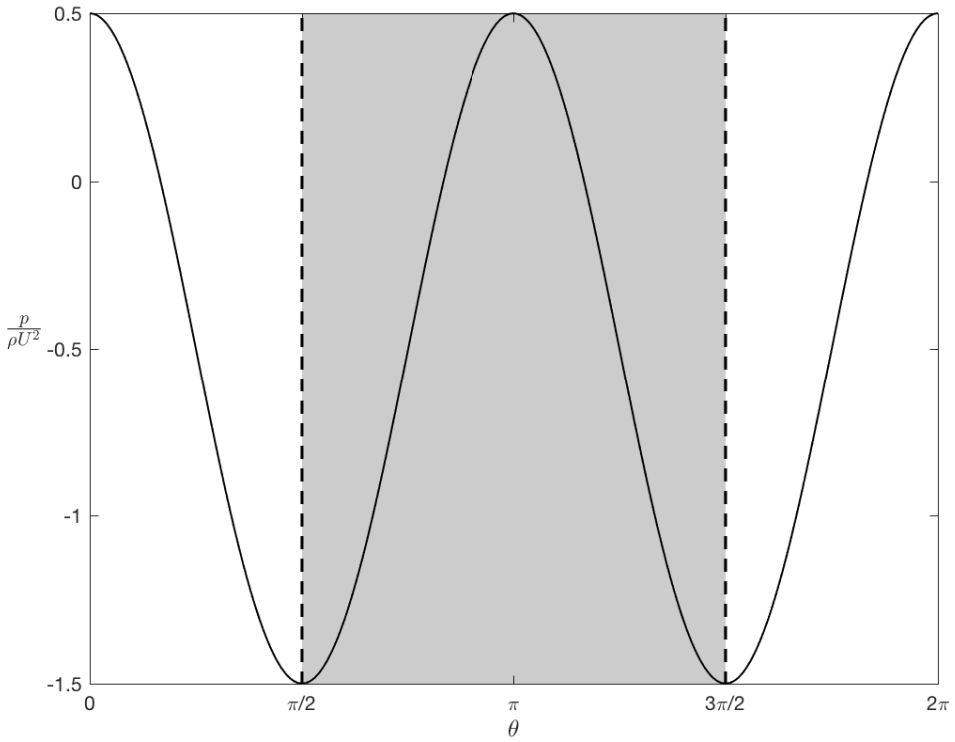

FIGURE 2.1: Pressure around a circular cylinder, in a steady inviscid flow, solved using Euler's equation (and the related Bernouilli equation). The angle θ is that made with the horizontal axis, hence the shaded area corresponds to the rear-facing half of the cylinder. Integrating the force per unit length on the cylinder gives a zero net force and hence no drag is experienced by the cylinder, contradicting experimental findings.

> *"... how one can explain the resistance of fluids by the theory in a satisfactory manner. It seems to me on the contrary that this theory, dealt with and studied with profound attention gives, at least in most cases, resistance absolutely zero: a singular paradox which I leave to geometricians [mathematicians] to explain"* (translated in [5]).

The problem was that Euler's equation was inviscid: in the list of forces on the right-hand side of equation (2.5), friction was missing. Also, it could not predict the separation of the flow over the cylinder and the resultant pressure drag. The field of hydrodynamics had, therefore, reached an impasse almost as soon as it had hatched: it was unable to predict the results that were seen in practice. This chasm was to be bridged by the discovery of the Navier–Stokes equations:

$$\rho\frac{\mathrm{D}\mathbf{u}}{\mathrm{D}t} = -\nabla p + \mu\nabla^2\mathbf{u}. \tag{2.6}$$

The viscosity (μ), which can be viewed as representing the 'thickness' of a fluid, and the frictional force (or viscous force) that was absent in Euler's equation was now included.

Hints as to the importance of friction had already appeared in the experimental work of Giovanni Venturi (1746–1822) and Pierre–Simon Girard (1765–1836). The former published a paper, *Recherches expérimentales sur le principe de communication latérale dans les fluides*[3], in 1799 in which he stated that the occurrence of eddies in pipes was due to the "motion communicated from the more rapid parts of the stream to the less rapidly moving lateral parts" [3], which encapsulates the idea of resistive forces existing between layers of fluid moving at different speeds. Girard carried out research on flow within capillary tubes and assumed that there existed a layer of fluid near the wall that remained at rest, with friction between this stationary layer and the main bulk of the flow [17]: although incorrect, it is hardly too much of a stretch of the imagination to go from this idea to the modern theory of boundary layers.

The incorporation of frictional forces in the governing equations of fluid dynamics then first came through the work of Navier in 1822, who was actually motivated by problems of rupture in elasticity. Over the next few decades, Cauchy (1823), Poission (1829), Saint-Venant (1837) and Stokes (1845) would re-derive the equations that became known as the Navier–Stokes equations, either unaware of Navier's earlier work or disagreeing with his approach. Poisson, for example, felt that the problem should be approached by considering the total force as a discrete sum over all the molecules, while Cauchy maintained that infinitesimal elements could be used, without a recourse to individual molecules. Navier, for his part, compromised between the two approaches, which led him to that lonely place in which engineers felt that his work was too mathematical, and mathematicians that it was based too much on engineering. Saint-Venant also adopted a compromise between Poisson and Cauchy's stances and it was he who first properly identified the concept of viscosity [17].

[3] *Experimental investigation on the principle of lateral communication in fluids*

Notwithstanding the discovery of the Navier–Stokes equations and the closure of a gap in the theory, the rift between mathematicians and experimentalists grew no less wide. As mentioned, this set of nonlinear equations was impossible to solve in almost all practical applications and the field of hydrodynamics continued to make use of Euler's inviscid flow theory, which, on top of its failure to correctly predict the behaviour and properties of near-surface flows, was hard enough to grapple with. In the words of the Nobel laureate Sir Cyril Hinshelwood, then, the study of fluid mechanics became split between those who observed things they could not explain and those who explained things they could not observe [26].

2.2 The gateway: Prandtl's boundary layer

We reach now the point where the past mingles with the present, as the work to follow makes use, like that of countless other researchers since 1905, of the ideas introduced by Ludwig Prandtl in his seminal 1904 talk, delivered to the Third International Mathematics Congress, held in Heidelberg, Germany, and published in its conference proceedings the following year. This paper, entitled *Über Flüsigkeitsbewegung bei sehr kleiner Reibung*[4], threw open the door to a practical treatment of the Navier–Stokes equations, bringing them down from the elevated heights of pure mathematical theory to join hands with the realm of mankind, and is described by Sydney Goldstein (who also played his own important role in the history of fluid dynamics—see chapter 4) as "one of the most extraordinary papers of this [20th] century, and probably of many centuries" [30].

Prandtl's presentation lasted a mere ten minutes [4] and the paper itself was only eight pages long but within its brevity and conciseness, Prandtl introduced the world to the concept of the boundary layer and its governing equations, discussed their application to flow along a flat plate and past a circular cylinder, suggested a description of separation and the role of the pressure gradient (discussed in §1.1) and proposed the use of suction as a means of avoiding the separation of the boundary layer from the surface [60]. In later years, Goldstein would ask Prandtl why the paper was so short, to which the reply was that Prandtl thought he could only include what he had time to say [30].

Of most importance to us is the idea of the boundary layer and its associated boundary layer equations, which will be described in this section. These equations, as we shall see, are much easier to solve than the full Navier–Stokes equations and yet are able to completely depict the behaviour of many flows and, in the cases where they cannot, the methodology developed indicates an approach to a solution. In the words of Prandtl,

> *"sufficient account can be taken of the physical phenomena in the boundary layer between the fluid and the solid body by assuming that the fluid adheres to the surface and that, therefore, the velocity is either zero or equal*

[4] *On the motion of fluids with very little friction*

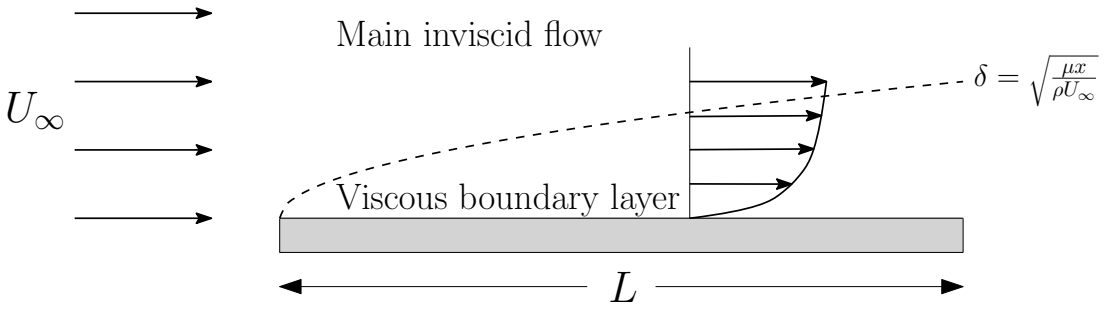

FIGURE 2.2: Schematic diagram (not to scale) showing the development of the boundary layer over the upper surface of a thin plate placed parallel to the flow.

> *to the velocity of the body. If, however, the viscosity is very slight and the path of the flow along the surface is not too long, then the velocity will have its normal [usual] value in immediate proximity to the surface. In the thin transition layer, the great velocity differences will then produce noticeable effects in spite of the small viscosity constants"* [60].

The idea (see figure 2.2) was that the flow remains inviscid almost everywhere in the flow field and the Euler equation (2.5) is therefore valid. This equation, having only a first order derivative, however, is unable to satisfy the full no-slip boundary condition on a solid surface: the velocity of the flow at a surface having to be "either zero or equal to the velocity of the body". Therefore, only the normal condition is imposed—that, in the absence of any blowing or suction, there is no flow through the boundary of the object—and there is a non-zero tangential 'slip' velocity at the surface.

A thin region of fluid where viscosity, although it might be very small, plays an important role is therefore needed to take the slip velocity predicted by inviscid theory to zero (relative to the velocity of the body) at the surface. Such a change in velocity over a small distance implies high velocity gradients and since, from Newton's shear stress law, the shear stress is proportional to the velocity gradient, this region must also be characterised by a large skin friction. Hence the 'thin transition layer', which has become known as the boundary layer.

An estimate of the size of the boundary layer, and how it develops along the surface of a body, can be obtained by determining when the inertial and frictional forces become of equivalent magnitude. The inertial force is that provided by momentum, or the left-hand side of the Navier–Stokes equation (2.6), and its magnitude is given by

$$\rho u \frac{\partial u}{\partial x} \sim \rho \frac{U_\infty^2}{x}.$$

Here, U_∞ is the uniform speed of the free-stream away from the body or, in a nod to the first inklings of the non-dimensionalisation that will follow shortly, some other reference velocity. The frictional force is given by $\mu \partial^2 u / \partial y^2$—which is one of the terms which was added to the right-hand side of Euler's equation (2.5) to obtain the Navier–Stokes

equation—and therefore has magnitude

$$\mu\frac{\partial^2 u}{\partial y^2} \sim \mu\frac{U_\infty}{\delta^2},$$

where δ denotes the thickness of the boundary layer. Equating the above then gives δ as

$$\delta \sim \sqrt{\frac{\mu x}{\rho U_\infty}}, \tag{2.7}$$

and hence the boundary layer thickness increases according to the square root of the distance along the surface of a body [76].

This form of the displacement thickness retains its dimensions: both δ and x retain their units of length. However, we can non-dimensionalise by dividing both left- and right-hand sides by some reference length scale (L)—the length of a flat plate, for example, or the chord of an airfoil—to obtain the non-dimensional version of (2.7):

$$\delta^* = \frac{\delta}{L} = \sqrt{\frac{\mu}{\rho L U_\infty}}\sqrt{\frac{x}{L}} = \frac{\sqrt{x^*}}{\sqrt{\mathrm{Re}}}. \tag{2.8}$$

For the rest of this chapter, unless otherwise stated, all asterisked variables will be non-dimensional (of dimension 1), with the non-dimensionalisation having been carried out through the division by some reference dimensional quantity. In particular, we define

$$\mathbf{x} = L\mathbf{x}^*, \quad \mathbf{u} = U_\infty \mathbf{u}^*, \quad t = \frac{L}{U_\infty}t^* \quad \text{and} \quad p = P_\infty + \rho U_\infty^2 p^*, \tag{2.9}$$

where, for our purposes, L is a typical horizontal length scale, U_∞ is the uniform horizontal velocity far upstream and P_∞ is the free-stream pressure.

In equation (2.8), we encounter also the Reynolds number, Re, defined as

$$\mathrm{Re} = \frac{\rho L U_\infty}{\mu},$$

or, in terms of the kinematic viscosity $\nu = \mu/\rho$,

$$\mathrm{Re} = \frac{L U_\infty}{\nu}. \tag{2.10}$$

The Reynolds number can be viewed as a ratio of inertial to viscous forces, since

$$\frac{\text{inertial forces}}{\text{viscous forces}} = \frac{\rho U_\infty^2}{L}\frac{L^2}{\mu U_\infty} = \frac{\rho L U_\infty}{\mu} = \frac{L U_\infty}{\nu},$$

and therefore is, in part, a measure of the importance of viscosity in the flow. This non-dimensionalisation process and the Reynolds number have other, extremely powerful, uses. If we apply (2.9) to the Navier–Stokes equation (2.6), we obtain the non-dimensional form

$$\frac{U_\infty^2}{L}\frac{\partial \mathbf{u}^*}{\partial t^*} + \frac{U_\infty^2}{L}\left(\mathbf{u}^* \cdot \nabla^*\right)\mathbf{u}^* = -\frac{U_\infty^2}{L}\nabla^* p^* + \frac{\nu U_\infty}{L}\nabla^{*2}\mathbf{u}^*,$$

which we can rearrange to obtain

$$\frac{\partial \mathbf{u}^*}{\partial t^*} + (\mathbf{u}^* \cdot \nabla^*)\,\mathbf{u}^* = -\nabla^* p^* + \frac{1}{\mathrm{Re}}\nabla^{*2}\mathbf{u}^*. \tag{2.11}$$

One sees, therefore, that the solution effectively only depends on the non-dimensional parameter Re and so the Reynolds number can be used to define similar flow behaviours: given a particular set-up, although the reference length, velocity or viscosity of two flows might differ, provided that the Reynolds number for both is the same, their solution (in the case of numerical experiments) or visualisation (in the case of physical experiments) will be identical (given the same initial and boundary conditions). This, then, is the secret behind the power of wind tunnels: the flow past small models can be analysed and the results extrapolated to hold for their larger scale counterparts, provided that the viscosity or wind speed is adjusted to ensure that the Reynolds number remains unaltered. The results of a single numerical simulation, too, hold for a whole swathe of the length, velocity and viscosity parameter space: namely those choices of L, U_∞ and ν that combine to give the same Reynolds number as that of the original computation.

Prandtl's idea was to suppose that viscosity is small ("very little friction"), which, from the definition (2.10), results in the Reynolds number being large and, from (2.8), the boundary layer being very thin (and becoming thinner as the Reynolds number increases). In the limit as $\mathrm{Re} \to \infty$, equation (2.11) reduces to Euler's equation

$$\frac{\partial \mathbf{u}^*}{\partial t^*} + (\mathbf{u}^* \cdot \nabla^*)\,\mathbf{u}^* = -\nabla^* p^*,$$

to which we suppose that the solution is known and, because it cannot in general satisfy the no-slip boundary condition, has an associated slip velocity of

$$\mathbf{u}^* = \left(U^*\left(x^*, t^*\right), 0\right),$$

where we have assumed that the flow is two-dimensional. As we have already described, there must then be a thin layer where the $\mathrm{Re}^{-1}\nabla^{*2}\mathbf{u}^*$ term of the non-dimensionalised Navier–Stokes equation (2.11) becomes important, i.e. of an order of magnitude comparable to the others. We first note that the Bernouilli equation (2.1) sets the pressure to be of the same order as the velocity squared; we secondly recall that the continuity equation (2.3) in two dimensions states that

$$\frac{\partial u^*}{\partial x^*} + \frac{\partial v^*}{\partial y^*} = 0,$$

which implies that

$$\mathcal{O}\left(\frac{u^*}{x^*}\right) = \mathcal{O}\left(\frac{v^*}{y^*}\right),$$

where $\mathcal{O}$ denotes the order of magnitude. Then, considering the x^*-momentum equation in the Navier–Stokes equations (2.11),

$$\frac{\partial u^*}{\partial t^*} + u^* \frac{\partial u^*}{\partial x^*} + v^* \frac{\partial u^*}{\partial y^*} = -\frac{\partial p^*}{\partial x^*} + \mathrm{Re}^{-1} \left(\frac{\partial^2 u^*}{\partial x^{*2}} + \frac{\partial^2 u^*}{\partial y^{*2}} \right),$$

we find that both the inertial terms on the left-hand side and the pressure gradient are of order u^{*2}/x^*. The viscous terms are then of order $\mathrm{Re}^{-1}u^*/x^{*2}$ and $\mathrm{Re}^{-1}u^*/y^{*2}$: the latter is the larger, since the height scale of the boundary layer is assumed smaller than the length scale. Then we are looking for a height scale where

$$\mathcal{O}\left(\frac{1}{\mathrm{Re}\, y^{*2}} \right) = \mathcal{O}\left(\frac{u^*}{x^*} \right).$$

The velocity in the boundary layer must match with the inviscid slip velocity, which is $\mathcal{O}(1)$, as is the length scale x^*, both having been non-dimensionalised. Thus we obtain the scaling law for the boundary layer, with

$$y^* \sim \mathrm{Re}^{-\frac{1}{2}}$$

and we can therefore define a new $\mathcal{O}(1)$ variable, Y^*, whereby

$$y^* = \mathrm{Re}^{-\frac{1}{2}} Y^*. \tag{2.12}$$

Note that in (2.8) we had already derived this result: in the above we confirm it by estimating directly the magnitude of each term in the Navier–Stokes equations.

The continuity equation then implies that the normal velocity v^* is of the same order of magnitude as the boundary layer height scale. The y^*-momentum equation in the Navier–Stokes equations reads

$$\frac{\partial v^*}{\partial t^*} + u^* \frac{\partial v^*}{\partial x^*} + v^* \frac{\partial v^*}{\partial y^*} = -\frac{\partial p^*}{\partial y^*} + \mathrm{Re}^{-1} \left(\frac{\partial^2 v^*}{\partial x^{*2}} + \frac{\partial^2 v^*}{\partial y^{*2}} \right):$$

in the boundary layer, the inertial terms on the left-hand side are of $\mathcal{O}(\mathrm{Re}^{-1/2})$; the pressure derivative is of $\mathcal{O}(\mathrm{Re}^{1/2})$; and the viscous terms are of $\mathcal{O}(\mathrm{Re}^{-3/2})$ and $\mathcal{O}(\mathrm{Re}^{-1/2})$. The dominant term is therefore that involving the pressure and the y^*-momentum equation is reduced to the statement that the pressure in the boundary layer is independent of the normal coordinate. This, along with Euler's equation and the requirement of matching between the inviscid flow and boundary layer, implies that the pressure gradient is

$$-\frac{\partial p^*}{\partial x^*}(x^*, t^*) = \frac{\partial U^*}{\partial t^*} + U^* \frac{\partial U^*}{\partial x^*}$$

and, noting that we have found that v^* is of order $\mathrm{Re}^{-1/2}$ (we have avoided introducing a new scaled variable in the hope of maintaining greater clarity), we obtain Prandtl's

boundary layer equations

$$\frac{\partial u^*}{\partial x^*} + \frac{\partial v^*}{\partial Y^*} = 0, \tag{2.13a}$$

$$\frac{\partial u^*}{\partial t^*} + u^*\frac{\partial u^*}{\partial x^*} + v^*\frac{\partial u^*}{\partial Y^*} = \frac{\partial U^*}{\partial t^*} + U^*\frac{\partial U^*}{\partial x^*} + \frac{\partial^2 u^*}{\partial Y^{*2}}, \tag{2.13b}$$

to be solved subject to the boundary conditions

$$u^* = v^* = 0 \quad \text{on} \quad Y^* = 0, \tag{2.13c}$$

$$u^* \to U^*(x^*, t^*) \quad \text{as} \quad Y^* \to \infty, \tag{2.13d}$$

along with some upstream matching conditions and, for unsteady flows, an initial condition. Here, the condition (2.13c) is the necessary no-slip boundary condition and (2.13d) is the requirement that the boundary layer flow match with the inviscid solution at the top of the boundary layer.

At first sight, it is perhaps unclear why this is an improvement to the Navier–Stokes equations: the boundary layer equations remain resolutely nonlinear. However, the Navier–Stokes equations are elliptic in nature, which means that there are both upstream and downstream influences on the flow at any given point and thus the whole flow field must be solved for simultaneously. The removal of the $\partial^2 u^*/\partial x^{*2}$ term in Prandtl's boundary layer equations, on the other hand, makes them parabolic: the flow at a particular point depends only on the upstream history. Hence the solution can be solved for numerically by a simple downstream marching, without needing to consider what happens downstream of the point being considered.

The system of equations (2.13), of course, serves to determine only the leading order term in the viscous boundary layer, which is affected by the need to match with the leading order inviscid solution. One can then continue the expansion by considering perturbations to the leading order inviscid velocities and pressure. The leading order boundary layer solution generates a correction, at $\mathcal{O}(\mathrm{Re}^{-1/2})$, to the inviscid flow, which then drives the second order viscous flow, and so on. This iterative process works without a problem, unless there is a singularity in the flow (which we will see in chapter 4 can occur at the separation point) or a need for a strong interaction between the viscous and inviscid flow, such as that which occurs at the trailing edge of a flat plate at 0° angle of attack, or along walls with considerable deformations (dents or humps), or in the presence of a shock wave [76].

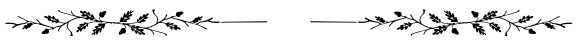

Prandtl's paper and ideas, in the years that followed its publication, remained largely unknown outside the hotpot of research that was sizzling away at the University of

Göttingen[5]—the fifth edition of Lamb's *Hydrodynamics*, published in 1924, contained only a single paragraph on Prandtl's boundary layer concept—and it wasn't until von Kármán derived the integral form of the boundary layer equations in 1921, which had direct and obvious applications to the field of engineering and aerodynamics in particular, that the world began to sit up and take notice [4]. Once it did, however, there was no looking back: engineers and mathematicians now had a language in which to communicate and together they ran enthusiastically through the gateway towards a more comprehensive understanding of fluid dynamics, with Sydney Goldstein proclaiming the wonders of Prandtl's 1905 paper.

2.3 The hitch: flows over humps

There was, however, a problem: Prandtl's beautiful structure of an outer inviscid flow setting the pressure gradient that drives a viscous boundary layer breaks down when separation occurs (see chapter 4). A singularity appears in classical boundary layer theory, which fails to incorporate the necessary interaction between the viscous and inviscid flow regimes as the separation point is approached and cannot predict the lift-off of the boundary layer from the wall. What is more, separation sets in train a region of reversed flow and the nice, simple, parabolic equations of Prandtl are unable to capture the resulting upstream influence.

Separation can occur due to the presence of a hump on the wall; and the study of the effect of such an obstacle on the flow, along with the development of relevant theories based on Prandtl's boundary layer idea, occupied the attention of many researchers in the decades that spanned the 1950s to 1980s: by the end, a comprehensive mathematical description of the flow past humps of various sizes was achieved [84], excellently outlined in Rothmayer & Smith (1998) [68]. The issue at hand was to determine the relevant length and height scales of the hump that would provoke separation, as functions of the Reynolds number (see figure 2.3), as well as the governing equations for each regime. In this section, we re-derive these scalings and highlight those that will be of interest to us in later chapters of this thesis.

2.3.1 A medley of humps

Steady flow along an infinite flat plate, with a constant free-stream velocity, develops a Blasius boundary layer, named after Paul Blasius (1883–1970), who was a student of Prandtl and first proposed the solution to such a scenario. Suppose now that a hump is placed along this flat plate, as shown in figure 2.3, and that the hump has a length scale of ℓ and a height scale of Δ, both of which are small and are some negative power

[5]Indeed, even today, the English translation of *Über Flüsigkeitsbewegung bei sehr kleiner Reibung* (as well as the original German text) remains very difficult to find. It does exist on the internet, but it is camouflaged behind a NACA technical report and I am indebted to Professor Arthur Veldman for providing me with a copy.

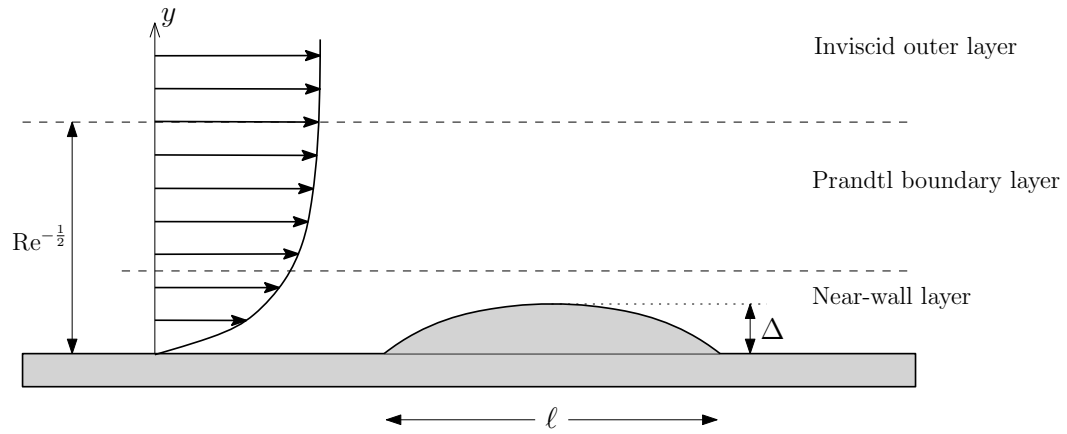

FIGURE 2.3: Blasius boundary layer flow along a flat plate encountering a hump of length scale ℓ and height scale Δ, with both ℓ and Δ being some power of the Reynolds number. The hump gives rise to a near-wall layer within Prandtl's boundary layer, the height of which depends upon the hump's size.

of the Reynolds number, which is taken to be large. The shape of the hump itself is not overly important in discussing separation: rather, it is its size relative to the boundary layer thickness, along with the Reynolds number, that are the key factors [68].

As we are still considering boundary layer flow, Prandtl's equations hold and thus the flow, at least upstream of the hump, can be described by

$$\frac{\partial u}{\partial x} + \frac{\partial v}{\partial Y} = 0, \tag{2.14a}$$

$$\frac{\partial u}{\partial t} + u\frac{\partial u}{\partial x} + v\frac{\partial u}{\partial Y} = -\frac{\partial p}{\partial x} + \frac{\partial^2 u}{\partial Y^2}, \tag{2.14b}$$

where, when compared to the version given in (2.13), we have removed the asterisks[6] and explicitly kept the pressure gradient, rather than representing it in terms of the slip velocity at the top of the boundary layer. The presence of the hump gives rise to a near-wall layer within Prandtl's original boundary layer, in which the flow is driven by the shear, $\partial u/\partial y$, rather than the inviscid pressure gradient. Indeed, the pressure can now be considered as an unknown in the problem and will be related to the slip velocity at the interface of this inner layer with the main boundary layer, as we shall see in forthcoming chapters.

We are now interested in the development of the flow over the length scale ℓ of the obstacle. If the origin is centred at the hump, then, with the inertial terms in the momentum equation (2.14b) of $\mathcal{O}(u^2/x)$ and the viscous term of $\mathcal{O}(u/Y^2)$, inertia will dominate viscosity if x is small (and Y is fixed). Hence we return once more to Euler's equation and obtain a slip velocity (traditionally denoted by A) that acts at some order of the Reynolds number, dependent on the scales of the obstacle. We therefore need a further viscous sublayer within the boundary layer that serves to satisfy the no-slip boundary condition at the surface of the wall. In particular, we want to find the scalings

[6]Henceforth, all variables will be assumed to be non-dimensional, unless otherwise stated.

such that all the terms in equation (2.14b) balance:

$$u\frac{\partial u}{\partial x} \sim \frac{\partial p}{\partial x} \sim \frac{\partial^2 u}{\partial Y^2}.$$

Short humps

Near the wall, the steady oncoming flow can be expanded using a Taylor series as

$$u = U_0 \sim \lambda Y + \mathcal{O}\left(Y^2\right),$$

where

$$\lambda = \left.\frac{\partial U_0}{\partial Y}\right|_{Y=0} \tag{2.15}$$

is the incoming wall shear and the no-slip boundary condition has been applied. Hence u is of order Y. Furthermore, for separation, we want the viscous sublayer to feel the influence of the hump, which has a height scale Δ, and thus we introduce a new normal coordinate $\hat{y}$, of $\mathcal{O}(1)$, which is given by

$$y = \Delta\hat{y},$$

or, in terms of the boundary layer coordinate Y,

$$Y = \mathrm{Re}^{\frac{1}{2}}\Delta\hat{y}.$$

For the inertial and viscous terms to match, we require

$$\frac{u^2}{x} \sim \frac{u}{Y^2} \quad \Longrightarrow \quad \frac{\mathrm{Re}\,\Delta^2}{\ell} \sim \frac{\mathrm{Re}^{\frac{1}{2}}\Delta}{\mathrm{Re}\Delta^2},$$

which gives a relationship between the length and height scales of the hump:

$$\Delta \sim \mathrm{Re}^{-\frac{1}{2}}\ell^{\frac{1}{3}}. \tag{2.16}$$

The pressure gradient then wants to match with the inertial and viscous terms, which sets $p \sim u^2$ and so

$$p \sim \ell^{\frac{2}{3}}.$$

The scaling of the normal velocity is derived from the continuity equation (2.14a) as

$$v \sim \frac{uY}{x} \sim \ell^{-\frac{1}{3}}.$$

Note that a natural time scaling, $t \sim \ell^{2/3}$, also appears for the cases where the flow becomes unsteady. Hence in the viscous sublayer we can define the following coordinate

system and scaled variables:

$$(x, y, t) = \left(\ell\hat{x}, \mathrm{Re}^{-\frac{1}{2}}\ell^{\frac{1}{3}}\hat{y}, \ell^{\frac{2}{3}}\hat{t}\right), \tag{2.17a}$$

$$(u, v, p) = \left(\ell^{\frac{1}{3}}\hat{u}, \mathrm{Re}^{-\frac{1}{2}}\ell^{-\frac{1}{3}}\hat{v}, \ell^{\frac{2}{3}}\hat{p}\right), \tag{2.17b}$$

where, in the scaling for the normal velocity, we recall that following our discussion of §2.2, the term v in equation (2.14) had already been scaled relative to $\mathrm{Re}^{-1/2}$.

The question now turns to how these scalings influence the full Navier–Stokes equations (2.6). The streamwise momentum equation with the scalings introduced in equation (2.17) becomes

$$\ell^{-\frac{1}{3}}\frac{\partial\hat{u}}{\partial\hat{t}} + \ell^{-\frac{1}{3}}\hat{u}\frac{\partial\hat{u}}{\partial\hat{x}} + \ell^{-\frac{1}{3}}\hat{v}\frac{\partial\hat{u}}{\partial\hat{y}} = -\ell^{-\frac{1}{3}}\frac{\partial\hat{p}}{\partial\hat{x}} + \mathrm{Re}^{-1}\left(\ell^{-\frac{5}{3}}\frac{\partial^2\hat{u}}{\partial\hat{x}^2} + \mathrm{Re}\,\ell^{-\frac{1}{3}}\frac{\partial^2\hat{u}}{\partial\hat{y}^2}\right).$$

The success of Prandtl's boundary layer theory lay in the removal of the $\partial^2\hat{u}/\partial\hat{x}^2$ term and, from the above, we see that the full Navier–Stokes equations are recovered when

$$\mathrm{Re}^{-1}\ell^{-\frac{5}{3}} \sim \ell^{-\frac{1}{3}} \quad \Longrightarrow \quad \ell \sim \mathrm{Re}^{-\frac{3}{4}}.$$

For obstacle length scales much smaller than this, we obtain Stokes flow, with $\partial^2\hat{u}/\partial\hat{x}^2$ dominating. However, we restrict our attention to those cases where

$$\ell \gg \mathrm{Re}^{-\frac{3}{4}}. \tag{2.18}$$

Long humps

The above analysis gives rise to the governing *condensed flow equations*,

$$\frac{\partial\hat{u}}{\partial\hat{x}} + \frac{\partial\hat{v}}{\partial\hat{y}} = 0, \tag{2.19a}$$

$$\frac{\partial\hat{u}}{\partial\hat{t}} + \hat{u}\frac{\partial\hat{u}}{\partial\hat{x}} + \hat{v}\frac{\partial\hat{u}}{\partial\hat{y}} = -\frac{\partial\hat{p}}{\partial\hat{x}}\left(\hat{x}, \hat{t}\right) + \frac{\partial^2\hat{u}}{\partial\hat{y}^2}, \tag{2.19b}$$

to be solved subject to the no-slip condition at the wall and the requirement that, to leading order at the top of the viscous sublayer,

$$\hat{u} \to \lambda\hat{y} \quad \text{as } \hat{y} \to \infty. \tag{2.19c}$$

As mentioned above, however, there is a slip velocity $A(\hat{x}, \hat{t})$ at the top of the sublayer, which is acting at some order Re^{γ} that is dependent on the length scale of the obstacle. Short humps are defined such that this slip velocity acts at higher order than that set by the oncoming shear. For humps that have a length of $\mathcal{O}(\mathrm{Re}^{-3/8})$, however, both the shear and slip velocity become of the same order of magnitude [68] and we recover the scalings of triple deck theory, first described by Neiland (1969) [55], Stewartson & Williams (1969) [91] and Messiter (1970) [53]. Humps on the length scale of the triple

deck will not be considered in this thesis but, briefly, the streamwise velocity in the viscous sublayer (known as the 'lower deck'), which has a height of $\mathcal{O}(\mathrm{Re}^{-5/8})$, tends to

$$\lambda\,(\hat{y}+A) \quad \text{as } \hat{y}\to\infty;$$

and the displacement A interacts, via the boundary layer of usual height $\mathcal{O}(\mathrm{Re}^{-1/2})$ (the 'main deck'), with an 'upper deck' of height scale $\mathrm{Re}^{-3/8}$ that extends into the inviscid flow field, setting a relationship between the pressure and displacement.

A similar structure is set up for longer humps, which are defined to be those that have a length scale greater than that of the triple deck, i.e.

$$\ell \gg \mathrm{Re}^{-\frac{3}{8}}. \tag{2.20}$$

In these cases, the pressure perturbation in the inviscid outer layer becomes of the same order as the obstacle slope, Δ/ℓ [84], and thus matching the pressure gradient and inertial terms in the viscous sublayer (2.14b), with the scaling on u being $u\sim\ell^{1/3}$ as before, gives

$$u^2\sim p \quad\Longrightarrow\quad \ell^{\frac{2}{3}}\sim\frac{\Delta}{\ell} \quad\Longrightarrow\quad \Delta\sim\ell^{\frac{5}{3}}. \tag{2.21}$$

A more detailed derivation of the scaling laws for these longer humps awaits us in chapter 6, where we make use of the framework of marginal separation theory, and so we postpone any further discussion until then.

In summary, therefore, we can classify a hump in the flow as being either 'short' or 'long', with the minimum obstacle height scale required for separation being of order $\mathrm{Re}^{-1/2}\ell^{1/3}$ and $\ell^{5/3}$ respectively; and triple deck theory sits comfortably at the interface of the two regimes. For height scales less than this minimum, a linearised approach, expanding about the hump height, can be used and the flow remains attached. Figure 2.4 summarises the discussion given in this section: our voyage will take us from short bumps lying in the range $\mathrm{Re}^{-3/4}\ll\ell\ll\mathrm{Re}^{-3/8}$ (chapters 3, which will make use of a linearised approach, and 5, which will not) to longer humps with $\ell\gg\mathrm{Re}^{-3/8}$ (chapter 6).

2.3.2 Simplifying matters: the Prandtl transposition

The no-slip condition sets the velocity at the wall to be zero, which, in the presence of a hump, no longer has the simple form $\hat{y}=0$. Rather, if we suppose that, in the notation of this section, we set the origin of the hump(s) at $\hat{x}=0$, with a flat plate parallel to the x-axis upstream, then the wall is given by

$$\hat{y}=\begin{cases}0 & \text{if } \hat{x}<0,\\ hF\left(\hat{x},\hat{t}\right) & \text{if } \hat{x}\geq 0,\end{cases}$$

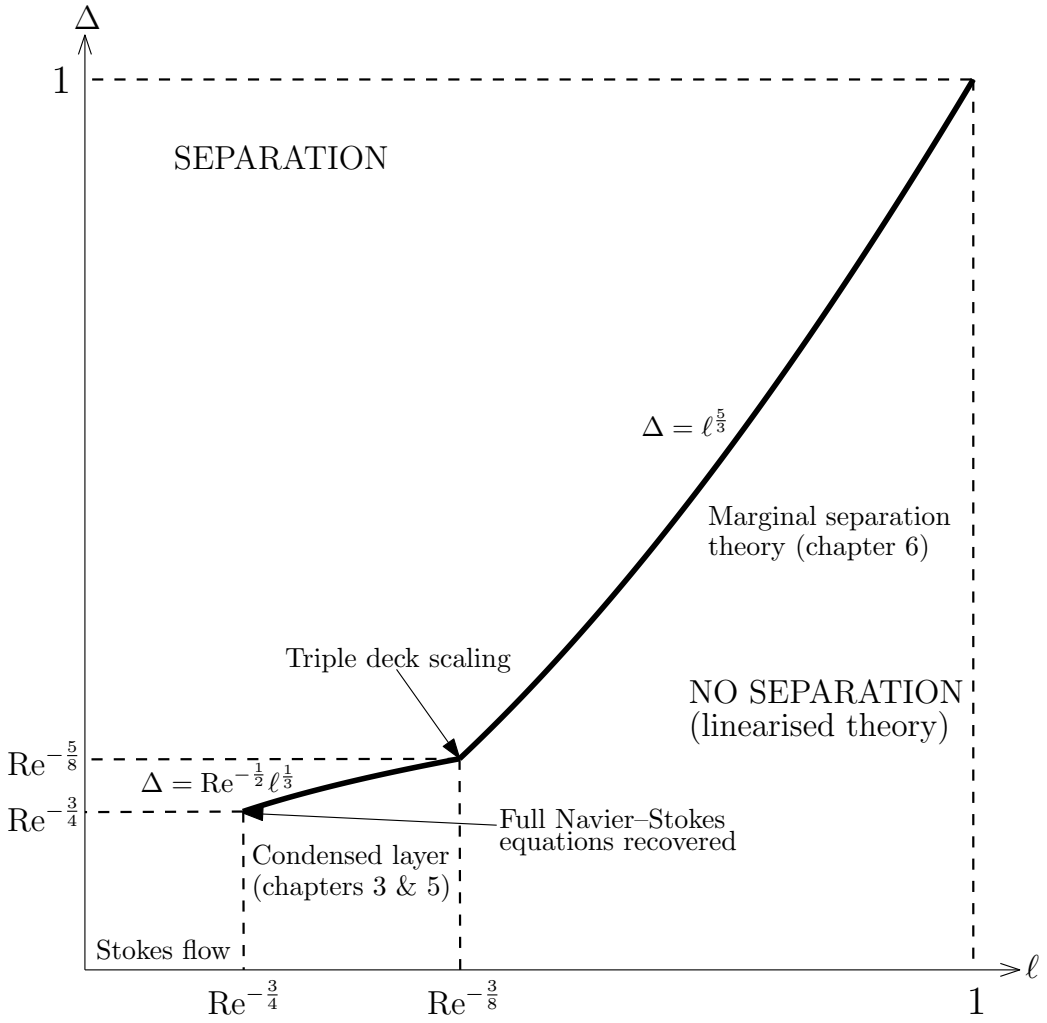

FIGURE 2.4: An overview of the hump length (ℓ) and height (Δ) scalings given in §2.3, with short/long humps being those having length less/greater than that of triple deck theory. The solid line indicates the relationship between length and height required for separation to first occur: obstacle sizes lying above this line can give rise to large regions of separated flow, while sizes below it have fully attached flow and the solution can be approached by linearisation about the small height parameter. An indication of which humps/roughnesses will be looked at in this thesis is also given, along with the relevant chapter.

where F is an $\mathcal{O}(1)$ function defining the actual shape of the hump, to be prescribed later, and h is its non-dimensional height. Then, for a time-dependent hump, the boundary conditions in the viscous sublayer are

$$\hat{u} = 0, \quad \hat{v} = h\left(\hat{u}\frac{\partial F}{\partial \hat{x}} + \frac{\partial F}{\partial \hat{t}}\right) \quad \text{on } \hat{y} = hF\left(\hat{x}, \hat{t}\right), \ \hat{x} \geq 0, \tag{2.22a}$$

$$\hat{u} = \lambda\hat{y}, \quad \hat{v} = 0, \quad \hat{p} = 0 \quad \text{when } \hat{x} < 0, \tag{2.22b}$$

$$\hat{u} \to \lambda\hat{y} \quad \text{as } \hat{y} \to \infty. \tag{2.22c}$$

The first condition (2.22a) is the requirement of no-slip on the surface of the hump, derived from the kinematic condition; the second (2.22b) represents matching with the oncoming boundary layer profile; and the third (2.22c) is the leading order matching condition as we move out of the viscous sublayer, as given in equation (2.19c).

The goal is to convert condition (2.22a) to the simpler form $\tilde{u} = \tilde{v} = 0$ on $\tilde{y} = 0$. This can be achieved using the Prandtl transposition, defined as

$$\tilde{x} = \hat{x}, \quad \tilde{y} = \hat{y} - hF\left(\tilde{x}, \tilde{t}\right), \quad \tilde{t} = \hat{t}, \tag{2.23a}$$

with the new flow variables

$$\tilde{u} = \hat{u}, \quad \tilde{v} = \hat{v} - h\tilde{u}\frac{\partial F}{\partial \tilde{x}} - h\frac{\partial F}{\partial \tilde{t}}, \quad \tilde{p} = \hat{p}, \tag{2.23b}$$

which has the happy added advantage that the governing boundary layer equations (2.19a) and (2.19b) remain unchanged. We arrive, therefore, at the system

$$\frac{\partial \tilde{u}}{\partial \tilde{x}} + \frac{\partial \tilde{v}}{\partial \tilde{y}} = 0, \tag{2.24a}$$

$$\frac{\partial \tilde{u}}{\partial \tilde{t}} + \tilde{u}\frac{\partial \tilde{u}}{\partial \tilde{x}} + \tilde{v}\frac{\partial \tilde{u}}{\partial \tilde{y}} = -\frac{\partial \tilde{p}}{\partial \tilde{x}}\left(\tilde{x}, \tilde{t}\right) + \frac{\partial^2 \tilde{u}}{\partial \tilde{y}^2}, \tag{2.24b}$$

with

$$\tilde{u} = \tilde{v} = 0 \quad \text{on } \tilde{y} = 0, \ \tilde{x} \geq 0, \tag{2.24c}$$

$$\tilde{u} = \lambda\left(\tilde{y} + hF\right), \quad \tilde{v} = 0, \quad \tilde{p} = 0, \quad \text{when } x < 0, \tag{2.24d}$$

$$\tilde{u} \to \lambda\left(\tilde{y} + hF\right) \quad \text{as } \tilde{y} \to \infty, \tag{2.24e}$$

which is the system that will concern us as we move on to chapter 3.

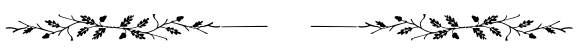

And so here we are. A patchwork of green, brown and golden fields thrown onto mountain slopes; leaves glinting in the early morning sunlight; the cacti shining. All around is the musky perfume of damp, fertile earth, the soothing wafts of pine and eucalyptus and freshly cut hay, arranged in mounds that dot the landscape. A sheep lifts its head

from sleep's embrace and stares warily at you. The air is full of the sweetly bitter hue of fire and incense, and pregnant with the promise of coffee and a warm welcome. It would be so easy to stay. But your boots are on and the dawn air stings and up ahead is an idea, and she's walking in a big blue sky.

3

Setting forth: the mean flow correction

"We should go forth on the shortest walk, perchance, in the spirit of undying adventure, never to return; prepared to send back our embalmed hearts only, as relics to our desolate kingdoms."

Henry David Thoreau, *Walking*

If the pressure gradient is key to driving a laminar boundary layer to separation, as we saw in chapter 1, then perhaps it makes sense to begin by focusing on what happens to this pressure as flow goes over an array of dynamic roughness elements. The work of Rothmayer & Huebsch (2011) [66] highlighted the possibility that such an array would give rise to Reynolds stress-like terms; due to these, airfoils inclined at angles of attack that would normally be expected to provoke aerodynamic stall were able to maintain attached flow.

Our aim in this chapter is maybe more humble: our array of short roughnesses—where we use the word 'short' in the sense in which it was defined in chapter 2—will be small in height, so that they lie under the separation curve of figure 2.4 and we are able to linearise the velocities and pressure using the height of the roughness as the expansion parameter. We search then for the effect of the roughness array on the pressure and determine how it modifies the behaviour of the mean flow: the time-averaged properties of the fluid as it goes over the obstacle field. Importantly, as we stroll through the trees under a canopy of foliage and birdsong, we seek to develop and establish the mathematical techniques on which we will rely as we climb the exposed scree slopes of the future.

Or perhaps, in accordance with the philosophy of Henry David Thoreau (1817–62), we should merely set out and immerse ourselves, fully and unquestioning, in a "wildness whose glance no civilisation can endure", rather than being like the "worldly miser [...] looking after his bounds, while heaven had taken place around him, and he did not see the angels going to and fro, but was looking for an old post-hole in the midst of paradise" [95].

3.1 Our surroundings

Rothmayer & Huebsch (2011) [66] considered a three-dimensional array of roughness elements, each with a length scale of $\mathcal{O}(\mathrm{Re}^{-1/2})$ and height scale of $\mathcal{O}(\mathrm{Re}^{-1})$. According to our nomenclature, this classifies the roughnesses as being 'short' and, with such a height scale, they lie below the dividing line of separation drawn in figure 2.4 (the critical height scale for a length of order $\mathrm{Re}^{-1/2}$ would be of order $\mathrm{Re}^{-2/3}$). In their case, however, separation is due to the angle of attack of an airfoil augmenting the adverse pressure gradients that follow the leading edge; and the aim was to determine whether the array of roughnesses was able to increase the angle of attack at which the skin friction goes to zero. The use of multiple flow scales—the array length was taken as $\mathcal{O}(1)$—assists in the generation of Reynolds stresses within the viscous sublayer (which has a height scale of order Re^{-1}): these are usually the result of the Reynolds averaging of the governing equations in turbulent flows [87], but here are driven by the velocity perturbations caused by the dynamic roughness elements.

In the work of this chapter, we scale out the Reynolds number from the non-dimensional Navier–Stokes equations by choosing the roughness scalings such that the condensed layer equations of (2.24) are valid. Thus the roughness length scale lies within the range

$$\mathrm{Re}^{-\frac{3}{4}} \ll \ell \ll \mathrm{Re}^{-\frac{3}{8}};$$

and the height scale obeys $\Delta \sim \ell^{1/3}$ and so lies in the range

$$\mathrm{Re}^{-\frac{1}{4}} \ll \Delta \ll \mathrm{Re}^{-\frac{1}{8}}.$$

We find ourselves, therefore, in the realm of the short roughness, as depicted in figure 2.4, and the results presented in this chapter hold for all roughnesses satisfying the above length and height scales.

The array of roughnesses sits on an otherwise flat plate, oriented parallel to the oncoming flow, and is given by the equation

$$y = hF\left(x, \bar{x}, t\right), \quad x, \bar{x} \geq 0, \tag{3.1}$$

where the trappings of chapter 2 and equation (2.24) have been removed: y is the non-dimensional normal coordinate in the viscous near-wall layer (see figure 2.3), which has been scaled relative to $\mathrm{Re}^{-1/2}\ell^{\frac{1}{3}}$; t is the non-dimensional scaled time (relative to $\ell^{2/3}$); and x is the non-dimensional streamwise (horizontal) coordinate, scaled relative to ℓ. There are, however, two horizontal length scales remaining in the problem: the first is that over a single roughness element; the second envelops the entire roughness array, which in general could be much longer than the length of a lone roughness. The former, shorter, coordinate is then of $\mathcal{O}(1)$ and we denote it by x; the latter, longer, coordinate

we take to be of order h^{-1}, and so

$$x = h^{-1}\bar{x}, \quad \bar{x} \sim 1, \tag{3.2}$$

where h is the same as that appearing as a coefficient in equation (3.1).

This h is the non-dimensional height of the roughness element and is taken to be small (hence h^{-1} is large). This implies that we move below the line of figure 2.4, the flow remains attached as it moves over the roughness and we can expand the velocities and pressure as

$$u = u_0(x, \bar{x}, y, t) + hu_1(x, \bar{x}, y, t) + h^2 u_2(x, \bar{x}, y, t) + \cdots, \tag{3.3a}$$

$$v = v_0(x, \bar{x}, y, t) + hv_1(x, \bar{x}, y, t) + h^2 v_2(x, \bar{x}, y, t) + \cdots, \tag{3.3b}$$

$$p = p_0(x, \bar{x}, t) + hp_1(x, \bar{x}, t) + h^2 p_2(x, \bar{x}, t) + \cdots. \tag{3.3c}$$

The function F is then the $\mathcal{O}(1)$ function that encodes the shape of an individual roughness, the whole array, and the dynamic motion of the surface perturbations. In §§3.2–3.4, we will consider what we shall call 'dynamic blips', these being roughness elements that are allowed to be both positive ($y \geq 0$) and negative ($y < 0$) over a cycle of oscillation; we then delay the study of proper dynamic roughness, as investigated in past numerical and experimental work (see §1.2), to §3.5. This first type of elements, the dynamic blips, can be represented by

$$F(x, \bar{x}, t) = 4G(\bar{x}) \sin(\alpha x) \sin(\omega t) = G(\bar{x}) \left(-E + \tilde{E} - E^{-1} + \tilde{E}^{-1}\right), \tag{3.4a}$$

where

$$E = \exp\left[\mathrm{i}\alpha(x + ct)\right] \quad \text{and} \quad \tilde{E} = \exp\left[\mathrm{i}\alpha(x - ct)\right] \tag{3.4b}$$

are complex exponentials that will simplify the analysis that is to follow. Here, α and c are the wavenumber and wave speed respectively, with $\omega = \alpha c$ the frequency of oscillation. Meanwhile, the function G, dependent only on the long coordinate $\bar{x}$, allows us to vary the maximum amplitude of the blips as we move along the array, as depicted in figure 3.1.

The governing system of equations is then adapted from the condensed flow equations (2.24) that closed chapter 2, with a slight modification to account for the two streamwise length scales:

$$\frac{\partial u}{\partial x} + h\frac{\partial u}{\partial \bar{x}} + \frac{\partial v}{\partial y} = 0, \tag{3.5a}$$

$$\frac{\partial u}{\partial t} + u\frac{\partial u}{\partial x} + hu\frac{\partial u}{\partial \bar{x}} + v\frac{\partial u}{\partial y} = -\frac{\partial p}{\partial x} - h\frac{\partial p}{\partial \bar{x}} + \frac{\partial^2 u}{\partial y^2}, \tag{3.5b}$$

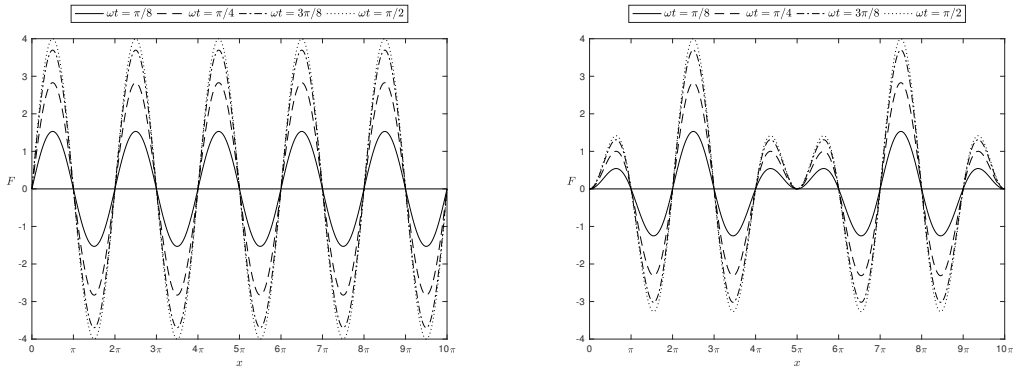

(A) $G(\bar{x}) = 1$ (B) $G(\bar{x}) = \sin \bar{x}$

FIGURE 3.1: Wall shape F for different functions $G(\bar{x})$, where $h = 0.1$ and $\alpha = \omega = 1$; the wall shape at different times—$\omega t = \pi/8$ (solid line), $\pi/4$ (dashed), $3\pi/8$ (dot–dashed) and $\pi/2$ (dotted)—is shown. Over a cycle of oscillation, the perturbations to the flat wall are allowed to be both positive and negative, creating a time dependent array of dips and humps. The function G allows one to change the maximum amplitude of oscillation of each blip: we focus in this chapter on the two forms depicted here.

subject to

$$u = v = 0 \quad \text{on } y = 0, \tag{3.5c}$$

$$u = \lambda y, \quad v = 0, \quad p = 0 \quad \text{when } x < 0, \tag{3.5d}$$

$$u \to \lambda (y + hF) \quad \text{as } y \to \infty. \tag{3.5e}$$

3.1.1 Peering back through the trees

Amidst the plethora of scalings and expansions that have been introduced in this and the preceeding chapter, we have, perhaps, immersed ourselves so totally in the dense forest of mathematics that we have lost sight of the dimensional counterparts of our various parameters and coordinates: values that are of most interest to the practical engineer. Table 3.1 is based on the data reported in the experiments of Grager et al. (2012) [33], which aimed to recreate as much as possible the numerical study of Huebsch et al. (2012) [41]. Four incoming flow speeds were studied, giving rise to four Reynolds numbers, based on this speed and the 0.15 m length of the airfoil chord.

With asterisked quantities once more referring to non-dimensional parameters—and corresponding to the space and time coordinates of system (3.5) and the whole of this chapter—the relationship between the dimensional (no asterisk) and non-dimensional versions is found by combining equations (2.9) and (2.17):

$$x = L\ell x^*, \quad y = \mathrm{Re}^{-\frac{1}{2}} L\ell^{\frac{1}{3}} y^*, \quad t = \frac{L}{U_\infty} \ell^{\frac{2}{3}} t^*.$$

The vertical y coordinate denotes also the height scale of the roughness element, which is of the same order as the sublayer height; and the frequency scale can be obtained by

U_∞ ($\mathrm{m\,s^{-1}}$)	Re	Width range (mm)	Height range (µm)	Frequency range (Hz)
2.7	25 000	0.075–3.36	75–268	226–2846
5.3	49 000	0.046–2.61	46–176	526–7821
7.8	73 000	0.033–2.25	34–137	855–14 050
10.4	97 000	0.027–2.02	27–115	1224–21 594

TABLE 3.1: Roughness dimensions and oscillation frequencies covered by the condensed flow theory and scalings of this chapter, at various Reynolds numbers, taken from the experimental work of Grager et al. (2012) [33].

recalling that it is the reciprocal of the time scaling, thus

$$\omega = \frac{U_\infty}{L}\ell^{-\frac{2}{3}}\omega^*.$$

The roughness elements used in Grager et al. (2012) had a diameter of 3 mm, a maximum height of 230 µm and oscillation frequency of 30–90 Hz. From table 3.1, therefore, at the lower Reynolds number of 25 000, our condensed flow theory encompasses the tested roughness diameter and height; with both the valid widths and heights decreasing with increasing Reynolds number, although remaining, at the upper end of the allowable range, within the correct order of magnitude. However, the frequency range associated with a scaling of $t \sim LU_\infty^{-1}\ell^{2/3}$ is far greater than the frequencies of Grager et al.—extending into the kilohertz, they are much larger than those that are likely to be achievable in practice.

Nevertheless, in the spirit of academic enquiry, we venture deeper into the mathematics.

3.2 The winding trail

We wish to solve for the terms in the asymptotic expansion of the horizontal (u) and vertical (v) velocities, as well as the pressure (p)—see equation (3.3)—by substituting the expansions into the governing system of equations (3.5) and then equating the terms multiplying given powers of h. In the subsections below, we follow the trail from $\mathcal{O}(1)$ to $\mathcal{O}(h^2)$, where we will suddenly lose it.

3.2.1 To the first bend

At $\mathcal{O}(1)$, the system of equations to solve is simply

$$\frac{\partial u_0}{\partial x} + \frac{\partial v_0}{\partial y} = 0, \tag{3.6a}$$

$$\frac{\partial u_0}{\partial t} + u_0\frac{\partial u_0}{\partial x} + v_0\frac{\partial u_0}{\partial y} = -\frac{\partial p_0}{\partial x} + \frac{\partial^2 u_0}{\partial y^2}, \tag{3.6b}$$

subject to

$$u_0 = v_0 = 0 \quad \text{on } y = 0, \tag{3.6c}$$

$$u_0 = \lambda y, \quad v_0 = p_0 = 0 \quad \text{when } x < 0, \tag{3.6d}$$

$$u_0 \to \lambda y \quad \text{as } y \to \infty, \tag{3.6e}$$

which has the straightforward solution

$$u_0 = \lambda y, \quad v_0 = 0, \quad p_0 = 0. \tag{3.7}$$

This is indeed as expected: to leading order, we obtain the incoming shear flow and the dynamic blips, being of small amplitude h, serve merely to perturb this solution at a higher order.

3.2.2 To the second bend

Things begin to get interesting at $\mathcal{O}(h)$, where the influence of the oscillating blips begins to be felt through the imposition of the matching condition at infinity (equivalent, due to the use of the Prandtl transposition described in §2.3.2, to the imposition of no slip at the surface of the dynamic blips). The governing system, substituting in the solution of (3.7), is

$$\frac{\partial u_1}{\partial x} + \frac{\partial v_1}{\partial y} = 0, \tag{3.8a}$$

$$\frac{\partial u_1}{\partial t} + \lambda y \frac{\partial u_1}{\partial x} + \lambda v_1 = -\frac{\partial p_1}{\partial x} + \frac{\partial^2 u_1}{\partial y^2}, \tag{3.8b}$$

with the boundary and matching conditions

$$u_1 = v_1 = 0 \quad \text{on } y = 0, \tag{3.8c}$$

$$u_1 = v_1 = p_1 = 0 \quad \text{when } x < 0, \tag{3.8d}$$

$$u_1 \to \lambda F \quad \text{as } y \to \infty. \tag{3.8e}$$

Given the form of F in equation (3.4), it makes sense to decompose our solution to u_1, v_1 and p_1 as

$$u_1(x, \bar{x}, y, t) = -u_{11}(\bar{x}, y)\, E + u_{12}(\bar{x}, y)\, \tilde{E} - u_{11}^*(\bar{x}, y)\, E^{-1} + u_{12}^*(\bar{x}, y)\, \tilde{E}^{-1}, \tag{3.9a}$$

$$v_1(x, \bar{x}, y, t) = -v_{11}(\bar{x}, y)\, E + v_{12}(\bar{x}, y)\, \tilde{E} - v_{11}^*(\bar{x}, y)\, E^{-1} + v_{12}^*(\bar{x}, y)\, \tilde{E}^{-1}, \tag{3.9b}$$

$$p_1(x, \bar{x}, t) = -p_{11}(\bar{x})\, E + p_{12}(\bar{x})\, \tilde{E} - p_{11}^*(\bar{x})\, E^{-1} + p_{12}^*(\bar{x})\, \tilde{E}^{-1}, \tag{3.9c}$$

where the asterisk denotes the complex conjugate.

The system (3.8) is best approached by solving for the second order shear stress,

$$\tau_1 = \frac{\partial u_1}{\partial y} = -\tau_{11}(\bar{x}, y)\, E + \tau_{12}(\bar{x}, y)\, \tilde{E} - \tau_{11}^*(\bar{x}, y)\, E^{-1} + \tau_{12}^*(\bar{x}, y)\, \tilde{E}^{-1},$$

for which we can obtain an equation by differentiating (3.8b) with respect to y:

$$\frac{\partial \tau_1}{\partial t} + \lambda y \frac{\partial \tau_1}{\partial x} = \frac{\partial^2 \tau_1}{\partial y^2}, \tag{3.10a}$$

subject to

$$\int_0^\infty \tau_1 \, \mathrm{d}y = \lambda F. \tag{3.10b}$$

This in turn gives equations for the various components of τ_1,

$$\frac{\partial^2 \tau_{11}}{\partial y^2} - (\mathrm{i}\alpha\lambda)\left(y + \frac{c}{\lambda}\right)\tau_{11} = 0, \tag{3.11a}$$

$$\frac{\partial^2 \tau_{12}}{\partial y^2} - (\mathrm{i}\alpha\lambda)\left(y - \frac{c}{\lambda}\right)\tau_{12} = 0, \tag{3.11b}$$

along with their complex conjugate versions. The transformation $\xi = (\mathrm{i}\alpha\lambda)^{1/3}(y \pm c/\lambda)$, where the positive sign is taken for (3.11a) and the negative sign for (3.11b), transforms these two equations into Airy's equation

$$\frac{\partial^2 \tau_{11,\,12}}{\partial \xi^2} = \xi \tau_{11,\,12},$$

which has the solution

$$\tau_{11,\,12} = A_{11,\,12}\left(\bar{x}\right)\mathrm{Ai}\left(\xi\right) + B_{11,\,12}\left(\bar{x}\right)\mathrm{Bi}\left(\xi\right).$$

For large values of y (and hence ξ), the Airy functions of the first and second kind take, respectively, the asymptotic form

$$\mathrm{Ai}(\xi) \sim \frac{1}{2\sqrt{\pi}}\xi^{-\frac{1}{4}}\exp\left(-\frac{2}{3}\xi^{\frac{3}{2}}\right),$$
$$\mathrm{Bi}(\xi) \sim \frac{1}{\sqrt{\pi}}\xi^{-\frac{1}{4}}\exp\left(\frac{2}{3}\xi^{\frac{3}{2}}\right),$$

thus forcing us to set $B_{11,\,12} = 0$ to ensure a bounded solution at infinity. So

$$\tau_{11,\,12}\left(\bar{x}, y\right) = A_{11,\,12}\left(\bar{x}\right)\mathrm{Ai}\left[(\mathrm{i}\alpha\lambda)^{\frac{1}{3}}\left(y \pm \frac{c}{\lambda}\right)\right], \tag{3.12a}$$

with the integral condition (3.10b) used to calculate the functions $A_{11,\,12}$:

$$A_{11,\,12}\left(\bar{x}\right) = \lambda G\left(\bar{x}\right)\left\{\int_0^\infty \mathrm{Ai}\left[(\mathrm{i}\alpha\lambda)^{\frac{1}{3}}\left(y \pm \frac{c}{\lambda}\right)\right]\,\mathrm{d}y\right\}^{-1}; \tag{3.12b}$$

with $\tau^*_{11,\,12}$ found by taking the complex conjugate of the above.

The pressure is determined by evaluating the momentum equation (3.8b) at $y = 0$: the no-slip boundary condition (3.8c) ensures that the only terms that remain are the pressure gradient and viscous term, which is the first derivative of the shear stress with

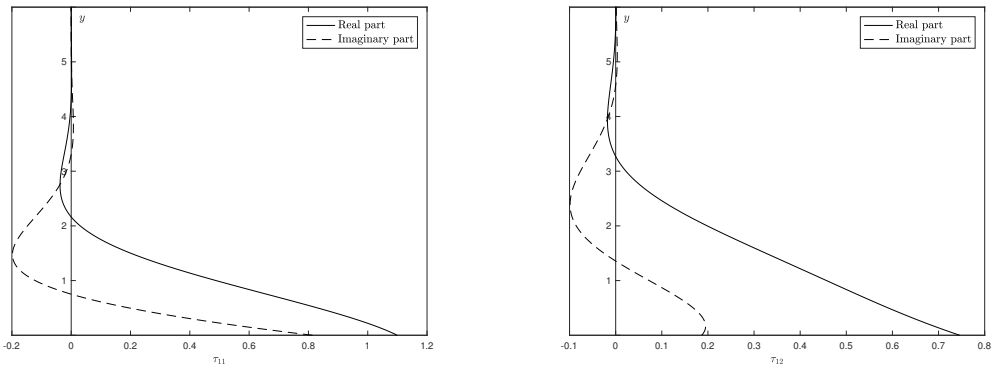

(A) τ_{11} (B) τ_{12}

FIGURE 3.2: Components of the shear stress multiplying (a) E, and (b) $\tilde{E}$, for an array of blips that have the same maximum amplitude throughout, i.e. $G = 1$. The wavenumber and frequency are both taken to be 1. The solid line denotes the real part of the solution and the dashed line is the imaginary part. Of course, for this choice of G, the pressure functions p_{1i} remain constant across the array, with $p_{11} = -1.5341 + 0.3730\mathrm{i}$ and $p_{12} = -0.0711 + 0.2392\mathrm{i}$.

respect to y,

$$\frac{\partial p_1}{\partial x} = \left.\frac{\partial \tau_1}{\partial y}\right|_{y=0}.$$

Hence

$$p_{11,\,12} = -\frac{\mathrm{i}}{\alpha}\left(\mathrm{i}\alpha\lambda\right)^{\frac{1}{3}} A_{11,\,12}\left(\bar{x}\right) \mathrm{Ai}'\left[\pm\frac{c}{\lambda}\left(\mathrm{i}\alpha\lambda\right)^{\frac{1}{3}}\right]; \tag{3.13a}$$

integration of the shear stress with respect to y gives the streamwise velocity $u_{11,\,12}$,

$$u_{11,\,12} = A_{11,\,12}\left(\bar{x}\right) \int_0^y \mathrm{Ai}\left[\left(\mathrm{i}\alpha\lambda\right)^{\frac{1}{3}}\left(s \pm \frac{c}{\lambda}\right)\right] \mathrm{d}s; \tag{3.13b}$$

and the continuity equation (3.8a) gives the normal velocity $v_{11,\,12}$,

$$v_{11,\,12} = -\mathrm{i}\alpha A_{11,\,12}\left(\bar{x}\right) \int_0^y \int_0^s \mathrm{Ai}\left[\left(\mathrm{i}\alpha\lambda\right)^{\frac{1}{3}}\left(r \pm \frac{c}{\lambda}\right)\right] \mathrm{d}r\,\mathrm{d}s. \tag{3.13c}$$

Graphs of the shear stress and pressure are shown in figures 3.2 and 3.3.

3.2.3 To the third bend

If things began to get interesting at $\mathcal{O}(h)$, the way becomes rather more involved at $\mathcal{O}(h^2)$, as the second order terms multiply each other to give rise to further complex exponentials at third order. The condensed flow equations (3.5) at $\mathcal{O}(h^2)$, making use of the results already obtained, are

$$\frac{\partial u_2}{\partial x} + \frac{\partial u_1}{\partial \bar{x}} + \frac{\partial v_2}{\partial y} = 0, \tag{3.14a}$$

$$\frac{\partial u_2}{\partial t} + \lambda y \frac{\partial u_2}{\partial x} + u_1 \frac{\partial u_1}{\partial x} + \lambda y \frac{\partial u_1}{\partial \bar{x}} + v_1 \frac{\partial u_1}{\partial y} + \lambda v_2 = -\frac{\partial p_2}{\partial x} - \frac{\partial p_1}{\partial \bar{x}} + \frac{\partial^2 u_2}{\partial y^2}, \tag{3.14b}$$

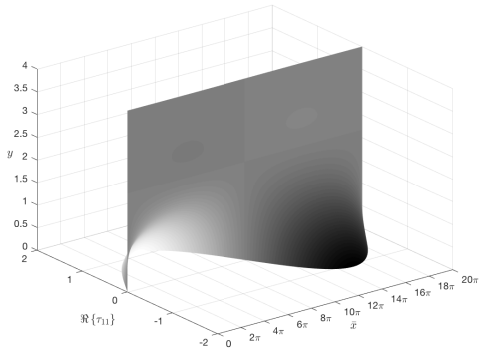

(A) τ_{11}, real part

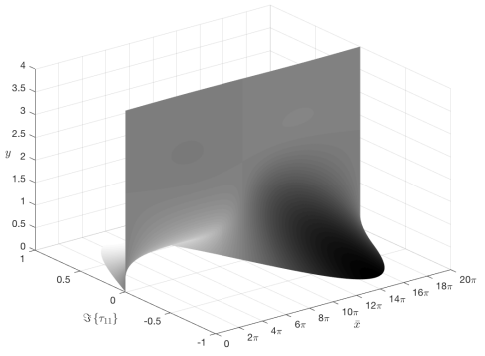

(B) τ_{11}, imaginary part

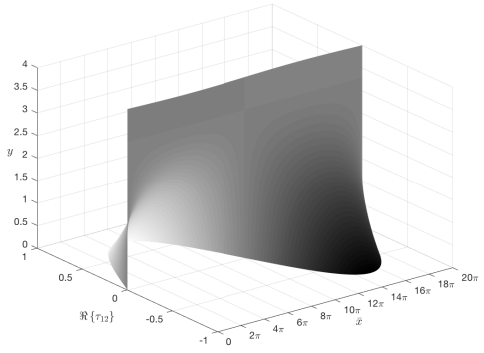

(C) τ_{12}, real part

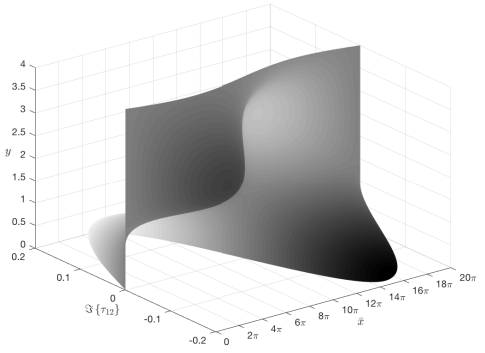

(D) τ_{12}, imaginary part

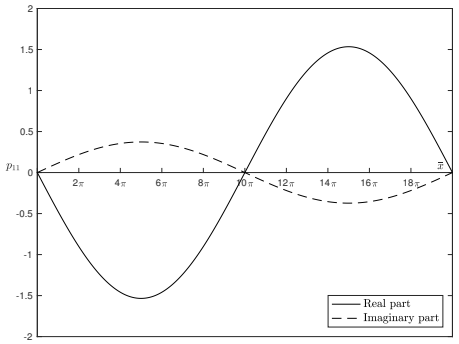

(E) p_{11}

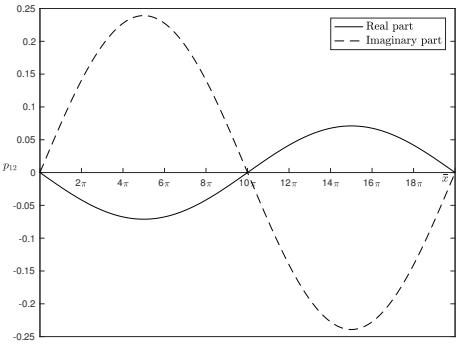

(F) p_{12}

FIGURE 3.3: Components of the shear stress (real and imaginary) and pressure, for blips that have varying maximum amplitude as one moves across the array, given by $G = \sin \bar{x}$. The wavenumber and frequency are both set to 1. For the graphs of the pressure (e) and (f), the solid line denotes the real part of the solution and the dashed line the imaginary part.

to be solved subject to

$$u_2 = v_2 = 0 \quad \text{on } y = 0, \tag{3.14c}$$

$$u_2 = v_2 = p_2 = 0 \quad \text{when } x < 0, \tag{3.14d}$$

$$u_2 \to 0 \quad \text{as } y \to \infty. \tag{3.14e}$$

Once more we aim to solve for the shear stress τ_2 first, rather than the velocities themselves. Hence differentiating the momentum equation (3.14b) with respect to y, and exploiting the continuity equations at both $\mathcal{O}(h)$ and $\mathcal{O}(h^2)$, gives us

$$\frac{\partial \tau_2}{\partial t} + u_1 \frac{\partial \tau_1}{\partial x} + \lambda y \left(\frac{\partial \tau_1}{\partial \bar{x}} + \frac{\partial \tau_2}{\partial x} \right) + v_1 \frac{\partial \tau_1}{\partial y} = \frac{\partial^2 \tau_2}{\partial y^2}, \tag{3.15a}$$

along with the conditions that τ_2 be bounded at infinity and

$$\int_0^\infty \tau_2 \, \mathrm{d}y = 0. \tag{3.15b}$$

The forcing terms $u_1 \partial \tau_1 / \partial x$ and $v_1 \partial \tau_1 / \partial y$ involve the multiplication among themselves of the complex exponentials E and $\tilde{E}$ (along with their complex conjugates), giving rise to the harmonics $E^2, \tilde{E}^2, E\tilde{E}$, and so on, along with a steady term that will prove to be of particular interest. We thus decompose the $\mathcal{O}(h^2)$ shear stress as

$$\begin{aligned} \tau_2 = \tau_{20} &- \tau_{21} E + \tau_{22} \tilde{E} + \tau_{23} E^2 + \tau_{24} \tilde{E}^2 + \tau_{25} E \tilde{E} + \tau_{26} E \tilde{E}^{-1} \\ &- \tau_{21}^* E^{-1} + \tau_{22}^* \tilde{E}^{-1} + \tau_{23}^* E^{-2} + \tau_{24}^* \tilde{E}^{-2} + \tau_{25}^* E^{-1} \tilde{E}^{-1} + \tau_{26}^* E^{-1} \tilde{E}, \end{aligned}$$

the choice of sign for E and $\tilde{E}$ informed only by a desire to maintain consistency with the convention used at $\mathcal{O}(h)$.

Leaving the most interesting component, τ_{20}, for later, the shear stress components $\tau_{2i}, i = 1, \ldots, 6$, then satisfy

$$\frac{\partial^2 \tau_{21}}{\partial y^2} - \mathrm{i}\alpha\lambda \left(y + \frac{c}{\lambda} \right) \tau_{21} = -\lambda y \frac{\partial \tau_{11}}{\partial \bar{x}}, \tag{3.16a}$$

$$\frac{\partial^2 \tau_{22}}{\partial y^2} - \mathrm{i}\alpha\lambda \left(y - \frac{c}{\lambda} \right) \tau_{22} = \lambda y \frac{\partial \tau_{12}}{\partial \bar{x}}, \tag{3.16b}$$

$$\frac{\partial^2 \tau_{23}}{\partial y^2} - 2\mathrm{i}\alpha\lambda \left(y + \frac{c}{\lambda} \right) \tau_{23} = \mathrm{i}\alpha u_{11} \tau_{11} + v_{11} \frac{\partial \tau_{11}}{\partial y}, \tag{3.16c}$$

$$\frac{\partial^2 \tau_{24}}{\partial y^2} - 2\mathrm{i}\alpha\lambda \left(y - \frac{c}{\lambda} \right) \tau_{24} = \mathrm{i}\alpha u_{12} \tau_{12} + v_{12} \frac{\partial \tau_{12}}{\partial y}, \tag{3.16d}$$

$$\frac{\partial^2 \tau_{25}}{\partial y^2} - 2\mathrm{i}\alpha\lambda y \tau_{25} = -\mathrm{i}\alpha \left(u_{12} \tau_{11} + u_{11} \tau_{12} \right) - \left(v_{11} \frac{\partial \tau_{12}}{\partial y} + v_{12} \frac{\partial \tau_{11}}{\partial y} \right), \tag{3.16e}$$

$$\frac{\partial^2 \tau_{26}}{\partial y^2} - 2\mathrm{i}\omega \tau_{26} = \mathrm{i}\alpha \left(u_{11} \tau_{12}^* - u_{12}^* \tau_{11} \right) - \left(v_{11} \frac{\partial \tau_{12}^*}{\partial y} + v_{12}^* \frac{\partial \tau_{11}}{\partial y} \right), \tag{3.16f}$$

with the integral condition (3.15b) then setting

$$\int_0^\infty \tau_{2i}\,\mathrm{d}y = 0,$$

along with boundedness at infinity.

We solve these six equations numerically using a finite difference scheme, with details given in appendix A.1: in particular, a check on the size of the mesh and the end point of the computational domain (representing 'infinity') indicates that we can use a step size of $\Delta_y = 0.01$ in the normal direction and terminate the domain at $y_M = 10$. The sampling size in the streamwise direction can be taken to be as fine or coarse as desired without affecting the accuracy of the solution, as there has been no approximation carried out in the $\bar{x}$ coordinate aside from the numerical representation of the function $G(\bar{x})$. The solutions to $\tau_{2i}, i = 1, \ldots, 6$, for constant G and $G = \sin\bar{x}$ are given in figures 3.4 and 3.5: we note that in the former case, the absence of any forcing in equations (3.16a) and (3.16b), along with the zero wall and integral conditions, ensure that the solutions to τ_{21} and τ_{22} are identically zero and thus these are not shown in figure 3.4.

The pressure can once more be found by evaluating the momentum equation (3.14b) at $y = 0$, giving a relationship between the pressure gradient and the shear stress

$$\frac{\partial p_2}{\partial x} = -\frac{\partial p_1}{\partial \bar{x}} + \left.\frac{\partial \tau_2}{\partial y}\right|_{y=0},$$

which, by expanding p_2 in a like manner to τ_2, provides a set of seven equations for the seven components of p_2:

$$\frac{\partial p_{20}}{\partial x} = \left.\frac{\partial \tau_{20}}{\partial y}\right|_{y=0}, \tag{3.17a}$$

$$\mathrm{i}\alpha p_{21} = \left.\frac{\partial \tau_{21}}{\partial y}\right|_{y=0} - \frac{\partial p_{11}}{\partial \bar{x}}, \tag{3.17b}$$

$$\mathrm{i}\alpha p_{22} = \left.\frac{\partial \tau_{22}}{\partial y}\right|_{y=0} - \frac{\partial p_{12}}{\partial \bar{x}}, \tag{3.17c}$$

$$2\mathrm{i}\alpha p_{23} = \left.\frac{\partial \tau_{23}}{\partial y}\right|_{y=0}, \tag{3.17d}$$

$$2\mathrm{i}\alpha p_{24} = \left.\frac{\partial \tau_{24}}{\partial y}\right|_{y=0}, \tag{3.17e}$$

$$2\mathrm{i}\alpha p_{25} = \left.\frac{\partial \tau_{25}}{\partial y}\right|_{y=0}, \tag{3.17f}$$

$$\frac{\partial p_{26}}{\partial x} = \left.\frac{\partial \tau_{26}}{\partial y}\right|_{y=0}. \tag{3.17g}$$

Where the function $G(\bar{x})$ that sets the maximum amplitude of the blips across the array is constant, the pressure functions p_{2i} at $\mathcal{O}(h^2)$ will also be constant across the

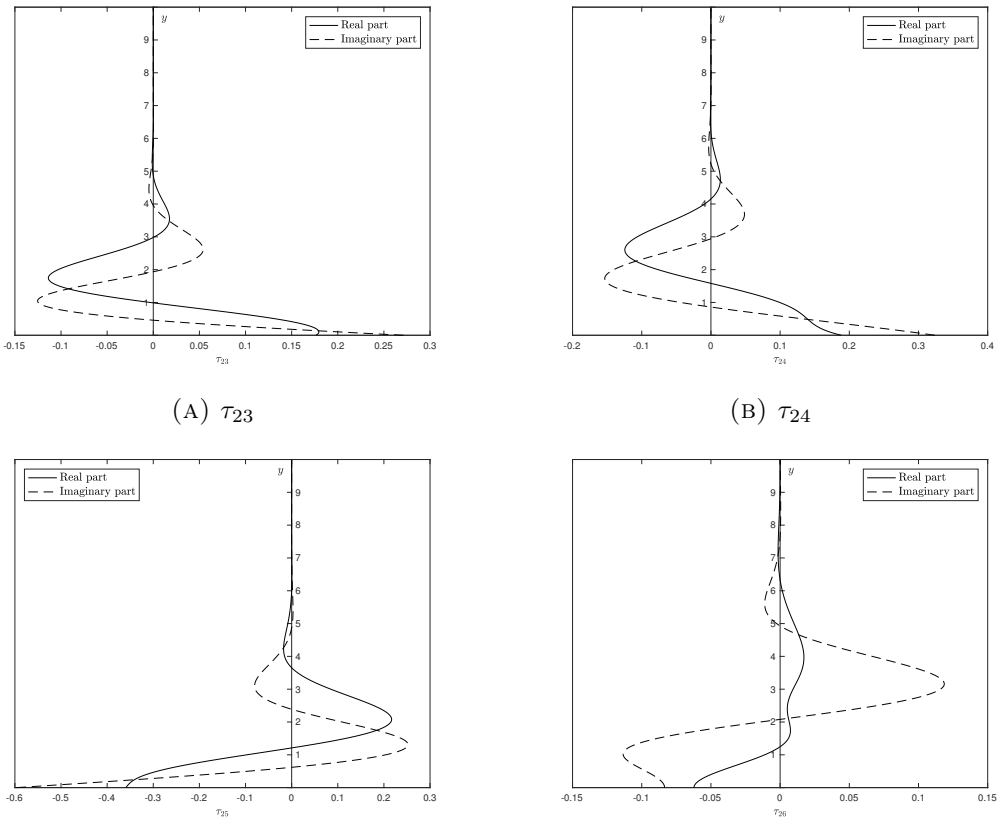

(A) τ_{23} (B) τ_{24}

(C) τ_{25} (D) τ_{26}

FIGURE 3.4: Components of the shear stress at $\mathcal{O}(h^2)$ for an array of blips with constant maximum amplitude, $G = 1$, with wavenumber and oscillation frequency both equal to one. The constant value of G implies that the components τ_{21} and τ_{22} are zero and are therefore not shown. A solid line denotes the real part of the solution, while the dashed line is the imaginary part.

array; the pressure in the case of $G(\bar{x}) = \sin \bar{x}$, however, is shown in figure 3.6 for $p_{21}, \ldots, p_{25}$: since p_{26} is independent of x, $\partial \tau_{26}/\partial y$ evaluated at the wall is zero.

3.2.4 We lose the path

The terms solved for thus far—both at $\mathcal{O}(h)$ and $\mathcal{O}(h^2)$—multiply complex exponentials and thus, on averaging either over a period of oscillation or over the short length scale x, are unable to adjust the mean flow over the blip array. The steady term that appears due to the nonlinear forcing in equation (3.14b), carrying the subscript '20', on the other hand, is able to modify this mean flow both over multiple cycles of oscillation and across the whole array. It is therefore of interest to us to solve for this component but, in trying to do so, we end up losing the path.

The normal velocity is straightforward to solve for: the continuity equation (3.14a), since u_{20} is independent of x, reduces to

$$\frac{\partial v_{20}}{\partial y} = 0,$$

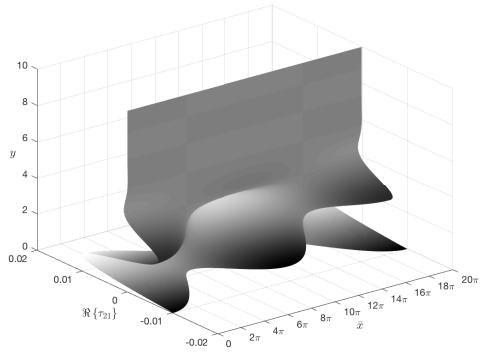

(A) τ_{21}, real part

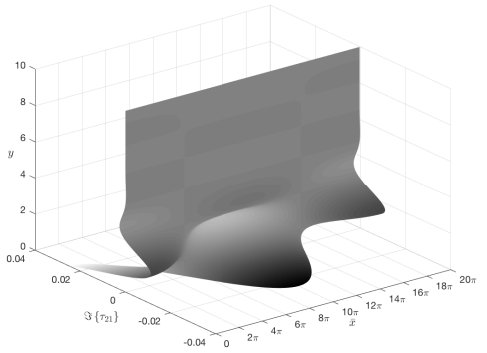

(B) τ_{21}, imaginary part

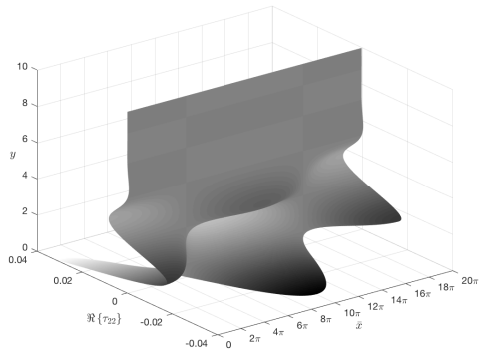

(C) τ_{22}, real part

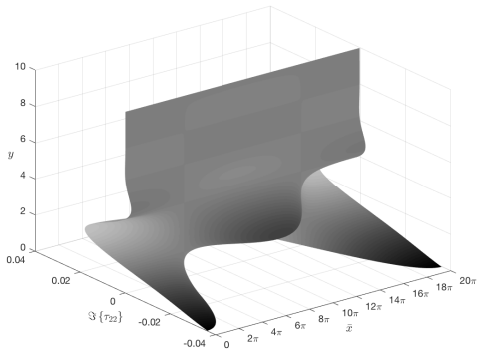

(D) τ_{22}, imaginary part

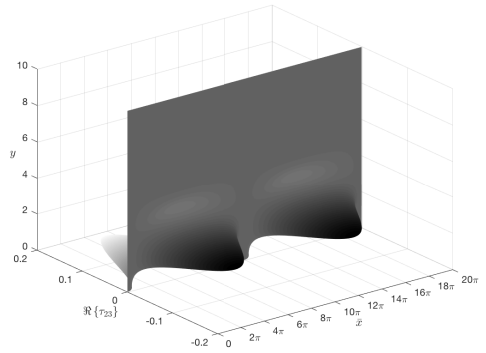

(E) τ_{23}, real part

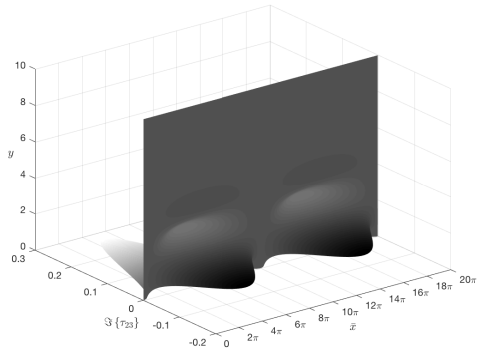

(F) τ_{23}, imaginary part

FIGURE 3.5: Components of the shear stress (real and imaginary) for blips that have varying maximum amplitude as one moves across the array, given by $G = \sin \bar{x}$, with $h = 0.1$. The wavenumber and frequency are both set to 1. (Continued on next page.)

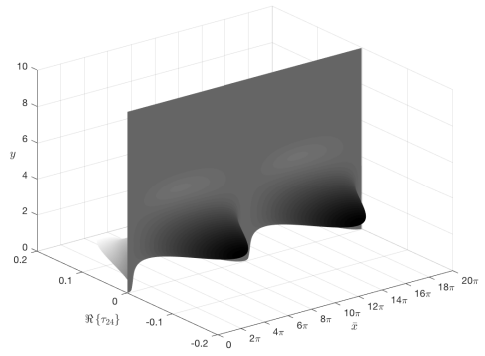

(G) τ_{24}, real part

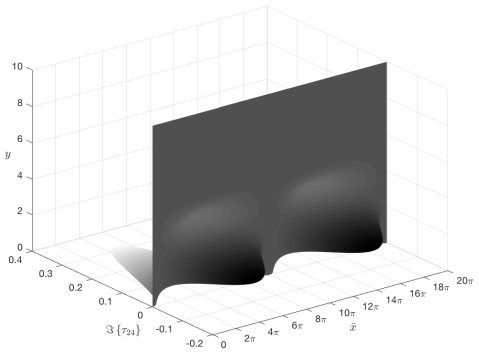

(H) τ_{24}, imaginary part

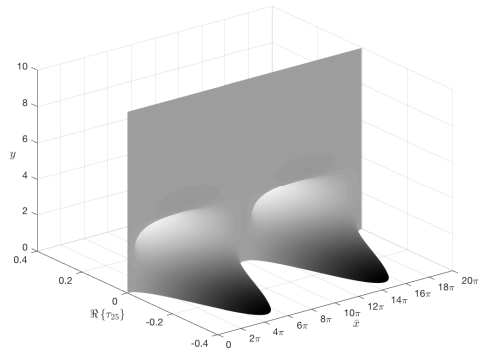

(I) τ_{25}, real part

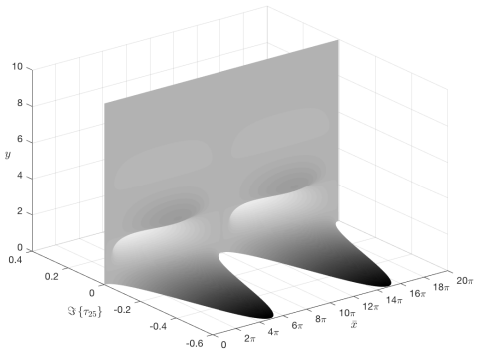

(J) τ_{25}, imaginary part

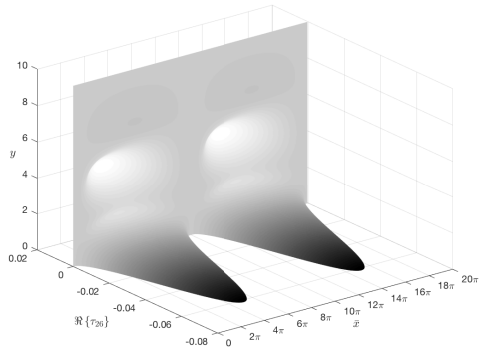

(K) τ_{26}, real part

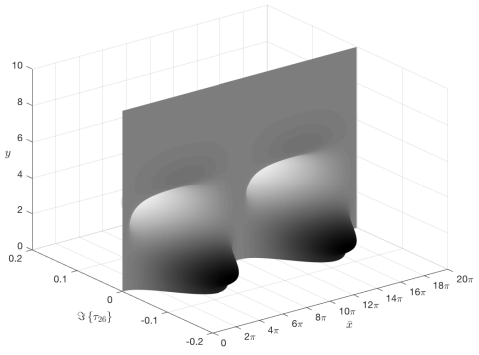

(L) τ_{26}, imaginary part

FIGURE 3.5: (Continued from previous page.)

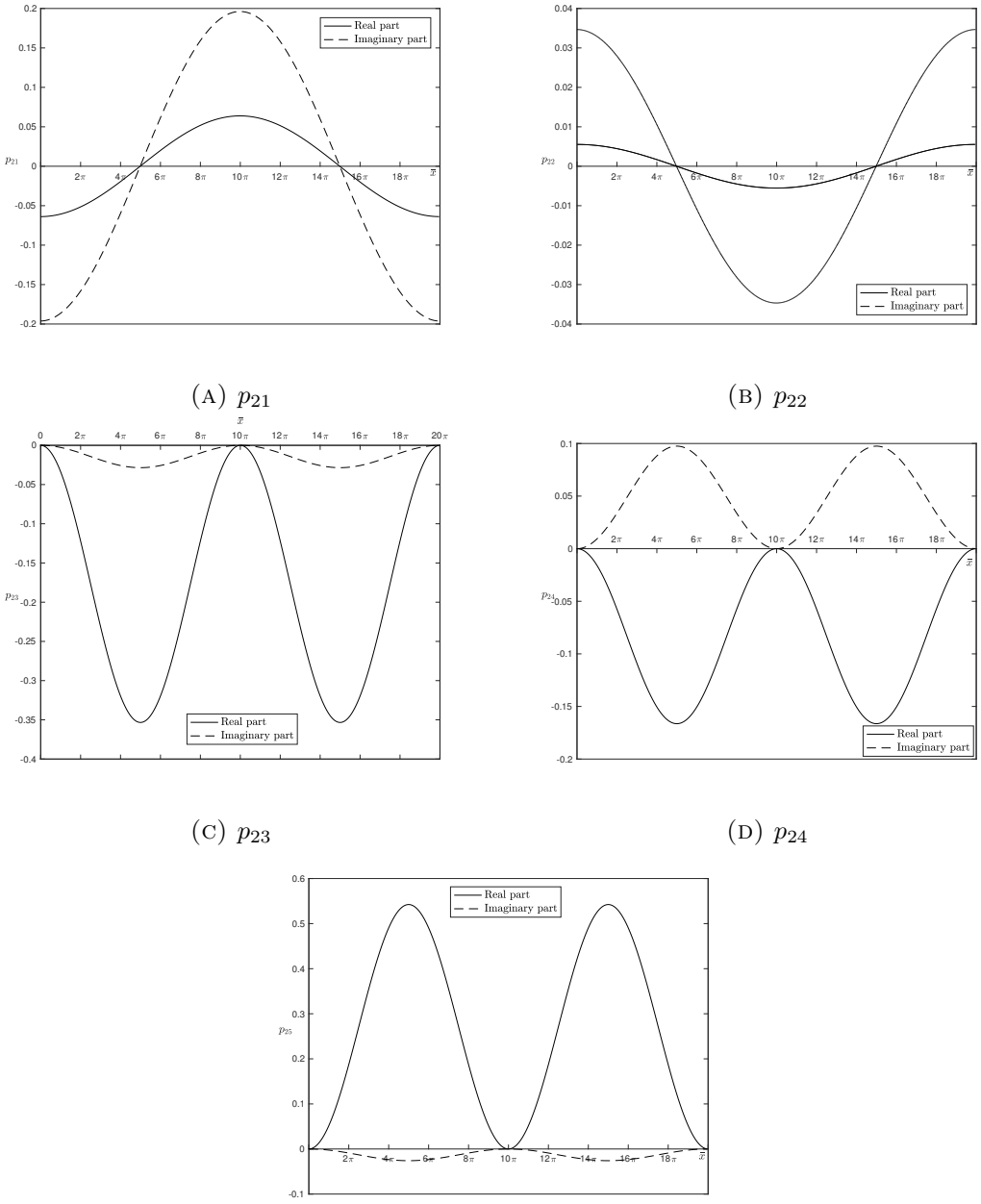

(A) p_{21}

(B) p_{22}

(C) p_{23}

(D) p_{24}

(E) p_{25}

FIGURE 3.6: Components of the pressure for blips that have varying maximum amplitude as one moves across the array, given by $G = \sin \bar{x}$, with $h = 0.1$. The wavenumber and frequency are both set to 1 and both the real (solid line) and imaginary (dashed line) parts are shown. The solution to p_{26} is not present as it multiplies the exponential $\exp(2\mathrm{i}\omega t)$ and thus differentiation with respect to the short coordinate x gives 0.

and application of the no-slip boundary condition then implies that $v_{20} = 0$. As in the work of Rothmayer & Huebsch (2011) [66], a term—which, following their lead, we will call a Reynolds stress (R)—then arises in the momentum equation due to the multiplication of the $\mathcal{O}(h)$ solution with itself. This Reynolds stress then drives u_{20}, with the system (3.14) becoming

$$\frac{\partial^2 u_{20}}{\partial y^2} = R\left(\bar{x}, y\right), \tag{3.18a}$$

where

$$R\left(\bar{x}, y\right) = 2\Re\left\{v_{11}\frac{\partial u_{11}^*}{\partial y} + v_{12}\frac{\partial u_{12}^*}{\partial y}\right\}; \tag{3.18b}$$

with the boundary conditions setting

$$u_{20} = 0 \quad \text{on } y = 0 \tag{3.18c}$$

and

$$u_{20} \to 0 \quad \text{as } y \to \infty. \tag{3.18d}$$

Note that the removal of the pressure gradient in (3.18a) makes sense: not only is p_{20} independent of x, its inclusion and evaluation of the momentum equation at the wall would set

$$\frac{\partial p_{20}}{\partial x} = \left.\frac{\partial \tau_{20}}{\partial y}\right|_{y=0},$$

which, from equation (3.15a), is

$$\frac{\partial p_{20}}{\partial x} = \int_{\infty}^{0}\left[-2\alpha\Im\left\{u_{11}^*\tau_{11} + u_{12}^*\tau_{12}\right\} + 2\Re\left\{v_{11}^*\frac{\partial \tau_{11}}{\partial y} + v_{12}^*\frac{\partial \tau_{12}}{\partial y}\right\}\right]\mathrm{d}y = 0$$

using integration by parts and the $\mathcal{O}(h)$ continuity equation (3.8a).

To the conditions on u_{20} must be added the behaviour that

$$\frac{\partial^2 u_{20}}{\partial y^2} \to 0 \quad \text{as } y \to \infty,$$

since the presence of Airy functions of the first kind ensures that R tends to zero at infinity. However, a solution to the second order differential equation (3.18a) with the three conditions (3.18c), (3.18d) and the one immediately above cannot, in general, be found. Lost in the undergrowth, the theory of steady streaming will come to the rescue.

3.3 The longer length scale and the mean flow correction

3.3.1 A historical refuge: steady streaming

Although hints towards the phenomenon of steady streaming date back to the work of Schlichting in 1932[1] and Longuet-Higgins in 1953 [51] (and possibly as far back as that of Lord Rayleigh in 1883), the foundations of its mathematical theory were first laid down in the papers of Riley [62] and Stuart [92] in the mid-1960s. Both considered flow around a circular cylinder oscillating along its diameter, as shown in figure 3.7, and obtained a horizontal velocity at the top of the boundary layer around the cylinder of

$$u \sim U_0(x)\cos\omega t + \frac{1}{\omega}U_0(x)\frac{\mathrm{d}U_0}{\mathrm{d}x}\left[2a_0\left(\frac{\omega}{2\nu}\right)^{\frac{1}{2}}y - \frac{3}{4}\right] + \cdots, \tag{3.19}$$

where U_0 is the steady part of the slip velocity given by inviscid flow theory and ω is the cylinder's oscillation frequency [62]. This fails to agree, regardless of the choice of a_0, with the required boundary condition that

$$u \to U_0(x)\cos\omega t$$

as $y \to \infty$; or, in other words, with the need for zero time-averaged velocities in the external flow.

In Schlichting's paper, it was argued that in order to maintain a finite velocity at the edge of what turns out to be an inner boundary layer, the coefficient a_0 in equation (3.19) can be set to zero, and Riley (1965) [62] proved this by carrying out a formal inner/outer layer expansion, with matching between the two layers. Letting $a_0 = 0$, then, still gives rise to a steady velocity of

$$-\frac{3}{4}\frac{1}{\omega}U_0\frac{\mathrm{d}U_0}{\mathrm{d}x}$$

and thus a second, outer boundary layer must be required to take this 'steady streaming' velocity to zero at the interface with the external potential flow. Formally, if the dimensional form of Prandtl's boundary layer equations is

$$\frac{\partial u}{\partial t} + u\frac{\partial u}{\partial x} + v\frac{\partial u}{\partial y} = -\frac{\partial p}{\partial x} + \nu\frac{\partial^2 u}{\partial y^2}, \tag{3.20}$$

then with known scalings of

$$u \sim U_\infty, \quad x \sim L, \quad t \sim \omega^{-1},$$

[1] Reference is made in various papers to Schlichting's *Berechnung ebner periodischer Grenzschichtströmungen* (*Calculation of planar oscillating boundary layer flow*, a translation for which I am indebted to my sister's memory of A-level German, Dr Martin Gebert and, somewhat tenuously, weekly games of football), published in the German journal *Zeitschrift für Physick* (Journal of Physics) in 1932. The journal itself has now mutated, joining with various other publications, to become the *European Physical Journal*.

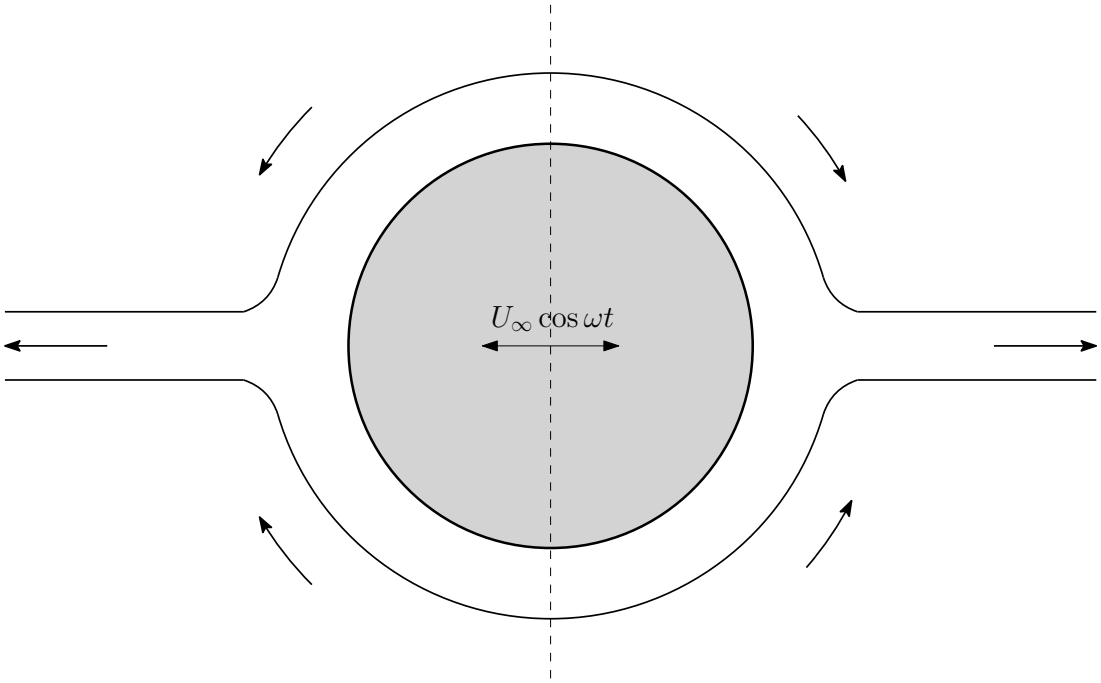

FIGURE 3.7: Cross-section of a circular cylinder oscillating about the dashed line with velocity $U_\infty \cos \omega t$, adapted from [92]. A steady streaming velocity is set up within an outer boundary layer (see text for details on scalings), which results in the ejection of two jets along the horizontal axis, as shown by the arrows.

where U_∞ and L are characteristic velocity and length scales (the oscillation amplitude of the cylinder, as shown in figure 3.7, and the cylinder's cross-sectional diameter, for example), and with an unknown height scaling $y \sim \Delta$, then a balance between the viscous term and the time derivative, gives

$$\Delta \sim \left(\frac{\nu}{\omega}\right)^{\frac{1}{2}}. \tag{3.21}$$

This ensures that both $\partial u/\partial t$ and $\nu \partial^2 u/\partial^2 y$ terms are of $\mathcal{O}(\omega U_\infty)$, while the nonlinear terms are of order U_∞^2/L; and so, if $U_\infty/\omega L \ll 1$, the linear terms will dominate and the nonlinear terms will only play a part at second order. These nonlinear terms then give rise to the Reynolds stresses in the viscous flow, resulting in the steady streaming velocity of order $U_\infty^2/\omega L$, which is an order above that of the oscillatory motion of the cylinder. Indeed, Batchelor (1967) [6] points out that the leading order velocity that goes on to act as a forcing, due to the nonlinearity, to the second order equations, is characterised by rapid variations in a thin layer near the boundary, and this behaviour is in fact seen in the graphs plotted in figures 3.2 and 3.3.

Taking this streaming velocity as the new scaling for the horizontal velocity gives terms in the governing equation (3.20) of orders

$$\frac{U_\infty^2}{L} \text{ (time derivative)}, \quad \frac{U_\infty^4}{\omega^2 L^2} \text{ (nonlinear terms)}, \quad \frac{\nu}{\omega}\frac{U_\infty^2}{L} y^{-2} \text{ (viscous term)},$$

along with the pressure gradient, which is imposed from the outer potential flow. Thus to have the nonlinear terms relevant at leading order, we seek a match between them and the last, viscous, term, resulting in a height scaling of

$$y \sim \frac{L}{U_\infty}(\omega\nu)^{\frac{1}{2}}, \tag{3.22}$$

which is much larger than the order $(\nu/\omega)^{1/2}$ height of the inner layer, provided that $U_\infty/\omega L \ll 1$, a condition that we have already imposed. In this layer, then, the non-zero mean velocity can be taken to zero.

The theory of steady streaming has gone on to be applied to scenarios with perhaps more obvious applications than that of an oscillating cylinder. In an embodiment of the sometimes beautifully cyclical nature of scientific research, it has given birth to the field of acoustic streaming, thereby closing the circle with Lord Rayleigh's 1883 work on Kundt's tube [6], an experimental apparatus in which particles gather at the nodes of standing waves created within the device. The above theory provides, for example, an explanation for the phenomenon of the 'quartz wind', which arises when an ultra-high frequency beam of sound interacts with a body of fluid [63]. Steady streaming flows possibly also exist within the body, especially in peristalsis: the contraction and relaxation of muscles in, for example, the intestines, helping to push the contents of a channel forward [35]. The generation of oscillatory flows is not limited to the periodic movement of a boundary, either: free-surface waves are also able to produce oscillatory motion and steady streaming has been used to study the transport of sediment along sea beds and proposed as a possible mechanism for the creation of sandbars running parallel to the seashore [63].

3.3.2 The mean flow correction

We had left ourselves staring, slightly bemused, at the governing system (3.18) for the steady velocity u_{20}. Following the above exposition of the theory of steady streaming, however, the situation has become a lot clearer. The term $R(\bar{x}, y)$ on the right-hand side of equation (3.18a) is indeed the Reynolds stress, which arises from the oscillatory boundary conditions at order ϵ (equation (3.18b)) and forces the solution at order ϵ^2. The left-hand side of the same equation involves only the diffusive term, now as expected, and we want u_{20} to satisfy both no-slip at the wall and tend to zero at the edge of our $\mathcal{O}(1)$ boundary layer. The complementary function for equation (3.18a) is

$$u_{20} = B + Ay,$$

but both A and B must be zero from the boundary conditions, which sets the onerous requirement on R that its double integral with respect to y satisfies both conditions listed above—a requirement that it is unable to meet. As in the work described in

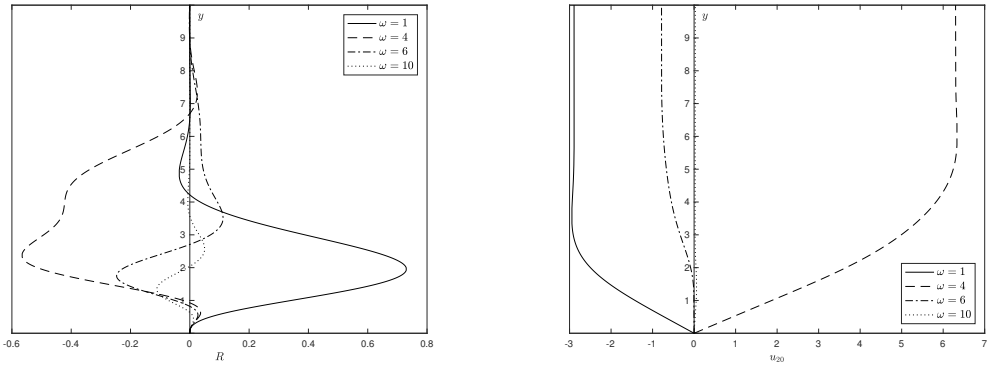

(A) Reynolds stress (B) Lower layer steady velocity

FIGURE 3.8: Reynolds stress and lower layer steady streaming velocity, with constant $G(\bar{x}) = 1$, and with the blips oscillating at frequencies $\omega = 1$ (solid line), 4 (dashed line), 6 (dot–dashed line) and 10 (dotted line). The last of these lies within the high frequency regime that will be studied in §3.4. The blip wavenumber α was set equal to 1 throughout.

§3.3.1, we replace the condition at infinity by the condition that

$$\frac{\partial u_{20}}{\partial y} \to 0 \quad \text{as } y \to \infty, \tag{3.23}$$

equivalent to the fact that outside the near-wall layer there is no source of rapid variations in the streamwise velocity [6].

The system of equations (3.18) along with our modified boundary condition (3.23) can now be solved numerically, employing a simple finite difference scheme and the Thomas algorithm (see appendix A.2), and the presence of a steady streaming velocity at the top of the lower layer can be confirmed. Figures 3.8, 3.10 and 3.11 plot both the Reynolds stress and steady velocity u_{20} for constant maximum blip height across the whole array (figure 3.8) at various oscillation frequencies and for varying maximum blip height, with $G(\bar{x}) = \sin \bar{x}$ (figure 3.10 for $\omega = 1$ and figure 3.11 for $\omega = 4$). Plots of u_{20} confirm the presence of the steady streaming velocity at the top of the lower layer, with both positive and negative velocities possible, depending on the frequency ω. This is further illustrated by figure 3.9, which plots the steady streaming velocity against ω: we note also that for high frequencies, the steady streaming velocity feeding into the upper layer remains positive, but tends to zero. This will be confirmed by the analysis of §3.4, but for now we comment that this agrees with the behaviour predicted by the theory outlined in §3.3.1 above, where the steady streaming velocity was $\mathcal{O}(U_\infty^2/\omega L)$.

Outer layer scaling

In the theory of steady streaming, the outer layer came about through a balance between the nonlinear and viscous terms in the governing equation, with the horizontal velocity scaling being that of the steady velocity at the outer edge of the inner layer. Here, however, the vertical scaling of the outer layer is deduced by taking into account the

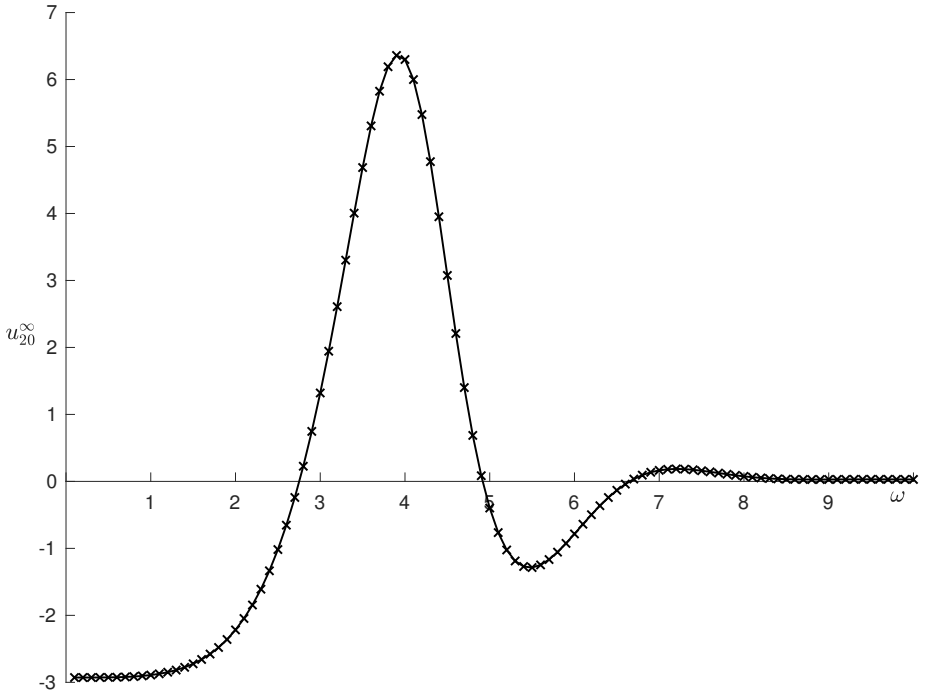

FIGURE 3.9: The steady streaming velocity feeding into the upper layer, obtained by taking the value of u_{20} at y_M and denoted by u_{20}^{∞}, as a function of the blip oscillation frequency ω. Both positive and negative velocities are seen; and, as will be confirmed through a high frequency analysis of the governing equations, the velocity tends to zero as ω becomes large. The blip amplitude function G was taken to be 1 to ensure that u_{20}^{∞} is constant across the blip array. The wavenumber was again kept at $\alpha = 1$.

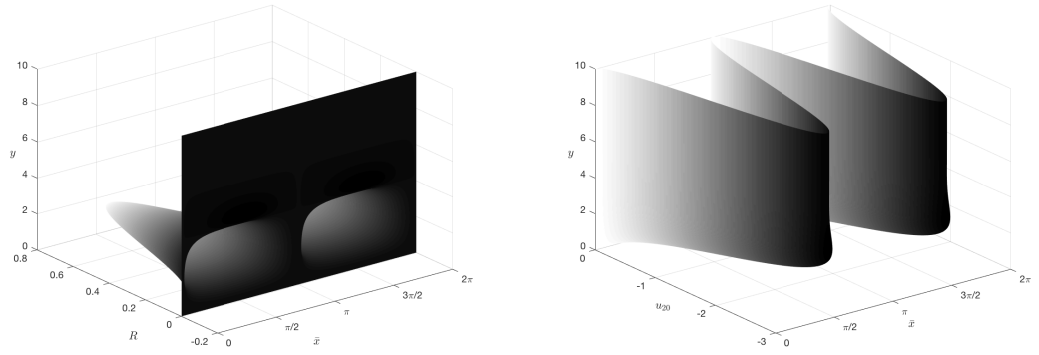

(A) Reynolds stress (B) Lower layer steady velocity

FIGURE 3.10: Reynolds stress and lower layer steady streaming velocity, for varying maximum blip amplitude given by $G(\bar{x}) = \sin \bar{x}$ and oscillation frequency $\omega = 1$. The blip wavenumber α was set equal to 1 as, for illustrative purposes, was h.

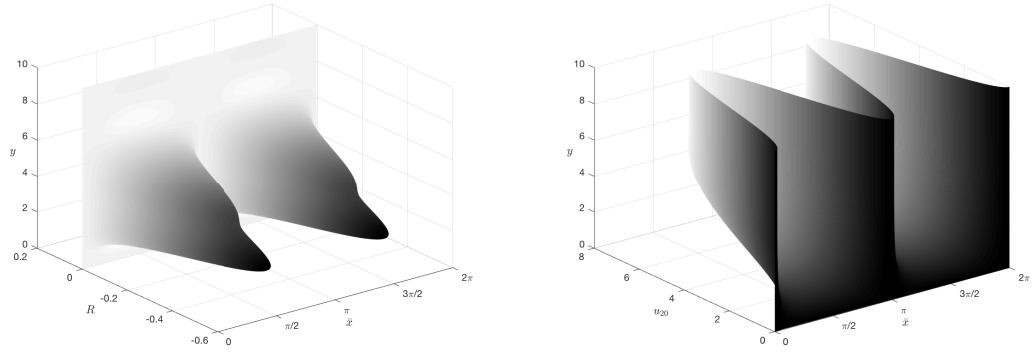

(A) Reynolds stress (B) Lower layer steady velocity

FIGURE 3.11: As figure 3.10, but with $\omega = 4$.

array length scale, $\mathcal{O}(h^{-1})$, and balancing the nonlinear $hu\partial u/\partial\bar{x}$ term and viscous $\partial^2 u/\partial y^2$ term in the governing equation (3.5b). Knowing that to leading order in the lower layer, $u \sim y$, this implies that

$$hy^2 \sim y^{-1}$$

and thus the upper layer has a height scale of $\mathcal{O}(h^{-1/3})$. We introduce then the upper layer normal coordinate $\bar{y}$, with

$$y = h^{-\frac{1}{3}}\bar{y}. \tag{3.24}$$

Remembering that $h \ll 1$, a schematic of the overall flow structure is shown in figure 3.12.

With this outer layer scaling, and with the horizontal and vertical velocities denoted by $\bar{u}$ and $\bar{v}$ respectively, the continuity and momentum equations become

$$\frac{\partial\bar{u}}{\partial x} + h\frac{\partial\bar{u}}{\partial\bar{x}} + h^{\frac{1}{3}}\frac{\partial\bar{v}}{\partial\bar{y}} = 0, \tag{3.25a}$$

$$\frac{\partial\bar{u}}{\partial t} + \bar{u}\frac{\partial\bar{u}}{\partial x} + h\bar{u}\frac{\partial\bar{u}}{\partial\bar{x}} + h^{\frac{1}{3}}\bar{v}\frac{\partial\bar{u}}{\partial\bar{y}} = -\frac{\partial p}{\partial x} - h\frac{\partial p}{\partial\bar{x}} + h^{\frac{2}{3}}\frac{\partial^2\bar{u}}{\partial\bar{y}^2}, \tag{3.25b}$$

the pressure remaining the same as that in the lower layer due to its independence on y.

Finding the mean flow correction

At the top of the inner layer, the horizontal velocity tends to

$$u \to \lambda y + h\lambda F + h^2 u_{20}^{\infty},$$

where u_{20}^{∞} denotes the steady streaming velocity that must go to zero as $\bar{y} \to \infty$. Given that the $\mathcal{O}(1)$ and $\mathcal{O}(h)$ terms already satisfy the required boundary conditions at the

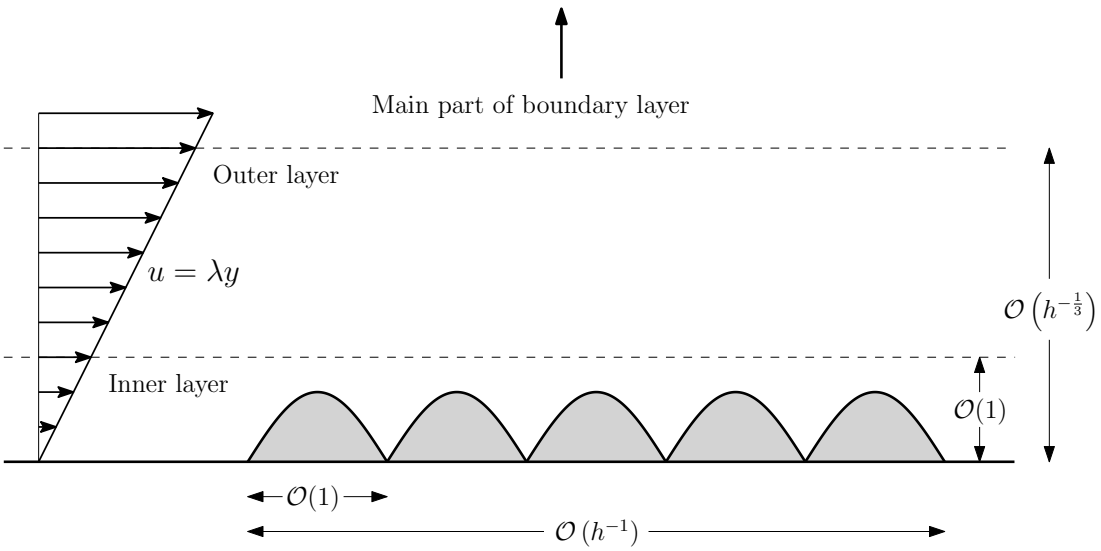

FIGURE 3.12: Schematic of the inner and outer layers present for flow over dynamic roughness (the same scalings hold for the positive roughness elements of §3.5), showing the horizontal and vertical length scales and with $h \ll 1$. Recall that this is within the condensed flow scalings already introduced in §3.1. The steady streaming velocity arises from the flow in the inner layer, while the mean flow correction is solved for in the outer layer. The core of the boundary layer sits above this two-layered structure, which does not see the boundary layer edge.

top of the viscous sublayer, the expansion

$$\bar{u} = h^{-\frac{1}{3}}\lambda\bar{y} + h\lambda F + h^2\bar{u}_M\left(\bar{x},\bar{y}\right) + \cdots, \tag{3.26a}$$

is suggested in the outer layer, with the continuity equation (3.25a) allowing us to calculate the normal velocity expansion

$$\bar{v} = -h^{\frac{2}{3}}\lambda\frac{\partial F}{\partial x}\bar{y} - h^{\frac{5}{3}}\lambda\frac{\partial F}{\partial \bar{x}}\bar{y} - h^{\frac{8}{3}}\bar{v}_M\left(\bar{x},\bar{y}\right) + \cdots, \tag{3.26b}$$

where any constants of integration in $\bar{v}$ have been set to zero from the requirement of matching with the inner layer solution. The terms subscripted with an M introduced here denote the mean flow correction of interest, dependent only on the normal coordinate $\bar{y}$ and the long horizontal length scale, $\bar{x}$, with

$$\bar{v}_M = \int \frac{\partial \bar{u}_M}{\partial \bar{x}}\,\mathrm{d}\bar{y}.$$

Since the pressure is independent of the normal coordinate, we can make use of the pressure expansion already found in the lower layer, with the one key difference being that a further term, dependent only on $\bar{x}$ and corresponding to a mean flow correction to the pressure, must be added at order $h^{5/3}$:

$$p = hp_1 + h^{\frac{5}{3}}\bar{p}_M\left(\bar{x}\right) + h^2p_2 + \cdots. \tag{3.27}$$

Note that this term would only appear in the expansion of the lower layer momentum equation (3.5b) at $\mathcal{O}(h^{8/3})$.

It is in fact the equation at order $h^{8/3}$ but in the upper layer, obtained by substituting (3.26) and (3.27) into (3.25b), that gives the governing equation for the mean flow correction:

$$\lambda\bar{y}\frac{\partial\bar{u}_M}{\partial\bar{x}} - \lambda\bar{v}_M = -\frac{\partial\bar{p}_M}{\partial\bar{x}} + \frac{\partial^2\bar{u}_M}{\partial\bar{y}^2}, \tag{3.28a}$$

with $\bar{u}_M$ and $\bar{v}_M$ having to match with the inner layer solution,

$$\bar{u}_M \to u_{20}^{\infty}, \quad \bar{v}_M \to 0, \quad \text{as } \bar{y} \to 0, \tag{3.28b}$$

and, of course,

$$\bar{u}_M \to 0 \quad \text{as } \bar{y} \to \infty. \tag{3.28c}$$

We proceed as previously by differentiating equation (3.28a) with respect to $\bar{y}$ and invoking continuity to obtain an expression for the mean flow correction shear stress. So

$$\lambda\bar{y}\frac{\partial\bar{\tau}_M}{\partial\bar{x}} = \frac{\partial^2\bar{\tau}_M}{\partial\bar{y}^2}, \tag{3.29a}$$

to be solved subject to the condition at infinity

$$\bar{\tau}_M \to 0 \quad \text{as } \bar{y} \to \infty \tag{3.29b}$$

and the integral

$$\int_0^{\infty} \bar{\tau}_M \,\mathrm{d}\bar{y} = -u_{20}^{\infty}. \tag{3.29c}$$

This system can be solved by taking a Fourier transform in $\bar{x}$, to give

$$\mathrm{i}\kappa\lambda\bar{y}\hat{\tau}_M = \frac{\partial^2\hat{\tau}_M}{\partial\bar{y}^2}, \tag{3.30a}$$

$$\hat{\tau}_M \to 0 \quad \text{as } \bar{y} \to \infty, \tag{3.30b}$$

$$\int_0^{\infty} \hat{\tau}_M \,\mathrm{d}\bar{y} = -\hat{u}_{20}^{\infty}, \tag{3.30c}$$

where an overhat denotes a transformed function and κ is the transform variable.

By imposing boundedness at infinity, we obtain the general solution

$$\hat{\tau}_M(\kappa, \bar{y}) = \hat{A}(\kappa)\,\mathrm{Ai}\left[(\mathrm{i}\kappa\lambda)^{\frac{1}{3}}\,\bar{y}\right];$$

to (3.30a); while (3.30c) serves to determine the function $\hat{A}$ as

$$\hat{A}(\kappa) = -3\,(\mathrm{i}\kappa\lambda)^{\frac{1}{3}}\,\hat{u}_{20}^{\infty},$$

where one must use a change of variables and the fact that the integral of the Airy function of the first kind from 0 to infinity is 1/3. Thus

$$\hat{\tau}_M(\kappa, \bar{y}) = -3(\mathrm{i}\kappa\lambda)^{\frac{1}{3}}\,\hat{u}_{20}^{\infty}(\kappa)\mathrm{Ai}\left[(\mathrm{i}\kappa\lambda)^{\frac{1}{3}}\,\bar{y}\right]. \tag{3.31}$$

The goal, ultimately, is to find the impact of the blip array on the pressure and to find the Fourier-transformed pressure, therefore, we first set $\bar{y} = 0$ in (3.28a) to obtain

$$\frac{\partial \bar{p}_M}{\partial \bar{x}} = \left.\frac{\partial \bar{\tau}_M}{\partial \bar{y}}\right|_{\bar{y}=0},$$

which we then Fourier transform to get, eventually,

$$\hat{p}_M = -3\lambda^{\frac{2}{3}}\mathrm{Ai}'(0)\,(\mathrm{i}\kappa)^{-\frac{1}{3}}\,\hat{u}_{20}^{\infty}. \tag{3.32}$$

The inverse Fourier transform is then computed using convolution and we end, at last, with the mean flow correction pressure

$$\bar{p}_M = -3\frac{\mathrm{Ai}'(0)}{\Gamma\left(\frac{1}{3}\right)}\lambda^{\frac{2}{3}}\int_0^{\bar{x}} u_{20}^{\infty}(s)\,(\bar{x}-s)^{-\frac{2}{3}}\,\mathrm{d}s, \tag{3.33}$$

where Γ is the Gamma function.

For a blip array with constant maximum amplitude, a simple analytic expression for the pressure gradient can be obtained from this, since the steady streaming velocity u_{20}^{∞} is independent of $\bar{x}$. Thus

$$\bar{p}_M(\bar{x}) = -9\frac{\mathrm{Ai}'(0)}{\Gamma\left(\frac{1}{3}\right)}\lambda^{\frac{2}{3}}u_{20}^{\infty}\bar{x}^{1/3}; \tag{3.34a}$$

and the pressure gradient is

$$\frac{\mathrm{d}\bar{p}_M}{\mathrm{d}\bar{x}} = -\gamma u_{20}^{\infty}\bar{x}^{-\frac{2}{3}}, \tag{3.34b}$$

where $\gamma = 3\lambda^{2/3}\mathrm{Ai}'(0)/\Gamma(1/3) < 0$. The aim is to introduce favourable pressure gradients into the flow, which can be achieved when u_{20}^{∞} is negative: this, in turn, depends on the frequency of oscillation of the blips, as shown in figure 3.9. Figure 3.13 plots both the pressure and pressure gradient for two different choices of ω: the first, $\omega = 1$, gave rise to a negative steady streaming and thus is associated with a favourable pressure gradient; while the second, $\omega = 4$, had a positive u_{20}^{∞} and thus gives rise to an adverse pressure gradient. Note the presence of a singularity at $\bar{x} = 0$: resolving the flow here would require a study of a smaller length scale, which we will ignore.

A similar conclusion is reached when considering an array of blips whose maximum amplitude varies according to $G(\bar{x}) = \sin\bar{x}$. The pressure in this case, since u_{20}^{∞} is no longer constant, must be computed numerically, with the singularity in the integrand dealt with as described in appendix A.3.1. In those cases where the steady streaming

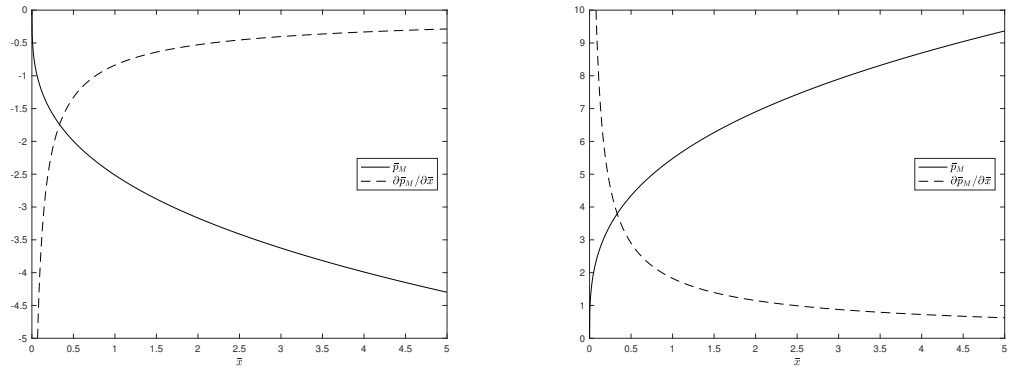

(A) $\omega = 1$ (B) $\omega = 4$

FIGURE 3.13: Mean flow correction pressure (solid line) and pressure gradient (dashed line) for flow over an array of blips, all with a maximum amplitude that remains constant across the array, oscillating at a frequency of $\omega = 1$ and $\omega = 4$, giving rise to a favourable and adverse pressure gradient respectively.

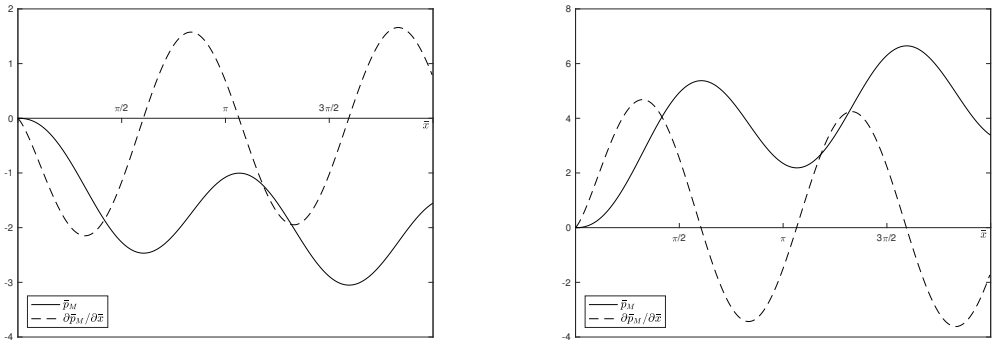

(A) $\omega = 1$ (B) $\omega = 4$

FIGURE 3.14: Mean flow correction pressure (solid line) and pressure gradient (dashed line) for flow over an array of blips, with a maximum amplitude that varies according to $G = \sin\bar{x}$ across the array, oscillating at a frequency of $\omega = 1$ and $\omega = 4$. The pressure gradient is, overall, favourable in the former case and adverse in the latter, but regions where the pressure gradient has opposite sign are possible in both cases.

velocity is negative, the pressure decreases overall across the bump array, and vice versa for when the steady streaming velocity is positive. The presence of varying maximum amplitudes, however, ensures that regions of both favourable and adverse pressure gradients can exist, as shown in figure 3.14. Where $\omega = 1$, the steady streaming velocity was negative (c.f. figure 3.10), and the pressure gradient is, on average, favourable across the array; where $\omega = 4$, the steady streaming velocity was positive (figure 3.11) and thus the opposite is the case.

Our array of blips is therefore able to introduce a pressure gradient into the flow that is non-zero when the mean over a cycle of oscillation or individual blip length is taken.

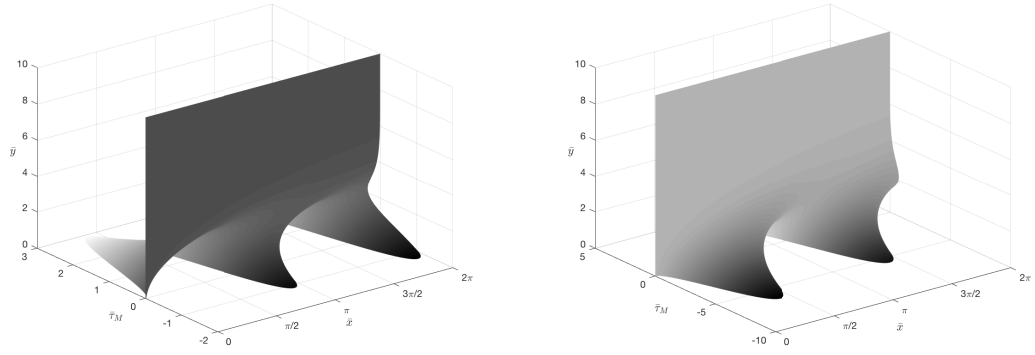

(A) $\omega = 1$ (B) $\omega = 4$

FIGURE 3.15: Mean flow correction shear stress, $\bar{\tau}_M$, acting at $\mathcal{O}(h^2)$, for flow over an array of blips, with a maximum amplitude that varies according to $G = \sin\bar{x}$ across the array, oscillating at a frequency of $\omega = 1$ and $\omega = 4$.

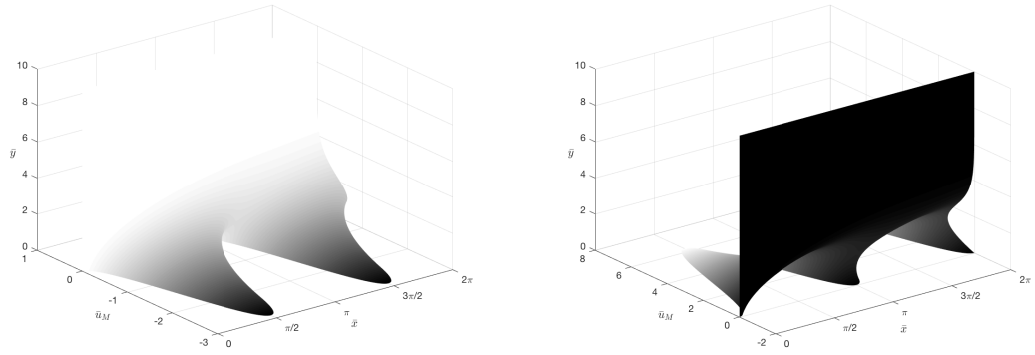

(A) $\omega = 1$ (B) $\omega = 4$

FIGURE 3.16: Mean flow correction velocity, $\bar{u}_M$, acting at $\mathcal{O}(h^2)$, for flow over an array of blips, with a maximum amplitude that varies according to $G = \sin\bar{x}$ across the array, oscillating at a frequency of $\omega = 1$ and $\omega = 4$.

This steady pressure, which we term a mean flow correction, arises due to the steady streaming velocity that is produced by Reynolds stresses in the lower layer, which in turn are produced by the oscillatory motion of the blips. This steady streaming velocity implies the need for an outer layer, of order $h^{-1/3}$, where the mean flow correction is solved for. Graphs of the velocity and shear for arrays of varying maximum amplitude, produced as described in appendix A.3.2, are shown in figures 3.15 and 3.16. The pressure gradient, which acts at order $h^{5/3}$, can then either be adverse or favourable, depending on the sign of the steady streaming velocity, which depends on the frequency ω. Although we have kept the wavenumber of the blips constant throughout ($\alpha = 1$), we note that changing the width of the blips—which would correspond to changing the wavenumber—would also affect the sign of the steady streaming velocity, as we had defined $\omega = \alpha c$.

3.4 Checking the map: the high frequency solution

Thoreau would not approve. To be immersed in one's surroundings involves ridding oneself of the human desire to illude itself that it knows where it is, where it's been and where the path ahead leads. To check a map is to rob yourself of the marvels of the unknown, to cheat yourself of the pleasure of discovery, to turn the unexpected into the mundane. Not only that, but the greatest joys of nature cannot be contained in the works of even the greatest of cartographers: rock giving birth to water, millennia old, but fresh and pure as innocence; the flash of a butterfly's wings as it catches a ray of sunlight, filtered through a canopy of green that stretches to the heavens; an ibex floating on an invisible ledge on the side of a cliff a thousand metres tall; or an arid, rocky ridge that hides behind it, stretching away to the mountains in the distant horizon, a valley so beautiful and bountiful you must have slipped from this life to Paradise.

But in our work, it is often worthwhile to pause for a moment and check a map. It is particularly of use to suppose that a certain parameter in the governing equations takes on values that are either very large or very small, in order to validate numerical results and perhaps gain some further insight into the problem at hand. In the preceding work of §§3.2 and 3.3, many of the solutions were solved for numerically and plotted graphically. Here, the oscillation frequency of our blips provides us with an opportunity to move away from the glare of the computer screen and the impenetrable thicket of lines of code, to pick up once more paper and pencil, and to attempt to confirm the high frequency behaviour of our solutions.

3.4.1 Checking the lower layer second order solution

The governing equations in the lower layer are, as before, those given in (3.5) and a solution is again sought by carrying out an asymptotic expansion in h as shown in (3.3)—but this time under the proviso that $\omega \gg 1$. For the admirable sake of avoiding confusion, we scale out the wavenumber α by transforming our coordinates and variables as

$$x = \alpha^{-1}\tilde{x}, \quad \bar{x} = \alpha^{-1}\tilde{\bar{x}}, \quad y = \alpha^{-1/3}\tilde{y}, \quad \omega = \alpha^{2/3}\tilde{\omega},$$
$$u = \alpha^{-1/3}\tilde{u}, \quad v = \alpha^{1/3}\tilde{v}, \quad p = \alpha^{-2/3}\tilde{p}, \quad G = \alpha^{-\frac{1}{3}}\tilde{G},$$

although we neglect the tilde from now on. In comparing with the solutions shown in preceding sections, this is equivalent to setting $\alpha = 1$, as was done throughout. The solution at $\mathcal{O}(1)$ is no different to that given previously: $u_0 = \lambda y$, $v_0 = 0$ and $p_0 = 0$ is independent of ω and thereby requires no further expansion.

At $\mathcal{O}(h)$ the governing system of equations is provided by (3.8) and it makes sense once more to decompose the pressure and velocities as shown in equation (3.9). The analysis for obtaining the high frequency approximation of the function multiplying E will be

presented below: the method for $\tilde{E}$ is identical except for some changes of sign. The equations to solve for u_{11} and v_{11} are then

$$\mathrm{i}u_{11} + \frac{\partial v_{11}}{\partial y} = 0, \tag{3.35a}$$

$$\mathrm{i}\omega u_{11} + \mathrm{i}\lambda y u_{11} + \lambda v_{11} = -\mathrm{i}p_{11} + \frac{\partial^2 u_{11}}{\partial y^2}, \tag{3.35b}$$

$$u_{11} = v_{11} = 0 \quad \text{on } y = 0, \tag{3.35c}$$

$$u_{11} \to \lambda G(\bar{x}) \quad \text{as } y \to \infty, \tag{3.35d}$$

under the assumption that ω is large.

With the pressure p_{11} of order ω, a Stokes layer of height scale $\omega^{-1/2}$ forms near the wall, in which the term in (3.35b) corresponding to the time derivative matches with the pressure and viscous forces. The same inner layer scaling of steady streaming, c.f. equation (3.21), is therefore obtained, albeit without the kinematic viscosity ν, which was scaled out in chapter 2. So writing $y = \omega^{-1/2}\hat{y}$ and, to leading order in ω,

$$p_{11} = \omega \hat{p}_{11} + \cdots, \tag{3.36a}$$

$$u_{11} = \hat{u}_{11} + \cdots, \tag{3.36b}$$

$$v_{11} = \omega^{-1/2}\hat{v}_{11} + \cdots, \tag{3.36c}$$

we have, to leading order in the Stokes layer,

$$\frac{\partial^2 \hat{u}_{11}}{\partial \hat{y}^2} - \mathrm{i}\hat{u}_{11} = \mathrm{i}\hat{p}_{11}.$$

This has solution

$$\hat{u}_{11} = \hat{A}(\bar{x}) \exp(\delta\hat{y}) + \hat{B}(\bar{x}) \exp(-\delta\hat{y}) - \hat{p}_{11}(\bar{x}), \tag{3.37a}$$

$$\hat{v}_{11} = \mathrm{i}\hat{p}_{11}(\bar{x})\,\hat{y} - \hat{A}(\bar{x})\,\delta \exp(\delta\hat{y}) + \hat{B}(\bar{x})\,\delta \exp(-\delta\hat{y}) + \hat{C}(\bar{x}), \tag{3.37b}$$

where $\delta = (1+\mathrm{i})/\sqrt{2}$, $\hat{p}_{11}$ is to be determined, and the unknown functions $\hat{A}$, $\hat{B}$ and $\hat{C}$ are related to each other by the imposition of the no-slip boundary condition (3.35c):

$$\hat{A}(\bar{x}) + \hat{B}(\bar{x}) = \hat{p}_{11}(\bar{x}),$$
$$\delta\hat{A}(\bar{x}) - \delta\hat{B}(\bar{x}) - \hat{C}(\bar{x}) = 0.$$

We appeal already to a desire for these solutions to remain bounded as $\hat{y}$ tends to infinity—a desire that is in fact a requirement, on considering the $y \sim 1$ layer—to set $\hat{A} = 0$. The pressure, and remaining functions, are then obtained in the layer above the Stokes layer, in which equation (3.35b) reduces to

$$\hat{u}_{11} = -\hat{p}_{11}.$$

The matching condition at infinity (3.35d) can be immediately applied here to give

$$\hat{p}_{11} = -\lambda G$$

and hence

$$\hat{B} = -\lambda G,$$
$$\hat{C} = \delta\lambda G.$$

(One could, if one wished, consider a further, larger layer of order ω, and apply the condition at infinity there, with matching between all three layers, but this gives the same result as that derived above and merely adds unnecessary complication.) The solution to leading order in the lower layer ($y \sim 1$) is therefore

$$p_{11} = -\omega\lambda G\left(\bar{x}\right), \tag{3.38a}$$
$$u_{11} = \lambda G\left(\bar{x}\right)\left[1 - \exp\left(-\delta\omega^{\frac{1}{2}}y\right)\right], \tag{3.38b}$$
$$v_{11} = \omega^{-\frac{1}{2}}\lambda G\left(\bar{x}\right)\left[\delta - \mathrm{i}\omega^{\frac{1}{2}}y - \delta\exp\left(-\delta\omega^{\frac{1}{2}}y\right)\right]. \tag{3.38c}$$

Comparison between the solutions obtained in the previous sections and the high frequency approximations derived here will be for dynamic blips that have a maximum amplitude that remains constant across the whole array: with the amplitude function G therefore set equal to 1, the pressure p_{11} is also constant and, for $\omega = 10$, one compares a value of $-10.2228 + 0.2121\mathrm{i}$ with the high frequency prediction of -10. Graphs of the $\mathcal{O}(h)$ velocities with $\omega = 10$ are shown in figure 3.17.

The solutions p_{12}, u_{12} and v_{12}, required later, are

$$p_{12} = \omega\lambda G\left(\bar{x}\right), \tag{3.39a}$$
$$u_{12} = \lambda G\left(\bar{x}\right)\left[1 - \exp\left(-\delta^{*}\omega^{\frac{1}{2}}y\right)\right], \tag{3.39b}$$
$$v_{12} = \omega^{-\frac{1}{2}}\lambda G\left(\bar{x}\right)\left[\delta^{*}\exp\left(-\delta^{*}\omega^{\frac{1}{2}}y\right) - \delta^{*} - \mathrm{i}\omega^{\frac{1}{2}}y\right]. \tag{3.39c}$$

The remaining functions are obtained by merely taking the complex conjugate of those in (3.38) and (3.39).

With fortuitous foresight, we will, before proceeding to $\mathcal{O}(h^2)$, expand our velocities and pressure at $\mathcal{O}(h)$ to second order in ω, where the exact power of ω must first be determined. The leading order solutions found above now act as forcing in the second order equation, via the nonlinear terms in the momentum equation (3.5b), which must be matched with the second order pressure gradient and viscous diffusion. This ensures

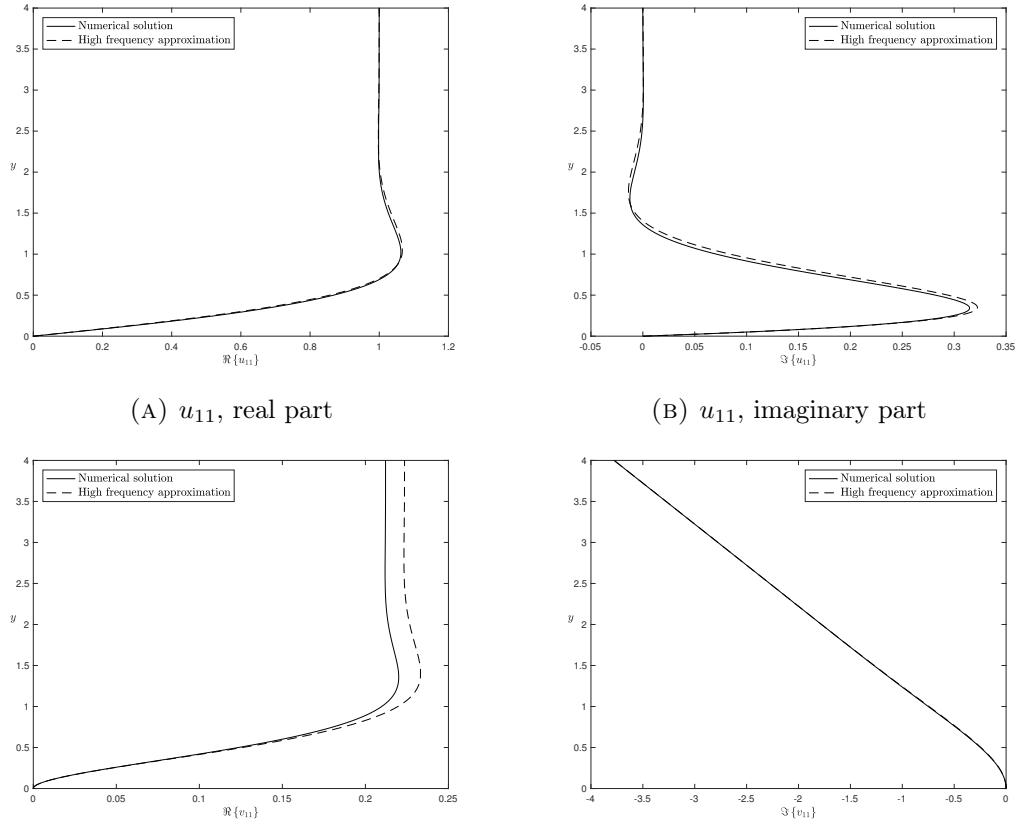

(A) u_{11}, real part

(B) u_{11}, imaginary part

(C) v_{11}, real part

(D) v_{11}, imaginary part

FIGURE 3.17: Comparison between the real and imaginary parts of u_{11} and v_{11} obtained as the solutions to the full problem described in §3.2.2 (solid line) and our high frequency approximation (dashed line), with $\omega = 10$. In these graphs, and in all other graphs in this section, the amplitude function G equals 1. The streamwise velocity plots agree very well, while the high frequency solution somewhat overestimates the size of the real part of v_{11}. Since $G = 1$, the pressure p_{11} is constant.

that the expansions reported in (3.36) can be extended to

$$u_{11} = u_{11}^{(0)} + \omega^{-\frac{3}{2}} u_{11}^{(3/2)} + \cdots, \tag{3.40a}$$

$$v_{11} = y v_{11}^{(0)} + \omega^{-\frac{1}{2}} v_{11}^{(1/2)} + \omega^{-\frac{3}{2}} v_{11}^{(3/2)} + \omega^{-2} v_{11}^{(2)} + \cdots \tag{3.40b}$$

$$p_{11} = \omega p_{11}^{(0)} + \omega^{-\frac{1}{2}} p_{11}^{(3/2)} + \cdots. \tag{3.40c}$$

The functions $u_1^{(0)}$, $v_1^{(0)}$, $v_1^{(1/2)}$ and $p_1^{(0)}$ are all contained in (3.38) and we have once more restricted our attention to the coefficients of E; those of $\tilde{E}$ being found in a similar fashion to that described below.

The momentum equation for u_{11} is

$$\begin{aligned} &\frac{\partial^2}{\partial y^2}\left(u_{11}^{(0)} + \omega^{-\frac{3}{2}} u_{11}^{(3/2)}\right) - \mathrm{i}\omega\left(u_{11}^{(0)} + \omega^{-\frac{3}{2}} u_{11}^{(3/2)}\right) - \mathrm{i}\omega p_{11}^{(0)} - \mathrm{i}\omega^{-\frac{1}{2}} p_{11}^{(3/2)} \\ &= \mathrm{i}\lambda y\left(u_{11}^{(0)} + \omega^{-\frac{3}{2}} u_{11}^{(3/2)}\right) + \lambda\left(y v_{11}^{(0)} + \omega^{-\frac{1}{2}} v_{11}^{(1/2)} + \omega^{-\frac{3}{2}} v_{11}^{(3/2)} + \omega^{-2} v_{11}^{(2)}\right). \end{aligned} \tag{3.41}$$

Looking within the Stokes layer, $y = \omega^{-\frac{1}{2}}\hat{y}$, at $\mathcal{O}(\omega^{-\frac{1}{2}})$ we find the equation for $u_{11}^{(3/2)}$ and $p_{11}^{(3/2)}$,

$$\frac{\partial^2 u_{11}^{(3/2)}}{\partial \hat{y}^2} - \mathrm{i} u_{11}^{(3/2)} = \mathrm{i} p_{11}^{(3/2)} + \lambda^2 G(\bar{x})\left[\delta - \exp(-\delta\hat{y})(\mathrm{i}\hat{y} + \delta)\right];$$

the two functions also related via the condition that $u_{11}^{(3/2)} \to 0$ as $y \to \infty$. The equation has solution

$$u_{11}^{(3/2)} = \hat{B}(\bar{x})\exp(-\delta\hat{y}) - p_{11}^{(3/2)} + \lambda^2\delta G(\bar{x})\left[\mathrm{i} + \frac{1}{8}\exp(-\delta\hat{y})\left(6\delta^*\hat{y} + 2\hat{y}^2 - 3\mathrm{i}\right)\right],$$

where we have already imposed the condition of no exponential growth as $\hat{y}$ goes to infinity. The no-slip boundary condition sets

$$\hat{B} = p_{11}^{(3/2)} - \frac{5}{8}\mathrm{i}\lambda^2\delta G.$$

Above the Stokes layer, $y \sim 1$, at $\mathcal{O}(\omega^{-\frac{1}{2}})$ in equation (3.41),

$$\mathrm{i} u_{11}^{(3/2)} + \lambda v_{11}^{(1/2)} = -\mathrm{i} p_{11}^{(3/2)},$$

on which we impose the boundary condition at infinity that $u_{11}^{(3/2)} \to 0$, giving

$$p_{11}^{(3/2)} = \mathrm{i}\lambda^2\delta G;$$

and, in turn,

$$u_{11}^{(3/2)} = \frac{1}{4}\lambda^2 G\left(3\hat{y} + \delta\hat{y}^2\right)\exp(-\delta\hat{y}).$$

The continuity equation then allows us to find

$$v_{11}^{(3/2)} + v_{11}^{(2)} = \frac{5}{4}\lambda^2 G\left[\exp\left(-\delta\hat{y}\right) - 1\right] + \frac{1}{4}\mathrm{i}\lambda^2 G\hat{y}^2 \exp\left(-\delta\hat{y}\right) + \frac{5}{4}\lambda^2 G\delta\hat{y}\exp\left(-\delta\hat{y}\right).$$

Hence, readjusting the expansion of equation (3.40), the above results at $\mathcal{O}(h)$ are collected below: the pressure is given by

$$p_{11} = \omega p_{11}^{(0)} + \omega^{-\frac{1}{2}} p_{11}^{(1/2)} + \cdots, \tag{3.42a}$$

with

$$p_{11}^{(0)} = -\lambda G\left(\bar{x}\right), \tag{3.42b}$$
$$p_{11}^{(1/2)} = \mathrm{i}\delta\lambda^2 G\left(\bar{x}\right); \tag{3.42c}$$

the streamwise velocity by

$$u_{11} = u_{11}^{(0)} + \omega^{-\frac{1}{2}} y^2 u_{11}^{(1/2)} + \omega^{-1} y u_{11}^{(1)} + \cdots, \tag{3.42d}$$

with

$$u_{11}^{(0)} = \lambda G\left(\bar{x}\right)\left[1 - \exp\left(-\delta\omega^{\frac{1}{2}}y\right)\right], \tag{3.42e}$$
$$u_{11}^{(1/2)} = \frac{1}{4}\delta\lambda^2 G\left(\bar{x}\right)\exp\left(-\delta\omega^{\frac{1}{2}}y\right), \tag{3.42f}$$
$$u_{11}^{(1)} = \frac{3}{4}\lambda^2 G\left(\bar{x}\right)\exp\left(-\delta\omega^{\frac{1}{2}}y\right); \tag{3.42g}$$

and the normal velocity by

$$v_{11} = y v_{11}^{(0)} + \omega^{-\frac{1}{2}} v_{11}^{(1/2)} + \omega^{-1} y^2 v_{11}^{(1)} + \omega^{-\frac{3}{2}} y v_{11}^{(3/2)} + \omega^{-2} v_{11}^{(2)} + \cdots, \tag{3.42h}$$

with

$$v_{11}^{(0)} = -\mathrm{i}\lambda G\left(\bar{x}\right), \tag{3.42i}$$
$$v_{11}^{(1/2)} = \delta\lambda G\left(\bar{x}\right)\left[1 - \exp\left(-\delta\omega^{\frac{1}{2}}y\right)\right], \tag{3.42j}$$
$$v_{11}^{(1)} = \frac{1}{4}\mathrm{i}\lambda^2 G\left(\bar{x}\right)\exp\left(-\delta\omega^{\frac{1}{2}}y\right), \tag{3.42k}$$
$$v_{11}^{(3/2)} = \frac{5}{4}\delta\lambda^2 G\left(\bar{x}\right)\exp\left(-\delta\omega^{\frac{1}{2}}y\right), \tag{3.42l}$$
$$v_{11}^{(2)} = \frac{5}{4}\lambda^2 G\left(\bar{x}\right)\left[\exp\left(-\delta\omega^{\frac{1}{2}}y\right) - 1\right]. \tag{3.42m}$$

A comparison between this, fuller, expansion and the solution obtained in previous sections is given in figure 3.18, which is compared favourably with the previous figure 3.17. Far more agreement between the two solutions for $\omega = 10$ is found, with the solid line being the high frequency approximation and the crosses the 'numerical solution' (although we recall that an expression in terms of integrals of the Airy function

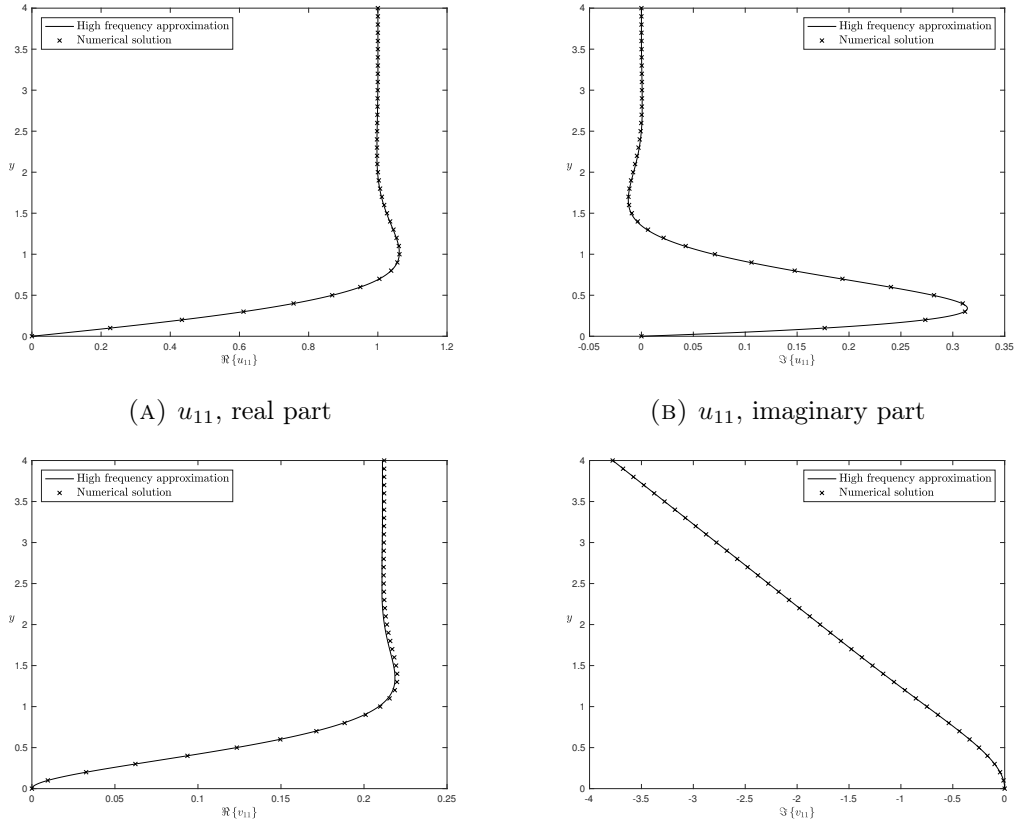

(A) u_{11}, real part

(B) u_{11}, imaginary part

(C) v_{11}, real part

(D) v_{11}, imaginary part

FIGURE 3.18: Comparison between the real and imaginary parts of u_{11} and v_{11}, obtained through the high frequency approximation carried out in this section and summarised in equations (3.42), represented by the solid line, and the solution in terms of the Airy function found in §3.2.2 (crosses), for a blip oscillation frequency of $\omega = 10$. As expected, far greater agreement is found between the two than that of figure 3.17.

was found for the velocities and pressures in §3.2.2). The estimate for the pressure is $-10.2236 + 0.2236\mathrm{i}$ compared with $-10.2228 + 0.2121\mathrm{i}$.

As mentioned, the coefficients of $\tilde{E}$ are obtained in a similar manner, and are listed below:

$$p_{12} = \omega p_{12}^{(0)} + \omega^{-\frac{1}{2}} p_{12}^{(1/2)} + \cdots , \tag{3.43a}$$

with

$$p_{12}^{(0)} = \lambda G(\bar{x}) , \tag{3.43b}$$

$$p_{12}^{(1/2)} = -\mathrm{i}\delta^* \lambda^2 G(\bar{x}) \tag{3.43c}$$

for the pressure;

$$u_{12} = u_{12}^{(0)} + \omega^{-\frac{1}{2}} y^2 u_{12}^{(1/2)} + \omega^{-1} y u_{12}^{(1)} + \cdots , \tag{3.43d}$$

with

$$u_{12}^{(0)} = \lambda G(\bar{x})\left[1 - \exp\left(-\delta^* \omega^{\frac{1}{2}} y\right)\right], \tag{3.43e}$$

$$u_{12}^{(1/2)} = -\frac{1}{4}\delta^* \lambda^2 G(\bar{x}) \exp\left(-\delta^* \omega^{\frac{1}{2}} y\right), \tag{3.43f}$$

$$u_{12}^{(1)} = -\frac{3}{4}\lambda^2 G(\bar{x}) \exp\left(-\delta^* \omega^{\frac{1}{2}} y\right) \tag{3.43g}$$

for the streamwise velocity; and

$$v_{12} = y v_{12}^{(0)} + \omega^{-\frac{1}{2}} v_{12}^{(1/2)} + \omega^{-1} y^2 v_{12}^{(1)} + \omega^{-\frac{3}{2}} y v_{12}^{(3/2)} + \omega^{-2} v_{12}^{(2)} + \cdots, \tag{3.43h}$$

with

$$v_{12}^{(0)} = -\mathrm{i}\lambda G(\bar{x}), \tag{3.43i}$$

$$v_{12}^{(1/2)} = \delta^* \lambda G(\bar{x})\left[\exp\left(-\delta^* \omega^{\frac{1}{2}} y\right) - 1\right], \tag{3.43j}$$

$$v_{12}^{(1)} = -\frac{1}{4}\mathrm{i}\lambda^2 G(\bar{x}) \exp\left(-\delta^* \omega^{\frac{1}{2}} y\right), \tag{3.43k}$$

$$v_{12}^{(3/2)} = \frac{5}{4}\delta^* \lambda^2 G(\bar{x}) \exp\left(-\delta^* \omega^{\frac{1}{2}} y\right), \tag{3.43l}$$

$$v_{12}^{(2)} = \frac{5}{4}\lambda^2 G(\bar{x})\left[\exp\left(-\delta^* \omega^{\frac{1}{2}} y\right) - 1\right] \tag{3.43m}$$

for the normal velocity.

Further terms can of course be computed to obtain an ever better approximation to the actual solutions: however, we have determined sufficiently many terms to find the leading order steady streaming velocity and we therefore proceed to order h^2.

3.4.2 Checking the Reynolds stress, steady streaming and mean flow correction

We will restrict our attention here to the high frequency expansion of the steady streaming velocity u_{20}, and leave the other subscripted terms, multiplying E, $\tilde{E}$ and their harmonics, aside in the interests of conciseness. The governing system of equations for u_{20} is that given by (3.18), with the infinity condition modified as discussed in §3.3, reproduced here below:

$$\frac{\partial^2 u_{20}}{\partial y^2} = R(\bar{x}, y),$$

$$R(\bar{x}, y) = 2\Re\left\{v_{11}\frac{\partial u_{11}^*}{\partial y} + v_{12}\frac{\partial u_{12}^*}{\partial y}\right\},$$

$$u_{20} = 0 \quad \text{on } y = 0,$$

$$\frac{\partial u_{20}}{\partial y} \to 0 \quad \text{as } y \to \infty.$$

We begin by considering the flow in the Stokes layer, where $y = \omega^{-\frac{1}{2}}\hat{y}$ and thus the solutions found at $\mathcal{O}(h)$, equations (3.42) and (3.43), can be written as

$$\hat{u}_1 = \hat{u}_1^{(0)} + \omega^{-\frac{3}{2}}\hat{u}_1^{(3/2)} + \cdots, \tag{3.44a}$$

$$\hat{v}_1 = \omega^{-\frac{1}{2}}\hat{v}_1^{(1/2)} + \omega^{-2}\hat{v}_1^{(2)} + \cdots; \tag{3.44b}$$

where

$$\hat{u}_1^{(0)} = u_1^{(0)}, \tag{3.44c}$$

$$\hat{u}_1^{(3/2)} = \hat{y}^2 u_1^{(1/2)} + \hat{y}u_1^{(1)}, \tag{3.44d}$$

$$\hat{v}_1^{(1/2)} = \hat{y}v_1^{(0)} + v_1^{(1/2)}, \tag{3.44e}$$

$$\hat{v}_1^{(2)} = \hat{y}^2 v_1^{(1)} + \hat{y}v_1^{(3/2)} + v_1^{(2)}. \tag{3.44f}$$

The Reynolds stress R in expanded form is then given by

$$\begin{aligned} R = 2\Re\Bigg\{ &\left[\hat{v}_{11}^{(1/2)}\frac{\partial \hat{u}_{11}^{*(0)}}{\partial \hat{y}} + \hat{v}_{12}^{(1/2)}\frac{\partial \hat{u}_{12}^{*(0)}}{\partial \hat{y}}\right] \\ &+ \omega^{-\frac{3}{2}}\left[\hat{v}_{11}^{(1/2)}\frac{\partial \hat{u}_{11}^{*(3/2)}}{\partial \hat{y}} + \hat{v}_{11}^{(2)}\frac{\partial \hat{u}_{11}^{*(0)}}{\partial \hat{y}} + \hat{v}_{12}^{(1/2)}\frac{\partial \hat{u}_{12}^{*(3/2)}}{\partial \hat{y}} + \hat{v}_{12}^{(2)}\frac{\partial \hat{u}_{12}^{*(0)}}{\partial \hat{y}}\right]\Bigg\}, \end{aligned}$$

but the terms in the first square brackets sum to an imaginary number, with zero real part. The Reynolds stress is, therefore, of order $\omega^{-3/2}$ and this is confirmed by the asymptote plotted in figure 3.19. This validates our expansion of the velocities at $\mathcal{O}(h)$ to second order in ω and, together with the equation for u_{20}, in turn indicates that the steady streaming velocity is of $\mathcal{O}(\omega^{-5/2})$.

Denoting by $\hat{u}_{20}$ the solution to u_{20} at order $\omega^{-5/2}$ expressed in the normal coordinate of the Stokes layer ($\hat{y}$), it must satisfy

$$\begin{aligned} \frac{\partial^2 \hat{u}_{20}}{\partial \hat{y}^2} = \lambda^3 G^2(\bar{x})\exp\left(-\hat{y}\sqrt{2}\right)\Bigg\{&\sqrt{2} + \hat{y}\left(6 + y\sqrt{2}\right) \\ &+ \exp\left(\frac{\hat{y}}{\sqrt{2}}\right)\Bigg[-\left(\sqrt{2} + \hat{y} - \hat{y}^3\right)\cos\left(\frac{\hat{y}}{\sqrt{2}}\right) \\ &- \left(4\sqrt{2} - 3\hat{y} + \hat{y}^2\sqrt{2}\right)\sin\left(\frac{\hat{y}}{\sqrt{2}}\right)\Bigg]\Bigg\}; \end{aligned}$$

which we integrate twice to obtain

$$\hat{u}_{20} = \frac{1}{\sqrt{2}}\lambda^3 G^2(\bar{x})\,\bar{R}(\hat{y}) + A(\bar{x})\,\hat{y} + B(\bar{x}),$$

where

$$\begin{aligned} \bar{R}(\hat{y}) = \exp\left(-\hat{y}\sqrt{2}\right)\Bigg[&10 + 5\hat{y}\sqrt{2} + \hat{y}^2 - \left(24 + 19\hat{y}\sqrt{2} + 8\hat{y}^2\right)\exp\left(\frac{\hat{y}}{\sqrt{2}}\right)\cos\left(\frac{\hat{y}}{\sqrt{2}}\right) \\ &- \left(-34 - 5\hat{y}\sqrt{2} + 6\hat{y}^2 + \hat{y}^3\sqrt{2}\right)\exp\left(\frac{\hat{y}}{\sqrt{2}}\right)\sin\left(\frac{\hat{y}}{\sqrt{2}}\right)\Bigg]. \end{aligned} \tag{3.45}$$

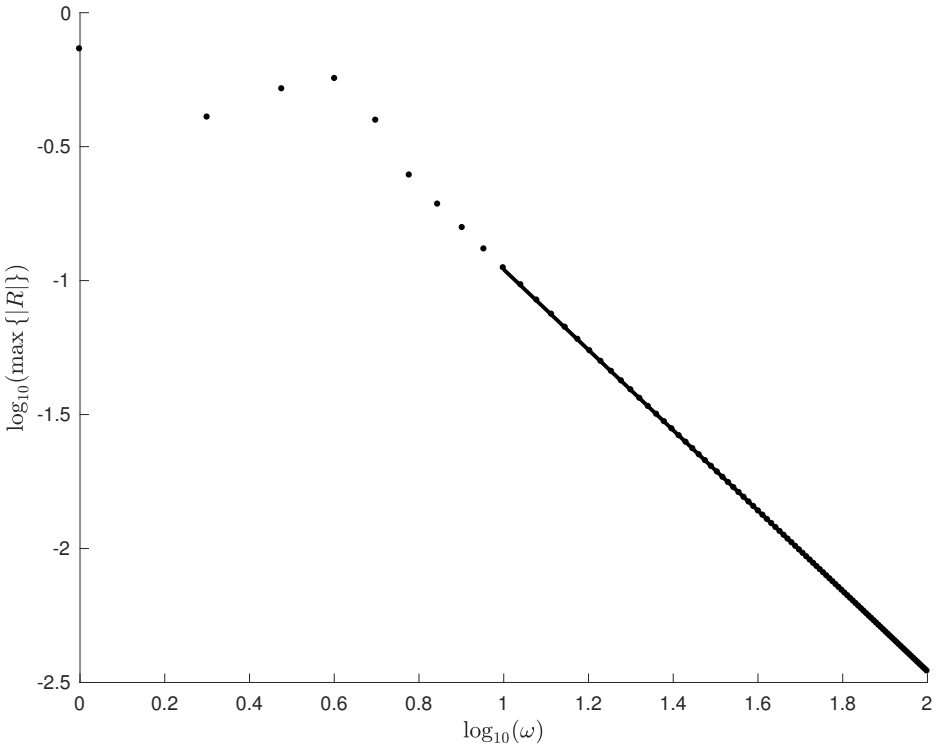

FIGURE 3.19: Maximum value of the Reynolds stress obtained in the interval $y \in [0, 10]$ against the blip oscillation frequency (dots). The logarithm to the base 10 of both is taken and the solid line indicates the asymptote with gradient $-3/2$, confirming the scaling of the Reynolds stress as $R \sim \omega^{-3/2}$.

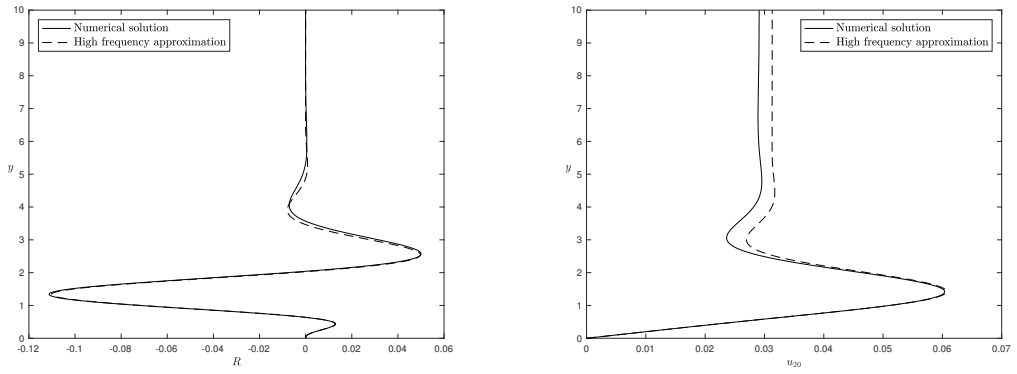

(A) Reynolds stress comparison (B) Steady streaming comparison

FIGURE 3.20: Comparison between the numerical solution (solid line) and the high frequency approximation (dashed line) to the Reynolds stress and steady streaming velocity for $\omega = 10$. The Reynolds stress shows excellent agreement, while the steady streaming high frequency solution overestimates its numerical counterpart. The predicted behaviour, however, is the same.

Imposing the no-slip boundary condition at the wall gives B as

$$B\left(\bar{x}\right) = -\frac{1}{\sqrt{2}}\lambda^3 G^2\left(\bar{x}\right)\bar{R}(0) = 7\sqrt{2}\lambda^3 G^2\left(\bar{x}\right),$$

while the requirement that the steady streaming velocity remains finite as $\hat{y} \to \infty$ dictates that $A\left(\bar{x}\right)$ be zero. Noticing that $\bar{R}\left(\hat{y}\right) \to 0$ as $\hat{y} \to \infty$, the steady streaming horizontal velocity is in fact

$$u_{20} = 7\sqrt{2}\lambda^3 G^2\left(\bar{x}\right)\omega^{-\frac{5}{2}}, \tag{3.46}$$

and an upper layer is thus once more required to take this velocity to zero. We conclude this high frequency study with figure 3.20: the high frequency expansion agrees well with the numerical solutions to the Reynolds stress and steady streaming velocities for $\omega = 10$. In theory, one could then proceed to the upper layer, of $\mathcal{O}(h^{-1/3})$, to find an analytic expression for the mean flow correction. In reality, its governing system of equations remains that of (3.28), with the only modification being the matching condition with the inner layer,

$$\bar{u}_M \to 7\sqrt{2}\omega^{-\frac{5}{2}}\lambda^3 G^2\left(\bar{x}\right) \quad \text{as } \bar{y} \to 0.$$

There is no scope, therefore, to change the analysis of the problem, but one would obtain the pressure correction

$$\bar{p}_M = -21\sqrt{2}\omega^{-\frac{5}{2}}\lambda^{\frac{1}{3}}\frac{\mathrm{Ai}'(0)}{\Gamma\left(\frac{1}{3}\right)}\int_0^{\bar{x}} G^2(s)\left(\bar{x}-s\right)^{-\frac{2}{3}}\,\mathrm{d}s, \tag{3.47}$$

which, overall, gives a positive, increasing pressure: in agreement with the conclusions of §3.3.

3.5 Staying positive

Dynamic blips, we have concluded, are able to introduce both a favourable and an adverse pressure gradient to the flow, this pressure gradient having non-zero mean over a cycle of oscillation or when the average over the periodic structure of our individual blips is taken. The sign of the pressure gradient was found to depend on the frequency of oscillation and the resulting direction of the steady streaming velocity. Previous experimental work, however, has focused on roughnesses that did not drop below the surface of the airfoil, i.e. remained non-negative throughout. In this section, therefore, we study the impact of dynamic roughnesses proper, which we represent by the equation

$$F(x,\bar{x},t) = G\left(\bar{x}\right)\sin^2\left(x\right)\sin^2\left(\omega t\right),$$

or, written once more in exponential form,

$$F(x,\bar{x},t) = G\left(\bar{x}\right)\left(E_1 + E_2 - 2E_3 - 2E_4 + \text{c.c.} + 4\right), \tag{3.48a}$$

where

$$E_1 = \exp\left[\mathrm{i}(x+\omega t)\right], \tag{3.48b}$$
$$E_2 = \exp\left[\mathrm{i}(x-\omega t)\right], \tag{3.48c}$$
$$E_3 = \exp\left(\mathrm{i}x\right), \tag{3.48d}$$
$$E_4 = \exp\left(\mathrm{i}\omega t\right), \tag{3.48e}$$

where we have removed the wavenumber α and re-scaled ω by dividing by two. The letters 'c.c.' denote the complex conjugate of the functions $E_1,\ldots,E_4$. The function G once more allows us to change the maximum height of oscillation across the roughness array: similar choices to before will again be made—the first is that of $G=1$, keeping all the roughness elements the same; the second is that of $G=\sin^2\bar{x}$, which gives a varying maximum amplitude while maintaining a non-negative shape throughout (figure 3.21). Conclusions for positive roughnesses can easily be extended to negative dips, however.

The governing equations in the lower layer remain the same as those of (3.5), with F now represented by equation (3.48). Expanding once more the velocities and pressure in powers of the small parameter h, the $\mathcal{O}(1)$ momentum equation, along with the continuity equation, continue to yield $u_0=\lambda y$ and $v_0=0$; but, as will be demonstrated later, the pressure is no longer zero, with

$$p_0 = p_0\left(\bar{x},t\right)$$

instead. The system at $\mathcal{O}(h)$, and most especially the matching condition at infinity, suggests the decomposition of the flow properties into

$$\zeta_1\left(x,\bar{x},y,t\right) = \zeta_{11}\left(\bar{x},y\right)E_1 + \zeta_{12}\left(\bar{x},y\right)E_2 - \zeta_{13}\left(\bar{x},y\right)E_3 - \zeta_{14}E_4\left(\bar{x},y\right) + \text{c.c.} + \zeta_{10}\left(\bar{x},y\right). \tag{3.49}$$

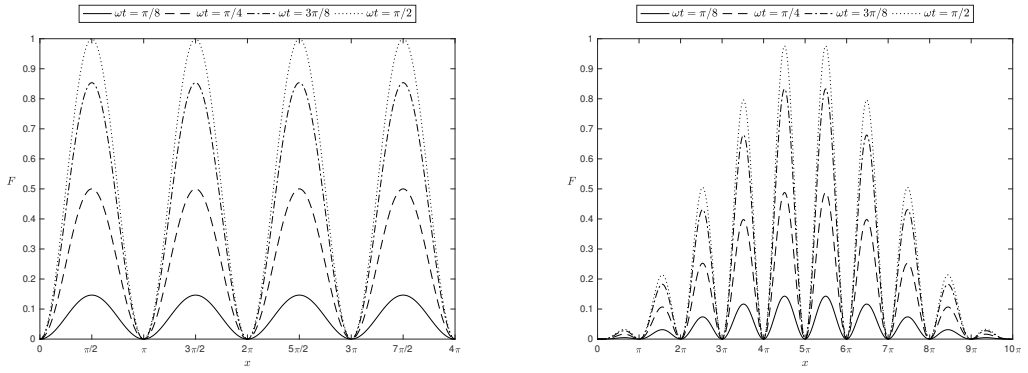

(A) $G(\bar{x}) = 1$ (B) $G(\bar{x}) = \sin^2 \bar{x}$

FIGURE 3.21: Time-dependent wall shape F for different functions $G(\bar{x})$, representing a roughness array with constant maximum oscillation amplitude (a) and varying maximum oscillation amplitude (b). The small parameter h, where $x = h^{-1}\bar{x}$, was set at $h = 0.1$. The wall shapes are shown at different times, corresponding to $\omega t = \pi/8$ (solid line), $\pi/4$ (dashed), $3\pi/8$ (dot–dashed) and $\pi/2$ (dotted).

The governing equations for the functions multiplying E_1 and E_2 are unchanged from those studied in the blip case and so the functions remain the same as those given in §3.2.2. The functions with the subscript '13' are new, and satisfy

$$\mathrm{i}u_{13} + \frac{\partial v_{13}}{\partial y} = 0, \tag{3.50a}$$

$$\mathrm{i}\lambda y u_{13} + \lambda v_{13} = -\mathrm{i}p_{13} + \frac{\partial^2 u_{13}}{\partial y^2}, \tag{3.50b}$$

$$u_{13} = v_{13} = 0 \quad \text{on } y = 0, \tag{3.50c}$$

$$u_{13} \to 2\lambda G(\bar{x}) \quad \text{as } y \to \infty. \tag{3.50d}$$

This is solved in an identical fashion to previous functions determined at $\mathcal{O}(h)$: the problem is reposed in terms of the shear stress τ_{13} by differentiating by y, and we obtain the solution

$$\tau_{13}(\bar{x}, y) = C(\bar{x}) \operatorname{Ai}\left[(\mathrm{i}\lambda)^{\frac{1}{3}} y\right], \tag{3.51a}$$

applying boundedness at infinity. The two boundary conditions (3.50c) and (3.50d) combine to determine C as

$$C(\bar{x}) = 2\lambda G(\bar{x}) \left\{ \int_0^\infty \operatorname{Ai}\left[(\mathrm{i}\lambda)^{\frac{1}{3}} y\right] \mathrm{d}y \right\}^{-1} = 6\lambda(\mathrm{i}\lambda)^{\frac{1}{3}} G(\bar{x}). \tag{3.51b}$$

The pressure is once more found by setting $y = 0$ in equation (3.50b), and so

$$p_{13} = -\mathrm{i}(\mathrm{i}\lambda)^{\frac{1}{3}} \operatorname{Ai}'(0) C(\bar{x}). \tag{3.51c}$$

These are plotted in figures 3.22 and 3.23.

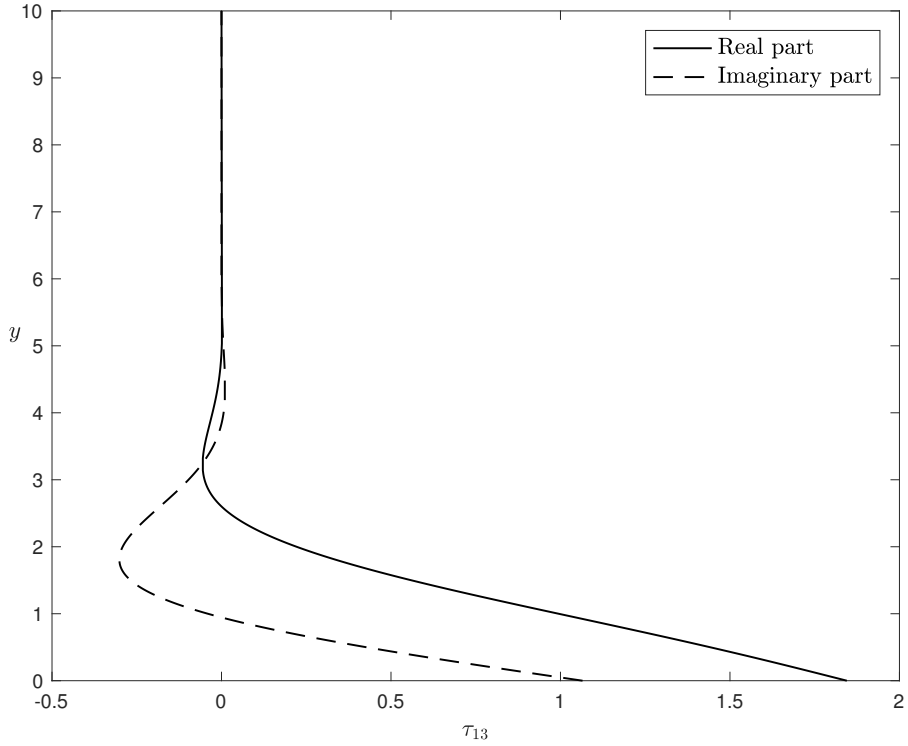

FIGURE 3.22: Real (solid line) and imaginary (dashed) components of τ_{13}, for the constant amplitude function $G(\bar{x}) = 1$. The pressure remains constant across the entirety of the array.

The function multiplying E_4 gives rise to the need for an $\mathcal{O}(1)$ pressure dependent on $\bar{x}$ and t, which we write as $p_0 = p_0(\bar{x}) \exp(\mathrm{i}\omega t)$, where $p_0(\bar{x})$ must be determined. Then, with the continuity equation setting $v_{14} = 0$, the momentum equation becomes

$$\frac{\partial^2 u_{14}}{\partial y^2} - \mathrm{i}\omega u_{14} = -p_0'(\bar{x}). \tag{3.52}$$

The solution, satisfying also the conditions of no-slip and $u_{14} \to 2\lambda G$ as $y \to \infty$, is

$$u_{14} = 2\lambda G\left[1 - \exp\left(-\delta\omega^{\frac{1}{2}} y\right)\right] \tag{3.53a}$$

$$p_0' = 2\mathrm{i}\lambda\omega G, \tag{3.53b}$$

with $\delta = (1+\mathrm{i})/\sqrt{2}$. The absence of the pressure p_0 from equation (3.52) would result, to avoid unbounded growth and to satisfy the no-slip boundary condition, in the trivial zero solution, which would obviously not satisfy the required behaviour at infinity. Alternatively, the pressure (3.53b) can be confirmed by considering flow moving over a flat surface for $x < 0$ and then impulsively starting the region $x \geq 0$ so that it moves up and down with normal velocity $\epsilon \exp(\mathrm{i}\omega t)$, where $\epsilon \ll 1$. For small x, the pressure behaves like $x^{1/3}$, while for large x, $p \sim x$: further analysis shows that it agrees with equation (3.53b).

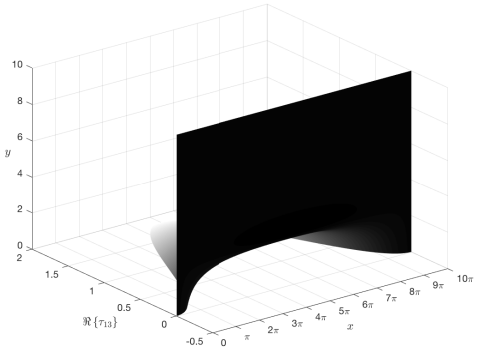

(A) Shear stress, real part

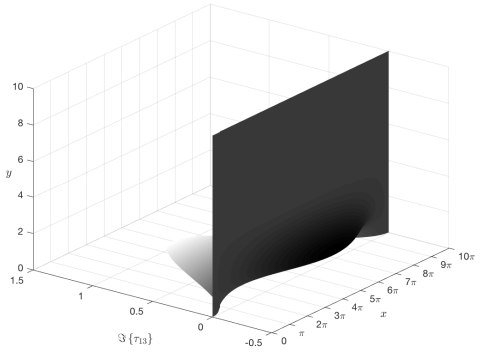

(B) Shear stress, imaginary part

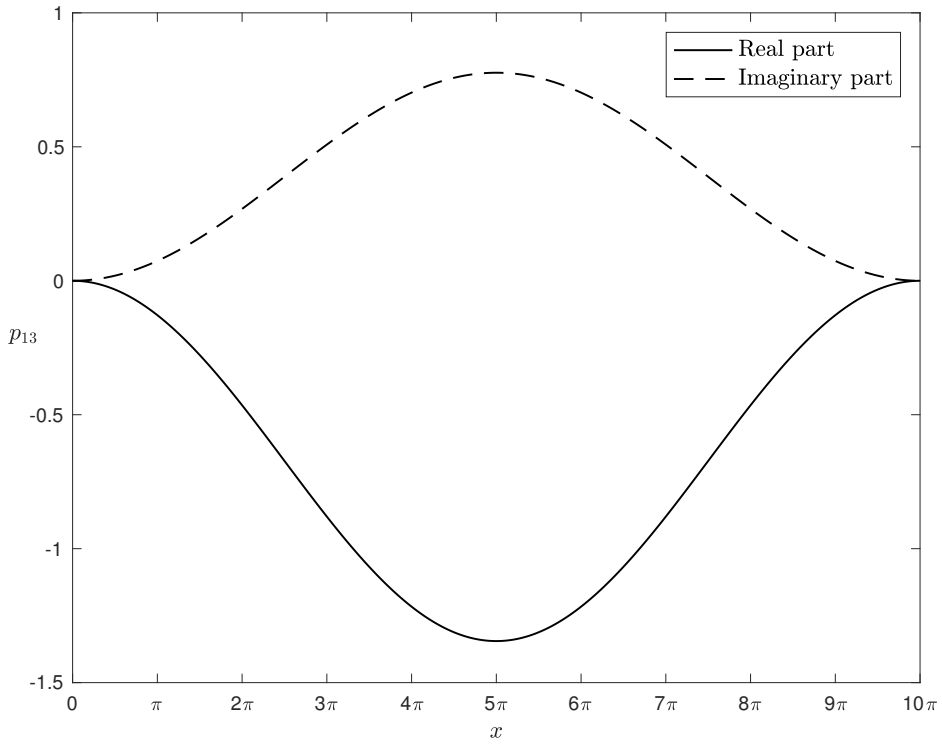

(C) Pressure

FIGURE 3.23: Real and imaginary components of τ_{13} and p_{13}, for the varying amplitude function $G(\bar{x}) = \sin^2 \bar{x}$.

3.5.1 The mean flow correction

The steady streamwise velocity at $\mathcal{O}(h)$ in the lower layer (the normal velocity being zero from the continuity equation) should satisfy the system

$$\frac{\partial^2 u_{10}}{\partial y^2} = 0,$$
$$u_{10} = 0 \quad \text{on } y = 0,$$
$$u_{10} \to 4\lambda G \quad \text{as } y \to \infty,$$

which it cannot. To satisfy the necessary boundary condition at infinity, we have to solve in the upper layer, where $y = h^{-1/3}\bar{y}$. The procedure is then analogous to that followed for the blips of §3.3: the velocities and pressure firstly expand as

$$\bar{u} = h^{-\frac{1}{3}}\lambda\bar{y} + h\left(\lambda\tilde{F} + \bar{u}_M\right) + \cdots, \tag{3.54a}$$
$$\bar{v} = -h^{\frac{2}{3}}\lambda\frac{\partial\tilde{F}}{\partial x}\bar{y} - h^{\frac{5}{3}}\left(\lambda\frac{\partial\tilde{F}}{\partial\bar{x}} + \bar{v}_M\right) + \cdots, \tag{3.54b}$$
$$p = p_0 + h^{\frac{2}{3}}\bar{p}_M + \cdots, \tag{3.54c}$$

where $\tilde{F}$ contains the exponential terms of (3.48); and the mean flow correction pressure now acts at $\mathcal{O}(h^{2/3})$ in order to force the momentum equation, in which the mean flow correction velocities are found, at $\mathcal{O}(h^{5/3})$. This equation is the same as that of (3.28a), with only the boundary conditions being different. In particular, we require

$$\frac{\partial^2\bar{u}_M}{\partial\bar{y}^2} - \lambda\bar{y}\frac{\partial\bar{u}_M}{\partial\bar{x}} - \lambda\bar{v}_M = \frac{\partial\bar{p}_M}{\partial\bar{x}}, \tag{3.55a}$$
$$\bar{u}_M = 0 \quad \text{on } \bar{y} = 0, \tag{3.55b}$$
$$\bar{u}_M \to 4\lambda G \quad \text{as } \bar{y} \to \infty, \tag{3.55c}$$

solved instead for the shear stress $\bar{\tau}_M$ (Fourier-transformed) and, in turn, the pressure gradient $\bar{p}_M$. The key difference is only in the integral condition for the Fourier-transformed shear stress, which now reads

$$\int_0^\infty \hat{\tau}_M \,\mathrm{d}\bar{y} = 4\lambda\hat{G}(\kappa)$$

(c.f. equation (3.29c)), and so, to save the reader from the same calculations as §3.3, we obtain

$$\bar{p}_M(\bar{x}) = 6\lambda^{\frac{5}{3}}\frac{\mathrm{Ai}'(0)}{\Gamma\left(\frac{1}{3}\right)}\left(\int_0^{\bar{x}} G(s)\,(\bar{x}-s)^{-\frac{2}{3}}\,\mathrm{d}s\right). \tag{3.56}$$

With the amplitude function G remaining positive to ensure that our dynamic roughness elements remain roughnesses rather than dips, the pressure will decrease overall across the roughness array. This is most easily seen for when G is a constant, when the pressure gradient becomes proportional to $\bar{x}^{-2/3}$, with the coefficient $6\lambda^{5/3}\mathrm{Ai}'(0)/\Gamma(1/3)$ being

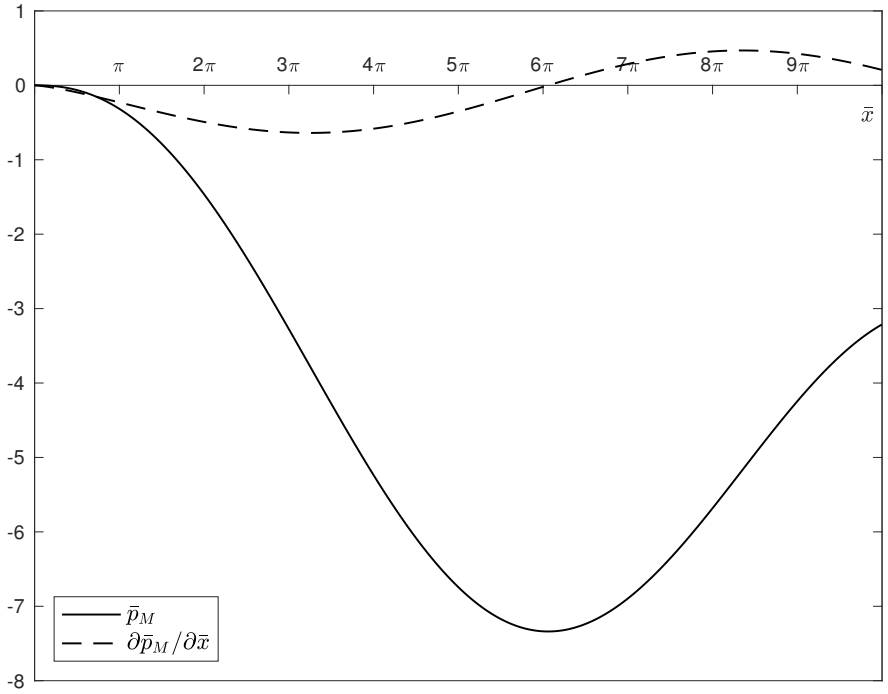

FIGURE 3.24: Mean flow correction pressure (solid line) and pressure gradient (dashed line) for a roughness amplitude function of $G(\bar{x}) = \sin^2 \bar{x}$. The fact that G is non-negative results in the pressure decreasing overall across the roughness array, although adverse gradients are also possible due to the varying nature of G.

negative; for varying G, adverse pressure gradients are present, but provided that G remains non-negative, the pressure will tend to fall, as shown in figure 3.24. For dips, the situation is reversed, and the pressure will tend to increase across the dip array.

For these roughnesses that remain single-signed throughout a cycle of oscillation, the steady streaming velocity as defined in §3.3.1—the result of a nonlinear forcing in the lower layer governing equations giving rise to Reynolds stresses—is no longer present. Rather, its existence comes about directly from the steady part of the boundary condition at infinity failing to be satisfied by the lower layer, which has a height scale associated with the shorter length of a single roughness element. In turn, this means that the mean flow correction is independent of the oscillation frequency of the roughness elements and depends only on how the maximum height of the roughnesses varies across the array; and, since it is the boundary conditions at $\mathcal{O}(h)$ in the lower layer that are not satisfied, the mean flow correction pressure can now act at lower order: $h^{2/3}$ as opposed to $h^{5/3}$.

3.6 Finding ourselves again

We had set out to analyse a similar scenario to that studied both numerically and experimentally by Rothmayer & Huebsch (2011) [66], Huebsch et al. (2012) [41] and Grager et al. (2012) [33], consisting of an array of roughness elements on a surface, over which fluid would travel. While experimental and numerical work is naturally limited to specific sizes of roughness elements, and the more analytical work of Rothmayer & Huebsch restricted itself to roughness elements of length $\mathcal{O}(\mathrm{Re}^{-1/2})$ and height $\mathcal{O}(\mathrm{Re}^{-1})$, we placed ourselves in the more generic setting of 'short' roughness elements and explored the condensed flow equations, valid for a range of roughness sizes. In particular, the analysis presented in this chapter is valid for elements of length between $\mathrm{Re}^{-3/4}$ and $\mathrm{Re}^{-3/8}$, and height between $\mathrm{Re}^{-1/4}$ and $\mathrm{Re}^{-1/8}$, where the Reynolds number is large. This choice was found to be relevant to the roughness array tested by Grager et al. (2012), except for the resultant time scaling, which gave rise to frequencies that were orders of magnitude too high.

Just as in previous work, we ensured that our dynamic roughnesses were unable to provoke separation: in our case, we did so by multiplying the roughness function F by a non-dimensional height h, where $h \ll 1$. This allowed us to linearise the governing equations and solve for the pressure correction introduced into the flow by the roughness elements. Importantly, we found a steady pressure that, when taking the average over a period of oscillation or the short length scale linked to the width of a single roughness, was non-zero: this was termed the 'mean flow correction' and could introduce favourable pressure gradients into the flow over an otherwise flat surface. The mechanism through which this correction came into being depended on the type of roughness present. For 'blips', which were allowed to oscillate both above and below the surface, it was due to the existence of Reynolds stresses, which arose due to the nonlinear inertial terms in the condensed flow equations, in agreement with the findings of Rothmayer & Huebsch (2011). In turn, these Reynolds stresses drove a steady streaming velocity that gave rise to the need for an upper layer, linked to the 'long' length scale of the entire blip array. The steady streaming velocity could be either positive or negative, dependent largely on the frequency of oscillation of the blips, and its sign determined whether the pressure increased or decreased as one proceeded downstream: a negative steady streaming velocity gave rise to stronger favourable pressure gradients, while a positive steady streaming velocity ensured that adverse pressure gradients dominated, although this depended also on how the maximum roughness amplitude, represented by the function $G(\bar{x})$, varied across the array. The fact that higher frequencies give rise to a positive steady streaming velocity at the top of a Stokes layer near the wall, confirmed by a high frequency analysis, ensured that these flows were detrimental to possible separation control, which requires favourable pressure gradients.

Roughnesses that remained single-signed throughout a cycle of oscillation (either positive or negative) produced a mean flow correction not through Reynolds stresses, but

directly through the boundary condition at the wall—or, due to the Prandtl transposition used, through the required behaviour at the top of the viscous sublayer. Contrary to experimental and numerical findings, this ensured that there was no dependence of the steady pressure on the oscillation frequency: rather, whether it was adverse or favourable depended only on whether the roughnesses were positive bumps or negative dips: for bumps, the pressure gradient is favourable; and vice versa for dips. The conclusion, at least, is that bumps should be better than dips when it comes to avoiding separation, partly validating previous work concentrating solely on positive roughnesses and providing some motivation for the focus on bumps that is to follow.

So we find ourselves once more. In a clearing, there is a way marker, left there by a ghost. One could continue straight, towards a mountain peak that glares back in the harsh midday sun. Although we have been motivated by questions of separation control, and we have concluded that the ability of roughnesses to introduce favourable pressure gradients has the potential to be beneficial to the avoidance of flow separation, nowhere in the work of this chapter have we encountered separation itself. Our roughnesses have been too small to provoke separation and we have not imposed any adverse pressure gradient, such as that existing over the upper surface of an airfoil, to drive the flow to separation. Rothmayer & Huebsch (2011) concluded that the angle of attack at which separation occurred could be increased due to the presence of a dynamic roughness array; we can make no such conclusion. The next step could be to mimic the approach of those who came before us and position our roughness array on an airfoil, thereby generalising the paper of Rothmayer and Huebsch [66] to arrays containing elements with any length and height scale in the range given above, rather than just a length and height of order $\mathrm{Re}^{-1/2}$ and Re^{-1} respectively. We note, however, that the cited paper considered three dimensional roughnesses and so, further down the path, a continuation into three dimensions would probably be inevitable.

Alternatively, one could consider separated flow by keeping our roughnesses on a flat surface but maintaining h at $\mathcal{O}(1)$, rather than making it small. In such a case, they would lie along the line of separation of figure 2.4 and each dynamic roughness would be sufficiently tall to provoke separation. From this, it could be interesting to determine what the impact of its oscillatory movement is on the separated flow: is separation suppressed, or delayed, or is there no effect at all? The dynamic motion of the roughness elements could consist either of $\mathcal{O}(1)$ oscillations, with the roughness dropping flush with the flat surface before increasing in amplitude again (as in this and following chapters); or could involve smaller vibrations about a base shape, as described by figure 3.25. By taking these vibrations to be of order $\epsilon \ll 1$, say, a more analytical approach may give some success and could be the appropriate starting point; the former full oscillations of the roughness would probably involve a fully numerical expedition.

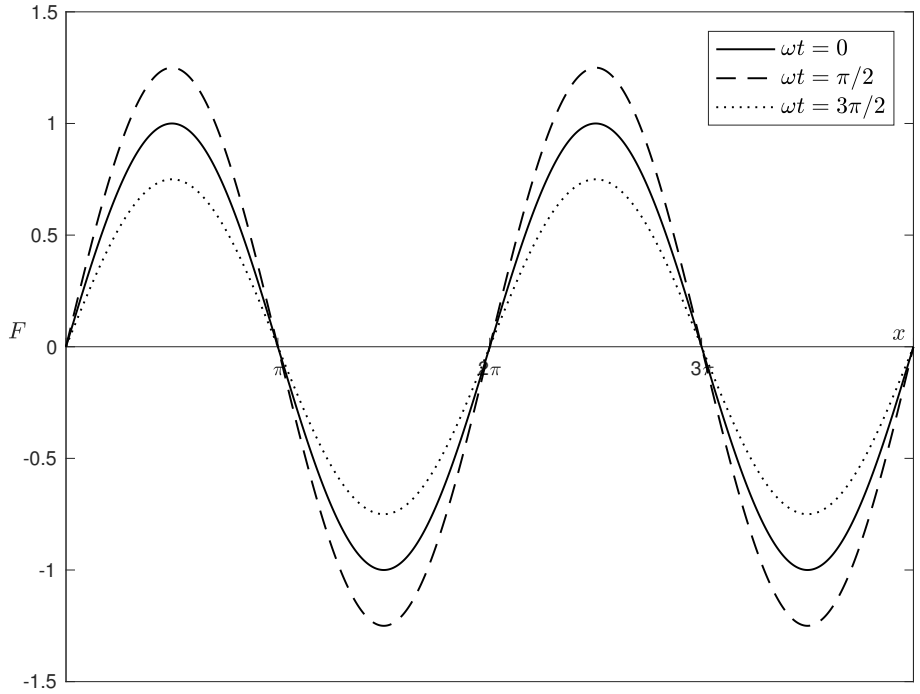

FIGURE 3.25: Dynamic blips, where the oscillatory motion consists of small amplitude vibrations about a base shape: for example $F(x,t) = \sin x + h \sin x \sin(\omega t)$, where h is small (here $h = 0.25$). Once more, one could multiply by an amplitude function $G(\bar{x})$, allowing one to change the height of the bumps as one moves across the array; one could also multiply the time-dependent term by some function that allows one to change the amplitude of the oscillations as one moves across the array. 'Blips' (positive and negative roughnesses) are shown in this figure, but the same principle could be applied to single-signed roughness elements.

We veer, however, westwards, for no good reason other than that, perhaps, "the earth seems more unexhausted and richer on that side" and a desire to follow the sun and "go to a West as distant and as fair as that into which the sun goes down", reaching at last "those mountain ridges in the horizon, though they may be of vapour only, which were last gilded by [the sun's] rays" [95].

4

The night drive: finding Goldstein's singularity

"It's like driving a car at night: you never see further than your headlights, but you can make the whole trip that way."

Edgar Lawrence Doctorow

There was a problem with the boundary layer equations. The two-layered structure, with Prandtl's equations holding in a thin layer, of height scale $\mathcal{O}(\mathrm{Re}^{-1/2})$, above the surface and Euler's equations governing the flow everywhere else, breaks down as the wall skin friction (τ_{wall}) tends to zero. The position of zero skin friction is associated with the separation of the boundary layer from the wall, with forward flow upstream resulting in positive τ_{wall} and reversed flow downstream giving rise to negative skin friction.

Mathematically, there is a singularity in the boundary layer equations (2.13) and its discovery is an admirable example of the insight that is possible when computational and analytical work combine. Although the singularity is now named after Sydney Goldstein, author of the paper that proved its existence [29], its presence had been felt for some time as numerical simulations of boundary layer flow, run on the computers of the first half of the twentieth century, failed to accurately predict what was happening near separation.[1] The work of Douglas Hartree, who solved the governing equations for boundary layer flow with a slip velocity of $U = 1 - x$ (i.e. a decreasing velocity and hence, from Bernouilli's equation (2.1), an increasing pressure)[2]—thankfully on

[1] See, for example, Douglas Hartree's *On an equation occurring in Falkner and Skan's approximate treatment of the equations of the boundary layer* [37], which also provides a fascinating insight into the intricacies involved in setting up and running a numerical simulation in 1937. As well as his many and varied contributions to the fields of physics and mathematics, he is famed (depending on one's definition of the term) for building a differential analyser from parts of Meccano; and his principle that

> *"no one, and no machine, is infallible, and it may fairly be said that the ideal to aim at is not to avoid mistakes entirely, but to find all mistakes that are made, and so free the work from any unidentified mistakes"* [38]

is a worthy foundation on which to base scientific research.

[2] The coefficients β_0 and β_1 appearing in [29] have been removed.

"hand calculating machines rather than on the Differential Analyser in order that more significant figures might be retained"—led him to become

> *"convinced that there was a singularity in the solution at the position of separation, and [Sydney Goldstein thus] undertook to try to find some formulae that would hold near this singularity and would help in finishing the computation"* [29].

This undertaking led to Goldstein's 1948 paper, *On laminar boundary-layer flow near a position of separation*, a *tour de force* of mathematical analysis. Guided in part by Hartree's conclusions, Goldstein set off into a darkness in which the most frightening of equations encircled, held at bay by the headlights of his mathematical dexterity as he drove along Doctorow's road. In this chapter, we will re-derive the existence of Goldstein's singularity and determine the necessity of analysing the flow on smaller length scales, two of which will appear in chapters 5 and 6.

4.1 Approaching the point of zero skin friction

The issue lies in the behaviour of the solution as the position of vanishing skin friction is approached and, in this section, we present the asymptotic structure of the stream function near this point. The detailed expansion was first presented by Goldstein [29], under the assumption—thanks to the work of Hartree—that a singularity existed. Below, we follow in the footsteps of Goldstein but prefer rather the exposition of reference [93], in which no such prior assumption is made.[3]

We consider two dimensional steady flow, which removes the time derivative in Prandtl's boundary layer equations and, with the continuity equation implying the existence of a stream function, as defined in §2.1, expanded in the boundary layer as

$$\psi = \mathrm{Re}^{-\frac{1}{2}}\psi_0 + \cdots ,$$

Prandtl's governing equation reads

$$\frac{\partial\psi_0}{\partial Y}\frac{\partial^2\psi_0}{\partial x\partial Y} - \frac{\partial\psi_0}{\partial x}\frac{\partial^2\psi_0}{\partial Y^2} = -\frac{\partial p}{\partial x} + \frac{\partial^3\psi_0}{\partial Y^3}; \tag{4.1a}$$

solved subject to no-slip,

$$\psi_0 = \frac{\partial\psi_0}{\partial Y} = 0 \quad \text{on } Y = 0, \tag{4.1b}$$

and matching with the inviscid slip velocity (U_e) at the top of the boundary layer,

$$\psi_0 \to U_\mathrm{e}(x) \quad \text{as } Y \to \infty. \tag{4.1c}$$

[3]Note that there are, however, some changes of notation in this section as compared to the cited references: the aim being to provide some greater detail to the derivation and, importantly, to maintain consistency with our forthcoming work in chapters 5 and 6.

The pressure is independent of the normal coordinate Y, which is that of the boundary layer ($y = \mathrm{Re}^{-1/2}Y$), and is therefore set by the external inviscid flow via Euler's equation, as described in chapter 2. Denoting by x_s the streamwise position of zero skin friction ($\tau_\mathrm{wall}(x_\mathrm{s}) = 0$), we are interested in the behaviour of the solution as x_s is approached from the upstream side ($x \to x_\mathrm{s}^-$) and hence we expand the pressure gradient using a Taylor expansion about x_s:

$$\frac{\partial p}{\partial x} = \mu_0 + \mu_1 (x_\mathrm{s} - x) + \cdots , \tag{4.2}$$

where μ_i are the known coefficients of the Taylor expansion and, for the adverse pressure gradient assumed necessary for flow retardation, $\mu_0 > 0$.

A Taylor expansion near the wall (small Y) at x_s can then also be carried out for the stream function: both the coefficients of Y^0 and Y must be zero from no-slip; the coefficient of Y^2 is also zero since we are at the point of vanishing skin friction ($\partial^2\psi_0/\partial Y^2 = 0$); and we end up with the first non-zero term

$$\psi_0 = \frac{1}{6}\mu_0 Y^3 + \cdots , \tag{4.3}$$

with the coefficient of Y^3 obtained by evaluating the momentum equation (4.1a) at the wall.

This process allows us to determine the height scale of the viscous layer near x_s, by balancing the viscous and inertial terms in (4.1a):

$$\frac{\partial \psi_0}{\partial Y}\frac{\partial^2 \psi_0}{\partial x \partial Y} \sim \frac{\partial^3 \psi_0}{\partial Y^3}$$

gives

$$Y \sim (x_\mathrm{s} - x)^{\frac{1}{4}} ; \tag{4.4a}$$

and we therefore introduce a new set of coordinates,

$$\xi = (x_\mathrm{s} - x)^{\frac{1}{4}} \quad \text{and} \quad \eta = Y (x_\mathrm{s} - x)^{-\frac{1}{4}} \tag{4.4b}$$

for the streamwise and normal directions respectively, with both ξ and η of order unity. The stream function expansion we seek therefore takes the form

$$\psi_0 = \xi^3 f_0(\eta) + \xi^{\alpha_1} f_1(\eta) + \xi^{\alpha_2} f_2(\eta) + \cdots , \tag{4.5}$$

where the functions f_i are to be found, and the choice of the exponent α_1, subject to the constraint (4.11) derived below, will give us either the Goldstein singularity of this chapter and the next, or the marginal separation singularity of chapter 6.

Substitution of the expansion (4.5) into the governing equation (4.1a), rewritten with the coordinates of (4.4b), gives the first of the equations which we must successfully

steer our way through,

$$
\begin{aligned}
&-\left(\xi^2 f_0' + \xi^{\alpha_1-1} f_1' + \xi^{\alpha_2-1} f_2'\right) \\
&\quad \left\{\frac{1}{4}\xi^{-2}\left(2f_0' - \eta f_0''\right) + \frac{1}{4}\xi^{\alpha_1-5}\left[\left(\alpha_1-1\right) f_1' - \eta f_1''\right] + \frac{1}{4}\xi^{\alpha_2-5}\left[\left(\alpha_2-1\right) f_2' - \eta f_2''\right]\right\} \\
&+ \left\{\frac{1}{4}\xi^{-1}\left(3f_0 - \eta f_0'\right) + \frac{1}{4}\xi^{\alpha_1-4}\left(\alpha_1 f_1 - \eta f_1'\right) + \frac{1}{4}\xi^{\alpha_2-4}\left(\alpha_2 f_2 - \eta f_2'\right)\right\} \\
&\quad \left(\xi f_0'' + \xi^{\alpha_1-2} f_1'' + \xi^{\alpha_2-2} f_2''\right) \\
&= -\mu_0 + f_0''' + \xi^{\alpha_1-3} f_1''' + \xi^{\alpha_2-3} f_2''', \qquad (4.6)
\end{aligned}
$$

where a prime denotes differentiation with respect to η. The solutions for f_i are found from the terms multiplying the various exponents of ξ, which is small. At order ξ^0, the equation to solve is

$$f_0''' - \frac{3}{4} f_0 f_0'' + \frac{1}{2}\left(f_0'\right)^2 = \mu_0.$$

Taken together with the conditions of no-slip and the form of (4.3), this has the solution

$$f_0\left(\eta\right) = \frac{1}{6}\mu_0 \eta^3. \qquad (4.7)$$

The function f_1 is then found from the terms in (4.6) at $\mathcal{O}(\xi^{\alpha_1-3})$, which give

$$f_1''' - \frac{1}{8}\mu_0 \eta^3 f_1'' + \frac{1}{8}\left(\alpha_1+1\right)\mu_0 \eta^2 f_1' - \frac{1}{4}\mu_0 \alpha_1 \eta f_1 = 0,$$

again to be solved subject to no-slip and a matching condition as $\eta \to \infty$: that the solution to f_1 matches the later terms in the Taylor expansion of the stream function (4.3). The solution is then

$$f_1 = a_0 \eta^2, \qquad (4.8)$$

where the constant a_0 cannot yet be determined. The next terms of interest appear at order ξ^{α_2-3} and at this point the relationship between α_1 and α_2 can be found: the non-linearity in the boundary layer equations and (4.6) allows the solution for f_1 to act as a forcing in the equation for f_2, provided that

$$\xi^{\alpha_1-1}\xi^{\alpha_1-5} \sim \xi^{\alpha_2-3},$$

or

$$\alpha = \alpha_1 = \frac{\alpha_2+3}{2}. \qquad (4.9)$$

The governing equation for f_2 is then

$$f_2''' - \frac{1}{8}\mu_0 \eta^3 f_2'' + \frac{1}{4}(\alpha-1)\mu_0 \eta^2 f_2' - \frac{1}{4}(2\alpha-3)\mu_0 \eta f_2 = \left(1 - \frac{\alpha}{2}\right) a_0^2 \eta^2, \qquad (4.10)$$

solved again subject to no-slip. The complementary function here is $a_1\eta^2$, but the particular integral involves the use of confluent hypergeometric functions, $F(\cdot,\cdot,\cdot)$,

$$f_2^{\mathrm{PI}} = 2\frac{a_0^2}{\mu_0}\eta^2 \int_0^\eta s^{-2}\left[F\left(1-\frac{\alpha}{2},\frac{5}{4},\frac{\mu_0}{32}s^4\right)-1\right]\,\mathrm{d}s,$$

a solution taken from references [69] and [93], but see also [32] for a more detailed treatment of hypergeometric functions in general. In chapter 6, we will follow the same procedure to that which would be required here to obtain the solution to a similar equation. This particular integral grows exponentially as η goes to infinity, unless

$$1-\frac{\alpha}{2} = -m, \quad m \in \mathbb{N},$$

in which case we get algebraic growth. Thus we obtain the condition on α we hinted at previously, namely that

$$\alpha = 2m+2, \quad m \in \mathbb{N},\ m \geq 1; \tag{4.11}$$

the requirement that m be non-zero coming from the fact that α must be strictly greater than 3 to ensure that the second term in the asymptotic expansion (4.5) is smaller than the first for small ξ.

The choice $m = 1$ ($\alpha = 4$) gives rise to the Goldstein singularity—shown below—whose removal provides the starting point of our work in chapter 5; the choice of $m = 2$ ($\alpha = 6$), on the other hand, is the basis for the marginal separation theory of chapter 6.

4.2 Reaching the Goldstein singularity

With $m = 1$, the exponent $\alpha_1 = \alpha$ in the stream function expansion (4.5) equals 4 and the governing equation for f_2 becomes

$$f_2''' - \frac{1}{8}\mu_0\eta^3 f_2'' + \frac{3}{4}\mu_0\eta^2 f_2' - \frac{5}{4}\mu_0\eta f_2 = -a_0^2\eta^2, \tag{4.12a}$$

the solutions for f_0 and f_1 remaining unchanged. The particular integral is then

$$f_2^{\mathrm{PI}} = -\frac{1}{60}a_0^2\eta^5, \tag{4.12b}$$

giving the solution

$$f_2(\eta) = a_1\eta^2 - \frac{1}{60}a_0^2\eta^5. \tag{4.12c}$$

The coefficient a_1, like a_0, remains unknown but can be shown to be proportional to a_0^2 [29]. Combining, therefore, the solutions (4.7), (4.8) and (4.12c), one obtains, in the viscous sublayer of order $\mathrm{Re}^{-1/2}(x_\mathrm{s}-x)^{1/4}$, the stream function expansion

$$\psi_0 = \frac{1}{6}\mu_0(x_\mathrm{s}-x)^{\frac{3}{4}}\eta^3 + a_0(x_\mathrm{s}-x)\eta^2 + (x_\mathrm{s}-x)^{\frac{5}{4}}\left(a_1\eta^2 - \frac{1}{60}a_0^2\eta^5\right) + \cdots \tag{4.13}$$

(c.f. equation (4.5)).

Hence we reach the square root singularity in the wall shear stress that, following the groundbreaking work of Goldstein, has become known as the Goldstein singularity: using the coordinates of the viscous sublayer,

$$\tau_{\text{wall}} = \mathrm{Re}^{\frac{1}{2}} \left(x_{\text{s}} - x\right)^{-\frac{1}{2}} \left.\frac{\partial^2 \psi_0}{\partial \eta^2}\right|_{\eta=0} \sim 2\,\mathrm{Re}^{\frac{1}{2}} a_0 \left(x_{\text{s}} - x\right)^{\frac{1}{2}} + \ldots \quad \text{as } x \to x_{\text{s}}^{-}. \tag{4.14}$$

The behaviour of the wall shear stress as $x^{1/2}$ implies, from the continuity equation, that the normal velocity has to be proportional to $x^{-1/2}$ and thus tends to infinity as the separation point is approached. This unbounded increase in the crossflow velocity results in the need for a greater interaction between the viscous sublayer and the pressure gradient set by the outer inviscid flow; and thence a breakdown in Prandtl's classical boundary layer approach occurs, accompanied by breakaway separation of the boundary layer from the surface.

A cogent mathematical description of the flow behaviour near the point of vanishing skin friction and the mechanisms through which the boundary layer's breakaway separation are possible came a couple of decades later, through the theory of the triple deck. Originally born out of a desire to describe boundary layer flow near the trailing edge of a flat plate [53], or to resolve the unseemly paradox of compressible transonic boundary layers separating prior to the impingement of a shock wave on the surface (despite the governing equations, as they stood at the time, being parabolic and there existing no obvious mechanism for the upstream propagation of disturbances) [55, 91], the triple deck structure allows one to solve for the flow in the vicinity and just downstream of the separation point, obtaining a reversed flow region beneath the separated boundary layer.

As suggested by its name, the triple deck consists of three regions, which are based on earlier work by Lighthill [48]. All three span the same streamwise length scale of order $\mathrm{Re}^{-3/8}$ around the separation point, with the change in velocity due to viscosity restricted to an inner part of the boundary layer, of height scale $\mathcal{O}(\mathrm{Re}^{-5/8})$. The bulk of the boundary layer, once more of height scale $\mathcal{O}(\mathrm{Re}^{-1/2})$, then serves only to deflect the streamlines as the boundary layer lifts itself off the surface—note that this process, however, does not occur under the influence of the pressure gradient in the main deck, since here the perturbation of the pressure acts at a higher order than that of the velocity. Finally, a relationship between the displacement function—describing the breakaway of the boundary layer from the wall—and the pressure perturbation is obtained in an exterior inviscid flow region, which stretches into the Euler flow with a height scale equal to the length scale, $\mathcal{O}(\mathrm{Re}^{-3/8})$.[4]

The above structure therefore allows for free interactions between a viscous sublayer and the inviscid flow and enables the boundary layer to spontaneously develop an adverse

[4]Note that in the case of supersonic flows, the interaction length also scales with $\mathrm{Ma}^{-3/4}$, while the height scale of the lower deck should be multiplied by $\mathrm{Ma}^{-1/4}$, where Ma is the Mach number [91].

pressure gradient and separate from the wall over a very short distance, avoiding the Goldstein singularity. However, Stewartson [89] would go on to show that a triple deck interaction is unable to take a classical boundary layer, acting under the influence of an adverse pressure gradient upstream of the separation point and join it onto another classical boundary layer, albeit with reversed flow, downstream; thereby indicating that the Goldstein singularity, when it occurs, heralds a breakdown of Prandtl's boundary layer theory. Of course, there are scenarios in which the singularity can be removed (chapter 5) or does not appear at all (chaper 6) and, as dawn breaks over the distant horizon and our night drive comes to an end, it is time to get out of the car and tread once more over the soft springiness of the earth, sparkling in the day's first few rays of sunshine, caught by the early morning dew.

5

Flow over a hump: shifting separation

"You can't see anything from a car; you've got to get out of the goddamned contraption and walk, better yet crawl, on hands and knees [...]. When traces of blood begin to mark your trail, you'll see something, maybe."

Edward Abbey, *Desert solitaire*

The quote by Edward Abbey (1927–89), who spent his life railing against the commercialisation of national parks in the US and the destruction of their sanctity by tourists in automobiles, is, perhaps, an odd way to begin a chapter in a thesis whose motivation is, ultimately, of an aerodynamical bent. The rapid and unchecked advance of technology in the last few centuries, since the Industrial Revolution took hold in Britain and was spread to the rest of the world, has, in the eyes of Abbey, led to a violent destruction of nature and, through it, caused humanity to forget what is important in life, "cutting itself off from its origins and betraying the principle of civilisation itself" [1]. He was probably right: the sight of people driving along scars in the earth, thinking that they've seen something, withers the soul a little. Even flying is humanity's way of jumping headfirst into discontinuities: we go from one place to another with no regard for how the terrain, people or cultures change along the way; a process that adds to our collective ignorance, while we delude ourselves to the contrary.

On the other hand, the urge to explore and the desire to immerse oneself in the wild—that place where "the tangible and the mythical became the same"—that drove Edward Abbey to spend time as a ranger at Arches National Monument in Utah, where he wrote the notes that became Desert solitaire, is often the same as that felt by mathematicians. And, even if we are only speaking metaphorically, we often share the crawling and the bleeding too...

In the previous chapter, we derived the existence of Goldstein's singularity in Prandtl's boundary layer equations (2.13) at the point of zero skin friction and described how a triple deck structure could be used to overcome it and incorporate the separation of the boundary layer from a surface. While the existence of the singularity usually causes an unavoidable breakdown in Prandtl's theory [89], in 1981 Smith & Daniels [85] showed that for the case of flow over a hump whose length scale satisfies the scalings of the condensed layer (see figure 2.4 and the discussion of §2.3), the Goldstein singularity can be removed in a physically realistic fashion. In this case, the solution passes regularly through the position of vanishing skin friction, which represents the local separation point, before encountering another singularity farther downstream, which is also removable and represents the global separation point and breakaway separation of the boundary layer from the hump.

In this chapter, our goal, our reason for getting out of the car and crawling on hands and knees through the undergrowth, is that of determining whether a roughness element, static or dynamic, is able to shift the local and global separation points downstream; and how that shift might depend upon the position, width, height and, in the case of a dynamic element, oscillation frequency of the roughness. The route is as follows: the governing equations, along with the asymptotic structure of the flow, are given in §5.1; we will move the Goldstein singularity slightly downstream in §5.2; in §5.3, we will obtain the scaling of the region in which we will both remove the singularity completely and introduce the roughness elements, and then derive the nonlinear equation for the skin friction in the presence of these roughness elements; linearised solutions will be studied in §5.4; while full nonlinear solutions for static and dynamic elements will be presented in §§5.6 and 5.7 respectively, focusing on their ability to shift both the local and global separation points; with conclusions closing in §5.8.

5.1 The landscape: the governing equations

We begin with a 'short' hump, as described by Smith & Daniels [85] and defined in §2.3.1: the characteristic length ℓ and height Δ of the hump satisfy $\mathrm{Re}^{-3/4} \ll \ell \ll \mathrm{Re}^{-3/8}$ and $\mathrm{Re}^{-3/4} \ll \Delta \ll \mathrm{Re}^{-5/8}$, with $\Delta \sim \mathrm{Re}^{-1/2}\ell^{1/3}$ so that we lie on the separation line of figure 2.4, within the realm of the condensed layer.[1] The hump length is therefore smaller than that of the triple deck and thus the flow cannot be resolved on the scales of triple deck theory, as was done in [77]. With x and y being the streamwise and normal coordinates of this sublayer, the governing equations in terms of the stream function ψ, on application of the Prandtl transposition to simplify the boundary

[1] Note that the time, velocities and pressure then scale as given in equation (2.17).

condition at the wall, follow from equations (2.24):

$$u = \frac{\partial \psi}{\partial y}, \quad v = -\frac{\partial \psi}{\partial x}, \tag{5.1a}$$

$$\frac{\partial^2 \psi}{\partial y \partial t} + \frac{\partial \psi}{\partial y}\frac{\partial^2 \psi}{\partial x \partial y} - \frac{\partial \psi}{\partial x}\frac{\partial^2 \psi}{\partial y^2} = -\frac{\partial p}{\partial x}(x,t) + \frac{\partial^3 \psi}{\partial y^3}, \tag{5.1b}$$

subject to

$$\psi = \frac{\partial \psi}{\partial y} = 0 \quad \text{on } y = 0, \tag{5.1c}$$

$$v, p \to 0, \quad u \to y \quad \text{as } x \to -\infty, \tag{5.1d}$$

$$u \to y + hF(x) + f(h,x,t) \quad \text{as } y \to \infty. \tag{5.1e}$$

The first of these boundary conditions represents that of no-slip applied at $y = 0$ due to the intervention of the Prandtl transposition; the second is the matching condition with the oncoming shear flow; and the third is the matching condition as one moves out of the condensed layer, with both the hump shape (hF) and the roughness element (f) that we introduce in this work appearing here.

The parameter h represents a non-dimensional height factor of the hump, within the condensed boundary layer. The above system (5.1) is valid for all finite values of h, with the only restriction being that $h \ll \Delta^{-1}\mathrm{Re}^{-5/8}$. For hump length scales equal to the boundary layer height, $\ell \sim \mathrm{Re}^{-1/2}$, for example, the height scale is $\Delta \sim \mathrm{Re}^{-2/3}$ and thus we require $h \ll \mathrm{Re}^{1/24}$. Since the Reynolds number tends to infinity, we are able to focus on choices where $h \gg 1$ and this is what we will do here: flows over a hump in a condensed boundary layer where $h \ll 1$ and $h = \mathcal{O}(1)$ were studied by Smith in [79] and [78] respectively. The function F is then the $\mathcal{O}(1)$ shape of the hump in the condensed layer, which will not be specified explicitly but must satisfy the following conditions: that it tends to zero far upstream and downstream, that a maximum is achieved at some $x = x_{\max}$, and that $F'(x) > 0$ for $x < x_{\max}$, while $F'(x) < 0$ for $x > x_{\max}$. The function f, meanwhile, represents the roughness elements, added in the appropriate region of the flow and with a non-dimensional height scale that will eventually be chosen as order $h^{-5/4}$.

With the boundary conditions (5.1c)–(5.1e) not allowing for the existence of a singularity in the flow, there must be some way to resolve the Goldstein singularity that is an almost inevitable consequence of equation (5.1b) when the skin friction goes to zero, provided that the pressure gradient is prescribed. Indeed there is: the strategy is that of considering ever smaller length scales around the point of vanishing skin friction, as shown in figure 5.1. The attached flow over the front of the hump, where a favourable pressure gradient exists, can be dealt with using classical boundary layer theory and is represented by region A in figure 5.1. Over the back of the hump, however, the pressure gradient becomes adverse and leads to the appearance of Goldstein's singularity, which can be shifted downstream by considering the flow on a length scale of $\mathcal{O}(h^{-3/2}\ln h)$

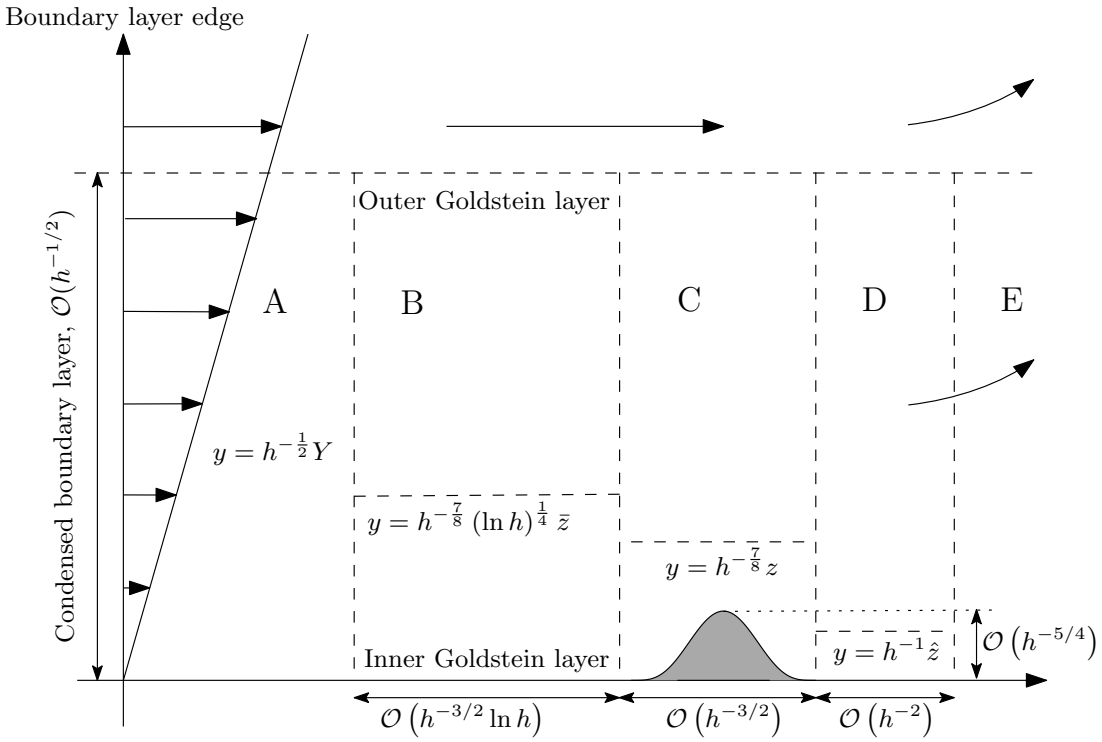

FIGURE 5.1: The development of the flow in the x, y-plane within the condensed boundary layer as it approaches the Goldstein singularity at the end of region A and proceeds downstream. Our roughness element (in grey) is placed in region C and a full description of each region is given in the text. Application of the Prandtl transposition on the hump has transformed it into the x-axis.

about the point of zero skin friction (region B). In this region, the vertical structure splits into two: an inner and an outer Goldstein layer. The singularity can then be removed completely by considering a still smaller length scale in region C, of $\mathcal{O}(h^{-3/2})$, and it is in this region that we place our roughness elements. Our solutions will indicate the presence of a further singularity downstream of the local separation point, and this can be resolved by considering a length scale of $\mathcal{O}(h^{-2})$ around the singularity (region D), which corresponds to the complete nonlinear breakaway of the boundary layer. The separated flow in region E then reattaches itself farther downstream.

Out of necessity, numerous coordinate systems and stream functions must be introduced throughout this chapter and, in a valiant attempt to avoid confusion, these are summarised in table 5.1 for each of the regions shown in figure 5.1. We begin by solving for the flow in regions A and B.

Region	Sub-region	Streamwise	Normal	Stream function	Pressure
Outer inviscid flow		x	$\tilde{y}$	$\tilde{\Psi}$	$\tilde{p}$
A	Upstream	x	Y	$\tilde{\psi}$	$\tilde{p}$
	Inner Goldstein layer	ξ	η	$\tilde{\psi}^{\mathrm{i}}$	$\tilde{p}$
	Outer Goldstein layer	x	Y	$\tilde{\psi}^{\mathrm{o}}$	$\tilde{p}$
B	Inner Goldstein layer	$\bar{x}$	$\bar{z}$	$\bar{\psi}$	$\bar{p}$
	Outer Goldstein layer	$\bar{x}$	Y	$\bar{\Psi}$	$\bar{p}$
C	Inner Goldstein layer	X	z	ψ	p
	Outer Goldstein layer	X	Y	Ψ	p
D	Inner Goldstein layer	$\hat{x}$	$\hat{z}$	$\hat{\psi}$	$\hat{p}$
	Outer Goldstein layer	$\hat{x}$	Y	$\hat{\Psi}$	$\hat{p}$
E		—	—	—	—

TABLE 5.1: List of coordinate systems, stream functions and pressures used in the various regions depicted in figure 5.1.

5.2 Getting out of the car: the Goldstein singularity

In chapter 4, we found the Goldstein singularity by considering a viscous sublayer, corresponding to the inner Goldstein layer of this chapter, near the point of zero skin friction. It remains in this section to complete the picture and find the expansion of the stream function in the attached flow upstream of the singularity, in the outer Goldstein layer and in the main bulk of the boundary layer sitting above the condensed flow layer, in order to provide ourselves with the necessary matching conditions. Finally, in §5.2.2, by considering a small length scale around the singularity, we will succeed in moving it slightly downstream.

5.2.1 Attached flow

Upstream of the roughness elements, the flow is steady (we assume that there are no influences coming from downstream, where the dynamic roughnesses are found) and thus the governing equations (5.1) are reduced to

$$u = \frac{\partial \psi}{\partial y}, \quad v = -\frac{\partial \psi}{\partial x}, \tag{5.2a}$$

$$\frac{\partial \psi}{\partial y}\frac{\partial^2 \psi}{\partial x \partial y} - \frac{\partial \psi}{\partial x}\frac{\partial^2 \psi}{\partial y^2} = -p'(x) + \frac{\partial^3 \psi}{\partial y^3}, \tag{5.2b}$$

$$\psi = \frac{\partial \psi}{\partial y} = 0 \quad \text{at } y = 0, \tag{5.2c}$$

$$u \to y, \quad v, p \to 0, \quad \text{as } x \to -\infty, \tag{5.2d}$$

$$u \sim y + hF(x) \quad \text{as } y \to \infty. \tag{5.2e}$$

With the scaled length of the hump being of $\mathcal{O}(1)$, we take $x \sim 1$ also. The boundary conditions (5.2d) and (5.2e) give rise to the scalings for u and y of $u \sim y \sim h$; and, from the definition of the stream function (5.2a), $\psi \sim h^2$. Then, since the left-hand side of (5.2b) is $\mathcal{O}(h^2)$ and the viscous term on the right-hand side is $\mathcal{O}(h^{-1})$, we must require $p \sim h^2$ for a non-trivial balance. The scalings for this regime, therefore, are

$$x \sim 1, \quad y \sim h, \quad u \sim h, \quad \psi \sim h^2, \quad p \sim h^2. \tag{5.3}$$

The condition at infinity (5.2e) can be expressed in terms of the stream function as

$$\tilde{\Psi} \sim \frac{1}{2}\left[y + hF\left(x\right)\right]^2 + \tilde{p}\left(x\right) \quad \text{as } y \to \infty, \tag{5.4}$$

where the pressure appears due to the evaluation of equation (5.2b) in the limit $y \to \infty$. (The tilde denotes a solution in the attached flow region A of figure 5.1, with the use of $\tilde{\Psi}$ referring to the outer inviscid layer and $\tilde{\psi}$ reserved for the viscous layer introduced shortly, as summarised in table 5.1.) Since the pressure is of order h^2, we can expand it as $\tilde{p} = h^2\tilde{p}_0 + \cdots$ and, introducing the scaled vertical height $\tilde{y}$ for the outer inviscid flow, $y = h\tilde{y}$, $\tilde{y} \sim 1$, we can write the stream function (5.4) as

$$\tilde{\Psi} = h^2\left[\frac{1}{2}\left(\tilde{y} + F\right)^2 + \tilde{p}_0\right] + \cdots, \tag{5.5a}$$

which can be differentiated with respect to $\tilde{y}$ to obtain the horizontal velocity

$$\tilde{U} = h\left(\tilde{y} + F\right) + \cdots. \tag{5.5b}$$

This stream function and streamwise velocity satisfy the system given in (5.2) except for the no-slip condition at the wall. As usual, we allow the tangential slip velocity $\tilde{U} = hF$ but set the normal velocity to be equal to zero at the wall, i.e. $\tilde{V} = -\tilde{\Psi}_x = 0$. This implies that

$$\tilde{p}_0 = -\frac{1}{2}F^2(x), \tag{5.6}$$

where (5.2d) sets the constant of integration equal to zero. The non-zero slip velocity, however, calls for the existence of a viscous sublayer near the wall. With the pressure $\mathcal{O}(h^2)$ and the slip velocity $\mathcal{O}(h)$, the viscous term in (5.2b) acts at leading order if $y \sim h^{-1/2}$. We define, therefore, the lower layer scaled normal coordinate

$$y = h^{-\frac{1}{2}}Y, \quad Y \sim 1; \tag{5.7}$$

this, coupled with the leading order term in $\tilde{U}$, allows us to expand the stream function in the lower layer as

$$\tilde{\psi} = h^{\frac{1}{2}}\tilde{\psi}_0 + \cdots. \tag{5.8}$$

Substituting this into the system (5.2), we obtain the governing equations for the leading order terms in our viscous layer expansion:

$$\frac{\partial\tilde{\psi}_0}{\partial Y}\frac{\partial^2\tilde{\psi}_0}{\partial x\partial Y} - \frac{\partial\tilde{\psi}_0}{\partial x}\frac{\partial^2\tilde{\psi}_0}{\partial Y^2} = FF' + \frac{\partial^3\tilde{\psi}_0}{\partial Y^3}, \tag{5.9a}$$

$$\tilde{\psi}_0 = \frac{\partial\tilde{\psi}_0}{\partial Y} = 0 \quad \text{at } Y = 0, \tag{5.9b}$$

$$\tilde{\psi}_0, \frac{\partial\tilde{\psi}_0}{\partial Y} \to 0 \quad \text{as } x \to -\infty, \tag{5.9c}$$

$$\frac{\partial\tilde{\psi}_0}{\partial Y} \to F \quad \text{as } Y \to \infty. \tag{5.9d}$$

This is classical boundary layer flow as obtained by Prandtl in 1904 [60]: the pressure gradient in this case is known ($-FF'$) and, given a positive hump ($F > 0$), is favourable upstream of the hump peak, allowing us to solve numerically as separation and reversed flow cannot occur [6].

Within this viscous layer, the boundary condition at infinity (5.9d), upon integrating, gives

$$\tilde{\psi}_0 \to F(x)\left[Y - \beta_0(x)\right] \quad \text{as } Y \to \infty, \tag{5.10}$$

where $\beta_0(x)$ is determined from the numerical solution to the system (5.9). The second order correction to the leading order solution in the inviscid layer (5.5) can now be computed by writing the above stream function using the coordinate $\tilde{y}$:

$$\tilde{\psi} = h^2 F\tilde{y} - h^{\frac{1}{2}}\beta_0 F + \cdots . \tag{5.11}$$

Matching between the outer inviscid and inner viscous layers determines the next term in the expansion of both the pressure and inviscid stream function, with

$$\tilde{p} = -\frac{1}{2}h^2F^2 - h^{\frac{1}{2}}\beta_0(x)F(x) + \cdots \tag{5.12a}$$

and

$$\tilde{\Psi} = \frac{1}{2}h^2\left[(\tilde{y}+F)^2 - F^2\right] - h^{\frac{1}{2}}\beta_0(x)F(x) + \cdots . \tag{5.12b}$$

Descending back down to the viscous layer will now allow us to determine the second order terms there. Writing (5.12b) in terms of the viscous layer coordinate Y indicates the next term in the stream function expansion, as well as the matching condition. Noting that $\tilde{y} = h^{-3/2}Y$,

$$\tilde{\Psi} = h^{\frac{1}{2}}\left(YF - \beta_0 F\right) + \frac{1}{2}h^{-1}\left[Y^2 + \mathcal{O}(1)\right] + \cdots ,$$

and hence the second order term in the viscous layer stream function is of order h^{-1},

$$\tilde{\psi} = h^{\frac{1}{2}}\tilde{\psi}_0 + h^{-1}\tilde{\psi}_1 + \cdots , \tag{5.13}$$

where $\tilde{\psi}_0$ would previously have been found numerically. Substituting the above into (5.2b) gives the governing equation for $\tilde{\psi}_1$

$$\frac{\partial\tilde{\psi}_0}{\partial Y}\frac{\partial^2\tilde{\psi}_1}{\partial x\partial Y}+\frac{\partial\tilde{\psi}_1}{\partial Y}\frac{\partial^2\tilde{\psi}_0}{\partial x\partial Y}-\frac{\partial\tilde{\psi}_0}{\partial x}\frac{\partial^2\tilde{\psi}_1}{\partial Y^2}-\frac{\partial\tilde{\psi}_1}{\partial x}\frac{\partial^2\tilde{\psi}_0}{\partial Y^2}=-\tilde{p}_1'+\frac{\partial^3\tilde{\psi}_1}{\partial Y^3}, \tag{5.14a}$$

$$\tilde{\psi}_1=\frac{\partial\tilde{\psi}_1}{\partial Y}=0 \quad \text{on } Y=0, \tag{5.14b}$$

$$\tilde{\psi}_1\to\frac{1}{2}Y^2 \quad \text{as } x\to-\infty, \tag{5.14c}$$

$$\tilde{\psi}_1\to\frac{1}{2}Y^2+\tilde{p}_2 \quad \text{as } Y\to\infty. \tag{5.14d}$$

Again we solve (5.14) numerically, allowing us to obtain the third order pressure term $\tilde{p}_2$ by matching with the inviscid layer, from which we could then calculate $\tilde{\psi}_2$ in the viscous layer, and the yo-yoing would continue until we have determined our solution to as accurate a level as we want. In our case, the first two terms in the viscous layer will suffice.

The inner Goldstein layer

As described in chapter 4, the numerical solution of system (5.9) breaks down in a singular manner when x approaches the separation point, labelled x_s. In the scenario considered here, the leading order term in the Taylor series expansion of the pressure gradient is

$$\tilde{p}'=-h^2F_\mathrm{s}F_\mathrm{s}',$$

where $F_\mathrm{s}=F(x_\mathrm{s})$, and hence, referring back to equation (4.2),

$$\mu_0=-F_\mathrm{s}F_\mathrm{s}'>0. \tag{5.15}$$

The appropriate streamwise and normal coordinates in the inner Goldstein layer remain

$$\xi=(x_\mathrm{s}-x)^{\frac{1}{4}} \text{ and } \eta=Y\,(x_\mathrm{s}-x)^{-\frac{1}{4}}=Y\xi^{-1}, \tag{5.16}$$

both of order 1; and the expansion of the stream function is given by equation (4.13), reproduced below:

$$\tilde{\psi}_0^\mathrm{i}=\frac{1}{6}\mu_0\,(x_\mathrm{s}-x)^{\frac{3}{4}}\,\eta^3+a_0\,(x_\mathrm{s}-x)\,\eta^2+(x_\mathrm{s}-x)^{\frac{5}{4}}\left(a_1\eta^2-\frac{1}{60}a_0^2\eta^5\right)+\cdots. \tag{5.17}$$

The outer Goldstein layer

Missing from the work of chapter 4 is the solution to the flow in the outer Goldstein layer, which keeps the normal coordinate $Y=\xi\eta$. Rewriting the stream function in the

inner Goldstein layer (5.17) in terms of Y gives

$$\tilde{\psi}_0^{\mathrm{i}} = \frac{1}{6}\mu_0 Y^3 + a_0\xi^2 Y^2 + a_1\xi^3 Y^2 - \frac{1}{60}a_0^2 Y^5 + \cdots$$

and so we seek an expansion in the outer Goldstein layer of the form

$$\tilde{\psi}_0^{\mathrm{o}} = \chi_0(Y) + \xi^2\chi_1(Y) + \xi^3\chi_2(Y) + \cdots .$$

Matching with the inner layer imposes the conditions

$$\chi_0(Y) \to \frac{1}{6}\mu_0 Y^3 - \frac{1}{60}a_0^2 Y^5 + \cdots , \tag{5.18a}$$

$$\chi_1(Y) \to a_0 Y^2 + \cdots , \tag{5.18b}$$

$$\chi_2(Y) \to a_1 Y^2 + \cdots , \tag{5.18c}$$

as $Y \to 0$. The boundary condition at infinity comes from that in the viscous layer (5.10), expanded using a Taylor series about the separation point

$$\tilde{\psi}_0 \to F_{\mathrm{s}}\left(Y - \beta_{\mathrm{s}}\right) + \mathcal{O}\left(\xi^4\right),$$

where $\beta_{\mathrm{s}} = \beta(x_{\mathrm{s}})$. So

$$\chi_0 \to F_{\mathrm{s}}\left(Y - \beta_{\mathrm{s}}\right) + o(1) \quad \text{as } Y \to \infty. \tag{5.19}$$

Noting that $\chi_1 \sim \chi_2 \sim \chi_0'$, we can rewrite the stream function in the outer Goldstein layer as

$$\tilde{\psi}_0^{\mathrm{o}} = \psi_{0\mathrm{s}}(Y) + \frac{2a_0}{\mu_0}\left(x_{\mathrm{s}} - x\right)^{\frac{1}{2}}\psi_{0\mathrm{s}}'(Y) + \frac{2a_1}{\mu_0}\left(x_{\mathrm{s}} - x\right)^{\frac{3}{4}}\psi_{0\mathrm{s}}'(Y), \tag{5.20a}$$

where

$$\psi_{0\mathrm{s}} \sim \frac{1}{6}\mu_0 Y^3 - \frac{1}{60}a_0^2 Y^5 + \ldots \quad \text{as } Y \to 0 \tag{5.20b}$$

and

$$\psi_{0\mathrm{s}} \sim F_{\mathrm{s}}\left(Y - \beta_{\mathrm{s}}\right) + o(1) \quad \text{as } Y \to \infty. \tag{5.20c}$$

Outside the Goldstein layers

Outside the Goldstein layers we encounter the inviscid region where the stream function was found to be (5.12b). Writing this in the form of the viscous layer coordinate Y and expanding about the separation point x_{s} gives

$$\tilde{\Psi} \sim h^{\frac{1}{2}}\left(YF_{\mathrm{s}} - \beta_0 F_{\mathrm{s}}\right) + \frac{1}{2}h^{-1}Y^2 + \cdots .$$

Then, if one also takes the limit $Y \to \infty$ of equation (5.20a),

$$\tilde{\psi}_0^{\mathrm{o}} \to F_{\mathrm{s}}\,(Y - \beta_{\mathrm{s}}) + \frac{2a_0}{\mu_0}\,(x_{\mathrm{s}} - x)^{\frac{1}{2}}\,F_{\mathrm{s}} + \frac{2a_1}{\mu_0}\,(x_{\mathrm{s}} - x)^{\frac{3}{4}}\,F_{\mathrm{s}},$$

and matching between the stream function in the outer Goldstein layer and inviscid region, one obtains the expansion of β_0 near the separation point:

$$\beta_0(x) \sim \beta_{\mathrm{s}} - \frac{2a_0}{\mu_0}\,(x_{\mathrm{s}} - x)^{\frac{1}{2}} - \frac{2a_1}{\mu_0}\,(x_{\mathrm{s}} - x)^{\frac{3}{4}} + \cdots . \tag{5.21}$$

With the aim being to remove the Goldstein singularity, we first turn our attention to region B of figure 5.1, where the singularity will be shifted downstream.

5.2.2 Shifting the Goldstein singularity

Our hope lies in finding some new streamwise length scale existing near the separation point, which will allow us to overcome the Goldstein singularity: the search for this new scaling must start with a solution to the second order stream function in the inner and outer Goldstein layers. As per the work of Smith & Daniels [85], we introduce the expansion for the second order stream function in the inner Goldstein layer,

$$\tilde{\psi}_1^{\mathrm{i}} = \ln\left(\xi^4\right) g_{0L}(\eta) + g_0(\eta) + \xi \ln\left(\xi^4\right) g_{1L}(\eta) + \xi g_1(\eta), \tag{5.22}$$

while keeping the expansion for $\tilde{\psi}_0^{\mathrm{i}}$ found earlier in (5.17). The aim is to substitute this into the governing equation (5.14a) to determine the functions g_i. Eventually, one ends up with the equation

$$\begin{aligned}
&-\frac{1}{4}\left[\frac{\mu_0}{2}\xi^2\eta^2 + 2a_0\xi^3\eta + \xi^4\left(2a_1\eta - \frac{1}{12}a_0^2\eta^4\right)\right] \\
&\quad\left\{\left[-\xi^{-1}\ln\left(\xi^4\right) + 4\xi^{-1}\right] g_{0L}' - \xi^{-1}g_0' + 4g_{1L}'\right. \\
&\qquad\left.-\eta\xi^{-1}\ln\left(\xi^4\right)g_{0L}'' - \eta\xi^{-1}g_0'' - \eta\ln\left(\xi^4\right)g_{1L}'' - \eta g_1''\right\} \\
&-\frac{1}{4}\left[\xi^{-1}\ln\left(\xi^4\right)g_{0L}' + \xi^{-1}g_0' + \ln\left(\xi^4\right)g_{1L}' + g_1'\right] \\
&\quad\left[4a_0\xi^3\eta + 4\xi^4\left(2a_1\eta - \frac{1}{12}a_0^2\eta^4\right) - \xi^4\eta\left(2a_1 - \frac{1}{3}a_0^2\eta^3\right)\right] \\
&+\frac{1}{4}\left[\xi^{-1}\ln\left(\xi^4\right)g_{0L}'' + \xi^{-1}g_0'' + \ln\left(\xi^4\right)g_{1L}'' + g_1''\right] \\
&\quad\left[2a_0\xi^3\eta^2 + 5\xi^4\left(a_1\eta^2 - \frac{1}{60}a_0^2\eta^5\right) - \xi^4\left(2a_1\eta^2 - \frac{1}{12}a_0^2\eta^5\right)\right] \\
&+\frac{1}{4}\left[\mu_0\eta\xi^2 + 2a_0\xi^3 + \xi^4\left(2a_1 - \frac{1}{3}a_0^2\eta^3\right)\right] \\
&\quad\left[4\xi^{-1}g_{0L} + \ln\left(\xi^4\right)g_{1L} + 4g_{1L} + g_1\right. \\
&\qquad\left.-\eta\xi^{-1}\ln\left(\xi^4\right)g_{0L}' - \eta\xi^{-1}g_0' - \eta\ln\left(\xi^4\right)g_{1L}' - \eta g_1'\right] \\
&= \frac{a_0}{\mu_0}F_{\mathrm{s}}\xi^2 + \frac{3}{2}\frac{a_1}{\mu_0}F_{\mathrm{s}}\xi^3 + \xi\ln\left(\xi^4\right)g_{0L}''' + \xi g_0''' + \xi^2\ln\left(\xi^4\right)g_{1L}''' + \xi^2 g_1'''.
\end{aligned}$$

The streamwise coordinate ξ is small and thus we look at its distinct powers to obtain the individual equations for g_i, which are solved subject to the no-slip boundary condition that sets $g_i(0) = g_i'(0) = 0$. At leading order, $\mathcal{O}(\xi \ln \xi^4)$,

$$\frac{1}{8}\mu_0\eta^3 g_{0L}'' - \frac{1}{8}\mu_0\eta^2 g_{0L}' = g_{0L}''' \tag{5.23a}$$

has solution

$$g_{0L}(\eta) = -\frac{1}{2}A_{0L}\eta^2. \tag{5.23b}$$

At the next order, $\mathcal{O}(\xi)$,

$$\frac{1}{8}\mu_0\eta^3 g_0'' - \frac{1}{8}\mu_0\eta^2 g_0' = g_0''' \tag{5.23c}$$

has solution

$$g_0(\eta) = \frac{1}{2}A_0\eta^2. \tag{5.23d}$$

Then, at $\mathcal{O}(\xi^2 \ln \xi^4)$,

$$\frac{1}{8}\mu_0\eta^3 g_{1L}'' - \frac{1}{4}\mu_0\eta^2 g_{1L}' + \frac{1}{4}\mu_0\eta g_{1L} = g_{1L}''' \tag{5.23e}$$

gives

$$g_{1L}(\eta) = \frac{1}{2}A_{1L}\eta^2. \tag{5.23f}$$

And finally, at $\mathcal{O}(\xi^2)$, the equation

$$g_1''' - \frac{1}{8}\mu_0\eta^3 g_1'' + \frac{1}{4}\mu_0\eta^2 g_1' - \frac{1}{4}\mu_0\eta g_1 = a_0\eta^2 A_{0L} - \frac{a_0}{\mu_0}F_\mathrm{s} \tag{5.23g}$$

is obtained, which can be rewritten in the form

$$\left(\eta^{-1}g_1\right)'' = -\eta^{-3}\exp\left(\frac{1}{32}\mu_0\eta^4\right)\int_0^\eta \left(\frac{a_0}{\mu_0}F_\mathrm{s} - a_0A_{0L}\hat{\eta}^2\right)\hat{\eta}^2\exp\left(-\frac{1}{32}\mu_0\hat{\eta}^4\right)\mathrm{d}\hat{\eta}.$$

In order for the expansion (5.22) to remain valid throughout the inner Goldstein layer, it is necessary that $g_1(\eta) \ll \mathcal{O}(\eta^2)$ else the fourth term in $\tilde{\psi}_1^\mathrm{i}$ becomes comparable to the third. The left-hand side of the reformulation above is then at most $\mathcal{O}(\eta^{-1})$; and the fact that the preceding argument must also be valid as $\eta \to \infty$ implies that the integral on the right-hand side must be zero, given the presence of the exponential multiplying it. In particular,

$$2\mu_0^{-\frac{5}{4}}\left[2^{\frac{3}{4}}a_0\mu_0^{-\frac{1}{2}}F_\mathrm{s}\Gamma\left(\frac{3}{4}\right) - 2^{\frac{13}{4}}a_0A_{0L}\Gamma\left(\frac{5}{4}\right)\right] = 0,$$

provided that μ_0 is positive, which it is from equation (5.15); and thus we find A_{0L} as

$$A_{0L} = \frac{F_\mathrm{s}\Gamma\left(\frac{3}{4}\right)}{2^{\frac{5}{2}}\mu_0^{\frac{1}{2}}\Gamma\left(\frac{5}{4}\right)}, \tag{5.24}$$

where $\Gamma(\cdot)$ is the Gamma function. We have therefore completely determined the first term in the expansion of $\tilde{\psi}_1^\mathrm{i}$ in the inner Goldstein layer as

$$\tilde{\psi}_1^\mathrm{i} = -\frac{1}{2}A_{0L}\left(x_\mathrm{s}-x\right)^{-\frac{1}{2}}\ln\left(x_\mathrm{s}-x\right)Y^2 + \cdots . \tag{5.25}$$

The second order stream function in the outer Goldstein layer, $\tilde{\psi}_1^\mathrm{o}$, can then be expanded as

$$\tilde{\psi}_1^\mathrm{o} = \left(x_\mathrm{s}-x\right)^{-\frac{1}{2}}\ln\left(x_\mathrm{s}-x\right)G(Y) + \cdots$$

and substituted, along with $\tilde{\psi}_0^\mathrm{o}$ (equation (5.20)), into equation (5.14a) to obtain

$$\begin{aligned}
&-\left[\psi_{0\mathrm{s}}' + 2\frac{a_0}{\mu_0}\left(x_\mathrm{s}-x\right)^{\frac{1}{2}}\psi_{0\mathrm{s}}'' + 2\frac{a_1}{\mu_0}\left(x_\mathrm{s}-x\right)^{\frac{3}{4}}\psi_{0\mathrm{s}}''\right] \\
&\quad\left[-\frac{1}{2}\left(x_\mathrm{s}-x\right)^{-\frac{3}{2}}\ln\left(x_\mathrm{s}-x\right)G' + \left(x_\mathrm{s}-x\right)^{-\frac{3}{2}}G'\right] \\
&-\left[\frac{a_0}{\mu_0}\left(x_\mathrm{s}-x\right)^{-\frac{1}{2}}\psi_{0\mathrm{s}}'' + \frac{3}{2}\frac{a_1}{\mu_0}\left(x_\mathrm{s}-x\right)^{-\frac{1}{4}}\psi_{0\mathrm{s}}''\right]\left(x_\mathrm{s}-x\right)^{-\frac{1}{2}}\ln\left(x_\mathrm{s}-x\right)G' \\
&+\left[\frac{a_0}{\mu_0}\left(x_\mathrm{s}-x\right)^{-\frac{1}{2}}\psi_{0\mathrm{s}}' + \frac{3}{2}\frac{a_1}{\mu_0}\left(x_\mathrm{s}-x\right)^{-\frac{1}{4}}\psi_{0\mathrm{s}}'\right]\left(x_\mathrm{s}-x\right)^{-\frac{1}{2}}\ln\left(x_\mathrm{s}-x\right)G'' \\
&+\left[-\frac{1}{2}\left(x_\mathrm{s}-x\right)^{-\frac{3}{2}}\ln\left(x_\mathrm{s}-x\right)G + \left(x_\mathrm{s}-x\right)^{-\frac{3}{2}}G\right] \\
&\quad\left[\psi_{0\mathrm{s}}'' + 2\frac{a_0}{\mu_0}\left(x_\mathrm{s}-x\right)^{\frac{1}{2}}\psi_{0\mathrm{s}}''' + 2\frac{a_1}{\mu_0}\left(x_\mathrm{s}-x\right)^{\frac{3}{4}}\psi_{0\mathrm{s}}'''\right] \\
&= -\frac{a_0}{\mu_0}F_\mathrm{s}\left(x_\mathrm{s}-x\right)^{-\frac{1}{2}} + \left(x_\mathrm{s}-x\right)^{-\frac{1}{2}}\ln\left(x_\mathrm{s}-x\right)G'''.
\end{aligned}$$

To determine G, we are interested only in the leading order terms in the above equation: namely, those appearing at order $\left(x_\mathrm{s}-x\right)^{-3/2}\ln\left(x_\mathrm{s}-x\right)$,

$$G'\psi_{0\mathrm{s}}' - G\psi_{0\mathrm{s}}'' = 0,$$

giving

$$G = -\mu_0^{-1}A_{0L}\psi_{0\mathrm{s}}',$$

where we have already matched with the inner layer as $Y \to 0$. The second order stream function in the outer Goldstein layer is therefore

$$\tilde{\psi}_1^\mathrm{o} = -\mu_0^{-1}A_{0L}\left(x_\mathrm{s}-x\right)^{-\frac{1}{2}}\ln\left(x_\mathrm{s}-x\right)\psi_{0\mathrm{s}}'(Y) + \cdots . \tag{5.26}$$

The method of matched asymptotic expansions that we have followed so far will break down when $h^{-1}\tilde{\psi}_1$ becomes of similar order of magnitude as $h^{1/2}\tilde{\psi}_0$: as we approach

the singular point and $x \to x_{\rm s}^-$, this will happen in both the inner and outer Goldstein layers when

$$(x_{\rm s} - x)^{-1} \ln (x_{\rm s} - x) \sim h^{\frac{3}{2}}$$

and this suggests looking at a critical scaling where

$$x_{\rm s} - x \sim h^{-\frac{3}{2}} \ln h.$$

The new length scale

We have successfully progressed, then, from region A to region B in figure 5.1 and the next step is to solve for the stream function in the latter, where we introduce the new streamwise coordinate $\bar{x}$, defined as

$$x = x_{\rm s} + h^{-\frac{3}{2}} \ln (h) \bar{x}, \tag{5.27}$$

with $\bar{x} \sim 1$. We are working again in the viscous layer where $y = h^{-1/2} Y$, within which there is the outer Goldstein layer ($Y \sim 1$) and inner Goldstein layer ($Y = (x_{\rm s} - x)^{1/4} \eta$, $\eta \sim 1$).

We begin by considering the outer Goldstein layer, where the stream function was expanded in the form

$$\tilde{\psi}^{\rm o} = h^{\frac{1}{2}} \tilde{\psi}_0^{\rm o} + h^{-1} \tilde{\psi}_1^{\rm o} + \cdots,$$

with $\tilde{\psi}_0^{\rm o}$ and $\tilde{\psi}_1^{\rm o}$ given by (5.20) and (5.26) respectively. Using the length scale of region B, this becomes

$$\begin{aligned}\tilde{\psi}^{\rm o} = & h^{\frac{1}{2}} \left[\psi_{0{\rm s}} + 2 \frac{a_0}{\mu_0} h^{-\frac{3}{4}} (\ln h)^{\frac{1}{2}} \bar{x}^{\frac{1}{2}} \psi'_{0{\rm s}} + 2 \frac{a_1}{\mu_0} h^{-\frac{9}{8}} (\ln h)^{\frac{3}{4}} \bar{x}^{\frac{3}{4}} \psi'_{0{\rm s}} \right] \\ & + h^{-\frac{1}{4}} (\ln h)^{-\frac{1}{2}} \bar{x}^{-\frac{1}{2}} \left\{ -A_{0L} \ln \left[h^{-\frac{3}{2}} \ln (h) \bar{x} \right] + A_0 + \right. \\ & \qquad \left. A_{1L} h^{-\frac{3}{8}} (\ln h)^{\frac{1}{4}} \bar{x}^{\frac{1}{4}} \ln \left[h^{-\frac{3}{8}} \ln (h) \bar{x} \right] + A_1 h^{-\frac{3}{8}} (\ln h)^{\frac{1}{4}} \bar{x}^{\frac{1}{4}} \right\}\end{aligned}$$

and suggests the stream function expansion

$$\begin{aligned}\bar{\Psi} = & h^{\frac{1}{2}} \psi_{0s}(Y) + h^{-\frac{1}{4}} (\ln h)^{\frac{1}{2}} J_1 (\bar{x}, Y) + h^{-\frac{1}{4}} (\ln h)^{-\frac{1}{2}} \ln (\ln h) J_{1L} (\bar{x}, Y) \\ & + h^{-\frac{1}{4}} (\ln h)^{-\frac{1}{2}} J_2 (\bar{x}, Y) + \cdots,\end{aligned} \tag{5.28}$$

where the functions J_i are to be found. From the expansion of the pressure (5.12a), carrying out a Taylor expansion of F about the separation point, using also equation (5.21), we can rewrite $\tilde{p}$ as

$$\begin{aligned}\tilde{p} = & -\frac{1}{2} h^2 \left[F_{\rm s}^2 + 2 F_{\rm s} F'_{\rm s} h^{-\frac{3}{2}} \ln (h) \bar{x} + \cdots \right] \\ & - h^{\frac{1}{2}} \left\{ \left[F_{\rm s} + F'_{\rm s} h^{-\frac{3}{2}} \ln (h) \bar{x} + \cdots \right] \left[\beta_{\rm s} + \mathcal{O} \left(h^{-\frac{3}{4}} (\ln h)^{\frac{1}{2}} \right) \right] \right\}\end{aligned}$$

and thus obtain the required expansion for the pressure in this region as

$$\begin{aligned}\bar{p} = {} & h^2\left(-\frac{1}{2}F_{\mathrm{s}}^2\right) + h^{\frac{1}{2}}\ln(h)\,(\mu_0\bar{x}) + h^{\frac{1}{2}}\,(-\beta_{\mathrm{s}}F_{\mathrm{s}}) \\ & + h^{-\frac{1}{4}}\,(\ln h)^{\frac{1}{2}}\,\bar{p}_1 + h^{-\frac{1}{4}}\,(\ln h)^{-\frac{1}{2}}\ln(\ln h)\bar{p}_{1L} + h^{-\frac{1}{4}}\,(\ln h)^{-\frac{1}{2}}\,\bar{p}_2 + \cdots, \end{aligned} \tag{5.29}$$

where the components $\bar{p}_i = \bar{p}_i(\bar{x})$ are also to be found.

Both J_i and $\bar{p}_i$ are determined by substituting the expansions for the stream function and pressure into the governing condensed layer equation (5.2b):

$$\begin{aligned} & \left[h\psi_{0\mathrm{s}}' + h^{\frac{1}{4}}\,(\ln h)^{\frac{1}{2}}\,\frac{\partial J_1}{\partial Y} + h^{\frac{1}{4}}\,(\ln h)^{-\frac{1}{2}}\ln(\ln h)\frac{\partial J_{1L}}{\partial Y} + h^{\frac{1}{4}}\,(\ln h)^{-\frac{1}{2}}\,\frac{\partial J_2}{\partial Y}\right] \\ & \left[h^{\frac{7}{4}}\,(\ln h)^{-\frac{1}{2}}\,\frac{\partial^2 J_1}{\partial\bar{x}\partial Y} + h^{\frac{7}{4}}\,(\ln h)^{-\frac{3}{2}}\ln(\ln h)\frac{\partial^2 J_{1L}}{\partial\bar{x}\partial Y} + h^{\frac{7}{4}}\,(\ln h)^{-\frac{3}{2}}\,\frac{\partial^2 J_2}{\partial\bar{x}\partial Y}\right] \\ - & \left[h^{\frac{5}{4}}\,(\ln h)^{-\frac{1}{2}}\,\frac{\partial J_1}{\partial\bar{x}} + h^{\frac{5}{4}}\,(\ln h)^{-\frac{3}{2}}\ln(\ln h)\frac{\partial J_{1L}}{\partial\bar{x}} + h^{\frac{5}{4}}\,(\ln h)^{-\frac{3}{2}}\,\frac{\partial J_2}{\partial\bar{x}}\right] \\ & \left[h^{\frac{3}{2}}\psi_{0\mathrm{s}}'' + h^{\frac{3}{4}}\,(\ln h)^{\frac{1}{2}}\,\frac{\partial^2 J_1}{\partial Y^2} + h^{\frac{3}{4}}\,(\ln h)^{-\frac{1}{2}}\ln(\ln h)\frac{\partial^2 J_{1L}}{\partial Y^2} + h^{\frac{3}{4}}\,(\ln h)^{-\frac{1}{2}}\,\frac{\partial^2 J_2}{\partial Y^2}\right] \\ = {} & -h^2\mu_0 - h^{\frac{5}{4}}\,(\ln h)^{-\frac{1}{2}}\,\bar{p}_1' - h^{\frac{5}{4}}\,(\ln h)^{-\frac{3}{2}}\ln(\ln h)\bar{p}_{1L}' - h^{\frac{5}{4}}\,(\ln h)^{-\frac{3}{2}}\,\bar{p}_2' \\ & + h^2\psi_{0\mathrm{s}}''' + h^{\frac{5}{4}}\,(\ln h)^{\frac{1}{2}}\,\frac{\partial^3 J_1}{\partial Y^3} + h^{\frac{5}{4}}\,(\ln h)^{-\frac{1}{2}}\ln(\ln h)\frac{\partial^3 J_{1L}}{\partial Y^3} + h^{\frac{5}{4}}\,(\ln h)^{-\frac{1}{2}}\,\frac{\partial^3 J_2}{\partial Y^3}, \end{aligned}$$

to be solved with the accompanying matching conditions with the inviscid layer above and the oncoming stream.

Once again, we follow the well-worn path of looking at the various orders of magnitude appearing in the above equation. The first three orders all result in the same equation

$$\psi_{0\mathrm{s}}'\frac{\partial^2 J_i}{\partial\bar{x}\partial Y} - \psi_{0\mathrm{s}}''\frac{\partial J_i}{\partial\bar{x}} = 0, \tag{5.30a}$$

with the solution

$$J_i(\bar{x}, Y) = \bar{\alpha}_i\,(\bar{x})\,\psi_{0\mathrm{s}}'(Y), \tag{5.30b}$$

for $i = 1, 1L, 2$. The functions $\bar{\alpha}_i$ remain unknown but are related to the pressure through the behaviour as $Y \to \infty$, equation (5.4). In detail,

$$\begin{aligned} & h^{\frac{1}{2}}F_{\mathrm{s}}\,(Y - \beta_{\mathrm{s}}) + h^{-\frac{1}{4}}\,(\ln h)^{\frac{1}{2}}\,\bar{\alpha}_1 F_{\mathrm{s}} + h^{-\frac{1}{4}}\,(\ln h)^{-\frac{1}{2}}\ln(\ln h)\bar{\alpha}_{1L}F_{\mathrm{s}} + h^{-\frac{1}{4}}\,(\ln h)^{-\frac{1}{2}}\,\bar{\alpha}_2 F_{\mathrm{s}} \\ \sim {} & \frac{1}{2}\left(h^{-\frac{1}{2}}Y + hF_{\mathrm{s}}\right)^2 + h^2\left(-\frac{1}{2}F_{\mathrm{s}}^2\right) + h^{\frac{1}{2}}\,(-F_{\mathrm{s}}\beta_{\mathrm{s}}) \\ & + h^{-\frac{1}{4}}\,(\ln h)^{\frac{1}{2}}\,\bar{p}_1 + h^{-\frac{1}{4}}\,(\ln h)^{-\frac{1}{2}}\ln(\ln h)\bar{p}_{1L} + h^{-\frac{1}{4}}\,(\ln h)^{-\frac{1}{2}}\,\bar{p}_2 \quad \text{as } Y \to \infty, \end{aligned}$$

gives the general form

$$\bar{p}_i = F_{\mathrm{s}}\bar{\alpha}_i. \tag{5.31}$$

To determine the functions $\bar{\alpha}_i$, we must turn to the inner Goldstein layer, whose normal coordinate is given by $y = h^{-7/8}(\ln h)^{1/4}\bar{x}^{1/4}\eta$, with $\bar{x}$ and η both of order unity. We thus introduce the new coordinate $\bar{z}$ such that

$$y = h^{-\frac{7}{8}}\,(\ln h)^{\frac{1}{4}}\,\bar{z}, \quad \Longleftrightarrow \quad Y = h^{-\frac{3}{8}}\,(\ln h)^{\frac{1}{4}}\,\bar{z}. \tag{5.32}$$

The expansion for the stream function was again $\tilde{\psi}^{\mathrm{i}} = h^{1/2}\tilde{\psi}^{\mathrm{i}}_0 + h^{-1}\tilde{\psi}^{\mathrm{i}}_1 + \cdots$, with $\tilde{\psi}^{\mathrm{i}}_0$ and $\tilde{\psi}^{\mathrm{i}}_1$ given by equations (5.17) and (5.22) respectively. Rewriting this in terms of the new normal coordinate $\bar{z}$,

$$\begin{aligned}\tilde{\psi}^{\mathrm{i}} =& h^{-\frac{5}{8}}\,(\ln h)^{\frac{3}{4}}\left(\frac{1}{6}\mu_0\bar{z}^3\right) + h^{-1}\,(\ln h)\left(a_0|\bar{x}|^{\frac{1}{2}}\bar{z}^2 + \frac{3}{4}A_{0L}\,|\bar{x}|^{-\frac{1}{2}}\,\bar{z}^2\right)\\ &+ h^{-1}\ln(\ln h)\left(-\frac{1}{2}A_{0L}\,|\bar{x}|^{-\frac{1}{2}}\,\bar{z}^2\right) + h^{-1}\left[-\frac{1}{2}A_{0L}\,|\bar{x}|^{-\frac{1}{2}}\,(\ln|\bar{x}|)\,\bar{z}^2 + \frac{1}{2}A_0\,|\bar{x}|^{-\frac{1}{2}}\,\bar{z}^2\right]\\ &+ h^{-\frac{11}{8}}\,(\ln h)^{\frac{5}{4}}\left(a_1\,|\bar{x}|^{\frac{3}{4}}\,\bar{z}^2 - \frac{3}{4}A_{1L}\,|\bar{x}|^{-\frac{1}{4}}\,\bar{z}^2 - \frac{1}{60}a_0^2\bar{z}^5\right),\end{aligned} \tag{5.33}$$

points the way to the required stream function expansion in this region

$$\begin{aligned}\bar{\psi} =& h^{-\frac{5}{8}}\,(\ln h)^{\frac{3}{4}}\left(\frac{1}{6}\mu_0\bar{z}^3\right) + h^{-1}\,(\ln h)\,\bar{\psi}_1\,(\bar{x},\bar{z}) + h^{-1}\ln(\ln h)\bar{\psi}_{1L}\,(\bar{x},\bar{z})\\ &+ h^{-1}\bar{\psi}_2\,(\bar{x},\bar{z}) + h^{-\frac{11}{8}}\,(\ln h)^{\frac{5}{4}}\,\bar{\psi}_3\,(\bar{x},\bar{z}) + \cdots.\end{aligned} \tag{5.34}$$

Since the pressure is independent of height, it remains as above with the relations of (5.31). Substitution into the condensed flow equation (5.2b) results in the now familiar quagmire

$$\begin{aligned}&\left[h^{\frac{1}{4}}\,(\ln h)^{\frac{1}{2}}\left(\frac{1}{2}\mu_0\bar{z}^2\right) + h^{-\frac{1}{8}}\,(\ln h)^{\frac{3}{4}}\,\frac{\partial\bar{\psi}_1}{\partial\bar{z}} + h^{-\frac{1}{8}}\,(\ln h)^{-\frac{1}{4}}\ln(\ln h)\frac{\partial\bar{\psi}_{1L}}{\partial\bar{z}}\right.\\ &\quad\left.+ h^{-\frac{1}{8}}\,(\ln h)^{-\frac{1}{4}}\,\frac{\partial\bar{\psi}_2}{\partial\bar{z}} + h^{-\frac{1}{2}}\,(\ln h)\,\frac{\partial\bar{\psi}_3}{\partial\bar{z}}\right]\\ &\left[h^{\frac{11}{8}}\,(\ln h)^{-\frac{1}{4}}\,\frac{\partial^2\bar{\psi}_1}{\partial\bar{x}\partial\bar{z}} + h^{\frac{11}{8}}\,(\ln h)^{-\frac{5}{4}}\ln(\ln h)\frac{\partial^2\bar{\psi}_{1L}}{\partial\bar{x}\partial\bar{z}} + h^{\frac{11}{8}}\,(\ln h)^{-\frac{5}{4}}\,\frac{\partial^2\bar{\psi}_2}{\partial\bar{x}\partial\bar{z}} + h\frac{\partial^2\bar{\psi}_3}{\partial\bar{x}\partial\bar{z}}\right]\\ -&\left[h^{\frac{1}{2}}\frac{\partial\bar{\psi}_1}{\partial\bar{x}} + h^{\frac{1}{2}}\,(\ln h)^{-1}\ln(\ln h)\frac{\partial\bar{\psi}_{1L}}{\partial\bar{x}} + h^{\frac{1}{2}}\,(\ln h)^{-1}\,\frac{\partial\bar{\psi}_2}{\partial\bar{x}} + h^{\frac{1}{8}}\,(\ln h)^{\frac{1}{4}}\,\frac{\partial\bar{\psi}_3}{\partial\bar{x}}\right]\\ &\left[h^{\frac{9}{8}}\,(\ln h)^{\frac{1}{4}}\,(\mu_0\bar{z}) + h^{\frac{3}{4}}\,(\ln h)^{\frac{1}{2}}\,\frac{\partial^2\bar{\psi}_1}{\partial\bar{z}^2} + h^{\frac{3}{4}}\,(\ln h)^{-\frac{1}{2}}\ln(\ln h)\frac{\partial^2\bar{\psi}_{1L}}{\partial\bar{z}^2}\right.\\ &\quad\left.+ h^{\frac{3}{4}}\,(\ln h)^{-\frac{1}{2}}\,\frac{\partial^2\bar{\psi}_2}{\partial\bar{z}^2} + h^{\frac{3}{8}}\,(\ln h)^{\frac{3}{4}}\,\frac{\partial^2\bar{\psi}_3}{\partial\bar{z}^2}\right]\\ =&-h^{\frac{5}{4}}\,(\ln h)^{-\frac{1}{2}}\,F_{\mathrm{s}}\bar{\alpha}_1' - h^{\frac{5}{4}}\,(\ln h)^{-\frac{3}{2}}\ln(\ln h)F_{\mathrm{s}}\bar{\alpha}_{1L}' - h^{\frac{5}{4}}\,(\ln h)^{-\frac{3}{2}}\,F_{\mathrm{s}}\bar{\alpha}_2'\\ &+ h^{\frac{13}{8}}\,(\ln h)^{\frac{1}{4}}\,\frac{\partial^3\bar{\psi}_1}{\partial\bar{z}^3} + h^{\frac{13}{8}}\,(\ln h)^{-\frac{3}{4}}\ln(\ln h)\frac{\partial^3\bar{\psi}_{1L}}{\partial\bar{z}^3}\\ &+ h^{\frac{13}{8}}\,(\ln h)^{-\frac{3}{4}}\,\frac{\partial^3\bar{\psi}_2}{\partial\bar{z}^3} + h^{\frac{5}{4}}\,(\ln h)^{\frac{1}{2}}\,\frac{\partial^3\bar{\psi}_3}{\partial\bar{z}^3},\end{aligned}$$

which can again be crossed by looking at the various orders of magnitude that appear.[2] At orders $h^{13/8}(\ln h)^{1/4}$, $h^{13/8}(\ln h)^{-3/4}\ln(\ln h)$ and $h^{13/8}(\ln h)^{-3/4}$, the equation has the same form

$$\frac{1}{2}\mu_0\bar{z}^2\frac{\partial^2\bar{\psi}_i}{\partial\bar{x}\partial\bar{z}} - \mu_0\bar{z}\frac{\partial\bar{\psi}_i}{\partial\bar{x}} = \frac{\partial^3\bar{\psi}_i}{\partial\bar{z}^3} \tag{5.35a}$$

with the no-slip boundary condition and matching requirement that

$$\bar{\psi}_i \to \frac{1}{2}\mu_0\bar{z}^2\bar{\alpha}_i \quad \text{as } \bar{z}\to\infty.$$

This gives the solution

$$\bar{\psi}_i = \frac{1}{2}\mu_0\bar{z}^2\bar{\alpha}_i(\bar{x}) \tag{5.35b}$$

for $i = 1, 1L, 2$. The equation for $\bar{\psi}_3$ appears at order $h^{5/4}(\ln h)^{1/2}$ and is

$$\frac{\partial^3\bar{\psi}_3}{\partial\bar{z}^3} = \frac{1}{2}\mu_0\bar{z}^2\frac{\partial^2\bar{\psi}_3}{\partial\bar{x}\partial\bar{z}} - \mu_0\bar{z}\frac{\partial\bar{\psi}_3}{\partial\bar{x}} + \frac{1}{2}\mu_0^2\bar{z}^2\bar{\alpha}_1\bar{\alpha}_1', \tag{5.36a}$$

which can be solved subject to the no-slip boundary condition and matching at infinity to obtain

$$\bar{\psi}_3 = \frac{1}{2}\mu_0\bar{z}^2\bar{\alpha}_3 + \frac{1}{120}\mu_0^2\bar{\alpha}_1\bar{\alpha}_1'\bar{z}^5. \tag{5.36b}$$

Matching with the solution in the outer Goldstein layer implies that $\mu_0^2\bar{\alpha}_1\bar{\alpha}_1'$ must be constant and hence, integrating,

$$\frac{1}{2}\mu_0^2\bar{\alpha}_1^2 = -2a_0^2\bar{x} + c, \tag{5.37}$$

with c being a constant that remains unknown for now.

To fully determine $\bar{\alpha}_1$, we must match with the stream function in the oncoming inner Goldstein layer, expanded as (5.33). Comparing this with the solution found here, equations (5.35b) and (5.36b), we can determine not only the asymptotic behaviour of $\bar{\alpha}_1$ as $\bar{x}\to-\infty$, but that of all $\bar{\alpha}_i$:

$$\frac{1}{2}\mu_0\bar{\alpha}_1 \sim a_0|\bar{x}|^{\frac{1}{2}} + \frac{3}{4}A_{0L}|\bar{x}|^{-\frac{1}{2}}, \tag{5.38a}$$

$$\frac{1}{2}\mu_0\bar{\alpha}_{1L} \sim -\frac{1}{2}A_{0L}|\bar{x}|^{-\frac{1}{2}}, \tag{5.38b}$$

$$\frac{1}{2}\mu_0\bar{\alpha}_2 \sim -\frac{1}{2}A_{0L}|\bar{x}|^{-\frac{1}{2}}\ln|\bar{x}| + \frac{1}{2}A_0|\bar{x}|^{-\frac{1}{2}}, \tag{5.38c}$$

$$\frac{1}{2}\mu_0\bar{\alpha}_3 \sim a_1|\bar{x}|^{\frac{3}{4}} - \frac{3}{4}A_{1L}|\bar{x}|^{-\frac{1}{4}}. \tag{5.38d}$$

[2] We're getting rather handy at this!

From (5.37), then, one finds $c = 3A_{0L}a_0$ and so we have completely determined $\bar{\alpha}_1$, as

$$\bar{\alpha}_1 = 2\mu_0^{-1}a_0\left(-\bar{x} + \frac{3A_{0L}}{2a_0}\right)^{\frac{1}{2}}. \tag{5.39a}$$

The solutions to $\bar{\alpha}_{1L}, \bar{\alpha}_2$ are found similarly and will be needed later in §5.3, but we limit ourselves to quoting the results from Smith & Daniels [85],

$$\bar{\alpha}_{1L} = -\mu_0^{-1}A_{0L}\left(-\bar{x} + \frac{3A_{0L}}{2a_0}\right)^{-\frac{1}{2}} \tag{5.39b}$$

$$\bar{\alpha}_2 = -\mu_0^{-1}A_{0L}\left(-\bar{x} + \frac{3A_{0L}}{2a_0}\right)^{-\frac{1}{2}}\ln\left(-\bar{x} + \frac{3A_{0L}}{2a_0}\right) + \mu_0^{-1}A_0\left(-\bar{x} + \frac{3A_{0L}}{2a_0}\right)^{-\frac{1}{2}}. \tag{5.39c}$$

For now, however, only $\bar{\alpha}_1$ is required to find the position of zero skin friction, since

$$\bar{\tau}_{\text{wall}}(\bar{x}, \bar{z}) = h^{\frac{7}{4}}(\ln h)^{-\frac{1}{2}}\left.\frac{\partial^2\bar{\psi}}{\partial\bar{z}^2}\right|_{\bar{z}=0} = 2a_0h^{\frac{3}{4}}(\ln h)^{\frac{1}{2}}\left(-\bar{x} + \frac{3A_{0L}}{2a_0}\right)^{\frac{1}{2}} + \cdots, \tag{5.40}$$

which takes the value of 0 at $\bar{x} = 3A_{0L}/2a_0$. The square root singularity still appears and the result of our endeavours so far has merely been a slight downstream shift in its position.

5.3 Walking: the roughness region

There is a freedom about walking that is impossible to find in a car, imprisoned in a steel box, constrained by white markings on a tarmac road. And the point is that you can't actually see anything from a car: your view on the world is a set of reinforced glass panes, one of which faces the backside of the vehicle in front, as it splutters out its refuse. Look up, and the big blue sky is replaced by the fuzzy felt of your limitations.

Even in the city, it is preferable to walk. How else do you spot the leaves frozen in place by the kerbside, white with frost and the ghostly memory of the spring in which they were young; or the great trees that stare back at you from the depths of a murky puddle, their roots stretching down to where nature still embraces them, their branches black rivers in the sky; or hear the call of the swallow and the robin and the seagull, or the coo of the pigeon—yes, even the pigeon—that, blackened by the smog and the city, can still fly free? How can you walk and discover, to your joy and amazement, that the lamp posts have become a forest; how can you climb a hill and see the city rolled out before you and stop and survey and know that it is all yours; how can you feel the pulse in the arteries of humanity if you are stuck in a car? How can you obey the whimsicalness of curiosity, follow imagination down an alley, hear history's whispers in the bricks, seek knowledge in the hidden, exploit the unexpected and feel the beckoning gaze of a pub,

that stands unobtrusively on the corner between past, present and future, if you shut it all out behind the barricades of a car?

It's time to go walking...

On having shifted the Goldstein singularity slightly downstream, Smith & Daniels [85] went on to remove it completely by considering an even smaller length (and corresponding height) scale, derived in §5.3.1 below, in which the skin friction goes through zero in a non-singular manner but in which a later singularity then appears, which will be dealt with in §5.5. In this region, which corresponds to region C in figure 5.1, we will diverge from the work of Smith & Daniels by introducing roughness elements in order to determine what impact they have, firstly, on the position of zero skin friction (local separation) and, secondly, on the new singularity (global separation). The length scale of the roughness elements will be the same as that of region D, but the scaling of the height and oscillation frequency (in the case of dynamic elements) will follow from a requirement that they act at an appropriate order in the governing equation, as explained in §5.3.2.

5.3.1 The scalings of region C

On getting out of the car in §5.2, we found that the Goldstein singularity could be shifted slightly downstream to the position $x = x_\mathrm{s} + h^{-3/2}\ln(h)3A_{0L}/2a_0$, with the square root singularity in the skin friction persisting. The hint as to the length scale of the region that could resolve this issue lies in comparing the behaviour of $\bar{\alpha}_1$ (equation (5.39a)) with that of $\bar{\alpha}_{1L}$ (equation (5.39b)) as $\bar{x}$ approaches $3A_{0L}/2a_0$. The function $\bar{\alpha}_{1L}$, appearing at higher order in the stream function expansion (5.34), grows at a faster rate ($s^{-1/2}$) than $\bar{\alpha}_1$ ($s^{1/2}$, with $s \to 0^+$) and hence the asymptotic expansion must break down in some smaller length scale around the point $3A_{0L}/2a_0$.

Indeed, this happens when

$$h^{-1}(\ln h)\left(-\bar{x} + \frac{3A_{0L}}{2a_0}\right)^{\frac{1}{2}} \sim h^{-1}\ln(\ln h)\left(-\bar{x} + \frac{3A_{0L}}{2a_0}\right)^{-\frac{1}{2}},$$

or

$$\left(-\bar{x} + \frac{3A_{0L}}{2a_0}\right) \sim (\ln h)^{-1}.$$

We thus introduce the new streamwise coordinate X, of order unity, holding in region C and as indicated in table 5.1, defined as

$$x - x_\mathrm{s} = h^{-\frac{3}{2}}\ln h\frac{3A_{0L}}{2a_0} + h^{-\frac{3}{2}}X. \tag{5.41}$$

The outer Goldstein layer keeps its normal coordinate $Y \sim 1$, but the inner Goldstein layer, which is dependent on the length scale, now has $y \sim h^{-7/8}$ and so we introduce the new normal coordinate $z \sim 1$,

$$y = h^{-\frac{7}{8}} z. \tag{5.42}$$

As per the variables defined in table 5.1, the inner Goldstein layer stream function is denoted by ψ while that of the outer layer is Ψ and the pressure is simply p. The flow in the inviscid layer above the Goldstein layers keeps the normal coordinate $\tilde{y}$, stream function $\tilde{\Psi}$ and pressure $\tilde{p}$.

5.3.2 The pressure–displacement equation

It behoves us now to derive the governing equation for the local displacement of the boundary layer from the wall, $-A(X)$, along with its relationship to the pressure perturbation and the wall skin friction in the presence of roughness elements. We will assume *a priori* that the roughness elements must have a height scale of $\mathcal{O}(h^{-5/4})$ and oscillation frequency of $\mathcal{O}(h^{11/8})$, introducing the scaled time

$$t = h^{-\frac{11}{8}} T, \quad T \sim 1, \tag{5.43}$$

and we will justify these choices later on.

Using this height scale, the boundary condition at infinity (5.1e), which now includes the roughness function f, is again integrated to obtain the stream function behaviour in the inviscid layer

$$\tilde{\Psi} \sim \frac{1}{2}\left(y + hF + h^{-\frac{5}{4}} f\right)^2 + q(x,t) \quad \text{as } y \to \infty.$$

The unknown function q is determined by taking the limit of the condensed flow equation (5.1b) as $y \to \infty$. This results in

$$h^{\frac{1}{8}} \frac{\partial f}{\partial T} - \frac{\partial q}{\partial x} = -\frac{\partial p}{\partial x},$$

or

$$q\,(x,T) = p\,(x,T) + h^{\frac{1}{8}} \int \frac{\partial f}{\partial T}\,\mathrm{d}x,$$

and gives a stream function behaviour of

$$\tilde{\Psi} \sim \frac{1}{2}\left(y + hF + h^{-\frac{5}{4}} f\right)^2 + p + h^{\frac{1}{8}} \int \frac{\partial f}{\partial T}\,\mathrm{d}x \tag{5.44}$$

as $y \to \infty$.

The pressure expansion in region C is inspired by the pressure in region B—encapsulated by equations (5.29), (5.31) and (5.39a)—rewritten in the new streamwise coordinate X

as

$$\bar{p} = -h^2\left(\frac{1}{2}F_\mathrm{s}^2\right) + h^{\frac{1}{2}}(\ln h)\,\frac{3A_{0L}}{2a_0}\mu_0 + h^{\frac{1}{2}}(\mu_0 X - \beta_\mathrm{s}F_\mathrm{s}) + h^{-\frac{1}{4}}2\mu_0^{-1}a_0F_\mathrm{s}\,|X|^{\frac{1}{2}} + \cdots,$$

and thus suggesting

$$p = -h^2\left(\frac{1}{2}F_\mathrm{s}^2\right) + h^{\frac{1}{2}}(\ln h)\,\frac{3A_{0L}}{2a_0}\mu_0 + h^{\frac{1}{2}}(\mu_0 X - \beta_\mathrm{s}F_\mathrm{s}) + h^{-\frac{1}{4}}p_1 + \cdots \tag{5.45}$$

as the appropriate expansion. The stream function (5.44) now also needs to be expanded about x_s: with $y = h^{-1/2}Y$,

$$\begin{aligned}\psi &\sim \frac{1}{2}\left\{h^{-\frac{1}{2}}Y + h\left[F_\mathrm{s} + F_\mathrm{s}'(x - x_\mathrm{s}) + \cdots\right] + h^{-\frac{5}{4}}f\right\}^2 + p + h^{-\frac{11}{8}}\int\frac{\partial f}{\partial T}\,\mathrm{d}X\\ &\sim h^{\frac{1}{2}}(F_\mathrm{s}Y - F_\mathrm{s}\beta_\mathrm{s}) + h^{-\frac{1}{4}}(F_\mathrm{s}f + p_1) + \cdots + h^{-\frac{11}{8}}\int\frac{\partial f}{\partial T}\,\mathrm{d}X + \cdots\end{aligned} \tag{5.46a}$$

as $Y \to \infty$; and thus the suggested expansion for the stream function in the outer Goldstein layer is

$$\Psi = h^{\frac{1}{2}}\Psi_1 + h^{-\frac{1}{4}}\Psi_2 + \cdots. \tag{5.46b}$$

The upstream matching condition is taken from the form of the oncoming stream function—equations (5.28), (5.30b) and (5.39a)—and is

$$\Psi \to h^{\frac{1}{2}}\psi_{0\mathrm{s}}(Y) + h^{-\frac{1}{4}}2\mu_0^{-1}a_0\psi_{0\mathrm{s}}'(Y)\,|X|^{\frac{1}{2}} + \cdots \quad \text{as } X \to -\infty. \tag{5.47}$$

It is time, now, to substitute the pressure expansion (5.45) and the stream function expansion (5.46b) into the condensed flow equation (5.1b), using the appropriate scalings, thereby obtaining the governing equation in the outer Goldstein layer:

$$\begin{aligned}&h^{\frac{19}{8}}\frac{\partial^2\Psi_1}{\partial Y\partial T} + h^{\frac{13}{8}}\frac{\partial^2\Psi_2}{\partial Y\partial T} + \left(h^{\frac{5}{2}}\frac{\partial\Psi_1}{\partial Y} + h^{\frac{7}{4}}\frac{\partial\Psi_2}{\partial Y}\right)\left(h\frac{\partial^2\Psi_1}{\partial X\partial Y} + h^{\frac{1}{4}}\frac{\partial^2\Psi_2}{\partial X\partial Y}\right)\\ &\quad - \left(h^{\frac{5}{2}}\frac{\partial\Psi_1}{\partial X} + h^{\frac{7}{4}}\frac{\partial\Psi_2}{\partial X}\right)\left(h\frac{\partial^2\Psi_1}{\partial Y^2} + h^{\frac{1}{4}}\frac{\partial^2\Psi_2}{\partial Y^2}\right)\\ &= -h^2\mu_0 - h^{\frac{5}{4}}\frac{\partial p_1}{\partial X} + h^2\frac{\partial^3\Psi_1}{\partial Y^3} + h^{\frac{5}{4}}\frac{\partial^3\Psi_2}{\partial Y^3}.\end{aligned}$$

To find the solutions to Ψ_i, we repeat the process of studying the terms appearing in the above equation at the various orders of magnitude, combining them with the relevant magnitudes in the matching conditions (5.46a) and (5.47). At $\mathcal{O}(h^{7/2})$, the system of equations is

$$\begin{aligned}&\frac{\partial\Psi_1}{\partial Y}\frac{\partial^2\Psi_1}{\partial X\partial Y} - \frac{\partial\Psi_1}{\partial X}\frac{\partial^2\Psi_1}{\partial Y^2} = 0,\\ &\Psi_1 \to \psi_{0\mathrm{s}}(Y) \quad \text{as } X \to -\infty,\\ &\Psi_1 \to F_\mathrm{s}(Y - \beta_\mathrm{s}) \quad \text{as } Y \to \infty,\end{aligned}$$

which has solution

$$\Psi_1 = \psi_{0s}(Y). \tag{5.48}$$

At $\mathcal{O}(h^{11/4})$, we solve

$$\psi'_{0s}\frac{\partial^2\Psi_2}{\partial X\partial Y} - \psi''_{0s}\frac{\partial\Psi_2}{\partial X} = 0,$$
$$\Psi_2 \to p_1 + F_s f \quad \text{as } Y \to \infty$$

to find

$$\Psi_2 = \psi'_{0s}(Y)\left[A(X,T) + f(X,T)\right], \tag{5.49a}$$

where $-A$ is the local displacement of the boundary layer. Here, too, imposing the condition at infinity, we find the relationship between the displacement and pressure

$$p_1 = F_s A(X,T) \tag{5.49b}$$

and we note its simplicity: the one being equal to the other, ignoring the multiplication by a positive constant.

To find A, we must turn to the inner Goldstein layer. First, though, the only unresolved issue that might give us pause is how the integral in the inviscid stream function (5.44) is accommodated by the outer Goldstein layer. The stream function in the latter region can be expanded up to $\mathcal{O}(h^{-11/8})$—taking in orders $h^{-5/8}$, where there is Ψ_3, and h^{-1}, where there is Ψ_4, along the way—and incorporated into the governing condensed flow equation, with each term solved for as above. The equation for Ψ_3 would then appear at $\mathcal{O}(h^{19/8})$ and has

$$\Psi_3 \propto \psi'_{0\mathrm{s}},$$

which implies, using the behaviour of $\psi_{0\mathrm{s}}$ as $Y \to 0$ (5.20b), that it behaves like $h^{-11/8}z^2$ in the inner Goldstein layer; the equation for Ψ_4 appears at $\mathcal{O}(h^2)$ and is

$$\psi'_{0\mathrm{s}}\frac{\partial^2\Psi_4}{\partial X\partial Y} - \psi''_{0\mathrm{s}}\frac{\partial\Psi_4}{\partial X} = -\mu_0 + \psi'''_{0\mathrm{s}} + (A+f)\frac{\partial}{\partial X}(A+f)\left[\psi'_{0\mathrm{s}}\psi'''_{0\mathrm{s}} - \left(\psi''_{0\mathrm{s}}\right)^2\right],$$

whose solution contains a term that behaves as $(1/2)h^{-11/8}(A+f)^2 z$ in the inner Goldstein layer; and, finally, the equation for Ψ_5 at order $h^{13/8}$ is

$$\psi'_{0\mathrm{s}}\frac{\partial^2\Psi_5}{\partial X\partial Y} - \psi''_{0\mathrm{s}}\frac{\partial\Psi_5}{\partial X} = -\psi''_{0\mathrm{s}}\frac{\partial}{\partial T}(A+f),$$

which has the particular solution

$$\int \frac{\partial}{\partial T}(A+f)\,\mathrm{d}X,$$

indicating that the integral term in the stream function expansion (5.44), present due to the addition of dynamic roughness elements, feeds straight through from the inviscid boundary layer flow to the inner Goldstein layer at order $h^{-11/8}$.

The displacement equation

To find the equation for the displacement function A, one must descend to the inner Goldstein layer. The upstream solution in region B was given by the stream function (5.34), with solutions (5.35b), (5.36b) and (5.39), rewritten in the (X, z) coordinates of region C's inner Goldstein layer as

$$\begin{aligned}\bar{\psi} = &h^{-\frac{5}{8}}\left(\frac{1}{6}\mu_0 z^3\right) + h^{-1}z^2\left(a_0\left|X\right|^{\frac{1}{2}} - \frac{1}{2}A_{0L}\left|X\right|^{-\frac{1}{2}}\ln\left|X\right| + \frac{1}{2}A_0\left|X\right|^{-\frac{1}{2}}\right)\\ &+ h^{-\frac{11}{8}}\left[-\frac{1}{60}a_0^2 z^5 + \mathcal{O}\left(z^2\right)\right],\end{aligned} \tag{5.50}$$

thus suggesting an expansion for the present stream function of

$$\psi = h^{-\frac{5}{8}}\psi_1 + h^{-1}\psi_2 + h^{-\frac{11}{8}}\psi_3 + \cdots; \tag{5.51}$$

an expansion that is confirmed by the matching condition with the stream function in the outer Goldstein layer, which, as $Y \to 0$, tends to

$$\begin{aligned}\Psi \to &h^{-\frac{5}{8}}\left(\frac{1}{6}\mu_0 z^3\right) + h^{-1}\left(\frac{1}{2}\mu_0 z^2\right)(A+f)\\ &+ h^{-\frac{11}{8}}\left[-\frac{1}{60}a_0^2 z^5 + A_3 z^2 + \frac{1}{2}(A+f)^2 z + \int\frac{\partial}{\partial T}(A+f)\,\mathrm{d}X\right] + \cdots.\end{aligned} \tag{5.52}$$

The condensed flow equation (5.1b) in the scalings of the inner Goldstein layer is

$$h^{\frac{9}{4}}\frac{\partial^2\psi}{\partial z\partial T} + h^{\frac{13}{4}}\frac{\partial\psi}{\partial z}\frac{\partial^2\psi}{\partial X\partial z} - h^{\frac{13}{4}}\frac{\partial\psi}{\partial X}\frac{\partial^2\psi}{\partial z^2} = -h^{\frac{3}{2}}\frac{\partial p}{\partial X} + h^{\frac{21}{8}}\frac{\partial^3\psi}{\partial z^3}, \tag{5.53}$$

into which we substitute the expansions for the pressure and stream function, (5.45) and (5.51) respectively,

$$\begin{aligned}&h^{\frac{13}{8}}\frac{\partial^2\psi_1}{\partial z\partial T} + h^{\frac{5}{4}}\frac{\partial^2\psi_2}{\partial z\partial T} + h^{\frac{7}{8}}\frac{\partial^2\psi_3}{\partial z\partial T}\\ &+ h^{\frac{13}{4}}\left(h^{-\frac{5}{8}}\frac{\partial\psi_1}{\partial z} + h^{-1}\frac{\partial\psi_2}{\partial z} + h^{-\frac{11}{8}}\frac{\partial\psi_3}{\partial z}\right)\left(h^{-\frac{5}{8}}\frac{\partial^2\psi_1}{\partial X\partial z} + h^{-1}\frac{\partial^2\psi_2}{\partial X\partial z} + h^{-\frac{11}{8}}\frac{\partial^2\psi_3}{\partial X\partial z}\right)\\ &- h^{\frac{13}{4}}\left(h^{-\frac{5}{8}}\frac{\partial\psi_1}{\partial X} + h^{-1}\frac{\partial\psi_2}{\partial X} + h^{-\frac{11}{8}}\frac{\partial\psi_3}{\partial X}\right)\left(h^{-\frac{5}{8}}\frac{\partial^2\psi_1}{\partial z^2} + h^{-1}\frac{\partial^2\psi_2}{\partial z^2} + h^{-\frac{11}{8}}\frac{\partial^2\psi_3}{\partial z^2}\right)\\ =&-h^2\mu_0 - h^{\frac{5}{4}}\frac{\partial p_1}{\partial X} + h^2\frac{\partial^3\psi_1}{\partial z^3} + h^{\frac{13}{8}}\frac{\partial^3\psi_2}{\partial z^3} + h^{\frac{5}{4}}\frac{\partial^3\psi_3}{\partial z^3}.\end{aligned}$$

The equations at $\mathcal{O}(h^2)$ and $\mathcal{O}(h^{13/8})$ are easy to deal with. The former gives

$$\frac{\partial\psi_1}{\partial z}\frac{\partial^2\psi_1}{\partial X\partial z} - \frac{\partial\psi_1}{\partial X}\frac{\partial^2\psi_1}{\partial z^2} = -\mu_0 + \frac{\partial^3\psi_1}{\partial z^3},$$

along with the matching conditions

$$\psi_1 \to \frac{1}{6}\mu_0 z^3 \quad \text{as } X \to -\infty,$$
$$\psi_1 \to \frac{1}{6}\mu_0 z^3 \quad \text{as } z \to \infty,$$

which has the solution

$$\psi_1(z) = \frac{1}{6}\mu_0 z^3; \tag{5.54}$$

while the latter gives

$$\frac{\partial^3 \psi_2}{\partial z^3} = \frac{1}{2}\mu_0 z^2 \frac{\partial^2 \psi_2}{\partial X \partial z} - \mu_0 z \frac{\partial \psi_2}{\partial X},$$

with

$$\psi_2 \to z^2 \left(a_0 |X|^{\frac{1}{2}} - \frac{1}{2} A_{0L} |X|^{-\frac{1}{2}} \ln |X| + \frac{1}{2} A_0 |X|^{-\frac{1}{2}} \right) \quad \text{as } X \to -\infty,$$
$$\psi_2 \to \frac{1}{2}\mu_0 z^2 (A + f) \quad \text{as } z \to \infty,$$

giving not only the solution to ψ_2,

$$\psi_2 (X, z, T) = \frac{1}{2}\mu_0 z^2 \left[A (X, T) + f (X, T) \right], \tag{5.55a}$$

but also the upstream matching condition on A,

$$A (X, T) \to 2\mu_0^{-1} a_0 |X|^{\frac{1}{2}} - \mu_0^{-1} A_{0L} |X|^{-\frac{1}{2}} \ln |X| + \mu_0^{-1} A_0 |X|^{-\frac{1}{2}} \tag{5.55b}$$

as $X \to -\infty$.

Compare this with the results obtained by Smith & Daniels [85]: the solution to ψ_1 is the same, with the solution to ψ_2 being modified by the addition of f, representing the roughness elements present here. This in turn adjusts the equation for ψ_3, which, considering terms at $\mathcal{O}(h^{5/4})$, is

$$\frac{\partial^3 \psi_3}{\partial z^3} + \mu_0 z \frac{\partial \psi_3}{\partial X} - \frac{1}{2}\mu_0 z^2 \frac{\partial^2 \psi_3}{\partial X \partial z} = \frac{\partial p_1}{\partial X} + \frac{1}{2}\mu_0 z^2 (A + f) \frac{\partial}{\partial X} (A + f) + \mu_0 z \frac{\partial}{\partial T} (A + f) \tag{5.56a}$$

to be solved subject to the matching conditions

$$\psi_3 \to -\frac{1}{60} a_0^2 z^5 + A_3 z^2 \quad \text{as } X \to -\infty, \tag{5.56b}$$
$$\psi_3 \to -\frac{1}{60} a_0^2 z^5 + A_3 z^2 + \frac{1}{2} (A + f)^2 z + \int \frac{\partial}{\partial T} (A + f) \, \mathrm{d}X \quad \text{as } z \to \infty. \tag{5.56c}$$

Note that evaluating equation (5.56a) using the boundary condition at infinity justifies the presence of the last two, roughness-dependent terms in condition (5.56c), since they account for the final two terms on the right-hand side of the governing equation for ψ_3. The $A_3 z^2$ term is also a solution to the homogeneous problem.

Our choice that the roughness height be of $\mathcal{O}(h^{-5/4})$ and time be of $\mathcal{O}(h^{-11/8})$ can be explained by reference to equation (5.56a). Of course, other scalings could be chosen, but, regarding firstly the height scale, the choice of $h^{-5/4}$ ensures that the roughness function f appears in the second term on the right-hand side of (5.56a), due to its inclusion as part of the solution to ψ_2, equation (5.55a)—which, in turn, is due to its presence in Ψ_2 in the outer Goldstein layer, equation (5.49a). Smaller height scales would merely be a subset of the chosen scaling, with f set to zero in equation (5.56a), no need for any time-dependent forcing and thus the same equation of Smith & Daniels would be obtained. Turning, secondly, to the time scaling: the primary motivation was to ensure that the time derivative appeared as a forcing term in the equation for ψ_3; or, more specifically, that the time derivative of ψ_i appeared in the equation for ψ_{i+1}. Increasing the time scaling to be $\mathcal{O}(h^{-1})$—equivalent to decreasing the oscillation frequency of the dynamic roughness—would make the time derivative of ψ_i appear in the governing equation for ψ_{i+2} and, since ψ_1 is independent of time, this would remove the time derivative from the right-hand side of equation (5.56a). The resulting equation,

$$\frac{\partial^3\psi_3}{\partial z^3} + \mu_0 z\frac{\partial\psi_3}{\partial X} - \frac{1}{2}\mu_0 z^2\frac{\partial^2\psi_3}{\partial X\partial z} = \frac{\partial p_1}{\partial X} + \frac{1}{2}\mu_0 z^2\,(A+f)\,\frac{\partial}{\partial X}\,(A+f)\,,$$

would still be time-dependent due to the presence of the roughness function f, but also turns out to be the same as that obtained for a steady roughness element and thus is studied in §5.6. Conversely, increasing the oscillation frequency by taking time to be $\mathcal{O}(h^{-7/4})$ would result in the time derivative of ψ_i appearing in the equation for ψ_i itself. The solution to ψ_2, which turns out to be the one we are interested in, would then be the solution to the system

$$\begin{aligned}\frac{\partial^3\psi_2}{\partial z^3} &= \frac{\partial^2\psi_2}{\partial z\partial T} + \frac{1}{2}\mu_0 z^2\frac{\partial^2\psi_2}{\partial X\partial z} - \mu_0 z\frac{\partial\psi_2}{\partial X},\\ \psi_2 \to \frac{1}{2}\mu_0 z^2(A+f) &+ \int\frac{\partial}{\partial T}(A+f)\,\mathrm{d}X \quad \text{as } z\to\infty,\end{aligned}$$

which contains no forcing from the pressure perturbation p_1. All of this is not to say that these other scalings should not be looked at—the scaling of height as $\mathcal{O}(h^{-5/4})$ and time as $\mathcal{O}(h^{-1})$, maintaining dynamic as opposed to static roughness elements, might be particularly interesting—but the above provides the reasoning behind the choice that is studied here.

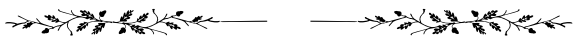

A rigorous derivation of how equation (5.56a), by finding the solvability criterion for it, is converted into an equation for the displacement A will be given in chapter 6 in the setting of marginal separation theory: a different scenario, but one which results in a similar equation.[3] For present purposes, we refer to the work of Smith on dynamic stall

[3]Note also the resemblance of equation (5.56a) with equation (4.10) in our derivation of the Goldstein singularity of chapter 4.

[82], who obtained fundamentally the same equation as ourselves (ignoring a change in some of the coefficients) but with $A + f$ replaced by the single function $\bar{A}$. The same procedure as is described admirably in his paper (as well as that of others, as will be mentioned in chapter 6) is carried out here to obtain the final equation

$$\begin{aligned}&(A+f)\,\frac{\partial}{\partial X}\,(A+f)+\sigma_1\int_{-\infty}^{X}(X-s)^{-\frac{1}{4}}\,\frac{\partial^2}{\partial s\partial T}\,(A+f)\;\mathrm{d}s+g\,(X)\\ =&-\sigma_2\int_{-\infty}^{X}(X-s)^{-\frac{1}{2}}\,\frac{\partial^2 p_1}{\partial s^2}\,\mathrm{d}s,\end{aligned}$$

where

$$\sigma_1 = 2^{\frac{5}{4}}\pi^{-1}\Gamma\left(\frac{3}{4}\right)\mu_0^{-\frac{3}{4}} \quad \text{and} \quad \sigma_2 = \pi^{-1}\Gamma^2\left(\frac{3}{4}\right)\mu_0^{-\frac{3}{2}}, \tag{5.57}$$

both positive.

Considering the upstream behaviour of A, equation (5.55b), allows us to find the (constant) function g as

$$g = 2\mu_0^{-2}a_0^2;$$

and we use also the pressure–displacement relation (5.49b) to finally arrive at the nonlinear integro–partial differential equation to be solved for A:

$$\begin{aligned}&(A+f)\,\frac{\partial}{\partial X}\,(A+f)+\sigma_1\int_{-\infty}^{X}(X-s)^{-\frac{1}{4}}\,\frac{\partial^2}{\partial s\partial T}\,(A+f)\;\mathrm{d}s+2\mu_0^{-2}a_0^2\\ =&-\sigma_2 F_s\int_{-\infty}^{X}(X-s)^{-\frac{1}{2}}\,\frac{\partial^2 A}{\partial s^2}\,\mathrm{d}s,\end{aligned} \tag{5.58}$$

subject to the upstream condition (5.55b).

To simplify the numerical work to come, and free ourselves from the trappings of extraneous notation, it makes sense to remove the constants σ_i, μ_0 and a_0 from both the governing equation and the upstream condition. Writing

$$A = \Gamma_A\tilde{A}, \quad f = \Gamma_A\tilde{f}, \quad X = \Gamma_X\tilde{X}, \quad T = \Gamma_T\tilde{T},$$

where the tilde is but a fleeting shadow, existing only briefly before vanishing, the upstream matching condition gives

$$\Gamma_A^2 = 4\mu_0^{-2}a_0^2\Gamma_X,$$

which we can substitute into (5.58), compare the coefficients of the various terms that appear, and obtain

$$\Gamma_X = \frac{1}{2}\frac{\mu_0}{a_0}\sigma_2 F_\mathrm{s}, \quad \Gamma_A = \left(2\frac{a_0}{\mu_0}\sigma_2 F_\mathrm{s}\right)^{\frac{1}{2}} \quad \text{and} \quad \Gamma_T = \frac{1}{2}\frac{\mu_0}{a_0}\sigma_1\left(\frac{1}{2}\frac{\mu_0}{a_0}\sigma_2 F_\mathrm{s}\right)^{\frac{1}{4}}. \tag{5.59}$$

The upstream condition (5.55b) also requires an origin shift in X: writing $X = \Gamma_X(\tilde{X} - \tilde{X}_0)$ allows us to rewrite it as

$$\begin{aligned}\tilde{A} \to &\left|\tilde{X}\right|^{\frac{1}{2}}\left(1 - \frac{1}{2}\left|\frac{\tilde{X}_0}{\tilde{X}}\right| + \cdots\right)\\ &- A_{0L}\left(\mu_0\sigma_2 F_\mathrm{s}\right)^{-1}\left|\tilde{X}\right|^{-\frac{1}{2}}\left(1 + \frac{1}{2}\left|\frac{\tilde{X}_0}{\tilde{X}}\right| + \cdots\right)\left[\ln\left|\tilde{X}\right| + \ln\left(1 + \cdots\right)\right]\\ &+ \left(\mu_0\sigma_2 F_\mathrm{s}\right)^{-1}\left|\tilde{X}\right|^{-\frac{1}{2}}\left(1 + \frac{1}{2}\left|\frac{\tilde{X}_0}{\tilde{X}}\right| + \cdots\right)\left[a_0 - A_{0L}\ln\left(\frac{1}{2}\frac{\mu_0}{a_0}\sigma_2 F_\mathrm{s}\right)\right] + \cdots,\end{aligned}$$

using the fact that $|\tilde{X}_0/\tilde{X}| \ll 1$. Removing the terms at order $|\tilde{X}|^{-1/2}$ gives the origin shift as

$$\left|\tilde{X}_0\right| = 2\left(\mu_0\sigma_2 F_\mathrm{s}\right)^{-1}\left[a_0 - A_{0L}\ln\left(\frac{1}{2}\frac{\mu_0}{a_0}\sigma_2 F_\mathrm{s}\right)\right]. \tag{5.60}$$

Combining the affine transformations (5.59) and (5.60) gives the final system for the local (negative) boundary layer displacement A that will concern us for the remainder of our journey in this chapter

$$\begin{aligned}&(A+f)\frac{\partial}{\partial X}(A+f) + \int_{-\infty}^{X}(X-s)^{-\frac{1}{4}}\frac{\partial^2}{\partial s\partial T}(A+f)\,\mathrm{d}s + \frac{1}{2}\\ &= -\int_{-\infty}^{X}(X-s)^{-\frac{1}{2}}\frac{\partial^2 A}{\partial s^2}\,\mathrm{d}s,\end{aligned} \tag{5.61a}$$

subject to

$$A \to |X|^{\frac{1}{2}} - \frac{1}{2}|X|^{-\frac{1}{2}}\ln|X| \quad \text{as } X \to -\infty. \tag{5.61b}$$

Compare this to the system of Smith & Daniels [85], whose scenario of condensed boundary layer flow over a hump has motivated this chapter. Their equation was

$$A\frac{\mathrm{d}A}{\mathrm{d}X} + \frac{1}{2} = -\int_{-\infty}^{X}(X-s)^{-\frac{1}{2}}A''(s)\,\mathrm{d}s, \tag{5.62}$$

with the same upstream condition as (5.61b). The introduction of our roughness element, with its accompanying time dependence in the dynamic case, at a height and time scale that forces the inclusion of the terms, previously discussed, in (5.56a) results in the presence of the roughness function and time derivative in our equation (5.61a). Setting f to zero and taking A to be steady would recover the above equation of Smith & Daniels. Indeed, the leading order solution in the linearised approach of the next section will be the same as that of equation (5.62).

Separation

The first two terms in the inner Goldstein layer stream function have thus been calculated as

$$\psi = h^{-\frac{5}{8}}\left(\frac{1}{6}\mu_0 z^3\right) + \frac{1}{2}h^{-1}\mu_0 z^2\left(A+f\right) + \cdots, \tag{5.63}$$

without the application of the affine transformation. These are sufficient to determine the skin friction at the wall,

$$\tau_{\text{wall}} = h^{\frac{7}{4}}\left.\frac{\partial^2\psi}{\partial z^2}\right|_{z=0} = h^{\frac{3}{4}}\mu_0\left(A+f\right), \tag{5.64a}$$

and thus separation will occur when

$$A\left(X,T\right) + f\left(X,T\right) = 0. \tag{5.64b}$$

And so our wanderings, thus far, have brought us here: in front of us is an equation for the local boundary layer displacement $-A$ (5.61); and, along the way, we have discovered that local separation occurs when $A+f$ equals zero and stumbled across the relationship relating the displacement to the pressure perturbation, (5.49b), which will guide us in understanding the results to be presented in later sections.

5.4 Crawling: linearised solutions

Before we learn to walk, we learn to crawl. Babies have it right: for when the going gets tough, and curiosity leads one to a scree slope, strewn with jagged flint, or a rocky descent that falls away precipitously, it is better to ignore one's adulthood and return to the state of an infant, crawling, a child before nature's majesty.

The governing system (5.61) that concerns us, albeit parabolic in space and thus amenable to downstream marching, is nonlinear and so, as a check on the numerical solutions that will follow, as well as to give an indication as to the behaviour of the negative boundary layer displacement, it makes sense to first study its linearised properties, through which we will discover also the existence of a singularity in the solution. To this end, we consider a small dynamic roughness f, with height of order ϵ, where $\epsilon \ll 1$, and A is expanded as

$$A\left(X,T\right) = A_0\left(X\right) + \epsilon A_1\left(X,T\right) + \epsilon^2 A_2\left(X,T\right) + \cdots. \tag{5.65}$$

The upstream boundary condition (5.61b) then dictates that

$$A_0 \to \left|X\right|^{\frac{1}{2}} - \frac{1}{2}\left|X\right|^{-\frac{1}{2}}\ln\left|X\right| \quad \text{as } X \to -\infty, \tag{5.66}$$

while all other A_i tend to 0. Substituting the expansion (5.65) into equation (5.61a) gives the linearised form

$$\begin{aligned}&\left[A_0+\epsilon\left(A_1+f\right)+\epsilon^2A_2+\cdots\right]\frac{\partial}{\partial X}\left[A_0+\epsilon\left(A_1+f\right)+\epsilon^2A_2+\cdots\right]\\&+\int_{-\infty}^{X}\left(X-s\right)^{-\frac{1}{4}}\frac{\partial^2}{\partial s\partial T}\left[\epsilon\left(A_1+f\right)+\epsilon^2A_2+\cdots\right]\,\mathrm{d}s+\frac{1}{2}\\=&-\int_{-\infty}^{X}\left(X-s\right)^{-\frac{1}{2}}\frac{\partial^2}{\partial s^2}\left(A_0+\epsilon A_1+\epsilon^2A_2+\cdots\right)\,\mathrm{d}s.\end{aligned}\tag{5.67}$$

5.4.1 First order solution

Taking the $\mathcal{O}(1)$ terms in equation (5.67) gives us the same equation for A_0 as that of Smith & Daniels [85],

$$A_0A_0'+\frac{1}{2}=-\int_{-\infty}^{X}\frac{A_0''}{\left(X-s\right)^{\frac{1}{2}}}\,\mathrm{d}s,\tag{5.68}$$

to be solved subject to (5.66). The numerical technique used is described in appendix B.1.1 and we will use throughout a step size of $\Delta=0.001$ and set the start of the computational domain at $X_{-\infty}=-10$, with the integral between $-\infty$ and $X_{-\infty}$ computed analytically using the leading order term in the upstream condition (5.66).

The solution to A_0 is given in figure 5.2 and seems to agree with that produced in Smith & Daniels (ignoring minor variations as a result of any differences in numerical technique or discretisation). We see that A_0 passes smoothly through the point of vanishing skin friction and can be continued past it until a further singularity is reached later downstream. The behaviour of this singularity can be determined analytically by supposing that A_0 behaves like $m(X_0-X)^n$ as X approaches X_0, where X_0 is the singular point. Both the coefficient m and the exponent n can be found by noting that the terms in equation (5.68) are of order $(X_0-X)^{2n-1}$, 1 and $(X_0-X)^{n-3/2}$ respectively, with the only possible balance that gives rise to a singularity being that between the first and third terms. Hence $n=-1/2$ and

$$\frac{1}{2}m^2\left(X_0-X\right)^{-2}=-\int_{-\infty}^{X}\frac{3}{4}m\left(X-s\right)^{-\frac{1}{2}}\left(X_0-s\right)^{-\frac{5}{2}}\,\mathrm{d}s,$$

giving $m=-2$; the sign agreeing with A_0 going to negative infinity in figure 5.2. Thus

$$A_0\sim-2\left(X_0-X\right)^{-\frac{1}{2}}\quad\text{as }X\to X_0^-,\tag{5.69}$$

as was found in Smith & Daniels. This singularity is far worse than that of Goldstein and we will see in §5.5 how it corresponds to the complete separation of the boundary layer from the surface.

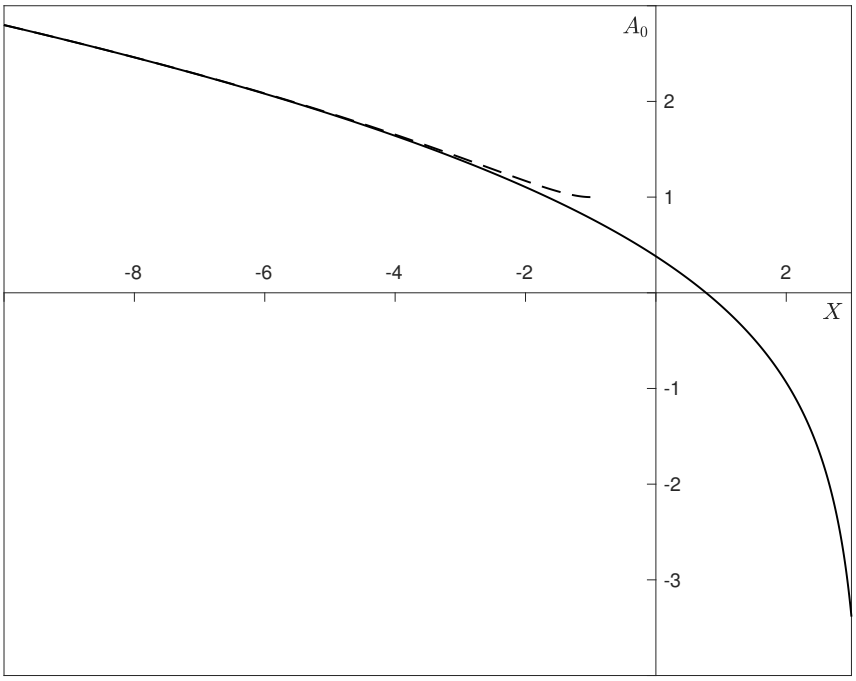

FIGURE 5.2: Solution of equation (5.68) for the leading order term (A_0) in the linearised displacement expansion (solid line). The step size is $\Delta = 0.001$ and the start point of the computational domain is $X_{-\infty} = -10$, a choice that will be maintained for the rest of §5.4. The solution, as expected, agrees with that shown in Smith & Daniels [85] and the upstream behaviour of A_0 is given by the dashed line.

5.4.2 The dynamic roughness

At $\mathcal{O}(\epsilon)$ in equation (5.67), the roughness elements make their appearance and so we define them here. As in chapter 3, their oscillatory motion is encapsulated in the use of complex exponentials, which are then multiplied by a function of the streamwise coordinate X, which represents the shape of the roughness,

$$f(X,T) = \bar{f}(X)\left[\exp(\mathrm{i}\omega T) + \exp(-\mathrm{i}\omega T)\right], \tag{5.70a}$$

where ω is the roughness oscillation frequency. To ensure that the roughness function $\bar{f}$ and its derivatives are sufficiently continuous at the left- and right-hand endpoints of the roughness, X_L and X_R respectively, we take our roughness shape to be given by

$$\bar{f}(X) = a(X - X_L)^4 (X - X_R)^4 \tag{5.70b}$$

for $X \in [X_L, X_R]$ and zero elsewhere. Changing a, which has been normalised by multiplying it by $256(X_L - X_R)^{-8}$ to give a peak height of 1 for a choice of $a = 1$, allows one to change the height of the roughness. Both position and width can be changed by choosing different values of X_L and X_R. A standard roughness, fully extended, is shown in figure 5.3 and note that the dynamic behaviour given by equation (5.70a) allows the roughness elements to oscillate both above and below the X-axis—positive (linearised) elements will be quickly looked at in §5.4.5, while the fully nonlinear problem will be studied for strictly positive (or negative) roughness elements only.

5.4.3 Second order solution

The $\mathcal{O}(\epsilon)$ terms in equation (5.67) give the governing equation for A_1:

$$\frac{\partial}{\partial X}\left[A_0(A_1 + f)\right] + \int_{-\infty}^{X} (X-s)^{-\frac{1}{4}} \frac{\partial^2}{\partial s \partial T}(A_1 + f)\,\mathrm{d}s = -\int_{-\infty}^{X} (X-s)^{-\frac{1}{2}} \frac{\partial^2 A_1}{\partial s^2}\,\mathrm{d}s.$$

The time dependence of f given in equation (5.70a) suggests writing A_1 as

$$A_1(X,T) = A_{11}(X)\exp(\mathrm{i}\omega T) + A_{11}^*(X)\exp(-\mathrm{i}\omega T),$$

where the asterisk denotes the complex conjugate. This allows us to deal with the time dependence and obtain an equation for A_{11}

$$\frac{\partial}{\partial X}\left[A_0\left(A_{11} + \bar{f}\right)\right] + \mathrm{i}\omega \int_{-\infty}^{X} (X-s)^{-\frac{1}{4}} \frac{\partial}{\partial s}\left(A_{11} + \bar{f}\right)\mathrm{d}s = -\int_{-\infty}^{X} (X-s)^{-\frac{1}{2}} \frac{\partial^2 A_{11}}{\partial s^2}\,\mathrm{d}s, \tag{5.71}$$

solved subject to the starting condition that A_{11} is zero upstream.

The solution is found in a similar manner to that of A_0 and the technique is described in appendix B.1.2, with figure 5.4 showing the solution to A_{11} for the choice $X_L = -3$, $X_R = 1$, $a = 1$ and $\omega = 1$. Focusing on the real part of the solution, A_{11} decreases over

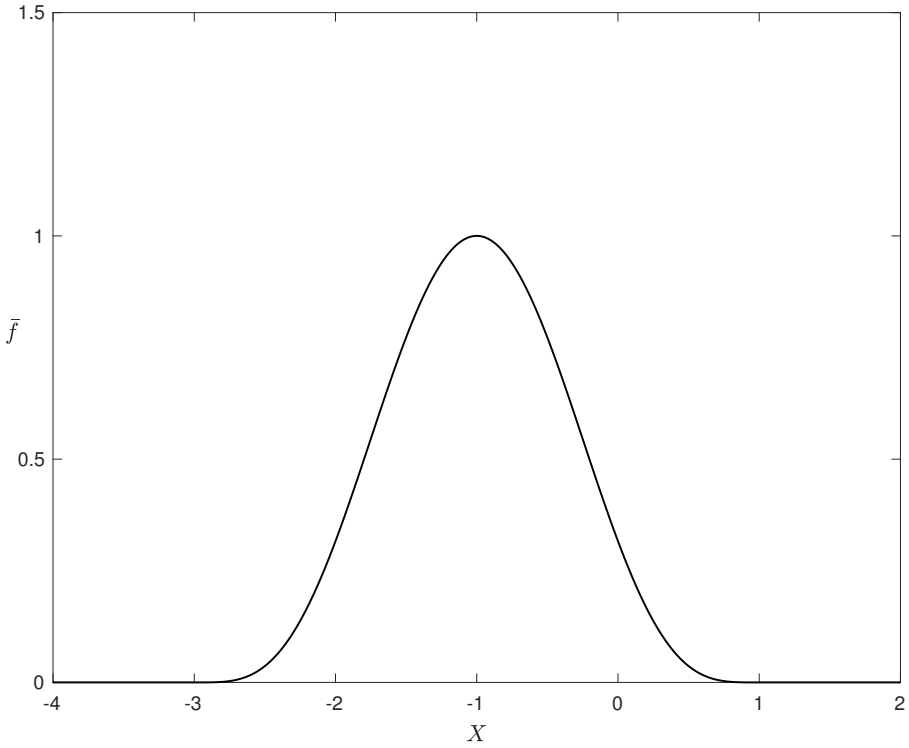

FIGURE 5.3: Roughness shape, with height $a = 1$, left-hand endpoint at $X_L = -3$ and right-hand endpoint at $X_R = 1$. The choice of shape function (5.70b) gives a sufficiently smooth behaviour at the endpoints of the roughness.

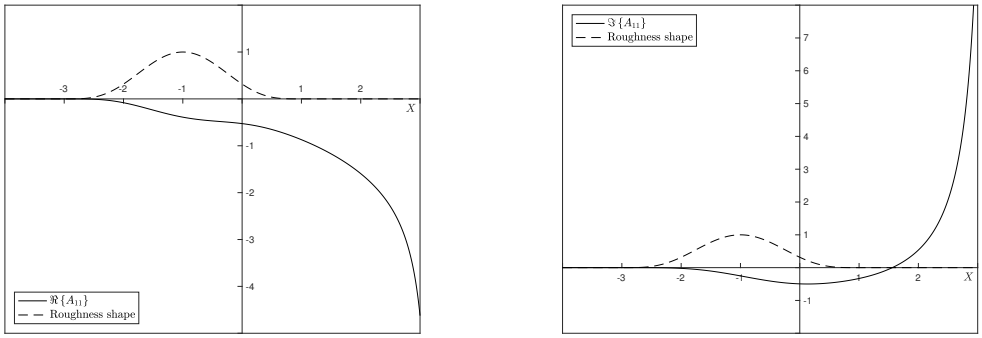

(A) Real part (B) Imaginary part

FIGURE 5.4: Solution to the real and imaginary parts of A_{11} (solid line), with a dynamic roughness (dashed line) oscillating at a frequency $\omega = 1$ and of height 1, placed between $X_L = -3$ and $X_R = 1$. The real part of the solution decreases over the front part of the roughness, levels off over the rear, and then reaches a singularity.

the front half of the roughness element before levelling off over the rear and then falling away into the singularity. We will describe in §5.6 how this behaviour makes physical sense and the high frequency behaviour in the solution to A_{11} will be referred to briefly in §5.8; in the meantime, we can once more determine the behaviour of the singularity.

Writing A_{11} as

$$A_{11} \sim m_{11}\,(X_0 - X)^n \quad \text{as } X \to X_0^-,$$

we aim to find the exponent n. Note that the linearity of equation (5.71) means that it is not possible to determine the coefficient m_{11}, but an analysis of the order of magnitude of the terms gives the value of n. Assuming that ω is of order 1, the first and third terms dominate the second and so the leading order balance is

$$\frac{\partial}{\partial X}\left(A_0 A_{11}\right) = -\int_{-\infty}^{X} (X-s)^{-\frac{1}{2}}\,\frac{\partial^2 A_{11}}{\partial s^2}\,\mathrm{d}s,$$

giving

$$2\left(n-\frac{1}{2}\right)(X_0 - X)^{n-\frac{3}{2}} = -n(n-1)\int_{-\infty}^{X} (X-s)^{-\frac{1}{2}}\,(X_0 - s)^{n-2}\,\mathrm{d}s,$$

which gives the solution $n = -3/2$. Thus at the singular point,

$$A_{11} \sim (X_0 - X)^{-\frac{3}{2}}, \tag{5.72}$$

which is confirmed in figure 5.5.

Once the average over a period of oscillation is taken, however, the solution to A_{11} does not contribute to any shifting of the position of zero skin friction: any movement that does occur is due to the mean flow correction that appears, just as in chapter 3, due to the nonlinear forcing at $\mathcal{O}(\epsilon^2)$.

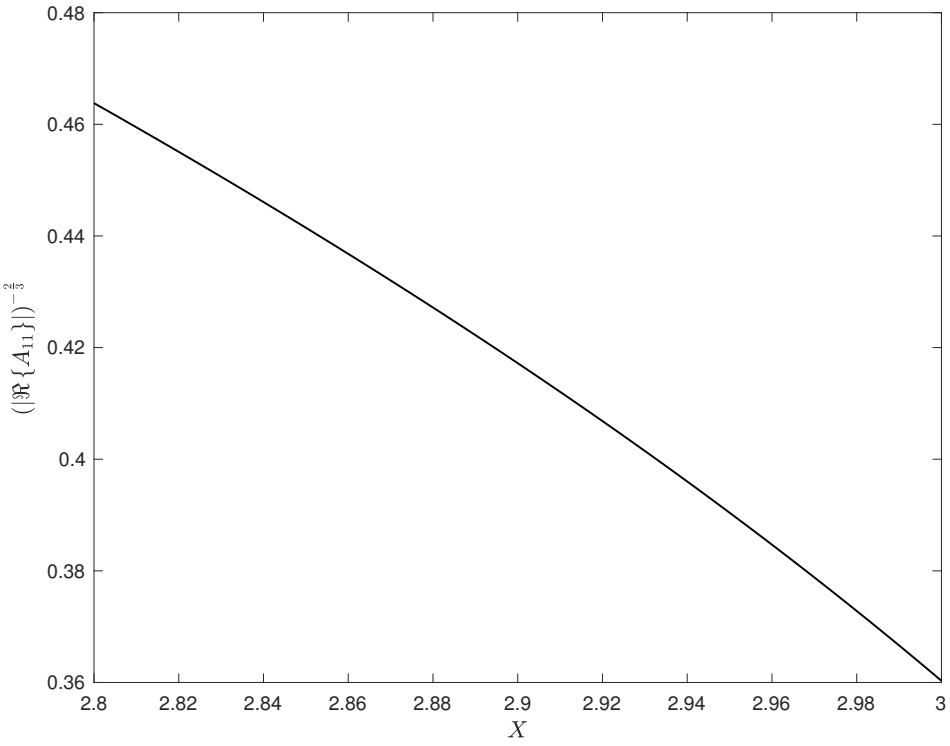

FIGURE 5.5: Graph of the real part of A_{11} (absolute value), raised to the power of $-2/3$ near the singular point. The (almost) straight line obtained confirms the conclusion of equation (5.72) that it behaves as $(X_0 - X)^{-3/2}$. The gradient of the straight line would then give the coefficient m_{11}.

5.4.4 Third order solution and the mean flow correction

The terms appearing at order ϵ^2 in equation (5.67) are

$$\begin{aligned} &A_0\frac{\partial A_2}{\partial X} + A_2\frac{\partial A_0}{\partial X} + \frac{1}{2}\frac{\partial}{\partial X}\left[(A_1+f)^2\right] + \int_{-\infty}^{X}(X-s)^{-\frac{1}{4}}\,\frac{\partial^2 A_2}{\partial s\partial T}\,\mathrm{d}s \\ &= -\int_{-\infty}^{X}(X-s)^{-\frac{1}{2}}\,\frac{\partial^2 A_2}{\partial s^2}\,\mathrm{d}s. \end{aligned} \tag{5.73}$$

The $(A_1+f)^2$ term hints at a form of A_2 of

$$A_2 = A_{21}(X)\exp(2\mathrm{i}\omega T) + A_{21}^*(X)\exp(-2\mathrm{i}\omega T) + A_M(X), \tag{5.74}$$

where the asterisk again denotes the complex conjugate and A_M is the mean flow correction of interest, since it is independent of time. Note that any function multiplying $\exp(\mathrm{i}\omega T)$ must be identically zero due to the lack of forcing in its governing equation and the upstream condition of zero.

The equation for A_{21} has been solved numerically but, since our main goal is to determine A_M, which allows us to shift (by a small amount) the position of vanishing skin friction, we do not present the results here. Rather, we turn straight to the equation for the mean flow correction, which, with the above expansion (5.74) of A_2 and that of A_1, is

$$\frac{\partial}{\partial X}(A_0A_M) + \frac{\partial}{\partial X}\left[\left(A_{11}+\bar{f}\right)\left(A_{11}^*+\bar{f}\right)\right] = -\int_{-\infty}^{X}(X-s)^{-\frac{1}{2}}\,\frac{\partial^2 A_M}{\partial s^2}\,\mathrm{d}s, \tag{5.75}$$

along with the boundary condition that A_M is zero upstream of the roughness element. This is solved numerically—details are found once more in appendix B.1.3, but the technique is essentially the same as that used to solve for A_0 and A_{11}—and the solution for when $\omega = 1$ is shown in figure 5.6. In a similar manner to that observed in the solution to A_{11}, A_M decreases over the front face of the roughness (for physical reasons that will be explained in §5.6) and increases over the rear—but only slightly due to the singular point that is encountered farther downstream, which causes A_M to fall away to negative infinity.

Writing this singular downstream behaviour as

$$A_M \sim m_M(X_0-X)^n \quad \text{as } X\to X_0^-,$$

substitution into (5.75), using also the singular behaviours of A_0 and A_{11} found previously, has a resulting equation, setting $\bar{f}=0$, of

$$\begin{aligned} &2m_Mn(X_0-X)^{n-\frac{3}{2}} - m_M(X_0-X)^{n-\frac{3}{2}} + 3m_{11}^2(X_0-X)^{-4} \\ &= -m_Mn(n-1)\int_{-\infty}^{X}(X-s)^{-\frac{1}{2}}(X_0-s)^{n-2}\,\mathrm{d}s, \end{aligned}$$

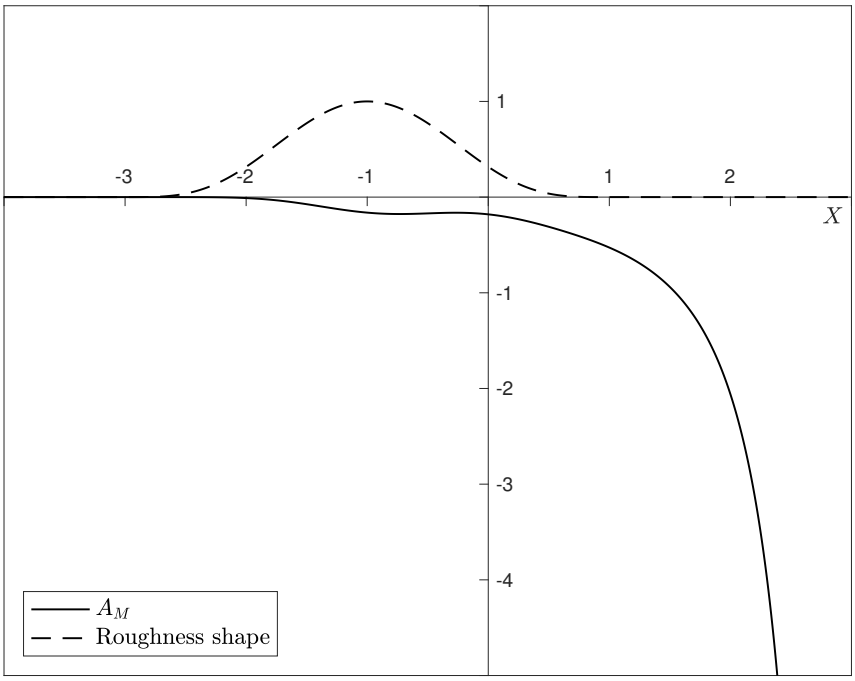

FIGURE 5.6: Mean flow correction to the displacement function, A_M, in the presence of a dynamic roughness element oscillating at frequency of $\omega = 1$, with height 1 and position between -3 and 1. Similarly to the solution to the real part of A_{11}, the solution decreases over the front face of the roughness, increases slightly on the back face and then falls away to negative infinity at the singular point.

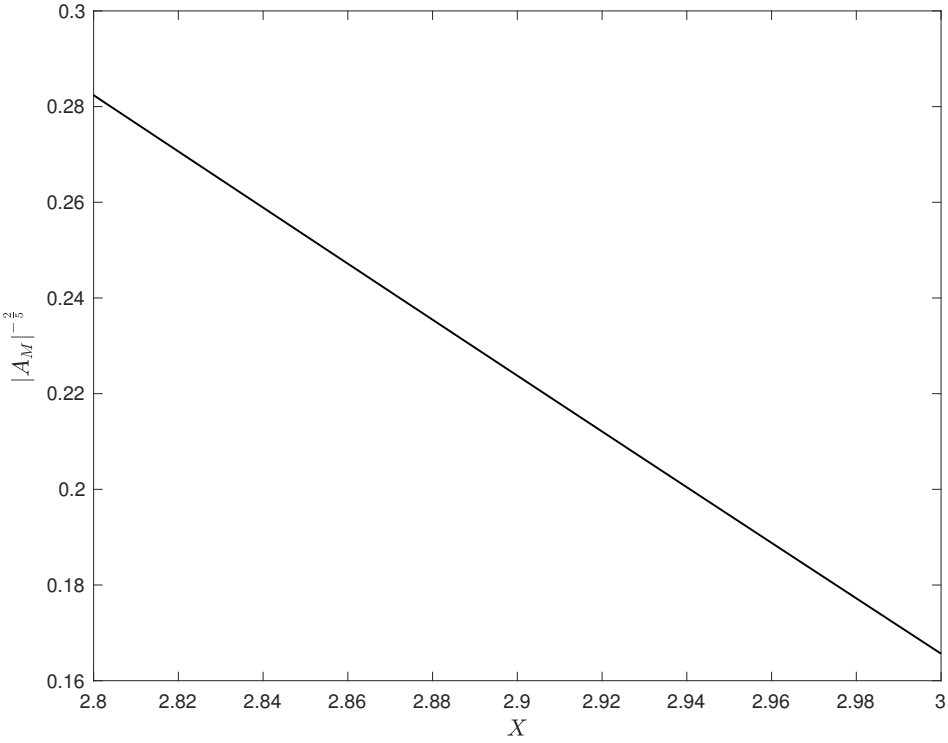

FIGURE 5.7: Graph of A_M (absolute value), raised to the power of $-2/5$ near the singular point. The straight line obtained confirms the conclusion of equation (5.76) that the mean flow correction behaves as $(X_0 - X)^{-5/2}$.

which has terms of order either $(X_0 - X)^{n-3/2}$ or $(X_0 - X)^{-4}$ and thus, keeping a balance between them all, we find that

$$A_M = -\frac{3}{2} m_{11}^2 \, (X_0 - X)^{-\frac{5}{2}} \quad \text{as } X \to X_0^-. \tag{5.76}$$

In particular, although m_{11} is unknown, we have proved that the solution will always tend towards negative infinity at the singularity. This will be seen in all of the graphs produced for dynamic roughness elements in this chapter, whether in the linear or nonlinear case. The choice of exponent as $-5/2$ is confirmed in figure 5.7.

For these 'small' dynamic roughness elements, the impact of their parameters on the local separation point is as follows: the roughness position (figure 5.8) obviously affects where the solution to A_M responds to the presence of the roughness, but the solution consistently decreases over the front half of the roughness and either levels out or increases slightly over the rear, depending on the vicinity of the roughness to the downstream singularity. For a midpoint of 1, for example, the roughness element has very little impact on the solution due to the nearby presence of this singularity. Modifying the width, but keeping the left-hand edge of the dynamic roughness element fixed at $X_L = -3$ (figure 5.9) indicates that the greater the width, the more negative the mean flow correction—probably due to it decreasing for a greater streamwise extent—but,

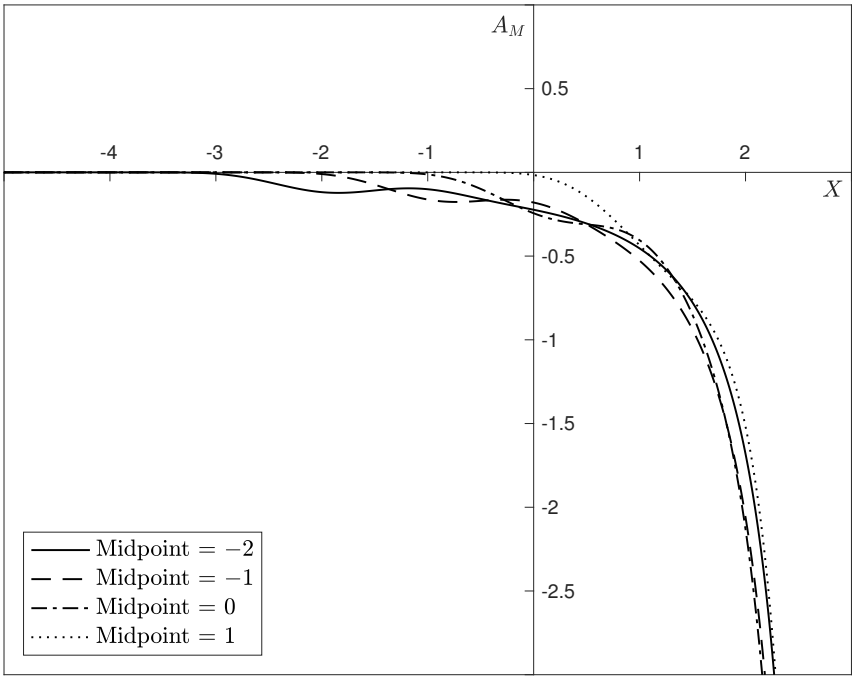

FIGURE 5.8: Impact of the roughness position on the mean flow correction, A_M. The midpoint of the roughness was changed as described in the legend, but the width was kept fixed at 4 and the oscillation frequency and maximum height of the roughness were both kept at 1. The shape of all solutions is similar, with the singularity having the effect of preventing an increase in A_M over the rear of the roughness for roughnesses that were placed too close to it.

interestingly, the position of the singularity seems to also advance (perhaps due to the more negative values of A_M obtained over the roughness element).

A similar behaviour as for the roughness width is observed for the roughness height (figure 5.10, reminding ourselves that height is of order ϵ). For a constant width of 4, larger heights result in a larger gradient over the front face of the roughness and hence the solution to the mean flow correction has a greater decrease, before recovering slightly over the rear. However, since A_M maintains a more negative solution over the rear half of the roughness for larger heights, the singularity again seems to move upstream. The impact of the rear half of the roughness in increasing A_M is also more readily seen for larger heights. The impact of frequency is shown in figure 5.11, both for lower and higher frequencies, the latter again suggesting an advance in the singular position. Of interest is the fact that at all frequencies, the solution over the front half of the roughness is virtually identical and the graphs of A_M only begin to diverge from each other over the rear side of the element: the higher the frequency, the sooner the divergence. This is also true for the real part of the solution to A_{11}, although not for the imaginary part, as would be expected.[4] An expansion of the solution to A_M near the

[4]Referring to equation (5.71), an expansion of A_{11} in powers of $\omega \ll 1$ would lead to a real leading order solution and an imaginary second order solution at $\mathcal{O}(\omega)$. Hence the imaginary part of A_{11},

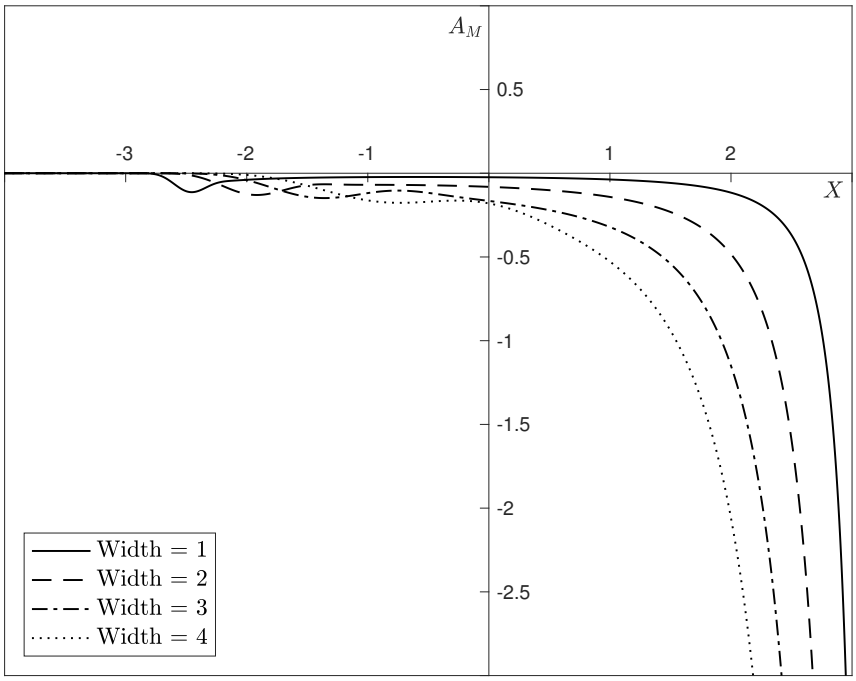

FIGURE 5.9: Impact of the roughness width on the mean flow correction, A_M. In all cases, the left-hand edge of the roughness was kept fixed at $X_L = -3$ but the width was changed as indicated in the legend. Both the height and oscillation frequency of the roughness were 1. Once more, the shape of all solutions is similar, with a greater width allowing the solution to A_M to decrease more over the front face of the roughness element, but also seeming to advance the position of the singularity.

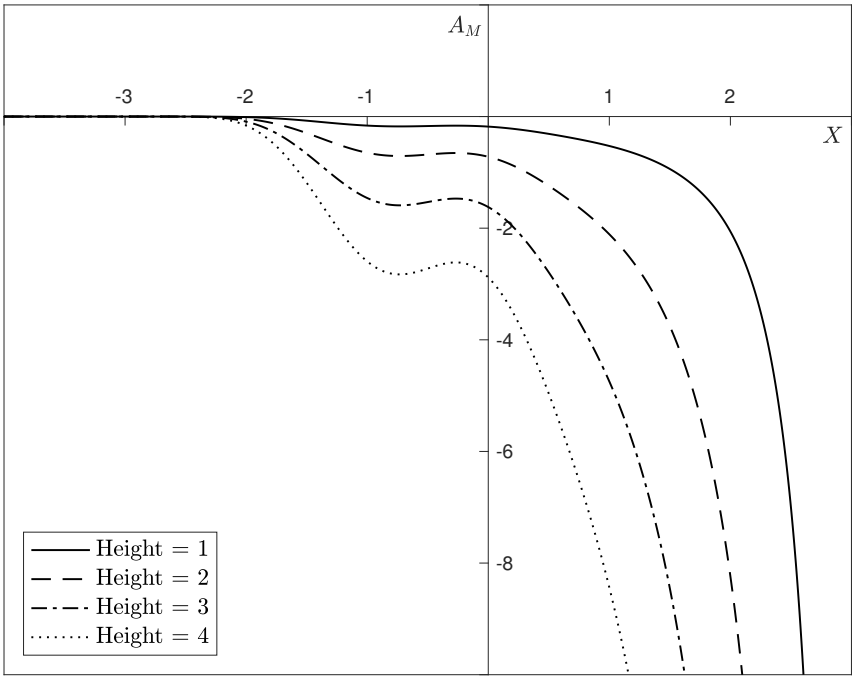

FIGURE 5.10: Impact of the roughness height, as given in the legend, on the mean flow correction, A_M. The roughness was placed between $X_L = -3$ and $X_R = 1$, with an oscillation frequency of $\omega = 1$. Similar behaviour as that of varying width is seen here, with advances in the singularity seemingly possible for larger heights.

leading edge of the roughness also indicates that a frequency dependence first appears at third and fourth order respectively,[5] although this expansion should only be valid for $X - X_L \ll 1$ and thus should not be sufficient to explain the excellent agreement found over a length scale that is of order unity.

5.4.5 Positive roughnesses

The linearised work described above has allowed our dynamic roughness elements to oscillate both above and below the X-axis, due to the form of the time-dependence chosen in equation (5.70a). In this section, we briefly comment on non-negative roughness elements, which will form the configuration in the nonlinear work to follow. The roughness function is then given by

$$f(X,T) = \bar{f}(X)\left[\exp(2\mathrm{i}\omega T) + \exp(-2\mathrm{i}\omega T) + 2\right], \tag{5.77}$$

at low frequencies, scales with ω: a self-similarity solution (by rescaling X) may exist, although this hasn't been checked. This implies, due to the forcing of equation (5.75) for the mean flow correction, that the second order term of A_M is $\mathcal{O}(\omega^2)$.

[5]This corresponds to orders $(X - X_L)^{21/4}$ and $(X - X_L)^{39/4}$ respectively, although the increase in the exponents of $(X - X_L)$ is not linear.

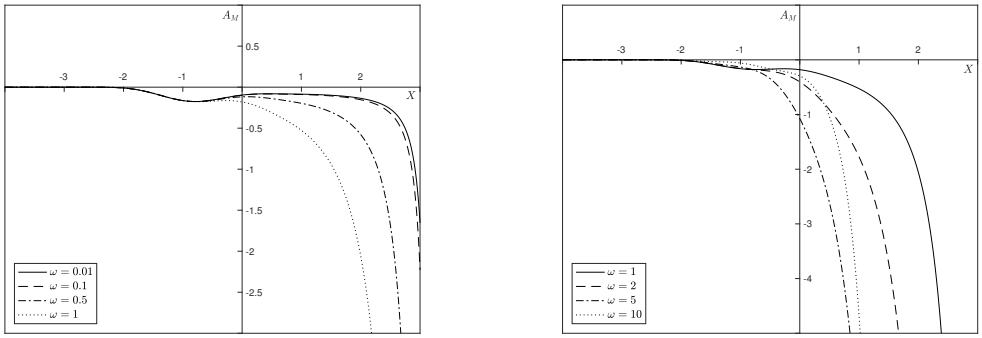

(A) Low frequencies (B) High frequencies

FIGURE 5.11: Impact of the roughness frequency on the mean flow correction, A_M for (a) lower and (b) higher frequencies, as given in the legends. The maximum roughness height was 1, with the roughness between $X_L = -3$ and $X_R = 1$. All solutions agree at the start of the roughness and over the majority of its front face; higher frequency solutions then diverge by becoming more negative sooner than lower frequency graphs, with the singularity therefore advancing.

again acting at $\mathcal{O}(\epsilon)$ and with $\bar{f}$ given by equation (5.70b). The mean flow correction, independent of time, will then also act at $\mathcal{O}(\epsilon)$ and arises due to the $+2$ term in (5.77), much as in the case of flow over an array of roughness elements on a plane, described in chapter 3. The negative boundary layer displacement is then expanded as

$$A\left(X,T\right) = A_0\left(X\right) + \epsilon\left[A_{11}\left(X\right)\exp\left(2\mathrm{i}\omega T\right) + A_{11}^*\left(X\right)\exp\left(-2\mathrm{i}\omega T\right) + A_M\left(X\right)\right] + \cdots . \tag{5.78}$$

Both the equations for A_0 and A_{11} remain the same as before (providing the frequency is rescaled), while the equation for the mean flow correction is now

$$\left(A_M + 2\bar{f}\right)\frac{\partial A_0}{\partial X} + A_0\frac{\partial}{\partial X}\left(A_M + 2\bar{f}\right) = -\int_{-\infty}^{X}\left(X-s\right)^{-\frac{1}{2}}\frac{\partial^2 A_M}{\partial s^2}\,\mathrm{d}s, \tag{5.79}$$

which is independent of frequency and whose numerical solution poses no new issues, with an example of A_M shown in figure 5.12a. Recall, from equation (5.64b), that separation occurs when $A + f$ equals zero: hence a permanent downstream shift in the local separation point is possible if

$$A_M + 2\bar{f} > 0$$

at the original (no roughness) position of vanishing skin friction. For roughness elements placed upstream of the original position of zero skin friction, the behaviour of A_M (decreasing over the front face of the roughness, increasing over the rear but not sufficiently for the solution to become positive again) implies that the local separation point will also move upstream: a roughness element therefore needs to be placed over the original separation point, so that $\bar{f}$ is positive there, in order to shift local separation downstream. An example of this is shown in figure 5.12b. This argument holds also for the nonlinear results presented later and we will see that for a negative roughness

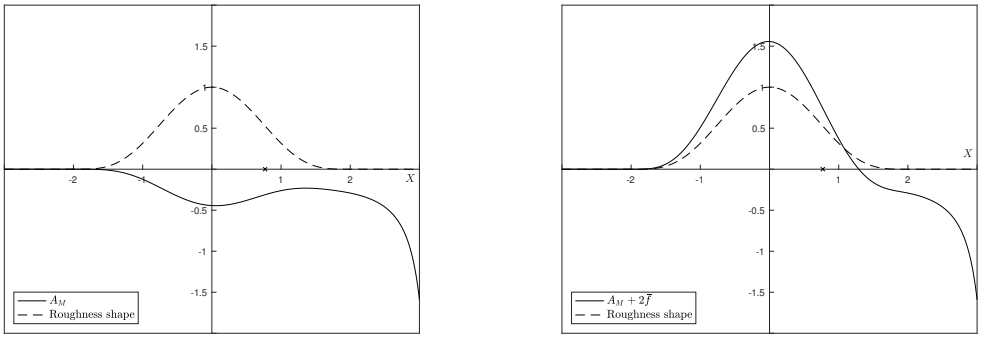

(A) Displacement function (B) Time-averaged skin friction (scaled)

FIGURE 5.12: Solution to both (a) the mean flow correction, A_M, and (b) $A_M + 2\bar{f}$ for a positive dynamic roughness element placed between $X_L = -2$ and $X_R = 2$ and of height 1. The solution is independent of frequency and so holds also for static roughness elements. The cross denotes the position at which $A_0 = 0$ and thus we see from (b) that this choice of roughness allows one to shift the local separation point downstream, by an amount of order ϵ.

element, the converse applies: a negative roughness must be placed far upstream of the local separation point in order to move it downstream.

Any shift in the marginal separation point, however, either upstream or downstream, will only be of order $\epsilon \ll 1$ in this linearised case. With results that suggest a downstream shift is possible depending on the position of the roughness element—and having learnt to crawl—we can proceed with optimism to the challenge of solving the full nonlinear system (5.61). We turn first, though, to describing the significance of the singularity that exists in all of our solutions and the potential impact of the roughness elements on it.

5.5 On hands and knees: breakaway separation

The focus so far has largely been on the local separation point—the position at which the skin friction equals zero. However, in all of the graphs of the linearised displacement solution presented so far, the presence of a singularity farther downstream looms ominously. Smith & Daniels [85] considered a length scale of order h^{-2} around it (region D in figure 5.1) and showed that it is removable in a physically sensible fashion. In fact, adjustments to the pressure in region C are infinitesimally small, acting at $\mathcal{O}(h^{-1/4})$, as per equation (5.45), and thus the corresponding displacement of the boundary layer from the wall is also small—of order h^{-1} from equation (5.51). However, as X approaches X_0 and

$$A \to -4\mu_0^{-1} A_{0L} \left(X_0 - X\right)^{-\frac{1}{2}}$$

—reintroducing the constants that were removed in the affine transformation of equation (5.59)—the pressure gradient behaves like

$$p' \sim h^2\mu_0 - 2h^{\frac{5}{4}}\mu_0^{-1}F_{\mathrm{s}}A_{0L}\left(X_0 - X\right)^{-\frac{3}{2}} + \cdots, \tag{5.80}$$

from equations (5.45) with (5.49b). Thus the second order term reduces the leading order adverse pressure gradient and becomes comparable in magnitude when $X \sim h^{-1/2}$ or, from equation (5.41), when $x \sim h^{-2}$, the aforementioned length scale of region D.

Following table 5.1, we denote the new streamwise coordinate as $\hat{x}$, with

$$x = x_{\mathrm{s}} + \frac{3A_{0L}}{2a_0}h^{-\frac{3}{2}}\ln h + h^{-\frac{3}{2}}X_0 + h^{-2}\hat{x}; \tag{5.81}$$

and the outer Goldstein layer keeps the normal coordinate $Y \sim 1$, while the inner Goldstein layer has the new normal coordinate $\hat{z} = hy \sim 1$. In the outer layer, the stream function expansion follows from that of the oncoming flow in region C, given in equation (5.46b) with (5.48) and (5.49a),

$$\hat{\Psi} = h^{\frac{1}{2}}\psi_{0\mathrm{s}}(Y) + \hat{A}\left(\hat{x}\right)\psi'_{0\mathrm{s}}(Y) + \cdots, \tag{5.82}$$

with $\hat{A}$ representing the negative boundary layer displacement to be found. Rewriting the pressure expansion in region C, equation (5.45) with (5.49b), one finds the required pressure expansion in region D

$$\hat{p} = -h^2\left(\frac{1}{2}F_{\mathrm{s}}^2\right) + h^{\frac{1}{2}}\left(\ln h\right)\frac{3A_{0L}}{2a_0}\mu_0 + h^{\frac{1}{2}}\left(\mu_0 X_0 - \beta_{\mathrm{s}}F_{\mathrm{s}}\right) + \hat{p}_1\left(\hat{x}\right) + \cdots. \tag{5.83}$$

The pressure–displacement relation is found as before by using condition (5.4) as Y tends to infinity on the stream function (5.82) and pressure (5.83), recalling the properties of $\psi_{0\mathrm{s}}$, equation (5.20c), giving

$$\hat{p}_1 = F_{\mathrm{s}}\hat{A}\left(\hat{x}\right) + \mu_0\hat{x} \tag{5.84a}$$

as the new pressure–displacement relation. Thus the pressure gradient is

$$\hat{p}' = F_{\mathrm{s}}\hat{A}'\left(\hat{x}\right) + \mu_0. \tag{5.84b}$$

In region D we are therefore able to change the adverse pressure gradient (μ_0) by a finite amount, proportional to $\hat{A}'$. From a match with the pressures far upstream, however, the negative boundary layer displacement must behave like

$$\hat{A}\left(\hat{x}\right) \sim -4\mu_0^{-1}A_{0L}\left|\hat{x}\right|^{-\frac{1}{2}} + \cdots, \tag{5.85}$$

indicating only a very small displacement of the boundary layer from the wall.

Taking the limit as $Y \to 0$, using equation (5.20b), gives the form of the stream function in the inner Goldstein layer:

$$\hat{\psi} = h^{-1}\hat{\psi}_1\left(\hat{x}, \hat{z}\right). \tag{5.86}$$

Substitution into the condensed flow equations (5.1) reproduces the steady version of the classical boundary layer equations

$$\hat{u}_1 = \frac{\partial \hat{\psi}_1}{\partial \hat{z}}, \quad \hat{v}_1 = -\frac{\partial \hat{\psi}_1}{\partial \hat{x}} \tag{5.87a}$$

$$\frac{\partial \hat{\psi}_1}{\partial \hat{z}} \frac{\partial^2 \hat{\psi}_1}{\partial \hat{x} \partial \hat{z}} - \frac{\partial \hat{\psi}_1}{\partial \hat{x}} \frac{\partial^2 \hat{\psi}_1}{\partial \hat{z}^2} = -\hat{p}_1'(\hat{x}) + \frac{\partial^3 \hat{\psi}_1}{\partial \hat{z}^3}; \tag{5.87b}$$

with boundary conditions

$$\hat{\psi}_1 = \frac{\partial \hat{\psi}_1}{\partial \hat{z}} = 0 \quad \text{at } \hat{z} = 0, \tag{5.87c}$$

$$\hat{\psi}_1 \to \frac{1}{6}\mu_0 \left[\hat{z} + \hat{A}(\hat{x})\right]^3 \quad \text{as } \hat{z} \to \infty, \tag{5.87d}$$

and

$$\hat{\psi}_1 \to \frac{1}{6}\mu_0 \hat{z}^3 \quad \text{as } \hat{x} \to -\infty. \tag{5.87e}$$

We seek a solution to the system (5.87) as $\hat{x} \to -\infty$, making use also of the behaviour of $\hat{A}$ upstream, equation (5.85), and obtain

$$\hat{\psi}_1 \sim \frac{1}{6}\mu_0 \hat{z}^3 - 2A_{0L} |\hat{x}|^{-\frac{1}{2}} \hat{z}^2 + \cdots, \tag{5.88a}$$

which implies that the dividing streamline, which has separated from the wall, is given by

$$\hat{z} = 12\mu_0^{-1} A_{0L} |\hat{x}|^{-\frac{1}{2}}, \tag{5.88b}$$

confirming the closeness of the boundary layer to the surface in region C.

If we consider instead what happens as we move downstream: the pressure gradient decreases until it eventually tends to zero and the pressure plateaus, with $\hat{p}_1 \to \hat{p}_{1\infty}$ as $\hat{x} \to \infty$ outside of region D. The displacement function, from equation (5.84a), must thence tend to

$$-\hat{A}(\hat{x}) \to -F_s' \hat{x} - F_s^{-1} \hat{p}_{1\infty}, \tag{5.89a}$$

indicating the linearly increasing displacement of the boundary layer. In fact, the dividing streamline now behaves as

$$\hat{z} \sim -F_s' \hat{x}, \tag{5.89b}$$

representing the complete separation of the boundary layer from the surface. The numerical solution of Smith & Daniels [85] shows that the system (5.87) removes the singularity that is found in region C.

To summarise: following the point of zero skin friction, which occurs in region C, the separated shear wall layer remains close to the wall, with the displacement behaving as $|\hat{x}|^{-1/2}$, until the occurrence of the singularity triggers a need to consider a still smaller length scale where the governing equations return to being the nonlinear Prandtl boundary layer equations. The solution here then forces the pressure gradient to go to zero and the separated streamline to move away from the surface in a linear manner, resulting in complete breakaway separation, with slow recirculating flow underneath the shear layer in region E. We therefore refer to the point of zero skin friction as the local separation point and the position of the singularity in our solutions as the global separation point, and aim to determine the impact of roughness elements on both.

5.6 Traces of blood: static roughness elements

In 1989, Edward Abbey started bleeding, but his bleeding marked no trail. The blood loss was internal, coming from an artery that was haemorrhaging. After a lifetime walking the great outdoors, he ended up under a surgeon's knife, in the clinical, artificial cleanliness of a hospital. When the operation failed to stop the bleeding, Abbey pulled the needles and tubes from his body and went back to the desert and back to his writing cabin, from where he had waged war for the wild with his pen and biting eloquence.

The linearised solution of §5.4.5, where the dynamic roughness elements were taken to be single-signed over a period of oscillation, had a mean flow correction that was completely independent of the oscillation frequency and therefore equivalent to that of a static element. Depending on the position of the element, the local separation point could be moved downstream. In this section, we will deal with the full nonlinear system (5.61) for static roughness elements and determine their impact on the local and global separation points, as defined previously. The roughness shape to be considered will remain the same as that introduced in equation (5.70b),

$$f(X) = a(X - X_L)^4 (X - X_R)^4$$

(dropping the use of the overscore), but will now be acting at $\mathcal{O}(1)$, rather than order ϵ. The time derivative is set to zero in equation (5.61a) and thus the system to solve numerically is

$$(A + f)\frac{\partial}{\partial X}(A + f) + \frac{1}{2} = -\int_{-\infty}^{X} (X - s)^{-\frac{1}{2}} \frac{\partial^2 A}{\partial s^2}\, \mathrm{d}s, \tag{5.90a}$$

subject to the upstream condition

$$A \to |X|^{\frac{1}{2}} - \frac{1}{2}|X|^{-\frac{1}{2}} \ln|X| \quad \text{as } X \to -\infty. \tag{5.90b}$$

An integration by parts is carried out on the integral in equation (5.90a) to remove the singularity in the integrand at the upper limit of integration. More accurate methods, which do not introduce a third order derivative, undoubtedly exist: these include, for example, the use of a linear approximation to the derivative at the integrand's singular point, which is the technique that will be used in chapter 6. However, we believe the results presented here to be qualitatively accurate at least and numerous mesh checks were carried out, presented in appendix B.2. As per the solution to A_0 in the linearised case, the semi-infinite integral is truncated at a finite $X_{-\infty}$ and the leading order term in the upstream matching condition (5.90b) used to compute the integral between $-\infty$ and $X_{-\infty}$ analytically. Writing, $\beta = \partial A/\partial X$ and $\gamma = \partial\beta/\partial X$, the nonlinearity is dealt with by using the solution to A at the $(n-1)$th mesh point in the calculation of γ (and hence A) at the nth mesh point. Full details are given in appendix B.2.

The solutions for both a positive and negative roughness element, whose shape is given by equation (5.70b), are shown in figure 5.13 and are seen to be qualitatively similar to the effect of the mean flow correction seen in §5.4. Referring back to the pressure–displacement equation (5.49b), which simply equates the negative boundary layer displacement with the pressure perturbation of figure 5.1's region C, we see that the solutions make physical sense. For a positive roughness element, we would expect the pressure to decrease as the flow accelerates over the front face of the roughness and hence, given the above pressure–displacement relation, the displacement function should also decrease, as indeed it does (dot–dashed line in figure 5.13a). Similarly, one would expect the accelerating flow to be associated with a greater skin friction and this, largely due to the fact that the wall skin friction is given by

$$\tau_{\text{wall}} = A + f,$$

is seen to be the case over the front half of a positive roughness element (solid line). Over the rear half of the element, where the pressure gradient becomes adverse and the flow decelerates again, we expect the opposite to occur: the pressure increases, hence the displacement also increases and the skin friction decreases. Again, this is the behaviour seen, although the increase in A is constrained by the presence of the singularity downstream, corresponding to the global separation of the boundary layer from the surface. The above argument is reversed for a negative roughness element, shown in figure 5.13b.

5.6.1 Static roughness elements and the local separation point

The form of the wall skin friction, equation (5.64a), suggests that for positive roughness, a downstream shift in the local separation point can only be achieved by placing the element over the position of vanishing skin friction in the clean case. For negative roughness, meanwhile, the roughness element must be positioned well upstream; placing either a positive or negative element downstream would have no impact on

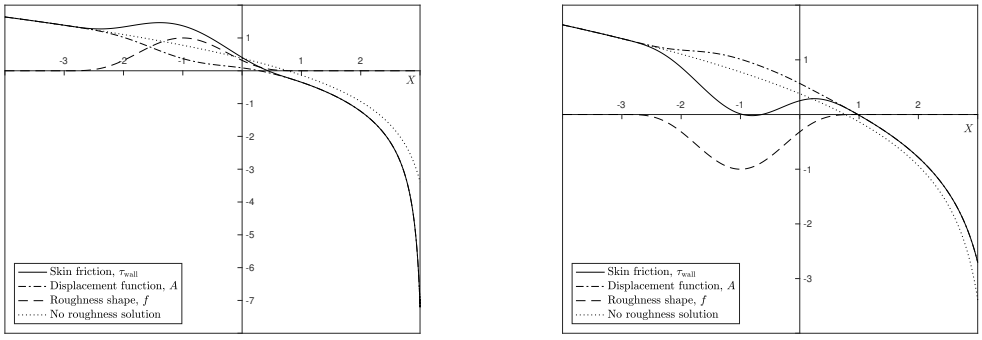

(A) Positive roughness, $a = 1$ (B) Negative roughness , $a = -1$

FIGURE 5.13: Solution to the wall skin friction (solid line) and negative boundary layer displacement function (dot–dashed line) for both (a) positive and (b) negative static roughness elements placed between $X_L = -3$ and $X_R = 1$, each having a height or depth respectively of 1 (dashed line). The clean roughness solution, as a tool for comparison, is given by the dotted line. For the chosen roughness parameters, a positive roughness element results in an advance in the local and global separation points, while the opposite is the case for a negative roughness element. The shape of both solutions makes physical sense, as described in the text.

local separation due to the parabolic nature of the governing system (5.90). Figures 5.14 and 5.15 for positive and negative roughness elements respectively indicate how the upstream (blue) and downstream (red) shifts in the point of vanishing skin friction depend on the width and position (represented by the midpoint, X_M) of the roughness.

The dependence of the local separation point on the roughness height for positive elements is shown in figure 5.16, for various roughness positions, all of which give a downstream shift in the position of vanishing skin friction. An increasing height is able to shift the local separation point farther downstream, largely due to the fact that the skin friction equals the displacement plus the roughness shape, but the greater deceleration of the flow that occurs over the lee side of the roughness element results in the advance of the singular point, as shown in figure 5.17, and thus places a limit on how far the position of zero skin friction can move downstream.

The effect of increasing the depth of a negative roughness element is interesting. We firstly note the clear distinction between an upstream and downstream movement of the local separation point seen in figure 5.15, which is explained in figure 5.18. For negative roughness elements placed sufficiently far upstream of the singular point, the skin friction goes negative due to the adverse pressure gradient over the front, rear-facing half of the roughness; but it then recovers over the rear, where there is a favourable pressure gradient, becoming positive again before reaching the local and global separation points, both of which occur farther downstream compared with the no-roughness solution (the dot–dashed line in figure 5.18, corresponding to $X_M = -1$). As the roughness element is moved downstream, however, such a separation bubble in the flow is no longer possible, since the skin friction, although it increases over the rear of the roughness, is prevented from increasing enough to become positive again due to the

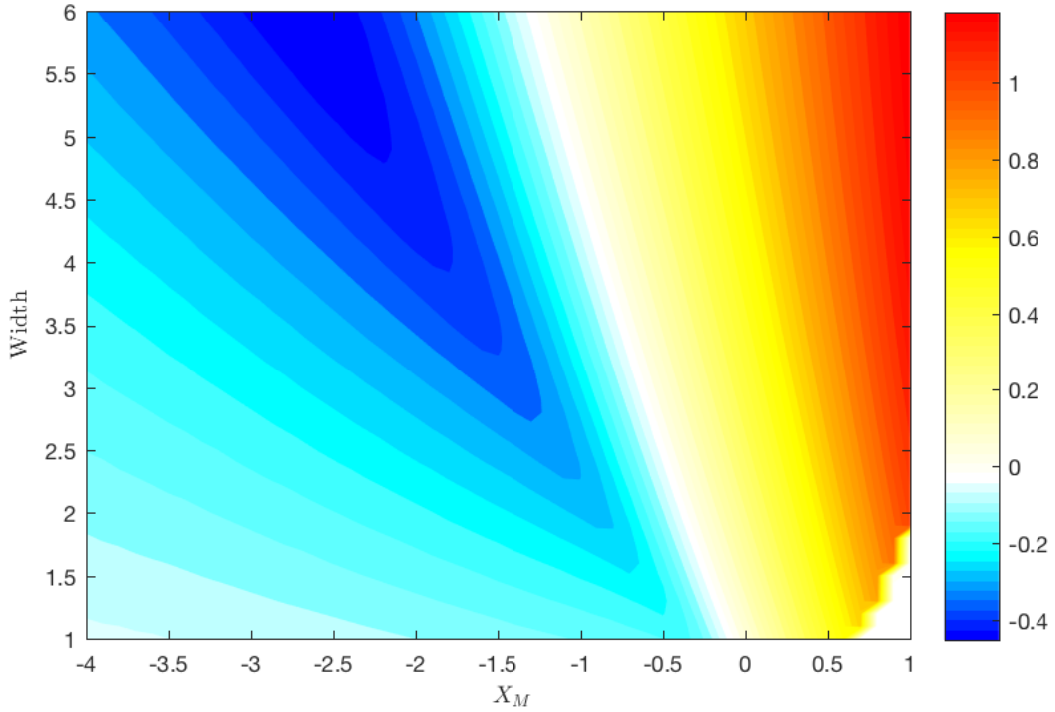

FIGURE 5.14: Influence of the width and position (represented by the midpoint X_M) of a positive roughness element on the local separation point. The upstream (negative numbers and blue tone) or downstream (positive numbers and red tone) shift is compared to the position of vanishing skin friction in the absence of roughness elements. Downstream shifts are seen to be possible provided that the roughness element covers the local separation point in the clean case, which occurs at $X \approx 0.769$. Placing the roughness upstream of this point results in an upstream shift in local separation.

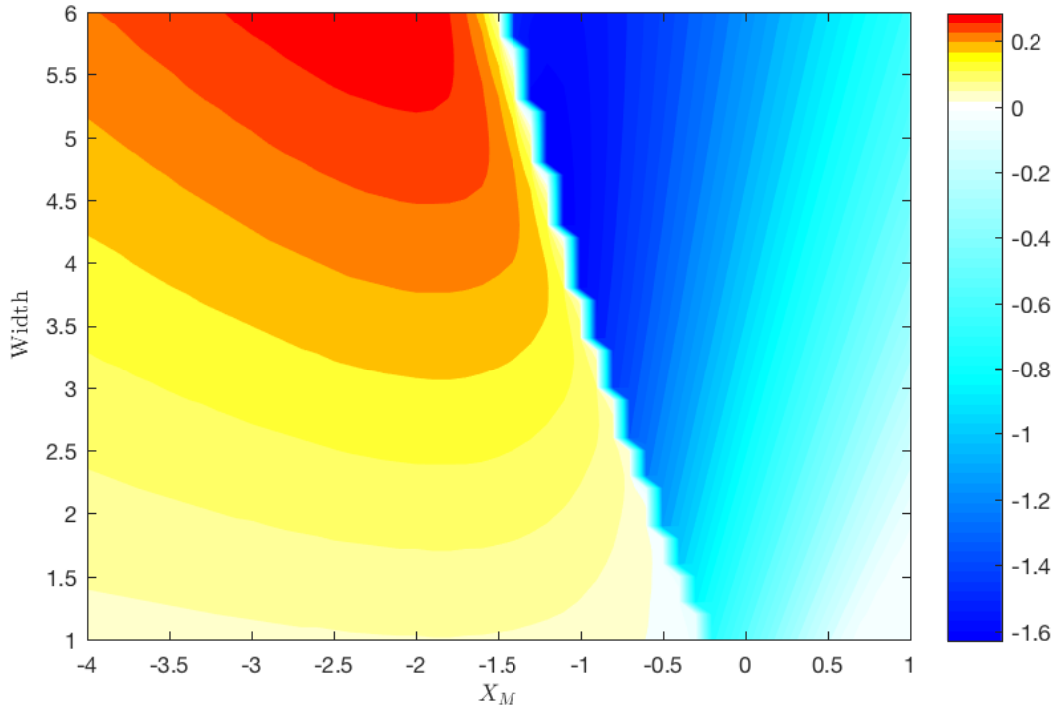

FIGURE 5.15: As per figure 5.14, but for negative roughness elements. A downstream shift is now only possible if the roughness is placed completely upstream of the local separation point in the no-roughness case and, as explained in the text, there is a clear demarcation between an upstream and downstream movement of the position of zero skin friction. Compared to positive roughness elements, any downstream shift is much smaller.

encroachment of the negative singularity, which, for $X_M = 0$ (solid line in figure 5.18), seems to be moving upstream.

Further behaviour can be seen as the depth is increased, as shown in figure 5.19 for a roughness placed between -5 and -1. For lower depths, the flow remains attached all the way across the roughness element until it separates as usual farther downstream. For depths of -3 and -3.5, the separation bubble develops, with final separation again occurring downstream. However, a small increase in depth ($a = -4$) causes the sudden and dramatic advance of the singular point. Physically speaking, at lower roughness depths, the flow separates over the front, backwards-facing half of the roughness under the action of an adverse pressure gradient, before it reattaches itself over the rear, forwards-facing half of the roughness and proceeds as normal along the original hump before eventually separating fully. A separation bubble therefore exists over the trough of the negative roughness element. As the depth increases, the point at which the skin friction goes negative occurs sooner along the negative roughness until eventually, at sufficiently large depth, the separated streamline is no longer able to reattach itself on the rear half of the roughness and full breakaway separation, indicated by the singularity, takes place. Narrower roughness elements admit larger depths before full breakaway separation occurs and this also makes physical sense: the front and rear of the roughness are closer together and thus any separated streamline has less streamwise distance available to it to detach itself sufficiently to clear the rear half of the roughness.

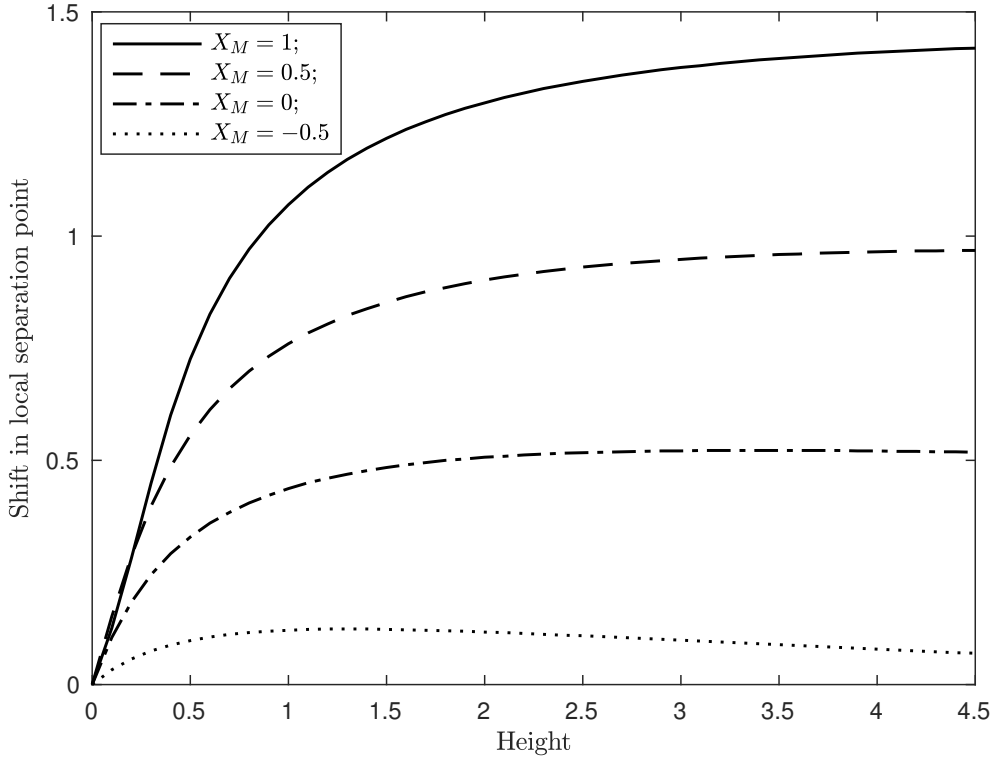

FIGURE 5.16: Change in the position of the local separation point, compared to the no-roughness case, as the height of a positive roughness element is varied, for different roughness midpoints, as given in the legend, but all with width equal to 4. The positive numbers all correspond to a downstream movement. Increasing the height tends to move the position of vanishing skin friction farther downstream, although this shift saturates at large amplitudes due to the upstream movement of the singular point.

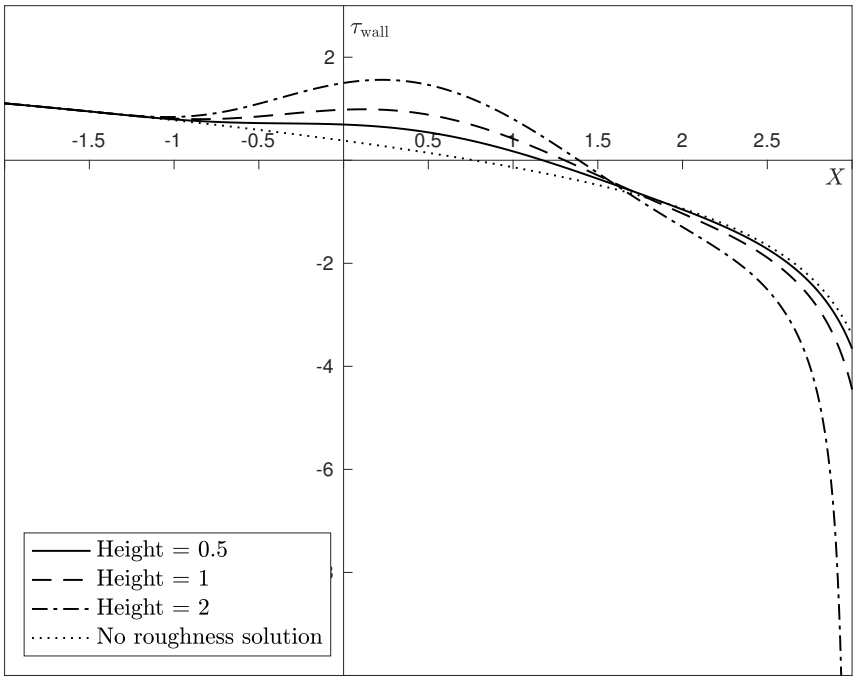

FIGURE 5.17: Influence of the height of positive roughness elements on the skin friction, τ_{wall}, with the roughness placed between $X_L = -1.5$ and $X_R = 2.5$ (dashed line of figure 5.16). Although greater roughness heights are able to move the local separation point farther downstream, the advance of the singular point limits this downstream movement.

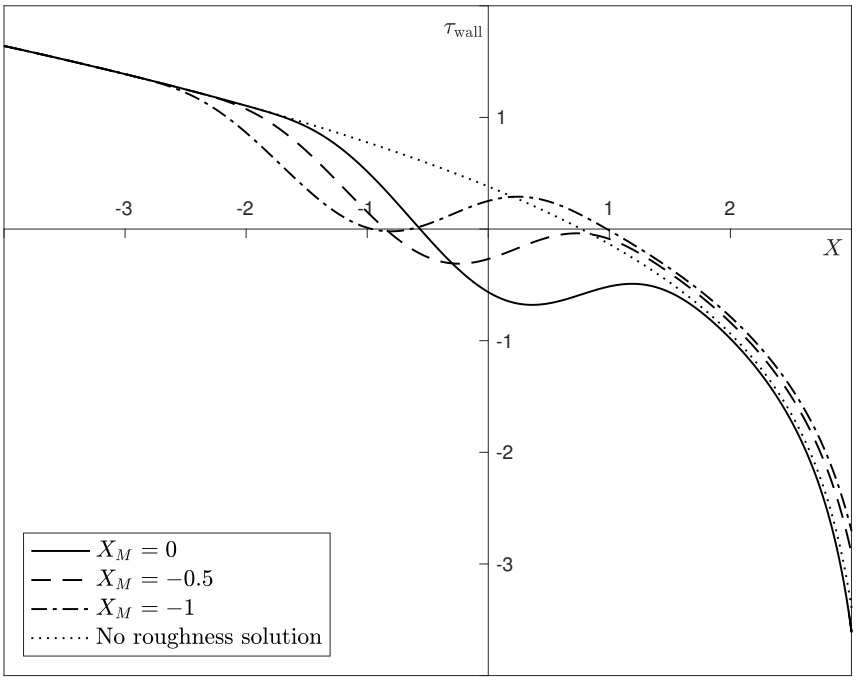

FIGURE 5.18: Formation and 'bursting' of separation bubbles, depending on the position of a negative roughness element, which has a width of 4 and depth of 1. For $X_M = -1$ (dot–dashed line), the skin friction goes negative before recovering, indicating the presence of a small bubble in the flow. As the roughness is moved downstream (dashed and solid lines), the increase in the skin friction over the rear side of the roughness is no longer sufficient to force reattachment ($\tau_{\text{wall}} > 0$), largely due to the presence of the negative singularity.

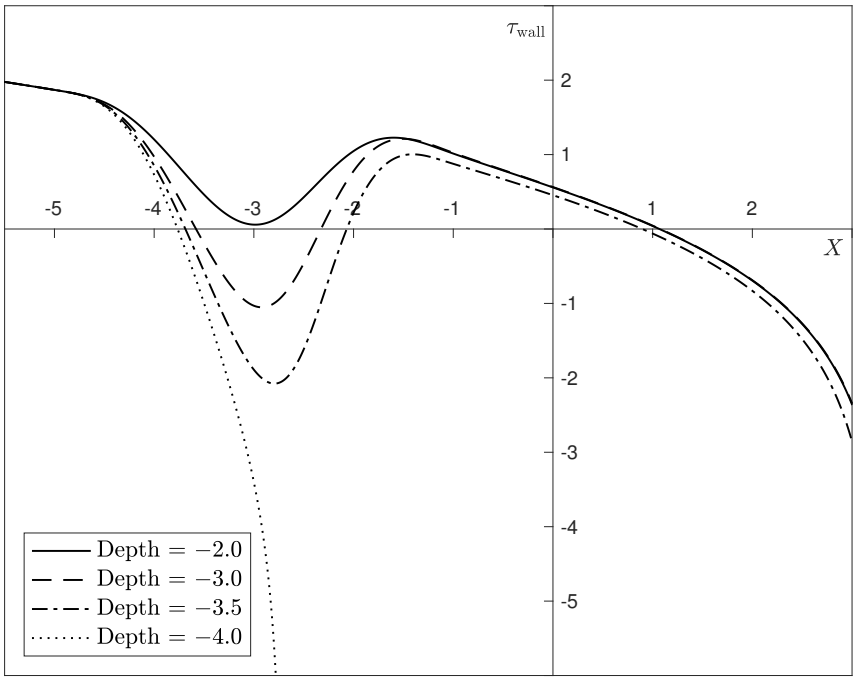

FIGURE 5.19: For a negative static roughness element placed between $X_L = -5$ and $X_R = -1$, for a sufficiently shallow depth ($a = -2$, solid line), the flow remains attached as it goes over the roughness element. As the depth is increased, a separation bubble forms as described in the text; but once the depth increases beyond some critical value, the separation bubble bursts as the singularity jumps forward dramatically ($a = -4$, dotted line).

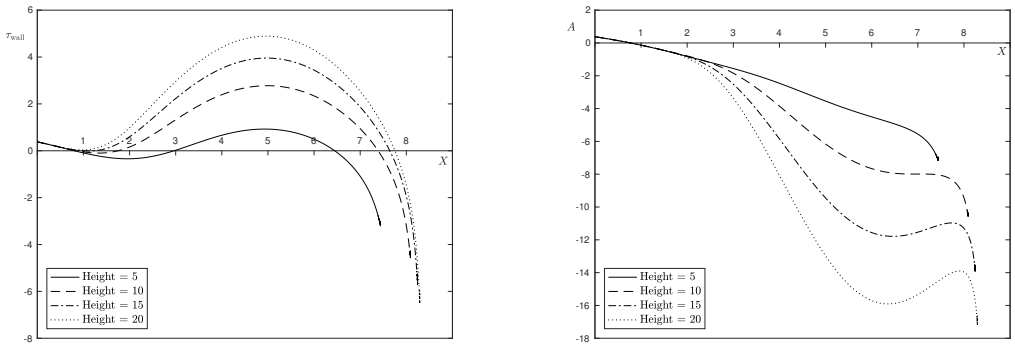

(A) Wall skin friction (B) Negative boundary layer displacement

FIGURE 5.20: Larger static roughness elements, with heights as given in the legend, centred at $X_M = 6$ with left-hand end point at $X_L = 0$, are able to considerably delay the singular position, which in the no-roughness case occurs at $X \approx 2.63$. In all cases shown, except for height equal to 20, a small separation bubble is formed soon after the start of the roughness, but attached flow is then maintained over the entire front half of the roughness, with local and global separation occurring on the rear half of the element. Both (a) the skin friction and (b) the displacement function, which equals the pressure, are shown.

5.6.2 Static roughness elements and the global separation point

As described in §5.5, the occurrence of the singularity is linked to the complete breakaway separation of the boundary layer from the surface and it is therefore of interest to move it downstream. In theory, we would expect that the introduction of a favourable pressure gradient, such as that provided by the front face of a positive roughness element, should help to keep the flow attached. We therefore position a positive roughness element with left-hand endpoint at $X_L = 0$ and midpoint at $X_M = 6$, thereby ensuring that the original, no-roughness singular point is covered by the front half of the element. The height of the roughness is taken to be larger than those considered previously, but we recall that the scaling of order $h^{-5/4}$, with $h \gg 1$, ensures that it is still small compared both to the height of the original hump (order h) and height scale of the inner Goldstein layer in the region C of the roughness (order $h^{-7/8}$). Numerically, one can define the singular position as being the mesh point X_n where $|X_{n+1} - X_n|$ is greater than some, moderately large (relative to the mesh size), finite value: in practice, the qualitative impact of the roughness on the singular point is clear from figure 5.20. Note that the mesh size has been reduced to $\Delta = 0.0001$ due to the sensitivity of the singular position to the mesh; smaller mesh steps require an unfeasibly large computational time for a solution to be obtained.

The positive static roughness elements have indeed been able to considerably delay the position of the singular point, which normally occurs, in the no-roughness case, at $X \approx 2.63$. Small separation bubbles can form near the start of the element, but the skin friction quickly becomes positive again, a state it maintains throughout the front half of the roughness element: see figure 5.20a. The displacement function A is also shown in figure 5.20b. Since it is equal to the pressure perturbation, we see that the pressure

decreases over the front face of the roughness, introducing a favourable pressure gradient into the flow, as expected. Over the rear half, the pressure then increases slightly, before falling away to a singularity. Larger heights are able to delay this singularity more than smaller heights (compare a height of $a = 5$ with one of $a = 10$, for example), but further increases in height do not have as beneficial an impact: perhaps the effect of an increased acceleration of the flow over the front half of the roughness is attenuated by the larger adverse pressure gradient that would exist over the rear.

Remaining with the pressure, we close this section by noting that the relation (5.49b) between the pressure and displacement, in which displacement equals pressure perturbation, might be viewed as being counterintuitive. In the absence of roughness elements, in which case the wall skin friction also equals the pressure perturbation, it implies that a decrease in pressure would lead to a decrease in skin friction, presumably corresponding to a deceleration of the flow—contrary to what would normally be expected. Even in the graphs given above, the singularity in A is negative, seemingly implying that a sudden large favourable pressure gradient is provoking breakaway separation. In reality, the discussion of §5.5 explains what is happening. In the region of our roughness elements, region C of figure 5.1, the overall, leading order pressure gradient ($h^2\mu_0$) is adverse and A (or, equivalently, p_1) represents a small, local adjustment to this (of order $h^{5/4}$): a decrease in A reduces the adverse pressure gradient slightly, and vice versa. The singular point, however, represents something more dramatic: the perturbation becomes of similar order of magnitude as the leading order pressure and the adverse pressure gradient then goes to zero, which is only possible if full breakaway separation has occurred upstream of the singularity and a recirculating region of fluid exists below the separated shear layer.

5.7 Marking the trail: dynamic roughness elements

The solution to the full, time-dependent, nonlinear system (5.61) is rather more complicated than the steady version considered in the above section. First and foremost, equation (5.61a) for the negative boundary layer displacement is ill-posed: a naive search for a solution by time marching will lead to a singularity at some finite time, when the displacement A becomes arbitrarily large at a (finite) streamwise position [82]. However, the fixed frequency oscillations of the dynamic roughness elements provides the suggestion that we write A—or, in the below, the skin friction—as the sum of Fourier modes, each mode forced either directly by the dynamic roughness function or by the nonlinearity present in the governing equation. The interest is then in the steady Fourier mode, as this represents a permanent, time-independent shift in the local and global separation points.

Rewriting the governing system (5.61) as an equation for the wall skin friction $\tau = A+f$ (we neglect the subscript 'wall' for ease of notation), we obtain

$$\begin{aligned}&\tau\frac{\partial\tau}{\partial X}+\int_{-\infty}^{X}(X-s)^{-\frac{1}{4}}\,\frac{\partial^2\tau}{\partial s\partial T}\,\mathrm{d}s+\int_{-\infty}^{X}(X-s)^{-\frac{1}{2}}\,\frac{\partial^2\tau}{\partial s^2}\,\mathrm{d}s\\&=\int_{-\infty}^{X}(X-s)^{-\frac{1}{2}}\,\frac{\partial^2 f}{\partial s^2}\,\mathrm{d}s-\frac{1}{2},\end{aligned}\tag{5.91a}$$

with the same upstream matching condition

$$\tau\to|X|^{\frac{1}{2}}-\frac{1}{2}\,|X|^{-\frac{1}{2}}\ln|X|\quad\text{as } X\to-\infty.\tag{5.91b}$$

With the linearised work of §5.4 seeming to suggest that non-negative roughness elements are more beneficial to delaying the separation points than elements that are allowed to be both positive and negative over a cycle of oscillation, we will focus here only on the former, thereby writing the dynamic roughness function f as in equation (5.77),

$$f(X,T)=\bar{f}(X)\left[\exp(2\mathrm{i}\omega T)+\exp(-2\mathrm{i}\omega T)+2\right].$$

As suggested, the skin friction is then expanded as

$$\tau=\sum_{k=-\infty}^{\infty}\tau_k(X)\exp(k\mathrm{i}\omega T),\tag{5.92}$$

where τ_{-k} and τ_k are complex conjugates of each other and we note that all odd Fourier modes are actually zero. Although the sum should run from negative to positive infinity, for a numerical solution it must be terminated at some finite M, with all higher modes being negligibly small. We do not set the value of M *a priori*: rather, the code described in appendix B.3 is run repeatedly with the value of M increased by a certain number each time, until the change in the solution to the steady mode τ_0 (which is the one of interest) is less than some small threshold value. For smaller roughness elements, the value of M required is moderately low (around ten), and so an increase of two each time is acceptable. However, for larger roughness elements (such as those used in §5.7.1), larger values of M were needed for convergence (in the tens) and thus the increase in M each time was greater.

The governing equation for each mode is then

$$\begin{aligned}&\sum_{k=-M}^{M}\tau_k\frac{\partial\tau_{m-k}}{\partial X}+m\mathrm{i}\omega\int_{-\infty}^{X}(X-s)^{-\frac{1}{4}}\,\frac{\partial\tau_m}{\partial s}\,\mathrm{d}s+\int_{-\infty}^{X}(X-s)^{-\frac{1}{2}}\,\frac{\partial^2\tau_m}{\partial s^2}\,\mathrm{d}s\\&=\delta_{0m}\left(-\frac{1}{2}+2\int_{-\infty}^{X}(X-s)^{-\frac{1}{2}}\,\frac{\partial^2\bar{f}}{\partial s^2}\,\mathrm{d}s\right)+\delta_{2m}\int_{-\infty}^{X}(X-s)^{-\frac{1}{2}}\,\frac{\partial^2\bar{f}}{\partial s^2}\,\mathrm{d}s,\end{aligned}\tag{5.93a}$$

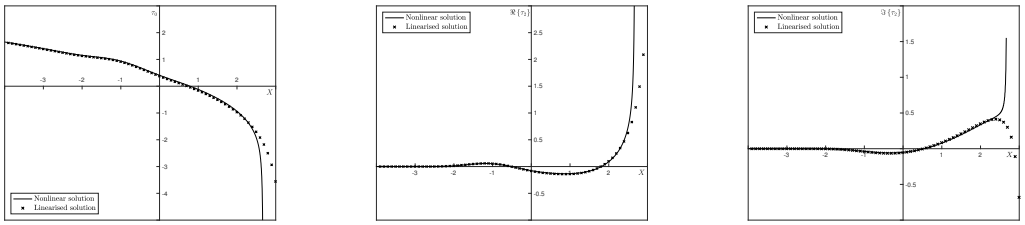

(A) Steady mode (B) Second mode, real part (C) Second mode, imaginary part

FIGURE 5.21: Comparison between the solution to the full nonlinear problem (5.91) and the linearised theory of §5.4 for a positive dynamic roughness element placed between $X_L = -3$ and $X_R = 1$, of oscillation frequency 1 and, in the nonlinear case (solid line), height 0.1 or, in the linearised case (crosses), height 1 but $\epsilon = 0.1$. The first two modes of the skin friction solution are shown.

subject to

$$\tau_m \to \begin{cases} |X|^{\frac{1}{2}} - \frac{1}{2}\,|X|^{-\frac{1}{2}} \ln|X|\,, & \text{if } m = 0; \\ 0, & \text{if } m \neq 0 \end{cases} \quad \text{as } X \to -\infty, \tag{5.93b}$$

where δ_{ij} equals 1 if $i = j$ and zero otherwise. This equation is then discretised in preparation for a numerical solution for each mode, τ_m, as described in appendix B.3. The terms containing τ_m need to be extracted from the sum and the remaining terms moved to the right-hand side, which acts as the forcing. The calculation of τ_m at the nth mesh point then needs to make use of the solutions to τ_i, $i \neq m$, at the mesh points up to the $(n-1)$th. The singularity in the integrand is once more dealt with by carrying out an integration by parts, which gives rise to a third derivative of the roughness shape $\bar{f}$. Hence we make use of a higher order polynomial for the roughness shape compared to that used in both the linearised and static cases, §§5.4 and 5.6 respectively, given by

$$\bar{f} = a\,(X - X_L)^6\,(X - X_R)^6\,, \tag{5.94}$$

where a is normalised by $(X_M - X_L)^{-6}(X_M - X_R)^{-6}$ to ensure that the maximum roughness height is one when $a = 1$. As previously, X_L, X_R and X_M refer to the left-hand edge, right-hand edge and midpoint of the roughness.

The linearised work of §5.4 allows us to check the nonlinear numerical solutions obtained. If we set the height of the dynamic roughness to be small, $a = 0.1$, this corresponds to taking a height of 1 in the linearised case, but with $\epsilon = 0.1$: a comparison between the results from the linearised theory and the nonlinear system (5.91) are shown in figure 5.21. The two agree very well with each other up until the singularity, where the linearised approach will break down in some region of order ϵ^2 about the singular point.

The shape of the steady mode of the wall skin friction and pressure perturbation in the presence of a dynamic roughness element remains similar to that of a static roughness,

and thus also agrees with expectations arising from previous physical arguments. Figure 5.22 shows the solution to both the skin friction and boundary layer displacement function, which we recall equals the pressure perturbation, for a dynamic roughness placed between -3 and 1, with maximum extended amplitude of 1 and oscillation frequency of 1. The pressure (or displacement) decreases over the front face of the roughness element, while the wall skin friction increases; and the opposite occurs over the rear half of the roughness. This agrees with the conclusions of, for example, Huebsch et al. [41], who suggested that the dynamic roughness elements used both in their numerical and experimental work were able to introduce favourable pressure perturbations in a region of predominantly increasing pressure. Compared with the solution to an equivalent static roughness element, shown in figure 5.13, the major difference here is found in the marked advance of the singular point, which occurs on the lee side of the roughness. Such an advance is affected by the frequency of oscillation, with larger frequencies provoking a more pronounced upstream jump, as shown in figure 5.23 for a dynamic roughness element placed slightly farther upstream, between -5 and -1. Notice also that, as was already highlighted in the linearised work of §5.4, remarkable agreement is found in the steady skin friction (or displacement) at all frequencies over the majority of the roughness element: the impact of increased frequency seems limited to the upstream movement of the singular point, rather than the shape of the solution over the roughness itself.

The form of the wall skin friction, as $\tau_{\text{wall}} = A + f$, again suggests placing our dynamic roughness element over the position of vanishing skin friction in the clean case in order to attempt to shift the local separation point downstream. In fact, considering the time-averaged position of the wall skin friction, denoted by an angled bracket, we find that

$$\langle \tau_{\text{wall}} \rangle = A_0 + 2\bar{f},$$

with the addition of twice the roughness shape allowing for this downstream movement. Such a conclusion is confirmed by figure 5.24, which shows the solution for dynamic roughness elements with varying midpoints, but all of width 4, frequency 1 and amplitude 1.

To investigate the impact of the width of the dynamic roughness element, we therefore fix the left-hand endpoint of the roughness at $X_L = -2$ (height and frequency both kept at 1). For small widths, we would expect an advance in the local separation point, given the considerable upstream movement of the singularity: this is indeed seen in figure 5.25 for a width of 2 (solid line). A wider roughness then introduces a more gradual favourable pressure gradient over the front half of the roughness, before pressure recovery occurs over the rear. The presence of the singularity just slightly downstream, however, ensures that for larger widths, no adverse pressure gradient exists over the second half of the roughness, with the favourable pressure gradient being only reduced before increasing again as it approaches the singular point (figure 5.25b).

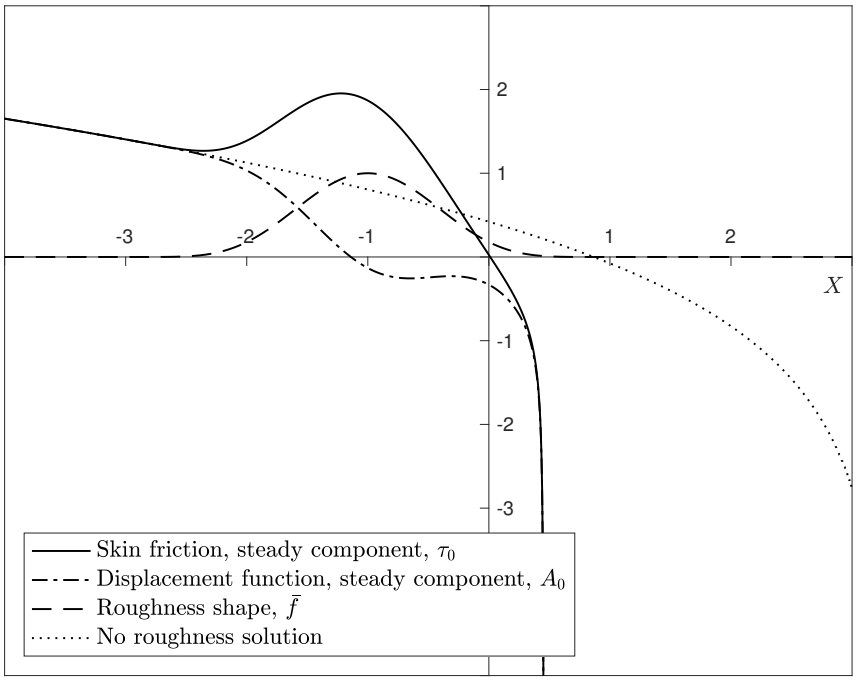

FIGURE 5.22: Solution to the steady components of the skin friction (τ_0, solid line) and boundary layer displacement function (A_0, dot–dashed line) in the presence of a dynamic roughness element (dashed line) placed between -3 and 1, of maximum amplitude 1 and oscillation frequency $\omega = 1$. Also shown is the no-roughness solution (dotted line). This is to be compared also to the solution for a static roughness element, shown in figure 5.13, although we note that the roughness shape is slightly different.

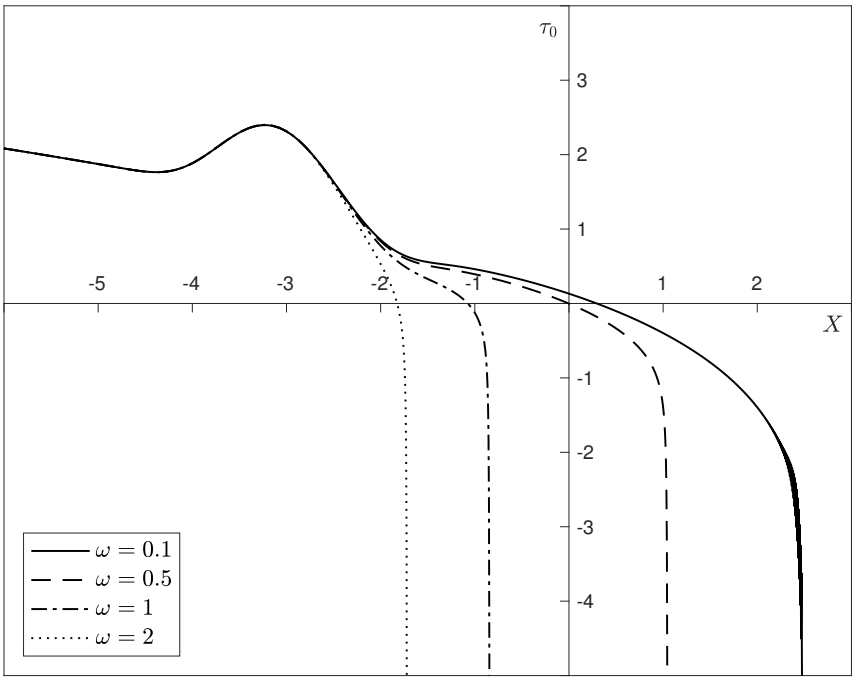

FIGURE 5.23: Impact of the oscillation frequency on the singularity in the solution to the wall skin friction (steady mode) in the presence of a dynamic roughness element. The element was placed farther upstream compared to that used in figure 5.22, between $X_L = -5$ and $X_R = -1$, to ensure that its right-hand edge was upstream of the no-roughness singularity. The maximum height was 1 and the frequencies of oscillation varied from 0.1 to 2, as indicated in the legend, with larger frequencies resulting in a greater upstream movement of the singularity.

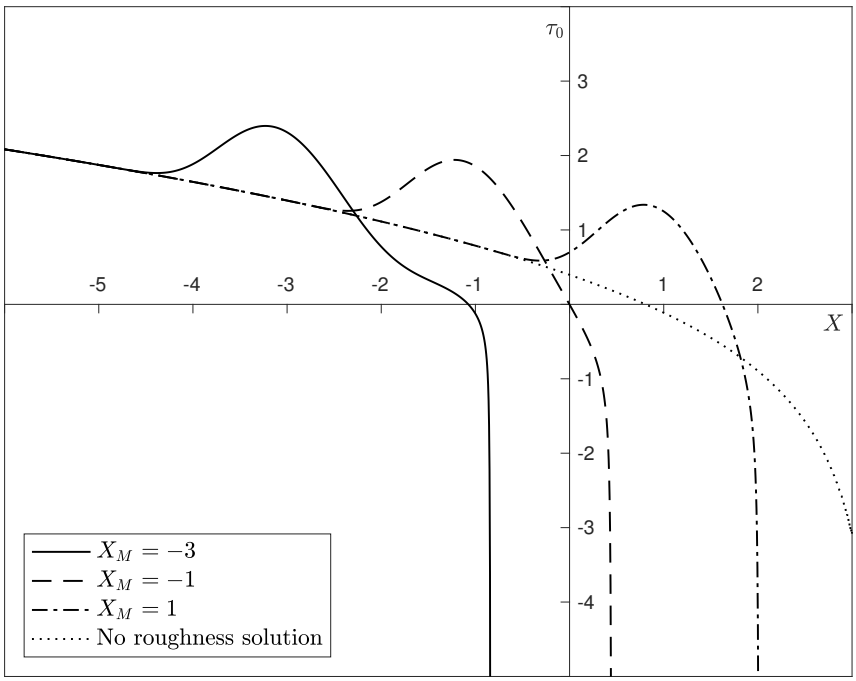

FIGURE 5.24: Impact of the position of the dynamic roughness element, represented by its midpoint X_M given in the legend, on the local separation point, which occurs when the (time-averaged) wall skin friction equals zero. The width of the roughness was 4, and the height and frequency were both 1. As expected from the text, any downstream movement of the position of vanishing skin friction occurs only when the roughness element is placed over the no-roughness zero skin friction point (dotted line): for elements placed upstream, the local separation point moves upstream. The parabolic nature of the governing equations (5.91) means that roughness elements placed downstream of the zero skin friction point will have no impact on it.

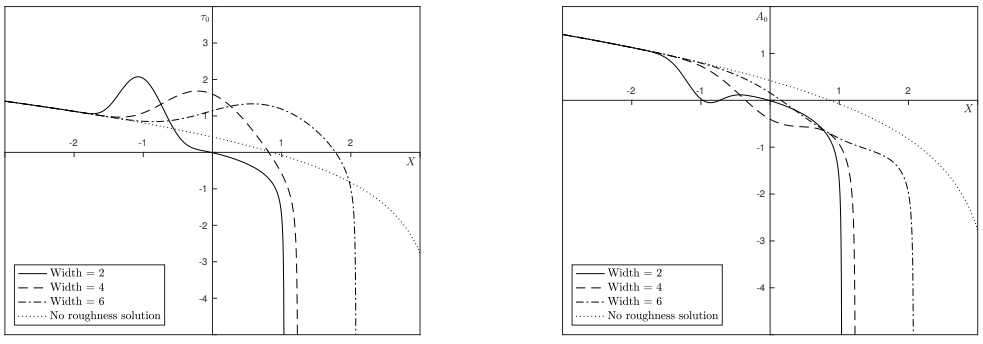

(A) Skin friction (B) Displacement function

FIGURE 5.25: Impact of the width of the dynamic roughness element on the position of the local separation point. The left-hand edge of the roughness was fixed at $X_L = -2$, while the width was changed as indicated in the legend. Both the maximum amplitude of the roughness and the frequency were equal to 1 throughout. Both (a) the skin friction; and (b) the displacement function, equal to the pressure perturbation, are shown and the no-roughness solution is given by the dotted line.

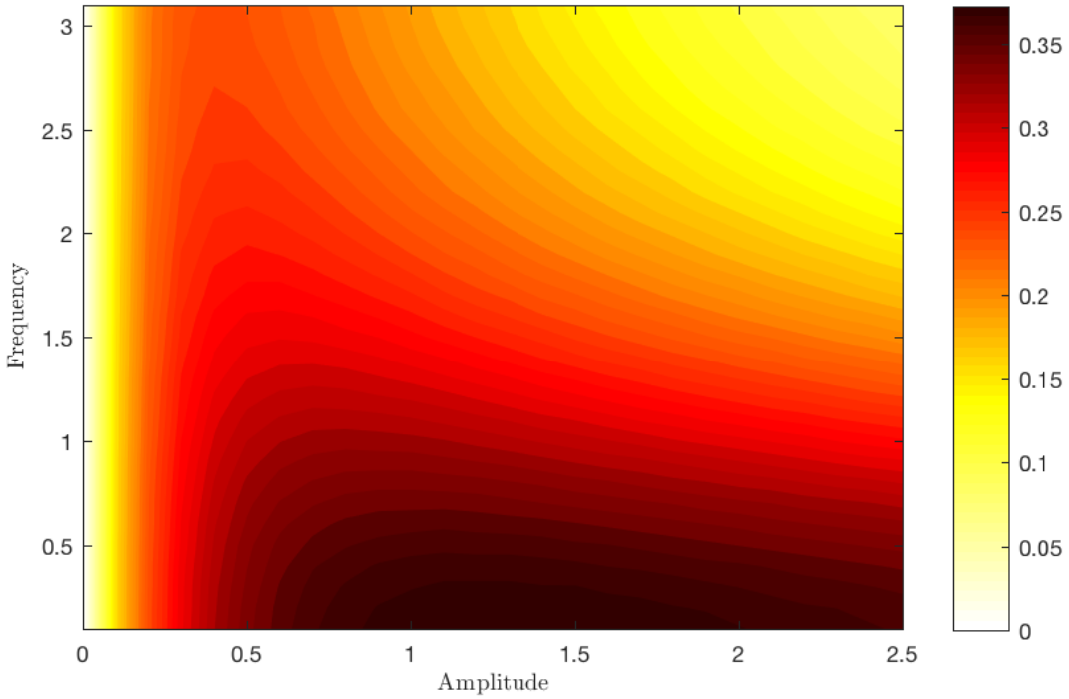

FIGURE 5.26: Impact of the height and oscillation frequency of a dynamic roughness placed between $X_L = -1$ and $X_R = 3$ on the (time-averaged) position of vanishing skin friction, compared to its position in the absence of any roughness elements. Due to the siting of the roughness element, with its rear half covering the no-roughness position of zero skin friction, the local separation point always moved downstream for the range of amplitudes and frequencies solved for, but by how much depended on both parameters. The numbers given in the legend therefore all correspond to the magnitude of the downstream movement of local separation.

We have mentioned already how an increase in the frequency of oscillation of any dynamic roughness results in a greater upstream movement of the singular point, and we have seen in all of the graphs thus far that the effect of the time-dependence on the flow has resulted in global separation occurring sooner. This seems to suggest that there is some limit to the downstream movement of the point of zero skin friction, and that higher frequencies have a detrimental impact. This is borne out by figure 5.26, which presents the impact of changing the amplitude and frequency of oscillation on the time-averaged local separation point, compared to its position where no roughness is present. The choice of position of the element, namely between -1 and 3, ensures that downstream shifts are always observed for the amplitudes and frequencies tested, but their magnitude is heavily dependent both on ω and the size of the roughness. At higher amplitudes, there seems also to be an inverse relationship between the amplitude and frequency: to maintain a given downstream shift in the local separation point, a decrease in frequency must be compensated by an increase in amplitude and a decrease in amplitude by an increase in frequency. The lower portion of the graph, at low frequencies, suggests that there is an optimal choice of roughness height and frequency (at this position) for the greatest downstream movement of the local separation point.

5.7.1 Dynamic roughness elements and the global separation point

Static roughness elements, with midpoints downstream of the original singular point and by a height of $a = 5$, were able to delay the global separation of the boundary layer quite considerably: until after the crest of the roughness. This made physical sense: the favourable pressure perturbation introduced over the front side was able to maintain attached flow, with larger roughness heights having a more beneficial impact. The question here is whether dynamic roughness elements can have the same effect.

We once more place the roughness with midpoint at $X_M = 6$ and left-hand edge at $X_L = 0$; again, the heights are larger than those looked at so far in this section, ranging from $a = 5$ to $a = 15$. Figure 5.27 shows that the downstream movement of the singular point is also possible with dynamic roughness elements, with larger heights once more being preferable, but with a saturation point seemingly being reached whereby further increases in height for a given frequency have only a very slight extra downstream shift. Static roughness elements, overall, are more effective (refer back to figure 5.20), although increasing frequencies in the dynamic case result in large movements of the singular point. Global separation still occurs on the front face of the roughness for the lower amplitudes of 5, with only a frequency of $\omega = 1$ and height equal to 15, and frequencies of $\omega = 1.5$ and heights greater than 10 able to move the singular point to the second, decreasing half of the roughness element. Increases in frequency allow one to decrease the roughness height and still obtain the same downstream shift in singular position.

Note once again that the solution at given roughness heights remains similar at all frequencies until the singularity, which occurs very suddenly, is reached. The numerical code itself needed a much larger number of Fourier modes M to be included in the expansion for the wall skin friction for there to be negligible change in the steady mode solution, due to the sudden occurrence of the singularity. Again, however, the code described in appendix B.3 was run until the difference between the use of successive values of M in the solution to τ_0 was less than 0.1 at each mesh point.

The dynamic motion of the roughness element, therefore, especially at higher frequencies, seems to counteract the favourable pressure gradient one would expect to find on the front face of a positive roughness and causes a breakdown in the solution at an earlier streamwise position than would be the case for a static roughness element. This singular point corresponds to the occurrence of the full separation of the boundary layer from the surface and so, at least for the frequencies studied here, a static element is preferable to a dynamic one. The large number of Fourier modes that must be used to find the solution at higher frequencies, and the corresponding computational time required, means that we do not know whether this conclusion also holds for higher frequencies, especially given the greatly beneficial impact greater frequencies have on the global separation point for roughness elements centred downstream of the

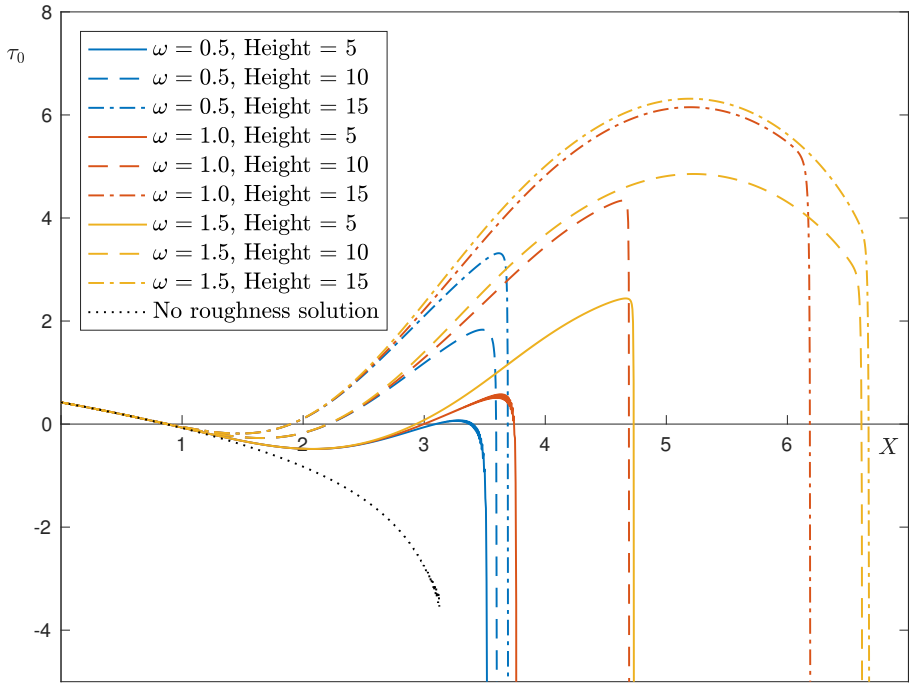

FIGURE 5.27: Downstream shift in the global separation point as a result of a dynamic roughness element centred at $X_M = 6$ and with left-hand edge at $X_L = 0$; and therefore with the singularity in the no-roughness case existing on the first half of the roughness element, where we would expect there to be a favourable pressure gradient. Various heights and frequencies of oscillation were looked at: these are listed in detail in the legend, but a blue line represents a frequency of $\omega = 0.5$, red $\omega = 1$ and yellow $\omega = 1.5$; while solid lines are a height of 5, dashed a height of 10 and dot–dashed a height of 15. The no-roughness solution is given by the black dotted line.

no-roughness singular point; a behaviour that is the opposite to that concluded for the local separation point when the roughness is placed farther upstream.

5.8 We'll see something, maybe

Motivated by the work of Smith & Daniels [85] on flow over a hump in a condensed boundary layer, we have moved on from the exposition of chapter 3, which studied flow over an array of roughness elements in which no separation was imposed, to consider a scenario in which the flow is known to separate, asking ourselves what the impact of roughness elements is on this separation. Smith & Daniels were able to first shift (§5.2) and then remove the Goldstein singularity at the point of vanishing skin friction, continuing the solution until a second singularity, corresponding to the nonlinear breakaway separation of the boundary layer from the surface (§5.5), was found farther downstream. The position of zero skin friction is viewed as the point at which the boundary layer begins to separate from the surface [27] and here we label it the 'local separation point', which must be considered in the time-averaged sense when dealing with dynamic roughness; while the later singularity is termed the 'global separation point'. With separation linked to increases in drag, as discussed in chapter 1, an ability to delay its (spatial) occurrence is of great benefit: the results of §§5.6 and 5.7 for static and dynamic roughness elements respectively indicate that such a delay is indeed possible.

Any downstream movement of the local and global separation points was, however, found to be heavily dependent on the parameters of the roughness element, which was placed in region C of figure 5.1 and had length, height and time scales appropriate to that region (§5.3). It was in region C that Smith & Daniels removed the Goldstein singularity. Summarising first the results dealing with a downstream shift in the local separation point, the equation for the wall skin friction (5.64a) suggests that any roughness element should be placed over the no-roughness zero skin friction point in order to bring about its downstream movement and this is indeed borne out in the graphs of τ_{wall} plotted in §§5.6 and 5.7. For both static and dynamic roughness elements, larger heights are preferable, as might be expected both, once more, from the form of the skin friction and physical arguments. For dynamic roughness elements, the solution to the governing system (5.61) was sought by writing the skin friction as a sum of Fourier modes, an approach that was deemed valid due to the fixed frequency forcing in the problem. The impact then of increasing the oscillation frequency tends to be adverse, resulting in smaller downstream movements in the occurrence of local separation or even upstream shifts compared with the no-roughness case—even for elements that would normally be expected to move separation downstream. This seems largely to be due to the advance of the singularity as ω is increased.

At all frequencies, however, with all other dynamic roughness parameters remaining the same, excellent agreement was found between the solutions to the steady mode

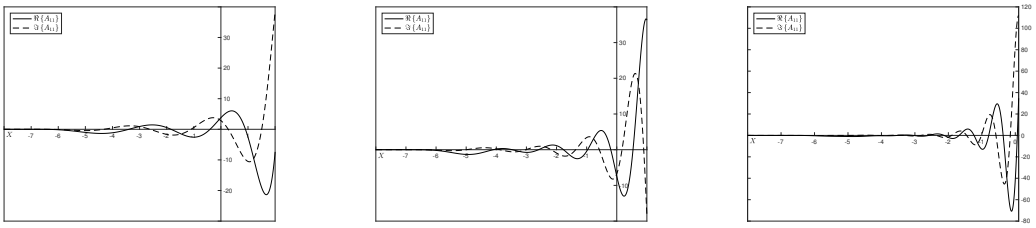

(A) $\omega = 5$ (B) $\omega = 10$ (C) $\omega = 20$

FIGURE 5.28: Real (solid) and imaginary (dashed) parts of the solution to the second order term in the linearised theory of §5.4 (A_{11}) for a roughness element placed between $X_L = -7$ and $X_R = -3$, of height 1 and with an oscillation frequency as given in the above captions. Oscillatory waves appear in the solution, starting over the roughness element and growing in amplitude as they propagate downstream. Note that the upper limit of the plot range is different in the three graphs, as the rate of growth of the waves increases with increasing frequency.

of the displacement function A_0, with the main difference being the greater advance of the singular point. The linearised approach of §5.4, in which the roughness acted at order ϵ, with ϵ small, also indicated the appearance of downstream waves in the solution to the second order term A_1, with the amplitude of the oscillations growing as they propagate downstream (figure 5.28). The properties of these waves are highly dependent on ω, with their wavelength decreasing and amplitude growth increasing with increasing roughness frequency. A high frequency analysis of equation (5.71) gives the correct scalings for the wavelength: the suggestion is to write A_{11} as

$$A_{11} = -\bar{f} + g\left(\omega^{\beta} X\right) + o(1), \tag{5.95}$$

and then the simple approach of balancing the second and third terms in equation (5.71) gives $\beta = 4/5$. A solution to g can be found by working in the complex plane (not shown here) and leads to a prediction that the wavelength λ is given by

$$\lambda = 2\pi^{\frac{7}{5}}\omega^{-\frac{4}{5}}\left[\Gamma\left(\frac{3}{4}\right)\right]^{-\frac{4}{5}}\left[\sin\left(\frac{2\pi}{5}\right)\right]^{-1}, \tag{5.96}$$

which agrees with that obtained numerically (figure 5.29). This approach, however, cannot predict the wavelengths that occur at lower frequencies and the growth in amplitude predicted by g as the waves proceed downstream does not agree with the numerical results.

In 1979, Smith [80, 81] showed that incompressible flow over an oscillating disturbance of various size within the lower deck of triple deck theory, oscillating with a frequency of order $\mathrm{Re}^{1/4}$, also, in a linearised setting, led to the existence of waves that grew exponentially as they propagated downstream. In our work, the full nonlinear system (5.61), due to the advance of the singularity, does not permit the presence of these waves; and a breakdown in the solution was also seen by Duck in the numerical solutions to his nonlinear equations governing flow over an oscillating hump, with height scale of $\mathcal{O}(\mathrm{Re}^{-5/8})$ [21]. Such an event turns out to be present in all unsteady interactive

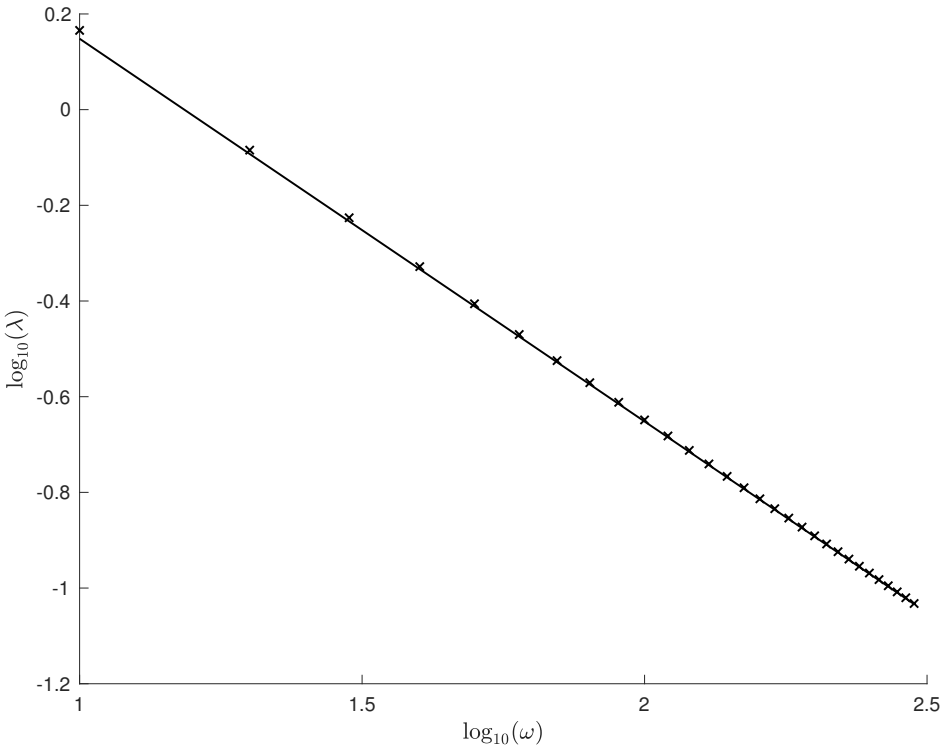

FIGURE 5.29: Graph of the wavelength (λ) of the waves in the solution to A_{11} existing downstream of a dynamic roughness oscillating at high frequency, for oscillation frequencies ω from 10 to 300. The roughness itself was placed between $X_L = -7$ and $X_R = -3$ and had height $a = 1$. The wavelength was computed from the numerical solution (crosses) by determining the points at which the real part of A_{11} crossed the X-axis and then computing the mean under the assumption, validated by solving for g in equation (5.95), that the wavelength did not vary with streamwise position. The solid line corresponds to the prediction of a high frequency analysis of equation (5.71) with (5.95), from which one finds that the wavelength is given by equation (5.96).

boundary layers after some finite time [83] and it is probable that our flow is merely another instance of this and a more in-depth analysis of the impact of the oscillation frequency on the solution would be of great interest in order to explain, firstly, the agreement in A_0 (or, equivalently, τ_0) over the vast majority of the roughness element at all values of ω until the singularity is reached; secondly, the occurrence of waves propagating downstream in the linearised theory and the link between the roughness oscillation frequency and the wavelength and amplitude of these waves, for ω small, $\mathcal{O}(1)$ and large; and thirdly, the disappearance of these waves in the solution to the nonlinear system, along with the influence of ω on the singular point. This was deemed to be beyond the scope of the present work, however.

The singularity that occurs downstream of the position of vanishing skin friction, representing global separation, can thus also be moved. This is not just as a result of the oscillatory motion of dynamic roughness elements either: interestingly, negative static elements give rise to a separation bubble—where the skin friction goes negative and then recovers to become positive again—at sufficiently large depths, but above some critical depth, linked also to the roughness width, the singularity suddenly and dramatically jumps upstream. Physically, this is presumably due to a failure of the separated streamline to reattach itself on the rear face of the negative roughness. More beneficially, to shift the global separation point downstream, any roughness element must be placed with its midpoint downstream and left-hand edge upstream of the original, no-roughness, singular position and must be rather large, although still within the height scaling $h^{-5/4}$, $h \gg 1$. Static elements are better than dynamic roughness for this purpose, with greater downstream shifts seen for these elements than for dynamic ones at the oscillation frequencies studied. For dynamic elements, both higher amplitudes and frequencies give rise to greater downstream shifts in the singular point, the latter effect being quite surprising given the upstream movement of the singularity if the roughness is placed completely upstream of its original position. It is, however, consistent with the experimental and numerical findings of earlier researchers for flow over an airfoil [33, 41]. Of course, the separated flow and any unsteadiness introduced by the dynamic roughness might result in downstream disturbances propagating upstream, which may manifest themselves as extra forcing terms in equation (5.61a), and the neglect of this possibility is a simplifying assumption made throughout the work of this chapter.

The results obtained throughout this chapter make physical sense: the front face of the roughness elements introduces a favourable pressure perturbation that enables attached flow to be maintained. This pressure perturbation acts as an $\mathcal{O}(h^{5/4})$ correction to the leading order (h^2) adverse pressure gradient and again agrees with past findings that suggested that dynamic roughness elements were able to favourably modify the adverse pressure gradient that exists over the upper surface of an airfoil [41]. We note, however, the simple form of the pressure–displacement relation (5.49b), which states that the pressure and negative boundary layer displacement function are interchangeable. This relationship is the result of the condensed boundary layer flow that has been studied

here, which has resulted in a two-layer structure being sufficient to describe the evolution of that flow. The equivalent relation that is standard in aerodynamics is considerably more complicated and introduces ellipticity into the governing equations: it is into this more challenging, and, for aeronautical applications, perhaps more relevant, scenario that we step into next.

Four days after walking out of hospital, on 14 March 1989, Edward Abbey bled to death. His friends placed his body into his old blue sleeping bag, packed it with dry ice, and drove into the Cabeza Prieta, deep in the desert of southwestern Arizona. He is buried, illegally, in a place only his close friends and family know, under a cactus or a cliff rose or a sage brush or a tree, for, in his words, if "my decomposing carcass helps nourish the roots of a juniper tree or the wings of a vulture—that is immortality enough for me. And as much as anyone deserves."

6

Roughness elements and the angle of attack

"Starting in a hollowed log of wood—some thousand miles up a river, with an infinitesimal prospect of returning! I ask myself 'Why?' and the only echo is 'Damned fool! The devil drives'."

Richard Burton

We began, in chapter 1, by emphasising the importance of separation delay in the world of aerodynamics. We have moved rather far away from these considerations, since we put on our boots and started walking. Indeed, our meanderings have hardly brought us into contact with the realm of Icarus and Daedalus: we first studied roughness elements on a plane (chapter 3) and then on a hump (chapter 5). In the former, we saw how an array of roughnesses was able to favourably modify the mean pressure gradient; in the latter, we discovered their ability to shift both the position of vanishing skin friction and global separation farther downstream. Numerical and experimental work, however, suggests that dynamic roughnesses are able to increase the angle of attack at which separation occurs on an airfoil.

In around AD150, the Greek geographer Ptolemy claimed, based on the travels of the trader Diogenes, that the origins of the Nile were to be found in a 'snowy range of mountains' that became known as the mythical Mountains of the Moon [44]. Although the source of the Blue Nile as Ethiopia's Lake Tana was found and documented by the Jesuit priest Pedro Paéz in 1618, the water basin of the White Nile, which joins the Blue at Khartoum, remained shrouded in mystery. In the 19th century, in a time before mechanisation, before instant communication, before cars and roads and aeroplanes, a group of men (and a woman)—including Richard Burton, driven by the devil—embarked, over a period of 23 years, on one of the greatest voyages of discovery ever attempted. They were looking for the source of the White Nile and, in so doing, they untangled the com-

plex water systems of the Nile and the Congo—and opened up the heart of Africa to the greed of European imperialism.

In searching for the effects shown by Huebsch et al. [41], Grager et al. [33] and others, we take ourselves to the setting of marginal separation theory, described in §6.1. As in chapter 5, the introduction of a roughness element, whether static or dynamic, in the appropriate region (§6.2) will allow us to increase (or decrease) the critical angle of attack at which an airfoil will stall (§6.3).

6.1 Marginal separation: the origins

Divided by the Iron Curtain, the theory of marginal separation was developed independently by Ruban [69] in the former USSR and Stewartson, Smith and Kaups [90] in the UK. The theory was designed to describe what happens near the position of vanishing skin friction in situations where the Goldstein singularity does not appear; such scenarios arise from a choice of $m = 2$ in equation (4.11) of chapter 4. As will be seen in §6.1.2, in these cases the skin friction still goes to zero, but does so linearly, thereby avoiding Goldstein's square root singularity. Instead, the wall skin friction recovers, returning to positive values in a linear manner once more, thereby giving rise to a discontinuity in the derivative of τ_{wall} with respect to the streamwise coordinate. Such a discontinuity implies the need for some sort of interaction structure around the point of vanishing skin friction, with this structure being described in §6.2, and it is there that our roughness elements will be placed.

The choice of $m = 2$ in equation (4.11) is possible provided that some critical parameter governing the flow is below a certain threshold value. The solutions of Stewartson, Smith and Kaups allowed for the presence of a small separation bubble within the interaction region, with non-uniqueness of the solution to the governing equations also possible: differences were embodied in the size of the separation region. Once the threshold value is surpassed, however, no solution of the governing equations can be found and the marginal separation singularity, for that is what it is, gives way to Goldstein's; we note, however, that there does not seem to be any way of proceeding continuously from a description of this 'small' separation bubble to larger bubbles or fully separated flows.

Since it was formulated by Ruban, Stewartson, Smith and Kaups, the theory of marginal separation has been applied to flow over smooth backward-facing steps [76], channel flows with suction [39] and viscous wall jets that are made to deflect [102], in which the critical parameter mentioned above was, respectively, the slope of the step, the magnitude of the suction and the deflection angle of the plate along which the jet flowed. Our interest, however, is in the use of marginal separation theory to study the flow over an airfoil flying at or near the critical angle of attack [70].

6.1.1 The airfoil: inviscid flow and the critical angle of attack

The equation that represents our airfoil is largely irrelevant, although our focus is mainly on slender airfoils (an example, the NACA 0012 airfoil, is shown in figure 1.1), and thus we represent the shape generally by

$$y = \epsilon G_{\pm}(x),$$

where ϵ is the relative thickness of the airfoil[1] and G_+, G_- denote its upper and lower surfaces respectively. For the sake of simplicity, we will consider only those airfoils that are symmetric and so $G_+ = -G_-$. All coordinates and dependent variables are in non-dimensional form, as given by equation (2.9), with the Reynolds number based on the radius (κ^{-1}) of the leading edge. The assumptions that permeate the entirety of this chapter are, firstly, that the flow remains laminar and, secondly, that the Reynolds number is large, the latter allowing us to take an asymptotic approach. The question is whether these two assumptions are compatible with each other: is the Reynolds number large enough to allow for an asymptotic approach, but low enough that the flow near the leading edge is not turbulent? The fact that the Reynolds number is based on the radius of the leading edge, which is much smaller than the chord length of the airfoil, means that it is, as it takes on values between 10^4 and 10^5 [22].

If we write

$$\epsilon^2 = (\kappa L)^{-1},$$

where L is the chord length, then the leading edge of a symmetrical four-digit NACA airfoil (designated by NACA 00xx, where 'xx' is the percentage thickness to chord) can be approximated as

$$G_{\pm} = \pm\sqrt{2x}.$$

If, furthermore, ϵ is much smaller than $\mathrm{Re}^{-1/16}$, with the airfoil leading edge being rounded, then, as we increase the angle of attack, the boundary layer will separate first at the leading, rather than trailing, edge [15, 90]. The angle of attack itself, α, is also of $\mathcal{O}(\epsilon)$ and thereby small.

We begin by considering the inviscid flow over the entirety of the airfoil, where both x and y are of order unity. Thin airfoil theory [98] gives, to a first approximation, a slip velocity on the surface of

$$U_{\mathrm{e}} = 1 + \epsilon\left[U_{1\mathrm{t}}(x) \pm U_{1\mathrm{c}}(x)\right] + \cdots, \tag{6.1}$$

where

$$U_{1\mathrm{t}}(x) = \frac{1}{\pi} \fint_0^1 \frac{G_1(s)}{x - s}\,\mathrm{d}s$$

[1] For the NACA 0012 airfoil, for example, the percentage thickness relative to chord length is 12% and so $\epsilon = 0.12$.

is related to the airfoil thickness [58]; and

$$U_{1c}(x) = \left(\frac{1-x}{x}\right)^{\frac{1}{2}} \left[\alpha + \frac{1}{\pi} \fint_0^1 \left(\frac{s}{1-s}\right)^{\frac{1}{2}} \frac{G_2(s)}{x-s}\,\mathrm{d}s\right]$$

is related to the airfoil camber and angle of attack (the chord length has been normalised to one) [54]. The functions G_1 and G_2 are

$$G_1(x) = -\frac{1}{2}\left(\frac{\mathrm{d}G_+}{\mathrm{d}x} - \frac{\mathrm{d}G_-}{\mathrm{d}x}\right) \quad \text{and} \quad G_2(x) = \frac{1}{2}\left(\frac{\mathrm{d}G_+}{\mathrm{d}x} + \frac{\mathrm{d}G_-}{\mathrm{d}x}\right).$$

In the limit $x \to 0$, as we approach the leading edge,

$$U_e \sim 1 \pm \epsilon \frac{k}{\sqrt{2x}} + \cdots, \tag{6.2a}$$

where

$$k = \sqrt{2}\left[\alpha - \frac{1}{\pi} \fint_0^1 \frac{G_2(s)}{\sqrt{s(1-s)}}\,\mathrm{d}s\right]. \tag{6.2b}$$

For our symmetric airfoil, the function G_2 is identically zero and thus the integral vanishes, making the parameter k effectively the angle of attack, $k = \alpha\sqrt{2}$. The expansion (6.2a), however, breaks down when $x \sim \epsilon^2$, as the first and second terms become of the same order of magnitude. Here, we introduce the new scaled coordinates

$$x = \epsilon^2 \tilde{x}, \quad y = \epsilon^2 \tilde{y},$$

with $\tilde{x}$ and $\tilde{y}$ both $\mathcal{O}(1)$. We neglect, though, the tilde henceforth, as the work of this chapter is focused solely within this leading edge region. The equation for the airfoil leading edge is then

$$y = \pm\sqrt{2x}$$

and the method of conformal mapping [98] produces the slip velocity

$$U_e = \left(\frac{2x}{2x+1}\right)^{\frac{1}{2}} \left(1 + \frac{k}{\sqrt{2x}}\right) = \frac{y+k}{(y^2+1)^{\frac{1}{2}}}. \tag{6.3}$$

Note that the stagnation point, where the slip velocity is zero, then occurs at $y = -k$ and so, for positive angles of attack, it will move to the pressure side of the airfoil. Furthermore, the slip velocity achieves a maximum of $(1+k^2)^{1/2}$ at $y = k^{-1}$, corresponding to $x = k^{-2}/2$, after which it decreases, eventually tending to one. This is shown in figure 6.1 for various values of the angle of attack k. From the inviscid Euler equation, one has also that

$$\frac{\mathrm{d}p_e}{\mathrm{d}x} = -U_e \frac{\mathrm{d}U_e}{\mathrm{d}x}$$

and thus the pressure gradient is initially favourable but then becomes adverse downstream of $x = k^{-2}/2$, as we discovered in chapter 1.

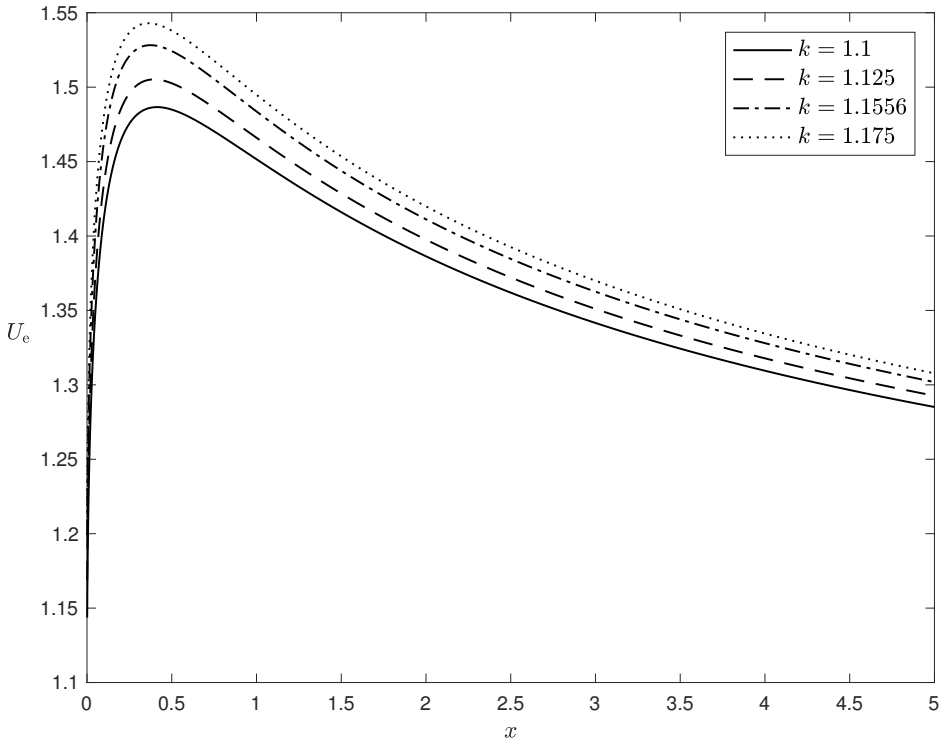

FIGURE 6.1: The slip velocity, U_e, for various angles of attack, k, as given in the legend, at the leading edge region of the airfoil. Rapid acceleration of the flow occurs as the air goes around the nose of the airfoil at the start of the leading edge, before it then decelerates and gives rise to an adverse pressure gradient. The critical angle of attack, above which one can expect leading edge separation to occur, is $k_c \simeq 1.1556$ (dot–dashed line).

Of course, the solution (6.3) for the slip velocity does not satisfy the no-slip condition and a boundary layer, with height scale of order $\mathrm{Re}^{-1/2}$, through which the tangential velocity component is able to become zero at the surface, is thus present. Solving within this boundary layer, the skin friction, dependent also on the angle of attack parameter k, can be obtained: a critical value of k, $k_\mathrm{c} \simeq 1.1556$ exists, below which the skin friction remains positive for all $x > 0$, reaching a positive minimum and then increasing again. Its increase is due to the diffusion of vorticity at the wall: for adverse pressure gradients, the shear stress would increase as we move farther from the wall, and frictional forces would then accelerate the neighbouring layers closer to the surface. If the adverse pressure gradient is weak enough, then the skin friction would increase once more [93]. At $k = k_\mathrm{c}$, the skin friction becomes zero at some point $x = x_0$ and for supercritical values of k, the position of vanishing skin friction moves upstream, and Goldstein's singularity appears [100].

However, for values of k sufficiently close to k_c, where exactly what is meant by 'sufficiently close' will be defined in §6.2, we obtain the marginal separation singularity: this is much weaker than Goldstein's singularity and we will see in §6.1.2 that Prandtl's boundary layer equations are still able to describe the flow both upstream and downstream of the singular point, with the continuous development of the solution from one to the other requiring an interaction region (§6.2).

6.1.2 The singularity near the critical angle of attack

In chapter 4, we derived the existence of the Goldstein singularity in Prandtl's boundary layer equations. Through this, we obtained also the condition (4.11) that set the exponents in the expansion (4.5) of the stream function in the inner Goldstein layer: this gave rise either to the Goldstein singularity (if $m = 1$), studied in §4.2 and chapter 5, or, as will be seen in this section, the marginal separation singularity. For as the parameter k representing the angle of attack is decreased from supercritical values ($k > k_\mathrm{c}$), the coefficient a_0 in the solution (4.8) to the second order term of the stream function expansion (4.5) also decreases until, at $k = k_\mathrm{c}$, it becomes equal to zero. In the condition (4.11), therefore, the choice $m = 1$ vanishes and we move on to the next option, $m = 2$.

The regions of the flow in which we must find a solution are shown in figure 6.2, while table 6.1 lists the notation that will be used for the dependent and independent variables in each region. Essentially, the structure is symmetric around the point of vanishing skin friction: there is the viscous near-wall region, equivalent to the inner Goldstein layer, both upstream ($\mathrm{A_u}$) and downstream ($\mathrm{A_d}$) of the position of zero skin friction; and an inviscid, rotational region, equivalent to the outer Goldstein layer, that consists of the rest of the classical Prandtl boundary layer ($\mathrm{B_u}$ and $\mathrm{B_d}$ for the upstream and downstream flow respectively). Above, as usual, is the external inviscid flow, described in §6.1.1.

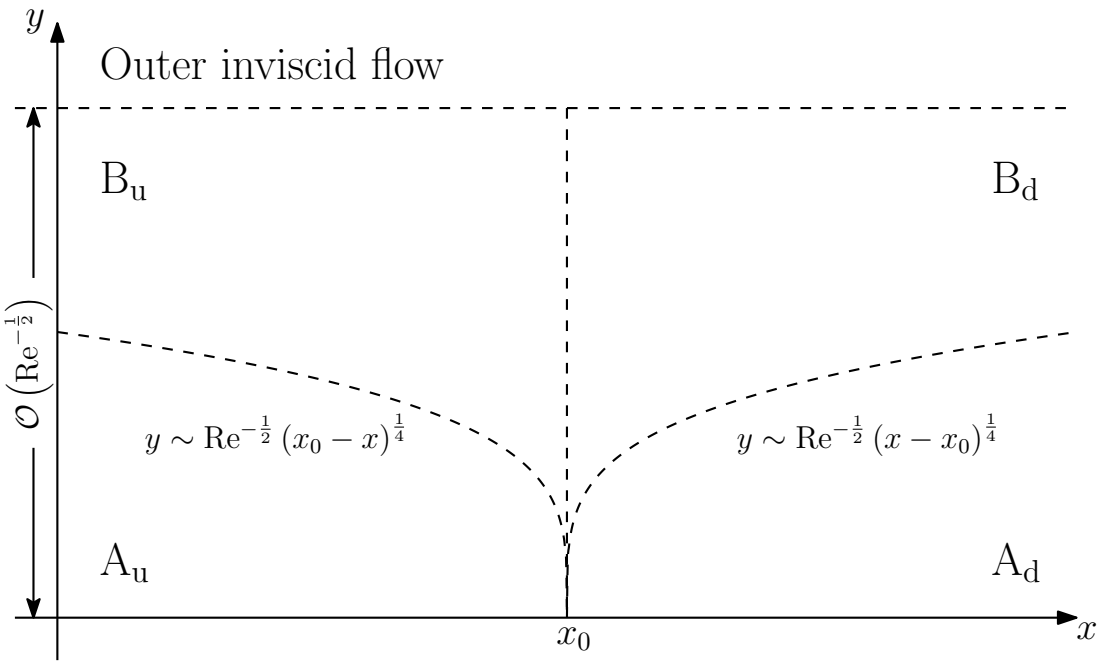

FIGURE 6.2: Schematic of the flow structure upstream and downstream of the position of vanishing skin friction, x_0. The solution in the outer inviscid layer is found in §6.1.1, while in §6.1.2, we find the stream function expansion in the regions $\mathrm{A_u}$, $\mathrm{B_u}$, $\mathrm{A_d}$ and $\mathrm{B_d}$, showing that no catastrophic breakdown of the solution occurs when the angle of attack is close to its critical value. The interaction structure required to smooth out a discontinuity in the streamwise derivative of the skin friction is shown in figure 6.3 and studied in §6.2.

Region	Streamwise	Normal	Stream function	Pressure
Outer inviscid flow	x	y	ψ	p_e
$\mathrm{A_u}$	ξ	η	$\tilde{\psi}^\mathrm{i}$	$\tilde{p}$
$\mathrm{B_u}$	ξ	Y	$\tilde{\psi}^\mathrm{o}$	$\tilde{p}$
$\mathrm{A_d}$	$\hat{\xi}$	$\hat{\eta}$	$\hat{\psi}^\mathrm{i}$	$\hat{p}$
$\mathrm{B_d}$	$\hat{\xi}$	Y	$\hat{\psi}^\mathrm{o}$	$\hat{p}$

TABLE 6.1: List of coordinate systems, stream functions and pressures used in the various regions depicted in figure 6.2. In general, a tilde denotes an upstream variable, while a hat denotes a downstream variable. To these must be added in §6.2 the coordinates and variables required in the interaction region: see table 6.2, later.

Upstream flow

Since we assume that we are 'close' to the critical angle of attack, k_c, the choice $m = 2$ in equation (4.11) gives rise to the stream function expansion in the lower, viscous layer, A_u, of

$$\tilde{\psi}_0^{\mathrm{i}} = \frac{1}{6}\mu_0\xi^3\eta^3 + \xi^6 f_1(\eta) + \xi^7 g_1(\eta) + \xi^9 f_2(\eta) + \cdots, \tag{6.4}$$

where $\xi = (x_0 - x)^{1/4}$ is the streamwise coordinate and $\eta = \mathrm{Re}^{1/2}(x_0 - x)^{-1/4}y$ is the normal coordinate, with both ξ and η of order 1. The above expansion (6.4) is obtained from the general form (4.5) introduced in chapter 4; with the addition of the function g_1 at $\mathcal{O}(\xi^7)$ due to the linear term $\mu_1 x$ in the Taylor expansion (4.2) of the pressure gradient (the leading order term, μ_0, is positive to ensure that there is an adverse pressure gradient reducing the wall skin friction to zero). Compare it also with the expansion (4.13) that was the solution in the case of the Goldstein singularity: the leading order term still acts at $\mathcal{O}(\xi^3)$; but the second and fourth terms act at higher order here—ξ^6 and ξ^9 instead of ξ^4 and ξ^5, indicating why the function g_1 must be considered now, while being absent in our previous work.

Substitution of the above expansion, as well as that of the pressure, equation (4.2), into the steady version of Prandtl's boundary layer equations (4.1) gives

$$\begin{aligned}
&\left(\frac{1}{2}\mu_0\xi^2\eta^2 + \xi^5 f_1' + \xi^6 g_1' + \xi^8 f_2'\right)\left(-\frac{1}{4}\mu_0\xi^{-2}\eta^2 - \frac{5}{4}\xi f_1' - \frac{3}{2}\xi^2 g_1' - 2\xi^4 f_2'\right)\\
&+\left(\frac{1}{8}\mu_0\xi^{-1}\eta^3 + \frac{3}{2}\xi^2 f_1 + \frac{7}{4}\xi^3 g_1 + \frac{9}{4}\xi^5 f_2\right)\left(\mu_0\xi\eta + \xi^4 f_1'' + \xi^5 g_1'' + \xi^7 f_2''\right)\\
&= -\mu_0 + \mu_1\xi^4 + \cdots + \mu_0 + \xi^3 f_1''' + \xi^4 g_1''' + \xi^6 f_2'''.
\end{aligned}$$

The $\mathcal{O}(1)$ equation is satisfied automatically, while the terms at order ξ^3 produce the solution

$$f_1(\eta) = a_0\eta^2$$

in exactly the same manner as in §4.1, since the solution to f_1 was independent of the exponent in the stream function expansion. At $\mathcal{O}(\xi^4)$, the governing equation for g_1 is

$$g_1''' + \frac{1}{8}\mu_0\eta^3 g_1'' - \mu_0\eta^2 g_1' + \frac{7}{4}\mu_0\eta g_1 = -\mu_1,$$

for which we can seek a solution by substituting in the general form

$$g_1(\eta) = \sum_{i=0}^{\infty} c_i\eta^i,$$

to find the only nonzero coefficients c_3 and c_7:

$$g_1(\eta) = -\frac{1}{6}\mu_1\eta^3 + \frac{2}{7!}\mu_0\mu_1\eta^7.$$

Finally, at order ξ^6, we obtain the equation for f_2, found also from equation (4.10),

$$f_2''' - \frac{1}{8}\mu_0\eta^3 f_2'' + \frac{5}{4}\mu_0\eta^2 f_2' - \frac{9}{4}\mu_0\eta f_2 = -2a_0^2\eta^2.$$

The homogeneous problem has the general solution $b_0\eta^2$, while the particular solution is again found by substituting in the polynomial

$$f_2(\eta) = \sum_{i=3}^{\infty} c_i\eta^i,$$

where the summation is started at $i = 3$ due to the no-slip boundary condition. The only nonzero coefficients turn out to be c_5 and c_9 and thus we have the solution

$$f_2(\eta) = b_0\eta^2 - \frac{4}{5!}a_0^2\eta^5 + \frac{4}{8!}\mu_0 a_0^2\eta^9.$$

Hence the stream function in the viscous near-wall layer, to leading order in k, is

$$\begin{aligned}\tilde{\psi}_0^{\mathrm{i}}(\xi,\eta) = &\frac{1}{6}\mu_0\xi^3\eta^3 + a_0\xi^6\eta^2 + \xi^7\left(-\frac{1}{6}\mu_1\eta^3 + \frac{2}{7!}\mu_0\mu_1\eta^7\right)\\ &+ \xi^9\left(b_0\eta^2 - \frac{4}{5!}a_0^2\eta^5 + \frac{4}{8!}\mu_0 a_0^2\eta^9\right) + \cdots. \end{aligned} \tag{6.5}$$

The main boundary layer solution ($\mathrm{B_u}$) must match with the viscous near-wall solution as $Y \to 0$. In a similar manner as was described in §5.2.1, equation (6.5) can be rewritten in terms of the normal coordinate Y as

$$\tilde{\psi}_0^{\mathrm{i}} = \left(\frac{1}{6}\mu_0 Y^3 + \frac{2}{7!}\mu_0\mu_1 Y^7 + \frac{4}{8!}\mu_0 a_0^2 Y^9\right) + \xi^4\left(a_0 Y^2 - \frac{1}{6}\mu_1 Y^3 - \frac{4}{5!}a_0^2 Y^5\right) + \cdots,$$

thereby suggesting a stream function expansion in the bulk of the boundary layer of

$$\tilde{\psi}_0^{\mathrm{o}}(\xi, Y) = \tilde{\psi}_{00}^{\mathrm{o}}(Y) + \xi^4\tilde{\psi}_{01}^{\mathrm{o}}(Y) + \cdots, \tag{6.6a}$$

with

$$\tilde{\psi}_{00}^{\mathrm{o}}(Y) \to \frac{1}{6}\mu_0 Y^3 + \frac{2}{7!}\mu_0\mu_1 Y^7 + \frac{4}{8!}\mu_0 a_0^2 Y^9, \tag{6.6b}$$

$$\tilde{\psi}_{01}^{\mathrm{o}}(Y) \to a_0 Y^2 - \frac{1}{6}\mu_1 Y^3 - \frac{4}{5!}a_0^2 Y^5 \tag{6.6c}$$

as $Y \to 0$.

This is substituted into the boundary layer equation (4.1) to obtain

$$-\tilde{\psi}_{01}^{\mathrm{o}\prime}\left(\tilde{\psi}_{00}^{\mathrm{o}\prime} + \xi^4\tilde{\psi}_{01}^{\mathrm{o}\prime}\right) + \tilde{\psi}_{01}^{\mathrm{o}}\left(\tilde{\psi}_{00}^{\mathrm{o}\prime\prime} + \xi^4\tilde{\psi}_{01}^{\mathrm{o}\prime\prime}\right) = -\mu_0 - \mu_1\xi^4 + \tilde{\psi}_{00}^{\mathrm{o}\prime\prime\prime} + \xi^4\tilde{\psi}_{01}^{\mathrm{o}\prime\prime\prime},$$

which gives the equation at $\mathcal{O}(1)$ of

$$\tilde{\psi}_{01}^{\mathrm{o}\prime} - \left(\frac{\tilde{\psi}_{00}^{\mathrm{o}\prime\prime}}{\tilde{\psi}_{00}^{\mathrm{o}\prime}}\right)\tilde{\psi}_{01}^{\mathrm{o}} = \frac{\mu_0}{\tilde{\psi}_{00}^{\mathrm{o}\prime}} - \frac{\tilde{\psi}_{00}^{\mathrm{o}\prime\prime\prime}}{\tilde{\psi}_{00}^{\mathrm{o}\prime}},$$

with solution

$$\tilde{\psi}_{01}^{\mathrm{o}}(Y) = \tilde{\psi}_{00}^{\mathrm{o}'}(Y)\left[2\frac{a_0}{\mu_0} + \int_0^Y \frac{\mu_0 - \tilde{\psi}_{00}^{\mathrm{o}'''}(s)}{\left[\tilde{\psi}_{00}^{\mathrm{o}'}(s)\right]^2}\,\mathrm{d}s\right],$$

where the matching conditions (6.6b) and (6.6c) have been used.

Thus the solution in region $\mathrm{B_u}$ just upstream of the position of vanishing skin friction is

$$\tilde{\psi}_0^{\mathrm{o}}(\xi, Y) = \tilde{\psi}_{00}^{\mathrm{o}}(Y) - (x - x_0)\,\tilde{\psi}_{00}^{\mathrm{o}'}(Y)\left[2\frac{a_0}{\mu_0} + \int_0^Y \frac{\mu_0 - \tilde{\psi}_{00}^{\mathrm{o}'''}(s)}{\left[\tilde{\psi}_{00}^{\mathrm{o}'}(s)\right]^2}\,\mathrm{d}s\right] + \mathcal{O}\left(\xi^7\right). \quad (6.7)$$

Downstream flow

The procedure for solving for the flow downstream of the point of zero skin friction, regions $\mathrm{A_d}$ and $\mathrm{B_d}$, is exactly the same as that described for the upstream flow, if we define $\hat{\xi}$ as $(x - x_0)^{1/4}$, and gives the valid solution in the main part of the boundary layer ($\mathrm{B_d}$)

$$\hat{\psi}_0^{\mathrm{o}}(\xi, Y) = \hat{\psi}_{00}^{\mathrm{o}}(Y) + (x - x_0)\,\hat{\psi}_{00}^{\mathrm{o}'}(Y)\left[2\frac{a_0}{\mu_0} - \int_0^Y \frac{\mu_0 - \hat{\psi}_{00}^{\mathrm{o}'''}(s)}{\left[\hat{\psi}_{00}^{\mathrm{o}'}(s)\right]^2}\,\mathrm{d}s\right] + \mathcal{O}\left(\xi^7\right),$$

with $\tilde{\psi}_{00}^{\mathrm{o}}(Y) = \hat{\psi}_{00}^{\mathrm{o}}(Y) = \psi_{00}^{\mathrm{o}}(Y)$. The solutions upstream and downstream of the position of vanishing skin friction in Prandtl's classical boundary layer can therefore be joined together into a single solution

$$\psi_0^{\mathrm{o}}(\xi, Y) = \psi_{00}^{\mathrm{o}}(Y) + \psi_{00}^{\mathrm{o}'}(Y)\left[2\frac{a_0}{\mu_0}\,|x - x_0| + (x - x_0)\int_0^Y \frac{\psi_{00}^{\mathrm{o}'''}(s) - \mu_0}{\left[\psi_{00}^{\mathrm{o}'}(s)\right]^2}\,\mathrm{d}s\right] + \mathcal{O}\left(\xi^7\right). \quad (6.8)$$

Within the setting of boundary layer theory, then, we have shown that it is possible to extend the stream function solution beyond the point of zero skin friction. However, from the definition of τ_{wall} and the matching condition (6.6b), the behaviour near the point x_0 is

$$\tau_{\mathrm{wall}} \sim 2a_0\,|x - x_0| + \cdots,$$

which is discontinuous at $x = x_0$ and calls for an interaction region, into which we shall place our roughness elements, in order to smooth it out.

On 10 November, 1871, at Ujiji, on the shores of Lake Tanganyika, Henry Morton Stanley (1841–1904), a journalist for the New York Herald, uttered the immortal phrase

"Dr Livingstone, I presume?".[2] *Dr David Livingstone (1813–1873)—both explorer and missionary priest; therefore driven, one presumes, more by God than the devil—had set off from Zanzibar in January 1866 and become lost to the outside world until he was found by Stanley with his reporter's notebook. Livingstone's mission, like that of those who had gone before, had been to find the source of the Nile and settle the bitter feud that had erupted between Richard Burton (1821–1890) and John Hanning Speke (1827–1864), once partners in adventure, now driven apart by jealousy and competing theories.*

Burton and Speke had drawn different conclusions from their 1856–59 expedition, in which they had become the first Westerners to set eyes on the great inland lake, Tanganyika, that was known to exist from the tales of Arab traders and slavers. The former claimed that it was the source of the Nile, with the River Ruzizi—which neither had actually seen—flowing out to the north, into Lake Albert—found in March 1864 by Samuel Baker and his eventual wife, Florence von Sass, bought at a slave market in Bulgaria—and then on to the White Nile. On the same expedition, however, Speke had discovered Lake Victoria and championed its cause; a later voyage, in 1860–64, brought him to its outlet at the Ripon Falls, which only strengthened his convictions. Shortly after his return, in 1864, almost a decade before Stanley and Livingstone found that the Ruzizi flowed into, not out of, Lake Tanganyika, and well before Stanley conclusively proved that Tanganyika was completely disconnected from the Nile, Speke died—a life of great adventure, enormous suffering, but so little recognition: cruelly ended by the highly unfortunate discharge of his own rifle as he was climbing over a stone wall in a field in Wiltshire.

David Livingstone and Henry Morton Stanley, after visiting the Ruzizi, separated at Tabora: Stanley went back to the coast and fame, and then more fame; Livingston was driven on by his God, his theories and his devil, which brought him to the River Lualaba and death.

6.2 Roughness elements and the interaction region

The work of §6.1.2 above was valid for values of the angle of attack k sufficiently close to the critical value k_c at which the skin friction goes to zero at some point x_0: no mention was made, however, of exactly what was meant by 'sufficiently close'. Here, we determine both the streamwise extent of the interaction region between the viscous, near-wall flow and the pressure in the external inviscid flow, required to remove the discontinuity in the wall skin friction at $x = x_0$; and the order of magnitude of the allowed deviation from the critical angle of attack. In §6.2.2, the structure of this interaction region, in which we will place our roughness elements, will be described

[2] It is quite likely, mind you, that he never actually asked this question, voicing instead something rather more prosaic, but a little poetic licence is probably not too much to begrudge the man who put the finishing touches to the map of the great African waterways.

and the governing equation for the boundary layer displacement, A, along with the pressure–displacement relation, will be found.

6.2.1 Orders of magnitude: the angle of attack and streamwise length scale

Suppose that the angle of attack of our airfoil is

$$k = k_{\mathrm{c}} + (\Delta k)k_1, \tag{6.9}$$

where k_1 is of $\mathcal{O}(1)$ and $\Delta k \ll 1$ is the order of magnitude of the increase (or decrease) in the angle of attack with respect to its critical value. We begin by again considering the external inviscid flow, which, in a similar way to triple deck theory, must play a part in the interaction structure. The slip velocity, found in equation (6.3), is a function of both x and k and can thus be expanded using a Taylor series about the critical angle of attack,

$$U_{\mathrm{e}}(x,k) = U_{\mathrm{e}}\left(x,k_{\mathrm{c}}\right) + (\Delta k)\left.\frac{\partial U_{\mathrm{e}}}{\partial k}\right|_{k=k_{\mathrm{c}}} + \cdots .$$

The inviscid Euler equation (2.5) then relates the slip velocity to the pressure as

$$\frac{\partial p}{\partial x} = \left[-U_{\mathrm{e}}\frac{\partial U_{\mathrm{e}}}{\partial x} - (\Delta k)\left(U_{\mathrm{e}}\frac{\partial^2 U_{\mathrm{e}}}{\partial x \partial k} + \frac{\partial U_{\mathrm{e}}}{\partial k}\frac{\partial U_{\mathrm{e}}}{\partial x}\right) + \cdots\right]_{k=k_{\mathrm{c}}},$$

and this dictates the form of the pressure expansion

$$p = \tilde{p}_0 + (\Delta k)\tilde{p}_1 + \cdots . \tag{6.10}$$

We next want to continue the expansion of the stream function in the viscous near-wall region of the boundary layer, $\mathrm{A_u}$, i.e.

$$\tilde{\psi}^{\mathrm{i}} = \tilde{\psi}_0^{\mathrm{i}} + (\Delta k)\,\tilde{\psi}_1^{\mathrm{i}} + \mathcal{O}\left[(\Delta k)^2\right], \tag{6.11}$$

with the solution to the leading order term $\tilde{\psi}_0^{\mathrm{i}}$ given in equation (6.5). The second order term can be expanded as

$$\tilde{\psi}_1^{\mathrm{i}}\left(\xi,\eta\right) = \xi^{\beta_1} g_1(\eta) + \xi^{\beta_2} g_2(\eta) + \cdots , \tag{6.12}$$

where (ξ,η) is the previously defined coordinate system in the viscous sublayer. The aim is to find the functions g_1, g_2 and the exponents β_1, β_2: this is done by substituting the above expansion and the solution (6.5) into terms appearing at order Δk in Prandtl's boundary layer equation,

$$\frac{\partial\tilde{\psi}_0^{\mathrm{i}}}{\partial Y}\frac{\partial^2\tilde{\psi}_1^{\mathrm{i}}}{\partial x\partial Y} + \frac{\partial\tilde{\psi}_1^{\mathrm{i}}}{\partial Y}\frac{\partial^2\tilde{\psi}_0^{\mathrm{i}}}{\partial x\partial Y} - \frac{\partial\tilde{\psi}_0^{\mathrm{i}}}{\partial x}\frac{\partial^2\tilde{\psi}_1^{\mathrm{i}}}{\partial Y^2} - \frac{\partial\tilde{\psi}_1^{\mathrm{i}}}{\partial x}\frac{\partial^2\tilde{\psi}_0^{\mathrm{i}}}{\partial Y^2} = -\frac{\partial\tilde{p}_1}{\partial x} + \frac{\partial^3\tilde{\psi}_1^{\mathrm{i}}}{\partial Y^3},$$

rewritten using the coordinates of region $\mathrm{A_u}$,

$$\begin{aligned}
&\frac{1}{4}\left(\frac{1}{2}\mu_0\xi^2\eta^2+2a_0\xi^5\eta\right)\left\{\xi^{\beta_1-5}\left[\eta g_1''-(\beta_1-1)\,g_1'\right]+\xi^{\beta_2-5}\left[\eta g_2''-(\beta_2-1)\,g_2'\right]\right\}\\
&-2a_0\xi\eta\left(\xi^{\beta_1-1}g_1'+\xi^{\beta_2-1}g_2'\right)+a_0\xi^2\eta^2\left(\xi^{\beta_1-2}g_1''+\xi^{\beta_2-2}g_2''\right)\\
&-\frac{1}{4}\left(\mu_0\xi\eta+2a_0\xi^4\right)\left[\xi^{\beta_1-4}\left(\eta g_1'-\beta_1 g_1\right)+\xi^{\beta_2-4}\left(\eta g_2'-\beta_2 g_2\right)\right]\\
=&\frac{1}{4}\xi^{-3}\frac{\partial\tilde{p}_1}{\partial\xi}+\xi^{\beta_1-3}g_1'''+\xi^{\beta_2-3}g_2'''.
\end{aligned}$$

At order ξ^{β_1-3}, the equation

$$g_1'''-\frac{1}{8}\mu_0\eta^3 g_1''+\frac{1}{8}\mu_0\left(\beta_1+1\right)\eta^2 g_1'-\frac{1}{4}\mu_0\beta_1\eta g_1=0,$$

coupled with the no-slip boundary condition, has solution

$$g_1(\eta)=a_1\eta^2,$$

with $a_1<0$ [93]. The relationship between β_1 and β_2 is found by ensuring that there are terms forcing the equation at next order, setting $\beta=\beta_1=\beta_2-3$. Thus, at $\mathcal{O}(\xi^\beta)$, we have

$$g_2'''-\frac{1}{8}\mu_0\eta^3 g_2''+\frac{1}{8}\mu_0\left(\beta+4\right)\eta^2 g_2'-\frac{1}{4}\left(\beta+3\right)\mu_0\eta g_2=\frac{1}{2}\left(\beta-2\right)a_0a_1\eta^2,$$

ignoring the second order pressure gradient. The hypergeometric function, $\mathcal{F}(\cdot,\cdot,\cdot)$ once more makes an appearance in the solution [93],

$$g_2(\eta)=4\frac{a_0a_1}{\mu_0}\eta^2\int_0^\eta s^{-2}\left[\mathcal{F}\left(-\frac{\beta}{4}-\frac{1}{2},\frac{5}{4},\frac{\mu_0}{32}s^4\right)-1\right]\mathrm{d}s+b_1\eta^2.$$

No exponential growth as $\eta\to\infty$ is ensured only if

$$\beta=4m-2,\quad m\in\mathbb{N}$$

and hence the first choice, $m=0$, provides $\beta=-2$ and the solution to g_2 of

$$g_2(\eta)=b_1\eta^2.$$

The second order term in the viscous near-wall layer stream function expansion is then

$$\tilde{\psi}_1^{\mathrm{i}}=a_1\xi^{-2}\eta^2+b_1\xi\eta^2, \tag{6.13}$$

indicating the breakdown of expansion (6.11) when

$$|x-x_0|\sim(\Delta k)^{\frac{1}{2}}, \tag{6.14}$$

since the first and second terms become of similar orders of magnitude.

The question now is what the magnitude of $|x - x_0|$, or Δk, is in terms of the Reynolds number. The leading order stream function expansion in the upstream viscous layer, $\mathrm{A_u}$, equation (6.5), gives rise to inertial terms of the form

$$u\frac{\partial u}{\partial x} \sim -a_0\mu_0 Y^3 - 4a_0\xi^6\eta^2 + \cdots ;$$

and the pressure perturbation, p_1, if it is to act both at order $\mathrm{Re}^{-1/2}$ in the outer inviscid flow and be able to affect the boundary layer displacement in the lower viscous layer, must satisfy

$$p_1 \sim \mathrm{Re}^{-\frac{1}{2}} \sim |x - x_0|^{\frac{5}{2}},$$

providing us with, firstly, the streamwise extent of the interaction region,

$$|x - x_0| \sim \mathrm{Re}^{-\frac{1}{5}}; \tag{6.15a}$$

and, secondly, the order of magnitude of the increment of angle attack from its critical value k_c,

$$\Delta k \sim \mathrm{Re}^{-\frac{2}{5}}. \tag{6.15b}$$

Having determined that an interaction region does exist, and defined rigorously what was meant by 'sufficiently close', we move on now to introduce the roughness elements and solve for the stream function in the vicinity of the point of zero skin friction. Through this, we will come across the critical parameter referred to towards the beginning of this chapter, which represents here a limiting increment in the angle of attack, and show that roughness elements are able to increase this parameter as compared to the no-roughness case.

6.2.2 The interaction region

The structure of the interaction region, which has a streamwise length scale of order $\mathrm{Re}^{-1/5}$, is similar to that of triple deck theory, and is shown in figure 6.3. The lower deck (denoted by a superscript A) is the continuation of the upstream region $\mathrm{A_u}$ and joins with the downstream region $\mathrm{A_d}$ of figure 6.2, where $y \sim \mathrm{Re}^{-1/2}|x - x_0|^{1/4}$, with x_0 being the point of vanishing skin friction. Since $|x - x_0|$ is of order $\mathrm{Re}^{-1/5}$, as found in equation (6.15a), we introduce the normal coordinate z, of order 1, defined as $z = \mathrm{Re}^{11/20}y$. Above this, we have the main deck (superscript B), which consists of the entirety of the boundary layer and serves to transmit perturbations to the flow in the viscous lower deck through to an upper deck (superscript C). This last deck extends out of the main boundary layer into the inviscid flow region with a height scale of the same order of magnitude as the streamwise length scale, hence allowing for leading

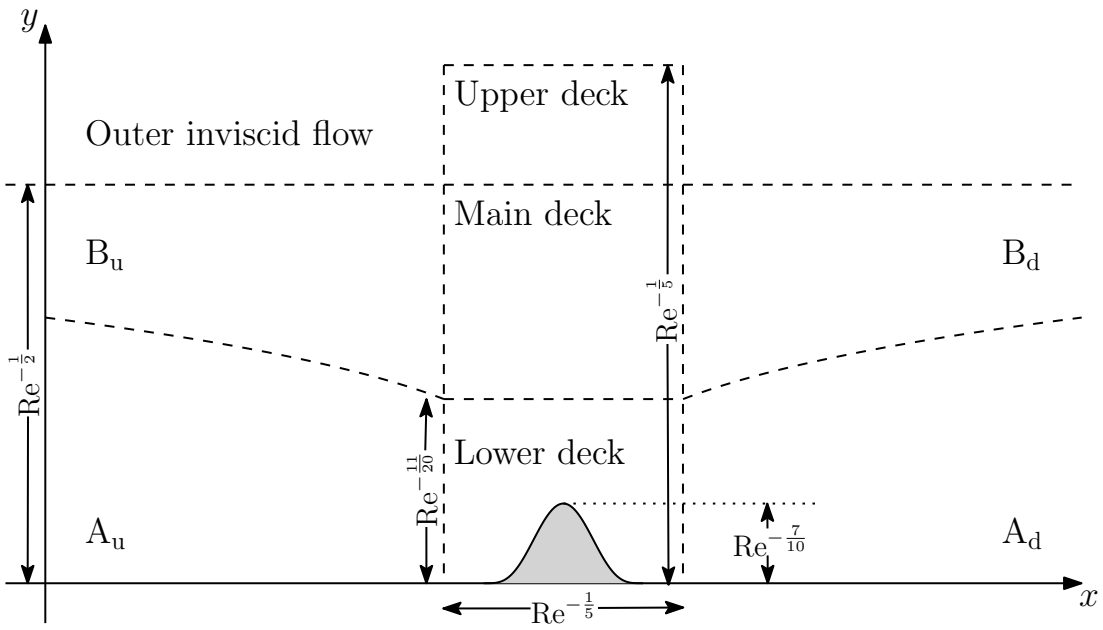

FIGURE 6.3: Schematic of the flow structure in the marginal separation region around the position of vanishing skin friction. The stream function in the regions upstream and downstream of the triple deck was found in §6.1.2; while in §6.2.2, we focus on finding the stream functions in the lower, main and upper decks, allowing us to determine the equations for the pressure and boundary layer displacement function. The presence of a roughness element within the lower deck is an addition to the classical theory of marginal separation.

order interactions between the inviscid and viscous flows. We retain then the normal coordinate $Y = \mathrm{Re}^{1/2}y$ for the main deck, introduce the normal coordinate $\bar{y} = \mathrm{Re}^{1/5}y$ for the upper deck[3] and define the streamwise coordinate $x - x_0 = \mathrm{Re}^{-1/5}X$. These are summarised in table 6.2, which completes the earlier table 6.1. The angle of attack k, is given, based on equation (6.15b), by

$$k = k_\mathrm{c} + \mathrm{Re}^{-\frac{2}{5}}k_1, \tag{6.16}$$

where k_c is its critical value and $k_1 \sim 1$ is an increment or reduction of it acting at order $\mathrm{Re}^{-2/5}$.

Within the lower deck, we introduce a roughness element, dynamic or static, represented for now by the general form

$$y = hF\left(X, \mathrm{Re}^{\gamma}t\right), \tag{6.17}$$

which has a height scale, h, that is some power of the Reynolds number—determined later based on the requirement that it is able to modify the wall skin friction to leading order—and some time scale, again due to the fixed frequency forcing, also acting at the appropriate order. For ease of notation, we introduce the scaled time $T = \mathrm{Re}^{\gamma}t$. We start with the Navier–Stokes equations (2.6), which must be studied in the context of the scalings of each layer, and the matching conditions that arise from the previous work of §6.1.2.

[3]These normal coordinates will be modified slightly later on by the application of the Prandtl transposition, but the fundamental height scalings remain the same.

Region	Streamwise	Normal	Stream function	Pressure
Outer inviscid flow	x	y	ψ	p_e
$\mathrm{A_u}$	ξ	η	$\tilde{\psi}^\mathrm{i}$	$\tilde{p}$
$\mathrm{B_u}$	ξ	Y	$\tilde{\psi}^\mathrm{o}$	$\tilde{p}$
Lower deck	X	z	ψ^A	p
Main deck	X	Y	ψ^B	p
Upper deck	X	$\bar{y}$	ψ^C	p
$\mathrm{A_d}$	$\hat{\xi}$	$\hat{\eta}$	$\hat{\psi}^\mathrm{i}$	$\hat{p}$
$\mathrm{B_d}$	$\hat{\xi}$	Y	$\hat{\psi}^\mathrm{o}$	$\hat{p}$

TABLE 6.2: List of coordinate systems, stream functions and pressures used in the marginal separation interaction region, as depicted in figure 6.3, along with the upstream and downstream variables used previously, thereby completing table 6.1. The pressure remains independent of the normal coordinate and thus is the same in all layers of the triple deck structure; while for the stream function, a superscript A, B and C denotes the lower, main and upper decks respectively.

The lower deck

The coordinate system for the lower deck is (X, z), where $X = \mathrm{Re}^{1/5}(x - x_0)$ is the streamwise coordinate and $z = \mathrm{Re}^{11/20}(y + hF)$ is the normal coordinate, with both X and z of order one and following the simplification of the no-slip boundary condition through the application of the Prandtl transposition. The lower deck is a continuation of the near-wall viscous layer $\mathrm{A_u}$ of §6.1.2 and then proceeds on to the downstream region $\mathrm{A_d}$, and thus the stream function expansion can be determined by combining equations (6.11), (6.5), (6.13) and (6.16), along with their downstream counterparts (not computed here), using the coordinate system of the lower deck,

$$\begin{aligned}\psi^\mathrm{i} = {}& \mathrm{Re}^{-\frac{13}{20}}\frac{1}{6}\mu_0 z^3 + \mathrm{Re}^{-\frac{4}{5}}\left(a_0\,|X|\,z^2 + a_1 k_1\,|X|^{-1}\,z^2\right) + \mathrm{Re}^{-\frac{17}{20}}\left(\frac{1}{6}\mu_1 X z^3 + \frac{2}{7!}\mu_0\mu_1 z^7\right) \\ & + \mathrm{Re}^{-\frac{19}{20}}\left(b_1 k_1 |X|^{-\frac{1}{4}} z^2 + \frac{4}{8!}\mu_0 a_0^2 z^9 + \frac{4}{5!}a_0^2 X z^5 + b_0 |X|^{\frac{7}{4}} z^2\right),\end{aligned}$$

to give

$$\psi^\mathrm{A}(X, z, T) = \mathrm{Re}^{-\frac{13}{20}}\frac{1}{6}\mu_0 z^3 + \mathrm{Re}^{-\frac{4}{5}}\psi_1^\mathrm{A} + \mathrm{Re}^{-\frac{17}{20}}\psi_2^\mathrm{A} + \mathrm{Re}^{-\frac{19}{20}}\psi_3^\mathrm{A} + \cdots; \tag{6.18a}$$

along with the upstream and downstream matching conditions

$$\psi_1^\mathrm{A}(X, z, T) \to a_0\,|X|\,z^2 + a_1 k_1\,|X|^{-1}\,z^2, \tag{6.18b}$$

$$\psi_2^\mathrm{A}(X, z, T) \to \frac{1}{6}\mu_1 X z^3 + \frac{2}{7!}\mu_0\mu_1 z^7, \tag{6.18c}$$

$$\psi_3^\mathrm{A}(X, z, T) \to b_1 k_1 |X|^{-\frac{1}{4}} z^2 + \frac{4}{8!}\mu_0 a_0^2 z^9 + \frac{4}{5!}a_0^2 X z^5 + b_0 |X|^{\frac{7}{4}} z^2. \tag{6.18d}$$

The pressure gradient, from equation (4.2), is

$$\frac{\partial p}{\partial x} = \mu_0 + \mathrm{Re}^{-\frac{1}{5}}\mu_1 X + \mathrm{Re}^{-\frac{3}{10}}\frac{\partial p_1}{\partial X} + \cdots, \tag{6.19}$$

where p_1 is the pressure perturbation induced by interactions between the viscous lower layer and outer inviscid flow, which must act at order $\mathrm{Re}^{-1/2}$.

Both in the lower and main decks, the normal momentum equation in the Navier–Stokes equations merely dictates that the pressure is independent of the normal coordinate, while the streamwise momentum equation in the lower deck becomes, substituting in the expansions (6.18a) and (6.19),

$$\begin{aligned}
&\mathrm{Re}^{-\frac{1}{4}+\gamma}\frac{\partial^2\psi_1^{\mathrm{A}}}{\partial z\partial T} + \mathrm{Re}^{-\frac{3}{10}+\gamma}\frac{\partial^2\psi_2^{\mathrm{A}}}{\partial z\partial T} + \mathrm{Re}^{-\frac{2}{5}+\gamma}\frac{\partial^2\psi_3^{\mathrm{A}}}{\partial z\partial T}\\
&+\left(\frac{1}{2}\mathrm{Re}^{\frac{13}{20}}\mu_0 z^2 + \mathrm{Re}^{\frac{1}{2}}\frac{\partial\psi_1^{\mathrm{A}}}{\partial z} + \mathrm{Re}^{\frac{9}{20}}\frac{\partial\psi_2^{\mathrm{A}}}{\partial z} + \mathrm{Re}^{\frac{7}{20}}\frac{\partial\psi_3^{\mathrm{A}}}{\partial z}\right)\\
&\quad\left(\mathrm{Re}^{-\frac{4}{5}}\frac{\partial^2\psi_1^{\mathrm{A}}}{\partial X\partial z} + \mathrm{Re}^{-\frac{17}{20}}\frac{\partial^2\psi_1^{\mathrm{A}}}{\partial X\partial z} + \mathrm{Re}^{-\frac{19}{20}}\frac{\partial^2\psi_1^{\mathrm{A}}}{\partial X\partial z}\right)\\
&-\left(\mathrm{Re}^{\frac{1}{2}}\frac{\partial\psi_1^{\mathrm{A}}}{\partial X} + \mathrm{Re}^{\frac{9}{20}}\frac{\partial\psi_2^{\mathrm{A}}}{\partial X} + \mathrm{Re}^{\frac{7}{20}}\frac{\partial\psi_3^{\mathrm{A}}}{\partial X}\right)\\
&\quad\left(\mathrm{Re}^{-\frac{13}{20}}\mu_0 z + \mathrm{Re}^{-\frac{4}{5}}\frac{\partial^2\psi_1^{\mathrm{A}}}{\partial z^2} + \mathrm{Re}^{-\frac{17}{20}}\frac{\partial^2\psi_2^{\mathrm{A}}}{\partial z^2} + \mathrm{Re}^{-\frac{19}{20}}\frac{\partial^2\psi_3^{\mathrm{A}}}{\partial z^2}\right)\\
&= -\mathrm{Re}^{-\frac{1}{5}}\mu_1 X - \mathrm{Re}^{-\frac{3}{10}}\frac{\partial p_1}{\partial X}\\
&\quad + \mathrm{Re}^{-\frac{17}{20}}\frac{\partial^3\psi_1^{\mathrm{A}}}{\partial X^2\partial z} + \mathrm{Re}^{-\frac{9}{10}}\frac{\partial^3\psi_2^{\mathrm{A}}}{\partial X^2\partial z} + \mathrm{Re}^{-1}\frac{\partial^3\psi_3^{\mathrm{A}}}{\partial X^2\partial z}\\
&\quad + \mathrm{Re}^{-\frac{3}{20}}\frac{\partial^3\psi_1^{\mathrm{A}}}{\partial z^3} + \mathrm{Re}^{-\frac{1}{5}}\frac{\partial^3\psi_2^{\mathrm{A}}}{\partial z^3} + \mathrm{Re}^{-\frac{2}{5}}\frac{\partial^3\psi_3^{\mathrm{A}}}{\partial z^3}.
\end{aligned}$$

At $\mathcal{O}(\mathrm{Re}^{-3/20})$, the equation

$$\frac{1}{2}\mu_0 z^2\frac{\partial^2\psi_1^{\mathrm{A}}}{\partial X\partial z} - \mu_0 z\frac{\partial\psi_1^{\mathrm{A}}}{\partial X} = \frac{\partial^3\psi_1^{\mathrm{A}}}{\partial z^3},$$

coupled with the no-slip boundary condition, has the solution

$$\psi_1^{\mathrm{A}}(X,z,T) = \frac{1}{2}\mu_0 z^2 A(X,T), \tag{6.20a}$$

where, just as in chapter 5, the function A represents the negative boundary layer displacement. The matching condition (6.18b) then gives the upstream and downstream behaviour of A as

$$A(X,T) \to 2\mu_0^{-1}\left(a_0|X| + a_1 k_1 |X|^{-1}\right) \quad \text{as } X \to \pm\infty. \tag{6.20b}$$

Both upstream and downstream conditions will be needed, as we will find that the final governing equation (6.38a) is elliptic in character.

At this point, we can already determine the necessary height scale of the roughness element. Using the Prandtl transposition, the normal velocity becomes

$$v = -\frac{\partial \psi}{\partial x} - h\frac{\partial \psi}{\partial y}\frac{\partial F}{\partial x} - h\frac{\partial F}{\partial t},$$

which, from equations (6.18a) and (6.20a), is

$$v^{\mathrm{A}} = -\mathrm{Re}^{-\frac{3}{5}}\left(\frac{1}{2}\mu_0 z^2 \frac{\partial A}{\partial X}\right) - h\mathrm{Re}^{\frac{1}{10}}\left(\frac{1}{2}\mu_0 z^2 \frac{\partial F}{\partial X}\right) - h\mathrm{Re}^{\gamma}\frac{\partial F}{\partial T}.$$

As we had in chapter 5, we want the roughness elements to act at the same order of magnitude as the boundary layer displacement function and thus we seek to balance the first two terms in the above, giving

$$h = \mathrm{Re}^{-\frac{7}{10}}, \tag{6.21}$$

while F remains an $\mathcal{O}(1)$ function. This agrees with the scaling of previous work on roughness elements [8].

Returning to the streamwise momentum equation, at $\mathcal{O}(\mathrm{Re}^{-1/5})$, we have

$$\frac{1}{2}\mu_0 z^2 \frac{\partial^2 \psi_2^{\mathrm{A}}}{\partial X \partial z} - \mu_0 z \frac{\partial \psi_2^{\mathrm{A}}}{\partial X} = -\mu_1 X + \frac{\partial^3 \psi_2^{\mathrm{A}}}{\partial z^3}$$

as the equation for ψ_2^{A}, which has solution equal to its upstream and downstream form,

$$\psi_2^{\mathrm{A}}(X, z, T) = \frac{1}{6}\mu_1 X z^3 + \frac{2}{7!}\mu_0 \mu_1 z^7. \tag{6.22}$$

We now stipulate the condition that the time derivative of the displacement A should be present in the equation at $\mathcal{O}(\mathrm{Re}^{-3/10})$, setting

$$\gamma = -\frac{1}{20}, \tag{6.23}$$

in agreement with the time scaling in the work of Smith on dynamic stall [82], among others: time of order $\mathrm{Re}^{1/20}$ is then equivalent to a frequency of order $\mathrm{Re}^{-1/20}$. The equation for ψ_3^{A} is therefore

$$\frac{\partial^3 \psi_3^{\mathrm{A}}}{\partial z^3} - \frac{1}{2}\mu_0 z^2 \frac{\partial^2 \psi_3^{\mathrm{A}}}{\partial X \partial z} + \mu_0 z \frac{\partial \psi_3^{\mathrm{A}}}{\partial X} = \mu_0 z \frac{\partial A}{\partial T} + \frac{1}{2}\mu_0^2 z^2 A \frac{\partial A}{\partial X} + \frac{\partial p_1}{\partial X}. \tag{6.24}$$

This, along with the no-slip boundary condition, is used to find a solvability condition for ψ_3^{A} involving the displacement A, as we saw in chapter 5. Here, however, we will, as promised, work through its derivation, but first the matching condition at infinity must be found by considering the solution in the main deck.

The main deck

The flow in the main deck of the interaction structure follows on from region $\mathrm{B_u}$ and proceeds on to region $\mathrm{B_d}$ of figure 6.3, where the solution, which spans the position of vanishing skin friction and therefore the interaction region itself, was given in equation (6.8). With the Prandtl transposition, and the roughness height scale (6.21), the normal coordinate in the main deck is defined by $y = \mathrm{Re}^{-1/2}Y + \mathrm{Re}^{-7/10}F$, with $Y \sim 1$. Combining the solution (6.8) with the second order solution (6.13) in the viscous sublayer, rewritten using the coordinates (X, Y) and making use of the matching condition (6.6b), gives

$$\begin{aligned}\psi^{\mathrm{o}} =& \,\mathrm{Re}^{-\frac{1}{2}}\psi_{00}(Y) \\ &+ \mathrm{Re}^{-\frac{7}{10}}\psi'_{00}(Y)\left[2\frac{a_0}{\mu_0}\left|X\right| + X\int_0^Y \frac{\psi'''_{00}(s)-\mu_0}{\left[\psi'_{00}(s)\right]^2}\,\mathrm{d}s + 2\frac{a_1}{\mu_0}k_1\left|X\right|^{-1}\right] + \cdots,\end{aligned}$$

where ψ_{00} is the same as the ψ^{o}_{00} used in equation (6.8) but with the superscript removed for beautification purposes. Thus the stream function expansion in the main deck takes the form

$$\psi^{\mathrm{B}}(X,Y,T) = \mathrm{Re}^{-\frac{1}{2}}\psi_{00} + \mathrm{Re}^{-\frac{7}{10}}\psi_1^{\mathrm{B}} + \mathrm{Re}^{-\frac{3}{4}}\psi_2^{\mathrm{B}} + \mathrm{Re}^{-\frac{9}{10}}\psi_3^{\mathrm{B}} + \mathrm{Re}^{-\frac{19}{20}}\psi_4^{\mathrm{B}} + \cdots, \quad (6.25)$$

with the continuation to $\mathcal{O}(\mathrm{Re}^{-19/20})$ designed to check the matching condition between the lower and main deck at that order.

The Navier–Stokes streamwise momentum equation in the main deck is then

$$\begin{aligned}&\mathrm{Re}^{-\frac{1}{4}}\frac{\partial^2\psi_1^{\mathrm{B}}}{\partial Y\partial T} + \mathrm{Re}^{-\frac{3}{10}}\frac{\partial^2\psi_2^{\mathrm{B}}}{\partial Y\partial T} + \mathrm{Re}^{-\frac{9}{20}}\frac{\partial^2\psi_3^{\mathrm{B}}}{\partial Y\partial T} + \mathrm{Re}^{-\frac{1}{2}}\frac{\partial^2\psi_4^{\mathrm{B}}}{\partial Y\partial T} \\ &+ \left(\mathrm{Re}^{\frac{7}{10}}\psi'_{00} + \mathrm{Re}^{\frac{1}{2}}\frac{\partial\psi_1^{\mathrm{B}}}{\partial Y} + \mathrm{Re}^{\frac{9}{20}}\frac{\partial\psi_2^{\mathrm{B}}}{\partial Y} + \mathrm{Re}^{\frac{3}{10}}\frac{\partial\psi_3^{\mathrm{B}}}{\partial Y} + \mathrm{Re}^{\frac{1}{4}}\frac{\partial\psi_4^{\mathrm{B}}}{\partial Y}\right) \\ &\quad\left(\mathrm{Re}^{-\frac{7}{10}}\frac{\partial^2\psi_1^{\mathrm{B}}}{\partial X\partial Y} + \mathrm{Re}^{-\frac{3}{4}}\frac{\partial^2\psi_2^{\mathrm{B}}}{\partial X\partial Y} + \mathrm{Re}^{-\frac{9}{10}}\frac{\partial^2\psi_3^{\mathrm{B}}}{\partial X\partial Y} + \mathrm{Re}^{-\frac{19}{20}}\frac{\partial^2\psi_4^{\mathrm{B}}}{\partial X\partial Y}\right) \\ &- \left(\mathrm{Re}^{\frac{1}{2}}\frac{\partial\psi_1^{\mathrm{B}}}{\partial X} + \mathrm{Re}^{\frac{9}{20}}\frac{\partial\psi_2^{\mathrm{B}}}{\partial X} + \mathrm{Re}^{\frac{3}{10}}\frac{\partial\psi_3^{\mathrm{B}}}{\partial X} + \mathrm{Re}^{\frac{1}{4}}\frac{\partial\psi_4^{\mathrm{B}}}{\partial X}\right) \\ &\quad\left(\mathrm{Re}^{-\frac{1}{2}}\psi''_{00} + \mathrm{Re}^{-\frac{7}{10}}\frac{\partial^2\psi_1^{\mathrm{B}}}{\partial Y^2} + \mathrm{Re}^{-\frac{3}{4}}\frac{\partial^2\psi_2^{\mathrm{B}}}{\partial Y^2} + \mathrm{Re}^{-\frac{9}{10}}\frac{\partial^2\psi_3^{\mathrm{B}}}{\partial Y^2} + \mathrm{Re}^{-\frac{19}{20}}\frac{\partial^2\psi_4^{\mathrm{B}}}{\partial Y^2}\right) \\ &= -\mu_0 - \mathrm{Re}^{-\frac{1}{5}}\mu_1 X - \mathrm{Re}^{-\frac{3}{10}}\frac{\partial p_1}{\partial X} \\ &\quad + \mathrm{Re}^{-\frac{4}{5}}\frac{\partial^3\psi_1^{\mathrm{B}}}{\partial X^2\partial Y} + \mathrm{Re}^{-\frac{17}{20}}\frac{\partial^3\psi_2^{\mathrm{B}}}{\partial X^2\partial Y} + \mathrm{Re}^{-1}\frac{\partial^3\psi_3^{\mathrm{B}}}{\partial X^2\partial Y} + \mathrm{Re}^{-\frac{21}{20}}\frac{\partial^3\psi_4^{\mathrm{B}}}{\partial X^2\partial Y} \\ &\quad + \psi'''_{00} + \mathrm{Re}^{-\frac{1}{5}}\frac{\partial^3\psi_1^{\mathrm{B}}}{\partial Y^3} + \mathrm{Re}^{-\frac{1}{4}}\frac{\partial^3\psi_2^{\mathrm{B}}}{\partial Y^3} + \mathrm{Re}^{-\frac{2}{5}}\frac{\partial^3\psi_3^{\mathrm{B}}}{\partial Y^3} + \mathrm{Re}^{-\frac{9}{20}}\frac{\partial^3\psi_4^{\mathrm{B}}}{\partial Y^3}.\end{aligned}$$

The $\mathcal{O}(1)$ terms,

$$\psi'_{00}\frac{\partial^2\psi_1^{\mathrm{B}}}{\partial X\partial Y} - \psi''_{00}\frac{\partial\psi_1^{\mathrm{B}}}{\partial X} = -\mu_0 + \psi'''_{00},$$

form an equation for ψ_1^{B} that has solution

$$\psi_1^{\mathrm{B}}(X,Y,T) = \psi_{00}'(Y)\left[A(X,T) + X\int_0^Y \frac{\psi_{00}'''(s)-\mu_0}{[\psi_{00}'(s)]^2}\,\mathrm{d}s\right], \tag{6.26}$$

noting the matching condition (6.20b).

For the purposes of the upper deck, an expansion to $\mathcal{O}(\mathrm{Re}^{-7/10})$ of the stream function in the main deck,

$$\psi^{\mathrm{B}}(X,Y,T) = \mathrm{Re}^{-\frac{1}{2}}\psi_{00}(Y) + \mathrm{Re}^{-\frac{7}{10}}\psi_{00}'(Y)\left[A(X,T) + X\int_0^Y \frac{\psi_{00}'''(s)-\mu_0}{[\psi_{00}'(s)]^2}\,\mathrm{d}s\right] + \cdots, \tag{6.27}$$

is sufficient. However, in order to fully determine the matching conditions with the lower deck, we should concern ourselves briefly with the terms at order $\mathrm{Re}^{-3/4}$ to $\mathrm{Re}^{-19/20}$. The equation at $\mathcal{O}(\mathrm{Re}^{-1/20})$ is

$$\psi_{00}'\frac{\partial^2\psi_2^{\mathrm{B}}}{\partial X\partial Y} - \psi_{00}''\frac{\partial\psi_2^{\mathrm{B}}}{\partial X} = 0,$$

whose solution,

$$\psi_2^{\mathrm{B}}(X,Y,T) = \psi_{00}'(Y)\,A_2(X,T),$$

would require a match with that at $\mathcal{O}(\mathrm{Re}^{-17/20})$ in the lower deck, equation (6.22), which is determined solely by the incoming pressure gradient: hence A_2 can safely be set to zero. At $\mathcal{O}(\mathrm{Re}^{-1/5})$,

$$\psi_{00}'\frac{\partial^2\psi_3^{\mathrm{B}}}{\partial X\partial Y} - \psi_{00}''\frac{\partial\psi_3^{\mathrm{B}}}{\partial X} = -\mu_1 X + \mathcal{C}_3,$$
$$\mathcal{C}_3 = \frac{\partial^3\psi_1^{\mathrm{B}}}{\partial Y^3} - \frac{\partial\psi_1^{\mathrm{B}}}{\partial Y}\frac{\partial^2\psi_1^{\mathrm{B}}}{\partial X\partial Y} + \frac{\partial\psi_1^{\mathrm{B}}}{\partial X}\frac{\partial^2\psi_1^{\mathrm{B}}}{\partial Y^2},$$

gives

$$\psi_3^{\mathrm{B}} = \psi_{00}'\left[A_3(X) + X\int_0^Y \left(\psi_{00}'\right)^{-2}\left(\mathcal{C}_2 - \mu_1 X\right)\,\mathrm{d}s\right];$$

which can be safely ignored, as it acts at order Re^{-1} in the lower deck. Finally, at $\mathcal{O}(\mathrm{Re}^{-1/4})$,

$$\psi_{00}'\frac{\partial^2\psi_4^{\mathrm{B}}}{\partial X\partial Y} - \psi_{00}''\frac{\partial\psi_4^{\mathrm{B}}}{\partial X} = -\frac{\partial^2\psi_1^{\mathrm{B}}}{\partial Y\partial T} + \mathcal{C}_4,$$
$$\mathcal{C}_4 = \frac{\partial^3\psi_2^{\mathrm{B}}}{\partial Y^3} + \frac{\partial\psi_1^{\mathrm{B}}}{\partial X}\frac{\partial^2\psi_2^{\mathrm{B}}}{\partial Y^2} + \frac{\partial\psi_2^{\mathrm{B}}}{\partial X}\frac{\partial^2\psi_1^{\mathrm{B}}}{\partial Y^2} - \frac{\partial\psi_1^{\mathrm{B}}}{\partial Y}\frac{\partial^2\psi_2^{\mathrm{B}}}{\partial X\partial Y} - \frac{\partial\psi_2^{\mathrm{B}}}{\partial Y}\frac{\partial^2\psi_1^{\mathrm{B}}}{\partial X\partial Y},$$

gives

$$\psi_4^{\mathrm{B}} = X\frac{\partial A}{\partial T} + \psi_{00}'\left[A_4 + X\int_0^Y \left(\psi_{00}'\right)^{-2}\mathcal{C}_4\,\mathrm{d}s\right],$$

with $X\partial A/\partial T$ feeding straight through to the lower deck at order $\mathrm{Re}^{-19/20}$. The presence of this term in the matching condition for the lower deck at infinity serves to justify the presence of the $\mu_0 z\partial A/\partial T$ term in equation (6.24) for ψ_3^{A}.

The solvability condition

Having satisfied ourselves that equation (6.24) is correct, with the time derivative that appears being adequately accounted for in the matching condition with the main deck as $z \to \infty$, we derive now the solvability condition for equation (6.24), which gives us the first relationship between the pressure and boundary layer displacement function. Differentiating first with respect to z gives

$$\frac{\partial^4 \psi_3^{\mathrm{A}}}{\partial z^4} - \frac{1}{2}\mu_0 z^2 \frac{\partial^3 \psi_3^{\mathrm{A}}}{\partial X \partial z^2} + \mu_0 \frac{\partial \psi_3^{\mathrm{A}}}{\partial X} = \mu_0 \frac{\partial A}{\partial T} + \mu_0^2 z A \frac{\partial A}{\partial X}$$

and we then take the Fourier transform in the streamwise coordinate, defined as

$$\hat{\psi}_3^{\mathrm{A}}(\kappa, z, T) = \frac{1}{\sqrt{2\pi}} \int_{-\infty}^{\infty} \exp(-\mathrm{i}\kappa X) \psi_3^{\mathrm{A}}(X, z, T)\, \mathrm{d}X$$

(both the overhat and $\mathcal{F}[\cdot]$ now denoting a Fourier transformed function, and κ being the transform variable), to obtain

$$\frac{\partial^4 \hat{\psi}_3^{\mathrm{A}}}{\partial z^4} - \frac{1}{2}\mathrm{i}\mu_0 \kappa z^2 \frac{\partial^2 \hat{\psi}_3^{\mathrm{A}}}{\partial z^2} + \mathrm{i}\mu_0 \kappa \hat{\psi}_3^{\mathrm{A}} = \mu_0 \frac{\partial \hat{A}}{\partial T} + \mu_0^2 z \mathcal{F}\left[A \frac{\partial A}{\partial X}\right](\kappa). \tag{6.28}$$

Applying the no-slip boundary condition, we substitute into equation (6.28) the polynomial solution

$$\hat{\psi}_3^{\mathrm{A}}(\kappa, z, T) = \sum_{i=2}^{\infty} \hat{c}_n(\kappa, T)\, z^n$$

and then equate coefficients of z^n. The coefficient $\hat{c}_3$ is found by evaluating equation (6.24) at $z = 0$; all other coefficients, apart from $\hat{c}_2$, whose calculation involves an expansion of the lower deck stream function to higher order than that needed here, can be found through recursion relations derived from equation (6.28).

The final Fourier-transformed version of ψ_3^{A} is a collection of three sums,

$$\begin{aligned}
\hat{\psi}_3^{\mathrm{A}} = {} & \hat{c}_2 z^2 + \frac{1}{\Gamma\left(\frac{1}{4}\right)} \mathrm{i}\kappa \hat{p}_1 \sum_{i=0}^{\infty} (8\mathrm{i}\kappa\mu_0)^i \frac{\Gamma(i+1)\,\Gamma\left(i+\frac{1}{4}\right)}{\Gamma(4i+4)} z^{4i+3} \\
& + \frac{1}{\Gamma\left(\frac{5}{4}\right)} \pi^{-\frac{1}{2}} \mu_0 \frac{\partial \hat{A}}{\partial T} \sum_{i=0}^{\infty} (8\mathrm{i}\kappa\mu_0)^i \frac{\Gamma\left(i+\frac{5}{4}\right)\Gamma\left(i+\frac{1}{2}\right)}{\Gamma(4i+5)} z^{4i+4} \\
& + \frac{1}{\Gamma\left(\frac{3}{4}\right)} \pi^{-\frac{1}{2}} \mathrm{i}\kappa \mu_0^2 \mathcal{F}\left[A^2\right] \sum_{i=0}^{\infty} (8\mathrm{i}\kappa\mu_0)^i \frac{\Gamma\left(i+\frac{3}{4}\right)\Gamma\left(i+\frac{3}{2}\right)}{\Gamma(4i+6)} z^{4i+5}
\end{aligned} \tag{6.29}$$

(where $\Gamma(\cdot)$ is the Gamma function), whose behaviour as z goes to infinity can be studied through the use of Struve and Bessel functions, as was done by Ruban [70], to obtain a relation involving the coefficients of the three sums, namely [82]

$$\mu_0^2 \mathrm{i}\kappa \mathcal{F}\left[A^2\right] + \frac{\Gamma\left(\frac{3}{4}\right)}{\Gamma\left(\frac{5}{4}\right)} 2^{\frac{3}{4}} \mu_0^{\frac{5}{4}} (\mathrm{i}\kappa)^{\frac{1}{4}} \frac{\partial \hat{A}}{\partial T} + \frac{\Gamma\left(\frac{3}{4}\right)}{\Gamma\left(\frac{1}{4}\right)} 2^{\frac{3}{2}} \pi^{\frac{1}{2}} \mu_0^{\frac{1}{2}} (\mathrm{i}\kappa)^{\frac{3}{2}} \hat{p}_1 = 0,$$

that ensures that there is no exponential growth in z. The inverse Fourier transform of this is then obtained using convolution as

$$A^2 + \sigma_1 \int_{-\infty}^{X} (X-s)^{-\frac{1}{4}} \frac{\partial A}{\partial T}\,\mathrm{d}s + g\,(X) = -\sigma_2 \int_{-\infty}^{X} (X-s)^{-\frac{1}{2}} \frac{\partial p_1}{\partial s}\,\mathrm{d}s,$$

with

$$\sigma_1 = 2^{\frac{9}{4}}\pi^{-1}\Gamma\left(\frac{3}{4}\right)\mu_0^{-\frac{3}{4}} \quad \text{and} \quad \sigma_2 = 2\pi^{-1}\Gamma^2\left(\frac{3}{4}\right)\mu_0^{-\frac{3}{2}}. \tag{6.30}$$

The function g is determined from the upstream condition on A: letting $X \to -\infty$ and using equation (6.20b), we find that

$$g(X) = -4\mu_0^{-2}\left(a_0^2 X^2 + 2a_0 a_1 k_1\right),$$

ignoring terms of order X^{-2}. Hence the first of the two equations relating the pressure and boundary layer displacement function is

$$\begin{aligned} &A^2 - \left(2\frac{a_0}{\mu_0}\right)^2 X^2 - 8\frac{a_0 a_1}{\mu_0^2}k_1 \\ &= -\sigma_1 \int_{-\infty}^{X} (X-s)^{-\frac{1}{4}} \frac{\partial A}{\partial T}\,\mathrm{d}s - \sigma_2 \int_{-\infty}^{X} (X-s)^{-\frac{1}{2}} \frac{\partial p_1}{\partial s}\,\mathrm{d}s. \end{aligned} \tag{6.31}$$

The constant on the left-hand side of equation (6.31) will go on to have a particular significance, explained later. First, we turn our attention to the upper deck, where the second pressure–displacement relation will be found, and thus the final governing equation for the displacement function determined.

Upper deck

The height and length scales in the upper deck are the same as each other, with the scaled length coordinate again given by $x - x_0 = \mathrm{Re}^{-1/5}X$, and the flow is therefore governed by the inviscid Euler equations (2.5). We introduce the normal coordinate $\bar{y}$, defined as

$$y = \mathrm{Re}^{-\frac{1}{5}}\bar{y},$$

and work with the velocities, rather than the stream function. The main deck solution (6.27), in the limit $Y \to \infty$, will give the matching condition between the main and upper decks. We first note that, if the inviscid slip velocity is given by U_e, then the behaviour of ψ_{00} as Y goes to infinity must be $\psi_{00} \to U_\mathrm{e}$ in order to ensure that there is a match between the flow in regions $\mathrm{B_u}$ or $\mathrm{B_d}$ with that in the inviscid flow region.

Thus, noting that the Prandtl transposition was applied in the main deck, the streamwise and normal velocity components there behave as

$$u^\mathrm{B} = \mathrm{Re}^{\frac{1}{2}}\frac{\partial \psi^\mathrm{B}}{\partial Y} \to U_\mathrm{e} - \mathrm{Re}^{-\frac{1}{5}}\frac{\mu_0}{U_\mathrm{e}}X + \cdots \tag{6.32a}$$

and

$$v^{\mathrm{B}} = -\mathrm{Re}^{\frac{1}{5}}\frac{\partial\psi^{\mathrm{B}}}{\partial X} + \frac{\partial\psi^{\mathrm{B}}}{\partial Y}\frac{\partial F}{\partial X} + \mathrm{Re}^{-\frac{3}{4}}\frac{\partial F}{\partial T}$$
$$\to \mathrm{Re}^{-\frac{1}{2}}\left[\frac{\mu_0}{U_{\mathrm{e}}}Y - U_{\mathrm{e}}\frac{\partial}{\partial X}(A-F)\right] + \mathcal{O}\left(\mathrm{Re}^{-\frac{7}{10}}\right) \tag{6.32b}$$

respectively as $Y \to \infty$. This therefore suggests the expansions

$$u^{\mathrm{C}} = U_{\mathrm{e}} - \mathrm{Re}^{-\frac{1}{5}}\frac{\mu_0}{U_{\mathrm{e}}}X + \cdots + \mathrm{Re}^{-\frac{1}{2}}u_1^{\mathrm{C}}(X,\bar{y},T) + \cdots \tag{6.33a}$$
$$v^{\mathrm{C}} = \mathrm{Re}^{-\frac{1}{5}}\frac{\mu_0}{U_{\mathrm{e}}}\bar{y} + \cdots + \mathrm{Re}^{-\frac{1}{2}}v_1^{\mathrm{C}}(X,\bar{y},T) + \cdots \tag{6.33b}$$

for the velocity components, with the same pressure gradient expansion as in equation (6.19).

The Navier–Stokes equations for u^{C} and v^{C} in the upper deck consist of the continuity equation,

$$\frac{\partial u_1^{\mathrm{C}}}{\partial X} + \frac{\partial v_1^{\mathrm{C}}}{\partial \bar{y}} = 0; \tag{6.34a}$$

and the streamwise and normal momentum equations, which reduce to

$$U_{\mathrm{e}}\frac{\partial u_1^{\mathrm{C}}}{\partial X} = -\frac{\partial p_1}{\partial X}, \tag{6.34b}$$
$$U_{\mathrm{e}}\frac{\partial v_1^{\mathrm{C}}}{\partial X} = -\frac{\partial p_1}{\partial \bar{y}}. \tag{6.34c}$$

From these, we obtain the Cauchy–Riemann equations relating v_1^{C} and p_1,

$$\frac{\partial v_1^{\mathrm{C}}}{\partial X} = -\frac{1}{U_{\mathrm{e}}}\frac{\partial p_1}{\partial \bar{y}}, \quad \frac{\partial v_1^{\mathrm{C}}}{\partial \bar{y}} = \frac{1}{U_{\mathrm{e}}}\frac{\partial p_1}{\partial X},$$

which can be solved by defining the complex-valued function $G(\bar{z}) = p_1 + \mathrm{i}U_{\mathrm{e}}v_1^{\mathrm{C}}$, where $\bar{z} = X + \mathrm{i}\bar{y}$ and Cauchy's residue theorem gives G as

$$G(\bar{z}) = \frac{1}{2\pi\mathrm{i}}\oint_C \frac{G(\zeta)}{\zeta - \bar{z}}\,\mathrm{d}\zeta,$$

$\bar{z}$ lying in the positive half plane and C being a semi-circular contour also in the upper half plane with diameter on the X-axis. For matching with the main deck as $\bar{y} \to 0$, we use the Sokhostki-Plemelj formula to calculate the above integral on the boundary:

$$G(X) = \frac{1}{2}G(X) + \frac{1}{2\pi\mathrm{i}}\int_{-\infty}^{\infty} \frac{G(s)}{s - X}\,\mathrm{d}s,$$

where the dashed integral indicates that the Cauchy principal value should be taken. Thus, considering only the real part, we find that

$$p_1(X,T) = \frac{U_{\mathrm{e}}}{\pi}\int_{-\infty}^{\infty} \frac{v_1^{\mathrm{C}}(s,0,T)}{s - X}\,\mathrm{d}s.$$

With the perturbation v_1^{C} evaluated at $\bar{y} = 0$ being found by comparing equations (6.32b) and (6.33b), giving

$$v_1^{\mathrm{C}}(X, 0, T) = -U_{\mathrm{e}} \frac{\partial}{\partial X}(A - F),$$

we thereby find the second relationship between the displacement function A and the pressure perturbation p_1,

$$p_1(X, T) = \frac{U_{\mathrm{e}}^2}{\pi} \int\!\!\!\!\!\!-_{-\infty}^{\infty} (X - s)^{-1} \frac{\partial}{\partial s}(A - F)\, \mathrm{d}s, \tag{6.35}$$

with which we close the system for A.

The boundary layer displacement equation

Equations (6.31) and (6.35) now need to be combined into a single equation and then, through the use of an affine transformation, cleared of extraneous constants in preparation for a numerical treatment. In equation (6.31), it is the derivative of the pressure that appears and so, assisted by the use of a Fourier transform, we rewrite equation (6.35) as

$$\frac{\partial p_1}{\partial X} = \frac{U_{\mathrm{e}}^2}{\pi} \int\!\!\!\!\!\!-_{-\infty}^{\infty} (X - s)^{-1} \frac{\partial^2}{\partial s^2}(A - F)\, \mathrm{d}s, \tag{6.36}$$

which will prove useful in our understanding of the physical mechanisms at play behind the results of §6.3. Substituting this into equation (6.31) gives

$$\begin{aligned} &A^2 - \left(2\frac{a_0}{\mu_0}\right)^2 X^2 - 8\frac{a_0 a_1}{\mu_0^2} k_1 \\ &= -\sigma_1 \int_{-\infty}^{X} (X - s)^{-\frac{1}{4}} \frac{\partial A}{\partial T}\, \mathrm{d}s \\ &\quad - \frac{\sigma_2 U_{\mathrm{e}}^2}{\pi} \int_{-\infty}^{X} (X - s)^{-\frac{1}{2}} \int\!\!\!\!\!\!-_{-\infty}^{\infty} (X - r)^{-1} \frac{\partial^2}{\partial r^2}(A - F)\, \mathrm{d}r\, \mathrm{d}s, \end{aligned}$$

which can be simplified to

$$\begin{aligned} &A^2 - \left(2\frac{a_0}{\mu_0}\right)^2 X^2 - 8\frac{a_0 a_1}{\mu_0^2} k_1 \\ &= \sigma_2 U_{\mathrm{e}}^2 \int_{X}^{\infty} (s - X)^{-\frac{1}{2}} \frac{\partial^2}{\partial s^2}(A - F)\, \mathrm{d}s - \sigma_1 \int_{-\infty}^{X} (X - s)^{-\frac{1}{4}} \frac{\partial A}{\partial T}\, \mathrm{d}s, \end{aligned} \tag{6.37a}$$

along with the up- and downstream matching condition

$$A^2 \to \left(2\frac{a_0}{\mu_0}\right)^2 X^2 + 8\frac{a_0 a_1}{\mu_0^2} k_1 + \cdots \quad \text{as } |X| \to \infty. \tag{6.37b}$$

The affine transformation

$$A = \sigma_2^{\frac{2}{5}} U_\mathrm{e}^{\frac{4}{5}} \left(2\frac{a_0}{\mu_0}\right)^{\frac{3}{5}} \bar{A}, \quad F = \sigma_2^{\frac{2}{5}} U_\mathrm{e}^{\frac{4}{5}} \left(2\frac{a_0}{\mu_0}\right)^{\frac{3}{5}} \bar{F},$$
$$X = \sigma_2^{\frac{2}{5}} U_\mathrm{e}^{\frac{4}{5}} \left(2\frac{a_0}{\mu_0}\right)^{-\frac{2}{5}} \bar{X}, \quad T = \sigma_1 \sigma_2^{-\frac{1}{10}} U_\mathrm{e}^{-\frac{1}{5}} \left(2\frac{a_0}{\mu_0}\right)^{-\frac{9}{10}} \bar{T},$$

then converts the system (6.37) into the more simple form, neglecting the overbar,

$$A^2 - X^2 + \Gamma = \int_X^\infty (s-X)^{-\frac{1}{2}} \frac{\partial^2}{\partial s^2}(A-F)\,\mathrm{d}s - \int_{-\infty}^X (X-s)^{-\frac{1}{4}} \frac{\partial A}{\partial T}\,\mathrm{d}s \tag{6.38a}$$
$$A \to \left(X^2 - \Gamma\right)^{\frac{1}{2}} \quad \text{as } X \to \pm\infty, \tag{6.38b}$$

where all remaining constants have been combined into the parameter Γ

$$\Gamma = \frac{-4a_1 k_1}{\left(2a_0 \mu_0^4 \sigma_2^4 U_\mathrm{e}^8\right)^{\frac{1}{5}}}. \tag{6.38c}$$

This equation differs from that originally derived by Ruban [70] and Stewartson, Smith & Kaups [90] through the addition of the time derivative; unsteadiness was then first introduced in the work of Smith [82], but the airfoil remained clean and there was no roughness function F. The work of Braun and Kluwick then saw the incorporation of roughness elements, first static [8] and then dynamic [9]: the latter had the same height and time scalings as those presented here, but our equation (6.38a) is a correction on their version (c.f. equation (2.7) of [9]), although the results that follow in their original paper, which will be commented on in more detail in §6.3, and subsequent publications (e.g. [75]), remain correct.[4]

Separation

The stream function expansion in the lower deck was found to be

$$\psi^\mathrm{A} = \frac{1}{6}\mathrm{Re}^{-\frac{13}{20}} \mu_0 z^3 + \frac{1}{2}\mathrm{Re}^{-\frac{4}{5}} \mu_0 z^2 A\,(X,T) + \cdots$$

and this gives rise to the wall skin friction

$$\tau_\mathrm{wall} = \mathrm{Re}^{\frac{3}{10}} \mu_0 A\,(X,T) + \cdots. \tag{6.39}$$

Hence separation is seen to occur when the boundary layer displacement function, A, is negative. Recalling that A was actually defined to be the negative displacement function, flow separation implies that the boundary layer displacement from the surface is positive, as would be expected.

[4] Private communication with the authors.

6.2.3 Increasing the angle of attack: the clean case

The definition (6.38c) of the critical parameter Γ includes the constant k_1 and thus Γ is related to a deviation in the angle of attack above or below the value $k = k_c$ where, from classical boundary layer theory, the skin friction first vanishes and then recovers in a discontinuous manner: the marginal separation singularity. The triple deck interaction structure introduced and described in §6.2.2 then allows one to remove this singularity and, by solving the resultant system

$$A^2 - X^2 + \Gamma = \int_X^\infty (s - X)^{-\frac{1}{2}} \frac{\partial^2 A}{\partial s^2} \, \mathrm{d}s \tag{6.40}$$

with the same boundary condition (6.38b), for different values of Γ, obtain physically realistic solutions for flows at angles of attack that are greater ($\Gamma > 0$) than the critical angle of attack, by an order of magnitude of $\mathrm{Re}^{-2/5}$. (Equation (6.40) is obtained from equation (6.38a) by removing both the roughness function F and the time dependence.)

Figure 6.4, in which we plot the displacement function A for different values of Γ, complements the discussion below.[5] Where Γ is negative, A remains positive throughout the domain, as would be expected: for $\Gamma < 0$, we are considering angles of attack that are less than k_c, when classical boundary layer theory first predicts that a position of vanishing skin friction will appear. At $\Gamma = 0$, giving an angle of attack $k = k_c$, the displacement function still remains positive and no separation occurs. Marginal separation theory therefore not only smooths out the discontinuity in the wall skin friction, but allows for fully attached flow over an airfoil leading edge at angles of attack that are greater than those predicted by classical boundary layer theory.

The minimum in A is, however, decreasing and moving slightly downstream as Γ increases and it eventually equals zero when $\Gamma \simeq 2.369$: note that this occurs at $X \simeq 0.40$ and therefore at a position downstream of the original point $x = x_0$, corresponding to $X = 0$. Further increases in Γ cause a separation bubble to form, where the skin friction (A) reaches a negative minimum before recovering, with larger separation bubbles forming for greater values of Γ: the separation point moves upstream and both the reattachment position and skin friction minimum move downstream. Such laminar separation bubbles are indeed found experimentally when the flow near the leading edge of an airfoil remains laminar and have a streamwise extent of around 1% of the chord length: so small that they have negligible effect on the lift and drag coefficients [93]. However, we then reach a choice of Γ for which numerical techniques used to solve equation (6.40) no longer converge and solutions for A do not exist. With the code used here, this occurs at $\Gamma \simeq 2.764$ and we denote this value by $\Gamma = \Gamma_c$.[6] This prediction of

[5] Details on the numerical technique are given later in §6.3 and appendix C. The algorithm used here corresponds to that developed for the dynamic roughness elements.

[6] Our result of $\Gamma_c \simeq 2.764$ compares with the original result of $\Gamma_c \simeq 2.75$ obtained by Stewartson, Smith & Kaups, who used a coarser mesh ($\Delta = 0.1$ or 0.25 compared to our $\Delta = 0.05$) and the later result of Braun & Kluwick of $\Gamma_c \simeq 2.66$. The former also predict that $A(0)$ will first vanish when $\Gamma \simeq 2.4$, compared to our 2.458 [90, 9].

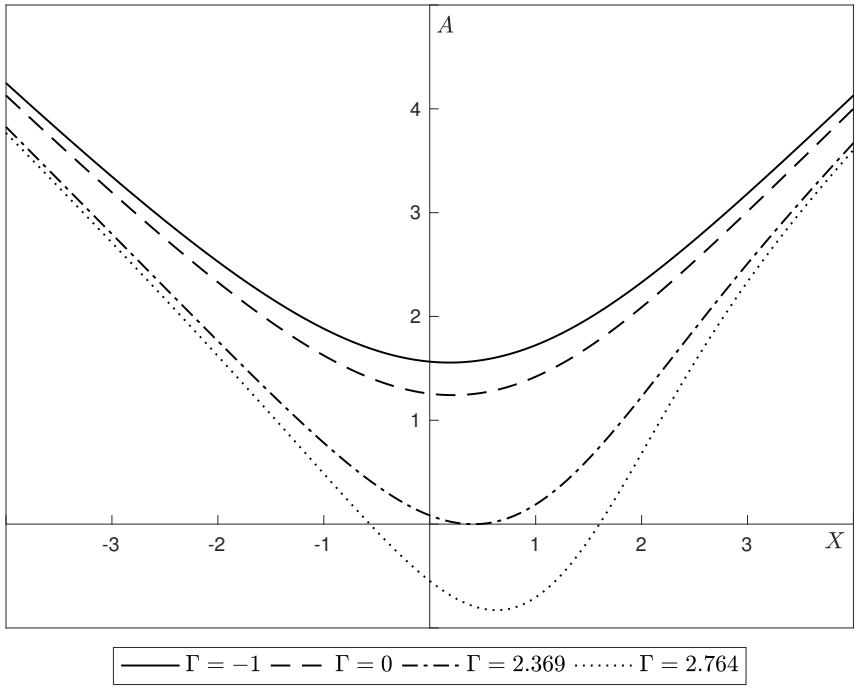

FIGURE 6.4: The solution, A, to equation (6.40) at different values of Γ. These represent: angles of attack less than the critical angle of attack as predicted by classical boundary layer theory ($\Gamma = -1$, solid line); angles of attack equal to the critical angle of attack, where the skin friction, as predicted by classical boundary layer theory, should vanish ($\Gamma = 0$, dashed line); the value of Γ where the skin friction first equals zero, as predicted by marginal separation theory ($\Gamma = 2.369$, dot–dashed line); and the value of Γ above which no solution to equation (6.40) exists ($\Gamma = 2.764$, dotted line).

marginal separation theory, that steady solutions can be obtained at angles of attack greater than that at which classical boundary layer theory breaks down, has been confirmed by past comparisons between Navier–Stokes computations and the asymptotic interaction approach presented above (see, for example, references [10, 39]).

The lack of a solution to equation (6.40) for $\Gamma > \Gamma_c$ corresponds to the 'bursting' of the short leading edge separation bubble into either a longer one or fully separated flow over the whole airfoil, with its resultant dramatic increase in the drag and decrease in lift.[7] By plotting in figure 6.5 the gradient of the pressure perturbation p_1, calculated from equation (6.36), we see that an increase in Γ not only results in an increase in the initially favourable pressure gradient that is encountered but, more pertinently, causes the later adverse pressure peak to increase quite dramatically and it is probable that, physically, it is this adverse pressure peak that leads to the bursting of the separation bubble and formation of larger regions of separated flow.

[7] As an aside—although it is a very interesting question—it seems to be currently unknown how one could pass continuously through the angle of attack represented by Γ_c to greater angles of attack and larger regions of separated flow, which cannot be accommodated by marginal separation theory—or, indeed, whether it is at all possible.

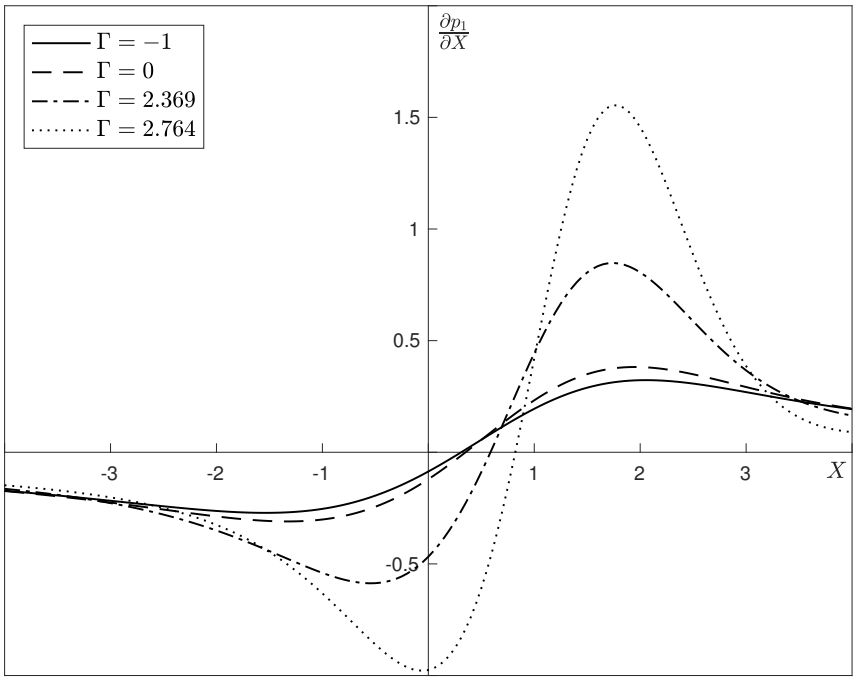

FIGURE 6.5: The gradient of the pressure perturbation p_1 at different values of Γ, as given in the legend and described in the caption of figure 6.4 and in the text. The growth of the adverse pressure peak as Γ is increased towards its critical value is clearly seen and it is possible that it is this large adverse pressure gradient that causes a fully separated flow, which cannot be described by marginal separation theory, to form at $\Gamma > \Gamma_c$.

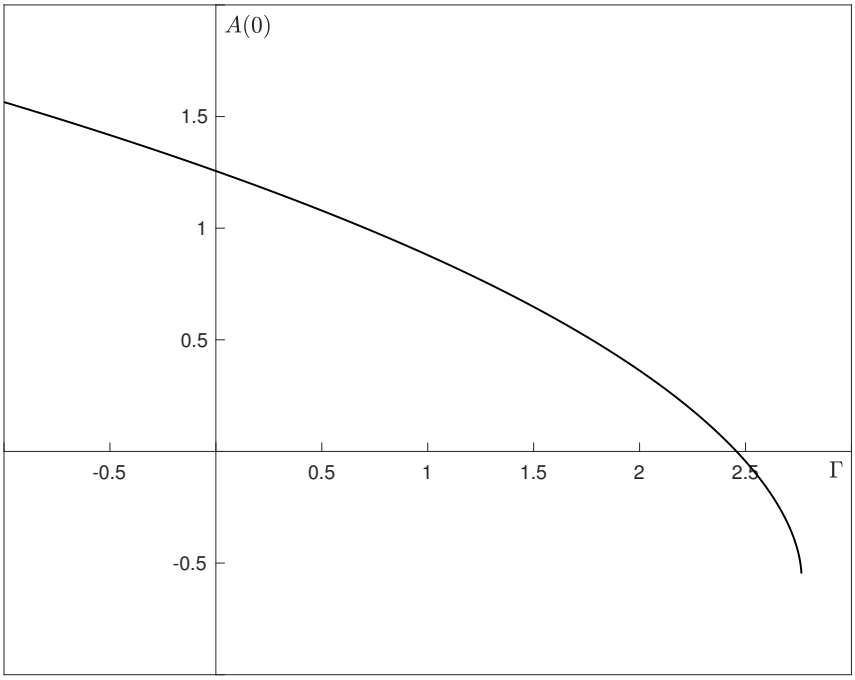

FIGURE 6.6: Upper branch solution for the displacement function, indicated by plotting the parameter Γ against $A(0)$. No solutions to A exist for $\Gamma > 2.764$; rather, the graph turns around and a lower branch exists for $\Gamma < 2.764$. Our focus, however, is on the value of Γ_c, approximately equal to 2.764 in the clean airfoil case.

Unperturbed by the nonexistence of a solution at $\Gamma > \Gamma_c$, Stewartson, Smith & Kaups modified their code so that instead of finding the displacement function for a fixed Γ, it sought both A and Γ from a preset $A(0)$. From the value determined at Γ_c, a decrease in $A(0)$ led to a second solution for the negative boundary layer displacement at $\Gamma < \Gamma_c$. The governing equation (6.40) and matching condition (6.38b) therefore admit non-uniqueness, with at least two branches existing for $0 < \Gamma < \Gamma_c$: indeed, it was later shown that for a certain range of Γ, four solutions are possible [12]. As Γ is increased along the upper branch, a separation bubble is formed that exists up until the critical value Γ_c; reductions in Γ could then cause the solution to move along the lower branch, where the separation bubble is much larger [90]. This can be visualised by plotting Γ against $A(0)$ and a graph of the upper branch, up to Γ_c, is shown in figure 6.6. As Γ approaches 0 again along the lower branch, the separation point tends to $x = x_0$, that predicted by classical boundary layer theory, and the reattachment point moves downstream towards positive infinity [12].

The lower branch was not computed in our case, as we are not overly interested in the solutions along the branches themselves, but rather in the value of Γ_c in the presence of roughness elements and in the solution to the boundary layer displacement function and perturbation pressure gradient at $\Gamma = \Gamma_c$. In particular, can the presence of roughness

elements (steady or dynamic) in equation (6.38a) result in solutions existing at higher values of Γ than are possible in equation (6.40), indicating the possibility of a small laminar separation bubble existing at higher angles of attack compared to the clean airfoil case? Furthermore, can the separation bubble be avoided altogether? And what is the effect on the pressure gradient through which this could all be possible? It is to these question that we will turn in the next section.

6.3 Roughness elements and the critical angle of attack

Henry Morton Stanley had had an upbringing of poverty and rejection. Actually born as John Rowlands in Wales in 1841, he was the son of an 18 year-old barmaid who didn't want him. At the age of 5, after having been shunted around from family to family, he was taken, under the pretence of buying cakes, to a workhouse, and left there. It was perhaps this sense of abandonment within the workhouse confines that drove him first to the US and then to Africa, where he made his name.

After leaving Livingstone at Tabora and returning to London, he planned never to return. But, once you have heard the voice of Africa, you are no longer your own. Regularly, often, repeatedly, at the most unpredictable of moments, it calls out to you again, and your blood starts to hum and your legs to buzz with an unquenchable restlessness, an unbearable need to immerse yourself once more in its being. When Livingstone died at Ilala on the Lualaba river, Stanley succumbed and went back.

He left Bagamayo, opposite Zanzibar on the Indian ocean on 17 November 1874 and, after circumnavigating both Lake Victoria and Lake Tanganyika, heard the crash of the ocean waves once more at the Portuguese trading post of Boma, near where the Ikuta Yacongo, the River Congo, flows into the Atlantic ocean, on 9 August 1877. It had been a journey of 11 000 km*, during which half of his companions had died—and Stanley's fiancée had married another—but the watersheds of the Nile and the Congo were at last untangled.*

The turn from Stanley's quest, and that of his contemporaries, to our own is perhaps[8] anticlimactic in its nature but, nevertheless, it is one we must take and, ultimately, might go on to provide us with sufficient adventure and excitement. With a steady solution to the governing system (6.38) existing only for $\Gamma < \Gamma_c$, our search is for the value of this critical parameter, in the presence of roughness elements, below which separation of the flow at the airfoil leading edge is restricted to a small laminar separation bubble, with little adverse effect on the lift and drag coefficients. Any increase in Γ_c may then be of significant interest in the development of flow control devices that can

[8] Probably?!

delay separation to higher angles of attack. For $\Gamma > \Gamma_c$, the separation bubble bursts and, if one considers the unsteady problem (6.38) but with the roughness function F set to zero, one finds that there occurs unbounded growth in the displacement function and a singularity at some finite time appears, linked to the abrupt thickening of the boundary layer and a vortex shedding phenomenon, studied by Smith in the context of dynamic stall [82].

In the case where our roughness element consists of a static bump,[9] we consider only the steady version of equation (6.38a), in which the time derivative is removed to obtain

$$A^2 - X^2 + \Gamma = \int_X^\infty (s - X)^{-\frac{1}{2}} \frac{\partial^2}{\partial s^2}(A - F)\,\mathrm{d}s \tag{6.41}$$

with the same boundary conditions (6.38b). The roughness shape is defined to be

$$F(X) = a\,(X - X_L)^4\,(X - X_R)^4 \tag{6.42}$$

between the left- and right-hand edge of the roughness (X_L and X_R respectively), but zero everywhere else. The numerical technique used to solve equation (6.41) is based on method 1 of Stewartson, Smith & Kaups [90], which involves the equation's rearrangement, via a Fourier transform, to

$$\pi\left[1 - \frac{\partial}{\partial X}(A - F)\right] = \int_X^\infty (s - X)^{-\frac{1}{2}}\left(A^2 - s^2 + \Gamma\right)\,\mathrm{d}s. \tag{6.43}$$

Further details on the iterative scheme, in which the guess of the solution to A, entered into the integral on the right-hand side of equation (6.43), is updated through the use of the derivative on the left-hand side, are given in appendix C.1.

Using this method, the value of the critical parameter in the absence of roughness elements is given by $\Gamma_c \simeq 2.756$ (slightly less than the value of 2.764 reported earlier, which was found using the technique devised for dynamic elements) and we seek to find out whether static roughness elements, of various positions, widths and heights, are able to increase this value, enabling steady solutions to the governing equations to be obtained for larger angles of attack. Such an analysis of the effect of static roughnesses was actually already carried out by Braun & Kluwick [9] and our results, as would be expected, then turn out to be qualitatively identical to theirs, with any quantitative variations due to the difference in roughness shape and numerical scheme or parameters. In §6.3.1, we plot also the boundary layer displacement function and pressure gradient, not done previously, in order to try to gain some physical understanding behind the changes in Γ_c.

The scenario of dynamic roughness elements, with its necessary inclusion of time-dependence in some form, is complicated by the fact that, as in chapter 5, the governing equation (6.38) is ill-posed and finite time blow-up can occur not only for values

[9] The results for negative roughness elements, whether static or dynamic, will not be presented, although tend to have a less beneficial effect than positive roughnesses.

of Γ greater than Γ_c (as mentioned previously), but also for $\Gamma \leq \Gamma_c$. This is due to the reversed flow that exists within the marginal separation interaction region giving rise to instabilities with short wavelengths that demonstrate exponentially fast growth. Equation (6.38) is based on the assumption of a quasi-steady boundary layer and, as a result of its development, cannot incorporate within its slower time scale the much faster Tollmien–Schlichting or Rayleigh instabilities, leading to its ill-posedness [71].

Once more, therefore, we must consider the forcing to be of fixed frequency (ω), as indeed it was in the reported experiments [33, 41], and deal with the time dependence by writing the solution to the boundary layer displacement as the (truncated) sum of Fourier modes,

$$A(X,T) = \sum_{k=-M}^{M} A_k(X) \exp(2\mathrm{i}k\omega T), \tag{6.44a}$$

with the roughness function given by

$$F(X,T) = f(X)\left[\exp(2\mathrm{i}\omega T) + \exp(-2\mathrm{i}\omega T) + 2\right] \tag{6.44b}$$

(ensuring that the element remains positive throughout a cycle of oscillation), and the roughness shape by

$$f(X) = a(X - X_L)^6 (X - X_L)^6. \tag{6.44c}$$

In both equations (6.42) and (6.44c), the roughness height a has been normalised to ensure that a choice of $a = 1$ gives a peak amplitude of 1 and we note that the static and dynamic roughness shapes have a slightly different form: a higher order polynomial being used for the latter due to the higher order derivative appearing in the governing equation. Although some comparison between the static and dynamic results is shown in §6.3.2, our main focus is solely on a comparison of the dynamic results with themselves and, in any case, any differences due to the roughness shape itself are likely to manifest themselves in small quantitative disagreements, rather than qualitative fall outs.

The method used to solve the static equation was found not to work in the dynamic case and so the second technique of Stewartson, Smith & Kaups, involving Newton's method, was adapted for use here. The system of equations to solve for the $M + 1$ Fourier modes (including the zeroth, and noting that negative and positive modes are complex conjugates of each other) are given, on substituting equations (6.44a) and

(6.44b) into equation (6.38), by

$$\begin{aligned}
&\sum_{k=-M}^{M} A_k A_{m-k} + \delta_{0m}\left(-X^2+\Gamma\right) \\
&= \int_X^\infty (s-X)^{-\frac{1}{2}}\, A_m''\,\mathrm{d}s - \delta_{2m}\int_X^\infty (s-X)^{-\frac{1}{2}}\, f''\,\mathrm{d}s \\
&\quad - 2\delta_{0m}\int_X^\infty (s-X)^{-\frac{1}{2}}\, f''\,\mathrm{d}s - 2\mathrm{i}m\omega\int_{-\infty}^X (X-s)^{-\frac{1}{4}}\, A_m\,\mathrm{d}s
\end{aligned} \tag{6.45a}$$

subject to

$$A_m \to \delta_{0m}\left(X^2-\Gamma\right)^{\frac{1}{2}} \quad \text{as } X \to \pm\infty. \tag{6.45b}$$

The δ_{ij} is the usual delta function, equal to 1 when $i = j$ and zero otherwise, and further details on the method used to solve the above system, including the analytical computation of the Jacobian matrix, are to be found in appendix C.2. Less iterations were required for convergence as compared to the technique used in the static case, although each individual iteration took considerably longer; the number of iterations needed for convergence when trying to determine Γ_c to the third decimal place became rather high (in the order of tens), but less than ten were needed in general for the calculation of Γ_c to two decimal places. A similar behaviour was seen for the static roughness elements as Γ_c was sought to higher levels of accuracy.

The question for the dynamic roughness is then whether there exists an equivalent value of Γ_c below which the governing equation admits some 'steady state' solution, where by 'steady state' we actually mean that the solution to each Fourier mode present in the system (6.44) and (6.45) must converge. And, if so, what is that value of Γ_c? This question will be dealt with in §6.3.2; we first turn briefly to static roughness elements to confirm and explain the results of Braun & Kluwick [9].

6.3.1 Static roughness elements

Braun & Kluwick, in their 2004 paper [9], demonstrated that static bumps can increase the value of Γ_c below which solutions to the steady equation (6.41) exist; while, conversely, negative bumps result in a decrease of Γ_c compared to the clean, no-roughness case. Similarly, suction tends to have a favourable impact but blowing does not. Our results for static elements, presented in this section, are, as would be expected, similar to those of Braun & Kluwick, but we note that any beneficial effect is highly dependent on the position of the roughness element, as indicated in figure 6.7a for humps and 6.7b for dents. For the latter, the arguments set forth in the paragraph below can largely be reversed and, due to their far more advantageous impact, we will focus from now onwards on positive roughnesses only.

Regarding the roughness position, the centre of the element, irrespective of width, must lie within the streamwise extent of the separation bubble that exists at Γ_c ($\simeq 2.756$) in the no-roughness case. Indeed, the position of maximum Γ_c seems largely invariant as

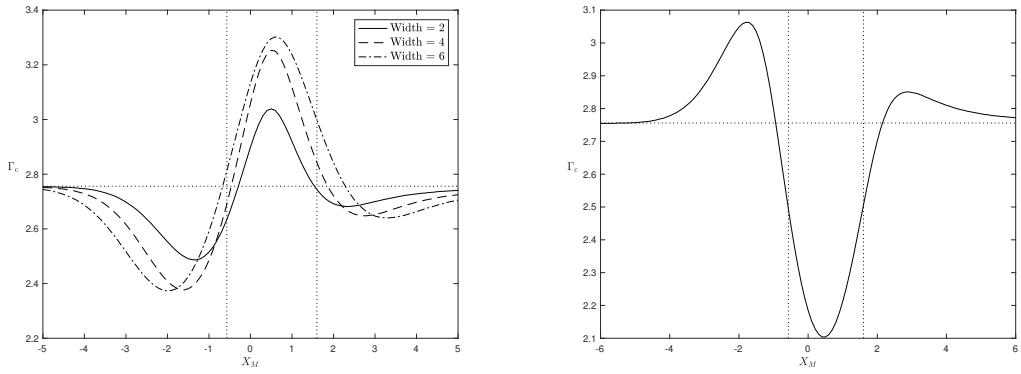

(A) $a = 1$ (B) $a = -1$

FIGURE 6.7: Impact of varying the position of a static roughness element on the critical parameter Γ_c for both (a) positive (height equal to 1) and (b) negative (depth equal to 1) elements. Various widths were studied in the case of a positive roughness, as shown in the legend. The two vertical dotted lines mark the start and end of the separation bubble that exists in the clean case at $\Gamma = \Gamma_c \simeq 2.756$, a value shown by the dotted horizontal line. The width in the negative roughness case was 4.

a function of width, occurring when the hump is centred at $X_M = 0.5$ or 0.6 for widths of 2, 4 and 6, which is approximately halfway along the length of the no-roughness separation bubble (extending from -0.57 to 1.60 at $\Gamma_c \simeq 2.756$). Such a placement of the element ensures that a favourable pressure gradient will exist in the portion of flow where the bubble in the clean case originally appears, with the effect that the separation point will move downstream, occurring only over the rear half of the roughness, provided that the height is large enough. Conversely, for elements centred immediately upstream of the no-roughness separation bubble (at, for example, $X_M = -1.6$ for a width of 4 in figure 6.7a), the favourable pressure perturbation that would be present were there no roughnesses is severely muted and this reduction (or, indeed, the favourable pressure gradient being replaced by an adverse gradient) could cause the separation bubble to burst at lower angles of attack when the static roughness is deployed. This impact on the pressure gradient for a roughness of height 1 and width 4 centred at $X_M = -1.6$ is shown in figure 6.8b, with figure 6.8a also indicating a slight upstream shift in the separation point and position of minimum skin friction. Roughness elements placed either far upstream or downstream have little impact on the interaction process and hence the critical parameter tends to its no-roughness value of approximately 2.756 there.

At this point, it is worth pausing briefly to explain how the value of Γ_c in figure 6.7 and later similar graphs, both in this section and the following one dealing with dynamic elements, was obtained. In the results of this section, the mesh size was set to $\Delta = 0.05$ and the endpoints of the computational domain were at ± 10 (checks on the impact of both are presented in appendix C.1; and slightly different values will be used in §6.3.2). Equation (6.43) (or equation (6.38a) for dynamic elements) was first solved for some integer $\Gamma \leq 0$ using the boundary condition (6.38b) as the initial guess. The value of Γ

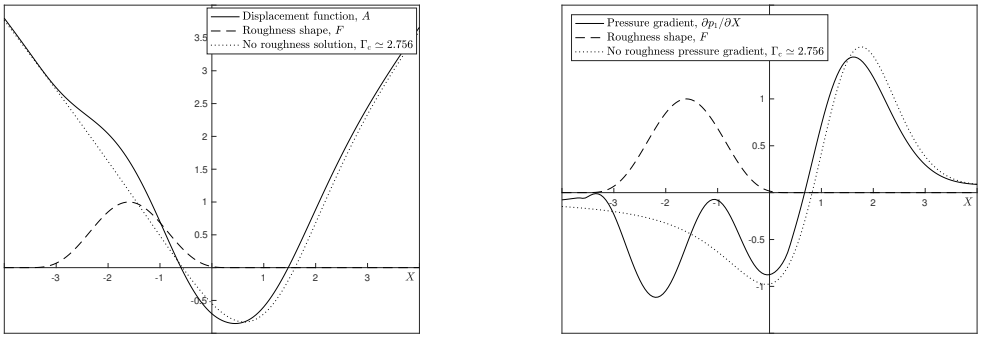

(A) Boundary layer displacement function, A (B) Perturbation pressure gradient, $\partial p_1/\partial X$

FIGURE 6.8: Solution in the case of a static roughness centred at $X_M = -1.6$, and thus with rear face covering the separation position of the flow in the no-roughness scenario at $\Gamma = \Gamma_c \simeq 2.756$ (compare dashed and dotted lines, representing the roughness shape and the no-roughness solution at $\Gamma_c \simeq 2.756$). The static roughness solution (solid line) is at $\Gamma_c \simeq 2.377$, just prior to the bubble bursting. Note that the critical value of Γ obtained is less than in the clean case. In (a), which shows the boundary layer displacement function, A, both the separation point and position of minimum skin friction occur farther upstream compared with the no-roughness solution, due to the retardation of the flow over the rear half of the roughness. This is linked to the pressure gradient, shown in (b), having a much lower favourable pressure gradient there, as expected. This considerable reduction in the favourable pressure gradient—and risk of it becoming adverse—may be the cause for the failure to sustain the laminar separation bubble at higher angles of attack.

was then increased by 1, and the solution at $\Gamma - 1$ used as the initial guess. This was repeated until no solution was found (either because the solution had diverged, with the residual greater than some large preset value, or because convergence had not been obtained within a certain predetermined maximum number of iterations). At this point, Γ was set to the last integer value at which a solution had been found and increased by 0.1, with $\Gamma - 0.1$ used as the initial guess. Repeated increases by 0.1 were performed until, once more, no convergence was achieved. A similar procedure was then repeated until Γ_c had been determined to three decimal places; and all solutions obtained along the way were stored.

Braun & Kluwick also suggested that the width of the roughness elements should be as large as possible for a favourable effect. From figure 6.9, however, we see that although this is indeed the case initially, a maximum is eventually obtained ($\Gamma_c \simeq 3.298$ for widths of 5.4–5.7 for a roughness midpoint of $X_M = 0.5$ and height of 1), with greater widths resulting in a decrease of Γ_c. Such an eventual decrease is, in truth, unavoidable, since as the width tends to infinity, the gradient of the roughness goes to zero and thus we would expect to approach the clean case solution. Further increases in width in our case were limited by the size of the computational domain.

A roughness of small width, centred at 0.5 and with a height of 1, has limited upstream influence and is thus unable to prevent separation of the flow prior to its encounter with the hump at sufficiently large angles of attack; the addition of a roughness, however, does allow for the reattachment of the flow over the front face, with separation occurring

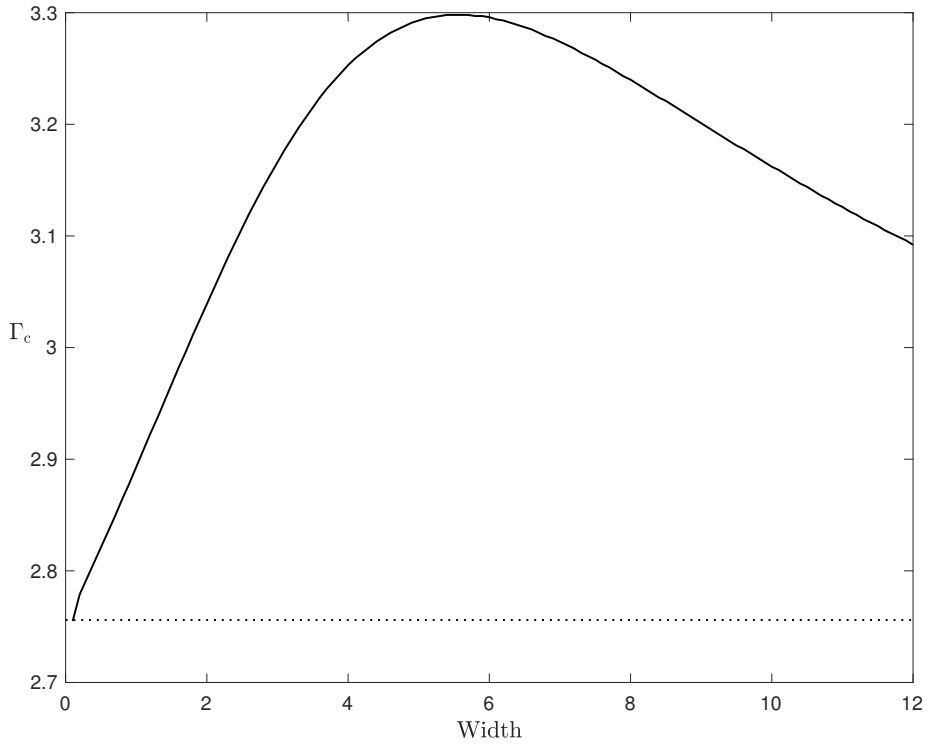

FIGURE 6.9: Impact of varying the width of a static roughness element, centred at $X_M = 0.5$ and of height 1, on the value of the critical parameter Γ_c. The horizontal dotted line gives the no-roughness value of $\Gamma_c \simeq 2.756$. A maximum in Γ_c of 3.298 is achieved for widths between 5.4 and 5.7 (the width was tested in intervals of 0.1).

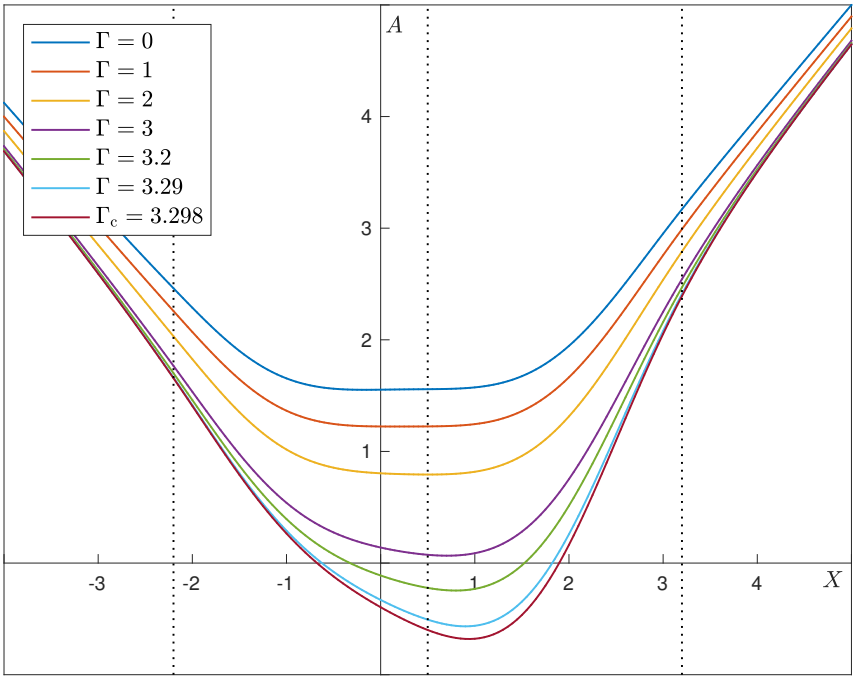

FIGURE 6.10: Plot of the boundary layer displacement function in the presence of a roughness element centred at $X_M = 0.5$, with width 5.4 and height 1, at various values of Γ (upper branch solutions), as given in the legend. At this width (which gives the maximum value of Γ_c for the above choice of roughness midpoint and height), the effect of the roughness element is to flatten out the bottom of the solution to A and attached flow is maintained even at $\Gamma = 3$. The minimum in A is also shifted downstream, occurring on the rear side of the hump, whose left-hand edge, peak and right-hand edge is indicated by the vertical dotted lines.

again over the rear, leading to the existence of two distinct separation bubbles for a range of angles of attack strictly less than that represented by Γ_c (upper branch solution only). At $\Gamma = \Gamma_c$, for all roughness widths, a single separation bubble exists, although for smaller widths an increase in the skin friction over the front face of the roughness can be seen. Larger widths, up to those corresponding to the maximum value of Γ_c, cause the boundary layer displacement function to flatten out at its minimum and the position of minimum skin friction, as Γ approaches Γ_c, is shifted considerably downstream compared to that of the no-roughness case and occurs on the rear half of the roughness element (see figure 6.10). As the width increases still further, the increase—due to the presence of the front face of the roughness—of the favourable pressure gradient as compared to the clean case begins to diminish again, as the slope of the roughness continues to decrease.

For a given width (and roughness midpoint), there is, as concluded by Braun & Kluwick, an optimal roughness height, and this is shown in figure 6.11 where, for a midpoint of $X_M = 0.5$ and width of 5.4, a maximum value of $\Gamma_c \simeq 4.057$ is obtained at heights of $a = 3.7$ and 3.8—indicating that the optimal height, since only heights that were

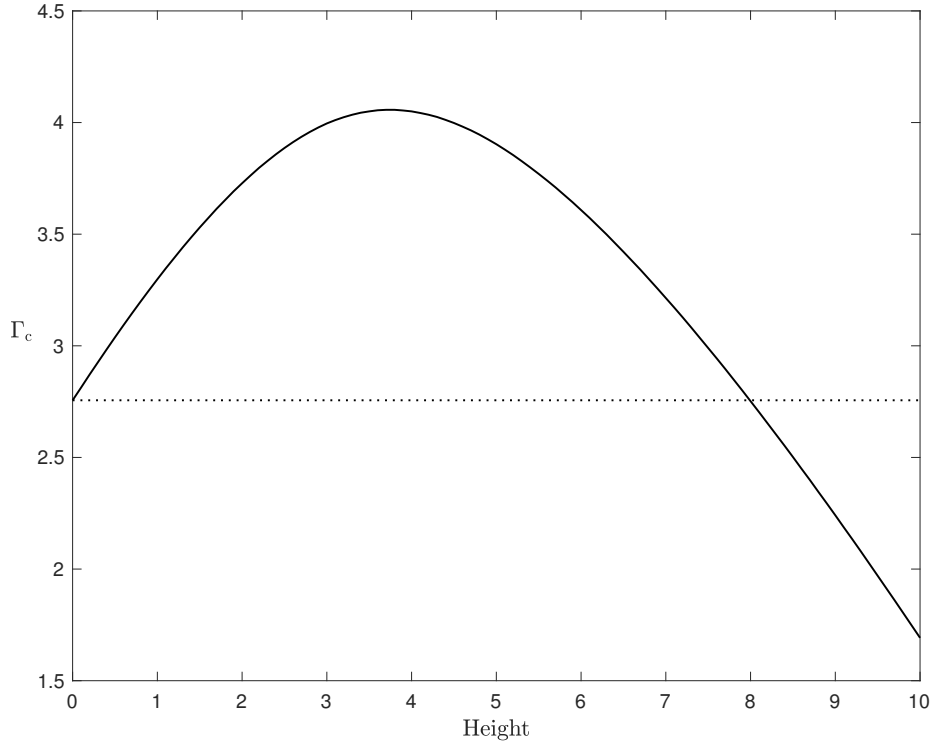

FIGURE 6.11: Impact of varying the height of a static roughness element, centred at $X_M = 0.5$ and of width 5.4, on the value of the critical parameter Γ_c, with the dotted line giving the no-roughness value of $\Gamma_c \simeq 2.756$. The impact of height is initially beneficial, with a maximum of $\Gamma_c \simeq 4.057$ reached at $a = 3.7$ and 3.8 (again, only intervals of 0.1 in the height were studied); this beneficial effect then decreases until eventually the presence of the roughness has a detrimental impact on Γ_c, at $a > 8$, approximately.

multiples of 0.1 were tested, is somewhere in-between. Increases in height are able to maintain attached flow across the whole of the airfoil leading edge region at greater angles of attack (values of Γ), although, as heights increase above 3.8, a separation bubble forms on the rear side of the roughness, due to the large adverse pressure gradient introduced. At $\Gamma = \Gamma_c$, heights greater than 3.8 are able to maintain attached flow over the roughness front face, but the flow separates over the rear and large negative values for the skin friction are obtained (dashed lines in figure 6.12a); while roughnesses with heights less than this fail to keep the flow attached over their front face, as it either separates and then reattaches ($a = 3$ in figure 6.12a) or forms a bubble extending over the roughness peak ($a = 1$ and 2 in figure 6.12a). In all cases, the front of the roughness, which, as discussed in previous chapters, would introduce a favourable pressure gradient (see figure 6.12b), causes the minimum in the skin friction to move downstream as compared to the clean case. Interestingly, this last figure indicates that for heights greater than 3.8, at which the maximum value of Γ_c is obtained, two adverse pressure peaks develop, both growing in magnitude as height increases.

The favourable impact of static roughness elements may go against conventional wisdom, which states that imperfections on a surface—due either to non-smoothness result-

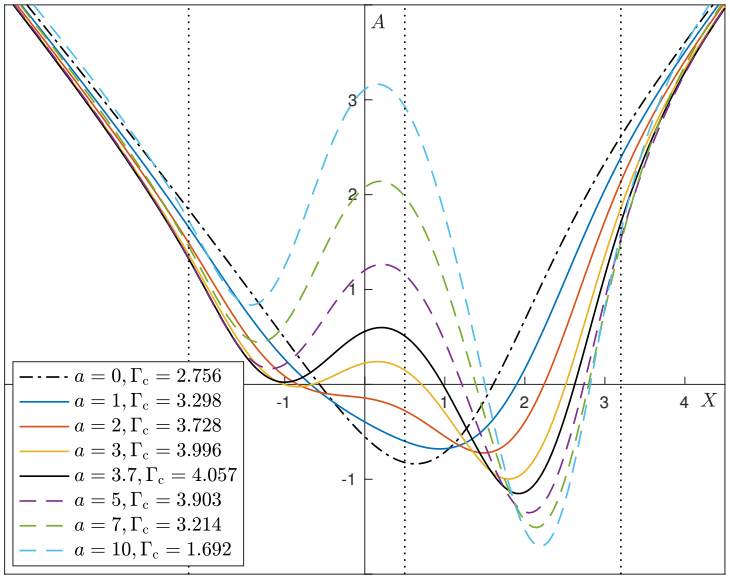

(A) Boundary layer displacement function, A

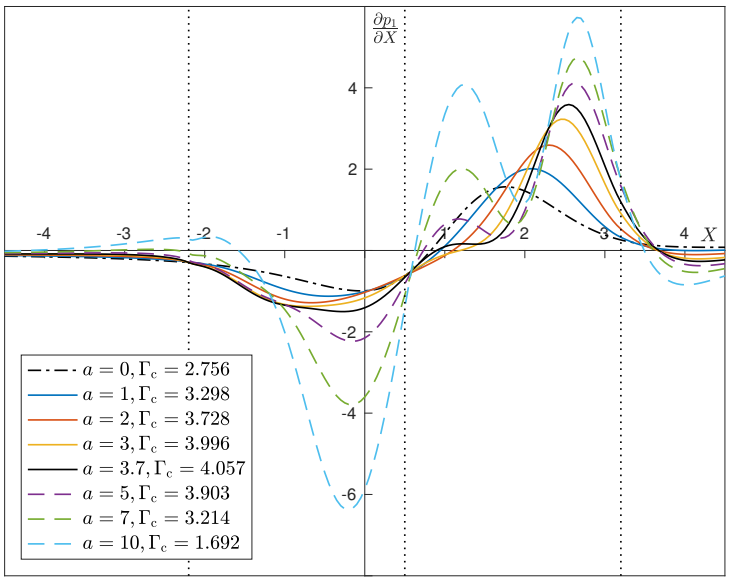

(B) Perturbation pressure gradient, $\partial p_1/\partial X$

FIGURE 6.12: The solution to (a) the boundary layer displacement function and (b) the perturbation pressure gradient at the critical value of the parameter Γ_c for various roughness heights, as given in the legend. The midpoint of the roughness element is at $X_M = 0.5$, and has left- and right-hand edges at $X_L = -2.2$ and $X_R = 3.2$, as indicated by the black dotted lines. The no-roughness solution is given by the black dot–dashed line and the solid black line is the solution for a height of 3.7, at which Γ_c obtains its maximal value. Quite distinct behaviour is seen for heights less than or greater than this. At lower heights (solid lines), separation bubbles can exist on the front half of the roughness element as well as the rear ($a = 3$, yellow line) or a continuous separation bubble can form over the front and rear halves of the element. At larger heights (dashed lines), the flow remains attached over the front half of the element, due to the larger favourable pressure gradient there, with a separation bubble, in which large negative skin frictions are found, present over the rear.

ing from the manufacturing process or dirt or debris on aircraft wings, not to mention icing—are highly detrimental to flow control and boundary layer separation [42]. Perhaps, however, the results are not so controversial: the prediction here seems to agree that large roughnesses can trigger the formation of long separation bubbles or fully separated flow at lower angles of attack than in the case of a clean airfoil; but suggests also that at smaller heights, their impact is actually advantageous. An analysis of the actual, real-life dimensions of the roughness parameters we are considering in both this section and the next will follow in §6.3.3.

On this note, we depart from the discoveries of Braun & Kluwick to determine whether similar results hold in the case of dynamic roughness elements, continuing along the Lualaba from where Dr David Livingstone's heart rests at Ilala. For upon his death, Livingston's heart was removed from his body and buried under a tree near to where he died, allowing part of him to forever remain, both emotionally and physically, in the land he loved and by the source of the quest that had consumed him. In a display of breathtaking devotion to their leader and employer, indicative of the great affection in which he was held, Amoda, Chowpereh, Chuma, Gardner, Mabruki, Sera, Susi and Uledi, along with many others whose names are lost to us, then decided to carry Livingstone's corpse, walking with it for over 1600 km *until they reached the coast at Bagamoyo and handed him over to the British, who took him away from his home and back to the isle of his birth, burying him at Westminster Abbey, where he now rests.*

6.3.2 Dynamic roughness elements

Although Braun & Kluwick introduced unsteady roughness elements into their work, which looked at the limit $\Gamma \to \Gamma_c$, the time-dependent oscillations (which were three-dimensional in character) were superimposed on a two-dimensional, steady, marginally separated boundary layer. To leading order, therefore, their hump was steady and 2D—giving rise to the same equation (6.41) and results presented in §6.3.1 above—with time dependence (and tridimensionality) appearing at second order, $\mathcal{O}(\Gamma_c - \Gamma) \ll 1$. One can consider their scenario, then, as consisting of small vibrations about a static hump shape, which go on to modify the boundary layer displacement function A at order $(\Gamma_c - \Gamma)^{1/2}$. With the second order term in A written as the product of two functions, one dependent only on the streamwise coordinate, the other on both the spanwise coordinate and time, the governing equation for the last of these was equivalent to the forced Fisher equation and allowed the authors to gain some insight into the bubble bursting phenomena both for when Γ was less than and greater than Γ_c. For $\Gamma > \Gamma_c$, infinitesimal disturbances caused the blow-up of the solution to the governing equation; while for $\Gamma < \Gamma_c$, the disturbances had to be of finite amplitude. In either case, however, the solution could be continued beyond the blow-up time and, for the latter, the upper branch solution was approached as $t \to \infty$. The lack of a steady solution when $\Gamma > \Gamma_c$, already discussed, means that a repeated pattern of bubble bursting (i.e. repeated blow-up) occurs [9].

In our work, on the other hand, we aim to keep the time dependence acting at leading order in the displacement function, with our roughness elements dropping flush with the surface before rising again, in exactly the same way as that of chapter 5. As already discussed, the fixed frequency nature of the oscillations means that we write A as the sum of Fourier modes, thereby obtaining equation (6.45a) and avoiding the need to march forward in time. The code used is described above and in appendix C.2 and gives a critical value of Γ in the no-roughness case of $\Gamma_c \simeq 2.764$: slightly higher than the value found using the numerical technique employed for the static roughness elements. The position of the separation bubble at $\Gamma = \Gamma_c$ remains between -0.55 and 1.60, however. As concluded from the numerical parameter checks presented in appendix C.2.3, in determining the impact of a roughness element on Γ_c, we used, for sweeps in roughness position and width (figures 6.13 and 6.16, along with graphs of individual solutions) a mesh size of $\Delta = 0.025$ and a computational domain between -15 and 15, with $M = 5$ in the sum (6.44a); while, for roughness height and frequency, for which simultaneous sweeps across parameter space were performed (figure 6.18), the mesh was coarsened to $\Delta = 0.05$ with endpoints at ± 10. We will look at positive roughness elements only.

Identifying first the impact of the roughness position on the value of Γ_c, figure 6.13, we find that dynamic elements seem to be less beneficial than static elements. The maximum value of Γ_c, for a dynamic roughness of width 4, height 1 and oscillation frequency $\omega = 1$, is lower than for an equivalent static roughness element: 3.039 instead of 3.253. (We remind the reader, however, that the roughness shape is slightly different in the cases of static and dynamic roughness elements, being given by the eighth-order polynomial (6.42) and the twelfth-order polynomial (6.44c) respectively. Added to this, of course, is the fact that the differing computational techniques, and associated parameters, give rise to small inconsistencies in the value of Γ_c. We trust, though, in the difference being quite minor and believe that the conclusions drawn from a comparison of the two solutions should not depend too much on the difference in shape.) The position of the roughness midpoint at which Γ_c achieves its maximal value is also shifted slightly downstream in the dynamic compared to the static case, occurring at $X_M = 0.8$ rather than $X_M = 0.5$. The shapes of the graphs are qualitatively similar: elements centred upstream of the clean separation bubble result in a decrease in Γ_c (more substantial for dynamic roughnesses—1.496 against 2.377—and a centre within the streamwise extent of the separation bubble does not guarantee an increase in Γ_c); following the peak in Γ_c, there is again a decrease with respect to the no-roughness value of $\Gamma_c \simeq 2.764$; with $\Gamma_c \to 2.764$ as $X_M \to \pm\infty$, due to the roughness' lessening impact on the interaction region.

For a roughness centred at $X_M = 0.5$, with width 4, height 1 and, in the case of a dynamic element, frequency 1, both static and dynamic roughnesses give an increase in Γ_c compared to the traditional clean airfoil scenario. Both have a convergent solution

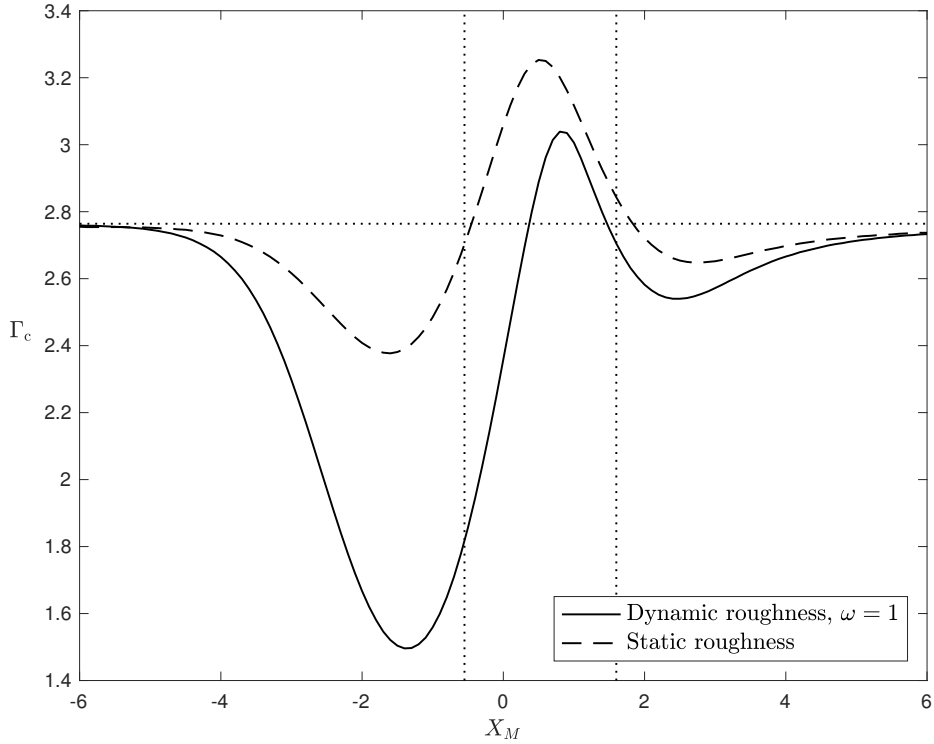

FIGURE 6.13: Impact of varying the midpoint of a dynamic roughness, which has a width of 4, a height of 1 and an oscillation frequency of $\omega = 1$, on the critical value of Γ (Γ_c). The results for a static roughness of the same width and height are also shown (dashed line), along with the value $\Gamma_c \simeq 2.764$ for the clean airfoil. The vertical dotted lines indicate the streamwise extent of the separation bubble at $\Gamma = \Gamma_c$ in the clean case.

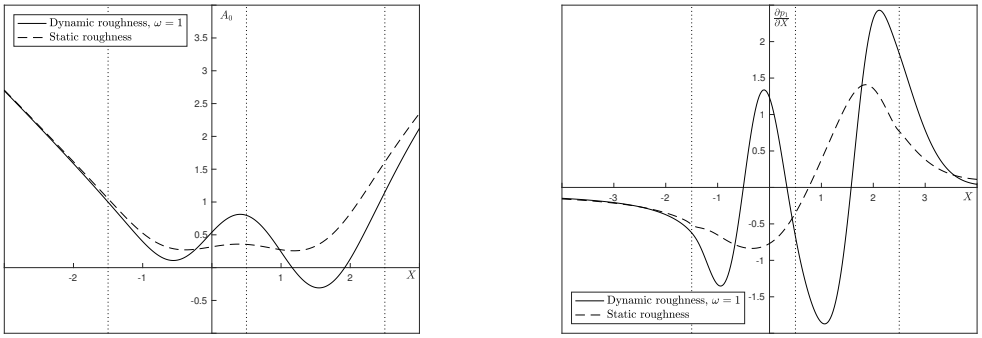

(A) Boundary layer displacement function, A_0 (B) Perturbation pressure gradient, $\partial p_1/\partial X$

FIGURE 6.14: Comparison of the dynamic (solid line) and static (dashed) roughness solutions for an element centred at $X_M = 0.5$, of width 1, height 1 and, in the case of a dynamic roughness, oscillation frequency $\omega = 1$. The parameter Γ equals 2.8 and thus it is the upper branch solution that is shown. The dotted lines indicate the start, midpoint and end of the roughness element.

at $\Gamma = 2.8$ and the upper branch result is plotted in figure 6.14.[10] Looking first at the displacement function—where we understand that both here and in the future, by displacement function we mean, for the dynamic roughness, the steady Fourier mode A_0—the impact of the front and rear faces of the roughness element is more clearly seen for a dynamic element: the increase in A_0 is greater over the front face of the roughness, as is the decrease over the rear face. At $\Gamma = 2.8$, the static roughness solution has not yet formed a separation bubble; but for the dynamic roughness, a small bubble is already visible over the rear face. The existence of this bubble persists all the way to $\Gamma_c \simeq 2.888$, above which no solution exists for the dynamic roughness defined above, but the flow continues to remain attached over the front face of the roughness (figure 6.15). This is to be contrasted with the static roughness solution at its $\Gamma_c \simeq 3.253$ (larger than for the dynamic roughness), where the bubble is much larger, separation having occurred on the increasing side of the roughness.

The behaviour of the perturbation pressure gradient (figures 6.14b and 6.15b) is rather different for the dynamic and static roughnesses. Although the latter largely follows the same shape as the clean case solution at $\Gamma < \Gamma_c$, the former has two favourable and two adverse pressure gradient peaks, with an adverse and favourable pressure gradient existing respectively over the front and back sides of the roughness, the physical reason behind their existence being unclear. All peaks are larger in the dynamic case than those present in the static for $\Gamma = 2.8$ (figure 6.14) and increase in size as Γ_c is approached.

Although an analysis of the impact of roughness position on the value of Γ_c suggests that dynamic roughnesses are less advantageous than static elements, a plot of the effect of roughness width (centred at $X_M = 0.5$, height 1, $\omega = 1$) indicates that this is not necessarily so. While, as discussed in §6.3.1, Γ_c initially increases with increasing static roughness width, before achieving a maximum and then decreasing, for a

[10] Again, only upper branch solutions or those at $\Gamma = \Gamma_c$ will be shown in this section.

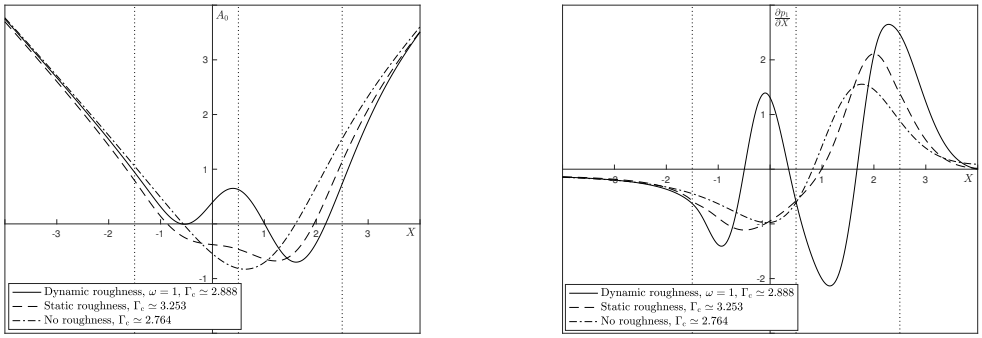

(A) Boundary layer displacement function, A_0 (B) Perturbation pressure gradient, $\partial p_1/\partial X$

FIGURE 6.15: Comparison of the dynamic (solid line) and static (dashed) roughness solutions for an element centred at $X_M = 0.5$, of width 1, height 1 and, in the case of a dynamic roughness, oscillation frequency $\omega = 1$, along with the no-roughness solution (dot–dashed). The solution for all is that at $\Gamma = \Gamma_c$, which equals approximately 2.888 in the dynamic case, 3.253 in the static and 2.764 in the clean. The separation bubble only exists on the rear half of the roughness element in the dynamic case, while the flow separates over the front half in the static case, although the increment in angle of attack is higher. The dotted lines indicate the start, midpoint and end of the roughness element.

dynamic roughness, at the widths plotted in figure 6.16, the value of the critical parameter continues to increase monotonically, becoming greater than its corresponding static roughness value at a width of 7.8, at which $\Gamma_c \simeq 3.247$. For the same reasons outlined previously, we predict that Γ_c will eventually reach a maximum at some dynamic roughness width (figure 6.16 suggests that this will indeed be the case) before decreasing again towards the clean airfoil value, but the width of the roughnesses tested was limited by the size of the computational domain.

The presence of a common $\Gamma_c \simeq 3.247$ at a width of 7.8 allows us to compare the solutions for the static and dynamic roughness elements. We note first that for the static roughness, from our analysis of it in §6.3.1 above, the value of Γ_c is decreasing and this leads to a behaviour in the displacement function that sees a 'bottoming out' of the minimum, with the impact of the front and rear halves of the roughness less clearly seen: it was suggested that this was due to the more gentle gradient of the roughness slopes. This is confirmed in figures 6.17a and 6.17c, for $\Gamma = 3$ and $\Gamma_c \simeq 3.247$ respectively. Comparing this now with a dynamic element, at $\Gamma = 3$, the flow remains fully attached across the whole interaction region, with the minimum in the skin friction being pushed quite significantly downstream due to the influence of the front half of the roughness. The double adverse/favourable pressure gradient peaks seen for smaller widths (figures 6.14 and 6.15) are no longer seen (figure 6.17b) but the magnitude of the favourable pressure gradient peak is less than that of the static roughness and the size of the adverse pressure peak is greater, despite the maintenance of attached flow for the dynamic element. This last fact is perhaps due to the extension of the region of favourable pressure gradients, with the position at which the gradient switches from being favourable to adverse being somewhat delayed and this may compensate for the

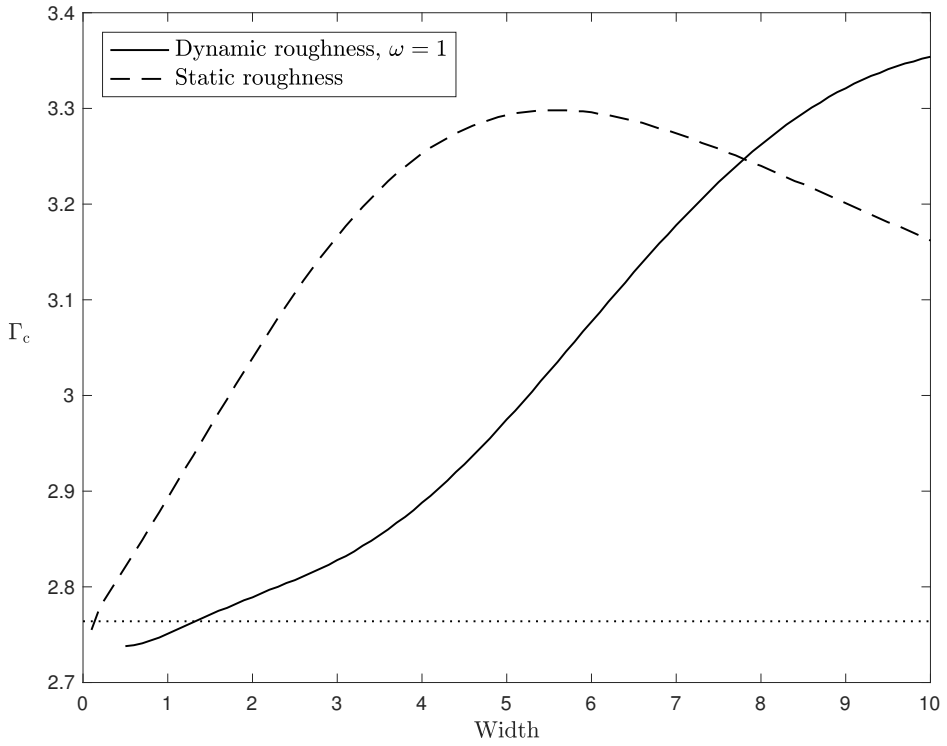

FIGURE 6.16: Impact of varying the roughness width on Γ_c for elements centred at $X_M = 0.5$, height 1 and oscillation frequency (in the case of a dynamic roughness, solid line) of $\omega = 1$. The maximum width tested was limited by the size of the computational domain. The graphs for a static and dynamic roughness cross at a width of 7.8. The horizontal dotted line once more denotes the no-roughness value of $\Gamma_c \simeq 2.764$.

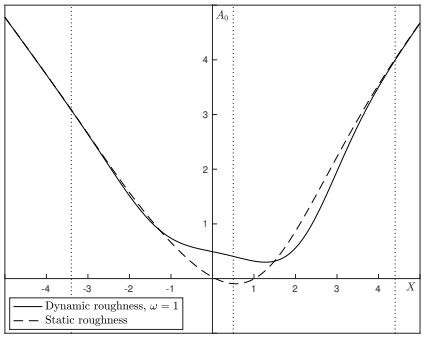

(A) Boundary layer displacement, $\Gamma = 3$

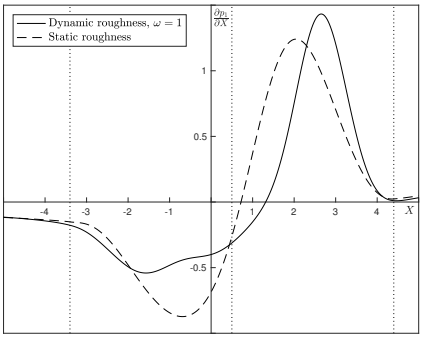

(B) Pressure gradient, $\Gamma = 3$

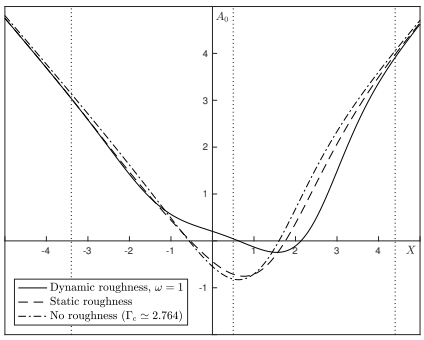

(C) Boundary layer displacement, $\Gamma_c \simeq 3.247$

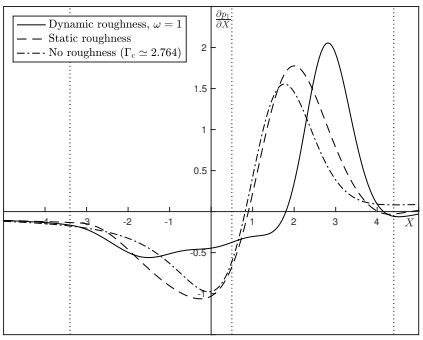

(D) Pressure gradient, $\Gamma_c \simeq 3.247$

FIGURE 6.17: Comparison of the dynamic (solid lines) and static (dashed lines) boundary layer displacements and perturbation pressure gradients for (a, b) $\Gamma = 3$ and (c, d) $\Gamma_c \simeq 3.247$, the critical value of the parameter Γ being shared by both static and roughness elements if they have a width of 7.8, a midpoint of 0.5 and a height of 1, along with an oscillation frequency of $\omega = 1$ for the dynamic roughness. As a means of comparison, the no-roughness solution at its $\Gamma_c \simeq 2.764$ (lower than in the roughness case) is shown as the dot–dashed line in (c) and (d).

decrease/increase in the favourable/adverse pressure gradient (see also figure 6.17d). This downstream shift in the position at which the pressure gradient becomes adverse is seen only for wider roughness elements, with narrow roughnesses, as seen in figures 6.14 and 6.15, introducing a double-peaked structure that provides for alternating regions of favourable and adverse pressure gradients.

Given the fact that greater increases in Γ_c were seen for the widest of the widths tested, for an analysis of the impact of the height (a) and oscillation frequency (ω) of the dynamic roughness on the value of Γ_c, we make use of a roughness element of width 10, centred at 0.8 (and hence with left-hand edge at -4.2 and right-hand edge at 5.8).[11]

[11] The first width tested was actually of 5.4, again centred at 0.8: the contours of Γ_c showed a similar behaviour to those in figure 6.18, for roughness amplitudes up to 2 and frequencies up to $\omega = 10$. The values of Γ_c obtained were, however, a lot lower than those for a width of 10, with decreases in Γ_c compared to the no-roughness case observed for much lower heights.

A contour plot of Γ_c, similar to those presented in chapter 5, is shown in figure 6.18. The value of Γ_c for each combination of height and frequency was once more obtained by starting off from a negative value of Γ, finding the solution for that value using the condition (6.38b) as the initial guess, then increasing Γ by 1 and finding the solution using that at $\Gamma - 1$ as the initial guess. The increases in Γ were then refined until we reached a value of Γ_c accurate to within 0.001. The resulting graph had some isolated regions, especially at higher frequencies, where the process of increasing Γ first by 1, then 0.1, then 0.01, then 0.001 had, for a reason that is unclear, failed to converge at choices of Γ that were far lower than the value of Γ_c for heights/frequencies immediately around them. In these cases, we began the above procedure at the value of Γ where convergence had not been achieved using as an initial guess the solution at the same Γ that was found at a neighbouring combination of (a, ω). This served to remove the discontinuities in Γ_c as a function of height and frequency, although some small kinks in the graph remain, especially at $\omega = 7.5$ and 9.4, where, regardless of the initial guess used, convergence was not obtained at larger Γ.

As already mentioned, due to the computational time required to produce figure 6.18, the mesh parameters were modified slightly compared to those used to produce previous figures, with $\Delta = 0.05$ and endpoints at ± 10. The accuracy of the results must necessarily suffer, but the mesh checks of appendix C.2.3 show good agreement throughout and the time required to produce figure 6.18 would otherwise have been prohibitively long. Further tests were performed to check that a choice of $M = 5$ in the sum (6.44a) was still sufficient, especially at high frequency and amplitude: there was no change in the value of Γ_c (to three decimal places) for both $M = 5$ and $M = 10$, with $\omega = 10$ and $a = 8, 9, 10$.

It was noticed that at larger heights, where Γ_c is much lower than its clean case value, convergence took a considerably large number of iterations (up to 100) as Γ approached Γ_c and there were problems with the iteration process as the Jacobian matrix became close to singular, as would be expected for $\Gamma \simeq \Gamma_c$. In these circumstances, a smaller increase in Γ from the previous convergent result, as imposed by the numerical scheme, often allowed for a solution at a higher value of Γ to be found: the final Γ_c was then the highest value of Γ at which convergence was obtained. For these reasons—the singular nature of the Jacobian matrix and the procedure through which Γ_c was chosen, along with the continuous behaviour of the contours in figure 6.18—we believe the results to be, if not completely quantitatively accurate, qualitatively robust and the elevated values of Γ_c seen, indicating an ability to maintain, at worst, a small laminar separation bubble at higher angles of attack (see also §6.3.3), are certainly promising.

The increases in Γ_c observed, on which we will focus, seem to be due to two distinct behaviours in the solution to the time-averaged displacement function (equivalently, the steady Fourier mode A_0 and the time-averaged skin friction) and, more pertinently, the interaction pressure gradient. The first of these behaviours occurs at lower roughness amplitudes and the graphs of both the displacement function and pressure gradient, at

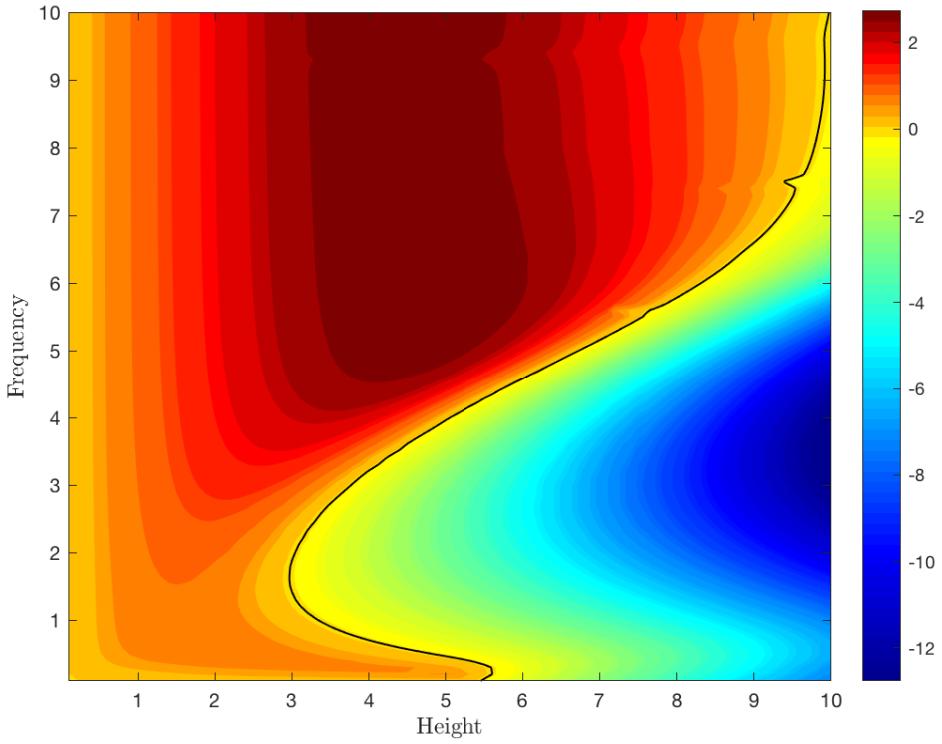

FIGURE 6.18: Impact of varying the roughness height (a) and oscillation frequency (ω) on the value of Γ_c, for an element centred at $X_M = 0.8$ and of width 10. The numbers represent an increase (red) or decrease (blue) on the critical value of Γ in the no-roughness case, $\Gamma_c \simeq 2.764$, while the contour depicted in black indicates the choice of height and frequency for which Γ_c is the same as in the clean case. The increment in both a and ω was of 0.1. Up to a height of approximately 2.9, therefore, only an increase in Γ_c is seen across all frequencies. At larger heights, decreases become possible and these can become quite significant at larger heights. An increase in oscillation frequency, however, is seen to be highly favourable, with beneficial values of Γ_c obtained provided that one lies above the curve shown in black. The maximum value of Γ_c obtained was at a height of 4.4 and frequency of 10, with $\Gamma_c \simeq 5.633$—over double the no-roughness figure.

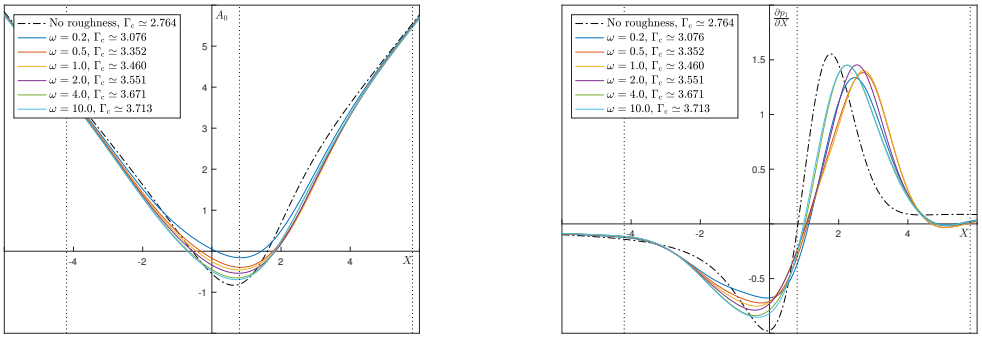

(A) Boundary layer displacement function, A_0 (B) Perturbation pressure gradient, $\partial p_1/\partial X$

FIGURE 6.19: The solution to (a) the boundary layer displacement function (or skin friction) and (b) the perturbation pressure gradient for a roughness of height 1, of various frequencies of oscillation (ω) and at $\Gamma = \Gamma_c$, as shown in the legend. The roughnesses were all centred at $X_M = 0.8$ and had width 10, giving a left-hand edge, midpoint and right-hand edge as indicated by the dotted lines in the figure. The roughness position will remain unchanged throughout the remainder of the graphs presented in this section. The no-roughness solution at $\Gamma_c \simeq 2.764$ is given by the black dot–dashed line. The value of Γ_c for the roughness elements is higher than that of the clean case at all frequencies shown and the minimum in the skin friction is greater and occurs farther downstream; the adverse pressure peak, meanwhile, is lower and is also positioned farther downstream.

$a = 1$, $\Gamma = \Gamma_c$ and for varying ω, are shown in figure 6.19. Studying first the skin friction, figure 6.19a, as ω increases, the size of the bubble that forms at Γ_c increases, with separation occurring farther upstream and reattachment farther downstream. Note, however, that the value of Γ_c is also increasing with ω. Hand in hand with this, the minimum in the skin friction decreases; although, at all frequencies, it remains higher than in the no-roughness case, which has a much lower value of Γ_c than that at all frequencies shown (2.764 compared with 3.076 at $\omega = 0.2$). The effect of the front face of the roughness element remains that of slowing down the decrease in skin friction by speeding up the flow, and the minimum in A_0 occurs at or just after the roughness peak.

The solution for the perturbation pressure gradient provides an indication into the physical mechanism through which the increase in Γ_c is possible. Figure 6.19b shows that, notwithstanding the fact that we are at Γ_c, which is higher than in the clean case, the adverse pressure peak is lower than that of the no-roughness solution at $\Gamma = \Gamma_c$. As might be expected, since the value of Γ_c increases with increasing ω, this peak becomes larger at the larger frequencies shown, but nevertheless remains smaller than the no-roughness peak, even at $\omega = 10$ and $\Gamma_c \simeq 3.713$. The adverse peak also occurs downstream of that in the clean case, moving upstream as ω increases; and we note that a high frequency solution seems to be approached, with little difference between the graphs at $\omega = 4$ (green line) and $\omega = 10$ (light blue line). The expected behaviour of this peak, increasing with Γ, is confirmed in figure 6.20b. In the presence of a dynamic roughness element, the position at which the perturbation pressure gradient becomes adverse also moves downstream compared to when the roughness is absent.

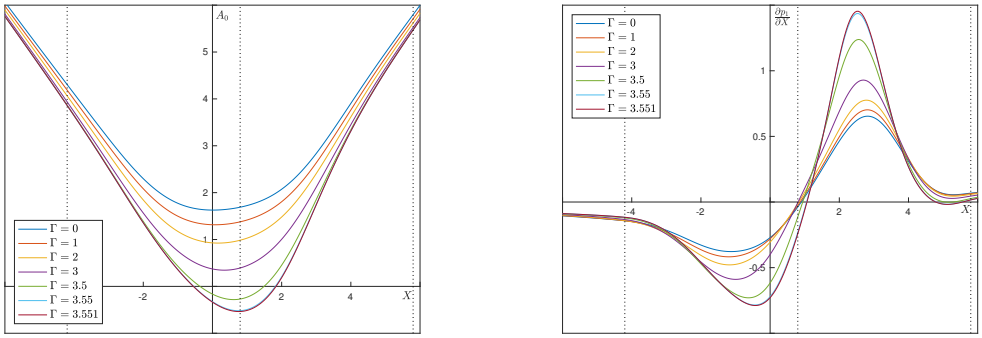

(A) Boundary layer displacement function, A_0 (B) Perturbation pressure gradient, $\partial p_1/\partial X$

FIGURE 6.20: The solution to (a) the boundary layer displacement function and (b) the perturbation pressure gradient for a dynamic roughness of height 1 and oscillation frequency 2, as Γ is increased towards Γ_c. As would be expected, the minimum in the skin friction decreases, with the separation bubble having formed by $\Gamma = 3.5$; and both the favourable and adverse pressure gradient peaks increase in magnitude.

This decrease in the peak of the adverse pressure gradient is not seen when the height is increased to 2. At all frequencies studied, and those plotted in figure 6.21b, the peak is higher than in the clean airfoil case at $\Gamma = \Gamma_c$, although we remind the reader that the value of Γ_c is much larger ($\Gamma_c \simeq 4.557$ at $\omega = 10$). If we expect it to be the adverse pressure peak that bursts the laminar separation bubble and produces fully separated flow, then the mechanism that keeps it in existence here must be different. Indeed, figure 6.21b suggests that it is the considerable extension of the region in which the pressure gradient is favourable (in some regions becoming adverse downstream of the adverse peak in the clean case) that allows for greater values of Γ at which a solution to the system (6.38) can be found. Such an impact on the pressure gradient is perhaps to be expected from the steeper slope of the front face of the roughness, which introduces favourable pressure perturbations; and then, also, the corresponding steeper slope on the rear face, which slows down the flow and gives rise to adverse pressure gradients. Figure 6.22, in which the solution for a roughness of height and oscillation frequency equal to 2 is plotted at increasing Γ, shows that, unsurprisingly now, the adverse pressure gradient peak is larger at larger angles of attack but that also the position at which the pressure gradient becomes adverse is also delayed further at greater Γ. It is unclear, physically, why this is the case but it does agree with the behaviour seen throughout, even in the clean case (figure 6.5).

The graph of the skin friction at Γ_c for $a = 2$, figure 6.21a, has another surprise in store: at lower oscillation frequencies, no separation bubble exists! (This is confirmed also in figure 6.22a, which plots the skin friction for $\omega = 2$ at increasing Γ, and in which A_0 remains resolutely positive throughout.) The minimum in the skin friction is shifted considerably downstream compared to the clean case solution, as would be expected if the perturbation pressure gradient remains favourable for a greater streamwise distance, but a passage from fully attached to fully separated flow (or the existence of a longer

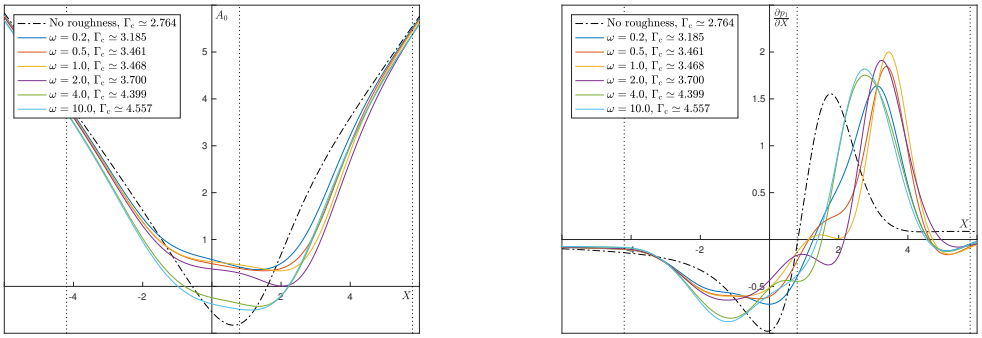

(A) Boundary layer displacement function, A_0 (B) Perturbation pressure gradient, $\partial p_1/\partial X$

FIGURE 6.21: As per figure 6.19, but for a roughness of height 2 and ω and Γ_c as shown in the legend. The displacement function (a) indicates that a separation bubble is not necessarily present at $\Gamma = \Gamma_c$; while the perturbation pressure gradient (b) has larger magnitudes in the peak adverse pressure gradient compared to the clean case (and the smaller roughnesses shown in figure 6.19b) but the gradient becomes adverse farther downstream.

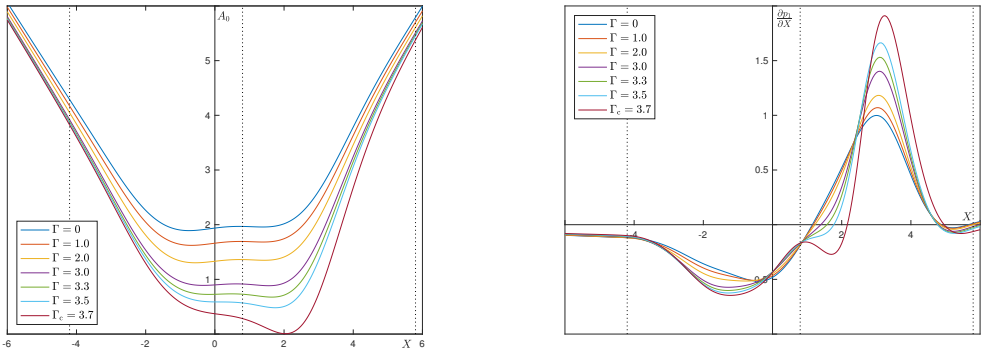

(A) Boundary layer displacement function, A_0 (B) Perturbation pressure gradient, $\partial p_1/\partial X$

FIGURE 6.22: The solution to (a) the boundary layer displacement function and (b) the perturbation pressure gradient for a dynamic roughness of height 2 and oscillation frequency 2, as Γ is increased towards Γ_c.

bubble) occurs without the bursting of any smaller bubble in the interaction region. With increasing frequency (and hence Γ_c), the minimum in A_0 decreases until eventually a bubble is formed, growing larger with ω.

At larger heights, as the oscillation frequency is increased from 0.1, figure 6.18 shows the value of Γ_c begin to decrease, reach a minimum, and then increase again. This minimum can be much less than the $\Gamma_c \simeq 2.764$ of the clean case. The behaviour when $a = 4$, for varying ω and at $\Gamma = \Gamma_c$, is given in figure 6.23. Once more, a separation bubble does not necessarily form and, when it does, it exists on the rear side of the roughness element, with $\omega = 6$ (where $\Gamma_c \simeq 5.558$) showing an additional small bubble over the front side. Looking at the perturbation pressure gradient, figure 6.23b, in all cases, including those in which Γ_c is lower, the adverse peak is higher than in the clean case, but is shifted considerably downstream; furthermore, at lower frequencies ($\omega = 2$,

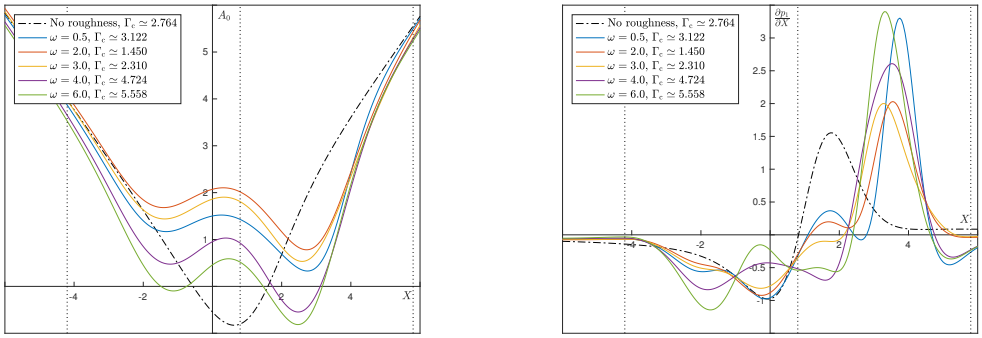

(A) Boundary layer displacement function, A_0 (B) Perturbation pressure gradient, $\partial p_1/\partial X$

FIGURE 6.23: As per figure 6.19, but for a roughness of height 4 and ω and Γ_c as shown in the legend. The frequencies chosen represent an initial increase in the value of Γ_c ($\omega = 0.5$, blue line) as compared to the clean case, the minimum in Γ_c obtained for a height of 4 ($\omega = 2$, red line), an increase in Γ_c compared to this minimum ($\omega = 3$, yellow line) and then the high values possible at large frequencies ($\omega = 4$ and 6, purple and green lines respectively).

red line), the downstream shift in the position at which the gradient becomes positive is small, while the favourable pressure gradients seen at larger frequencies remain quite considerable for an extended streamwise distance. At $\omega = 0.5$ ($\Gamma_c \simeq 3.122$), the pressure gradient becomes favourable early on relative to the solution at higher frequencies, but a second small region of favourable pressure gradient occurs later downstream.

The suggestion, therefore, is that although the heights are larger than those corresponding to the two behaviours described previously ($a = 1$ and 2), those amplitudes where Γ_c decreases compared to its value in the clean case show a mixture of these two behaviours. The solutions for $\omega = 0.5$, 1, 2 and 4—corresponding, respectively, to Γ_c being higher (3.122) than its clean case value; lower (2.270) and still decreasing with increasing ω; the minimum (1.450) for $a = 4$; and higher (4.724) than the clean case value—are shown in figure 6.24 for $\Gamma = 0, 1, 1.4$ and 1.45, the latter being approximately equal to Γ_c at $\omega = 2$. Focusing first on the pressure gradient (e, f, g, h), at all values of Γ, the adverse pressure peak is largest for $\omega = 2$ (dot–dashed line) and increases quite dramatically, compared to the other solutions shown, between $\Gamma = 0$ and $\Gamma = 1$. (Comparing the solutions at $\Gamma = 1$ and 1.4 show the peak move noticeably downstream rather than increase; and a further increase to $\Gamma_c \simeq 1.450$ actually sees the peak decrease in size.) The solution for $\omega = 1$ (dashed line), where $\Gamma_c \simeq 2.270$ and thus is also less than the clean case, has a peak that, by $\Gamma = 1.45$, is of similar size as that for $\omega = 4$ but does not benefit from the latter's downstream shift in the position at which the pressure gradient becomes adverse. Throughout, the solution for $\omega = 0.5$ retains the smallest peak and the position at which the gradient switches from favourable to adverse remains largely unchanged.

Similarly, the minimum in the skin friction (a, b, c, d) is lowest for $\omega = 2$ and, by the time $\Gamma = 1.45$, the solution for $\omega = 1$ has the second-lowest minimum. From the graphs of A_0, it is unclear why the minimum could not decrease further until a separation

bubble, which then bursts, is formed: perhaps it is the pressure gradient that provides the clue here, with only a maximum adverse pressure gradient being supported before an extended region of separated flow forms that cannot be accommodated by marginal separation theory.

6.3.3 The maths to engineering dictionary

Having dwelt for so long in the mathematical setting of marginal separation theory, we extricate ourselves now from the thicket of Reynolds numbers, non-dimensional parameters and scalings in order to compare the dynamic roughness elements and results we have studied and obtained with the experimental work of Grager et al. [33]. As referred to in chapter 1, these experiments consisted of air flowing over an array of elements mounted on a NACA 0012 airfoil, with the roughnesses oscillating at frequencies between 30 and 90 Hz. The Reynolds number was changed by modifying the incoming velocity in the wind tunnel and the roughness elements were able to increase the angle of attack, which was in the teens, at which separated flow was first observed by 2 to 3 degrees (refer back to figure 1.4).

Our results agree that, in the presence of either static (§6.3.1) or dynamic (§6.3.2) roughness elements, it is possible to increase the critical angle of attack at which a larger region of separated flow, either in the form of a large separation bubble or complete airfoil stall, will develop from the leading edge of a wing. Such an increase is, however, highly sensitive on the physical parameters of the roughness—its position, width, height and oscillation frequency—and the incorrect choice of any of these will lead to a decrease in the angle of attack. In the above §6.3.2, we focused mainly on dynamic roughnesses centred at the non-dimensional streamwise position $X_M = 0.8$ and non-dimensional width 10 and, from this choice, produced figure 6.18 to illustrate the impact of the height and frequency on the value of Γ_c.

This showed that up to a certain height (approximately equal to 2.9), an increase in the critical angle of attack was possible at all oscillation frequencies, with greater heights and frequencies being most beneficial. In certain regions of figure 6.18, there seems to be an inverse relationship between amplitude and frequency as suggested by Huebsch et al. [41] and, although heights larger than 2.9 can give rise to decreases in Γ_c as compared to the no-roughness case, by increasing the frequency one can return to larger values of Γ_c; and larger frequencies, for all heights plotted, are most effective.

There are, of course, some fundamental differences between our mathematical study and the experiments of Grager et al. Firstly, the latter looked at an array of three dimensional roughness elements rather than our solitary, 2D element. This array spanned a region from 1.07 % chord to 10.76 % chord and hence was much larger than the marginal separation length scale in which our roughness was found, although we can compare the width of our element with the diameter of theirs. Secondly, for the roughnesses studied experimentally, the oscillations were not of the same order as the roughness

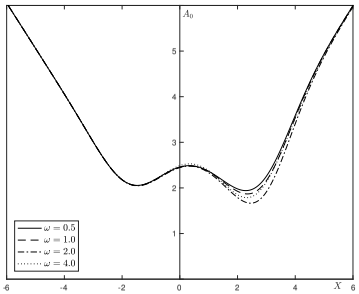

(A) $\Gamma = 0$, A_0

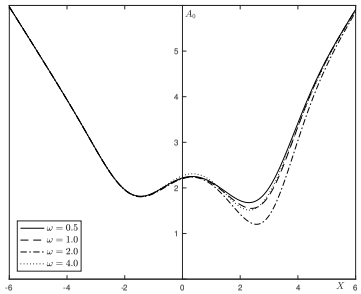

(B) $\Gamma = 1$, A_0

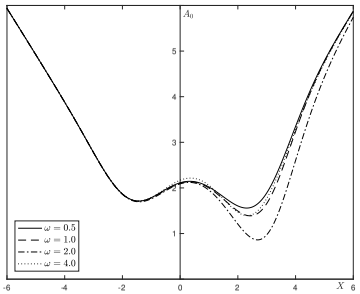

(C) $\Gamma = 1.4$, A_0

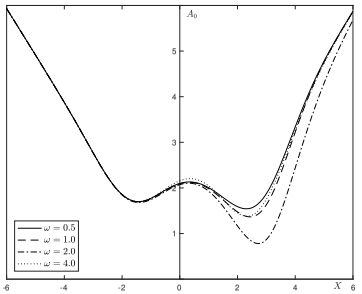

(D) $\Gamma = 1.45$, A_0

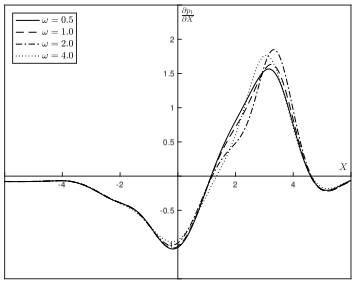

(E) $\Gamma = 0$, $\partial p_1/\partial X$

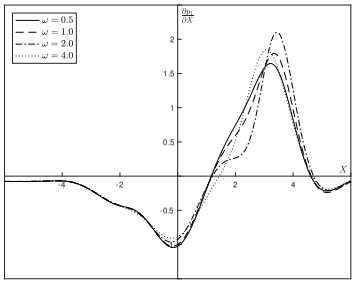

(F) $\Gamma = 1$, $\partial p_1/\partial X$

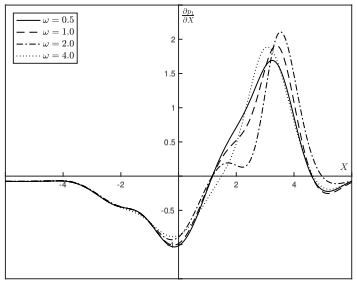

(G) $\Gamma = 1.4$, $\partial p_1/\partial X$

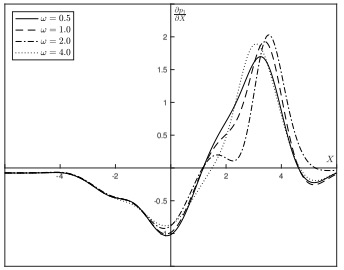

(H) $\Gamma = 1.45$, $\partial p_1/\partial X$

FIGURE 6.24: Solution to the skin friction (a–d) and perturbation pressure gradient (e–h) for a dynamic roughness element with height 4 and oscillation frequencies $\omega = 0.5$ (solid line), 1 (dashed), 2 (dot–dashed) and 4 (dotted) at various values of Γ, as given in the captions, up to $\Gamma = 1.45$. This value is, for fixed $a = 4$, the minimum in Γ_c as a function of ω, occurring at $\omega = 2$. The corresponding solution at $\omega = 2$ has many of the traits in skin friction and pressure gradient indicative of an imminent failure of the system (6.38) to converge to a solution occurring at lower values of Γ. These include the lower minimum in A_0 as compared to that obtained at other frequencies for the same choice of Γ and an elevated adverse peak in the pressure gradient, which may play a role in triggering the onset of larger regions of separated flow not accommodated by marginal separation theory despite the absence of any small laminar separation bubble.

height but were vibrations of around 25 % of the maximum height. In this way, the experimental set-up perhaps corresponds more closely with the work of Braun & Kluwick [9] described throughout §6.3, which showed similar favourable results but linked the increase in critical angle of attack to the presence of a bump on the surface and the latter's oscillatory motion to the control of the blow-up of laminar separation bubbles and shedding of vortices into the bulk of the boundary layer.

Nevertheless, it is of interest to convert the scaled roughness parameters introduced here into their dimensional counterparts, with a view then to determining whether they are comparable with those that have been studied in the past and whether the results predict similar increases in the angle of attack. The properties of a single roughness appearing in Grager et al. are as follows: the diameter was 3 mm, the height 230 µm and the frequencies tested were from 30 Hz to 90 Hz. The Reynolds numbers tested were of 25 000, 49 000, 73 000 and 97 000 and these were based on the airfoil chord length, which was of 0.15 m, and corresponded to an incoming air speed of $2.7\,\mathrm{m\,s^{-1}}$, $5.3\,\mathrm{m\,s^{-1}}$, $7.3\,\mathrm{m\,s^{-1}}$ and $9.7\,\mathrm{m\,s^{-1}}$. From this, we will take the kinematic viscosity of air to be $1.6 \times 10^{-5}\,\mathrm{m^2\,s^{-1}}$.

The Reynolds number used throughout this section was, however, based on the leading edge radius of the airfoil, which, in Grager et al., was a NACA 0012. For these four-digit '00xx' airfoils, the leading edge can be approximated by a cylinder of radius

$$r = 1.1019 \left(\frac{\mathrm{xx}}{100}\right)^2 L$$

[43], where L is the chord length. Hence, for the airfoil of Grager et al., we obtain $r \approx 2.4 \times 10^{-3}\,\mathrm{m}$ and leading edge Reynolds numbers of 405, 795, 1170 and 1560. In §6.1.1, we stated that the angle of attack (α) was of order $(L/r)^{-1/2}$ and we later worked with k, which was related to α by the expression

$$k = \alpha\sqrt{2}.$$

We therefore find ourselves at angles of attack of around 10°, similar to the experimental study. The roughness parameter scalings were derived in §6.2 and are dependent on the Reynolds number itself: table 6.3 therefore presents the corresponding width, height and oscillation frequency for a roughness in which all of the three are set to unity and, importantly, the order of magnitude of the increment in Γ_c. This ignores, admittedly, the affine transformation that was introduced in §6.2.2, containing as it does various constants whose values have not been introduced, but all the same it gives a rough estimate of the sizes involved.

As shown in table 6.3, the scalings of marginal separation theory give rise to roughness elements that are an order of magnitude smaller than those studied previously, and a frequency that is several orders of magnitude larger (kilohertz as opposed to tens of hertz). The dynamic roughnesses themselves are therefore not comparable, but the magnitude of the increase in angle of attack possible prior to stall occurring is

Reynolds number Re	Width $\mathrm{Re}^{-\frac{1}{5}}r$	Height $\mathrm{Re}^{-\frac{7}{10}}r$	Frequency $\mathrm{Re}^{-\frac{1}{20}}(U_\mathrm{e}/r)$	Angle of attack increment $\mathrm{Re}^{-\frac{2}{5}}$
405	0.72 mm	36 µm	800 Hz	5.2°
795	0.63 mm	22 µm	1.5 kHz	4.0°
1170	0.58 mm	17 µm	2.1 kHz	3.4°
1560	0.55 mm	14 µm	2.8 kHz	3.0°

TABLE 6.3: Dimensional roughness parameters, based on the Reynolds number reported in Grager et al. [33], converted so as to use the airfoil leading edge radius ($r \approx 2.4 \times 10^{-3}$ m) as the length scale. These parameters, and the increase in angle of attack possible, are to be compared with the values given in the text.

significantly larger than the couple of degrees identified by Grager et al.[12] The fact that we are acting at such high frequencies also perhaps provides further support for previous conclusions that suggest greater scope for flow control at higher frequencies. Moreover, although the scalings of marginal separation theory are undoubtedly coincidental, it is striking that they seem to validate the numerical and experimental results of Huebsch et al. that required smaller roughness amplitudes to be compensated by greater roughness frequencies to maintain attached flow [41]. On the other hand, the detrimental impact of increasing the roughness height, as it tends towards the heights studied previously, and the continued necessary increases in ω to retain a beneficial effect, does not agree with existing experimental observations.

6.4 The final few paces, and then some

The ability of marginal separation theory, described in §6.2, to predict not only the presence of laminar separation bubbles, which have been observed experimentally near the leading edge of an airfoil, but also the angle of attack at which such bubbles no longer exist, has been exploited in this chapter to determine the impact of roughness elements on aerodynamic stall. The prevailing belief is that the breakdown of marginal separation theory is caused by the bursting of its small regions of separated flow into larger regions that extend over a significant proportion of an aircraft wing, resulting in increased drag and decreased lift [93]. The idea here was to identify whether roughness elements are able to increase the value of Γ above which no solutions to the governing system of equations (6.38) exist: such a Γ being denoted by Γ_c.

Three questions were therefore posed: the first, obviously, was whether a small laminar separation bubble, which has negligible impact on the lift and drag coefficients, can exist at higher angles of attack in the presence of roughness elements than on a clean

[12] On the other hand, if we keep the Reynolds number based on the airfoil chord length, the roughness parameters become of a similar order of magnitude as those used in the experiments. For the range of Reynolds numbers 25 000–97 000, with the same airfoil, the roughness widths are in the range 15 mm–20 mm, the heights between 50 µm and 130 µm, and the frequencies span 10 Hz to 40 Hz. The order of magnitude of the increment in angle of attack decreases slightly, to between 0.5° and 1.0°

airfoil. As an extension to this, the second asked whether it is at all possible for a separation bubble not to exist, with attached flow existing at all values of Γ up to Γ_c; and the third aimed to determine what the impact of the roughness elements is on the interaction pressure gradient and how this might be linked to an increase, or decrease, in Γ_c.

The answer to the first of these questions is affirmative for both static and dynamic elements, with the latter allowing for a doubling in the value of Γ_c. The impact is, however, highly sensitive to the choice of roughness parameters. It was found that the roughness has to be placed such that its midpoint lies within the streamwise extent of the laminar separation bubble that exists in the clean airfoil case at $\Gamma = \Gamma_c \simeq 2.764$ or 2.756 (depending on the code used to solve the governing system): anywhere else and the value of Γ_c decreases, significantly so if the midpoint is placed upstream, due partly to the diminution of the peak in the favourable pressure gradient. For a static roughness element, a maximum effective width (for a given choice of roughness position and height) was found, as would be expected if an initial increase in Γ_c with width must be reconciled with the fact that, as the width tends to infinity and the hump slopes tend to zero, we should approach the clean airfoil solution once more. Although such a width was not found for dynamic roughness elements at the widths tested, the shape of figure 6.16 suggests that there is eventually a maximum in Γ_c as a function of width: we were, however, limited by the size of the computational domain.

In a similar manner to the width, an increase in height initially causes Γ_c to increase, until a maximum is reached and it begins to decrease. For static roughness elements (figure 6.11), the impact of height eventually becomes detrimental to the value of Γ_c and this perhaps corresponds with existing knowledge about the adverse effects of surface roughnesses on separation and stall. The situation is rather more complicated in the case of dynamic elements due to the interdependency between the height and a new parameter, the oscillation frequency, not present in static roughnesses. An increase in height could again be viewed unfavourably, but this can in fact be compensated for by an increase in frequency, which allows for elevated values of Γ_c (figure 6.18). A translation from these scaled roughness parameters to their real-world counterparts appears in §6.3.3 and a comparison between our results and those obtained in past experimental work—indicating that the inverse relationship between height and frequency predicted by Huebsch et al. [41] to maintain a given increase in critical angle of attack is present for certain ranges of the two parameters and that greater frequencies do indeed have a more beneficial impact—was presented there.

With regards to the second of the questions enumerated above, it was found to be possible, for certain choices of the dynamic roughness parameters, for no separation bubble to appear in the leading edge region even at $\Gamma = \Gamma_c$: i.e. at all angles of attack up to the one above which the airfoil presumably stalls, since marginal separation theory ceases to apply. It is unclear whether this has any practical implications, given the aforementioned negligible effect of the separation bubble on the lift and drag, but the

result certainly suggests that it is not necessarily only the, possibly repeated, bursting of the separation bubble and/or injection of vorticity into the bulk of the boundary layer that causes full breakaway separation. For static roughness elements, on the other hand, a separation bubble was found always to exist, although it is often smaller than the clean case version, appearing over the rear half of the roughness.

This answer to the second question brings us to the last, as it is the sudden growth of the peak in the adverse pressure gradient that may cause the failure of marginal separation theory to describe the flow at angles of attack greater than that represented by the increment Γ_c, despite the lack of a bubble within the interaction region. The impact of dynamic roughness elements on the interaction pressure gradient, at least for a roughness positioned between $X_L = -4.2$ and $X_R = 5.8$, takes two forms and depends on the height and frequency of the roughness: either the size of the peak in the adverse pressure gradient is decreased or the streamwise extent of favourable pressure gradients increased, despite a greater adverse peak compared to the no-roughness case.

Oscillating flows, with a modal approach to the solution, have been shown in the past to increase the range of angles of attack for which Goldstein's singularity does not appear. Timoshin demonstrated, in 1988 [96], that cosine perturbations in the external, inviscid flow (due, for example, to acoustic disturbances) at large frequencies (large Strouhal number, $S = (L\omega/U_\infty)^{1/2}$) but small amplitudes[13] give rise to a Stokes layer that induces a steady flow in the bulk of the boundary layer; and that this steady flow then results in a similar interaction structure to that described in this chapter, with a solution to the governing equation existing provided that the increase in the angle of attack satisfies

$$\Gamma < \frac{3\mu_0^2}{4a_0\,|a_1|}\left(\frac{\sigma}{S}\right)^2.$$

It would be interesting to determine whether a similar estimate could be made for our system (6.38), even if we restrict ourselves to extreme values of the roughness oscillation frequency and/or amplitude. An attempt at determining the interdependence of frequency and amplitude, where both were assumed large, in maintaining a fixed, order 1 value of Γ_c was made by considering the order of magnitude of the terms present in equation (6.38a) and gave the prediction that height should behave as ω^2, but this is not borne out by figure 6.18. Similarly, can we obtain an equation (again within certain ranges of amplitude or frequency) for the black solid contour in figure 6.18 that separates increases from decreases in Γ_c, as compared to the no-roughness case?

The time-dependent system (6.38), ultimately, seems to be mathematically rich, with various behaviours that remain to be explored. These include not only low/high amplitude/frequency asymptotics, but also the explanation behind the switch from one

[13]The amplitude of the disturbances was written as $\sigma = S\sigma_1$, with $S \gg 1$, but then σ_1 was taken to tend to zero.

type of pressure gradient (a decrease in adverse gradient peak) to another (an extension of the region of favourable gradients) and a more rigorous justification for why no separation bubble exists for certain roughness parameters. The passage through Γ_c to larger values of Γ, building on recent work [11, 46, 75], and the search for a possible link between the small bubble of marginal separation theory and larger separated flows, where boundary layer separation is described through the smaller streamwise length scale of triple deck theory, also poses interesting questions.

Remaining with both marginal separation theory in general, as well as its specific application to roughness elements, it could be interesting to combine the Newton's method that was used in this chapter with the relatively new algorithm of deflation, which can be applied in physical scenarios in which there exist bifurcations and multiple solutions in the governing systems of equations—these include the Allen–Cahn equation in phase separation, Yamabe problems in differential geometry and, in fluid dynamics, flows in channels that suddenly expand, among others [23]. Exactly as in our system (6.38), these equations take the form

$$\mathcal{S}\left(A, \Gamma\right) = 0,$$

where $\mathcal{S}$ is some operator, A is the function sought and Γ is some relevant parameter that appears in the governing equation. In the numerical scheme applied here, where the displacement function depended on the parameter Γ, the use of the solution $A(X, T, \Gamma_1)$ was used as the initial guess to proceed along the upper branch of the bifurcation diagram (see figure 6.6) to obtain the next solution $A(X, T, \Gamma_2)$, where $\Gamma_2 = \Gamma_1 + \epsilon$, ϵ being some (small, depending on the radius of convergence) positive number. Once Γ_c is reached, a modification of the discretisation process is needed, where Γ becomes unknown but A at $X = 0$ (say) is fixed, in order to start reversing back along the lower branch of the bifurcation diagram (not done here).

The deflation method, which merely involves a preconditioning of the Jacobian matrix and a modification of the residual (details are in the cited paper), would allow one to jump easily from the upper branch to the lower branch (or vice versa) as follows: suppose that the solution to A is obtained at some $\Gamma = \Gamma_1 < \Gamma_c$. One then sets $\Gamma = \Gamma_2 < \Gamma_c$ and uses $A^+(X, T, \Gamma_1)$ as the initial guess to obtain, as usual, the solution $A^+(X, T, \Gamma_2)$, with the positive superscript indicating that our result lies upon the upper branch (for example) for both values of Γ. Having done this, one keeps $\Gamma = \Gamma_2$ and uses, once more, $A^+(X, T, \Gamma_1)$ as the initial guess. The deflation process then removes the previously obtained $A^+(X, T, \Gamma_2)$ as a viable solution to converge to and instead converges to $A^-(X, T, \Gamma_2)$ on the lower branch. Curiosity then dictates that it could be worthwhile repeating the process a third time to see if any other, as yet unidentified and disconnected branches, exist: probably not, but it would do no harm to try.

Returning to our roughness elements, both the frequency and height scales were chosen so that both the roughness and its time-dependence acted at the appropriate order to appear in the governing equation (6.38a), but can marginal separation theory accom-

modate other scalings that would modify equation (6.38a) and its associated solutions? This would be linked, potentially, to the high frequency and/or amplitude investigations mentioned above. And, finally, what is the effect of 3D roughness elements, either static [8] or dynamic,[14] on the value of Γ_c?

6.4.1 The legacy of the Nile explorers

At Marseilles' railway station, on his way back to London from the Congo, Henry Morton Stanley was approached by two men. The first was Baron Jules Greindl, a diplomat; the second was Henry Shelton Sanford, a US businessman and aristocrat with a name remarkably similar to our hero's; both were acting on behalf of King Leopold II of Belgium. Between them, they persuaded Stanley to return to the Congo to set up a system of trading stations and build roads into the interior. This he did in 1879, opening up the river's surrounding regions to commerce and allowing the pillage of the Congo to begin. Still today, the theft of its riches continues; still today, the suffering has not ended.

Similarly, Samuel Baker, accompanied by his wife Florence, led a military expedition to a region now within South Sudan and all of its troubles, snatching away territory from the local chieftains and combining them into a new administrative area, Equatoria, of which he later became governor–general. James Grant served in the punitive Napier expedition of 1868, which marched into Ethiopia, freed the missionaries and representatives of the British government who had been imprisoned by Emperor Tewodros II, and marched out again carrying the loot taken from Ethiopia's cultural and religious history. Much of that treasure remains in the British Museum and Library. Perhaps only Richard Burton, who was nursing his bitterness in Trieste, and Livingston and Speke, who were dead, remain largely untainted.

It is a sad legacy that they leave behind, these great explorers, despite their best of intentions—which, in most cases, included the goals of destroying the slave trade and spreading what they saw as the benefits of their civilisation. They had set off in a spirit of undying adventure, driven by the devil, to conquer the Nile and our human limitations. They succeeded; but in so doing they ended up opening the way for the conquest of Africa, the scramble for its riches and the subjugation of its people through the medium of colonialism.

[14] The governing unsteady equation for a three dimensional roughness element is given in our oft-cited paper of Braun & Kluwick [9], but it would need to be corrected similarly to how our equation (6.38a) is the corrected version of their equation (2.7).

7

The mountains ahead

"I arrived in Kumasi with no particular goal. Having one is generally deemed a good thing, the benefit of having something to stride toward. This can blind you, however: you see only your goal, and nothing else, while this something else—wider, deeper—may be considerably more interesting and important."

Ryszard Kapuściński, *The Shadow of the Sun*

Ryszard Kapuściński (1932–2007) spent his life having no particular goal. Or rather, he had goals, but these were the unimportant ones set by his employer, the Polish Press Agency, and were dealt with in one of the two notebooks he always travelled around with; the second notebook, on the other hand, was far more important, filled as it was with the jottings of a mind that was very open to the 'something else', carried by legs that didn't so much stride as wander slowly, with great pauses, in whatever direction curiosity and chance pulled them. Following a breakthrough as a young journalist exposing the inhumane working and living conditions of those involved in the construction of one of the first socialist municipalities in Poland, he was hired by his aforementioned employers in 1958 and sent to Africa. For Kapuściński's inquisitiveness, and for those who have followed vicariously in his footsteps, this was a happening of great fortuitousness: in 1957, the Gold Coast had declared its independence and become Ghana, with other countries swift to follow suit in a spasm of hope that settled into shudders of violence; and the Polish Press Agency was virtually skint, which meant that Kapuściński had to travel in the most economical way possible and invest his time in forging contacts with people who might help him get around.

In the course of his eventful career, Kapuściński sent back to his employers the events of 27 coups, revolutions and wars. But he understood that what was important was not what went into his telegrams and filled his newspaper columns, but the stories of the eclectic mixture of ordinary people he met, lived with and travelled with along the way. Ghana, Liberia, Senegal, Tanzania; Kenya, Rwanda, Congo, Uganda: everywhere he went, he stayed amongst those most affected by the tumult, amongst the grass that gets

trampled when the elephants fight. Having been brought up amidst the destruction of Warsaw in the Second World War, he was well aware of "how difficult it is to convey the truth about [war] to those for whom that experience is [. . .] unfamiliar": how it "is, finally, incommunicable".

And yet he tried: by putting on his boots and walking; by standing for countless hours on the kerbside, waiting for a bus that would not come; by making friends with the revolutionaries and the guerrillas, the victors and the losers, the great and the once-great and the soon-to-be-great (however briefly); by living with the families in their homes; and, most of all, by moving impulsively, without a goal. In so doing, he formed the backbone of the books that he wrote: the fall of Haile Selassie and the haunting memories of a medieval régime that crumbled away, eroded by the contradictions of its existence; the chaos and confusion of Portugal's withdrawal from Angola, as capitalism and communism collided in the chasm into which the little people fell; the inevitable overthrow of Mohammad Reza Pahlavi, last Shah of Iran, and the quickening march of disaster as its drums sounded out their beats of doom, . . .

It takes great courage to move as Kapuściński moved, 'with no particular goal'. Our goal, on setting out, was to determine the impact of roughness elements on flow separation over an airfoil, such an effort being motivated by past experimental, numerical and analytical work, which suggested that dynamic roughnesses are able to increase the angle of attack at which a boundary layer will separate. If this is the case, the use of these elements could have a beneficial impact for the drones, turbines and propellors that operate within the range of Reynolds numbers (10^4–10^6) in which laminar flow prevails: separation carries with it increased drag and decreased lift and so its avoidance has great financial and safety implications.

Despite this, only at the very end did we turn to the question of roughnesses on an airfoil, setting them within the context of marginal separation theory [69, 70, 90]. We began by considering an array of roughnesses on a flat plate, and this led us to delve into the phenomenon of steady streaming (chapter 3). These roughnesses, however, were too small to provoke separation, although they did allow us to favourably modify the mean pressure gradient. Separation was eventually provoked through the use of the hump of Smith & Daniels [85], with a height scale that placed it within a condensed boundary layer: small roughness elements were then placed on the lee side of this hump—in the region where the adverse pressure gradient drives the boundary layer to separate—and their impact on the local and global separation points (the position of vanishing skin friction and its later singularity) was determined (chapter 5). Our final arrival at roughness elements positioned near the leading edge of the airfoil, where the skin friction goes to zero and a a small separation bubble can be created, was then driven by a desire to discover whether the small bubbles, which have negligible impact

on the lift and drag coefficients, can exist for larger angles of attack before 'bursting' into larger, aerodynamically undesirable regions of separated flow (chapter 6).

As implied, the scenario presented in the previous chapter was the most similar to past experimental work, in which the roughness array (admittedly, we looked only at a single element) consisted of bumps with heights that were a finite fraction of that of the local boundary layer [33, 40, 41]. The general scientific consensus has tended to be that static roughness elements are detrimental to flow control, and thus previous work on dynamic elements has understandably ignored such steady humps, although one paper agreed that they have an adverse effect [40]. Our analytical approach, however, has allowed us to easily incorporate such elements into the model and the results suggest that provided they are small enough—and certainly smaller than those of [40], which were of the order of the boundary layer height, $\mathrm{Re}^{-1/2}$—static roughnesses can also have a favourable impact, both in delaying the separation point on the hump of Smith & Daniels and increasing the angle of attack at which breakaway separation occurs on an airfoil. As the heights tend towards larger scales, though, at least in the case of aerodynamic stall, we also predict an adverse effect. In this, we agree with past analytical work [9].

The conclusion from the numerical and wind tunnel experiments was that the benefits of dynamic roughnesses are highly dependent on the roughness parameters. Firstly, the roughness array has to start at or just upstream of the separation point and, in this, our results concur, both for flow over a hump and marginally separated flow over an airfoil: in the former, the front side of the roughness element had to be placed over the local and global separation points; in the latter, the roughness had to be placed such that its midpoint lay at a streamwise station within the region in which a separation bubble can exist on a clean airfoil.

Secondly, in previous work, a preference was shown, at least with regards to dynamic roughnesses, for larger roughness heights [41]. The same conclusions were presented for the scenario of chapter 5, but we found that this was not necessarily the case for that of chapter 6, where increases in height were initially beneficial, but then detrimental—unless the oscillation frequency was increased. The benefits of increasing the frequency on the value of Γ_c, which is the increment in the angle of attack, in the last chapter were similar to previous conclusions that found that flow control is lost once the frequency falls below a certain value [33]. Lower roughness heights also require higher oscillation frequencies [41]: the conclusions from our figure 6.18 did not necessarily support this, although there are regions of that graph in which an inverse relationship between the two parameters can be seen. We note, however, that if we base our scalings on a Reynolds number that has a length scale equal to the radius of the airfoil leading edge, we find ourselves in a completely different parameter space to that of previous experimentalists, with smaller roughness elements and frequencies in the kilohertz range—far higher than

those achievable in reality.[1] For flow over a bump, on the other hand, the lessening effect of lower heights could be compensated by higher frequencies when it comes to moving the global separation point downstream, provided that the front face of the roughness covered the original singularity that represents breakaway separation: the opposite was the case if the roughness was centred upstream, with increased frequencies advancing the singular position over the rear half of the element.

Contributing factors to the possible success of dynamic roughness elements have been proposed by past authors. Vortex shedding from a single element has been studied by Rothmayer & Huebsch (2012) as a means of stabilising the boundary layer and maintaining attached flow [67], but this phenomenon has not been touched upon in this study. Chapter 3 did, however, confirm the possibility of modifying the mean flow within the boundary layer through Reynolds stress-like terms that arose from the oscillatory motion of dynamic roughness elements, as was found by Rothmayer & Huebsch (2011) for a roughness of height scale $\mathcal{O}(\mathrm{Re}^{-1})$, oscillation frequency of order the Reynolds number and width of the same order as the boundary layer height [66]. In particular, a favourable pressure gradient, that is nonzero over a cycle of oscillation, could be introduced.

Such a favourable modification of the pressure gradient agrees also with the conclusions of others [41], as well as our results in chapters 5 and 6. In the former, for flow over a hump in a condensed boundary layer, this was partly due to the simple form of the pressure–displacement relation that arose from matching between the core flow in the condensed layer and that in the rest of Prandtl's classical boundary layer, which set the pressure to be equal to the boundary layer displacement function. In the case of roughness elements mounted on an airfoil, on the other hand, the viscous–inviscid interactions gave rise to the standard integral of aerodynamics, equation (6.35), and the solutions to the governing system (6.38) suggested that the dynamic roughnesses were able to increase the critical angle of attack as compared to the clean airfoil case either by maintaining a favourable perturbation pressure gradient over a greater streamwise extent, or by reducing the magnitude of the peak in the adverse perturbation pressure gradient.

Turning to negative static roughness elements, their presence on the lee side of the hump in chapter 5 produced some interesting results: if positioned far upstream of the position of vanishing skin friction on a clean hump and of sufficiently large depth, they gave rise to a small separation bubble in the flow; but if the depth was too large, the bubble burst and breakaway separation, represented by a singularity in the asymptotic region in which the roughness was placed (region C of figure 5.1), was greatly advanced. Such a phenomenon seemed to depend both on the depth and width of the roughness, with narrower elements allowing for larger roughness depths before bubble bursting

[1] On the other hand, if we take the Reynolds number to be based on the chord length, our roughness height becomes slightly smaller than that studied experimentally, and our width slighter wider, but the frequencies now lie in the tens of hertz: see §6.3.3. The difficulty here is in determining which Reynolds number is appropriate—the belief is that it is the one reported in the main text.

occurred. A more in-depth study of this behaviour, perhaps focusing on the critical values of the width/depth, could be worthwhile.

7.1 Journey's end, and journey's beginning

It was easy setting out. You could see the top of the mountain straight ahead of you—and it didn't look so tall, nor was the granite underfoot so uncomfortable. The path was clear and well-marked and putting one foot in front of the other was the easiest thing in the world. Just one foot in front of the other, one foot in front of the other, all the way to your destination. But then all of a sudden it wasn't so easy anymore, and the destination wasn't so obvious. The path forked into two and then more and then many and it was dark up ahead and you couldn't see where they led. Then eventually, after stumbling around for a while, you began to forget exactly where it was you wanted to go; so you turned away from the path and lost yourself in wherever it was you happened to be. And what you discovered might have had nothing to do with what you thought you'd discover, but that didn't matter: what mattered was the finding of it. When you finally stopped, and paused for a while, and searched for the person that had set out, you chuckled a little: for that person started walking confident that they would find the answer to a question, but all they found was more questions; and the more they walked, the more they realised that it was the questions that were the most important things in the world.

The conclusions to chapters 3, 5 and 6 contain the questions we identified along the way and the directions in which our wanderings could take us next; these are summarised briefly here. The advance of the singular position with increasing frequency for flow over a hump in the presence of dynamic roughnesses has already been mentioned and it would be interesting to determine why this is the case and to describe more accurately the growth of waves, linked again to the oscillation frequency, downstream of the roughness in the linearised solutions of §5.4. The marginally separated flow of chapter 6 seems to be mathematically rich, and the governing system when dynamic roughnesses are included hides a plethora of interesting behaviours. From these, we can ask ourselves why no separation bubbles exist at all possible values of Γ for certain choices of roughness height, width, position and frequency; and why and when in parameter space the pressure gradient switches from one behaviour, touched upon above and described in detail in §6.3.2, to another. A study of low or high frequencies or amplitudes, and the response of Γ_c in each case, would also be interesting.

Very high frequency and low amplitude surface forcing through alternating suction and blowing (perhaps more feasible from an engineering viewpoint) has recently also been shown to be able to maintain attached flow during an airfoil pitching motion and therefore prevent the occurrence of dynamic stall [99]. One possible limitation, however, is that at higher Reynolds numbers, separation from the airfoil's trailing edge and the ensuing turbulent motion may move upstream and cause a marginal separation

bubble to burst.[2] This question is linked to the general phenomenon of bubble bursting and the investigation into what happens as the angle of attack increases beyond that represented by $\Gamma = \Gamma_c$: how, mathematically, can one describe the transition from a small laminar separation bubble to separated flow on a larger scale? Described in chapter 6 was also the potential application of a deflation algorithm to the nonlinear system (6.40) with the aim of checking that no other disconnected branches exist in the bifurcation diagram of Γ against $A(0)$.

The work of chapter 3, where an array of oscillating roughnesses was placed on a plane, should be viewed as merely the first step in an extension to the study of Rothmayer & Huebsch (2011) [66] to length and height scales of the order $\mathrm{Re}^{-3/4}$–$\mathrm{Re}^{-3/8}$ and $\mathrm{Re}^{-1/4}$–$\mathrm{Re}^{-1/8}$ respectively. Although we confirmed the presence of Reynolds stress-like terms and identified the existence of a steady streaming velocity feeding from an inner layer into an outer layer, no separation was present in our study: one should move next to introducing an adverse pressure gradient—such as that which exists on the suction side of an airfoil, for example—that drives the flow towards separation to determine, as done in [66], whether greater adverse gradients can be withstood without separation occurring. Alternatively (or rather, additionally), the roughness elements could be taken to be sufficiently large ($h \sim 1$ in the setting of chapter 3) to provoke separation, but then made to vibrate up and down (time-dependent perturbations with amplitudes much smaller than the roughness height) or drop flush to the surface before returning to maximum amplitude: their impact on separation, as opposed to that of static elements, could then be studied.

The array of roughnesses in Rothmayer & Huebsch (2011), however, was also three dimensional, while throughout the entirety of this study, the roughnesses remained two dimensional. Given the tridimensionality of the real world, it would be worthwhile to extend this work, especially in the case of marginally separated flow, into three dimensions to identify what impact the spanwise direction has on the conclusions. Nevertheless, we believe that a 2D approach makes for a valid first attempt in gaining an understanding of the physics involved in the problem.

The role of turbulence has also been completely ignored and we turn, all too briefly, to this question now. Moving aside from flow separation to transition, the amplification of Tollmien-Schlichting instabilities in the presence of an array of static surface roughnesses has been studied in the past: the flow in the space between the elements has been modelled as a Stokes flow and that in the bulk of the boundary layer above found by solving the Orr-Sommerfield equation, along with matching at the interface between the two [28]. The presence of spanwise periodic roughness elements on a wing has been seen to be successful in maintaining laminar flow during wind tunnel experiments, due

[2] The impact of cyclical blowing/suction from a surface on a boundary layer, along with a discussion of the upstream movement of the trailing edge separation point at higher Reynolds numbers, was presented by Visbal and Gormann at the US Air Force Office of Scientific Research (AFOSR) flow interactions and control portfolio review, Arlington (2017).

potentially to their ability to control crossflow instabilities [72], but this success has not been carried over to in-flight tests [74].

Numerous other studies carried out over the years on the role of static roughness elements in transition to turbulence exist; more recently, the incorporation of dynamic effects, through the use, for example, of electro-active polymers (EAPs) has also been attempted, mainly experimentally, as a means of reducing skin friction drag in turbulent flows. These EAPs are able to form dimples (as opposed to roughnesses) on a surface that oscillate [19] and inject vorticity into the boundary layer [18]. Recalling also that turbulence tends to keep the flow attached to the surface through momentum mixing (see chapter 1), it would be interesting to determine the impact of dynamic roughness elements on the growth of instabilities, and how the growth of unstable modes could be linked to the oscillation frequency of the roughnesses. Such an effort could also have implications to the studies on EAPs.

The approach taken in this work has been almost wholly analytical, with only the final equations solved numerically, although asymptotic techniques have been used in places, partly to further analyse the flow behaviour and partly to validate the numerical results. Such an approach has allowed us to determine the influence of roughness parameters on the separation of a boundary layer and gain some understanding of the physical phenomena present. Along the way, we have tried, where possible, to compare our conclusions with those of past experimental and computational studies.

The growth of computing power in recent decades, along with the continued presence of sophisticated wind tunnels, has revolutionised our attempts to understand and exploit fluid flows, as well as thrown open the doors to new collaborations between different, but increasingly blurred, research approaches: computational, experimental and mathematical. This last component should not be forgotten or allowed to fall by the wayside: the insight it can give, in guiding the other two and understanding their results—in, if the answer is a needle in the proverbial haystack, at least pointing us to the right haystack—has a vital role to play in the marriage between all three; and it is this marriage that holds the most potential in allowing humankind to peek behind the curtain that shrouds the mysteries of nature. And, most of all, it is their merging that will give the greatest enjoyment.

And so here we are, perched on a mountainside, looking out at day's end. The sun is an orange orb slipping below the vanishing horizon. Dusk, encroaching, is held at bay by a dull red glow and, all around, the mountains are fading away from this world and passing into the next. They become dark blue shadows; ghostly echoes of what may once

have been before the earth and the sky melted and the distinction between the two ceased to exist. The wind blows through your memories. It's the end of the day, and journey's end, but we're perched on an ethereal mountainside and there's still a long way to go.

Appendices

A

Roughnesses on a plane: numerical techniques

This appendix outlines the numerical techniques used in chapter 3. These largely involve solving simple systems of linear equations through matrix inversion in MATLAB. Throughout, the subscripts m, n refer to the (m, n)th position in a matrix, corresponding to the mth mesh point in the normal direction and the nth mesh point in the horizontal direction.

A.1 Lower layer solution, third order

The six equations to solve for the components of the oscillatory shear stress at order h^2, $(\tau_{2i}, i = 1, \ldots, 6)$ are those given in equations (3.16), reproduced here below:

$$\frac{\partial^2 \tau_{21}}{\partial y^2} - \mathrm{i}\alpha\lambda\left(y + \frac{c}{\lambda}\right)\tau_{21} = -\lambda y \frac{\partial \tau_{11}}{\partial \bar{x}}, \tag{A.1a}$$

$$\frac{\partial^2 \tau_{22}}{\partial y^2} - \mathrm{i}\alpha\lambda\left(y - \frac{c}{\lambda}\right)\tau_{22} = \lambda y \frac{\partial \tau_{12}}{\partial \bar{x}}, \tag{A.1b}$$

$$\frac{\partial^2 \tau_{23}}{\partial y^2} - 2\mathrm{i}\alpha\lambda\left(y + \frac{c}{\lambda}\right)\tau_{23} = \mathrm{i}\alpha u_{11}\tau_{11} + v_{11}\frac{\partial \tau_{11}}{\partial y}, \tag{A.1c}$$

$$\frac{\partial^2 \tau_{24}}{\partial y^2} - 2\mathrm{i}\alpha\lambda\left(y - \frac{c}{\lambda}\right)\tau_{24} = \mathrm{i}\alpha u_{12}\tau_{12} + v_{12}\frac{\partial \tau_{12}}{\partial y}, \tag{A.1d}$$

$$\frac{\partial^2 \tau_{25}}{\partial y^2} - 2\mathrm{i}\alpha\lambda_0 y\tau_{25} = -\mathrm{i}\alpha\left(u_{12}\tau_{11} + u_{11}\tau_{12}\right) - \left(v_{11}\frac{\partial \tau_{12}}{\partial y} + v_{12}\frac{\partial \tau_{11}}{\partial y}\right), \tag{A.1e}$$

$$\frac{\partial^2 \tau_{26}}{\partial y^2} - 2\mathrm{i}\omega\tau_{26} = \mathrm{i}\alpha\left(u_{11}\tau_{12}^* - u_{12}^*\tau_{11}\right) - \left(v_{11}\frac{\partial \tau_{12}^*}{\partial y} + v_{12}^*\frac{\partial \tau_{11}}{\partial y}\right). \tag{A.1f}$$

To these is added the condition

$$\int_0^\infty \tau_{2i}\,\mathrm{d}y = 0,$$

which comes from no-slip and matching at the top of the viscous sublayer, and the requirement that τ_2 tends to zero as y tends to infinity.

The right-hand side of the above, for which an analytical expression in term of the Airy function is known, acts as the forcing for the shear stress, and can be labelled $\mathcal{F}_{m,n}$, where the matrix $\mathcal{F}$ depends on which of the six equations (A.1a)–(A.1f) we are trying to solve. The left-hand side of each equation is converted into a set of linear equations by using a second order accurate centred difference on the derivative. This gives the following six systems of equations, for the (m,n)th mesh point, each corresponding to the equivalent partial differential equation of (A.1):

$$\tau_{m+1,n} - \left[2 + \Delta_y^2 \mathrm{i}\alpha\lambda\left(m\Delta_y + \frac{c}{\lambda}\right)\right]\tau_{m,n} + \tau_{m-1,n} = \Delta_y^2 \mathcal{F}_{m,n}, \tag{A.2a}$$

$$\tau_{m+1,n} - \left[2 + \Delta_y^2 \mathrm{i}\alpha\lambda\left(m\Delta_y - \frac{c}{\lambda}\right)\right]\tau_{m,n} + \tau_{m-1,n} = \Delta_y^2 \mathcal{F}_{m,n}, \tag{A.2b}$$

$$\tau_{m+1,n} - 2\left[1 + \Delta_y^2 \mathrm{i}\alpha\lambda\left(m\Delta_y + \frac{c}{\lambda}\right)\right]\tau_{m,n} + \tau_{m-1,n} = \Delta_y^2 \mathcal{F}_{m,n}, \tag{A.2c}$$

$$\tau_{m+1,n} - 2\left[1 + \Delta_y^2 \mathrm{i}\alpha\lambda\left(m\Delta_y - \frac{c}{\lambda}\right)\right]\tau_{m,n} + \tau_{m-1,n} = \Delta_y^2 \mathcal{F}_{m,n}, \tag{A.2d}$$

$$\tau_{m+1,n} - 2\left(1 + \Delta_y^2 \mathrm{i}\alpha\lambda\right)\tau_{m,n} + \tau_{m-1,n} = \Delta_y^2 \mathcal{F}_{m,n}, \tag{A.2e}$$

$$\tau_{m+1,n} - 2\left[1 + \Delta_y^2 \mathrm{i}\omega\right]\tau_{m,n} + \tau_{m-1,n} = \Delta_y^2 \mathcal{F}_{m,n}; \tag{A.2f}$$

where Δ_y is the step size in the normal direction and all other symbols are as defined in chapter 3.

Two further equations are required to define the boundary conditions and close the system: we set $\tau_{M,n} = 0$ to satisfy the condition at infinity; and the integral condition is defined using trapezoidal integration:

$$\tau_{1,n} + \tau_{M,n} + \sum_{i=2}^{M-1} \tau_{i,n} = 0, \tag{A.3}$$

where 1 and M denote the first and last mesh points in the normal direction.

The linear system of equations can then be written in the form

$$\mathbf{A}\tau_n = \mathcal{F}_n,$$

for each horizontal station n, where we note that the matrix $\mathbf{A}$ does not depend on the horizontal coordinate. It therefore needs only be inverted once and we have

$$\tau_n = \mathbf{A}^{-1}\mathcal{F}_n, \ \forall n. \tag{A.4}$$

Equivalently, the MATLAB backslash command can be used to solve the system (A.2) and (A.3), with $\tau_{M,n} = 0$.

There has been no approximation in the horizontal direction: we thus only need to check the influence of the mesh size and finite termination of the computational domain in the normal direction (i.e. Δ_y and y_M). This is shown in figures A.1 and A.2 for the case where all blips have the same maximum amplitude (i.e. $G = 1$). Note that this implies that τ_{21} and τ_{22} are necessarily zero, since the forcing is zero and both the no-slip and

integral condition allow for the solution to be zero at the wall and at infinity. Hence only $\tau_{2i}, i = 3, \ldots 6$ are shown.

In figure A.1, the mesh sizes $\Delta_y = 0.01$ (solid line), 0.005 (dashed line) and 0.001 (dot–dashed line) are tested, with the upper limit of the computational domain set at $y_M = 10$. There is almost perfect agreement at all mesh sizes; figure A.2 therefore takes the mesh step to be $\Delta_y = 0.01$ and the upper limits $y = 10$ (solid line), 15 (dashed) and 20 (dot–dashed) are tested. Once more, agreement is obtained in all cases. All plots for the shear stress components $\tau_{2i}, i = 1, \ldots, 6$ in chapter 3 use $\Delta_y = 0.01$ and $y_M = 10$.

A.2 Steady streaming solution

The system to solve for the steady streaming velocity is that given by (3.18), along with the modified boundary condition (3.23), reproduced here without the subscripts:

$$\frac{\partial^2 u}{\partial y^2} = R\left(\bar{x}, y\right), \tag{A.5a}$$

$$u = 0 \quad \text{on } y = 0, \tag{A.5b}$$

$$\frac{\partial u}{\partial y} \to 0 \quad \text{as } y \to \infty. \tag{A.5c}$$

The function R here is the Reynolds stress (3.18b) and, although it depends both on y and the long streamwise coordinate $\bar{x}$, we can treat equation (A.5a) as an ordinary differential equation for u. In order to ensure that the correct boundary conditions (A.5b) and (A.5c) are imposed, the system (A.5) is solved using the Thomas algorithm.

We first discretise equation (A.5a) using a second order accurate centred difference to give

$$u_{m+1} - 2u_{m,n} + u_{m-1,n} = \Delta^2 R_m, \tag{A.6}$$

where Δ refers to the step size in y (the subscript y present in §A.1 has been dropped due to its obsolescence). We can replace u_{m+1} by

$$u_{m+1} = p_m u_m + q_m, \tag{A.7}$$

where p_m, q_m will be determined shortly, to obtain

$$u_m = \frac{\Delta^2 R_m - q_m}{p_m - 2} - \frac{u_{m-1}}{p_m - 1}.$$

However, u_m is necessarily

$$u_m = p_{m-1} u_{m-1} + q_{m-1}$$

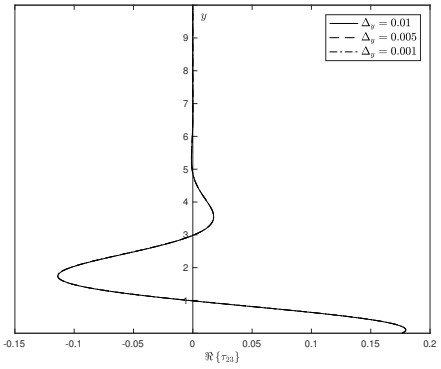

(A) $\Re\{\tau_{23}\}$

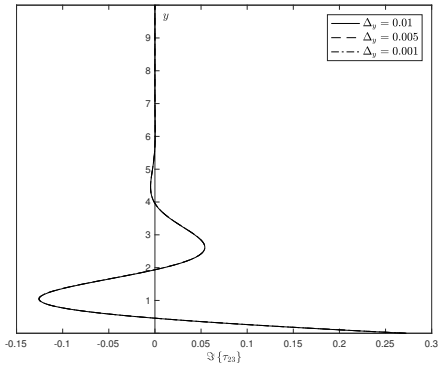

(B) $\Im\{\tau_{23}\}$

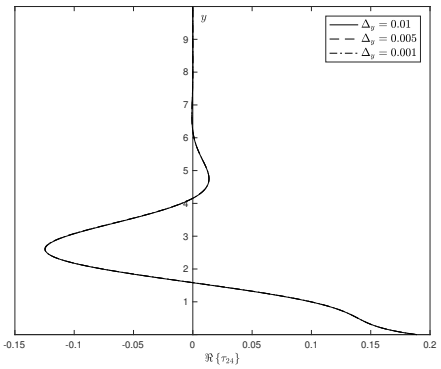

(C) $\Re\{\tau_{24}\}$

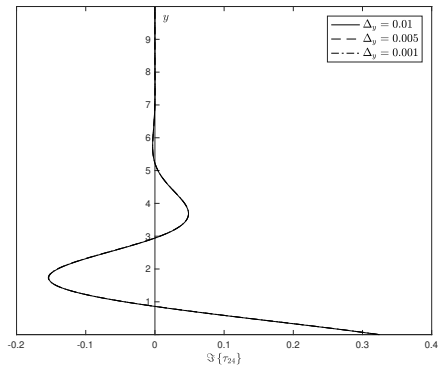

(D) $\Im\{\tau_{24}\}$

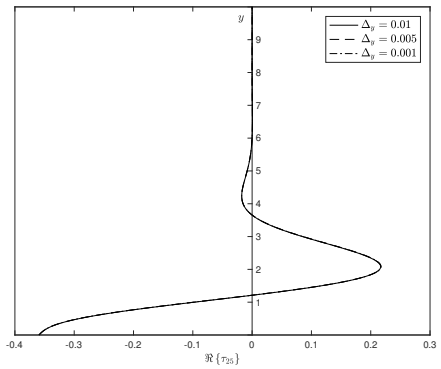

(E) $\Re\{\tau_{25}\}$

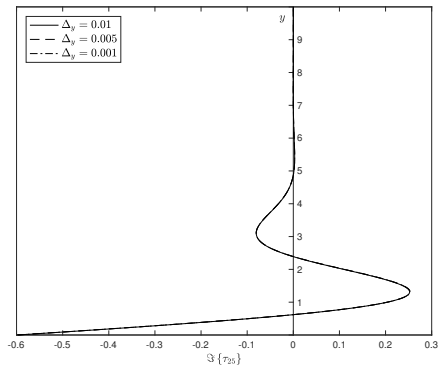

(F) $\Im\{\tau_{25}\}$

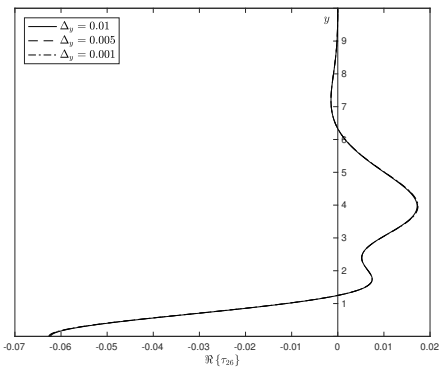

(G) $\Re\{\tau_{26}\}$

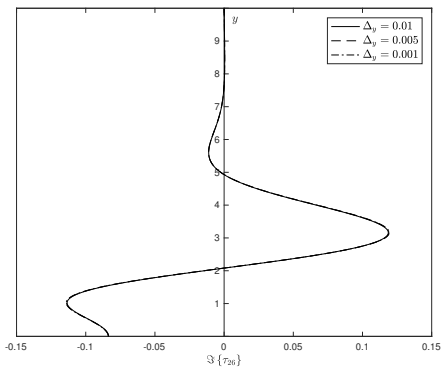

(H) $\Im\{\tau_{26}\}$

FIGURE A.1: Influence of changing the mesh size in the wall-normal direction (Δ_y) on the solution for the shear stress components $\tau_{2i}, i = 3, \ldots, 6$, as described in the text.

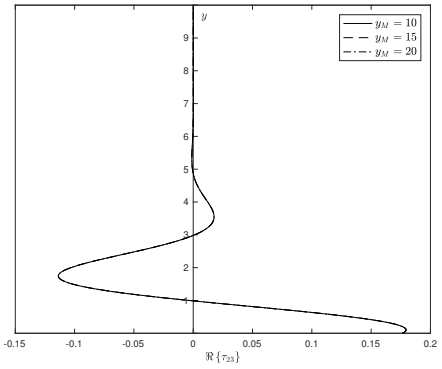

(A) $\Re\{\tau_{23}\}$

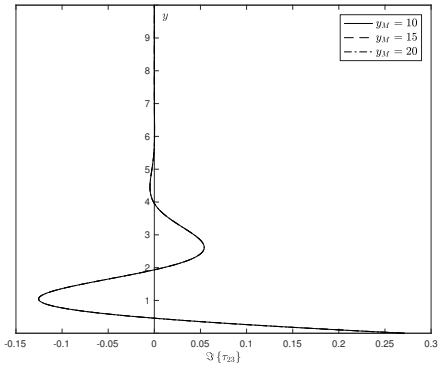

(B) $\Im\{\tau_{23}\}$

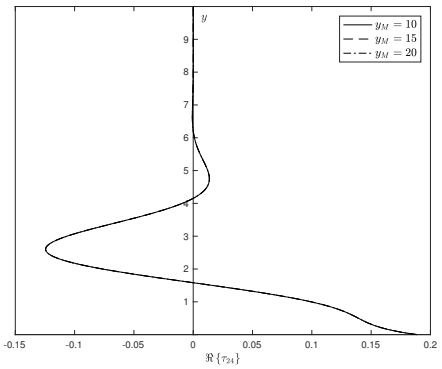

(C) $\Re\{\tau_{24}\}$

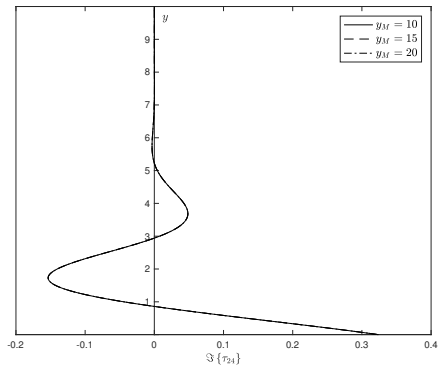

(D) $\Im\{\tau_{24}\}$

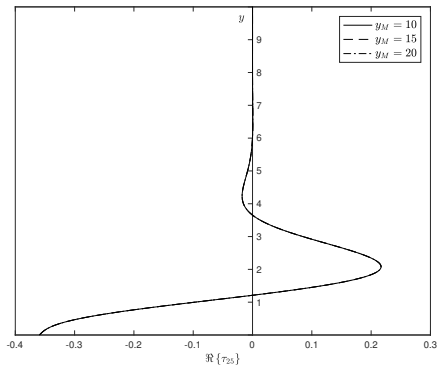

(E) $\Re\{\tau_{25}\}$

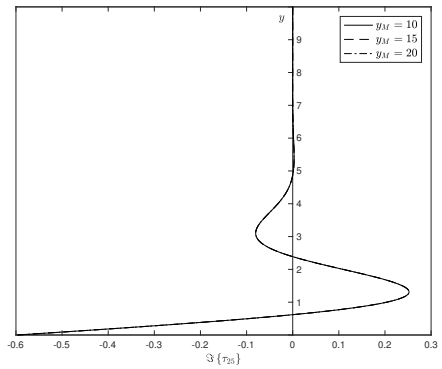

(F) $\Im\{\tau_{25}\}$

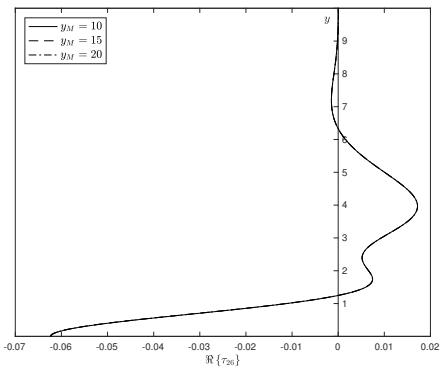

(G) $\Re\{\tau_{26}\}$

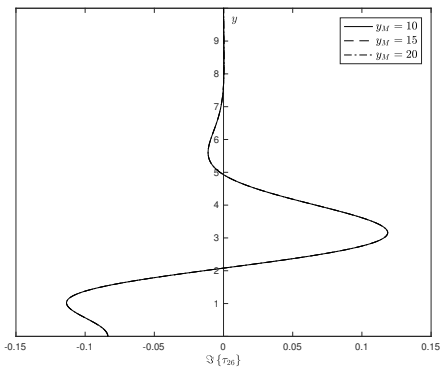

(H) $\Im\{\tau_{26}\}$

FIGURE A.2: Influence of changing the end of the computational domain in the wall-normal direction (y_M) on the solution for the shear stress components $\tau_{2i}, i = 3, \ldots, 6$, as described in the text.

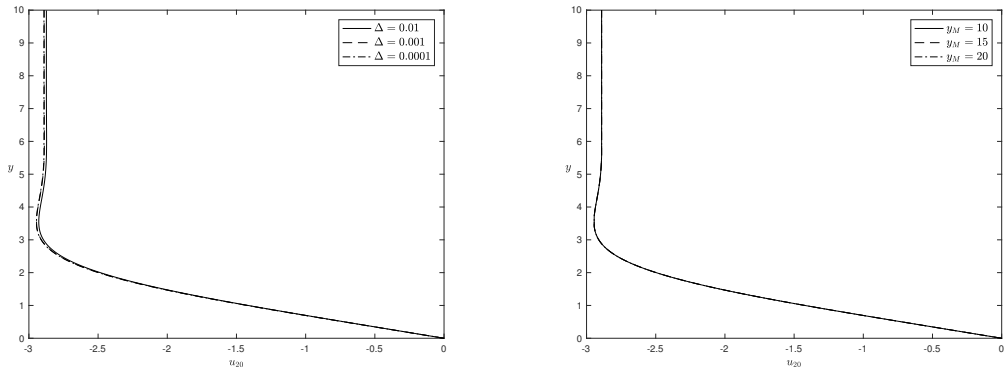

(A) Mesh check (B) End check

FIGURE A.3: Check on the mesh size and termination point of the computational domain, at which the boundary condition (A.5c) is applied, for the numerical calculation of the steady velocity u_{20} for flow over a blip array with constant maximum amplitude $G(\bar{x}) = 1$. The frequency of oscillation and wavenumber of the blip elements are both equal to 1. In §3.3, $\Delta = 0.0001$ and $y_M = 10$ will be used.

and so, by comparison with (A.7),

$$p_{m-1} = -\frac{1}{p_m - 2}, \tag{A.8a}$$

$$q_{m-1} = \frac{\Delta^2 R_m - q_m}{p_m - 2}. \tag{A.8b}$$

Furthermore, we know from the boundary conditions that $u_1 = 0$ and that $u_M = u_{M-1}$, which implies that $p_{M-1} = 1$ and $q_{M-1} = 0$, where M is the subscript corresponding to the final mesh point (at 'infinity'). Hence one first computes p_m and q_m from $m = M-1$ to 1 using (A.8), and then u_m from $m = 2$ to M using (A.7).

The effect of changing the mesh size and end point of the computational domain is shown in figure A.3 for the constant function $G(\bar{x})$ and $\omega = \alpha = 1$. Good agreement is seen for all termination points tested and so y_M will be set at 10 in §3.3, but a small difference is seen as we refine the mesh from $\Delta = 0.01$ to $\Delta = 0.0001$. The Thomas algorithm used is, however, remarkably fast and does not impose too onerous a weight on the computational time required; on top of this, the solutions at $\mathcal{O}(\epsilon)$ that are needed to compute the forcing have analytic expressions and are thus also easy and quick to compute. We choose therefore to use $\Delta = 0.0001$ to solve for the steady streaming velocity, noting that smaller values could be used without heavily impacting the time required to obtain a solution.

A.3 Mean flow correction

A.3.1 Pressure

The mean flow correction pressure is given by equation (3.33) as

$$p = -\gamma \int_0^x u(s)(x-s)^{-\frac{2}{3}}\,\mathrm{d}s, \tag{A.9}$$

where γ is a constant, u here refers to the steady streaming velocity at the top of the inner layer and the overbar and all subscripts have been removed. Evaluation of the integral is through the trapezium rule, with the singularity at x resolved by supposing that u is linear there.

Hence we can write $u_n = g_n s + c_n$ for $s \in [x_{n-1}, x_n]$, with

$$g_n = \frac{u_n - u_{n-1}}{x_n - x_{n-1}},$$

and

$$\begin{aligned} p_n =& -\gamma \int_{x_1}^{x_{n-1}} u(s)\,(x_n - s)^{-\frac{2}{3}}\,\mathrm{d}s - \gamma \int_{x_{n-1}}^{x_n} (gs + c)\,(x_n - s)^{-\frac{2}{3}}\,\mathrm{d}s \\ =& -\gamma\Delta \left[\frac{1}{2}u_1\,(x_n - x_1)^{-\frac{2}{3}} + \frac{1}{2}u_{n-1}\,(x_n - x_{n-1})^{-\frac{2}{3}} + \sum_{i=2}^{n-2} u_i\,(x_n - x_i)^{-\frac{2}{3}}\right] \\ & - \frac{3}{4}\gamma\,(x_n - x_{n-1})^{\frac{1}{3}}\left[4u_{n-1} + 3g_{n-1}\,(x_n - x_{n-1})\right], \end{aligned} \tag{A.10}$$

valid for $n \geq 4$. Note that $x_1 = 0$. For the subscripts $n < 4$, we have

$$p_1 = 0, \tag{A.11a}$$

$$p_2 = -\frac{3}{4}\gamma\,(x_2 - x_1)^{\frac{1}{3}}\left[4u_1 + 3g_1\,(x_2 - x_1)\right], \tag{A.11b}$$

$$p_3 = -\frac{1}{2}\gamma\Delta\left[u_1\,(x_3 - x_1)^{-\frac{2}{3}} + u_2\,(x_3 - x_2)^{-\frac{2}{3}}\right] - \frac{3}{4}\gamma\,(x_3 - x_2)^{\frac{1}{3}}\left[4u_2 + 3g_2\,(x_3 - x_2)\right]. \tag{A.11c}$$

A.3.2 Shear

Although an expression for the Fourier-transformed shear stress $\bar{\tau}_M$ was found in (3.31), the relevant figures plotted in §3.3.2 are obtained by numerically solving the partial differential equation (3.29):

$$\lambda y \frac{\partial \tau}{\partial x} = \frac{\partial^2 \tau}{\partial y^2}, \tag{A.12a}$$

$$\tau \to 0 \quad \text{as } y \to \infty, \tag{A.12b}$$

$$\int_0^\infty \tau\,\mathrm{d}y = -u. \tag{A.12c}$$

To this is added the boundary condition for x: $\tau = 0$ on $x = 0$. If $\tau_{i,j}$ denotes the ith mesh point in the normal direction (y) and the jth mesh point in the horizontal direction (x), the solution is found by discretising (A.12a) as

$$\tau_{m+1,n} - 2\tau_{m,n} + \tau_{m-1,n} = \Delta y_m \left(\tau_{m,n} - \tau_{m,n-1}\right),$$

using a second order accurate centred difference on the y derivative and a first order accurate backwards difference on the x derivative, with $\Delta = \lambda \Delta_y^2 \Delta_x^{-1}$.

This is rearranged as

$$\tau_{m+1,n} - (2 + \Delta y_m)\, \tau_{m,n} + \tau_{m-1,n} = \Delta y_m \tau_{m,n-1} \tag{A.13}$$

and solved by marching downstream in x, obtaining all y values at each streamwise mesh point along the way, in a similar manner to that described in §A.1. The upper vertical limit of the computational domain is once more set at $y_M = 10$ and the step size in both x and y directions is $\Delta_x = \Delta_y = 0.001$. The streamwise velocity in the upper layer is then obtained by an integration of τ using the definition

$$\tau = \frac{\partial \bar{u}}{\partial y}.$$

B

Roughnesses on a hump: numerical techniques

This appendix outlines the numerical techniques used in chapter 5. These include a variety of methods, which solve the simpler linearised equations of §5.4 to the more complex nonlinear parabolic system (5.61), which, in the case of dynamic roughness elements, is also time-dependent. There is, however, only the streamwise spatial direction to consider and thus, unless we are dealing with the dynamic case, the subscript n will refer to the nth mesh point in the horizontal direction. In the case of dynamic roughness elements, where the solution is found as the sum of Fourier modes, the subscripts m, n refer to the mth mode and the nth streamwise mesh point. The step size is Δ and the computational domain starts with the mesh point x_1 and ends with the mesh point x_N; any subscripts less than 1 have been set using the starting condition.

B.1 Linearised solutions

For simplicity, the subscripts appearing in this section, which deals with the linearised theory of §5.4, refer either to the mesh points, as described above, or, if x and s, to a derivative. The notation introduced in table 5.1 is suspended and x is the streamwise coordinate.

B.1.1 First order solution

To remove the singularity in the integrand of equation (5.68), we use an integration by parts to obtain

$$AA' + \frac{1}{2} = \frac{1}{x_1^2}\left[\frac{1}{2}\left|x_1\right|^{\frac{1}{2}} + \frac{3}{4}\left|x_1\right|^{-\frac{1}{2}}\ln\left|x_1\right| - 2\left|x_1\right|^{-\frac{1}{2}}\right](x - x_1)^{\frac{1}{2}} + \frac{1}{2x}\left[-1 + \left(1 - \frac{x}{x_1}\right)^{\frac{1}{2}}\right] - 2\int_{x_1}^{x}(x-s)^{\frac{1}{2}}\,\alpha'''\,\mathrm{d}s, \tag{B.1}$$

to be solved subject to the condition

$$A \to |x|^{\frac{1}{2}} - \frac{1}{2}\,|x|^{-\frac{1}{2}} \ln|x| \quad \text{as } x \to -\infty.$$

We set $\beta = A_x$ and $\gamma = \beta_x = A_{xx}$. Thus:

$$A\beta = \delta - 2\int_{x_1}^{x} \gamma_s (x-s)^{\frac{1}{2}}\,\mathrm{d}s = \delta - 2I, \tag{B.2}$$

where

$$\begin{aligned}\delta = &-\frac{1}{2} + \frac{1}{x_1^2}\left[\frac{1}{2}\,|x_1|^{\frac{1}{2}} + \frac{3}{4}\,|x_1|^{-\frac{1}{2}}\ln|x_1| - 2\,|x_1|^{-\frac{1}{2}}\right](x-x_1)^{\frac{1}{2}} \\ &+ \frac{1}{2x}\left[-1 + \left(1 - \frac{x}{x_1}\right)^{\frac{1}{2}}\right],\end{aligned}$$

with the final term coming from the effect of truncating the semi-infinite integral at some finite x_1, prior to which the leading order term in the upstream condition is applied to compute the integral from $-\infty$ to x_1 analytically.

We use trapezoidal integration on the integral I:

$$\begin{aligned} I_n &= \int_{x_1}^{x_n} \gamma_s (x_n - x_s)^{\frac{1}{2}}\,\mathrm{d}s \\ &= \frac{1}{2}(n-1)^{\frac{1}{2}}\Delta^{\frac{3}{2}}\gamma_s(x_1) + \Delta^{\frac{3}{2}}\sum_{j=2}^{n-1}\gamma_s(x_j)(n-j)^{\frac{1}{2}}.\end{aligned}$$

The derivative γ_s is discretised using a second order accurate centred difference to obtain

$$\begin{aligned} I_n &= \frac{1}{4}\Delta^{\frac{1}{2}}(n-1)^{\frac{1}{2}}(\gamma_2 - \gamma_0) + \frac{1}{2}\Delta^{\frac{1}{2}}\sum_{j=2}^{n-1}(n-j)^{\frac{1}{2}}(\gamma_{j+1} - \gamma_{j-1}) \\ &= \frac{1}{2}\Delta^{\frac{1}{2}}\gamma_n + \epsilon_n,\end{aligned}$$

where

$$\epsilon_n = -\frac{1}{2}\Delta^{\frac{1}{2}}\gamma_{n-2} + \frac{1}{4}\Delta^{\frac{1}{2}}(n-1)^{\frac{1}{2}}(\gamma_2 - \gamma_0) + \frac{1}{2}\Delta^{\frac{1}{2}}\sum_{j=2}^{n-2}(n-j)^{\frac{1}{2}}(\gamma_{j+1} - \gamma_{j-1}). \tag{B.3}$$

Here, ϵ_n contains terms up to at most γ_{n-1} and so is known at the n^{th} mesh point.

Equation (B.2) can be discretised as

$$A_{n-1}\beta_n = \delta_n - \Delta^{\frac{1}{2}}\gamma_n - 2\epsilon_n.$$

But $\gamma = \beta_x$, which is discretised using a second order accurate backwards difference, to obtain both

$$\beta_n = \frac{2}{3}\left(\Delta\gamma_n + 2\beta_{n-1} - \frac{1}{2}\beta_{n-2}\right), \tag{B.4}$$

and

$$\gamma_n = \left(\frac{2}{3}\Delta A_{n-1} + \Delta^{\frac{1}{2}}\right)^{-1}\left(\delta_n - 2\epsilon_n - \frac{4}{3}A_{n-1}\beta_{n-1} + \frac{1}{3}A_{n-1}\beta_{n-2}\right). \tag{B.5}$$

Discretising $\beta = A_x$ using a second order accurate backwards difference gives us A_n:

$$A_n = \frac{2}{3}\left(\Delta\beta_n + 2A_{n-1} - \frac{1}{2}A_{n-2}\right). \tag{B.6}$$

Hence the scheme is as follows:

1. Compute ϵ_n using (B.3);
2. Compute γ_n using (B.5);
3. Compute β_n using (B.4);
4. Compute A_n using (B.6).

Note that $A_{-3}, \cdots, A_1$ need to be set from the upstream boundary condition; then

$$\begin{aligned}
\gamma_0 &= \Delta^{-2}\left(2A_0 - 5A_{-1} + 4A_{-2} - A_{-3}\right),\\
\gamma_1 &= \Delta^{-2}\left(2A_1 - 5A_0 + 4A_{-1} - A_{-2}\right),\\
\gamma_2 &= \Delta^{-2}\left(2A_2 - 5A_1 + 4A_0 - A_{-1}\right),\\
\beta_0 &= \Delta^{-1}\left(\frac{3}{2}A_0 - 2A_{-1} + \frac{1}{2}A_{-2}\right),\\
\beta_1 &= \Delta^{-1}\left(\frac{3}{2}A_1 - 2A_0 + \frac{1}{2}A_{-1}\right),\\
\beta_2 &= \Delta^{-1}\left(\frac{3}{2}A_2 - 2A_1 + \frac{1}{2}A_0\right);
\end{aligned}$$

and ϵ_3 takes the slightly different form

$$\epsilon_3 = -\frac{1}{2}\Delta^{\frac{1}{2}}\gamma_1 + \frac{1}{4}\Delta^{\frac{1}{2}}2^{\frac{1}{2}}(\gamma_2 - \gamma_0).$$

Figure B.1 indicates the influence of changing the mesh size and start of the computational domain on the solution. The agreement is promising in all cases, as well as agreeing with that presented in Smith & Daniels [85], with whose solution it should coincide. However, we note that the position of the singularity is markedly advanced for a step size of $\Delta = 0.0001$, although in the linearised solutions we will only be interested in the position of vanishing skin friction. Throughout §5.4, a step size of $\Delta = 0.001$ and start point of $x_1 = -10$ will be used.

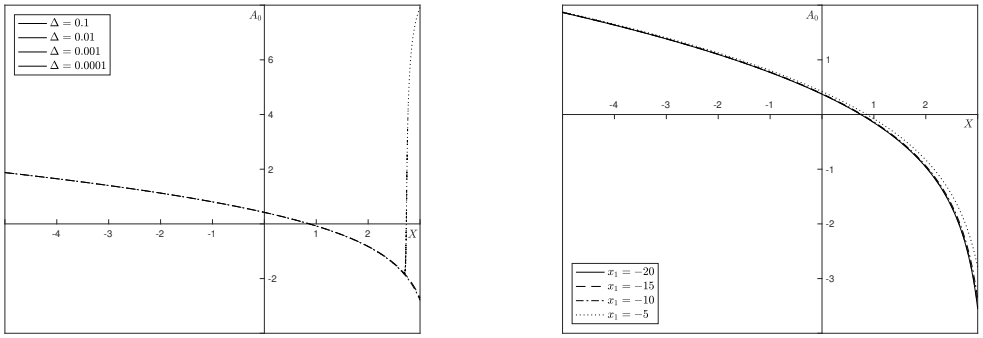

(A) Mesh size, $x_1 = -5$ (B) Domain start, $\Delta = 0.001$

FIGURE B.1: Influence of both (a) the mesh size and (b) the start of the computational domain on the solution for the leading order linearised solution to the displacement A_0, which coincides with the solution of Smith & Daniels [85].

B.1.2 Second order solution

We remove the singularity in the integrand by carrying out an integration by parts on equation (5.71) to obtain

$$\alpha\frac{\partial A}{\partial x}+A\frac{\partial \alpha}{\partial x}+\frac{\partial}{\partial x}(\alpha f)=-\frac{4}{3}\mathrm{i}\omega\int_{x_1}^{x}(x-s)^{\frac{3}{4}}\frac{\partial^2}{\partial s^2}(A+f)\,\mathrm{d}s-2\int_{x_1}^{x}(x-s)^{\frac{1}{2}}\frac{\partial^3 A}{\partial s^3}\,\mathrm{d}s, \quad \text{(B.7)}$$

where α corresponds to the A_0 of §5.4 and A is the function we are solving for (A_{11}). Note that there is no issue with starting at a finite value x_1 here, since both A and the roughness shape f are zero upstream. We rewrite this as

$$\alpha\frac{\partial A}{\partial x}+AB=-C-\frac{4}{3}\mathrm{i}\omega I-\frac{4}{3}\mathrm{i}\omega J-2K, \quad \text{(B.8)}$$

with

$$\begin{aligned}
\alpha &= A_0,\\
B &= \frac{\partial \alpha}{\partial x},\\
C &= \frac{\partial}{\partial x}\left(\alpha f\right),\\
I &= \int_{x_1}^{x}(x-s)^{\frac{3}{4}}\frac{\partial^2 f}{\partial s^2}\,\mathrm{d}s,\\
J &= \int_{x_1}^{x}(x-s)^{\frac{3}{4}}\frac{\partial^2 A}{\partial s^2}\,\mathrm{d}s,
\end{aligned}$$

and

$$K=\int_{x_1}^{x}(x-s)^{\frac{1}{2}}\frac{\partial^3 A}{\partial s^3}\,\mathrm{d}s.$$

The upstream boundary condition of α is used to set the first few terms of B, then a second order accurate backwards difference scheme is used. The roughness shape f is 0 upstream, so C can be set to 0 upstream and then a second order accurate backwards difference scheme is also used. Trapezoidal integration is used on the integral I, with the definition of f used to compute the second derivative analytically. The integral J can be discretised as

$$J_n = \Delta^{-\frac{1}{4}} \left[\frac{1}{2}(n-1)^{\frac{3}{4}} \left(A_2 - 2A_1 + A_0\right) + \sum_{j=2}^{n-1} (n-j)^{\frac{3}{4}} \left(A_{j+1} - 2A_j + A_{j-1}\right) \right], \quad \text{(B.9)}$$

where a second order accurate centred difference is used on the derivative. The integral K is discretised as

$$K_n = \frac{1}{2}\Delta^{-\frac{3}{2}} A_{n+1} + \epsilon_n, \quad \text{(B.10a)}$$

with

$$\begin{aligned} \epsilon_n = &\frac{1}{4}\Delta^{-\frac{3}{2}}(n-1)^{\frac{1}{2}} \left(A_3 - 2A_2 + 2A_0 - A_{-1}\right) + \frac{1}{2}\Delta^{-\frac{3}{2}} \left(-2A_n + 2A_{n-2} - A_{n-3}\right) \\ &+ \frac{1}{2}\Delta^{-\frac{3}{2}} \sum_{j=2}^{n-2} (n-j)^{\frac{1}{2}} \left(A_{j+2} - 2A_{j+1} + 2A_{j-1} - A_{j-2}\right), \end{aligned} \quad \text{(B.10b)}$$

where, again, the trapezoidal rule and a second order accurate centred difference on the derivative is used.

We then rearrange equation (B.8) as

$$\begin{aligned} A_{n+1} = &\left(\frac{1}{2}\Delta^{-1}\alpha_n + \Delta^{-\frac{3}{2}} \right)^{-1} \\ &\left(-C_n - \frac{4}{3}\mathrm{i}\omega I_n - \frac{4}{3}\mathrm{i}\omega J_n - 2\epsilon_n - A_n B_n + \frac{1}{2}\Delta^{-1}\alpha_n A_{n-1} \right) \end{aligned} \quad \text{(B.11)}$$

for A_{n+1}. The strategy is therefore as follows:

1. Compute J_n using (B.9);

2. Compute ϵ_n using (B.10b);

3. Compute A_{n+1} using (B.11).

With x_1 set at -5 and a dynamic roughness element, of height 1 and frequency 1, positioned between -3 and -1, the influence of changing the mesh size is shown in figure B.2. There is near perfect agreement between all mesh sizes throughout the computational domain, except as the singularity is approached, where the solution becomes unstable sooner for smaller mesh sizes, especially for $\Delta = 0.0001$. We are, in this linearised scenario, only interested in the position of vanishing skin friction, where all four mesh sizes agree, and thus we will ignore this behaviour here.

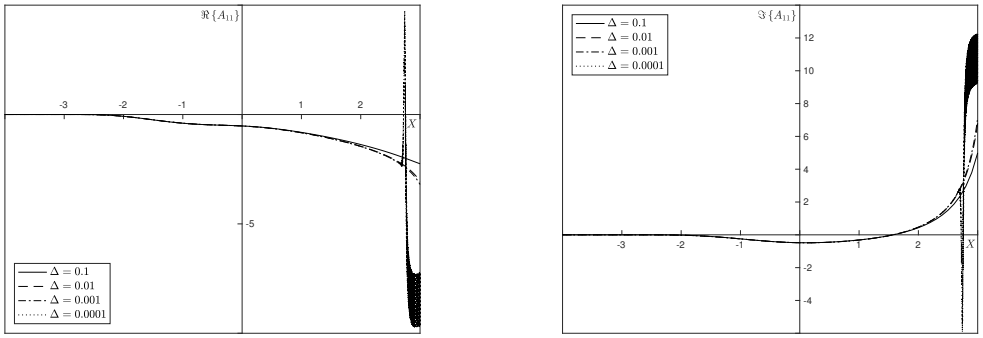

(A) Real part (B) Imaginary part

FIGURE B.2: Influence of the mesh size Δ on the solution to A_{11} for both real and imaginary parts. The roughness is placed between -3 and 1 and has both height and oscillation frequency equal to 1. Good agreement is found throughout, until the singularity is approached, with the appearance of an instability advancing as the mesh is refined, a behaviour particularly noticeable when $\Delta = 0.0001$.

B.1.3 The mean flow correction

Equation (5.75), once an integration by parts is performed, becomes

$$A_0 \frac{\partial A_M}{\partial x} + A_M \frac{\partial A_0}{\partial x} + \frac{\partial}{\partial x}\left[\left(A_{11} + \bar{f}\right)\left(A_{11}^* + \bar{f}\right)\right] = -2\int_{-\infty}^{x} (x-s)^{\frac{1}{2}} \frac{\partial^3 A_M}{\partial s^3}\,\mathrm{d}s. \quad \text{(B.12)}$$

There is nothing new here compared to equations (B.1) and (B.7): the integral on the right-hand side is treated in exactly the same way as before and the derivative of A_M is written using a second order accurate centred difference.

Figure B.3 shows the impact of changing the mesh size on the solution, for a roughness placed between -3 and -1, with height and oscillation frequency both 1. Once more, good agreement is found for all mesh sizes up until the point where the singularity is reached downstream of the position of vanishing skin friction. Although the solutions for the two coarser grids are similar, when the mesh is refined to have a step size of $\Delta = 0.0001$, the solution breaks down noticeably sooner.

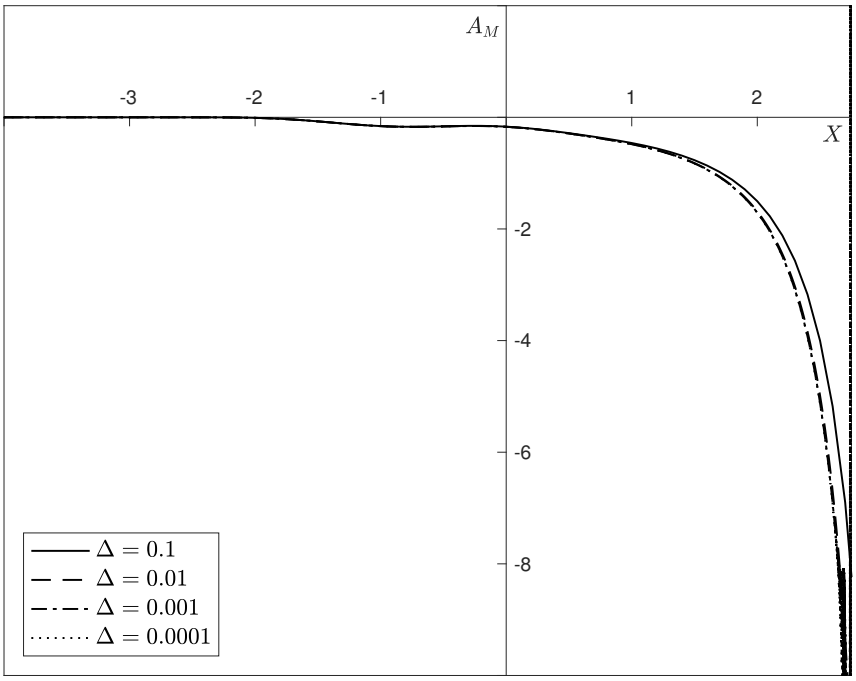

FIGURE B.3: Influence of the mesh size Δ on the solution to the mean displacement correction, A_M. The roughness is placed between -3 and 1 and has both height and oscillation frequency equal to 1. Once more, good agreement is found until the singularity is approached, when the solution for the mesh size of $\Delta = 0.0001$ breaks down sooner.

B.2 Nonlinear solution: static roughness

The numerical method used to solve the governing nonlinear system (5.90) for static bumps is very similar to that used to solve for A_0 in the linearised case (appendix B.1.1). The governing equation (5.90a), following an integration by parts, becomes

$$AA_x + fA_x + Af_x + ff_x + \frac{1}{2} = \frac{1}{4}\int_{-\infty}^{x_1} (x-s)^{-\frac{1}{2}}(-s)^{-\frac{3}{2}}\,\mathrm{d}s - 2\,(x-x_1)^{\frac{1}{2}}\left.\frac{\partial^2 A}{\partial x^2}\right|_{x=x_1} - 2\int_{x_1}^{x}(x-s)^{\frac{1}{2}}\,A_{sss}\,\mathrm{d}s \tag{B.13}$$

to be solved subject to the boundary condition

$$A \to |x|^{\frac{1}{2}} - \frac{1}{2}|x|^{-\frac{1}{2}}\ln|x| \quad \text{as } x \to x_1.$$

Calling $\beta = A_x$ and $\gamma = \beta_x = A_{xx}$, this can be rewritten as

$$A\beta + f\beta + Af_x + C = -2I, \tag{B.14}$$

where

$$C = ff_x + \frac{1}{2} - \frac{1}{2x}\left[-1 + \left(1 - \frac{x}{x_1}\right)^{\frac{1}{2}}\right] + 2\,(x-x_1)^{\frac{1}{2}}\left.\frac{\partial^2 A}{\partial s^2}\right|_{x=x_1}$$

and

$$I = \int_{x_1}^{x}(x-s)^{\frac{1}{2}}\gamma_s\,\mathrm{d}s.$$

We can use the boundary condition to compute the final term in C and the roughness function f can be differentiated either analytically or numerically. The integral I is identical to that in Appendix B.1.1 and is dealt with in exactly the same way. Thus the governing equation is discretised as

$$A_{n-1}\beta_n + f_n\beta_n + A_{n-1}\,(f_x)_n + C_n = -\Delta^{\frac{1}{2}}\gamma_n - 2\epsilon_n,$$

where ϵ_n is as given in equation (B.3). We use equations (B.4) and (B.6) to obtain, in turn, β_n from γ_n and A_n from β_n, where γ_n is given by

$$\gamma_n = \left[\frac{2}{3}\Delta\,(A_{n-1}+f_n) + \Delta^{\frac{1}{2}}\right]^{-1} \left[-2\epsilon_n - A_{n-1}\,(f_x)_n - C_n - \frac{2}{3}\,(A_{n-1}+f_n)\left(2\beta_{n-1} - \frac{1}{2}\beta_{n-2}\right)\right], \tag{B.15}$$

similar to (B.5) but including the extra terms appearing in (B.13). The procedure is then the same: compute ϵ_n using (B.3); then γ_n using (B.15); then β_n using (B.4); and finally A_n using (B.6).

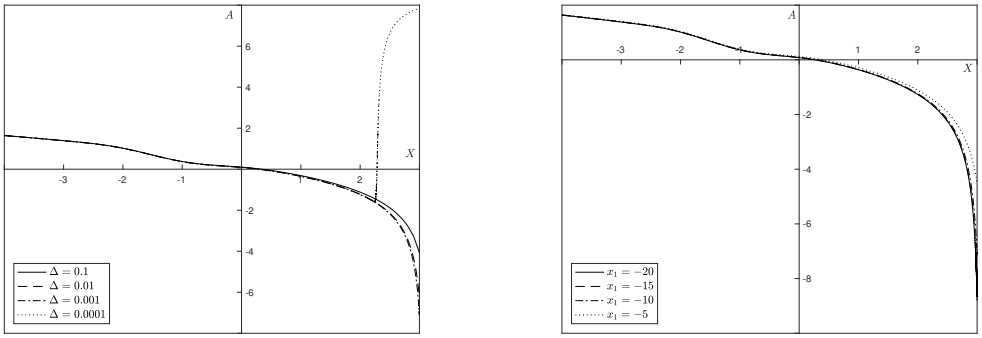

(A) Mesh size, $x_1 = -5$ (B) Domain start, $\Delta = 0.001$

FIGURE B.4: Influence of both (a) the mesh size and (b) the start of the computational domain for the numerical solution to the boundary layer displacement function A for flow over a static roughness element.

The influence of the computational parameters on the numerical solution to the boundary layer displacement is given in figure B.4. As per the linearised solution, there is good agreement between the various mesh sizes except for as the singularity is approached, when the finer mesh, with $\Delta = 0.0001$, breaks down sooner (figure B.4a). There is little difference in the solutions when the start of the computational domain is changed (figure B.4b), although the singularity in the case of $x_1 = -5$ seems to occur slightly farther downstream than when the computational domain is started farther upstream. In the solutions presented in §5.6.1, we set $x_1 = -10$ and $\Delta = 0.001$; while for the analysis of the position of global separation, §5.6.2, which coincides with the occurrence of the singularity, we set $x_1 = -10$ and $\Delta = 0.0001$. Any further refinement of the mesh is unfeasible in terms of the computational time required.

B.3 Nonlinear solution: dynamic roughness

In the case of the dynamic roughness, the equation for the negative boundary layer displacement A was converted into one for the skin friction, equation (5.93), which was decomposed into its various Fourier modes, τ_m, with

$$\begin{aligned}
&\sum_{k=-M}^{M} \tau_k \frac{\partial \tau_{m-k}}{\partial x} + \frac{4}{3} m\mathrm{i}\omega \int_{x_1}^{x} (x-s)^{\frac{3}{4}} \frac{\partial^2 \tau_m}{\partial s^2}\,\mathrm{d}s + 2\int_{x_1}^{x} (x-s)^{\frac{1}{2}} \frac{\partial^3 \tau_m}{\partial s^3}\,\mathrm{d}s \\
&= \delta_{0m}\left\{-\frac{1}{2} + 4\int_{x_1}^{x} (x-s)^{\frac{1}{2}} \frac{\partial^3 \bar{f}}{\partial s^3}\,\mathrm{d}s + \frac{1}{2x}\left[-1 + \left(1 - \frac{x}{x_1}\right)^{\frac{1}{2}}\right]\right\} \\
&\quad + 2\delta_{2m}\int_{x_1}^{x} (x-s)^{\frac{1}{2}} \frac{\partial^3 \bar{f}}{\partial s^3}\,\mathrm{d}s - 2\,(x-x_1)^{\frac{1}{2}} \left.\frac{\partial^2 \tau_m}{\partial x^2}\right|_{x=x_1}, \qquad \text{(B.16a)}
\end{aligned}$$

$$\tau_m \to \begin{cases} |x|^{\frac{1}{2}} - \frac{1}{2}|x|^{-\frac{1}{2}} \ln|x|, & \text{if } m = 0; \\ 0, & \text{if } m \neq 0, \end{cases} \quad \text{as } x \to x_1. \qquad \text{(B.16b)}$$

Once more, integration by parts was used to removed the singularities in the integrands of equation (5.93) and the upstream boundary condition was used to truncate the integrals at some finite x_1. Only one of the integrals needs to be dealt with in this way, since the coefficient m multiplying the other ensures that it does not appear in the steady equation, which is the only one in which the upstream condition is non-zero.

When solving for τ_m, the terms in the sum involving τ_m are extracted and kept on the left-hand side, while all other terms are moved over to the right-hand side, which acts as the forcing throughout. Thus when solving at the nth mesh point, all terms on the right-hand side and those multiplying τ_m on the left-hand side must involve at most the solution at the $(n-1)$th mesh point, which have already been found due to the process of downstream marching. The system of equations to be solved is then

$$\begin{aligned}
&\tau_0\frac{\partial\tau_0}{\partial x}+2\int_{x_1}^{x}(x-s)^{\frac{1}{2}}\frac{\partial^3\tau_0}{\partial s^3}\,\mathrm{d}s\\
&=-\frac{1}{2}+4\int_{x_1}^{x}(x-s)^{\frac{1}{2}}\frac{\partial^3\bar{f}}{\partial s^3}\,\mathrm{d}s+\frac{1}{2x}\left[-1+\left(1-\frac{x}{x_1}\right)^{\frac{1}{2}}\right]\\
&\quad-2\,(x-x_1)^{\frac{1}{2}}\left.\frac{\partial^2\tau_0}{\partial x^2}\right|_{x=x_1}-\sum_{\substack{k=-M,\\ k\neq 0}}^{M}\tau_k\frac{\partial\tau_{-k}}{\partial x},
\end{aligned}\tag{B.17a}$$

$$\tau_0\to|x_1|^{\frac{1}{2}}-\frac{1}{2}|x|^{-\frac{1}{2}}\ln|x|\quad\text{as } x\to x_1,\tag{B.17b}$$

for τ_0; and

$$\begin{aligned}
&\tau_0\frac{\partial\tau_m}{\partial x}+\tau_m\frac{\partial\tau_0}{\partial x}+\frac{4}{3}m\mathrm{i}\omega\int_{x_1}^{x}(x-s)^{\frac{3}{4}}\frac{\partial^2\tau_m}{\partial s^2}\,\mathrm{d}s+2\int_{x_1}^{x}(x-s)^{\frac{1}{2}}\frac{\partial^3\tau_m}{\partial s^3}\,\mathrm{d}s\\
&=2\delta_{2m}\int_{x_1}^{x}(x-s)^{\frac{1}{2}}\frac{\partial^3\bar{f}}{\partial s^3}\,\mathrm{d}s-\sum_{\substack{k=-M,\\ k\neq 0,m}}^{M}\tau_k\frac{\partial\tau_{m-k}}{\partial x},
\end{aligned}\tag{B.17c}$$

with $\tau_m\to 0$ as $x\to x_1$ for τ_m, $m\neq 0$.

In the following, $\tau_{m,n}$ refers to the solution to the mth Fourier mode of the skin friction at the nth mesh point. We deal first with the case where $m=0$, which is the steady mode of interest. We define $\beta_0=\partial\tau_0/\partial x$ and $\gamma_0=\partial\beta_0/\partial x$ and discretise (B.17a) as

$$\tau_{0,n-1}\beta_{0,n}=R_{0,n-1}-2I_{0,n},\tag{B.18a}$$

where

$$\begin{aligned}
R_{0,n}=&-\frac{1}{2}-2\Delta^{\frac{1}{2}}(n-1)^{\frac{1}{2}}\left.\frac{\partial^2\tau_0}{\partial x^2}\right|_{x_1}+4\int_{x_1}^{x}(x-s)^{\frac{1}{2}}\frac{\partial^3\bar{f}}{\partial s^3}\,\mathrm{d}s\\
&+\frac{1}{2x}\left[-1+\left(1-\frac{x}{x_1}\right)^{\frac{1}{2}}\right]-\Delta^{-1}\sum_{\substack{k=-M\\ k\neq 0}}^{M}\tau_{k,n}\left(\frac{3}{2}\tau_{-k,n}-2\tau_{-k,n-1}+\frac{1}{2}\tau_{-k,n-2}\right),
\end{aligned}\tag{B.18b}$$

$$I_{0,n} = \frac{1}{2}\Delta^{\frac{1}{2}}\gamma_{0,n} + \epsilon_{0,n-1}, \tag{B.18c}$$

and

$$\epsilon_{0,n} = \begin{cases} 0, & \text{if } n = 1; \\ \frac{1}{4}\Delta^{\frac{1}{2}}2^{\frac{1}{2}}\left(\gamma_{0,2} - \gamma_{0,0}\right) - \frac{1}{2}\Delta^{\frac{1}{2}}\gamma_{0,1}, & \text{if } n = 2; \\ -\frac{1}{2}\Delta^{\frac{1}{2}}\gamma_{0,n-1} + \frac{1}{4}\Delta^{\frac{1}{2}}n^{\frac{1}{2}}\left(\gamma_{0,2} - \gamma_{0,0}\right) & \\ \quad + \frac{1}{2}\Delta^{\frac{1}{2}}\sum_{j=2}^{n-1}(n+1-j)^{\frac{1}{2}}\left(\gamma_{0,j+1} - \gamma_{0,j-1}\right), & \text{if } n \geq 3. \end{cases} \tag{B.18d}$$

The first few terms, from $\tau_{0,-2}$ to $\tau_{0,2}$ need to be set from the boundary condition (B.17b), from which one also computes $\beta_{0,-1}$ to $\beta_{0,2}$ and $\gamma_{0,0}$ to $\gamma_{0,2}$.

Substituting (B.18c) into (B.18a) and using a backwards difference on the definition of γ_0,

$$\gamma_{0,n} = \Delta^{-1}\left(\frac{3}{2}\beta_{0,n} - 2\beta_{0,n-1} + \frac{1}{2}\beta_{0,n-2}\right), \tag{B.19a}$$

allows one to solve for

$$\gamma_{0,n} = \left(\frac{2}{3}\Delta\tau_{0,n-1} + \Delta^{\frac{1}{2}}\right)^{-1}\left[R_{0,n-1} - 2\epsilon_{0,n-1} - \frac{2}{3}\tau_{0,n-1}\left(2\beta_{0,n-1} - \frac{1}{2}\beta_{0,n-2}\right)\right]; \tag{B.19b}$$

a backwards difference on the definition of β_0, rearranged, then computes

$$\tau_{0,n} = \frac{2}{3}\left(\Delta\beta_{0,n} + 2\tau_{0,n-1} - \frac{1}{2}\tau_{0,n-2}\right). \tag{B.19c}$$

Once the initial terms are set, the numerical solution proceeds by computing $\gamma_{0,n}$ from (B.19b), then $\beta_{0,n}$ from (B.19a) and finally $\tau_{0,n}$ from (B.19c).

Of course, before proceeding to the $(n+1)$th mesh point, one must solve for the solution at the nth point of all the other modes, $m \neq 0$. This is done similarly to τ_0 above, but with some extra terms appearing in (B.17c). We first write $\beta_m = \partial\tau_m/\partial x$ and $\gamma_m = \partial\beta_m/\partial x$ to obtain

$$\tau_{0,n-1}\beta_{m,n} + \tau_{m,n-1}\frac{\partial\tau_{0,n-1}}{\partial x} + \frac{4}{3}m\mathrm{i}\omega I_{m,n} + 2J_{m,n} = R_{m,n-1}, \tag{B.20a}$$

where

$$R_{m,n} = 2F_{m,n} - \Delta^{-1}\sum_{\substack{k=-M,\\ k\neq 0, k\neq m}}^{M}\tau_{k,n}\left(\frac{3}{2}\tau_{m-k,n} - 2\tau_{m-k,n-1} + \frac{1}{2}\tau_{m-k,n-2}\right) \tag{B.20b}$$

and

$$F_{m,n} = \begin{cases} 0, & m \neq 2; \\ \displaystyle\int_{x_1}^{x_n} (x_n - s)^{\frac{1}{2}} \frac{\partial^3 \bar{f}}{\partial s^3} \, \mathrm{d}s, & m = 2. \end{cases} \tag{B.20c}$$

Note that a backwards difference will be used on the derivative of $\tau_{0,n-1}$ in (B.20a). Then

$$\begin{aligned} I_{m,n} &= \int_{x_1}^{x_n} (x_n - s)^{\frac{3}{4}} \, \gamma_m \mathrm{d}s \\ &= \begin{cases} 0, & n = 1; \\ \dfrac{1}{2}\Delta^{\frac{7}{4}} \gamma_{m,1}, & n = 2; \\ \dfrac{1}{2}\Delta^{\frac{7}{4}} (n-1)^{\frac{3}{4}} \gamma_{m,1} + \Delta^{\frac{7}{4}} \displaystyle\sum_{j=2}^{n-1} (n-j)^{\frac{3}{4}} \gamma_{m,j}, & n \geq 3; \end{cases} \end{aligned} \tag{B.21a}$$

and

$$J_{m,n} = \int_{x_1}^{x_n} (x_n - s)^{\frac{1}{2}} \frac{\partial \gamma_m}{\partial s} \, \mathrm{d}s = \frac{1}{2}\Delta^{\frac{1}{2}} \gamma_{m,n} + \epsilon_{m,n-1}, \tag{B.21b}$$

where

$$\epsilon_{m,n-1} = \begin{cases} 0, & n = 2; \\ \dfrac{1}{4}\Delta^{\frac{1}{2}} 2^{\frac{1}{2}} \left(\gamma_{m,2} - \gamma_{m,0}\right) - \dfrac{1}{2}\Delta^{\frac{1}{2}} \gamma_{m,1}, & n = 3; \\ \dfrac{1}{4}\Delta^{\frac{1}{2}} (n-1)^{\frac{1}{2}} \left(\gamma_{m,2} - \gamma_{m,0}\right) - \dfrac{1}{2}\Delta^{\frac{1}{2}} \gamma_{m,n-2} & \\ \quad + \dfrac{1}{2}\Delta^{\frac{1}{2}} \displaystyle\sum_{j=2}^{n-2} (n-j)^{\frac{1}{2}} \left(\gamma_{m,j+1} - \gamma_{m,j-1}\right), & n \geq 4. \end{cases} \tag{B.21c}$$

Once again, the terms $\tau_{m,-2}, \cdots, \tau_{m,2}$ must be set from the upstream boundary condition, allowing one to compute $\beta_{m,-1}, \cdots, \beta_{m,2}$ and $\gamma_{m,0}, \cdots, \gamma_{m,2}$. From then on, however, we substitute (B.21b) into (B.20a) and use the fact that γ_m is the first derivative of β_m to obtain

$$\begin{aligned} \gamma_{m,n} = \left(\frac{2}{3}\Delta\tau_{0,n-1} + \Delta^{\frac{1}{2}}\right)^{-1} \Bigg[& R_{m,n-1} - \Delta^{-1}\tau_{m,n-1}\left(\frac{3}{2}\tau_{0,n-1} - 2\tau_{0,n-2} + \frac{1}{2}\tau_{0,n-3}\right) \\ & - \frac{4}{3} m \mathrm{i}\omega I_{m,n} - 2\epsilon_{m,n-1} - \frac{2}{3}\tau_{0,n-1}\left(2\beta_{m,n-1} - \frac{1}{2}\beta_{m,n-2}\right)\Bigg]; \end{aligned} \tag{B.22a}$$

from which we retrieve $\beta_{m,n}$ and $\tau_{m,n}$ in turn as

$$\beta_{m,n} = \frac{2}{3}\left(\Delta\gamma_{m,n} + 2\beta_{m,n-1} - \frac{1}{2}\beta_{m,n-2}\right) \tag{B.22b}$$

and

$$\tau_{m,n} = \frac{2}{3}\left(\Delta\beta_{m,n} + 2\tau_{m,n-1} - \frac{1}{2}\tau_{m,n-2}\right). \tag{B.22c}$$

Note that $I_{m,n}$ above contains only the solution at mesh points up to $\tau_{m,n-1}$ and so is known in (B.22a).

Thus the strategy is as follows:

1. Set the upstream condition at the required mesh points;
2. Set the number of Fourier modes one wishes to compute, M;
3. Solve for the solution at mesh point n for all modes;
4. Proceed to the next mesh point, $n+1$, until one reaches the end of the computational domain;
5. Set $M = M + 2$ and repeat steps 3 and 4;
6. Compare the two steady solutions (τ_0) obtained. If

$$\max_{1\leq n\leq N_s}\left|\tau_{0,n}^{(M+2)} - \tau_{0,n}^{(M)}\right| < \text{tolerance},$$

where the superscript denotes the solution when M or $M+2$ modes are used and N_s is the number of streamwise mesh points up to when the solution starts falling away to the singularity, stop. Otherwise set $M = M + 2$ and repeat until convergence in the solution to τ_0 is obtained. The tolerance was set equal to 0.01.

Figure B.5 determines the impact of changing both the mesh size and start of the computational domain on the solution for the steady mode τ_0 in the presence of a dynamic roughness element, of height 1 and oscillation frequency 1, placed between -3 and 1. The singular point again advances slightly as the mesh is refined (figure B.5a), but an upstream jump similar to the one seen for static roughness elements is not seen, although only mesh sizes down to $\Delta = 0.0005$ were tested. Finer meshes required a considerable amount of computational time to solve for, especially since the code is run repeatedly to determine the appropriate number of Fourier modes that should be used in the expansion of the skin friction. The impact of changing the start of the computational domain, figure B.5b, was also deemed to be negligible and so in the graphs presented in §5.7, the mesh size was set to $\Delta = 0.005$ and the domain was started at $x_1 = -5$ as this was felt to represent a good balance between accuracy and speed of computation.

Although the number of modes used in the expansion of τ were determined by the code by comparing the solutions to τ_0 as more modes were added, figure B.6 indicates the impact of adding further modes to the expansion. Once again, there is no recognisable difference until the singular point is reached: then, it moves slightly upstream as more

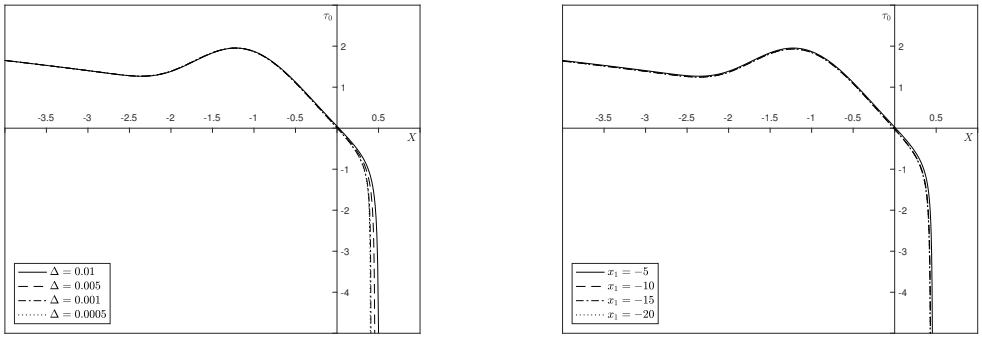

(A) Mesh size, $x_1 = -5$ (B) Domain start, $\Delta = 0.005$

FIGURE B.5: Influence of both (a) the mesh size and (b) the start of the computational domain on the numerical solution to the steady component of the skin friction, τ_0, in the presence of a dynamic roughness element, placed between -3 and 1, with maximum amplitude 1 and oscillation frequency 1.

modes are included but there is no noticeable difference in the solution for $M > 12$ for that choice of roughness parameters.

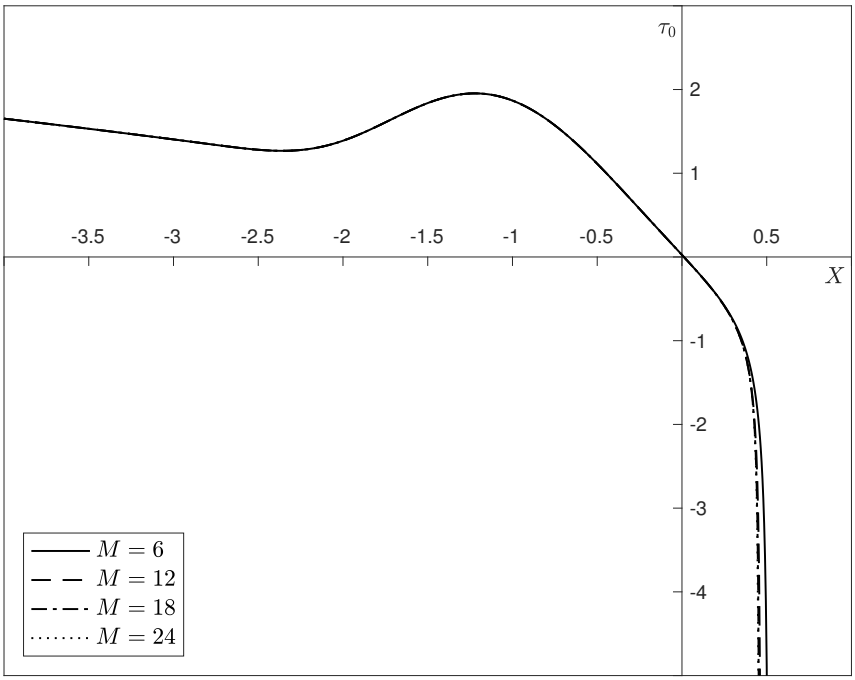

FIGURE B.6: Although the number of Fourier modes M used in the expansion of the skin friction is not predetermined but is rather set by the code as described in the text, the above graph indicates the impact of changing the number of modes used on the solution to the steady component of the skin friction, τ_0. We see that the only differences between all four solutions, with different values of M as indicated in the legend, occur near the singular point and any difference is very small. The dynamic roughness used is the same as that used in figure B.5.

C

Roughnesses on an airfoil: numerical techniques

The system to be solved in chapter 6 is that given by equation (6.38), where the function F represents either static or dynamic roughness elements. In the latter case, the full system (6.38) must be solved; in the former case, the flow is steady and thus the time derivative equals zero. A different numerical technique was used in each scenario, both derived from those presented in the work of Stewartson, Smith & Kaups [90]. Their first method was used for static roughness elements (§C.1), while their second method was adapted for use in the dynamic case (§C.2). Upper branch solutions only are obtained, the main interest being in the value of Γ_c and its accompanying boundary layer displacement function and pressure gradient.

Once more, the subscript m, n denotes the solution to the mth Fourier mode at the nth streamwise mesh point, except for in the steady case, where there are obviously no Fourier modes and thus only the mesh point is referred to. The mesh size is Δ, and we replace the streamwise coordinate X used in the interaction region of §6.2.2 with x, as in previous appendices (although all graphs plotted will retain the use of X). The computational domain starts at x_1 and ends at x_N.

C.1 Static roughness

The system to solve in the steady roughness case is given by equation (6.43), reproduced below

$$\pi\left[1-\frac{\partial}{\partial x}\left(A-F\right)\right]=\int_x^\infty (s-x)^{-\frac{1}{2}}\left(A^2-s^2+\Gamma\right)\,\mathrm{d}s, \tag{C.1a}$$

along with the upstream and downstream boundary condition

$$A\to\left(x^2-\Gamma\right)^{\frac{1}{2}}\quad \text{as } x\to\pm\infty, \tag{C.1b}$$

which fixes the values of A at the first and last mesh points of the computational domain. The strategy is as follows: we guess a solution for the displacement function A, compute

the integral, denoted by $I(x)$, using trapezoidal integration and then update the guess for the displacement function by applying equation (C.1a), which is discretised by using a first-order accurate backwards difference on the derivative. Hence, if the subscript 'n' denotes the nth mesh point and the superscript '(k)' the kth guess, we have

$$\tilde{A}_n^{(k)} = \tilde{A}_{n-1}^{(k)} + \Delta \left[1 + \left(\frac{\partial F}{\partial x} \right)_n - \pi^{-1} I_n^{(k-1)} \right] \tag{C.2a}$$

initially, but then an under-relaxation parameter, δ, must be applied to obtain the final guess

$$A^{(k)} = \delta \tilde{A}^{(k)} + (1-\delta) A^{(k-1)}. \tag{C.2b}$$

An under-relaxation value of $\delta = 0.6$ was used throughout, with a lower value of 0.1 used to confirm divergence of the solution. The iterative procedure is terminated once the residual, defined as being

$$r = \max \left| \pi \left[1 - \frac{\partial}{\partial x} (A - F) \right] - I(x) \right|, \tag{C.3}$$

is less than some small tolerance, taken to be 10^{-4}. The rate of convergence, for a roughness of height 1 and width 4, centred at 0, and for $\Gamma = 0$ and $\Gamma = 2.5$, is shown in figure C.1, with the initial guess equal to the matching condition (C.1b) when $\Gamma = 0$ and the solution at $\Gamma = 0$ used as the initial guess for the solution at $\Gamma = 2.5$ (for illustrative purposes, the requirement for convergence was taken to be much smaller here, equal to 10^{-6}).

Some care needs to be taken with the integral $I(x)$ due, firstly, to the existence of a singularity in the integrand at the lower limit of integration and, secondly, because of the replacement of the upper limit at infinity by some finite x-station, x_N. The former is dealt with by approximating $A^2 - s^2 + \Gamma$ as a linear function in s between x and $x + \Delta$ and then integrating analytically in this interval; the latter by using the downstream condition (C.1b) and again integrating analytically. Hence the integral I is split as follows:

$$I_n = I(x_n) = \left(\int_{x_n}^{x_{n+1}} + \int_{x_{n+1}}^{x_N} + \int_{x_N}^{x_\infty} \right) (s - x_n)^{-\frac{1}{2}} \left(A^2 - s^2 + \Gamma \right) \mathrm{d}s, \tag{C.4a}$$

where

$$\int_{x_n}^{x_{n+1}} (s - x_n)^{-\frac{1}{2}} \left(A^2 - s^2 + \Gamma \right) \mathrm{d}s = \frac{2}{3} \Delta^{\frac{1}{2}} \left[2 \left(A_n^2 - x_n^2 \right) + A_{n+1}^2 - x_{n+1}^2 + 3\Gamma \right]; \tag{C.4b}$$

and the condition (C.1b) can be rewritten for large x as

$$A \sim x - \frac{\Gamma}{2x} + \cdots,$$

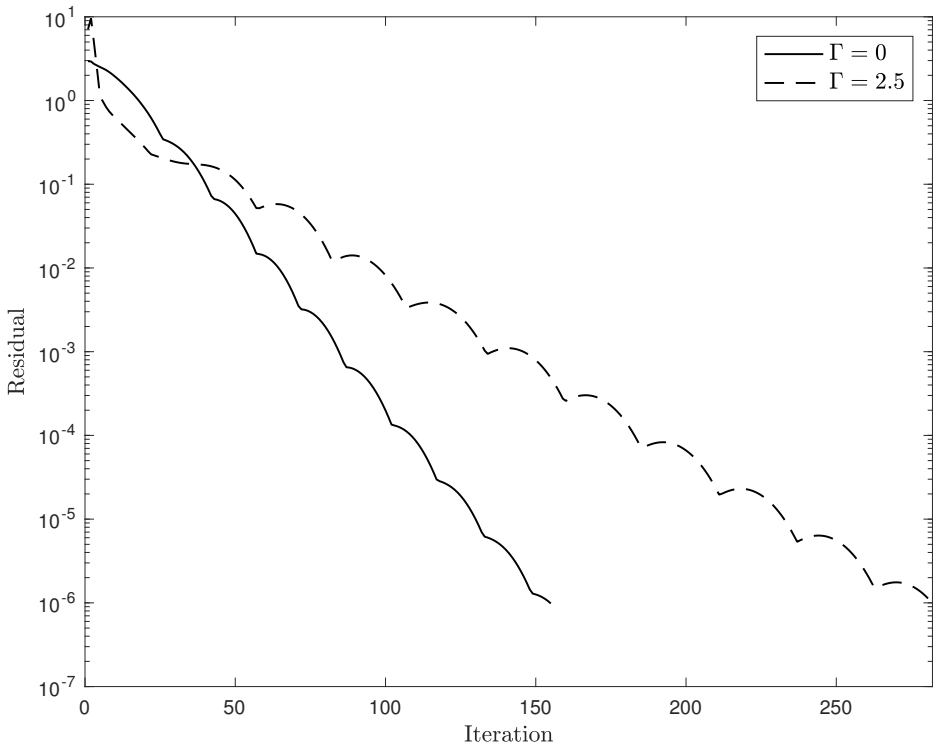

FIGURE C.1: Convergence of the solution for a static roughness element, of width 4, centred at 0, and height 1 and with $\Gamma = 0$ (solid line) and $\Gamma = 2.5$ (dashed line). The initial guess for the former was that given by equation (C.1b), while for the latter it was the solution obtained at $\Gamma = 0$. The calculation was terminated when the residual was less than 10^{-6}, which took, respectively, 155 and 282 iterations. The endpoints of the computational domain were at ± 10 and the mesh size was $\Delta = 0.05$.

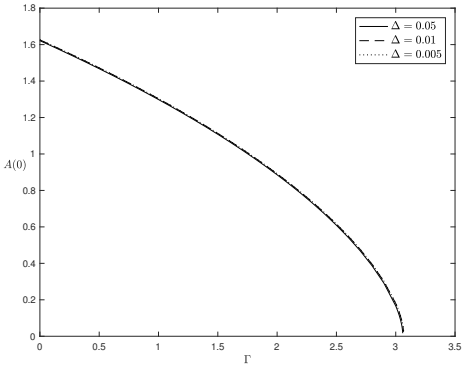

(A) Upper branch of $A(0)$ against Γ

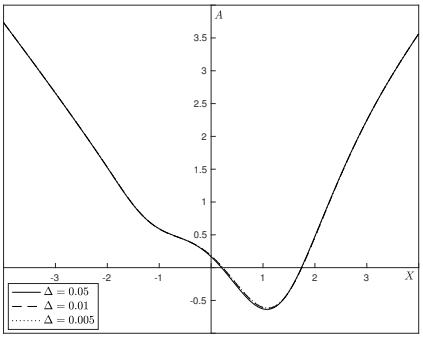

(B) Solution to A at $\Gamma = 3$

FIGURE C.2: The effect of changing the mesh size Δ, as given in the legend, for a static roughness centred at $X_M = 0$, with width 4 and height 1. The ends of the computational domain were at ± 10. Good agreement is found at all mesh sizes down to $\Delta = 0.005$.

substituted into the original governing equation (6.41) to obtain the behaviour

$$A^2 - x^2 + \Gamma \sim -\frac{3}{8}\pi\Gamma x^{-\frac{5}{2}} + \cdots ,$$

and hence

$$\int_{x_N}^{\infty} (s - x_n)^{-\frac{1}{2}} \left(A^2 - s^2 + \Gamma\right) \mathrm{d}s = \frac{1}{4}\pi\Gamma x_n^{-2} \left[x_N^{-\frac{3}{2}} (x_N - x_n)^{\frac{1}{2}} (2x_N + x_n) - 2\right]. \tag{C.4c}$$

Although equation (C.4c) has a singularity at $x_n = 0$, the use of L'Hôpital's rule gives the value $-(3/16)\pi\Gamma x_N^{-2}$ there.

The effects of changing the mesh size and endpoints of the computational domain are presented in figures C.2 and C.3 respectively, with both the graph of $A(0)$ against Γ and the graph of A at $\Gamma = 3$ (the largest integer value below Γ_c in all computational figurations tested) shown. In both cases, the static roughness was centred at $X_M = 0$, had width 4 and height 1.

Refining the mesh size has the effect of increasing Γ_c, although the change is extremely small (3.059 at $\Delta = 0.05$, 3.066 at $\Delta = 0.01$ and 3.067 at $\Delta = 0.005$); and the effect of varying the endpoints of the computational domain is negligible. Given this, for all graphs produced in §6.3.1, the endpoints were taken to be at ± 10 and the step size was chosen to be $\Delta = 0.05$. Finer meshes require a greater amount of computational time, not only due to the increased number of mesh points, but also as a larger number of iterations are required for convergence. The use of $\Delta = 0.05$ was deemed to be sufficient, especially as it seems to underestimate the value of Γ_c.

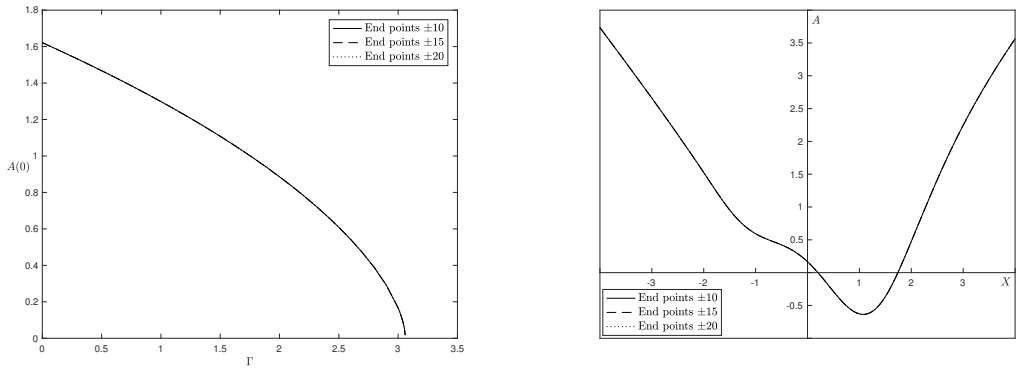

(A) Upper branch of $A(0)$ against Γ (B) Solution to A at $\Gamma = 3$

FIGURE C.3: The effect of changing the endpoints, as given in the legend, for a static roughness element as defined in figure C.2. The mesh size was $\Delta = 0.05$ and the solutions for endpoints between ± 10 and ± 20 are indistinguishable from each other.

C.2 Dynamic roughness

The system to be solved in the case of dynamic roughnesses, for each Fourier mode $m \geq 0$, is that given by equation (6.45), reproduced here below:

$$\begin{aligned}
&\sum_{k=-M}^{M} A_k A_{m-k} + \delta_{0m}\left(-x^2 + \Gamma\right) \\
&= \int_x^\infty (s-x)^{-\frac{1}{2}} A_m'' \,\mathrm{d}s - \delta_{2m} \int_x^\infty (s-x)^{-\frac{1}{2}} f'' \,\mathrm{d}s \\
&\quad - 2\delta_{0m} \int_x^\infty (s-x)^{-\frac{1}{2}} f'' \,\mathrm{d}s - 2\mathrm{i}m\omega \int_{-\infty}^x (x-s)^{-\frac{1}{4}} A_m \,\mathrm{d}s, \qquad \text{(C.5a)}
\end{aligned}$$

subject to

$$A_m \to \delta_{0m}\left(x^2 - \Gamma\right)^{\frac{1}{2}} \quad \text{as } x \to \pm\infty. \qquad \text{(C.5b)}$$

The δ_{ij} is the standard delta function, defined as being 1 when $i = j$ and 0 otherwise, and f is the roughness shape (independent of time).

As per the static roughness elements in §C.1, we look once again at the effects of the integral truncation. The only integral to worry about is the first in equation (C.5a) for A_0, since for all modes except the zeroth, the displacement tends to zero and, for the final integral, the coefficient m means that the steady mode ($m = 0$) will not contribute. So, from the downstream condition (C.5b), we have

$$A_0'' \sim -\Gamma x^{-3} + \cdots$$

as $x \to \pm\infty$ and hence

$$\int_{x_N}^\infty (s-x)^{-\frac{1}{2}} s^{-3} \,\mathrm{d}s$$

equals

$$\frac{1}{4}\left|x\right|^{-\frac{5}{2}} x_N^{-\frac{3}{2}} \left[2x^2\sqrt{\frac{1}{x_N}-\frac{1}{x}} - 3\sqrt{xx_N\left(x-x_N\right)} + 3x_N^{\frac{3}{2}}\mathrm{arsinh}\left(\sqrt{\frac{|x|}{x_N}}\right)\right] \tag{C.6a}$$

if $x < 0$,

$$\frac{2}{5}x_N^{-\frac{5}{2}} \tag{C.6b}$$

if $x = 0$, and

$$\frac{1}{8}x^{-\frac{5}{2}}x_N^{-2}\left\{-6x_N\sqrt{x\left(x_N-x\right)} - 4\sqrt{x^3\left(x_N-x\right)} + 3x_N^2\left[\pi - 2\arctan\left(\sqrt{\frac{x_N}{x}-1}\right)\right]\right\} \tag{C.6c}$$

if $x > 0$.

The nonlinear system (C.5) is then solved by applying Newton's method. Noting that we terminate the infinite sum at some finite M (so k varies from $-M$ to M), we are looking for the $(M+1)\times N$ matrix of unknowns

$$\mathbf{A} = \begin{pmatrix} A_{0,1} & A_{0,2} & \cdots & A_{0,N-1} & A_{0,N} \\ A_{1,1} & A_{1,2} & \cdots & A_{1,N-1} & A_{1,N} \\ \vdots & \vdots & \ddots & \vdots & \vdots \\ A_{M-1,1} & A_{M-1,2} & \cdots & A_{M-1,N-1} & A_{M-1,N} \\ A_{M,1} & A_{M,2} & \cdots & A_{M,N-1} & A_{M,N} \end{pmatrix},$$

where N is the number of streamwise mesh points. In the above, the entry A_{ij} corresponds to the solution of the ith mode at the jth mesh point. In order to apply Newton's method, the matrix is converted into a vector $\tilde{\mathbf{A}}$, where each mode follows on successively from the preceding one. This matrix (equivalently, vector) then needs to satisfy

$$\mathcal{H}(\mathbf{A}) = 0,$$

where $\mathcal{H}$ is the operator embodied in equation (C.5a).

The procedure is then as follows: one sets an initial guess for the solution, $\mathbf{A}^{(0)}$, and evaluates $\mathcal{H}(\mathbf{A}^{(0)})$, giving the residue $\tilde{\mathbf{R}}^{(0)}$, which is written as a vector. The updated guess then becomes, in general,

$$\tilde{\mathbf{A}}^{(k+1)} = \tilde{\mathbf{A}}^{(k)} - \mathbf{J}^{-1}\tilde{\mathbf{R}}^{(k)}, \tag{C.7}$$

which follows from a Taylor expansion about the kth guess, with $\mathbf{J}$ the Jacobian matrix. One repeats the process until either convergence is achieved, or the solution diverges, or the maximum number of iterations allowed is reached. Convergence is taken to be

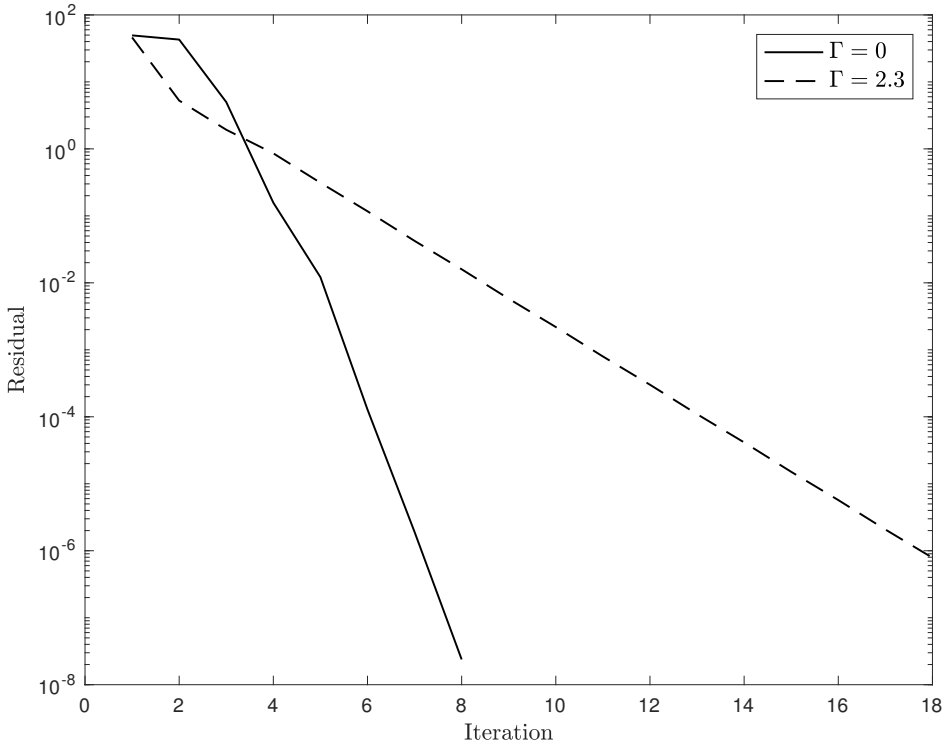

FIGURE C.4: Convergence of the solution for a dynamic roughness element, of width 4, centred at 0, height 1 and oscillation frequency 1 and with $\Gamma = 0$ (solid line) and $\Gamma = 2.3$ (dashed line). The initial guess for the former was that given by equation (C.5b), while for the latter it was the solution obtained at $\Gamma = 0$. The calculation was terminated when the residual was less than 10^{-6}, which took, respectively, 8 and 18 iterations. The endpoints of the computational domain were at ± 10 and the mesh size was $\Delta = 0.05$.

when the residue, defined as

$$r = \left(\sum_{m=1}^{M} \sum_{n=1}^{N} |\mathcal{H}_{m,n}|^2 \right)^{\frac{1}{2}}, \tag{C.8}$$

noting that $\mathcal{H}_{m,n}$ will contain complex terms, is less than a small tolerance, set again as 10^{-4}. Checks on the convergence of the solution, as was done in figure C.1 of §C.1, were performed for a dynamic roughness element centred at 0, of width 4, height 1 and oscillation frequency 1 and are shown in figure C.4.

C.2.1 Calculation of the operator $\mathcal{H}$

As in the static roughness case, all of the integrands in equation (C.5a) have a singularity either at the lower or upper limit of integration. This is dealt with in the same way as described in §C.1: by assuming that the function multiplying the term responsible for the singularity is linear between x and $x \pm \Delta$ (depending on whether the singularity is at the upper or lower limit of integration) and then integrating analytically to give

$$\int_{x_n}^{x_N} (s - x_n)^{-\frac{1}{2}} f'' \, \mathrm{d}s = \frac{2}{3}\Delta^{\frac{1}{2}} \left(f''_{n+1} + 2f''_n \right) + \int_{x_{n+1}}^{x_N} (s - x_n)^{-\frac{1}{2}} f'' \, \mathrm{d}s, \tag{C.9a}$$

$$\int_{x_n}^{x_N} (s - x_n)^{-\frac{1}{2}} A''_m \, \mathrm{d}s = \frac{2}{3}\Delta^{\frac{1}{2}} \left(A''_{m,n+1} + 2A''_{m,n} \right) + \int_{x_{n+1}}^{x_N} (s - x_n)^{-\frac{1}{2}} A''_m \, \mathrm{d}s, \tag{C.9b}$$

$$\int_{x_1}^{x_n} (x_n - s)^{-\frac{1}{4}} A_m \, \mathrm{d}s = \int_{x_1}^{x_{n-1}} (x_n - s)^{-\frac{1}{4}} A_m \, \mathrm{d}s + \frac{4}{21}\Delta^{\frac{3}{4}} \left(4A_{m,n} + 3A_{m,n-1} \right). \tag{C.9c}$$

The remaining integral is then evaluating using the trapezium rule and the derivatives appearing are approximated using a second-order accurate centred difference.

C.2.2 Computing the Jacobian

The Jacobian $\mathbf{J}$ is the matrix with entries

$$J_{ij} = \frac{\partial \tilde{R}_i}{\partial \tilde{A}_j},$$

or, in slightly different notation,

$$J_{ij} = \frac{\partial \mathcal{H}_i \left(\tilde{\mathbf{A}} \right)}{\partial \tilde{A}_j}, \tag{C.10}$$

where by $\mathcal{H}_i$ we understand that the operator $\mathcal{H}$ can be discretised to form a set of $(M+1)N$ equations for the $(M+1)N$ unknowns A_{ij}. The Jacobian is thus an $(M+1)N \times (M+1)N$ matrix and it is of great interest to us to be able to compute it analytically.

Since differentiation by A_j will result in all terms in equation (C.5a) not involving at least one of the modes of the displacement function vanishing, we can consider the operator $\mathcal{H}$, for the purposes of computing the Jacobian, to be given by

$$\mathcal{H}(\mathbf{A}) = \sum_{k=-M}^{M} A_k A_{m-k} - \int_x^{x_N} (s - x)^{-\frac{1}{2}} A''_m \, \mathrm{d}s + 2\mathrm{i}m\omega \int_{x_1}^{x} (x - s)^{-\frac{1}{4}} A_m \, \mathrm{d}s. \tag{C.11}$$

We then note that the Jacobian itself can be split into smaller matrices—

$$\mathbf{J} = \begin{pmatrix} \frac{\partial \mathcal{H}_0}{\partial A_0} & \cdots & \frac{\partial \mathcal{H}_0}{\partial A_M} \\ \vdots & \ddots & \vdots \\ \frac{\partial \mathcal{H}_M}{\partial A_0} & \cdots & \frac{\partial \mathcal{H}_M}{\partial A_M} \end{pmatrix} \tag{C.12}$$

—corresponding to the derivative of the N equations governing the mth mode ($\mathcal{H}_m$) with respect to the N mesh points of the $\tilde{m}$th mode ($A_{\tilde{m}}$).

For $m \neq \tilde{m}$, all integral terms vanish and the only contribution comes from the nonlinear sum,

$$\frac{\partial \mathcal{H}_m}{\partial A_{\tilde{m}}} = \frac{\partial}{\partial A_{\tilde{m}}} \left(\sum_{k=-M}^{M} A_k A_{m-k} \right) = 2A_{m-\tilde{m}}, \tag{C.13}$$

giving an $N \times N$ diagonal matrix with the entries of the guess for $2A_{m-\tilde{m}}$ along the main diagonal. This result is valid also for the $m = \tilde{m}$ matrices in the definition (C.12), with $2A_0$ being one component of their main diagonal. The situation is, however, complicated by the presence of the integral terms, which also contribute. Labelling

$$I_m = \int_x^{x_N} (s - x)^{-\frac{1}{2}} A_m'' \, \mathrm{d}s$$

and

$$K_m = \int_{x_1}^{x} (x - s)^{-\frac{1}{4}} A_m \, \mathrm{d}s,$$

the matrices along the main diagonal of $\mathbf{J}$ take the form

$$\frac{\partial \mathcal{H}_m}{\partial A_m} = 2A_0 - \frac{\partial I_m}{\partial A_m} + 2\mathrm{i}m\omega \frac{\partial K_m}{\partial A_m}. \tag{C.14}$$

Note that the linearity of A_m in the integrals I_m and K_m means that their differentiation with respect to A_m gives the same result regardless of the choice of mode m and thus we neglect the subscript m in what follows, to avoid confusion also with the mesh point, which will now appear as the sole subscript.

We deal first with the integral I. Using equation (C.9b), along with a second-order accurate centred difference on the derivative, we obtain

$$I_i = \frac{2}{3}\Delta^{-\frac{3}{2}} \left(A_{i+2} - 3A_i + 2A_{i-1} \right) + \Delta^{-2} \int_{x_{i+1}}^{x_N} (s - x_i)^{-\frac{1}{2}} \left(A_{s+1} - 2A_s + A_{s-1} \right) \mathrm{d}s; \tag{C.15a}$$

and hence, for $i = 1$, we have

$$\frac{\partial I_1}{\partial A_j} = \begin{cases} \frac{7}{6}\Delta^{-\frac{3}{2}}, & j = 1; \\ -\frac{4}{3}\Delta^{-\frac{3}{2}} + \left(2^{-\frac{1}{2}} - 1\right)\Delta^{-1}, & j = 2 \end{cases} \tag{C.15b}$$

due to the imposition of the upstream matching condition (C.5b), and then, for $j > 2$, we revert to the form given in equation (C.15c) below; for $2 \leq i \leq N-4$,

$$\frac{\partial I_i}{\partial A_j} = \begin{cases} 0, & j \leq i-2; \\ \frac{4}{3}\Delta^{-\frac{3}{2}}, & j = i-1; \\ -\frac{3}{2}\Delta^{-\frac{3}{2}}, & j = i; \\ \left(2^{-\frac{1}{2}} - 1\right)\Delta^{-\frac{3}{2}}, & j = i+1; \\ \left(\frac{7}{6} - 2^{\frac{1}{2}} + 3^{-\frac{1}{2}}\right)\Delta^{-\frac{3}{2}}, & j = i+2; \\ \Big[(x_{j-1}-x_i)^{-\frac{1}{2}} - 2\,(x_j - x_i)^{-\frac{1}{2}} & \\ \quad + (x_{j+1}-x_i)^{-\frac{1}{2}}\Big]\,\Delta^{-1}, & i+3 \leq j \leq N-2; \\ \Big[(x_{N-2}-x_i)^{-\frac{1}{2}} - 2\,(x_{N-1}-x_i)^{-\frac{1}{2}}\Big]\,\Delta^{-1}, & j = N-1; \\ (x_{N-1}-x_i)^{-\frac{1}{2}}\,\Delta^{-1}, & j = N. \end{cases} \tag{C.15c}$$

There are then some further slight modifications to the general representation of $\partial I_i/\partial A_j$ in equation (C.15c) due to the imposition of the downstream matching condition:

$$\frac{\partial I_{N-3}}{\partial A_{N-1}} = \left(\frac{7}{6} - 2^{\frac{1}{2}}\right)\Delta^{-\frac{3}{2}}; \tag{C.15d}$$

$$\frac{\partial I_{N-2}}{\partial A_j} = \begin{cases} -\Delta^{-\frac{3}{2}}, & j = N-1; \\ \frac{7}{6}\Delta^{-\frac{3}{2}}, & j = N; \end{cases} \tag{C.15e}$$

$$\frac{\partial I_{N-1}}{\partial A_j} = \begin{cases} 0, & j \leq N-3; \\ \frac{4}{3}\Delta^{-\frac{3}{2}}, & j = N-2; \\ -\frac{8}{3}\Delta^{-\frac{3}{2}}, & j = N-1; \\ \frac{4}{3}\Delta^{-\frac{3}{2}}, & j = N; \end{cases} \tag{C.15f}$$

and

$$\frac{\partial I_N}{\partial A_j} = 0, \quad \forall j. \tag{C.15g}$$

The second integral K is treated in a similar manner, the lack of a derivative making the procedure slightly less involved. The form

$$K_i = \int_{x_1}^{x_{i-1}} (x_i - s)^{-\frac{1}{4}}\, A_s \,\mathrm{d}s + \frac{4}{21}\Delta^{\frac{3}{4}}\,(4A_i + 3A_{i-1}) \tag{C.16a}$$

leads to

$$\frac{\partial K_i}{\partial A_j} = \begin{cases} \frac{1}{2}\left(x_i - x_1\right)^{-\frac{1}{4}}\Delta, & j = 1; \\ \left(x_i - x_j\right)^{-\frac{1}{4}}\Delta, & j \leq i-2; \\ \frac{15}{14}\Delta^{\frac{3}{4}}, & j = i; \\ 0, & j > i; \end{cases} \tag{C.16b}$$

valid for $i \geq 3$. The first row $\partial K_1/\partial A_j$ is zero for all j, while the second is given by

$$\frac{\partial K_2}{\partial A_j} = \begin{cases} \frac{12}{21}\Delta^{\frac{3}{4}}, & j = 1; \\ \frac{16}{21}\Delta^{\frac{3}{4}}, & j = 2; \\ 0, & j > 2. \end{cases} \tag{C.16c}$$

Hence the Jacobian can be fully defined by equations (C.12)–(C.16), speeding up its computation considerably and ensuring that the limiting factor on the speed of the algorithm is the calculation of the solution to the linear set of equations

$$\tilde{\mathbf{R}}^{(k)} = \mathbf{J}\left(\tilde{\mathbf{A}}^{(k)} - \tilde{\mathbf{A}}^{(k-1)}\right), \tag{C.17}$$

c.f. equation (C.7). Tests (not shown) were carried out, confirming that the Jacobian computed analytically as described above agreed with its numerical calculation.

C.2.3 Discretisation checks

As with the static roughness, checks need to be made on the effects of the mesh size (Δ), domain endpoints and, for dynamic roughness elements, the number of modes M that are included in the solution. Graphs of the upper branch of the displacement function (steady mode) against Γ and of the solution A_0 at $\Gamma = 2.35$, near $\Gamma_c \in [2.358, 2.363]$ for the configurations tested and for the same dynamic roughness element as used in the creation of figure C.4, are shown in figures C.5–C.7.

Mesh sizes of $\Delta = 0.1, 0.05$ and 0.025 were tested, with the size of the Jacobian matrix $\mathbf{J}$, containing $(M+1)^2N^2$ elements, and the process of solving the linear system (C.17), limiting the ability to test finer meshes. The results are presented in figure C.5. The difference between the solution at different mesh sizes is small, with a small decrease in the critical value of Γ as Δ is decreased (2.360 at $\Delta = 0.025$ compared to 2.363 at $\Delta = 0.05$ and 0.1). The solution for the steady mode of the displacement function at $\Gamma = 2.35$ is similar for all mesh sizes.

Using a mesh size of $\Delta = 0.025$, one next tested the effect of changing the endpoints of the computational domain, as shown in figure C.6. This has a small impact on the

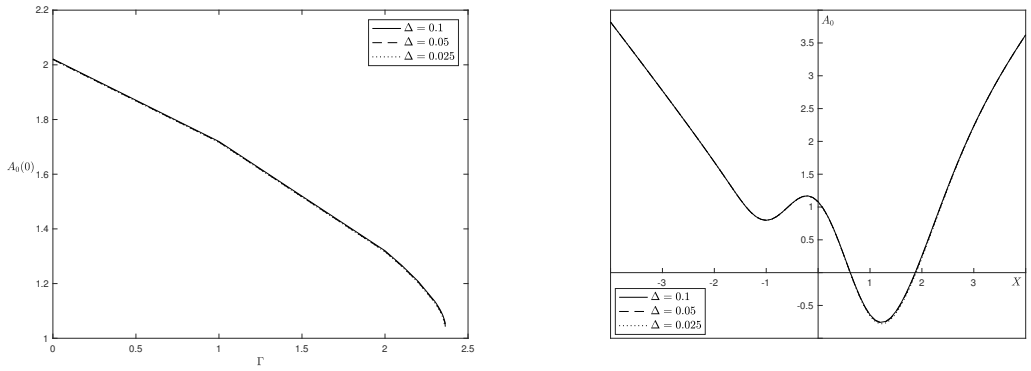

(A) Upper branch of $A_0(0)$ against Γ (B) Solution to A_0 at $\Gamma = 2.35$

FIGURE C.5: The effect of changing the mesh size Δ, as given in the legend, on the solution for a dynamic roughness centred at 0, with width 4, height 1 and oscillation frequency 1. In (a) the upper branch solutions are computed but, unlike in the case of the static roughness shown in §C.1, in which the solution to A at steps of 0.1 in Γ was computed, here the solution at integer values of Γ was computed until divergence occurred, then the step size was of 0.1 until divergence, then 0.01, then 0.001. The solution to the steady mode of the displacement function is then plotted in (b) for $\Gamma = 2.53$. The endpoints of the computational domain were at ± 10 and 6 modes, including the zeroth, were used.

critical value Γ_c, which equals 2.360 for endpoints at ± 10, 2.359 for endpoints at ± 15 and 2.358 for endpoints at ± 20.

Perhaps surprisingly, the solutions where 6, 11 and 16 modes were used ($M = 5$, 10 and 15 respectively in the sum of equation (C.5a)) show no difference—see figure C.7: differences in the plots of higher modes of the displacement function at $\Gamma = 2.35$ (not shown) are only noticeable from the fourth mode upwards. We recall, though, that the fact that all odd Fourier modes are necessarily zero implies that in setting $M = 5$ we are effectively expanding up to the tenth mode. Indeed, the solution at the fifth mode is of order 10^{-3}, at the tenth mode of order 10^{-5} and at the fifteenth mode of order 10^{-7}; hence higher modes should be expected to have little impact on the solution to the lowest modes. The critical value of Γ, for a mesh size of $\Delta = 0.025$ and endpoints at ± 10, is 2.360 for all cases.

Although Newton's method requires less iterations for convergence than the iterative scheme of §C.1, the need to solve a large system of linear equations, given by equation (C.7), at each iteration limited the formulation of the computational domain used in §6.3.2, especially taking into account the sweeps in the roughness parameter space that are carried out there. The number of modes used was $M = 5$, with an increase in M seeming to have no impact on the solution to the steady mode and the value of Γ_c computed to the third decimal place. The step size for the sweeps in roughness position and width was set at $\Delta = 0.025$ and the endpoints of the computational domain were at ± 15. For the simultaneous sweeps in frequency and amplitude space, however, these values were deemed prohibitively small and large respectively: thus here, $\Delta = 0.05$ and the endpoints were at ± 10.

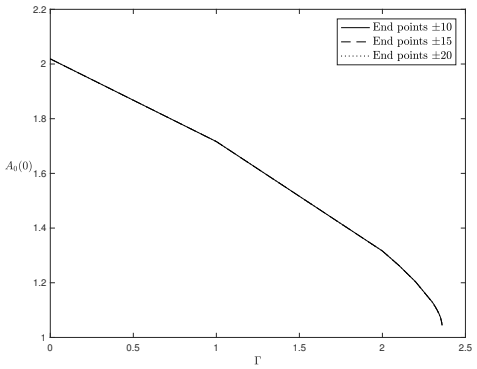

(A) Upper branch of $A_0(0)$ against Γ

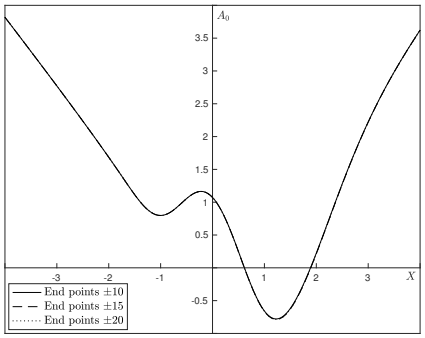

(B) Solution to A_0 at $\Gamma = 2.35$

FIGURE C.6: The effect of changing the endpoints of the computational domain, as given in the legend, on the solution for the same dynamic roughness as defined in figure C.5. The mesh size was $\Delta = 0.025$, $M = 5$ and the graphs shown agree very well with each other.

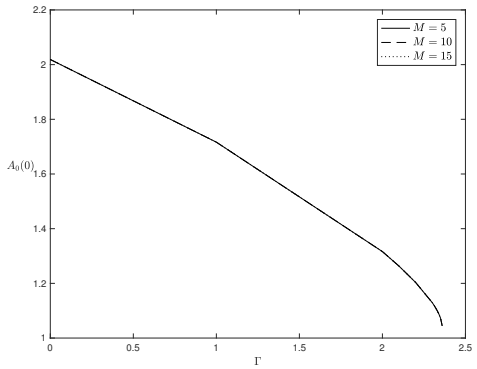

(A) Upper branch of $A_0(0)$ against Γ

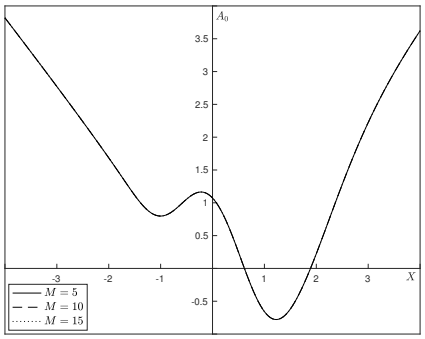

(B) Solution to A_0 at $\Gamma = 2.35$

FIGURE C.7: The effect of changing the number of modes used in the expansion of A, as given in the legend, on the solution for the same dynamic roughness as defined in figure C.5. The mesh size was $\Delta = 0.025$ and the endpoints of the computational domain were at ± 10: the graphs shown agree very well with each other.

Bibliography

[1] Abbey, E. *Desert solitaire: a season in the wilderness.* McGraw-Hill, 1968.

[2] Álvarez, J. C., Meseguer, J., Meseguer, E., and Pérez, A. On the role of the alula in the steady flight of birds. *Ardeola 48*, 2 (2001), 161–173.

[3] Anderson, J. D. *A History of Aerodynamics.* Cambridge University Press, 1997.

[4] Anderson, J. D. Ludwig Prandtl's boundary layer. *Physics Today 58*, 12 (2005), 42–48.

[5] Anderson, J. D. *Fundamentals of Aerodynamics*, 5 ed. McGraw-Hill, 2011.

[6] Batchelor, G. K. *An Introduction to Fluid Dynamics.* Cambridge Mathematical Library, 1967.

[7] Bomphrey, R. J., Taylor, G. K., and Thomas, A. L. R. Smoke visualization of free-flying bumblebees indicates independent leading-edge vortices on each wing pair. *Experiments in Fluids 46*, 5 (2009), 811–821.

[8] Braun, S., and Kluwick, A. The effect of three-dimensional obstacles on marginally separated laminar boundary layer flows. *Journal of Fluid Mechanics 460* (2002), 57–82.

[9] Braun, S., and Kluwick, A. Unsteady three-dimensional marginal separation caused by surface-mounted obstacles and/or local suction. *Journal of Fluid Mechanics 514* (2004), 121–152.

[10] Braun, S., Kluwick, A., and Trenker, M. Leading edge separation: a comparison between interaction theory and Navier–Stokes computations. *PAMM 2*, 1 (2003), 312–313.

[11] Braun, S., and Scheichl, S. On recent developments in marginal separation theory. *Philosophical Transactions of the Royal Society A 372*, 2020 (2014), 20130343.

[12] Brown, S. N., and Stewartson, K. On an integral equation of marginal separation. *SIAM Journal on Applied Mathematics 43*, 5 (1983), 1119–1126.

[13] Bushnell, D. M., and Moore, K. J. Drag reduction in nature. *Annual Review of Fluid Mechanics 23*, 1 (1991), 65–79.

[14] Chang, P. K. *Separation of flow.* Pergamon Press, 1970.

[15] Cheng, H. K., and Smith, F. T. The influence of airfoil thickness and Reynolds number on separation. *Zeitschrift für Angewandte Mathematik und Physik ZAMP 33*, 2 (1982), 151–180.

[16] Craik, A. D. D. "Continuity and change": representing mass conservation in fluid mechanics. *Archive for History of Exact Sciences 67*, 1 (2013), 1–38.

[17] Darrigol, O. Between hydrodynamics and elasticity theory: the first five births of the Navier-Stokes equation. *Archive for History of Exact Sciences 56*, 2 (2002), 95–150.

[18] Dearing, S. S., Lambert, S., and Morrison, J. F. Flow control with active dimples. *Aeronautical Journal 111*, 1125 (2007), 705–714.

[19] Dearing, S. S., Morrison, J. F., and Iannucci, L. Electro-active polymer (EAP) "dimple" actuators for flow control: design and characterisation. *Sensors and Actuators A: Physical 157* (2010), 210–218.

[20] DeMauro, E. P., Dell'Orso, H., Zaremski, S., Leong, C. M., and Amitay, M. Control of laminar separation bubble on NACA 0009 airfoil using electroactive polymers. *AIAA Journal 53*, 8 (2015), 2270–2279.

[21] Duck, P. W. Laminar flow over unsteady humps: the formation of waves. *Journal of Fluid Mechanics 160* (1985), 465–498.

[22] Ely, W., and Herring, R. Laminar leading edge stall prediction for thin airfoils. In *11th Fluid and Plasma Dynamics Conference* (1978), p. 1222.

[23] Farrell, P. E., Birkisson, A., and Funke, S. W. Deflation techniques for finding distinct solutions of nonlinear partial differential equations. *SIAM Journal on Scientific Computing 37*, 4 (2015), A2026–A2045.

[24] Fish, F. E., and Lauder, G. V. Passive and active flow control by swimming fishes and mammals. *Annual Review of Fluid Mechanics 38* (2006), 193–224.

[25] Flatt, J. The history of boundary layer control research in the United States of America. *Boundary Layer and Flow Control 1* (1961), 122–143.

[26] Gad el Hak, M. Fluid mechanics from the beginning to the third millennium. *International Journal of Engineering Education 14*, 3 (1998), 177–185.

[27] Gad el Hak, M. *Flow Control: Passive, Active and Reactive Flow Management.* Cambridge University Press, 2000.

[28] Gaster, M. Understanding the effects of surface roughness on the growth of disturbances. In *46th AIAA Fluid Dynamics Conference* (2016), p. 4384.

[29] Goldstein, S. On laminar boundary-layer flow near a position of separation. *The Quarterly Journal of Mechanics and Applied Mathematics 1*, 1 (1948), 43–69.

[30] Goldstein, S. Fluid mechanics in the first half of this century. *Annual Review of Fluid Mechanics 1*, 1 (1969), 1–29.

[31] Gouder, K., Potter, M., and Morrison, J. F. Turbulent friction drag reduction using electroactive polymer and electromagnetically driven surfaces. *Experiments in Fluids 54*, 1 (2013), 1441.

[32] Gradshteyn, I. S., and Ryzhik, I. M. *Table of integrals, series and products*. Academic Press, 2014.

[33] Grager, T., Rothmayer, A. P., Huebsch, W. W., and Hu, H. Low Reynolds number stall suppression with dynamic roughness. In *6th AIAA Flow Control Conference* (2012), American Institute of Aeronautics and Astronautics, pp. 25–28.

[34] Greenblatt, D., and Wygnanski, I. J. The control of flow separation by periodic excitation. *Progress in Aerospace Sciences 36*, 7 (2000), 487–545.

[35] Grotberg, J. B., and Jensen, O. E. Biofluid mechanics in flexible tubes. *Annual Review of Fluid Mechanics 36* (2004), 121–147.

[36] Hain, R., Kähler, C. J., and Radespiel, R. Dynamics of laminar separation bubbles at low-Reynolds-number aerofoils. *Journal of Fluid Mechanics 630* (2009), 129–153.

[37] Hartree, D. R. On an equation occurring in Falkner and Skan's approximate treatment of the equations of the boundary layer. In *Mathematical Proceedings of the Cambridge Philosophical Society* (1937), vol. 33, Cambridge University Press, pp. 223–239.

[38] Hartree, D. R. *Numerical analysis*. Oxford Clarendon Press, 1958.

[39] Hsiao, C.-T., and Pauley, L. L. Comparison of the triple-deck theory, interactive boundary layer method, and Navier–Stokes computation for marginal separation. *Journal of Fluids Engineering 116* (1994), 22–28.

[40] Huebsch, W. W. Two-dimensional simulation of dynamic surface roughness for aerodynamic flow control. *Journal of Aircraft 43*, 2 (2006), 353–362.

[41] Huebsch, W. W., Gall, P. D., Hamburg, S. D., and Rothmayer, A. P. Dynamic roughness as a means of leading-edge separation flow control. *Journal of Aircraft 49*, 1 (2012), 108–115.

[42] Huebsch, W. W., and Rothmayer, A. P. Effects of surface ice roughness on dynamic stall. *Journal of Aircraft 39*, 6 (2002), 945–953.

[43] Jacobs, E. N., Ward, K. E., and Pinkerton, R. M. The characteristics of 78 related airfoil sections from tests in the variable-density wind tunnel. Tech. rep., NACA, 1933.

[44] Jeal, T. *Explorers of the Nile*. Faber and Faber, 2011.

[45] Joslin, R. D. Aircraft laminar flow control. *Annual Review of Fluid Mechanics 30*, 1 (1998), 1–29.

[46] Kluwick, A., Braun, S., and Cox, E. A. Near critical phenomena in laminar boundary layers. *Journal of Fluids and Structures 24*, 8 (2008), 1185–1193.

[47] Ladson, C. L., Brooks, C. W., Hill, A. S., and Sproles, D. W. Computer program to obtain ordinates for NACA airfoils. Tech. rep., NASA, 1996.

[48] Lighthill, M. J. On boundary layers and upstream influence. II. supersonic flows without separation. In *Proceedings of the Royal Society of London A: Mathematical, Physical and Engineering Sciences* (1953), vol. 217, The Royal Society, pp. 478–507.

[49] Lin, J. C. M., and Pauley, L. L. Low-Reynolds-number separation on an airfoil. *AIAA Journal 34*, 8 (1996), 1570–1577.

[50] Lissaman, P. B. S. Low-Reynolds-number airfoils. *Annual Review of Fluid Mechanics 15*, 1 (1983), 223–239.

[51] Longuet-Higgins, M. S. Mass transport in water waves. *Philosophical Transactions of the Royal Society of London A: Mathematical, Physical and Engineering Sciences 245*, 903 (1953), 535–581.

[52] McCroskey, W. J. The phenomenon of dynamic stall. Tech. rep., NASA, 1981.

[53] Messiter, A. F. Boundary-layer flow near the trailing edge of a flat plate. *SIAM Journal on Applied Mathematics 18*, 1 (1970), 241–257.

[54] Munk, M. Elements of wing section theory and of the wing theory. Tech. rep., NACA, 1925.

[55] Neiland, V. Y. Theory of laminar boundary layer separation in supersonic flow. *Fluid Dynamics 4*, 4 (1969), 33–35.

[56] Ovenden, N. C., and Smith, F. T. Vortices and flow reversal due to suction slots. *Philosophical Transactions of the Royal Society of London A: Mathematical, Physical and Engineering Sciences 363*, 1830 (2005), 1199–1208.

[57] Ovid. *The Metamorphoses, Book VIII. Translated by A. S. Kline*, 2 ed. Poetry in Translation, 2014.

[58] Pistolesi, E. *Sulla teoria delle ali sottili.* Pontificia Accademia delle Scienze, 1937.

[59] Poppleton, E. D. *Boundary-layer Control for High Lift by Suction at the Leading-edge of a 40 deg Swept-back Wing.* HM Stationery Office, 1955.

[60] Prandtl, L. Motion of fluids with very little viscosity. Technical Memorandum 452, NACA, 1928.

[61] Pruessner, L., and Smith, F. T. Enhanced effects from tiny flexible in-wall blips and shear flow. *Journal of Fluid Mechanics 772* (2015), 16–41.

[62] Riley, N. Oscillating viscous flows. *Mathematika 12* (1965), 161–175.

[63] Riley, N. Steady streaming. *Annual Review of Fluid Mechanics 33* (2001), 43–65.

[64] Roberts, D. *Alone on the Ice: The Greatest Survival Story in the History of Exploration.* W. W. Norton & Company, 2013.

[65] Roberts, W. B. Calculation of laminar separation bubbles and their effect on airfoil performance. *AIAA Journal 18*, 1 (1980), 25–31.

[66] Rothmayer, A. P., and Huebsch, W. W. On the modification of laminar boundary layers using unsteady surface actuation. In *6th AIAA Theoretical Fluid Mechanics Conference, AIAA Paper* (2011), vol. 4016, American Institute of Aeronautics and Astronautics.

[67] Rothmayer, A. P., and Huebsch, W. W. Flow about large unsteady two-dimensional humps in a boundary layer. In *42nd AIAA Fluid Dynamics Conference and Exhibit* (2012), p. 2950.

[68] Rothmayer, A. P., and Smith, F. T. *The Handbook of Fluid Dynamics*. CRC Press, 1998, ch. 23.

[69] Ruban, A. I. Singular solution of boundary layer equations which can be extended continuously through the point of zero surface friction. *Fluid Dynamics 16*, 6 (1981), 835–843.

[70] Ruban, A. I. Asymptotic theory of short separation regions on the leading edge of a slender airfoil. *Fluid Dynamics 17*, 1 (1982), 33–41.

[71] Ryzhov, O. S., and Smith, F. T. Short-length instabilities, breakdown and initial value problems in dynamic stall. *Mathematika 31*, 62 (1984), 163–177.

[72] Saric, W., Carpenter, A. L., and Reed, H. L. Passive control of transition in three-dimensional boundary layers, with emphasis on discrete roughness elements. *Philosophical Transactions of the Royal Society of London A: Mathematical, Physical and Engineering Sciences 369*, 1940 (2011), 1352–1364.

[73] Saric, W., and Reed, H. Toward practical laminar flow control—remaining challenges. *AIAA Paper 2311* (2004), 2004.

[74] Saric, W., West, D., Tufts, M., and Reed, H. L. Flight test experiments on discrete roughness element technology for laminar flow control. *AIAA Paper 539* (2015), 2015.

[75] Scheichl, S., Braun, S., and Kluwick, A. On a similarity solution in the theory of unsteady marginal separation. *Acta Mechanica 201* (2008), 153–170.

[76] Schlichting, H., and Gersten, K. *Boundary Layer Theory*. Springer, 2000.

[77] Smith, F. T. Laminar flow over a small hump on a flat plate. *Journal of Fluid Mechanics 57*, 4 (1973), 803–824.

[78] Smith, F. T. Flow through constricted or dilated pipes and channels: Part 1. *The Quarterly Journal of Mechanics and Applied Mathematics 29*, 3 (1976), 343–364.

[79] Smith, F. T. Flow through constricted or dilated pipes and channels: Part 2. *The Quarterly Journal of Mechanics and Applied Mathematics 29*, 3 (1976), 365–376.

[80] Smith, F. T. Nonlinear stability of boundary layers for disturbances of various sizes. In *Proceedings of the Royal Society of London A: Mathematical, Physical and Engineering Sciences* (1979), vol. 368, The Royal Society, pp. 573–589.

[81] Smith, F. T. On the non-parallel flow stability of the Blasius boundary layer. In *Proceedings of the Royal Society of London A: Mathematical, Physical and Engineering Sciences* (1979), vol. 366, The Royal Society, pp. 91–109.

[82] Smith, F. T. Concerning dynamic stall. *Aeronautical Quarterly 33* (1982), 331–352.

[83] Smith, F. T. Finite-time break-up can occur in any unsteady interacting boundary layer. *Mathematika 35*, 2 (1988), 256–273.

[84] Smith, F. T., Brighton, P. W. M., Jackson, P. S., and Hunt, J. C. R. On boundary-layer flow past two-dimensional obstacles. *Journal of Fluid Mechanics 113* (1981), 123–152.

[85] Smith, F. T., and Daniels, P. G. Removal of Goldstein's singularity at separation, in flow past obstacles in wall layers. *Journal of Fluid Mechanics 110* (1981), 1–37.

[86] Smith, F. T., and Elliott, J. W. On the abrupt turbulent reattachment downstream of leading-edge laminar separation. In *Proceedings of the Royal Society of London A: Mathematical, Physical and Engineering Sciences* (1985), vol. 401, pp. 1–27.

[87] Speziale, C. G., and So, R. M. C. *The Handbook of Fluid Dynamics*. CRC Press, 1998, ch. 14.

[88] Stack, J. The NACA high-speed wind tunnel and tests of six propeller sections. Tech. rep., NACA, 1933.

[89] Stewartson, K. Is the singularity at separation removable? *Journal of Fluid Mechanics 44*, 2 (1970), 347–364.

[90] Stewartson, K., Smith, F. T., and Kaups, K. Marginal separation. *Studies in Applied Mathematics 67* (1982), 45–61.

[91] Stewartson, K., and Williams, P. G. Self-induced separation. In *Proceedings of the Royal Society of London A: Mathematical, Physical and Engineering Sciences* (1969), vol. 312, The Royal Society, pp. 181–206.

[92] Stuart, J. T. Double boundary layers in oscillatory viscous flow. *Journal of Fluid Mechanics 24*, 4 (1966), 673–687.

[93] Sychev, V. V., Ruban, A. I., Sychev, V. V., and Korolev, G. L. *Asymptotic theory of separated flows*. Cambridge University Press, 1998.

[94] Tani, I. Boundary-layer transition. *Annual Review of Fluid Mechanics 1*, 1 (1969), 169–196.

[95] Thoreau, H. D. Walking, 1861.

[96] Timoshin, S. N. Elimination of edge rupture caused by the effect of flow pulsations. *Journal of Applied Mathematics and Mechanics 52*, 1 (1988), 59–62.

[97] United States, D. o. T. Fuel cost and consumption. `http://www.transtats.bts.gov/FUEL/`.

[98] Van Dyke, M. D. Second-order subsonic airfoil theory including edge effects. Tech. Rep. 1274, NACA, 1956.

[99] Visbal, M. R., and Garmann, D. J. Control of dynamic stall over a pitching finite-aspect-ration wing. In *47th AIAA Fluid Dynamics Conference* (2017), p. 4118.

[100] Werle, M. J., and Davis, R. T. Incompressible laminar boundary layers on a parabola at angle of attack: a study of the separation point. *Journal of Applied Mechanics 39*, 1 (1972), 7–12.

[101] White, L. Eilmer of Malmesbury, an eleventh century aviator: a case study of technological innovation, its context and tradition. *Technology and Culture 2*, 2 (1961), 97–111.

[102] Zametaev, V. B. Existence and nonuniqueness of local separation zones in viscous jets. *Fluid Dynamics 21*, 1 (1986), 31–38.